

Physics Performance Report for:

$\bar{\text{P}}\text{ANDA}$

(AntiProton Annihilations at Darmstadt)

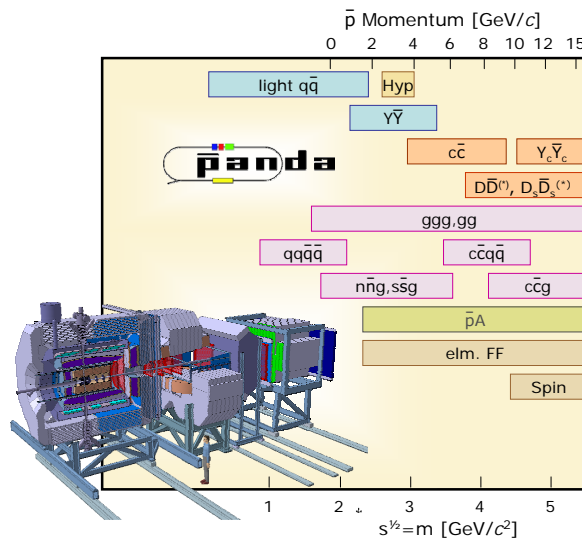
Strong Interaction Studies with Antiprotons

$\bar{\text{P}}\text{ANDA}$ Collaboration

December 1, 2008 - Revision: 683

To study fundamental questions of hadron and nuclear physics in interactions of antiprotons with nucleons and nuclei, the universal $\bar{\text{P}}\text{ANDA}$ detector will be build. Gluonic excitations, the physics of strange and charm quarks and nucleon structure studies will be performed with unprecedented accuracy thereby allowing high-precision tests of the strong interaction. The proposed $\bar{\text{P}}\text{ANDA}$ detector is a state-of-the-art internal target detector at the HESR at FAIR allowing the detection and identification of neutral and charged particles generated within the relevant angular and energy range.

This report presents a summary of the physics accessible at $\bar{\text{P}}\text{ANDA}$ and what performance can be expected.



The \bar{P} ANDA Collaboration

Universität **Basel**, Switzerland

W. Erni, I. Keshelashvili, B. Krusche, M. Steinacher

Institute of High Energy Physics, Chinese Academy of Sciences, **Beijing**, China

Y. Heng, Z. Liu, H. Liu, X. Shen, O. Wang, H. Xu

Universität **Bochum**, I. Institut für Experimentalphysik, Germany

F.-H. Heinsius, T. Held, H. Koch, B. Kopf, M. Pelizäus, M. Steinke, U. Wiedner, J. Zhong

Università di Brescia, **Brescia**, Italy

A. Bianconi

Institutul National de C&D pentru Fizica si Inginerie Nucleara "Horia Hulubei", **Bukarest-Magurele**,
Romania

M. Bragadireanu, P. Dan, T. Preda, A. Tudorache

Dipartimento di Fisica e Astronomia dell'Università di **Catania** and INFN, Sezione di Catania, Italy

M. De Napoli, F. Giacoppo, G. Raciti, E. Rapisarda

IFJ, Institute of Nuclear Physics PAN, **Cracow**, Poland

E. Bialkowski, A. Budzanowski, B. Czech, S. Kliczewski, A. Kozela, P. Kulesa, K. Malgorzata,
K. Pysz, W. Schäfer, R. Siudak, A. Szczurek

Instytut Fizyki, Uniwersytet Jagiellonski, **Cracow**, Poland

W. Bardan, P. Brandys, T. Czyżewski, W. Czyżewski, M. Domagala, G. Filo, D. Gil, P. Hawranek,
B. Kamys, P. Kazmierczak, St. Kistryn, K. Korcyl, M. Krawczyk, W. Krzemień, E. Lisowski,
A. Magiera, P. Moskal, J. Pietraszek, Z. Rudy, P. Salabura, J. Smyrski, L. Wojnar, A. Wrońska

Gesellschaft für Schwerionenforschung mbH, **Darmstadt**, Germany

M. Al-Turany, I. Augustin, H. Deppe, H. Flemming, J. Gerl, K. Götzen, G. Hohler, D. Lehmann,
B. Lewandowski, J. Lühning, F. Maas, D. Mishra, H. Orth, K. Peters, T. Saito, G. Schepers,
L. Schmitt, C. Schwarz, C. Sfienti, P. Wiczorek, A. Wilms

Technische Universität **Dresden**, Germany

K.-T. Brinkmann, H. Freiesleben, R. Jäkel, R. Kliemt, T. Würschig, H.-G. Zaunick

Veksler-Baldin Laboratory of High Energies (VBLHE), Joint Institute for Nuclear Research. **Dubna**,
Russia

V.M. Abazov, G. Alexeev, A. Arefiev, V.I. Astakhov, M.Yu. Barabanov, B.V. Batyunya, Yu.I. Davydov,
V.Kh. Dodokhov, A.A. Efremov, A.G. Fedunov, A.A. Feshchenko, A.S. Galoyan, S. Grigoryan,
A. Karmokov, E.K. Koshurnikov, V.Ch. Kudaev, V.I. Lobanov, Yu.Yu. Lobanov, A.F. Makarov,
L.V. Malinina, V.L. Malyshev, G.A. Mustafaev, A. Olshevski, M.A. Pasyuk, E.A. Perevalova,
A.A. Piskun, T.A. Pocheptsov, G. Pontecorvo, V.K. Rodionov, Yu.N. Rogov, R.A. Salmin,
A.G. Samartsev, M.G. Sapozhnikov, A. Shabratova, G.S. Shabratova, A.N. Skachkova, N.B. Skachkov,
E.A. Strokovsky, M.K. Suleimanov, R.Sh. Teshev, V.V. Tokmenin, V.V. Uzhinsky A.S. Vodopianov,
S.A. Zaporozhets, N.I. Zhuravlev, A.G. Zorin

University of **Edinburgh**, United Kingdom

D. Branford, K. Föhl, D. Glazier, D. Watts, P. Woods

Friedrich Alexander Universität **Erlangen-Nürnberg**, Germany

W. Eyrich, A. Lehmann, A. Teufel

Northwestern University, **Evanston**, U.S.A.

S. Dobbs, Z. Metreveli, K. Seth, B. Tann, A. Tomaradze

Università di **Ferrara** and INFN, Sezione di Ferrara, Italy

D. Bettoni, V. Carassiti, A. Cecchi, P. Dalpiaz, E. Fioravanti, M. Negrini, M. Savriè, G. Stancari

INFN-Laboratori Nazionali di **Frascati**, Italy

B. Dulach, P. Gianotti, C. Guaraldo, V. Lucherini, E. Pace

INFN, Sezione di **Genova**, Italy

A. Bersani, M. Macri, M. Marinelli, R.F. Parodi

Justus Liebig-Universität **Gießen**, II. Physikalisches Institut, Germany

W. Döring, P. Drexler, M. Düren, Z. Gagyi-Palfy, A. Hayrapetyan, M. Kotulla, W. Kühn, S. Lange,
M. Liu, V. Metag, M. Nanova, R. Novotny, C. Salz, J. Schneider, P. Schönmeier, R. Schubert,
S. Spataro, H. Stenzel, C. Strackbein, M. Thiel, U. Thöring, S. Yang,

University of **Glasgow**, United Kingdom

T. Clarkson, E. Downie, M. Hoek, D. Ireland, R. Kaiser, J. Kellie, I. Lehmann, K. Livingston,
S. Lumsden, D. MacGregor, B. McKinnon, M. Murray, D. Protopopescu, G. Rosner, B. Seitz, G. Yang

Kernfysisch Versneller Instituut, University of **Groningen**, Netherlands

M. Babai, A.K. Biegun, A. Bubak, E. Guliyev, V.S. Jothi, M. Kavatsyuk, H. Löhner, J. Messchendorp,
H. Smit, J.C. van der Weele

Helsinki Institute of Physics, **Helsinki**, Finland

F. Garcia, D.-O. Riska

Forschungszentrum Jülich, Institut für Kernphysik, **Jülich**, Germany

M. Büscher, R. Dossall, A. Gillitzer, F. Goldenbaum, F. Hügging, M. Mertens, T. Randriamalala,
J. Ritman, S. Schadmand, A. Sokolov, T. Stockmanns, P. Wintz

University of Silesia, **Katowice**, Poland

J. Kisiel

Chinese Academy of Science, Institute of Modern Physics, **Lanzhou**, China

S. Li, Z. Li, Z. Sun, H. Xu

Lunds Universitet, Department of Physics, **Lund**, Sweden

S. Fissum, K. Hansen, L. Isaksson, M. Lundin, B. Schröder

Johannes Gutenberg-Universität, Institut für Kernphysik, **Mainz**, Germany

P. Achenbach, M.C. Mora Espi, J. Pochodzalla, S. Sanchez, A. Sanchez-Lorente

Research Institute for Nuclear Problems, Belarus State University, **Minsk**, Belarus

V.I. Dormenev, A.A. Fedorov, M.V. Korzhik, O.V. Missevitch

Institute for Theoretical and Experimental Physics, **Moscow**, Russia

V. Balanutsa, V. Chernetsky, A. Demekhin, A. Dolgolenko, P. Fedorets, A. Gerasimov, V. Goryachev

Moscow Power Engineering Institute, **Moscow**, Russia

A. Boukharov, O. Malyshev, I. Marishev, A. Semenov

Technische Universität **München**, Germany

C. Höppner, B. Ketzer, I. Konorov, A. Mann, S. Neubert, S. Paul, Q. Weitzel

Westfälische Wilhelms-Universität **Münster**, Germany

A. Khoukaz, T. Rausmann, A. Täschner, J. Wessels

IIT Bombay, Department of Physics, **Mumbai**, India

R. Varma

Budker Institute of Nuclear Physics, **Novosibirsk**, Russia

E. Baldin, K. Kotov, S. Peleganchuk, Yu. Tikhonov

Institut de Physique Nucléaire, **Orsay**, France

J. Boucher, T. Hennino, R. Kunne, S. Ong, J. Pouthas, B. Ramstein, P. Rosier, M. Sudol,

J. Van de Wiele, T. Zerguerras

Warsaw University of Technology, Institute of Atomic Energy, **Otwock-Swierk**, Poland

K. Dmowski, R. Korzeniewski, D. Przemyslaw, B. Slowinski

Dipartimento di Fisica Nucleare e Teorica, Università di Pavia, INFN, Sezione di Pavia, **Pavia**, Italy

G. Boca, A. Braghieri, S. Costanza, A. Fontana, P. Genova, L. Lavezzi, P. Montagna, A. Rotondi

Institute for High Energy Physics, **Protvino**, Russia

N.I. Belikov, A.M. Davidenko, A.A. Derevschikov, Y.M. Goncharenko, V.N. Grishin, V.A. Kachanov,
D.A. Konstantinov, V.A. Kormilitsin, V.I. Kravtsov, Y.A. Matulenko, Y.M. Melnik A.P. Meschanin,
N.G. Minaev, V.V. Mochalov, D.A. Morozov, L.V. Nogach, S.B. Nurushev, A.V. Ryazantsev,
P.A. Semenov, L.F. Soloviev, A.V. Uzunian, A.N. Vasiliev, A.E. Yakutin

Kungliga Tekniska Högskolan, **Stockholm**, Sweden

T. Bäck, B. Cederwall

Stockholms Universitet, **Stockholm**, Sweden

C. Bargholtz, L. Gerén, P.E. Tegnér

Petersburg Nuclear Physics Institute of Academy of Science, Gatchina, **St. Petersburg**, Russia

S. Belostotski, G. Gavrilo, A. Itzotov, A. Kisselev, P. Kravchenko, S. Manaenkov, O. Miklukho,
Y. Naryshkin, D. Veretennikov, V. Vikhrov, A. Zhadanov

Università del Piemonte Orientale Alessandria and INFN, Sezione di Torino, **Torino**, Italy

L. Fava, D. Panzieri

Università di Torino and INFN, Sezione di Torino, **Torino**, Italy

D. Alberto, A. Amoroso, M. Anselmino, E. Botta, T. Bressani, M.P. Bussa, L. Busso, F. De Mori,
L. Ferrero, A. Grasso, M. Greco, T. Kugathasan, M. Maggiora, S. Marcello, C. Mulatera,
G.C. Serbanut, S. Sosio

INFN, Sezione di Torino, **Torino**, Italy

R. Bertini, D. Calvo, S. Coli, P. De Remigis, A. Feliciello, A. Filippi, G. Giraudo, G. Mazza, A. Rivetti,
K. Szymanska, F. Tosello, R. Wheadon

INAF-IFSI and INFN, Sezione di Torino, **Torino**, Italy

O. Morra

Politecnico di Torino and INFN, Sezione di Torino, **Torino**, Italy

M. Agnello, F. Iazzi, K. Szymanska

Università di Trieste and INFN, Sezione di Trieste, **Trieste**, Italy

R. Birsa, F. Bradamante, A. Bressan, A. Martin

Universität Tübingen, **Tübingen**, Germany

H. Clement

The Svedberg Laboratory, **Uppsala**, Sweden

C. Ekström

Uppsala Universitet, Institutionen för Strålningsvetenskap, **Uppsala**, Sweden

H. Calén, S. Grape, B. Höistad, T. Johansson, A. Kupsc, P. Marciniwski, E. Thomé, J. Zlomanczuk

Universitat de Valencia, Dpto. de Física Atómica, Molecular y Nuclear, **Valencia**, Spain

J. Díaz, A. Ortiz

Soltan Institute for Nuclear Studies, **Warsaw**, Poland

S. Borsuk, A. Chlopik, Z. Guzik, J. Kopec, T. Kozlowski, D. Melnychuk, M. Plominski, J. Szewinski,
K. Traczyk, B. Zwieglinski

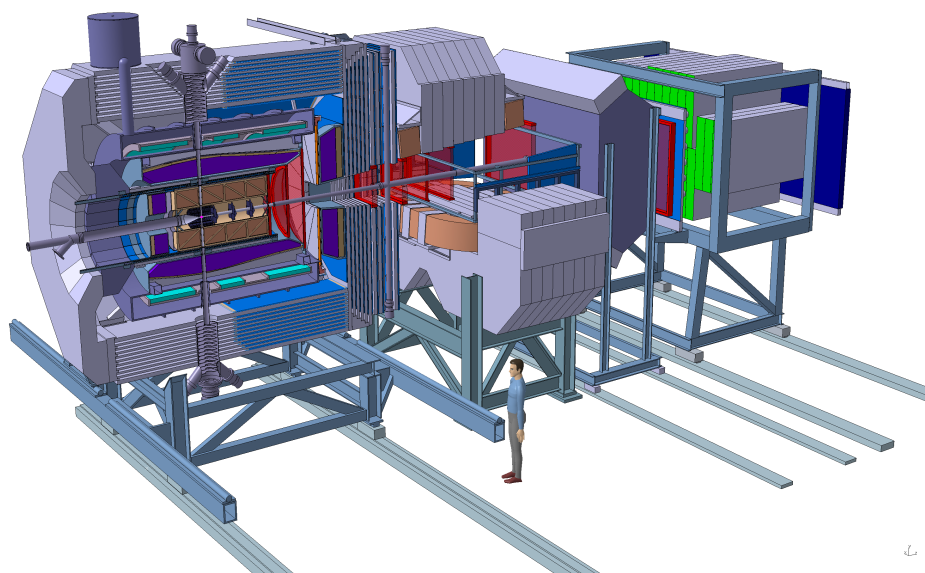
Österreichische Akademie der Wissenschaften, Stefan Meyer Institut für Subatomare Physik, **Wien**,
Austria

P. Bühler, A. Gruber, P. Kienle, J. Marton, E. Widmann, J. Zmeskal

Editor:	Diego Bettoni	Email: bettoni@fe.infn.it
Physics Coordinator:	Klaus Peters	Email: k.peters@gsi.de
Spokesperson:	Ulrich Wiedner	Email: ulrich.wiedner@tsl.uu.se
Deputy:	Paola Gianotti	Email: paola.gianotti@lnf.infn.it

Preface

This document shows the expected physics performance of the PANDA detector. With ongoing R&D, significant progress has been made since the Technical Progress Report (TPR). The proposed setup as of XXX 2007 is the basis for the physics simulations presented in this report.



The use of registered names, trademarks, *etc.* in this publication does not imply, even in the absence of specific statement, that such names are exempt from the relevant laws and regulations and therefore free for general use.

Contents

Preface	vii	3 Software	39
1 Introduction	1	3.1 Event Generation	39
1.1 The challenge of QCD	1	3.1.1 EvtGen Generator	39
1.1.1 Quantum chromodynamics	1	3.1.2 Dual Parton Model	39
1.1.2 The QCD coupling constant	2	3.1.3 UrQMD	41
1.1.3 The symmetries of QCD	2	3.2 Particle Tracking and Detector Simulation	43
1.1.4 Theoretical approaches to non-perturbative QCD	3	3.2.1 Detector Setup	43
1.2 Lattice QCD: status and prospects	4	3.2.2 Digitisation	44
1.3 EFT with quark and gluon degrees of freedom	6	3.3 Reconstruction	46
1.3.1 Non-relativistic QCD	6	3.3.1 Charged Particle Track Reconstruction	46
1.4 EFT with hadronic degrees of freedoms	7	3.3.2 Photon Reconstruction	48
1.4.1 Chiral symmetry and open-charm meson systems	8	3.3.3 Charged Particle Identification	50
1.4.2 Phenomenology of open-charm baryon systems	10	3.4 Physics Analysis	55
References	10	3.4.1 Analysis Tools	56
2 Experimental Setup	13	3.5 Data Production	56
2.1 Overview	13	3.5.1 Filter on generator level	57
2.2 The PANDA Detector	13	3.6 Software developments	57
2.2.1 Target Spectrometer	13	References	60
2.2.2 Forward Spectrometer	22	4 Physics Performance	63
2.2.3 Luminosity monitor	23	4.1 Overview	63
2.2.4 Data Acquisition	24	4.2 QCD Bound States	64
2.2.5 Infrastructure	25	4.2.1 The QCD Spectrum	64
2.3 The HESR	27	4.2.2 Charmonium	64
2.3.1 A quick description of the HESR	27	4.2.3 Exotic Excitations	87
2.3.2 Beam Equilibria and Luminosity Estimates	27	4.2.4 Heavy-Light Systems	108
2.4 Precision measurements of resonance parameters	31	4.2.5 Strange and Charmed Baryons	117
2.4.1 Experimental technique	33	4.3 Non-perturbative QCD Dynamics	122
2.4.2 Mass measurements	34	4.3.1 Previous Experiments	122
2.4.3 Total and partial widths	34	4.3.2 Experimental Aims	123
2.4.4 Line shapes	36	4.3.3 Reconstruction of the $\bar{p}p \rightarrow \bar{Y}Y$ Reaction	123
2.4.5 Achievable precision	36	4.4 Hadrons in the Nuclear Medium	132
References	37	4.4.1 In-Medium Properties of Charmed Hadrons	132
		4.4.2 Charmonium Dissociation	133

4.4.3	J/ψ N Dissociation Cross Section in $\bar{p}A$ Collisions	134
4.4.4	Antibaryons and antikaons Pro- duced in $\bar{p}A$ Collisions	138
4.5	Hypernuclear Physics	140
4.5.1	Physics Goals	140
4.5.2	Experimental Integration and Simulation	142
4.6	The structure of the nucleon using electromagnetic processes	149
4.6.1	Distribution amplitudes in hard exclusive $p\bar{p}$ -annihilation	149
4.6.2	Transverse Parton Distribution Functions in Drell-Yan Production	154
4.6.3	Electromagnetic Form Factors in the Time-like Region	166
4.7	Electroweak Physics	174
4.7.1	CP-Violation and Mixing in the Charm-Sector	175
4.7.2	CP-Violation in Hyperon Decays .	175
4.7.3	Rare Decays	176
	References	176
5	Summary and Outlook	189
	References	189
	Acknowledgements	191
	List of Acronyms	193
	List of Figures	195
	List of Tables	201

1 Introduction

COMMENT: Author(s): R. Timmermans, D. Bettoni, K. Peters

1.1 The challenge of QCD

The modern theory of the strong interactions is Quantum Chromodynamics (QCD), the quantum field theory of quarks and gluons based on the non-abelian gauge group SU(3). Together with the SU(2)×U(1) electroweak theory, QCD is part of the Standard Model of particle physics. QCD is well tested at high energies, where the strong coupling constant becomes small and perturbation theory applies. In the low-energy regime, however, QCD becomes a strongly-coupled theory, many aspects of which are not understood. The thriving questions are: How can we bring order into the rich phenomena of low energy QCD? Are there effective degrees of freedoms in terms of which we can understand the resonances and bound states of QCD efficiently and systematically? Does QCD generate exotic structures so far undiscovered? $\overline{\text{PANDA}}$ will be in a unique position to provide answers to such important questions about non-perturbative QCD. A major part of the physics program of $\overline{\text{PANDA}}$ is designed to collect high-quality data that allow a clean interpretation in terms of the predictions of non-perturbative QCD. In this introductory Chapter, we first summarize the basics of QCD and then review the theoretical approaches that can be justified rigorously within QCD and provide testable predictions for experiments like $\overline{\text{PANDA}}$.

1.1.1 Quantum chromodynamics

The development of QCD as the theory of strong interactions is a success story. Its quantitative predictions at high energies, in the perturbative regime, are such that it is beyond serious doubt that QCD is the correct theory of the strong interactions. Nevertheless, in the non-perturbative low-energy regime, it remains very hard to make quantitative predictions starting from first principles, *i.e.* from the QCD Lagrangian. Conceptually, QCD is simple: it is a relativistic quantum field theory of quarks and gluons interacting according to the laws of non-abelian forces between colour charges. The starting point of all considerations is the celebrated QCD

Lagrangian density:

$$\mathcal{L}_{QCD} = -\frac{1}{4} G_a^{\mu\nu} G_{\mu\nu}^a + \sum_f \bar{q}_f [i \gamma^\mu D_\mu - m_f] q_f, \quad (1.1)$$

where

$$G_a^{\mu\nu} = \partial^\mu A_a^\nu - \partial^\nu A_a^\mu + g f_a^{bc} A_b^\mu A_c^\nu, \quad (1.2)$$

is the gluon field strength tensor, and

$$D^\mu = \partial^\mu - i \frac{g}{2} A_a^\mu \lambda^a, \quad (1.3)$$

the gauge covariant derivative involving the gluon field A_a^μ ; g is the strong coupling constant, $\alpha_S = g^2/4\pi$; f denotes the quark flavour, where for the energy regime of $\overline{\text{PANDA}}$, the relevant quark flavours are u , d , s , c : up, down, strange, and charm. We take $\hbar = 1 = c$.

This deceptively simple looking QCD Lagrangian is at the basis of the rich and complex phenomena of nuclear and hadronic physics. How this complexity arises in a theory with quarks and gluons as fundamental degrees of freedom is only qualitatively understood. The QCD field equations are non-linear, since the gluons that mediate the interaction carry colour charge, and hence interact among themselves. This makes every strongly-interacting system intrinsically a many-body problem, wherein apart from the valence quarks many quark-antiquark pairs and many gluons are always involved. These non-abelian features of QCD are believed to lead to the phenomenon that the basic degrees of freedom, the quarks and the gluons, cannot be observed in the QCD spectrum: the confinement of colour charge is the reason behind the complex world of nuclear and hadronic physics.

The process of renormalisation in quantum field theory generates an intrinsic QCD scale Λ_{QCD} through the mechanism of dimensional transmutation; Λ_{QCD} is, loosely speaking, the scale below which the coupling constant becomes so large that standard perturbation theory no longer applies. All hadron masses are in principle calculable within QCD in terms of Λ_{QCD} . This dynamical generation of the mass scale of the strong interactions is the famous QCD gap phenomenon: the proton mass is non-zero because of the energy of the confined quarks and gluons. Although a mathematical proof

of colour confinement is lacking, qualitatively this is thought to be linked to the fact that the quark and gluon bilinears $\bar{q}_a q^a$ and $G_{\mu\nu}^a G_a^{\mu\nu}$ acquire non-zero vacuum expectation values.

Now, some 35 years after the discovery of QCD, it is fair to say that strong interactions are understood in principle, but a long list of unresolved questions about low-energy QCD remains. Our present understanding of QCD thereby serves as the basis to set priorities for theoretical and experimental research. Clearly, not all phenomena in nuclear physics need to be understood in detail from QCD. Many areas of nuclear physics will be happily described in terms of well-established phenomenology with its own degrees of freedom, just like many complex phenomena in atomic physics and chemistry do not have to be understood directly in terms of QED. Likewise, while not all experiments in nuclear and hadronic physics should be guided by QCD, dedicated experiments that test QCD in the non-perturbative regime and to improve our limited understanding of these aspects of QCD are crucial. In its choice of topics, the $\overline{\text{PANDA}}$ physics program aims to achieve precisely this.

1.1.2 The QCD coupling constant

The qualitative understanding of QCD as outlined above is to a large extent based on the classical calculation of the renormalisation scale dependence of the QCD coupling constant α_S as given by the β -function at an energy scale μ ,

$$\beta(\alpha_S) \equiv \frac{\mu}{2} \frac{\partial \alpha_S}{\partial \mu} = -\frac{\beta_0}{4\pi} \alpha_S^2 - \frac{\beta_1}{8\pi^2} \alpha_S^3 - \dots \quad (1.4)$$

where

$$\beta_0 = 11 - \frac{2}{3} n_f, \quad (1.5)$$

$$\beta_1 = 51 - \frac{19}{3} n_f, \quad (1.6)$$

where n_f is the number of quarks with mass less than μ ; expressions for β_2 and β_3 exist. In solving this differential equation for $\alpha_S(\mu)$, one introduces the scale Λ to provide the μ dependence of α_S . The solution then demonstrates the famous properties of asymptotic freedom, $\alpha_S \rightarrow 0$ when $\mu \rightarrow \infty$, and of strong coupling at scales below $\mu \sim \Lambda$. Based on this result for the scale dependence of the QCD coupling constant, one may roughly divide the field of strong interaction physics into the areas of perturbative QCD (pQCD) and of non-perturbative QCD. QCD has been very successful in quantitatively describing phenomena where

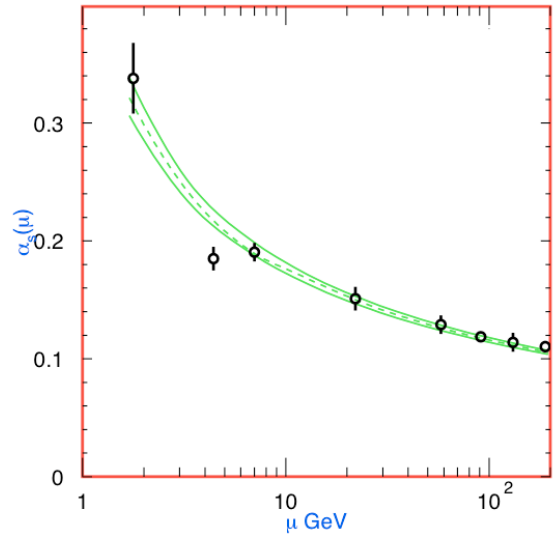


Figure 1.1: The running of the strong coupling constant as function of the scale μ [1].

perturbation theory with its standard machinery of Feynman rules applies. An important example is e^+e^- annihilation in the area of the Z^0 boson, where the multi-particle hadronic final-state system reveals the perturbative QCD physics in the form of the quark and gluon jets. In this perturbative regime predictions can be made on the basis of the magnitude of the QCD coupling constant. Its value as a function of energy determines a host of phenomena, such as scaling violations in deep inelastic scattering, the τ lifetime, high-energy hadron collisions, heavy-quarkonium (in particular bottomonium) decay, e^+e^- collisions, and jet rates in ep collisions. The coupling constants derived from these processes are consistent and lead to an average value [1]

$$\alpha_S(M_Z) = 0.1176 \pm 0.0002. \quad (1.7)$$

The non-perturbative regime is the area of strong nuclear forces and hadronic resonances, which is quantitatively much less well understood and where important questions still have to be addressed. In between are areas like deep inelastic lepton-hadron scattering where perturbation theory is used, however, with non-perturbative input.

1.1.3 The symmetries of QCD

It has been said that QCD is a most elegant theory in physics, since its structure is solely determined by symmetry principles: QCD is the most general renormalisable quantum field theory based on the gauge group $SU(3)$. In addition to exact

Lorentz invariance and SU(3) colour gauge invariance, it has several other important symmetry properties. The QCD Lagrangian as given above has a number of “accidental” symmetries, *i.e.* symmetries that are an automatic consequence of the assumed gauge invariance. The discrete symmetries parity and charge conjugation are such accidental symmetries (we ignore here the mysterious θ -term that results in the still unsolved strong CP-problem of QCD). Flavour conservation is another: the number of quarks (minus antiquarks) of each flavour (*e.g.* strangeness) is conserved, corresponding to an automatic invariance of the QCD Lagrangian under phase rotations of the quark fields of each flavour separately.

Additional symmetries result from the consideration that the masses of the up, down, and strange quarks can be considered small compared to the typical hadronic scale Λ_{QCD} . To the extent that these masses can be ignored, the QCD Lagrangian is invariant under unitary transformations of the quark fields of the form $q'_i = U_{ij} q_j$. This accounts for the rather accurate SU(2)-isospin and the approximate SU(3)-flavour symmetries of nuclear and hadronic physics. Moreover, when the u , d , and s masses can be ignored, QCD is invariant under separate unitary transformations among the left- and right-handed quarks, $q_i^{L'} = U_{ij}^L q_j^L$ and $q_i^{R'} = U_{ij}^R q_j^R$, resulting in the chiral symmetry group $U(3)_L \times U(3)_R$. The diagonal subgroup ($U_L = U_R$) corresponds to the SU(3)-flavour (and baryon number) symmetry mentioned. The remaining chiral SU(3) symmetry ($U_L^{-1} = U_R$) is believed to be spontaneously broken by the vacuum state of QCD, resulting in the existence of an octet of Goldstone bosons identified with the pseudoscalar mesons π , K , η .

These approximate flavour and chiral symmetries due to the smallness of the u , d , and s quark masses, are important, since they can be exploited to formulate effective field theories that are equivalent to QCD in a certain energy range. A classic example is chiral perturbation theory for the interaction of baryons with the octet of the pseudoscalar mesons, which results in an expansion of matrix elements in terms of small momenta or light-quark masses [2]. On similar footing is heavy-quark effective theory (HQET) for hadrons containing a quark (c , b , t) with mass $m_Q \gg \Lambda_{QCD}$. In the limit $m_Q \rightarrow \infty$, the heavy quark becomes on-shell and the dynamics becomes independent of its mass. The hadronic matrix elements can be expanded as a power series in $1/m_Q$, resulting in symmetry relations between various matrix elements [3].

Generalizing QCD to an SU(N_c) gauge theory, the inverse of the number of colours, $1/N_c$, is a hidden expansion parameter [4]. This theory, wherein the coupling is decreased such that $g^2 N_c$ is constant, is “large- N_c QCD”. Diagrammatic considerations suggest that large- N_c QCD is a weakly-coupled theory of mesons and baryons, wherein baryons are heavy semiclassical objects. Significant, mostly qualitative, insight into QCD can be obtained from considering the large- N_c limit, especially when combined with the techniques of effective field theory.

1.1.4 Theoretical approaches to non-perturbative QCD

In this brief introduction, we focus on theoretical frameworks that have a rigorous justification in QCD and that, with allowance for further progress in the coming years and with a reasonable extrapolation of available computing resources, can be expected to provide a direct confrontation of the data from experiments like PANDA with the predictions of non-perturbative QCD. Among these theoretical approaches the best established are (i) lattice QCD, which attempts a direct attack to solve QCD non-perturbatively by numerical simulation, and (ii) effective field theories, which exploit the symmetries of QCD and the existence of hierarchies of scales to provide predictions from effective Lagrangians that are equivalent to QCD; among the latter we distinguish systematic effective field theories formulated in terms of quark-gluon and in terms of hadronic degrees of freedom.

It should be kept in mind that the theoretical approaches will, in many cases, calculate quantities that require an additional step to be compared with measured data. This is because a full computation of the cross section as measured by experimentalists in antiproton-proton collisions demands significantly more effort. Such an additional step may involve a partial-wave analysis of the measured data, in order to, for instance determine the quantum numbers of a resonance. Effective field theory with hadronic degrees of freedom offers some advantages in this respect. In the case of PANDA, an example is the associated production of hyperon-antihyperon pairs in the reactions $\bar{p}p \rightarrow \bar{Y}Y$, where the spin observables in the final state can be precisely measured [5]. Therefore, the possibility exists in this case to perform a full partial-wave analysis of the data to study in detail the contribution of resonances.

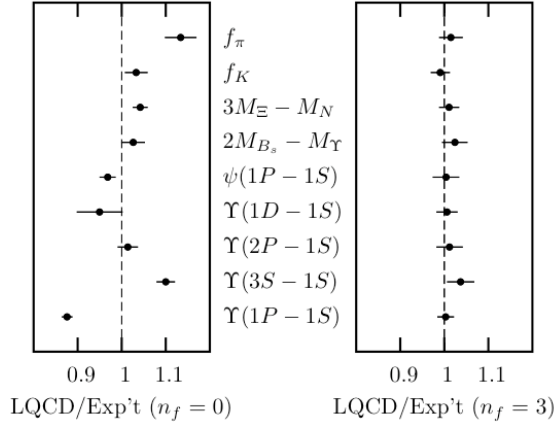


Figure 1.2: LQCD results divided by experimental values for selected quantities in hadronic physics. On the left the quenched calculations are shown, on the right the corresponding unquenched ones. While the former exhibit systematic deviations of some 10 % from experiment, the latter are in impressive agreement with experiment.

1.2 Lattice QCD: status and prospects

Lattice QCD (LQCD) is an *ab initio* approach to deal with QCD in the non-perturbative low-energy regime. The equations of motion of QCD are discretised on a 4-dimensional space-time lattice and solved by large-scale numerical simulations on big computers. For numerical reasons the QCD action is Wick rotated into Euclidean space-time. The lattice spacing, a , acts as the ultraviolet regulator of the theory. By letting $a \rightarrow 0$, the regulator is removed and continuum results are obtained. LQCD (originally proposed by Wilson in 1974) has made enormous progress over the last decades. In the past, the accuracy of LQCD results were limited by the use of the “quenched approximation” (*i.e.* the neglect of sea quarks), by unrealistic heavy up and down quarks, and by the use of only two instead of three light quark flavours. These deviations from “real QCD” were partly mandated by the limited availability of CPU-time. In recent years, all these limiting aspects (finite volume effects, lattice artefacts, unrealistic quark masses, exclusion of sea quarks) are being improved upon gradually. Thus, there is every reason to expect that progress in LQCD will continue in the future, to the extent that precise LQCD predictions will be available when the PANDA experiment starts.

In LQCD, the SU(3) group elements $U_{x,\mu}$ are 3×3 matrices defined on the links that connect the

neighbouring sites x and $x + a\hat{\mu}$ on the lattice. Traces of products of such matrices along closed paths, so-called Wilson loops, are gauge invariant. The elementary building block is the “plaquette,” the 1×1 lattice square. The simplest discretised action is then the Wilson action, which is proportional to the (gauge-invariant) trace of the sum over all plaquettes,

$$S_W = -\frac{6}{g^2} \text{Re} \sum_{x,\mu>\nu} \text{Tr} \Pi_{x,\mu,\nu}, \quad (1.8)$$

where $\Pi_{x,\mu\nu} = U_{x,\mu} U_{x+a\hat{\mu},\nu} U_{x+a\hat{\nu},\mu}^\dagger U_{x,\nu}^\dagger$. In the continuum limit, this action agrees with the (Yang-Mills part of the) QCD action (in 4D Euclidean space) to order $\mathcal{O}(a^2)$,

$$\begin{aligned} S_{YM} &= -\frac{1}{4g^2} \int d^4x G_a^{\mu\nu}(x) G_{\mu\nu}^a(x) \\ &= S_W + \text{constant} + \mathcal{O}(a^2). \end{aligned} \quad (1.9)$$

The simplest discretised version for the fermionic quark part of the QCD action reads

$$\begin{aligned} S_f &= \sum_x \left(\frac{1}{2} \gamma_\mu \bar{\psi}_x \left[U_{x+a\hat{\mu},\mu} \psi_{x+a\hat{\mu}} \right. \right. \\ &\quad \left. \left. - U_{x-a\hat{\mu},\mu}^\dagger \psi_{x-a\hat{\mu}} \right] + m a \bar{\psi}_x \psi_x \right), \end{aligned} \quad (1.10)$$

which again corresponds to the continuum action up to order $\mathcal{O}(a^2)$ terms. A major part of the progress in LQCD has consisted in developing improved versions of these naive discretised actions for the gluon and the quark fields, for instance to remove the order $\mathcal{O}(a^2)$ artefacts when taking the continuum limit. Improved fermionic actions have been developed for instance to implement an exact chiral symmetry on the lattice that in the continuum limit corresponds to the usual continuum chiral symmetry.

In LQCD the expectation values of n -point Green functions are calculated in the path integral sense, by evaluating their averages over all possible gauge field configurations on the lattice, weighted with the exponent of the action. For instance, for a hadron mass a zero-momentum two-point Green function with the desired quantum numbers is calculated that creates the hadron at Euclidean time zero and annihilates it at time t . For large t , this quantity will decay as $\exp(-mt)$, from which the mass can be extracted. In such a LQCD calculation it is the production of the gauge-field configurations that consumes the bulk of the CPU-time, especially in (“unquenched”) calculations that include sea quarks.

Many impressive results have been obtained for hadron spectroscopy within LQCD. As an example

of great relevance to the $\overline{\text{PANDA}}$ program, we discuss briefly (quenched) lattice calculations for the glueball spectrum. One first chooses an interpolating operator for a glueball with specific quantum numbers, *e.g.* for a scalar glueball one can take

$$O(\vec{x}, t) = \sum_{i < j = x, y, z} \text{Re Tr } U_{ij}(\vec{x}), \quad (1.11)$$

where U_{ij} is the plaquette in the ij -plane. The glueball masses are then obtained from the asymptotic behaviour of the time correlator

$$\begin{aligned} C(t) &= \sum_{x, x', t} \langle O(\vec{x}, t) O^\dagger(\vec{x}', 0) \rangle \\ &= \sum_i |\langle 0 | O | i \rangle|^2 \exp(-m_i t). \end{aligned} \quad (1.12)$$

However, because the scalar glueball has vacuum quantum numbers, it provides from the simulation point of view a particular “noisy” signal. The mass must be obtained from a fit to a function of the type $C(t) \simeq C_0 + C_1 \exp(-m t)$. Special techniques have been developed to improve the signal-to-noise quality of the glueball signal on the lattice. For instance, one can use an anisotropic lattice with a smaller lattice spacing in the temporal direction. The glueball spectrum obtained in this manner [6] is shown in the Figure 1.3.

While this LQCD result for the glueball spectrum is already very impressive, further improvement is clearly needed in order to compare ultimately to spectroscopic results obtained from a partial-wave analysis of the experimental data. The glueballs from a quenched calculations, for instance, decay only to lighter glueballs and the η' meson. Moreover, significant limitations will have to be overcome for LQCD to become as predictive for dynamical (scattering) observables as it is for spectroscopy. Lattice QCD applications in the charm sector constitute an important test for applications to hadronic corrections required in B physics.

From lattice calculation of various quantities the QCD coupling constant can be determined. For instance, from the bottomonium spectrum, the value $\alpha_S(M_Z) = 0.1170 \pm 0.0012$ was extracted. Also the running of α_S was studied and the results are in good agreement with the two-loop result calculated within pQCD.

An area that so far has proven challenging for LQCD, but where it is foreseeable that significant progress will be made in the coming years, is the (ground-state) structure of the nucleon. The nucleon electromagnetic form factors, measured with increasing precision in electron scattering, are clas-

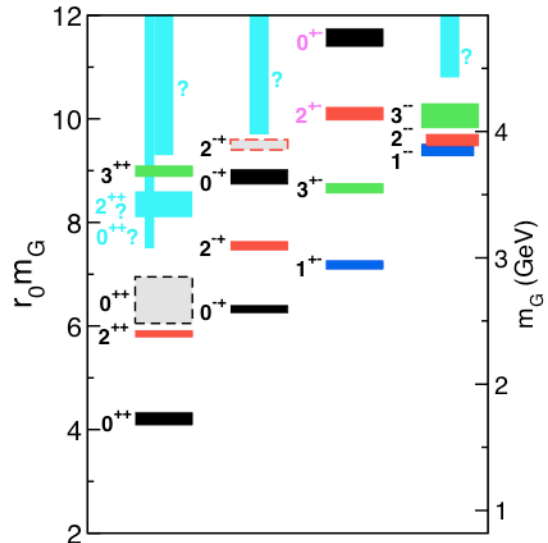


Figure 1.3: The LQCD glueball spectrum in pure SU(3) gauge theory [6].

sical observables in this respect, but recent surprising results obtained at JLAB demonstrate that our understanding is far from complete. The proton charge form factor falls off more rapidly than the standard dipole form supported by pQCD, and also the neutron data are not consistent with pQCD. LQCD results are becoming more accurate, but at present only the space-like region, in a limited q^2 -range, can be handled. Significant progress has been achieved in recent years by applying dispersion relation techniques to relate the space-like and the time-like regime [7]. The latter can be addressed by $\overline{\text{PANDA}}$ in a wide q^2 -range via the reaction $\overline{\text{p}}\text{p} \rightarrow e^+e^-$.

Certain hard exclusive processes in electron scattering have offered more detailed probes of the transition from the non-perturbative to the perturbative regime in QCD. The success of the theoretical framework of generalized parton distributions (GPDs) to describe the “soft” part of deeply virtual Compton scattering is a case in point. With $\overline{\text{PANDA}}$ the opportunity exists to measure the time-like counterparts of such processes, *viz.* antiproton-proton annihilation with crossed kinematics, as in $\overline{\text{p}}\text{p} \rightarrow \gamma\gamma$. A framework analogous to the GPDs for the space-like case has been developed: the amplitudes that encode the soft part of these annihilation reactions are the generalized distribution amplitudes (GDAs). The theoretical description within QCD of such time-like dynamical processes needs to be developed.

1.3 EFT with quark and gluon degrees of freedom

Ab initio calculations from QCD, be it pQCD or LQCD, are and will remain very difficult, especially in situations where several dynamical scales are involved. Effective field theory (EFT) techniques in many such cases can provide a solution. For instance, LQCD is particularly powerful when it is combined with EFT. A variety of EFTs with quark and gluon degrees of freedom have been developed in recent years. Exploiting a scale separation a simpler theory is obtained that it is equivalent to full QCD in the energy region considered. The degrees of freedom above a chosen energy scale are integrated out (in a path-integral sense) and the resulting field theory is organized as a power series of operators containing the low-energy degrees of freedom over the heavy scales. The high-energy physics is encoded in the coupling constants multiplying these operators, which are calculated by “matching” selected observables in the EFT and in full QCD. In the process, the symmetries of QCD need to be obeyed.

1.3.1 Non-relativistic QCD

Applications of QCD to systems involving charm, beauty or top quarks, can be simplified significantly by the use of effective field theory methods. It is not always necessary to solve the dynamics of such systems based on the QCD Lagrangian (Eq. 1.1) directly. One may integrate out fast modes of the heavy quarks by a systematic non-relativistic expansion [8]. The role of the four-component Dirac spinor fields q_f is taken over by two-component Pauli spinor fields ψ_f and χ_f describing heavy quarks and antiquarks. For the purpose of charm physics as studied with PANDA at FAIR it is useful to integrate out the b and t quarks and keep u , d , s , and c quarks as active degrees of freedom only. The resulting effective Lagrangian of QCD reads

$$\begin{aligned} \mathcal{L}_{QCD}^{\text{eff}} = & -\frac{1}{4} G_a^{\mu\nu} G_{\mu\nu} \\ & + \sum_{f=u,d,s} \bar{q}_f [i \gamma^\mu D_\mu - m_f] q_f \\ & + \psi^\dagger \left[i D_0 + \frac{1}{2m_c} \mathbf{D}^2 \right] \psi \\ & + \chi^\dagger \left[i D_0 - \frac{1}{2m_c} \mathbf{D}^2 \right] \chi + \sum_{n=0}^{\infty} \mathcal{L}_n, \end{aligned} \quad (1.13)$$

where the non-trivial terms \mathcal{L}_n are expanded in inverse powers of the charm-quark mass. The index n

denotes the number of heavy-quark and antiquark fields involved. Terms with $n \geq 4$ arise only if part of the gluon dynamics is integrated out, as will be discussed below. For a given heavy-quark species we illustrate the form of typical one-body terms,

$$\begin{aligned} \mathcal{L}_2 = & \frac{c_1}{8m_f^3} \left(\psi^\dagger (\mathbf{D}^2)^2 \psi - \chi^\dagger (\mathbf{D}^2)^2 \chi \right) \\ & + \frac{c_2}{8m_f^2} \left(\psi^\dagger (\mathbf{D} \cdot g \mathbf{E} - g \mathbf{E} \cdot \mathbf{D}) \psi \right. \\ & \quad \left. + \chi^\dagger (\mathbf{D} \cdot g \mathbf{E} - g \mathbf{E} \cdot \mathbf{D}) \chi \right) \\ & + \frac{c_3}{8m_f^2} \left(\psi^\dagger (i \mathbf{D} \times g \mathbf{E} - g \mathbf{E} \times i \mathbf{D}) \cdot \boldsymbol{\sigma} \psi \right. \\ & \quad \left. + \chi^\dagger (i \mathbf{D} \times g \mathbf{E} - g \mathbf{E} \times i \mathbf{D}) \cdot \boldsymbol{\sigma} \chi \right) \\ & + \frac{c_4}{2m_f} \left(\psi^\dagger (g \mathbf{B} \cdot \boldsymbol{\sigma}) \psi - \chi^\dagger (g \mathbf{B} \cdot \boldsymbol{\sigma}) \chi \right) \\ & + \dots, \end{aligned} \quad (1.14)$$

where $E^i = G^{0i}$ and $B^i = \frac{1}{2} \epsilon^i{}_{jk} G^{jk}$ are the electric and magnetic components of the gluon field strength tensor $G^{\mu\nu}$. The coefficients c_i in (Eq. 1.14) are calculable in perturbation theory with $c_i = 1 + \mathcal{O}(\alpha_s)$. The relevance of the various terms in (Eq. 1.14) is predicted by power-counting rules [9].

The characteristic quantity that controls the relative importance of the infinite number of terms in \mathcal{L}_n is the typical velocity v of the heavy quark. By assumption it must hold $v \ll 1$, as to justify the use of the non-relativistic fields in (Eq. 1.13). The precise realization of the power-counting rules depends on the system, whether for instance heavy-light or heavy-heavy systems are studied. We focus on heavy-quarkonium systems [10] for which the two terms D_0 and $\mathbf{D}^2/(2m_f)$ in (Eq. 1.13) are of equal importance. This is reflected in the counting rules with $D_0 \sim m_f v^2$ and $\mathbf{D} \sim m_f v$. If supplemented by the identification $\alpha_S(m_c) \sim v$ and $g \mathbf{E} \sim m_f^2 v^3$ and $g \mathbf{B} \sim m_f^2 v^4$ all terms displayed in (Eq. 1.14) are of equal relevance [9].

The effective Lagrangian (Eq. 1.13) defines still a quite complicated theory, since it is not always justified to treat the gluon dynamics in an expansion in powers of α_S . Nevertheless, it is a powerful tool since it can be and is used for simulations on the lattice. Depending on the typical velocity v of the heavy quark it is possible to integrate out the gluon dynamics at least in part. This is desirable since it would make contact with the phenomenological quark-potential model [11]. The one-gluon exchange part of such models follows by the assumption of perturbative gluon dynamics. A corresponding contribution in \mathcal{L}_4 of (Eq. 1.13) would

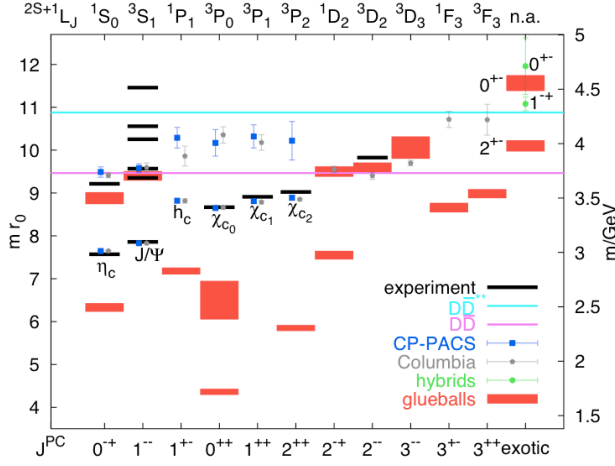


Figure 1.4: LQCD predictions for the charmonium, the glueball and the spin-exotic $\bar{c}c$ -glue hybrids spectrum in quenched lattice QCD.

arise. For charmonium systems there are three relevant scales: the mass m_c (the “hard scale”), the momentum transfer $m_c v$ (the “soft scale”, proportional to the inverse of the typical size of the system), and the binding energy $m_c v^2$ (the “ultra-soft scale”, proportional to the inverse of the typical time of the system). In charmonium $v^2 \simeq 0.3$. The crucial question is how Λ_{QCD} relates to the three scales discussed above. If $\Lambda_{QCD} > m_c v^2$ there must be non-perturbative physics involved when integrating out gluon dynamics. Since one expects $m_c > m_c v \sim \Lambda_{QCD}$, part of the gluon dynamics is perturbative [12, 13].

One can integrate out the soft scale $m_c v$ by employing a matching procedure keeping only dynamical ultra-soft degrees. This results in potential Non-relativistic QCD (pNRQCD). In lowest order the problem reduces to solving a Schrödinger equation for the $c\bar{c}$ states. The quark-potential model is recovered from pNRQCD, with potentials calculated from QCD following a formal non-perturbative procedure. An actual evaluation of the low-energy part requires a calculation on a lattice or QCD vacuum models. Some actual examples are shown in Figure 1.4. The charmonium ground-state hyperfine splitting has been calculated at NLO.

1.4 EFT with hadronic degrees of freedoms

We discuss the concepts of EFT with hadronic degrees of freedom at hand of open-charm systems in some detail. This is a sector most relevant for the

\bar{P} ANDA experiment with its goal to study properties of the spectrum of the D mesons in free-space and in nuclear matter. Analogous developments are possible in the light sector of QCD with up, down and strange quarks only. The description of baryon resonances with double strangeness, another important topic of the PANDA experiment, will profit from such developments. The study of hyper nuclei with PANDA is motivated in part as a mean to learn on the interaction of hyperons. For the latter chiral effective field theories are being developed [14]. In the charmonium sector, the construction of an EFT with hadronic degrees of freedom is in its infancy, though further developments would be important for the charmonium program at \bar{P} ANDA.

There are three important steps in the course of constructing an EFT. The first step is the choice of degrees of freedom. In most cases this can not be derived from QCD, but must be conjectured and then falsified by explicit computations to be confronted with QCD lattice results or experiments. Most predictive are EFTs involving Goldstone boson fields, since the interaction of the latter with matter fields is strongly constrained by the spontaneously broken chiral SU(3) symmetry QCD. The second step is of more technical nature, the construction of the effective Lagrangian, in a manner consistent with the symmetries of QCD. Though the second step is least controversial, it involves an infinite number of unknown parameters. This leads to the third crucial step: the identification of a suitable approximation scheme for the effective Lagrangian based on power-counting rules. This program is quite rewarding since the leading order Lagrangian involves typically a few unknown parameters only, in terms of which a lot of physics can be understood.

A quite radical approach is the hadrogenesis conjecture [15], which postulates the spectrum of QCD to be generated by the interaction of a few “quasi-fundamental” hadronic degrees of freedom, the selection of which is guided by symmetry properties of QCD. Clearly, alternative or complementary assumptions may be used at this stage. It is an important goal of the \bar{P} ANDA project to give answers to the fundamental question how QCD manifests itself in the hadronic spectrum.

1.4.1 Chiral symmetry and open-charm meson systems

In the open-charm sector consider the flavour-octet of Goldstone bosons

$$\Phi = \begin{pmatrix} \pi^0 + \frac{1}{\sqrt{3}}\eta & \sqrt{2}\pi^+ & \sqrt{2}K^+ \\ \sqrt{2}\pi^- & -\pi^0 + \frac{1}{\sqrt{3}}\eta & \sqrt{2}K^0 \\ \sqrt{2}K^- & \sqrt{2}\bar{K}^0 & -\frac{2}{\sqrt{3}}\eta \end{pmatrix} \quad (1.15)$$

and the flavor anti-triplets of pseudo-scalar and vector open-charm mesons

$$\begin{aligned} P &= (D^0, -D^+, D_s^+), \\ P_{\mu\nu} &= (D_{\mu\nu}^{*0}, -D_{\mu\nu}^{*+}, D_{s,\mu\nu}^{*+}), \end{aligned} \quad (1.16)$$

where one may represent the vector states by anti-symmetric tensors fields. In the limit of an infinite charm-quark mass the properties of pseudo-scalar and vector D mesons are closely related, in particular they are mass degenerate. In order to construct the effective Lagrangian describing the interaction of Goldstone bosons and the D mesons it is useful to identify building blocks that have convenient transformation properties under chiral transformations

$$\begin{aligned} U_\mu &= \frac{1}{2} u^\dagger \left(\left(\partial_\mu e^{i\frac{\Phi}{f}} \right) + i e A_\mu \left[Q, e^{i\frac{\Phi}{f}} \right] \right) u^\dagger, \\ u &= \exp\left(\frac{i\Phi}{2f}\right), \\ \chi_\pm &= \frac{1}{2} u \chi_0 u \pm \frac{1}{2} u^\dagger \chi_0 u^\dagger, \\ \chi_0 &= 2B_0 \begin{pmatrix} m_u & 0 & 0 \\ 0 & m_d & 0 \\ 0 & 0 & m_s \end{pmatrix}, \end{aligned} \quad (1.17)$$

where the parameter $f \simeq f_\pi$ may be identified with the pion-decay constant, $f_\pi = 92.4 \text{ MeV}$, at leading order. A precise determination of f requires a chiral SU(3) extrapolation of some data set. The field U_μ involves the photon field A_μ and the electromagnetic coupling constant $e \simeq 0.303$ and the quark charge matrix $Q = \text{diag}(2, -1, -1)/3$. The building blocks in (Eq. 1.17) illustrate two important aspects of EFTs: first the Goldstone boson field Φ enters in a non-linear fashion and second the chiral symmetry breaking fields χ_\pm are proportional to the quark-mass matrix of QCD. The parameter B_0 is related to the chiral quark condensate.

The chiral Ward identities of QCD are transported into the EFT by the use of a covariant derivative,

D_μ ,

$$\begin{aligned} D_\mu U_\nu &= \partial_\mu U_\nu + [\Gamma_\mu, U_\nu] + i e A_\mu [Q, U_\nu], \\ D_\mu P &= \partial_\mu P - P \Gamma_\mu + i e P Q' A_\mu, \\ \Gamma_\mu &= \frac{1}{2} \left(u^\dagger \partial_\mu u + u \partial_\mu u^\dagger \right), \end{aligned} \quad (1.18)$$

with $Q' = (0, 1, 1)$. Given the building blocks Eqs. (1.17, 1.18) it is straightforward to write down interaction terms that are compatible with the chiral constraints of QCD. This is because a covariant derivative D_μ acting on the fields U_μ , P , $P_{\mu\nu}$ or χ_\pm does not alter their transformation properties under chiral transformation [16].

We display the leading order Lagrangian constructed in terms of the building blocks Eqs. (1.17, 1.18)

$$\begin{aligned} \mathcal{L} &= f^2 \text{tr} \left\{ U^\mu U_\mu^\dagger \right\} + \frac{1}{2} \text{tr} (\chi_+) \\ &+ (D_\mu P) (D^\mu \bar{P}) - P M_{0-}^2 \bar{P} \\ &- (D_\mu P^{\mu\alpha}) (D^\nu \bar{P}_{\nu\alpha}) + \frac{1}{2} P^{\mu\alpha} M_{1-}^2 \bar{P}_{\mu\alpha} \\ &+ 2g_P \left\{ P_{\mu\nu} U^\mu (D^\nu \bar{P}) - (D^\nu P) U^\mu \bar{P}_{\mu\nu} \right\} \\ &- i \frac{\tilde{g}_P}{2} \epsilon^{\mu\nu\alpha\beta} \left\{ P_{\mu\nu} U_\alpha (D^\tau \bar{P}_{\tau\beta}) \right. \\ &\left. + (D^\tau P_{\tau\beta}) U_\alpha \bar{P}_{\mu\nu} \right\}, \end{aligned} \quad (1.19)$$

where we use the notation $\bar{P} = P^\dagger$. The decay of the charged D^* -mesons implies $|g_P| = 0.57 \pm 0.07$. The parameter \tilde{g}_P in (Eq. 1.19) can not be extracted from empirical data directly. In the absence of an accurate evaluation within unquenched lattice QCD, the size of \tilde{g}_P can be estimated using the heavy-quark symmetry, one expects $\tilde{g}_P = g_P$ at leading order [17]. In that limit it holds also that $M_{0-} = M_{1-}$.

If we admit isospin-breaking effects, *i.e.* $m_u \neq m_d$, there is a term in Eq. 1.19) after insertion of Eq. 1.15 proportional to $(m_u - m_d) \pi^0 \eta$. A unitary transformation is required such that the transformed fields $\tilde{\pi}^0$ and $\tilde{\eta}$ decouple. The Lagrangian density (Eq. 1.19), when written in terms of the new fields and a mixing angle ϵ , does not show a $\tilde{\pi}^0 \tilde{\eta}$ term if and only if

$$\frac{\sin(2\epsilon)}{\cos(2\epsilon)} = \sqrt{3} \frac{m_d - m_u}{2m_s - m_u - m_d}, \quad (1.20)$$

where we recalled the value for the mixing angle $\epsilon = 0.010 \pm 0.001$ as determined in Ref. [18].

We give a brief discussion of the power-counting rules underlying (Eq. 1.19). Such counting rules are

based on naive dimensional counting supplemented by a naturalness assumption. Dimensional counting rules are realized in a computation of a given Feynman diagram if the theory is treated in dimensional regularization. It is an important issue to devise renormalisation schemes that are compatible with a given counting scheme. To be specific we collect some counting rules

$$\begin{aligned} U_\mu &\sim Q, \\ D_\mu U_\mu &\sim Q^2, \\ D_\mu P &\sim Q^0, \\ \chi_\pm &\sim Q^2. \end{aligned} \quad (1.21)$$

The fact that a covariant derivative acting on U_μ must be counted Q reflects the “lightness” of the Goldstone boson fields: the squared mass of the Goldstone boson is proportional to the current quark mass of QCD. On the other hand the mass of a D meson is much larger than the masses of the Goldstone bosons. Thus, at a formal level one must assign a covariant derivative acting on a D -meson field the order Q^0 . A systematic approach arises if one orders the interaction terms of the chiral Lagrangian according to inverse powers in the charm-quark mass. The leading-order term is then linear in the charm quark mass, like the QCD action is linear in that parameter.

The central guiding rule of EFTs is the derivation of most general approximations compatible with the symmetries of the underlying theory but also the fundamental concepts of local quantum field theory like micro-causality, covariance, unitarity, and crossing symmetry. As emphasized by Weinberg for the case of nucleon-nucleon scattering a systematic approximation scheme can be devised if one evaluates a two-body potential based on power-counting rules in a perturbative manner [19]. The latter should then be used in a Schrödinger-type equation as to arrive at scattering amplitude compatible with the unitarity constraint. It is important to realize that within this type of EFT one does not apply the counting rules to the scattering amplitude directly, rather to the subset or irreducible diagrams. The rationale behind this approach is the observation that the “naive” counting rules are spoiled for a Feynman diagram in phase-space regions close to the opening of thresholds: an appropriate summation is required.

We illustrate the power of the effective Lagrangian (Eq. 1.19) and extract the leading order two-body interaction terms of the Goldstone bosons with the

D mesons

$$\begin{aligned} \mathcal{L}_{WT} = & \frac{1}{8f^2} \left\{ (\partial^\mu P) [\Phi, (\partial_\mu \Phi)] \bar{P} \right. \\ & \left. - P [\Phi, (\partial_\mu \Phi)] (\partial^\mu \bar{P}) \right\}, \\ & - \frac{1}{8f^2} \left\{ (\partial^\nu P_{\nu\alpha}) [\Phi, (\partial_\mu \Phi)] \bar{P}^{\mu\alpha} \right. \\ & \left. - P_{\nu\alpha} [\Phi, (\partial_\nu \Phi)] (\partial_\mu \bar{P}^{\mu\alpha}) \right\}. \end{aligned} \quad (1.22)$$

The Weinberg-Tomozawa interaction (Eq. 1.22) is a direct consequence of the chiral SU(3) symmetry of QCD and illustrates the predictive power of chiral EFT: the interaction is determined by one parameter $f \simeq 90$ MeV only that is known from the pion-decay process. Analogous interactions of the Goldstone bosons with other matter fields were derived and studied in detail in the recent literature [20, 21, 22, 23, 24]. It was shown that the chiral interaction (Eq. 1.22) is relevant for the study of open-charm resonances with $J^P = 0^+$ or 1^+ quantum number: it implies unambiguously the existence of two resonances with masses below the DK and D^*K thresholds and astonishingly close to the empirical masses of the $D_{s0}^*(2317)$ and $D_{s1}^*(2460)$ [25]. Such states manifest themselves as poles in the S -wave scattering amplitude of Goldstone bosons with the pseudo-scalar or vector open-charm ground states. For the formation of the scalar $D_{s0}^*(2317)$ resonance the four isospin states $\langle K D, I \rangle$, $\langle \pi D_s, 1 \rangle$ and $\langle \eta D_s, 0 \rangle$ are relevant with their coupled-channel interactions determined by (Eq. 1.22) at leading order. In the presence of isospin mixing all channels couple. The mixing of the two isospin sectors is of order ϵ . It predicts the leading isospin-violating hadronic decay $D_{s0}^*(2317) \rightarrow \pi^0 D_s$. Analogous statements hold for the axial-vector state.

The detailed consequence of the EFT approach for the properties of scalar and axial vector open-charm states has been addressed in the recent literature where chiral correction terms were considered systematically [26, 27]. In particular their electromagnetic and isospin-violating decay properties have been computed and confronted with experimental bounds successfully [26]. The leading order interaction predicts sizeable attraction in channels only that have an interpretation as $c\bar{q}$ states. Exotic channels, which would require tetra-quark configurations, are sensitive to chiral correction terms. Since the latter involve further a priori unknown parameters, the predictions in exotic channel are more uncertain. Nevertheless, it was shown that if further constraints of QCD, which arise in the limit of large number of colours N_c , are considered one

would expect exotic signals in the invariant mass distribution of the πD and ηD^* channels. It would be an important step towards a better understanding of the physics of open-charm meson systems to measure such mass distributions with high accuracy [26].

Further studies of open-charm systems that involve light vector mesons as active degrees of freedom are necessary. Within the hadrogenesis conjecture one would expect further resonance states, like tensor states, to be formed.

1.4.2 Phenomenology of open-charm baryon systems

While EFT is a rigorous and systematic approach to solve QCD, there are many systems for which such tools are not yet available. In such cases it is useful to develop schematic models to pave the way towards more systematic approaches. A good example is the interaction of D mesons with nucleons. The theoretical efforts to describe such systems with hadronic degrees of freedom are few so far. Since the experimental study of the open-charm baryon spectrum and properties of D mesons in cold nuclear matter may be feasible with \bar{P} ANDA, it is important to work out the relevance of this physics for the better understanding of strong QCD. One may model the interaction of D mesons with matter fields by a t -channel exchange of universally coupled light vector mesons. If written down for all two-body channels that are implied by the presence of up, down, strange and charm quarks such an interaction is compatible with the leading order chiral interaction in the case where the initial and final state involves a Goldstone boson [28]. For instance, the chiral interaction of Goldstone bosons with the open-charm baryon ground state, that is analogous to (Eq. 1.22), is recovered. The open-charm baryon systems are considerably more complicated than the open-charm meson systems since the charm quark may be exchanged from a meson to baryon and vice versa. For instance such processes are implied by the t -channel exchanges of D mesons. This complicates the construction of an EFT considerably. On the other hand, coupled-channel models based on that simple t -channel exchange force predict a surprising rich phenomenology. Thus a dedicated theoretical and experimental study appears quite rewarding and should be undertaken.

References

- [1] W. M. Yao et al., J. Phys. **G33**, 1 (2006).
- [2] V. Bernard, Prog. Part. Nucl. Phys. **60**, 82 (2008).
- [3] A. V. Manohar and M. B. Wise, Camb. Monogr. Part. Phys. Nucl. Phys. Cosmol. **10**, 1 (2000).
- [4] G. 't Hooft, Nucl. Phys. **B72**, 461 (1974).
- [5] K. D. Paschke et al., Phys. Rev. **C74**, 015206 (2006).
- [6] C. J. Morningstar and M. Peardon, Phys. Rev. D **60**, 034509 (1999).
- [7] S. Pacetti, Eur. Phys. J. **A32**, 421 (2007).
- [8] G. T. Bodwin, E. Braaten, and G. P. Lepage, Phys. Rev. D **51**, 1125 (1995).
- [9] G. T. Bodwin, E. Braaten, and G. P. Lepage, Phys. Rev. **D51**, 1125 (1995).
- [10] N. Brambilla et al., (2004).
- [11] E. S. Swanson, Phys. Rept. **429**, 243 (2006).
- [12] M. Luke and A. V. Manohar, Phys. Rev. D **55**, 4129 (1997).
- [13] N. Brambilla, A. Pineda, J. Soto, and A. Vairo, Rev. Mod. Phys. **77**, 1423 (2005).
- [14] H. Polinder, J. Haidenbauer, and U.-G. Meissner, Nucl. Phys. **A779**, 244 (2006).
- [15] M. F. M. Lutz and E. E. Kolomeitsev, Nucl. Phys. **A700**, 193 (2002).
- [16] A. Krause, Helv. Phys. Acta **63**, 3 (1990).
- [17] T.-M. Yan et al., Phys. Rev. D **46**, 1148 (1992).
- [18] J. Gasser and H. Leutwyler, Nucl. Phys. **B250**, 465 (1985).
- [19] S. Weinberg, Nucl. Phys. **B363**, 3 (1991).
- [20] N. Kaiser, T. Waas, and W. Weise, Nucl. Phys. **A612**, 297 (1997).
- [21] J. A. Oller, E. Oset, and J. R. Pelaez, Phys. Rev. **D59**, 074001 (1999).
- [22] C. Garcia-Recio, M. F. M. Lutz, and J. Nieves, Phys. Lett. **B582**, 49 (2004).

- [23] E. E. Kolomeitsev and M. F. M. Lutz, Phys. Lett. **B585**, 243 (2004).
- [24] M. F. M. Lutz and E. E. Kolomeitsev, Nucl. Phys. **A730**, 392 (2004).
- [25] E. E. Kolomeitsev and M. F. M. Lutz, Phys. Lett. **B582**, 39 (2004).
- [26] M. F. M. Lutz and M. Soyeur, Nucl. Phys. **A**, **in print** (2007).
- [27] F.-K. Guo, C. Hanhart, S. Krewald, and U.-G. Meissner, Phys. Lett. **B666**, 251 (2008).
- [28] J. Hofmann and M. F. M. Lutz, Nucl. Phys. **A763**, 90 (2005).

2 Experimental Setup

COMMENT: Author(s): A. Lehrach, L. Schmitt, G. Stancari

2.1 Overview

COMMENT: Author(s): K. Peters

2.2 The $\bar{\text{P}}\text{ANDA}$ Detector

COMMENT: Author(s): L. Schmitt

The main objectives of the design of the $\bar{\text{P}}\text{ANDA}$ experiment pictured in Fig. 2.1 are to achieve 4π acceptance, high resolution for tracking, particle identification and calorimetry, high rate capabilities and a versatile readout and event selection. To obtain a good momentum resolution the detector is split into a *target spectrometer* based on a superconducting solenoid magnet surrounding the interaction point and measuring at high angles and a *forward spectrometer* based on a dipole magnet for small angle tracks. A silicon vertex detector surrounds the interaction point. In both spectrometer parts tracking, charged particle identification, electromagnetic calorimetry and muon identification are available to allow to detect the complete spectrum of final states relevant for the $\bar{\text{P}}\text{ANDA}$ physics objectives.

In the following paragraphs the components of all detector subsystems are briefly described.

2.2.1 Target Spectrometer

The target spectrometer surrounds the interaction point and measures charged tracks in a solenoidal field of 2 T. It consists of detector layers arranged in an onion shell configuration. Pipes for the injection of target material have to cross the spectrometer perpendicular to the beam pipe.

The target spectrometer is arranged in a barrel part for angles larger than 22° and an end-cap part for the forward range down to 5° in the vertical and 10° in the horizontal plane. A side view of the target spectrometer is shown in Fig. 2.2.

One of the main design requirements is compactness to avoid a too large and a too costly magnet and crystal calorimeter.

2.2.1.1 Target

The compact geometry of the detector layers nested inside the solenoidal magnetic field combined with the request of minimal distance from the interaction point to the vertex tracker leaves very restricted space for the target installations. The situation is displayed in Fig. 2.3, showing the intersection between the antiproton beam pipe and the target pipe being gauged to the available space. In order to reach the design luminosity of $2 \cdot 10^{32} \text{ cm}^{-2} \text{ s}^{-1}$ a target thickness of about $4 \cdot 10^{15}$ hydrogen atoms per cm^2 is required assuming 10^{11} stored anti-protons in the HESR ring.

These are conditions posing a real challenge for an internal target inside a storage ring. At present, two different, complementary techniques for the internal target are being developed: the cluster-jet target and the pellet target. Both techniques are capable of providing sufficient densities for hydrogen at the interaction point, but exhibit different properties concerning their effect on the beam quality and the definition of the interaction point. In addition, internal targets also of heavier gases, like deuterium, nitrogen or argon can be made available.

For non-gaseous nuclear targets the situation is different in particular in case of the planned hyper-nuclear experiment. In these studies the whole upstream end cap and part of the inner detector geometry will be modified.

Cluster-Jet Target The expansion of pressurized cold hydrogen gas into vacuum through a Laval-type nozzle leads to a condensation of hydrogen molecules forming a narrow jet of hydrogen clusters. The cluster size varies from $\cdot 10^3$ to $\cdot 10^6$ hydrogen molecules tending to become larger at higher inlet pressure and lower nozzle temperatures. Such a cluster-jet with density of $\cdot 10^{15} \text{ atoms/cm}^3$ acts as a very diluted target since it may be seen as a localized and homogeneous mono-layer of hydrogen atoms being passed by the antiprotons once per revolution.

Fulfilling the luminosity demand for $\bar{\text{P}}\text{ANDA}$ still requires a density increase compared to current applications. Additionally, due to detector constraints, the distance between the cluster-jet nozzle and the target will be larger. The size of the target region will be given by the lateral spread of hydro-

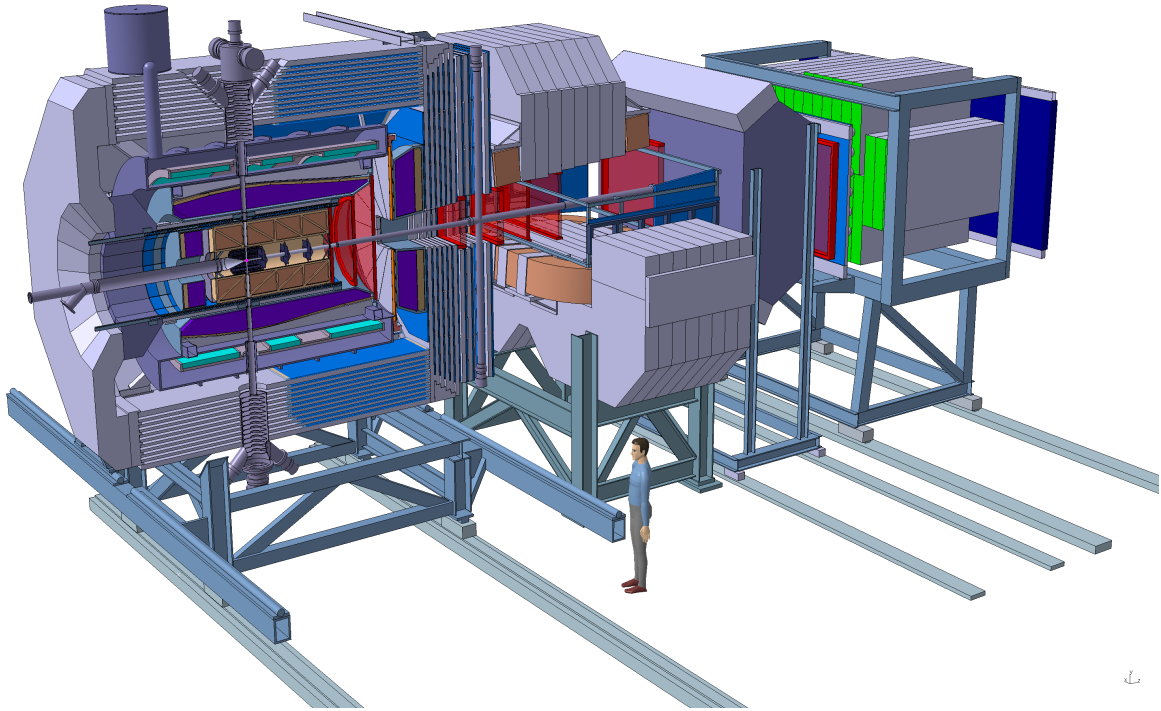


Figure 2.1: Artistic view of the \bar{P} ANDA Detector

gen clusters. This width should stay smaller than 10 mm when optimized with skimmers and collimators both for maximum cluster flux as well as for minimum gas load in the adjacent beam pipes. The great advantage of cluster targets is the homogeneous density profile and the possibility to focus the antiproton beam at highest phase space density. Hence, the interaction point is defined transversely but has to be reconstructed longitudinally in beam direction. In addition the low β -function of the antiproton beam keeps the transverse beam target heating effects at the minimum. The possibility of adjusting the target density along with the gradual consumption of antiprotons for running at constant luminosity will be an important feature.

Pellet Target The pellet target features a stream of frozen hydrogen micro-spheres, called pellets, traversing the antiproton beam perpendicularly. Pellet targets are presently in use at the WASA at COSY experiment [1] and were previously developed at TSL [2]. Typical parameters for pellets at the interaction point are the rate of $1.0 - 1.5 \cdot 10^4 \text{ s}^{-1}$, the pellet size of 25 - 40 μm , and the velocity of about 60 m/s. At the interaction point the pellet train has a lateral spread of $\sigma \approx 1 \text{ mm}$ and an inter spacing

of pellets that varies between 0.5 to 5 mm. With proper adjustment of the β -function of the coasting antiproton beam at the target position, the design luminosity for \bar{P} ANDA can be reached. The present R&D is concentrating on minimizing the luminosity variations such that the instantaneous interaction rate does not exceed the acceptance of the detector systems. Since a single pellet becomes the vertex for more than hundred nuclear interactions with antiprotons during the time a pellet traverses the beam, it will be possible to determine the position of individual pellets with the resolution of the micro-vertex detector averaged over many events. R&D is going on to devise an optical pellet tracking system. Such a device could determine the vertex position to about 50 μm precision for each individual event independently of the detector. It remains to be seen if this device can later be implemented in \bar{P} ANDA.

The production of deuterium pellets is also well established, the use of other gases like N_2 , Ar or Xe as pellet target material does not pose problems [3].

Other Targets are under consideration for the hyper-nuclear studies where a separate target sta-

may be employed to study antiproton-nucleus interactions.

2.2.1.2 Solenoid Magnet

The magnetic field in the target spectrometer is provided by a superconducting solenoid coil with an inner radius of 90 cm and a length of 2.8 m. The maximum magnetic field is 2 T. The field homogeneity is foreseen to be better than 2% over the volume of the vertex detector and central tracker. In addition the transverse component of the solenoid field should be as small as possible, in order to allow a uniform drift of charges in the time projection chamber. This is expressed by a limit of $\int B_r/B_z dz < 2$ mm for the normalized integral of the radial field component.

In order to minimize the amount of material in front of the electromagnetic calorimeter, the latter is placed inside the magnetic coil. The tracking devices in the solenoid cover angles down to $5^\circ/10^\circ$ where momentum resolution is still acceptable. The dipole magnet with a gap height of 1.4 m provides a continuation of the angular coverage to smaller polar angles.

The cryostat for the solenoid coils has two warm bores of 100 mm diameter, one above and one below the target position, to allow for insertion of internal targets.

2.2.1.3 Microvertex Detector

The design of the micro-vertex detector (MVD) for the target spectrometer is optimized for the detection of secondary vertices from D and hyperon decays and maximum acceptance close to the interaction point. It will also strongly improve the transverse momentum resolution. The setup is depicted in Fig. 2.4.

The concept of the MVD is based on radiation hard silicon pixel detectors with fast individual pixel readout circuits and silicon strip detectors. The layout foresees a four layer barrel detector with an inner radius of 2.5 cm and an outer radius of 13 cm. The two innermost layers will consist of pixel detectors while the outer two layers are considered to consist of double sided silicon strip detectors.

Eight detector wheels arranged perpendicular to the beam will achieve the best acceptance for the forward part of the particle spectrum. Here again, the inner two layers are made entirely of pixel detectors, the following four are a combination of strip detectors on the outer radius and pixel detectors closer

to the beam pipe. Finally the last two wheels, made entirely of silicon strip detectors, are placed further downstream to achieve a better acceptance of hyperon cascades.

The present design of the pixel detectors comprises detector wafers which are 200 μm thick (0.25% X_0). The readout via bump-bonded wafers with ASICs as it is used in ATLAS and CMS [4, 5] is foreseen as the default solution. It is highly parallelised and allows zero suppression as well as the transfer of analog information at the same time. The readout wafer has a thickness of 300 μm (0.37% X_0). A pixel readout chip based on a 0.13 μm CMOS technology is under development for \bar{P} ANDA. This chip allows smaller pixels, lower power consumption and a continuously sampling readout without external trigger.

2.2.1.4 Central Tracker

The charged particle tracking devices must handle the high particle fluxes that are anticipated for a luminosity of up to several $10^{32} \text{ cm}^{-2} \text{ s}^{-1}$. The momentum resolution $\delta p/p$ has to be on the percent level. The detectors should have good detection efficiency for secondary vertices which can occur outside the inner vertex detector (e.g. K_S^0 or Λ). This is achieved by the combination of the silicon vertex detectors close to the interaction point (MVD) with two outer systems. One system is covering a large area and is designed as a barrel around the MVD. This will be either a stack of straw tubes (STT) or a time-projection chamber (TPC). The forward angles will be covered using three sets of GEM trackers similar to those developed for the COMPASS experiment [6] at CERN. The two options for the central tracker are explained briefly in the following.

Straw Tube Tracker (STT) This detector consists of aluminized mylar tubes called *straws*, which are self supporting by the operation at 1 bar overpressure. The straws are arranged in planar layers which are mounted in a hexagonal shape around the MVD as shown in Fig. 2.5. In total there are 24 layers of which the 8 central ones are tilted to achieve an acceptable resolution of 3 mm also in z (parallel to the beam). The gap to the surrounding detectors is filled with further individual straws. In total there are 4200 straws around the beam pipe at radial distances between 15 cm and 42 cm with an overall length of 150 cm. All straws have a diameter of 10 mm. A thin and light space frame will hold the straws in place, the force of the wire however is kept solely by the straw itself. The mylar foil is

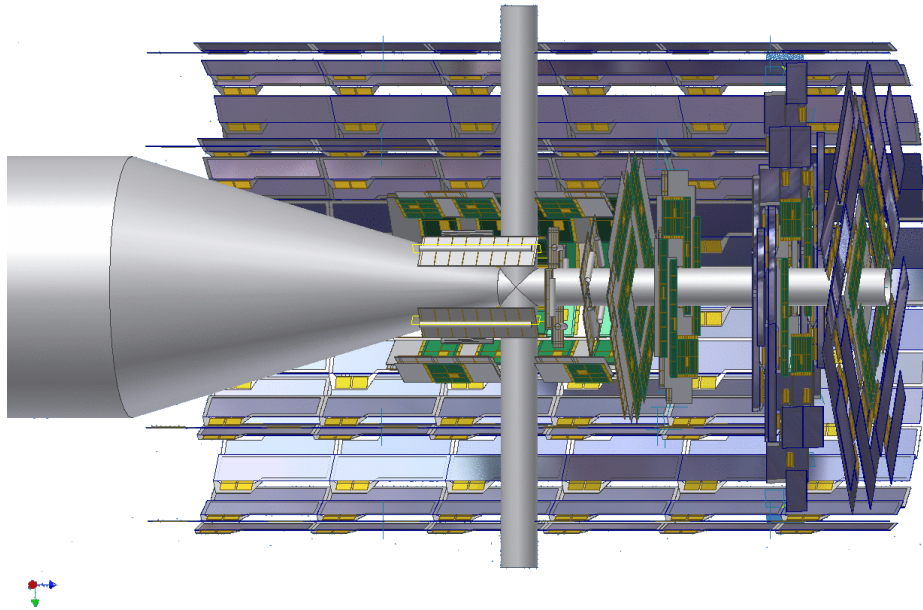


Figure 2.4: The Micro-vertex detector of \bar{P} ANDA

30 μm thick, the wire is made of 20 μm thick gold plated tungsten. This design results in a material budget of 1.3 % of a radiation length.

The gas mixture used will be Argon based with CO_2 as quencher. It is foreseen to have a gas gain no greater than 10^5 in order to warrant long term operation. With these parameters, a resolution in x and y coordinates of about 150 μm is expected.

Time Projection Chamber (TPC) A challenging but advantageous alternative to the STT is a TPC, which would combine superior track resolution with a low material budget and additional particle identification capabilities through energy loss measurements.

The TPC depicted in a schematic view in Fig. 2.6 consists of two large gas-filled half-cylinders enclosing the target and beam pipe and surrounding the MVD. An electric field along the cylinder axis separates positive gas ions from electrons created by ionizing particles traversing the gas volume. The electrons drift with constant velocity towards the anode at the upstream end face and create an avalanche detected by a pad readout plane yielding information on two coordinates. The third coordinate of the track comes from the measurement of the drift time of each primary electron cluster. In common TPCs the amplification stage typically occurs in multi-wire proportional chambers. These are gated by

an external trigger to avoid a continuous backflow of ions in the drift volume which would distort the electric drift field and jeopardize the principle of operation.

In \bar{P} ANDA the interaction rate is too high and there is no fast external trigger to allow such an operation. Therefore a novel readout scheme is employed which is based on GEM foils as amplification stage. These foils have a strong suppression of ion backflow, since the ions produced in the avalanches within the holes are mostly caught on the backside of the foil. Nevertheless about two ions per primary electron are drifting back into the ionisation volume even at moderate gains. The deformation of the drift field can be measured by a laser calibration system and the resulting drift can be corrected accordingly. In addition a very good homogeneity of the solenoid field with a low radial component is required.

A further challenge is the large number of tracks accumulating in the drift volume because of the high rate and slow drift. While the TPC is capable of storing a lot of tracks at the same time, their assignment to specific interactions has to be done by time correlations with other detectors in the target spectrometer. To achieve this, first a tracklet reconstruction has to take place. The tracklets are then matched against other detector signals or are pointed to the interaction. This requires either high

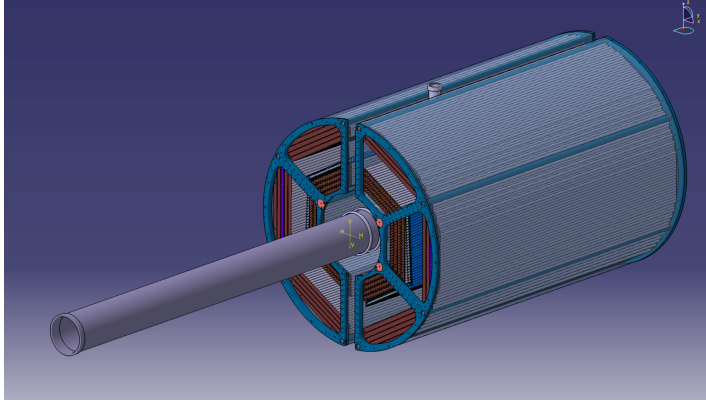


Figure 2.5: Straw Tube Tracker in the Target Spectrometer.

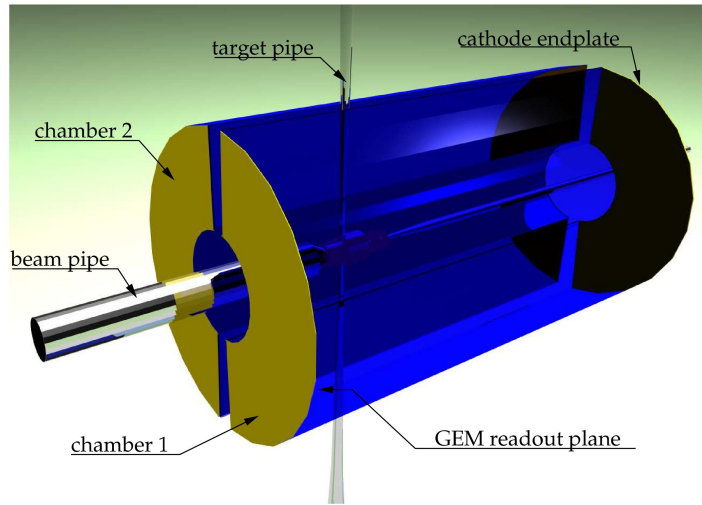


Figure 2.6: GEM Time Projection Chamber in the Target Spectrometer.

computing power close to the readout electronics or a very high bandwidth at the full interaction rate.

Forward GEM Detectors Particles emitted at angles below 22° which are not covered fully by the Straw Tube Tracker or TPC will be tracked by three stations of GEM detectors placed 1.1 m, 1.4 m and 1.9 m downstream of the target. The chambers have to sustain a high counting rate of particles peaked at the most forward angles due to the relativistic boost of the reaction products as well as due to the small angle $\bar{p}p$ elastic scattering. With the envisaged luminosity, the expected particle flux in the first chamber in the vicinity of the 5 cm diameter beam pipe is about $3 \cdot 10^4 \text{ cm}^{-2} \text{ s}^{-1}$. In addition it is required that the chambers work in the 2 T magnetic field produced by the solenoid. Drift chambers cannot fulfil the requirements here since they would suffer from aging and the occupancy would be too high. Therefore gaseous micropattern detec-

tors based on GEM foils as amplification stages are chosen. These detectors have rate capabilities three orders of magnitude higher than drift chambers.

In the current layout there are three double planes with two projections per plane. The readout plane is subdivided in an outer ring with longer and an inner ring with shorter strips. The strips are arranged in two orthogonal projections per readout plane. Owing to the charge sharing between strip layers a strong correlation between the orthogonal strips can be found giving an almost 2D information rather than just two projections.

The readout is performed by the same front-end chips as are used for the silicon microstrips. The first chamber has a diameter of 90 cm, the last one of 150 cm. The readout boards carrying the ASICs are placed at the outer rim of the detectors.

2.2.1.5 Cherenkov Detectors and Time-of-Flight

Charged particle identification of hadrons and leptons over a large range of angles and momenta is an essential requirement for meeting the physics objectives of $\bar{\text{P}}\text{ANDA}$. There will be several dedicated systems which, complementary to the other detectors, will provide means to identify particles. The main part of the momentum spectrum above 1 GeV/c will be covered by Cherenkov detectors. Below the Cherenkov threshold of kaons several other processes have to be employed for particle identification: The tracking detectors are able to provide energy loss measurements. Here in particular the TPC with its large number of measurements along each track excels. In addition a time-of-flight barrel can identify slow particles.

Barrel DIRC Charged particles in a medium with index of refraction n , propagating with velocity $\beta c < 1/n$, emit radiation at an angle $\Theta_C = \arccos(1/n\beta)$. Thus, the mass of the detected particle can be determined by combining the velocity information determined from Θ_C with the momentum information from the tracking detectors.

A very good choice as radiator material for these detectors is fused silica (*i.e.* artificial quartz) with a refractive index of 1.47. This provides pion-kaon-separation from rather low momenta of 800 MeV/c up to about 5 GeV/c and fits well to the compact design of the target spectrometer. In this way the loss of photons converting in the radiator material can be reduced by placing the conversion point as close as possible to the electromagnetic calorimeter.

At polar angles between 22° and 140°, particle identification will be performed by the detection of internally reflected Cherenkov (DIRC) light as realized in the BaBar detector [7]. It will consist of 1.7 cm thick quartz slabs surrounding the beam line at a radial distance of 45 - 54 cm. At BaBar the light was imaged across a large stand-off volume filled with water onto 11 000 photomultiplier tubes. At $\bar{\text{P}}\text{ANDA}$, it is intended to focus the images by lenses onto micro-channel plate photomultiplier tubes (MCP PMTs) which are insensitive to magnetic fields. This fast light detector type allows a more compact design and the readout of two spatial coordinates. In addition MCP PMTs provide good time resolution to measure the time of light propagation for dispersion correction and background suppression.

Forward Endcap DIRC A similar concept can be employed in the forward direction for particles between 5° and 22°. The same radiator, fused silica, is to be employed however in shape of a disk. At the rim around the disk focussing will be done by mirroring quartz elements reflecting onto MCP PMTs. Once again two spatial coordinates plus the propagation time for corrections will be read. The disk will be 2 cm thick and will have a radius of 110 cm. It will be placed directly upstream of the forward end-cap calorimeter.

Barrel Time-of-Flight For slow particles at large polar angles particle identification will be provided by a time-of-flight detector. In the target spectrometer the flight path is only of the order of 50 - 100 cm. Therefore the detector must have a very good time resolution between 50 and 100 ps.

Implementing an additional start detector would introduce too much material close to the interaction point deteriorating considerably the resolution of the electromagnetic crystal calorimeter. In the absence of a start detector relative timing of a minimum of two particles has to be employed.

As detector candidates scintillator bars and strips or pads of multi-gap resistive plate chambers are considered. In both cases a compromise between time resolution and material budget has to be found. The detectors will cover angles between 22° and 140° using a barrel arrangement around the STT/TPC at 42 - 45 cm radial distance.

2.2.1.6 Electromagnetic Calorimeters

Expected high count rates and a geometrically compact design of the target spectrometer require a fast scintillator material with a short radiation length and Molière radius for the construction of the electromagnetic calorimeter (EMC). Lead tungstate (PbWO_4) is a high density inorganic scintillator with sufficient energy and time resolution for photon, electron, and hadron detection even at intermediate energies [8, 9, 10]. For high energy physics PbWO_4 has been chosen by the CMS and ALICE collaborations at CERN [11, 12] and optimized for large scale production. Apart from a short decay time of less than 10 ns good radiation hardness has been achieved [13]. Recent developments indicate a significant increase of light yield due to crystal perfection and appropriate doping to enable photon detection down to a few MeV with sufficient resolution. The light yield can be increased by a factor of about 4 compared to room temperature by cooling the crystals down to -25°C.

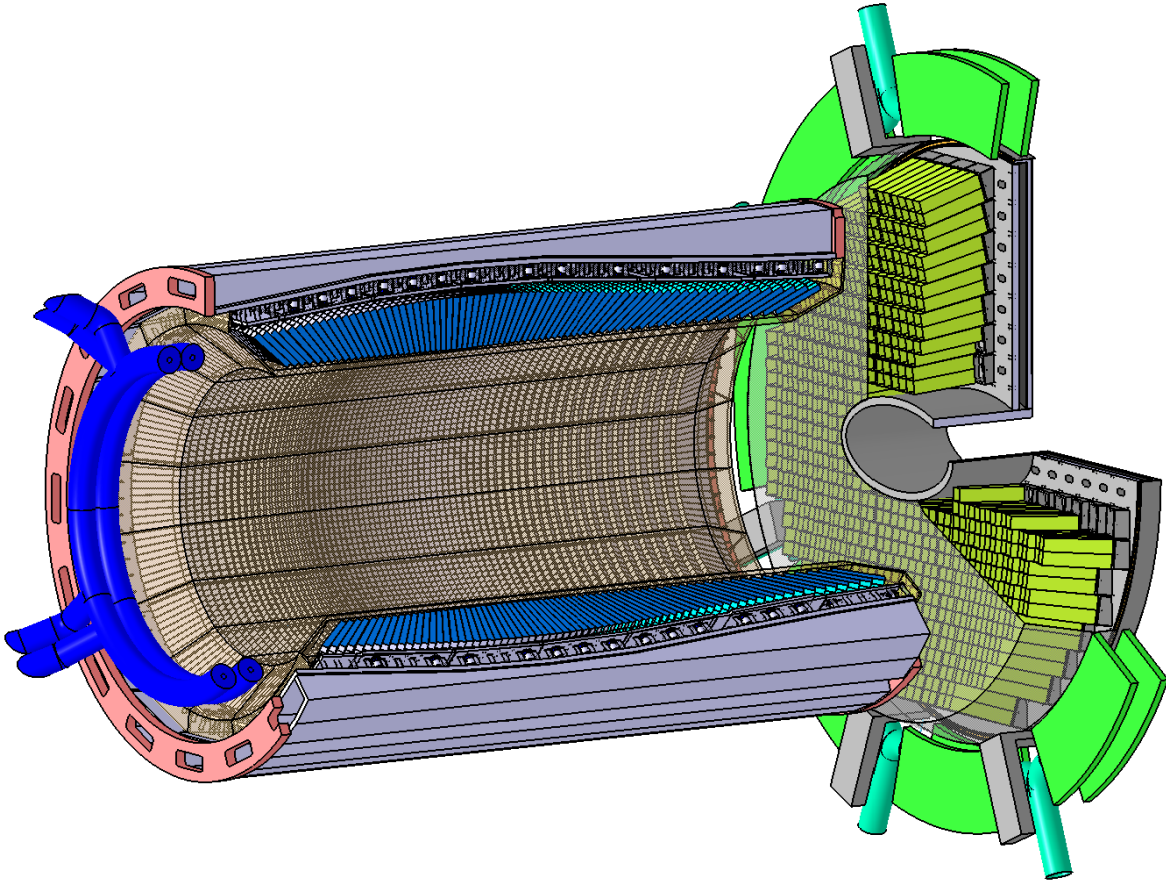


Figure 2.7: The \bar{P} ANDA barrel and forward end-cap EMC

The crystals will be 20 cm long, *i.e.* approximately $22 X_0$, in order to achieve an energy resolution below 2% at 1 GeV [8, 9, 10] at a tolerable energy loss due to longitudinal leakage of the shower. Tapered crystals with a front size of $2.1 \times 2.1 \text{ cm}^2$ will be mounted with an inner radius of 57 cm. This implies 11 360 crystals for the barrel part of the calorimeter. The forward end-cap calorimeter will have 3600 tapered crystals, the backward end-cap calorimeter 592. The readout of the crystals will be accomplished by large area avalanche photo diodes in the barrel and vacuum photo-triodes in the forward and backward endcaps.

The barrel part and the forward endcap of the target spectrometer EMC are depicted in Fig. 2.7.

2.2.1.7 Muon Detectors

Muons are an important probe for, among others, J/ψ decays, semi-leptonic D -meson decays and the Drell-Yan process. The strongest background are pions and their decay daughter muons. However at the low momenta of \bar{P} ANDA the signature is less

clean than in high energy physics experiments. To allow nevertheless a proper separation of primary muons from pions and decay muons a range tracking system will be implemented in the yoke of the solenoid magnet. Here a fine segmentation of the yoke as absorber with interleaved tracking detectors allows the distinction of energy loss processes of muons and pions and kinks from pion decays. Only in this way a high separation of primary muons from the background can be achieved.

In the barrel region the yoke is segmented in a first layer of 6 cm iron followed by 12 layers of 3 cm thickness. The gaps for the detectors are 3 cm wide. This is enough material for the absorption of pions in the momentum range in \bar{P} ANDA at these angles. In the forward end-cap more material is needed. Since the downstream door of the return yoke has to fulfil constraints for space and accessibility, the muon system is split in several layers. Six detection layers are placed around five iron layers of 6 cm each within the door, and a removable muon filter with additional five layers of 6 cm iron is located in the space between the solenoid and the dipole. This

filter has to provide cut-outs for forward detectors and pump lines and has to be built in a way that it can be removed with few crane operations to allow easy access to these parts.

As detector within the absorber layers rectangular aluminium drift tubes are used as they were constructed for the COMPASS muon detection system [14]. They are essentially drift tubes with additional capacitively coupled strips read out on both ends to obtain the longitudinal coordinate.

2.2.1.8 Hypernuclear Detector

The hypernuclei study will make use of the modular structure of PANDA. Removing the backward end-cap calorimeter will allow to add a dedicated nuclear target station and the required additional detectors for γ spectroscopy (see Fig. 2.8) close to the entrance of PANDA. While the detection of anti-hyperons and low momentum K^+ can be ensured by the universal detector and its PID system, a specific target system and a γ -detector are additional components required for the hypernuclear studies.

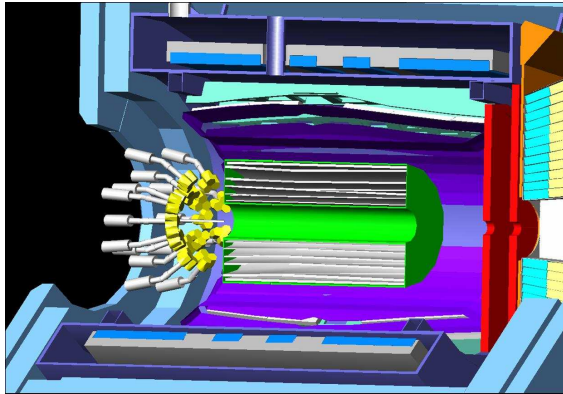


Figure 2.8: Integration of the secondary target and the germanium Cluster-array in the PANDA detector. The beam enters from left.

Active Secondary Target The production of hypernuclei proceeds as a two-stage process. First hyperons, in particular $\Xi\Xi$, are produced on a primary nuclear target. The slowing down of the Ξ proceeds through a sequence of nuclear elastic scattering processes inside the residual nucleus in which the antiproton annihilation has occurred and by energy loss during the passage through an active absorber. If decelerated to rest before decaying, the particle can be captured in a nucleus, eventually releasing two Λ hyperons and forming a double hypernucleus.

The geometry of this secondary target is essentially determined by the short mean life of the Ξ^- of only 0.164 ns and its stopping time in solid material. This limits the required thickness of the active secondary target to about 25–30 mm. The present layout shows a compact structure of 26 mm thickness, consisting out of 20 layers of silicon strip detectors with alternating layers of absorber material (Fig. 2.9). The active silicon layers provide also tracking information on the emitted weak decay products of the produced hypernuclei (see Fig. 4.75 in Sec. 4.5.2).

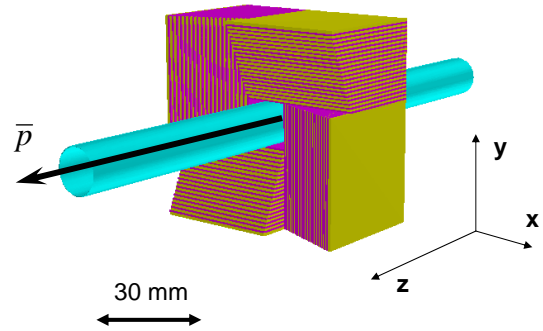


Figure 2.9: Layout out the secondary sandwich target. The active silicon layers provide also tracking information on the emitted weak decay products of the produced hypernuclei.

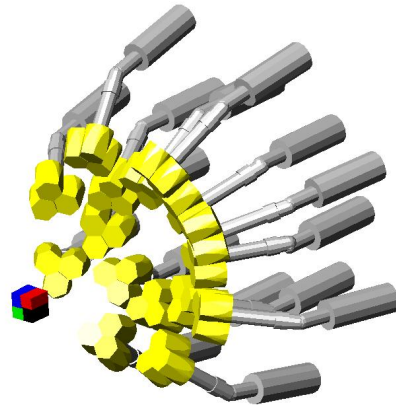


Figure 2.10: Design of the γ -ray spectroscopy setup with 15 germanium cluster detector, each comprising 3 germanium crystals.

Germanium Array An existing germanium-array with refurbished readout is planned to be used for the γ -spectroscopy of the nuclear decay cascades of hypernuclei. The main limitation will be the

load due to neutral or charged particles traversing the germanium detectors. Therefore, readout schemes and tracking algorithms are presently being developed which will enable high resolution γ -spectroscopy in an environment of high particle flux. The germanium-array crystals will be grouped asymmetrically by forming triple clusters. Each cluster consists of three encapsulated n-type Germanium crystals of the Euroball type. The total γ -array set-up consists of 15 triple Germanium clusters positioned at backward axial angle around the target region as shown in Fig. 2.10.

2.2.2 Forward Spectrometer

2.2.2.1 Dipole Magnet

A dipole magnet with a window frame, a 1 m gap, and more than 2 m aperture will be used for the momentum analysis of charged particles in the forward spectrometer. In the current planning, the magnet yoke will occupy about 2.5 m in beam direction starting from 3.5 m downstream of the target. Thus, it covers the entire angular acceptance of the target spectrometer of $\pm 10^\circ$ and $\pm 5^\circ$ in the horizontal and in the vertical direction, respectively. The maximum bending power of the magnet will be 2 Tm and the resulting deflection of the antiproton beam at the maximum momentum of 15 GeV/c will be 2.2° . The design acceptance for charged particles covers a dynamic range of a factor 15 with the detectors downstream of the magnet. For particles with lower momenta, detectors will be placed inside the yoke opening. The beam deflection will be compensated by two correcting dipole magnets, placed around the PANDA detection system.

2.2.2.2 Forward Trackers

The deflection of particle trajectories in the field of the dipole magnet will be measured with a set of wire chambers (either small cell size drift chambers or straw tubes), two placed in front, two within and two behind the dipole magnet. This will allow to track particles with highest momenta as well as very low momentum particles where tracks will curl up inside the magnetic field.

The chambers will contain drift cells of 1 cm width. Each chamber will contain three pairs of detection planes, one pair with vertical wires and two pairs with wires inclined by $+10^\circ$ and -10° . This configuration will allow to reconstruct tracks in each chamber separately, also in case of multi-track events. The beam pipe will pass through central holes in

the chambers. The most central wires will be separately mounted on insulating rings surrounding the beam pipe. The expected momentum resolution of the system for 3 GeV/c protons is $\delta p/p = 0.2\%$ and is limited by the small angle scattering on the chamber wires and gas.

2.2.2.3 Forward Particle Identification

RICH Detector To enable the π/K and K/p separation also at the very highest momenta a RICH detector is proposed. The favoured design is a dual radiator RICH detector similar to the one used at Hermes [15]. Using two radiators, silica aerogel and C_4F_{10} gas, provides $\pi/K/p$ separation in a broad momentum range from 2–15 GeV/c. The two different indices of refraction are 1.0304 and 1.00137, respectively. The total thickness of the detector is reduced to the freon gas radiator (5% X_0), the aerogel radiator (2.8% X_0), and the aluminium window (3% X_0) by using a lightweight mirror focusing the Cherenkov light on an array of photo tubes placed outside the active volume. It has been studied to reuse components of the HERMES RICH.

Time-of-Flight Wall A wall of slabs made of plastic scintillator and read out on both ends by fast photo tubes will serve as time-of-flight stop counter placed at about 7 m from the target. In addition, similar detectors will be placed inside the dipole magnet opening, to detect low momentum particles which do not exit the dipole magnet. The relative time of flight between two charged tracks reaching any of the time-of-flight detectors in the experiment will be measured. The wall in front of the forward spectrometer EMC will consist of vertical strips varying in width from 5 to 10 cm to account for the differences in count rate. With the expected time resolution of $\sigma = 50$ ps π - K and K/p separation on a 3σ level will be possible up to momenta of 2.8 GeV/c and 4.7 GeV/c, respectively.

2.2.2.4 Forward Electromagnetic Calorimeter

For the detection of photons and electrons a Shashlyk-type calorimeter with high resolution and efficiency will be employed. The detection is based on lead-scintillator sandwiches read out with wavelength shifting fibres passing through the block and coupled to photomultipliers. The technique has already been successfully used in the E865 experiment [16]. It has been adopted for various other experiments [17, 18, 19, 20, 21, 22]. An energy resolution of $4\%/\sqrt{E}$ [20] has been achieved. To cover

the forward acceptance, 26 rows and 54 columns are required with a cell size of 55 mm, *i.e.* 1404 modules in total, which will be placed at a distance of 7–8 m from the target.

2.2.2.5 Forward Muon Detectors

For the very forward part of the muon spectrum a further range tracking system consisting of interleaved absorber layers and rectangular aluminium drift-tubes is being designed, similar to the muon system of the target spectrometer, but laid out for higher momenta. The system allows discrimination of pions from muons, detection of pion decays and, with moderate resolution, also the energy determination of neutrons and anti-neutrons.

2.2.3 Luminosity monitor

In order to determine the cross section for physical processes, it is essential to determine the time integrated luminosity L for reactions at the PANDA interaction point that was available while collecting a given data sample. Typically the precision for a relative measurement is higher than for an absolute measurement. For many observables connected to narrow resonance scans a relative measurement might be sufficient for PANDA, but for other observables an absolute determination of L is required. The absolute cross section can be determined from the measured count rate of a specific process with known cross section. In the following we concentrate on elastic antiproton-proton scattering as the reference channel. For most other hadronic processes that will be measured concurrently in PANDA the precision with which the cross section is known is poor.

The optical theorem connects the forward elastic scattering amplitude to the total cross section. The total reaction rate and the differential elastic reaction rate as a function of the 4-momentum transfer t can be used to determine the total cross section.

The differential cross section $d\sigma_{el}/dt$ becomes dominated by Coulomb scattering at very low values of t . Since the electromagnetic amplitude can be precisely calculated, Coulomb elastic scattering allows both the luminosity and total cross section to be determined without measuring the inelastic rate [23].

Due to the 2 T solenoid field and the existence of the MVD it appears most feasible to measure the forward going antiproton in PANDA. The Coulomb-nuclear interference region corresponds to

4-momentum transfers of $-t \approx 0.001 \text{ GeV}^2$ at the beam momentum range of interest to PANDA. At a beam momentum of 6 GeV/ c this momentum transfer corresponds to a scattering angle of the antiproton of about 5 mrad.

The basic concept of the luminosity monitor is to reconstruct the angle (and thus t) of the scattered antiprotons in the polar angle range of 3–8 mrad with respect to the beam axis. Due to the large transverse dimensions of the interaction region when using the pellet target, there is only a weak correlation of the position of the antiproton at e.g. $z = +10.0 \text{ m}$ to the recoil angle. Therefore, it is necessary to reconstruct the angle of the antiproton at the luminosity monitor. As a result the luminosity monitor will consist of a sequence of four planes of double-sided silicon strip detectors located as far downstream and as close to the beam axis as possible. The planes are separated by 20 cm along the beam direction. Each plane consists of 4 wafers (e.g. $2 \text{ cm} \times 5 \text{ cm} \times 200 \mu\text{m}$, with $50 \mu\text{m}$ pitch) arranged radially to the beam axis. Four planes are required for sufficient redundancy and background suppression. The use of 4 wafers (up, down, right, left) in each plane allows systematic errors to be strongly suppressed.

The silicon wafers are located inside a vacuum chamber to minimize scattering of the antiprotons before traversing the 4 tracking planes. The acceptance for the antiproton beam in the HESR is $\pm 3 \text{ mrad}$, corresponding to the 89 mm inner diameter of the beam pipe at the quadrupoles located at about 15 m downstream of the interaction point. The luminosity monitor can be located in the space between the downstream side of the forward spectrometer hadronic calorimeter and the HESR dipole needed to redirect the antiproton beam out of the PANDA chicane back into the direction of the HESR straight stretch (*i.e.* between $z = +10.0 \text{ m}$ and $z = +12.0 \text{ m}$ downstream of the target). At this distance from the target the luminosity monitor needs to measure particles at a radial distance of between 3 and 8 cm from the beam axis. A sketch of the detector concept is given in Fig. 2.11. As pilot simulations show, at a beam momentum of 6.2 GeV/ c the proposed detector measures antiprotons elastically scattered in the range $0.0006 \text{ GeV}^2 < -t < 0.0035 \text{ GeV}^2$, which spans the Coulomb-nuclear interference region. Based upon the granularity of the readout the resolution of t could reach $\sigma_t \approx 0.0001 \text{ GeV}^2$. In reality this value is expected to degrade to $\sigma_t \approx 0.0005 \text{ GeV}^2$ when taking small-angle scattering into account. At the nominal PANDA interaction rate of $2 \cdot 10^7/\text{s}$ there

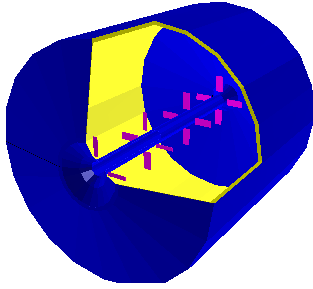


Figure 2.11: Schematic overview of the luminosity monitor concept.

will be an average of 10 kHz/cm^2 in the sensors. In comparison with other experiments an absolute precision of about 3% is considered feasible for this detector concept at \bar{P} ANDA, which will be verified by more detailed simulations.

2.2.4 Data Acquisition

In many contemporary experiments the trigger and data acquisition (DAQ) system is based on a two layer hierarchical approach. A subset of specially instrumented detectors is used to evaluate a first level trigger condition. For the accepted events, the full information of all detectors is then transported to the next higher trigger level or to storage. The available time for the first level decision is usually limited by the buffering capabilities of the front-end electronics. Furthermore, the hard-wired detector connectivity severely constrains both the complexity and the flexibility of the possible trigger schemes.

In \bar{P} ANDA, a data acquisition concept is being developed which is better matched to the high data rates, to the complexity of the experiment and the diversity of physics objectives and the rate capability of at least $2 \cdot 10^7$ events/s.

In our approach, every sub-detector system is a self-triggering entity. Signals are detected autonomously by the sub-systems and are preprocessed. Only the physically relevant information is extracted and transmitted. This requires hit-detection, noise-suppression and clustering at the readout level. The data related to a particle hit, with a substantially reduced rate in the preprocessing step, is marked by a precise time stamp and buffered for further processing. The trigger selection finally occurs in computing nodes which access the buffers via a high-bandwidth network fabric. The new concept provides a high degree of flexi-

bility in the choice of trigger algorithms. It makes trigger conditions available which are outside the capabilities of the standard approach. One obvious example is displaced vertex triggering.

In this scheme, sub-detectors can contribute to the trigger decision on the same footing without restrictions due to hard-wired connectivity. Different physics can be accessed either in parallel or via software reconfiguration of the system.

High speed serial (10 Gb/s per link and beyond) and high-density FPGA (field programmable gate arrays) with large numbers of programmable gates as well as more advanced embedded features are key technologies to be exploited within the DAQ framework.

The basic building blocks of the hardware infrastructure which can be combined in a flexible way to cope with varying demands, are the following:

- Intelligent front-end modules capable of autonomous hit detection and data preprocessing (e.g. clustering, hit time reconstruction, and pattern recognition) are needed.
- A precise time distribution system is mandatory to provide a clock norm from which all time stamps can be derived. Without this, data from subsystems cannot be correlated.
- Data concentrators provide point-to-point communication, typically via optical links, buffering and online data manipulation.
- Compute nodes aggregate large amounts of computing power in a specialized architecture rather than through commodity PC hardware. They may employ fast FPGAs (Fast Programmable Gate Arrays), DSPs (Digital Signal Processors), or other computing units. The nodes have to deal with feature extraction, association of data fragments to events, and, finally, event selection.

A major component providing the link for all building blocks is the network fabric. Here, special emphasis is put on embedded switches which can be cascaded and reconfigured to reroute traffic for different physics selection topologies. Alternatively, with an even higher aggregate bandwidth of the network, which according to projections of network speed evolution will be available by the time the experiment will start, a flat network topology where all data is transferred directly to processing nodes may be feasible as well. This requires a higher total bandwidth but would have a simpler architecture and allow event selection in a single environment.

The bandwidth required in this case would be at least 200 GB/s. After event selection in the order of 100-200 MB/s will be saved to mass storage.

An important requirement for this scheme is that all detectors perform a continuous online calibration with data. The normal data taking is interleaved with special calibration runs. For the monitoring of the quality of data, calibration constants and event selection a small fraction of unfiltered raw data is transmitted to mass storage.

To facilitate the association of data fragments to events the beam structure of the accelerator is exploited: Every 1.8 μ s there is a gap of about 400 ns needed for the compensation of energy loss with a bucket barrier cavity. This gap provides a clean division between consistent data blocks which can be processed coherently by one processing unit.

2.2.5 Infrastructure

The target for antiproton physics is located in the straight section at the east side of the HESR. At this location an experimental hall of 43 m \times 29 m floor space and 14.5 m height is planned (see Fig. 2.12). A concrete radiation shield of 2 m thickness on both sides along the beam line is covered by concrete bars of 1 m thickness to suppress the neutron sky shine. Within the elongated concrete cave the $\bar{\text{PANDA}}$ detector together with auxiliary equipment, beam steering, and focusing elements will be housed. The roof of the cave can be opened and heavy components hoisted by crane. The shielded beam line area for the $\bar{\text{PANDA}}$ experiment including dipoles and focusing elements is foreseen to have 37 m \times 9.4 m floor space and a height of 8.5 m with the beam line at a height of 3.5 m. The general floor level of the HESR is 2 m higher. This level will be kept for a length of 4 m in the north of the hall (right part in Fig. 2.12), to facilitate transport of heavy equipment into the HESR tunnel.

The target spectrometer with electronics and supplies will be mounted on rails which makes it retractable to a parking position outside the HESR beam line *i.e.* into the lower part of the hall in Fig. 2.12). The experimental hall provides additional space for delivery of components and assembly of the detector parts. In the south corner of the hall, a counting house complex with five floors is foreseen. The lowest floor will contain various supplies for power, high voltage, cooling water, gases *etc.*. The next level is planned for readout electronics including data concentrators. The third level will house the online computing farm. The fourth floor is at level with the surrounding ground and

will house the control room, a meeting room and social rooms for the shift crew. Above this floor, hall electricity supplies and ventilation is placed. A crane (15 t) spans the whole area with a hook at a height of about 10 m. Sufficient (300 kW) electric power will be available.

Liquid helium coolant may come from the main cryogenic liquefier for the SIS rings. Alternatively, a separate small liquefier (50 W cooling power at 4 K) would be mounted. The temperature of the building will be moderately controlled. The more stringent requirements with respect to temperature and humidity for the detectors have to be maintained locally. To facilitate cooling and avoid condensation the target spectrometer will be kept in a tent with dry air at a controlled temperature.

2.3 The HESR

COMMENT: Author(s): A. Lehrach

by two long straight sections. One straight section will mainly be occupied by the electron cooler. The other section will host the experimental installation with internal H₂ pellet target, RF cavities, injection kickers and septa (see Fig. 2.13). For stochastic cooling pickup (P) and kicker (K) tanks are also located in the straight sections, opposite to each other. Special requirements for the lattice are dispersion free straight sections and small betatron amplitudes in the range of a few meters at the internal interaction point. In addition the betatron amplitudes at the electron cooler are adjustable within a large range.

Table 2.1 summarizes the specified injection parameters, experimental requirements and operation modes.

2.3.2 Beam Equilibria and Luminosity Estimates

The equilibrium beam parameters are most important for the high-resolution mode. Calculations of beam equilibria for beam cooling, intra-beam scattering and beam-target interaction are being performed utilizing different simulation codes like BETACOOOL (JINR, Dubna), MOCAC (ITEP, Moscow), and PTARGET (GSI, Darmstadt). Cooled beam equilibria calculations including special features of pellet targets have been carried out with a simulation code based on PTARGET.

2.3.1 A quick description of the HESR

The HESR is being realized by a consortium consisting of IKP at Forschungszentrum Jülich, TSL at Uppsala University, and GSI Darmstadt [24]. An important feature of this new facility is the combination of phase-space cooled beams and dense internal targets, comprising challenging beam parameters in two operation modes: high-luminosity mode with beam intensities up to 10^{11} , and high-resolution mode with a momentum spread down to a few times 10^{-5} , respectively. Powerful electron and stochastic cooling systems are necessary to meet the experimental requirements.

The HESR lattice is designed as a racetrack shaped ring, consisting of two 180° arc sections connected

2.3.2.1 Beam equilibria with Electron Cooling

An electron beam with up to 1 A current, accelerated in special accelerator columns to energies in the range of 0.4 to 4.5 MeV is proposed for the HESR. Since the design is modular it facilitates future increase of the high voltage to 8 MV. The 22 m long solenoidal field in the cooler section has a longitudinal field strength of 0.2 T with a magnetic field straightness on the order of 10^{-5} [24]. This arrangement allows beam cooling for beam momentum between 1.5 GeV/c and 8.9 GeV/c.

To simulate the dynamics of the core particles, an analytic “rms” model was applied [25]. The empirical magnetized cooling force formula by V. V. Parkhomchuk for electron cooling [26] and an analytical description for intra-beam scattering [27] was used. Beam heating by beam-target interaction is described by transverse and longitudinal emittance growth due to Coulomb scattering and energy straggling, respectively [28, 29]. In the HR mode,

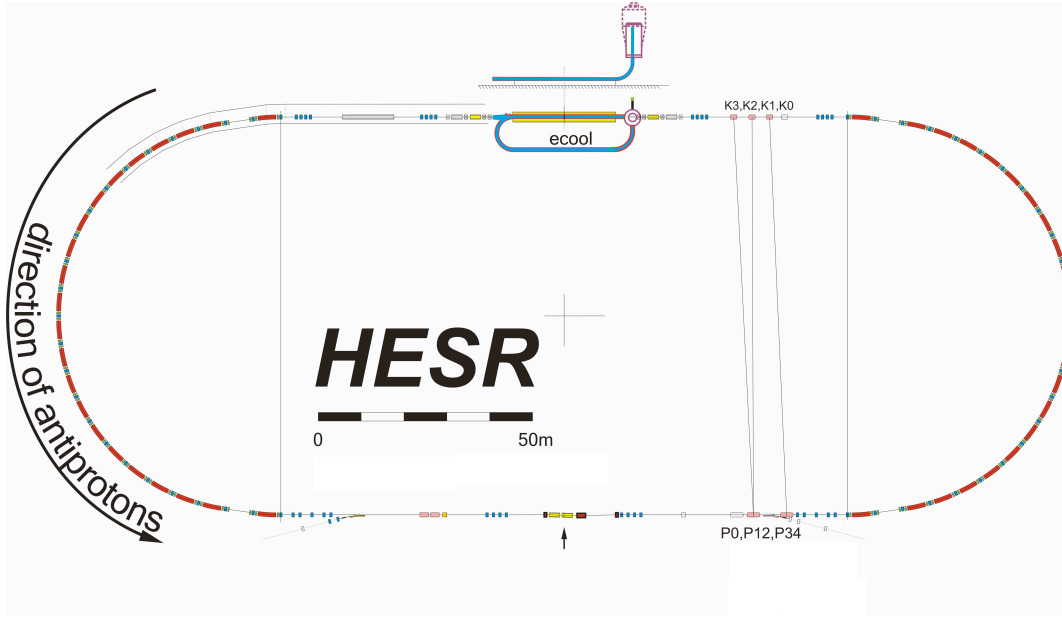


Figure 2.13: Schematic view of the HESR. Tentative positions for injection, cooling devices and experimental installations are indicated.

Injection Parameters	
Transverse emittance	0.25 mm · mrad (normalized, rms) for $3.5 \cdot 10^{10}$ particles, scaling with number of accumulated particles: $\varepsilon_{\perp} \sim N^{4/5}$
Relative momentum spread	$3.3 \cdot 10^{-4}$ (normalized, rms) for $3.5 \cdot 10^{10}$ particles, scaling with number of accumulated particles: $\sigma_p/p \sim N^{2/5}$
Bunch length	150 m
Injection Momentum	3.8 GeV/c
Injection	Kicker injection using multi-harmonic RF cavities
Experimental Requirements	
Ion species	Antiprotons
\bar{p} production rate	$2 \cdot 10^7$ /s ($1.2 \cdot 10^{10}$ per 10 min)
Momentum / Kinetic energy range	1.5 to 15 GeV/c / 0.83 to 14.1 GeV
Number of particles	10^{10} to 10^{11}
Target thickness	$4 \cdot 10^{15}$ atoms/cm ² (H ₂ pellets)
Transverse emittance	< 1 mm · mrad
Betatron amplitude E-Cooler	25–200 m
Betatron amplitude at IP	1–15 m
Operation Modes	
High resolution (HR)	Luminosity of $2 \cdot 10^{31}$ cm ⁻² s ⁻¹ for 10^{10} \bar{p} rms momentum spread $\sigma_p/p \leq 2 \cdot 10^{-5}$, 1.5 to 9 GeV/c, electron cooling up to 9 GeV/c
High luminosity (HL)	Luminosity of $2 \cdot 10^{32}$ cm ⁻² s ⁻¹ for 10^{11} \bar{p} rms momentum spread $\sigma_p/p \sim 10^{-4}$, 1.5 to 15 GeV/c, stochastic cooling above 3.8 GeV/c

Table 2.1: Injection parameters, experimental requirements and operation modes.

rms relative momentum spreads are 7.9×10^{-6} at 1.5 GeV/c, 2.7×10^{-5} at 8.9 GeV/c, and 1.2×10^{-4} at 15 GeV/c [30].

Heating process	$(\tau_{\text{loss}}^{-1}) / \text{s}^{-1}$		
	1.5 GeV/c	9 GeV/c	15 GeV/c
Hadronic Interaction	$1.8 \cdot 10^{-4}$	$1.2 \cdot 10^{-4}$	$1.1 \cdot 10^{-4}$
Single Coulomb	$2.9 \cdot 10^{-4}$	$6.8 \cdot 10^{-6}$	$2.4 \cdot 10^{-6}$
Energy Straggling	$1.3 \cdot 10^{-4}$	$4.1 \cdot 10^{-5}$	$2.8 \cdot 10^{-5}$
Touschek Effect	$4.9 \cdot 10^{-5}$	$2.3 \cdot 10^{-7}$	$4.9 \cdot 10^{-8}$
Total relative loss rate	$6.5 \cdot 10^{-4}$	$1.7 \cdot 10^{-4}$	$1.4 \cdot 10^{-4}$
$1/e$ beam lifetime $t_{\bar{p}} / \text{s}$	~ 1540	~ 6000	~ 7100
$L_{\text{max}} / 10^{32} \text{ cm}^{-2} \text{ s}^{-1}$	0.82	3.22	3.93

Table 2.2: Upper limit for relative beam loss rate, $1/e$ beam lifetime $t_{\bar{p}}$, and maximum average luminosity L_{max} for a H_2 pellet target.

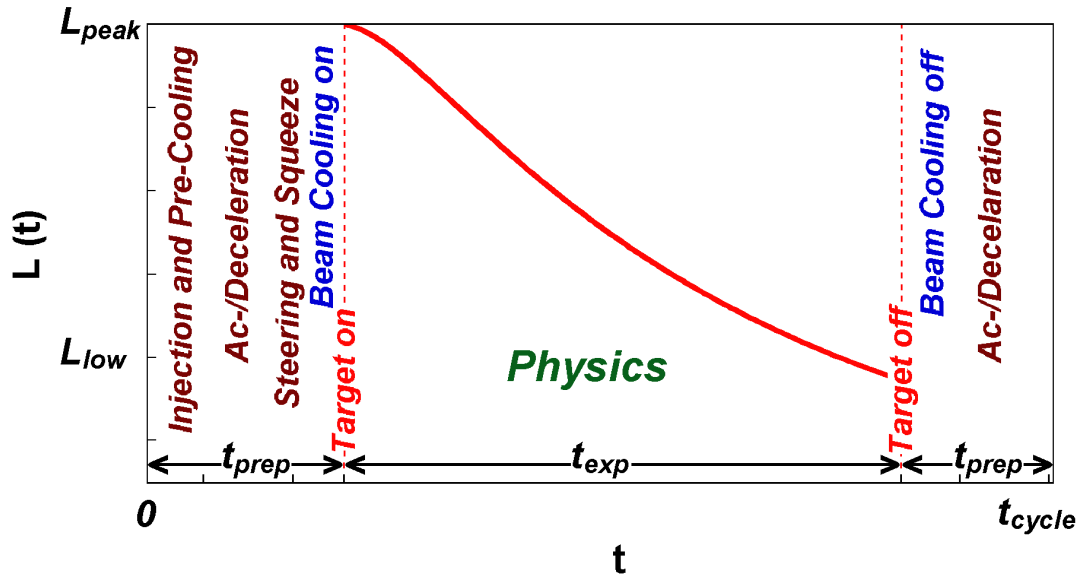


Figure 2.14: Time dependent luminosity during the cycle $L(t)$ versus the time in the cycle. Different measures for beam preparation are indicated.

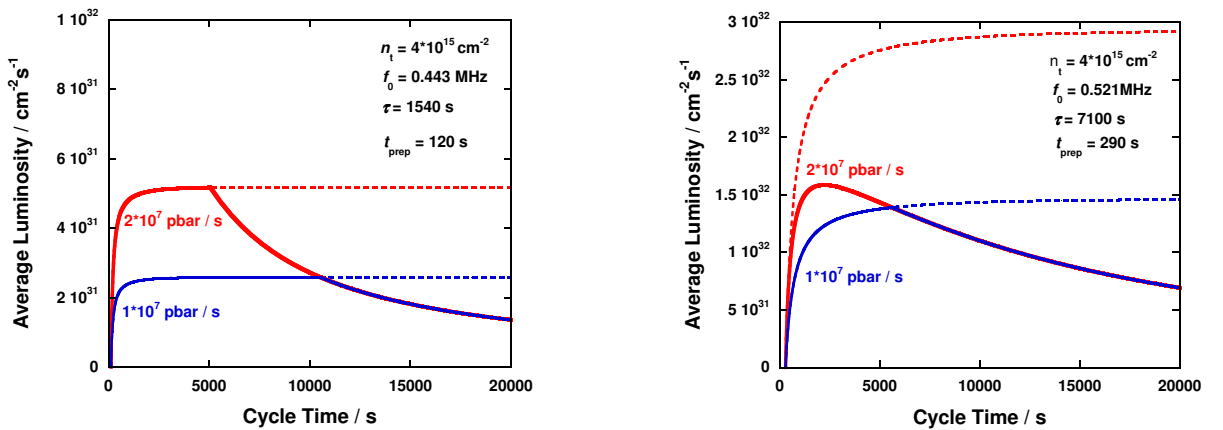


Figure 2.15: Cycle average luminosity vs. cycle time at 1.5 (left) and 15 GeV/c (right). The maximum number of particles is limited to 10^{11} (solid line), and unlimited (dashed lines).

2.3.2.2 Beam Equilibria with Stochastic Cooling

kickers with a band-width of 2 – 4 GHz and the

The main stochastic cooling parameters were determined for a cooling system utilizing pickups and

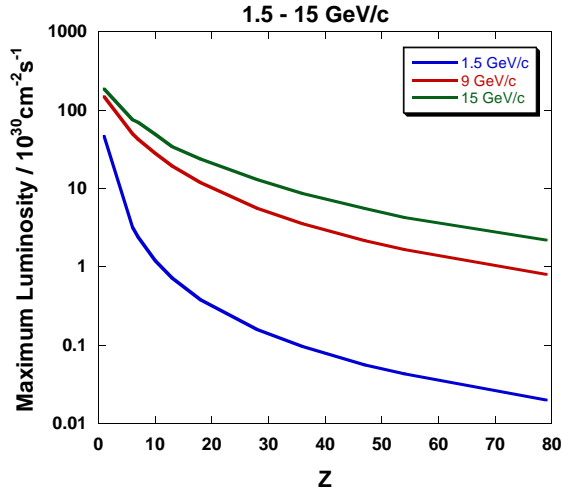


Figure 2.16: Maximum average luminosity L_{\max} vs. atomic charge Z for three different beam momenta.

option for an extension to 4 – 6 GHz. Stochastic cooling is presently specified above 3.8 GeV/c [31]. Beam equilibria have been simulated based on a Fokker-Planck approach. Applying stochastic cooling, one can achieve rms relative momentum spreads of 5.1×10^{-5} at 3.8 GeV/c, 5.4×10^{-5} at 8.9 GeV/c, and 3.9×10^{-5} at 15 GeV/c for the HR mode. With a combination of electron and stochastic cooling the beam equilibria can be further improved. In the HL mode, rms relative momentum spread of roughly 10^{-4} can be expected. Transverse stochastic cooling can be adjusted independently to ensure sufficient beam-target overlap.

2.3.2.3 Beam Losses and Luminosity Estimates

Beam losses are the main restriction for high luminosities, since the antiproton production rate is limited. Three dominating contributions of beam-target interaction have been identified: Hadronic interaction, single Coulomb scattering and energy straggling of the circulating beam in the target. In addition, single intra-beam scattering due to the Touschek effect has also to be considered for beam lifetime estimates. Beam losses due to residual gas scattering can be neglected compared to beam-target interaction, if the vacuum is better than 10^{-9} mbar. A detailed analysis of all beam loss processes can be found in [32, 33].

2.3.2.4 Beam lifetime

The relative beam loss rate for the total cross section σ_{tot} is given by the expression

$$(\tau_{\text{loss}}^{-1}) = n_t \sigma_{\text{tot}} f_0 \quad (2.1)$$

where $(\tau_{\text{loss}}^{-1})$ is the relative beam loss rate, n_t the target thickness and f_0 the reference particle's revolution frequency. In Table 2.2 the upper limit for beam losses and corresponding lifetimes are listed for a transverse beam emittance of $1 \text{ mm} \cdot \text{mrad}$, a longitudinal ring acceptance of $\Delta p/p = \pm 10^{-3}$ and 10^{11} circulating particles in the ring.

For beam-target interaction, the beam lifetime is independent of the beam intensity, whereas for the Touschek effect it depends on the beam equilibria and beam intensity. Beam lifetimes are ranging from 1540s to 7100s. Beam lifetimes at low momenta strongly depend on the beam cooling scenario and the ring acceptance. Beam losses corresponding to beam lifetimes below half an hour obviously cannot be compensated by the antiproton production rate.

2.3.2.5 Luminosity Considerations for Hydrogen-Pellet Targets

The maximum average luminosity depends on the antiproton production rate $dN_{\bar{p}}/dt = 2 \cdot 10^7 / \text{s}$ and loss rate

$$L_{\max} = \frac{dN_{\bar{p}}/dt}{\sigma_{\text{tot}}} \quad (2.2)$$

and is also given in Table 2.2 for different beam momenta. The maximum average luminosity for 1.5 GeV/c is below the specified value for the HL mode.

To calculate the cycle average luminosity, machine cycles and beam preparation times have to be specified. After injection, the beam is pre-cooled to equilibrium (with target off) at 3.8 GeV/c. The beam is then accelerated or decelerated to the desired beam momentum. A maximum ramp rate of 25 mT/s is specified. After reaching the final momentum, beam steering and focusing in the target and beam cooler region takes place. The total beam preparation time t_{prep} ranges from 120s for 1.5 GeV/c to 290s for 15 GeV/c. A typical example for the evolution of the luminosity during a cycle is plotted in Fig. 2.14 versus the time in the cycle.

In the high-luminosity mode, particles should be re-used in the next cycle. Therefore the used beam is transferred back to the injection momentum and merged with the newly injected beam. A bucket

scheme utilizing broad-band cavities is foreseen for beam injection and the refill procedure. During acceleration 1% and during deceleration 5% beam losses are assumed. The cycle average luminosity reads

$$\bar{L} = f_0 N_{i,0} n_t \frac{\tau [1 - e^{-t_{\text{exp}}/\tau}]}{t_{\text{exp}} + t_{\text{prep}}} \quad (2.3)$$

where τ is the $1/e$ beam lifetime, t_{exp} the experimental time (beam on target time), and t_{cycle} the total time of the cycle, with $t_{\text{cycle}} = t_{\text{exp}} + t_{\text{prep}}$. The dependence of the cycle average luminosity on the cycle time is shown for different antiproton production rates in Fig. 2.15.

With limited number of antiprotons of 10^{11} , as specified for the high-luminosity mode, cycle average luminosities of up to $1.6 \cdot 10^{32} \text{ cm}^{-2} \text{ s}^{-1}$ can be achieved at 15 GeV/c for cycle times of less than one beam lifetime. If one does not restrict the number of available particles, cycle times should be longer to reach maximum average luminosities close to $3 \cdot 10^{32} \text{ cm}^{-2} \text{ s}^{-1}$. This is a theoretical upper limit, since the larger momentum spread of the injected beam would lead to higher beam losses during injection due to the limited longitudinal ring acceptance. For the lowest momentum, more than 10^{11} particles can not be provided in average, due to very short beam lifetimes. As expected, cycle average luminosities are below $10^{32} \text{ cm}^{-2} \text{ s}^{-1}$.

2.3.2.6 Luminosity Considerations for Nuclear Targets

The hadronic cross section for the interaction of antiprotons with nuclear targets can be estimated from geometric considerations. Starting from the antiproton-proton hadronic cross section $\sigma_{\text{H}}^{\bar{\text{p}}\text{p}}$ for 1.5 GeV/c

$$\sigma_{\text{H}}^{\bar{\text{p}}\text{p}} \approx 100 \text{ mbarn} := \pi r_{\text{p}}^2$$

with the proton radius of $r_{\text{p}} = 0.9 \text{ fm}$, the antiproton-nucleus hadronic cross section can be deduced to be

$$\sigma_{\text{H}}^{\bar{\text{p}}\text{A}} = \pi (R_{\text{A}} + r_{\text{p}})^2. \quad (2.4)$$

The radius of a spherical nucleus as a first approximation reads $R_{\text{A}} = r_0 A^{1/3}$, with $r_0 = 1.2 \text{ fm}$ and the mass number A . The total hadronic cross section decreases with the beam momentum from 100, 60 to 50 mb for hydrogen targets at 1.5, 9, and 15 GeV/c, respectively. The cross sections for nuclear targets is scaled with beam momentum accordingly [34]. To evaluate beam losses also single

Coulomb scattering and energy straggling of the circulating beam in the target have been calculated [35]. Fig. 2.16 shows maximum average luminosities for nuclear targets under the same conditions as for hydrogen targets.

For the specified antiproton production rate maximum average luminosities of $5 \cdot 10^{31}$, $4 \cdot 10^{29}$ to $4 \cdot 10^{28} \text{ cm}^{-2} \cdot \text{s}^{-1}$ (deuterium, argon to gold) are achieved at 1.5 GeV/c beam momentum. For maximum beam momentum of 15 GeV/c the maximum average luminosities increase by more than one order of magnitude to $1.9 \cdot 10^{32}$, $2.4 \cdot 10^{31}$ to $2.2 \cdot 10^{30} \text{ cm}^{-2} \cdot \text{s}^{-1}$ (deuterium, argon to gold) for 10^{11} circulating antiprotons.

In order to reach these values an effective target thickness of $3.6 \cdot 10^{15} \text{ atoms/cm}^2$ for a deuterium target, $4.6 \cdot 10^{14} \text{ atoms/cm}^2$ for an argon target to $4.1 \cdot 10^{13} \text{ atoms/cm}^2$ for gold at $10^{11} \bar{\text{p}}$ is required. The optimum effective target thickness can be adjusted by proper beam focussing and steering onto the target.

2.4 Precision measurements of resonance parameters

COMMENT: Author(s): G. Stancari

The study of resonances is an important part of the PANDA physics program. Masses, widths and decay fractions are measured by scanning the beam energy across the resonance under study. In antiproton-proton annihilations, there are two main advantages over inclusive production: (a) resonances can be formed directly; (b) the detector is used as an event counter (y axis of the excitation curve), while the energy determination (x axis) relies entirely on the precisely-calibrated and cooled antiproton beam.

This is an area where a close interplay between machine and detector is needed, and this is why this discussion is included here. In this section, we describe the technique of resonance scans for precise determination of resonance parameters. A discussion of the main sources of uncertainty is given, as it is an important input for the following physics chapters. The issue of determining line shapes is also briefly addressed.

Much of the discussion is based upon E835 experience with charmonium resonances [36, 37]. We assume Breit-Wigner resonant shapes and constant backgrounds, but the analysis can be easily extended to more general cases.

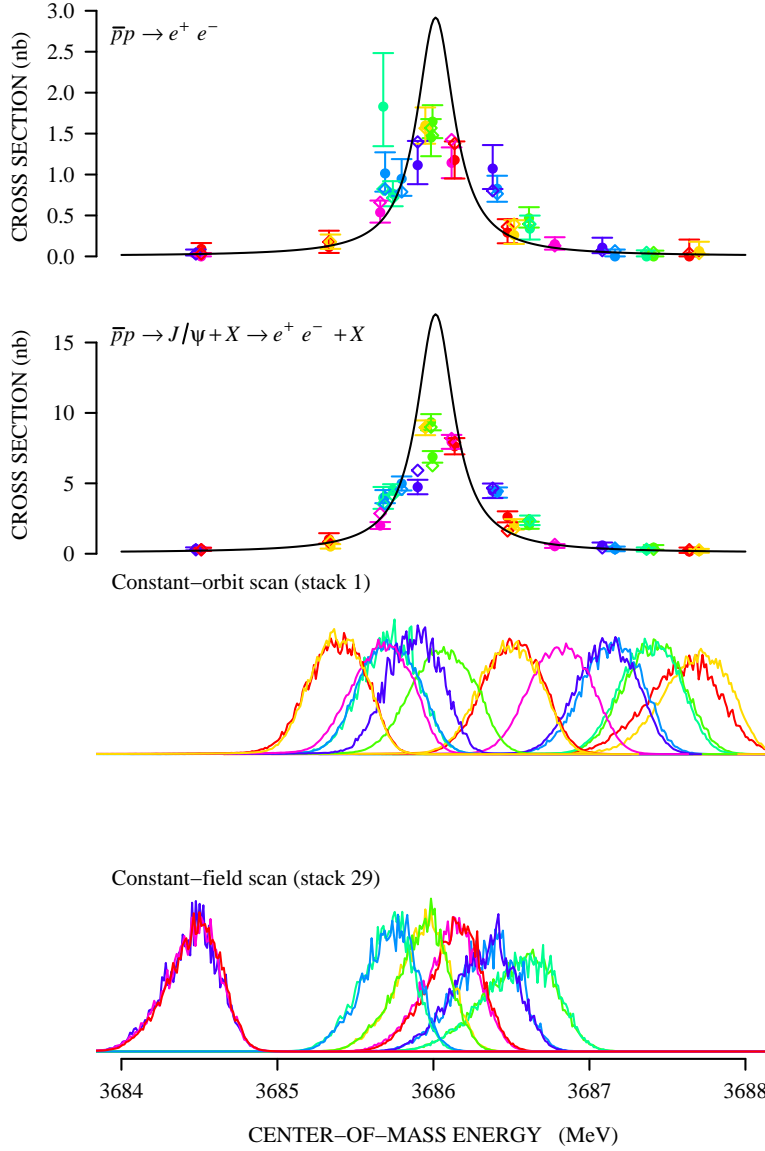


Figure 2.17: $\psi(2S)$ resonance scans: the observed cross section (excitation curve) for each channel (filled dots); the expected cross section from the fit (open diamonds); the ‘bare’ resonance curves σ_{BW} from the fit (solid lines). The two bottom plots show the normalized energy distributions B_i (from Ref. [37]).

	statistical	systematic
mass M	3 keV	– J/ψ or $\psi(2S)$ mass from resonant depolarization: 10 keV – ΔL : 5 keV (single scan), 100 keV (scans at different energies)
width Γ	1.9 %	– η : $\sim 5\%$ – ΔL (BPM noise): ~ 5 keV
‘area’ $\Gamma_{\text{in}}\Gamma_{\text{out}}/\Gamma$	1.5 %	– efficiency: a few % – luminosity: a few %

Table 2.3: Summary of the sources of uncertainty in the resonance parameters. Statistical errors refer to $\mathcal{N} \equiv \varepsilon\mathcal{L}\sigma = 10^4$ and scale as $1/\sqrt{\mathcal{N}}$. It is assumed that the luminosity distribution is optimized and that the beam width is negligible, and so they represent lower limits for a given \mathcal{N} .

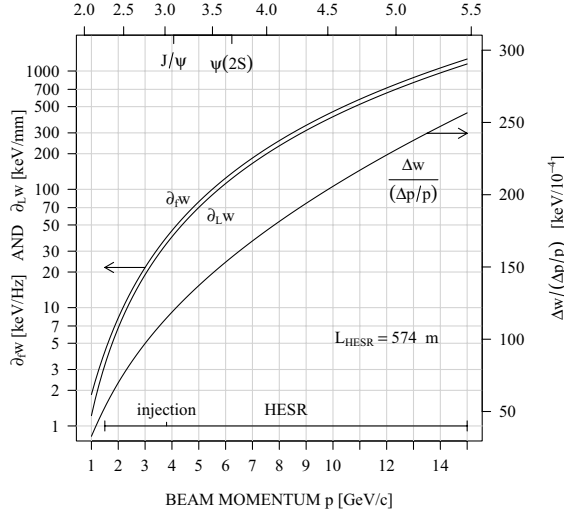


Figure 2.18: Kinematical factors used in the determination of the center-of-mass energy from the velocity of antiprotons in the rf bucket. Left vertical axis: partial derivatives of the center-of-mass energy w with respect to revolution frequency f and orbit length L . Right vertical axis: energy spread in the center of mass Δw for a given momentum spread $\Delta p/p$.

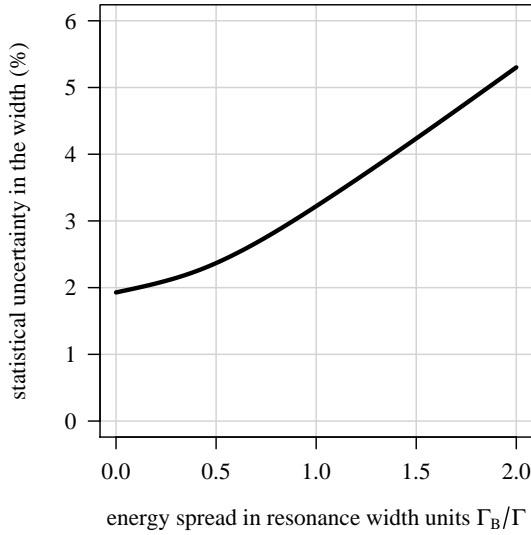


Figure 2.19: Statistical uncertainty in the resonance width as a function of the ratio between energy spread (Gaussian FWHM Γ_B) and resonance width Γ . The amount of data is $\mathcal{N} \equiv \varepsilon \mathcal{L} \sigma_p = 10^4$ in this example. An optimal luminosity distribution is assumed.

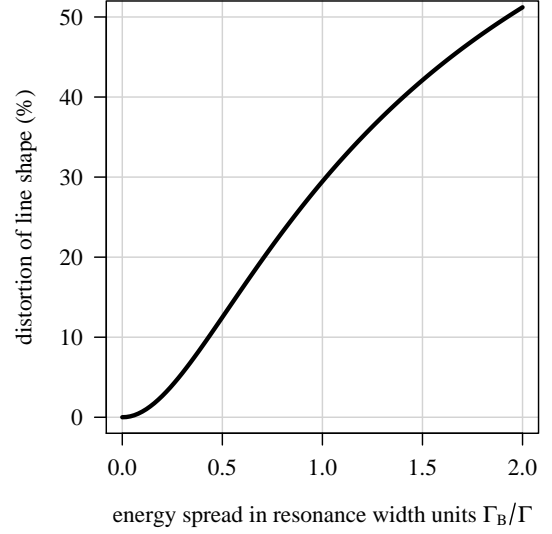


Figure 2.20: Distortion of the resonance shape as a function of the ratio between energy spread (Gaussian FWHM Γ_B) and resonance width Γ .

2.4.1 Experimental technique

The resonance parameters are determined from a maximum-likelihood fit to the excitation curve (Fig. 2.17). For each data-taking run (subscript i), we assume that the average number of observed events μ_i in each channel depends on a Breit-Wigner cross section σ_{BW_r} and on the center-of-mass energy distribution, B_i , as follows:

$$\mu_i = \varepsilon_i \mathcal{L}_i \left[\int \sigma_{\text{BW}_r}(w) B_i(w) dw + \sigma_{\text{bkg}} \right], \quad (2.5)$$

where w is the center-of-mass energy, ε_i is the detector efficiency, \mathcal{L}_i is the integrated luminosity, and σ_{bkg} is a constant background cross section. The integral is extended over the energy acceptance of the machine. The spin-averaged Breit-Wigner cross section for a spin- J resonance of mass M and width Γ formed in $\bar{p}p$ annihilations is

$$\sigma_{\text{BW}}(w) = \frac{(2J+1)}{(2S+1)^2} \frac{16\pi}{w^2 - 4m^2} \frac{(\Gamma_{\text{in}}\Gamma_{\text{out}}/\Gamma) \cdot \Gamma}{\Gamma^2 + 4(w-M)^2}; \quad (2.6)$$

m and S are the (anti)proton mass and spin, while Γ_{in} and Γ_{out} are the partial resonance widths for the entrance ($\bar{p}p$, in our case) and exit channels. The Breit-Wigner cross section is corrected

for initial-state radiation to obtain σ_{BWR} [38, 39]:

$$\begin{aligned} \sigma_{\text{BWR}}(w) = & \\ & b \int_0^{w/2} \frac{dk}{k} \left(\frac{2k}{w}\right)^b \sigma_{\text{BW}}(\sqrt{w^2 - 2kw}) = \\ & (2/w)^b \int_0^{(w/2)^b} dt \sigma_{\text{BW}}(\sqrt{w^2 - 2t^{1/b}w}), \end{aligned}$$

where the second form is more suitable for numerical integration and $b(w)$ is the semiclassical collinearity factor [39], equal to 0.00753 at the $\psi(2S)$.

The resonance mass M , width Γ , ‘area’ $A \equiv (\Gamma_{\text{in}}\Gamma_{\text{out}}/\Gamma)$ and the background cross section σ_{bkg} are left as free parameters in the maximization of the log-likelihood function $\log(\Lambda) = \sum_i \log P(\mu_i, N_i)$, where $P(\mu, N)$ are Poisson probabilities of observing N events when the mean is μ . N_i are the observed number of events, and $\sigma_i \equiv N_i/(\varepsilon_i \mathcal{L}_i)$ is the observed cross section. The area parameter is usually chosen in the parameterization of the resonance shape because it is proportional to the total number of events in each channel. It is less correlated with the width than the product of branching fractions.

The detector determines the cross section (y -axis) measurements and their uncertainty. Here we focus on energy measurements (x -axis), their uncertainty and their impact on the determination of resonance parameters through B_i .

2.4.2 Mass measurements

The center-of-mass energy distribution $B_i(w)$ of the $\bar{p}p$ system can be determined from the velocity of the antiproton beam, since revolution frequencies and orbit lengths can be measured very precisely.

The revolution-frequency distribution of the antiprotons can be measured by detecting the Schottky noise signal generated by the coasting beam. The signal is sensed by a longitudinal Schottky pickup and recorded on a spectrum analyzer. An accuracy of 0.05 Hz can be achieved on a revolution frequency of 0.52 MHz, over a wide dynamic range in intensity (60 dBm), using commercial spectrum analyzers.

The beam is slightly bunched by an rf cavity operating at $f^{\text{cav}} \sim 0.52$ MHz, the first harmonic ($h = 1$) of the revolution frequency. The beam is bunched both for stability (ion clearing) and for making the beam position monitors (BPMs) sensitive to a portion of the beam. Therefore, recorded orbits refer to particles bunched by the rf system, and their revolu-

tion frequency is $f^{\text{rf}} = f^{\text{cav}}/h$. The bunched-beam revolution frequency f^{rf} is usually close to the average revolution frequency of the beam. Each orbit consists of several horizontal and vertical readings. BPM noise is an important consideration for precision energy measurements.

From the BPM readings and the HESR lattice model, differences ΔL in the length of one orbit and another can be calculated accurately. The main systematic uncertainties come from lattice differences, from BPM calibrations, from bend-field drifts, and from neglecting second-order terms in the orbit length. In the Fermilab Antiproton Accumulator, the systematic uncertainty in ΔL was estimated to be 0.05 mm out of 474 m during the E835 run within a single $\psi(2S)$ scan [37], and about 1 mm over the entire run.

The absolute length L of an orbit can be calculated from a reference orbit of length L_0 : $L = L_0 + \Delta L$. The calibration of L_0 is done by scanning a resonance (the $\psi(2S)$, for instance) the mass of which is precisely known from the resonant-depolarization method in e^+e^- experiments [40].

For particles in the bunched portion of the beam (rf bucket), the relativistic parameters β^{rf} and γ^{rf} are calculated from their velocity $v^{\text{rf}} = f^{\text{rf}} \cdot L$, from which the center-of-mass energy w of the $\bar{p}p$ system is calculated: $w^{\text{rf}} = w(f^{\text{rf}}, L) \equiv m\sqrt{2(1 + \gamma^{\text{rf}})}$. (The superscript rf is omitted from orbit lengths because they always refer to particles in the rf bucket.) In the charmonium region, this method yields good accuracies on w . Figure 2.18 shows the magnitude of the partial derivatives of w with respect to f^{rf} and L , $\partial_{f^{\text{rf}}}w$ and $\partial_L w$. Being based upon velocity measurements, the precision is quickly degraded as the beam energy increases. At constant L and relativistic energies, the partial derivatives scale as the fifth power of the center-of-mass energy: $\partial_{f,L}w \sim w^5$. From the uncertainties in the orbit length and in the revolution frequency, it is reasonable to expect absolute measurements of the beam energy with an uncertainty of the order of 0.1 MeV in the charmonium region.

2.4.3 Total and partial widths

For width and area determinations, energy differences are crucial, and they must be determined precisely. During normal data taking, the beam is kept near the central orbit of the machine. A particular run is chosen as the reference (subscript 0). Energy differences between the reference run and other runs in the scan (subscript i), for particles in the rf

bucket, are simply

$$w_i^{\text{rf}} - w_0^{\text{rf}} = w(f_i^{\text{rf}}, L_0 + \Delta L_i) - w(f_0^{\text{rf}}, L_0). \quad (2.7)$$

Within the energy range of a resonance scan, these differences are largely independent of the choice of L_0 . For this reason, the absolute energy calibration is irrelevant for width and area measurements. Only uncertainties coming from ΔL are to be considered.

Once the energy w_i^{rf} for particles in the rf bucket is known, the complete energy distribution is obtained from the Schottky spectrum using the relation between frequency differences and momentum differences at constant magnetic field:

$$\frac{\Delta p}{p} = -\frac{1}{\eta} \frac{\Delta f}{f}, \quad (2.8)$$

where η is the energy-dependent phase-slip factor of the machine, which is one of the parameters governing synchrotron oscillations. (The dependence of η on beam energy is chosen during lattice design; the variation of η within a scan can usually be neglected.) In terms of the center-of-mass energy,

$$w - w_i^{\text{rf}} = -\frac{1}{\eta} \frac{(\beta_i^{\text{rf}})^2 (\gamma_i^{\text{rf}})^2 m^2 f - f_i^{\text{rf}}}{w_i^{\text{rf}} f_i^{\text{rf}}}. \quad (2.9)$$

Within a run, rf frequencies, beam-frequency spectra, and BPM readings are to be updated frequently with respect to expected variations in energy or luminosity. Frequency spectra can then translated into center-of-mass energy through Eq. 2.9, weighted by luminosity and summed, to obtain the luminosity-weighted normalized energy spectra $B_i(w)$ for each data-taking run.

The phase-slip factor is usually determined from the slope of the measured synchrotron frequency f_s as a function of rf voltage settings V^{rf} :

$$f_s^2 = -\frac{\eta \cos \phi_s (f^{\text{rf}})^2 q V^{\text{rf}}}{2\pi h \beta^2 E_s}, \quad (2.10)$$

where ϕ_s is the synchronous phase, q is the particles' charge, E_s their energy and β^2 is the relativistic factor. The main uncertainty comes from the absolute calibration of the rf voltage and it is usually of the order of a few percent.

The resonance width and area are affected by a systematic error due to the uncertainty in η . This effect is most noticeable when the beam width is not negligible compared to the resonance width. Usually, the resonance width and area are positively correlated with the phase-slip factor. A larger η implies a narrower energy spectrum, as described

in Eq. 2.9. As a consequence, the fitted resonance will more closely resemble the measured excitation curve, yielding a larger resonance width.

For precision measurements, one needs a better estimate of the phase-slip factor or determinations that are independent of η , or both. In E760, the ‘double scan’ technique was used [38]. It yielded η with an uncertainty of 6% at the $\psi(2S)$ and width determinations largely independent of the phase-slip factor, but it had the disadvantage of being operationally complex. For E835, a new method of ‘complementary scans’ was developed [37]. It resulted in a similar precision on η and arbitrarily small correlations between resonance parameters and phase-slip factor; the technique is also operationally simpler.

The resonance is scanned once on the central orbit, as described above. A second scan is then performed at constant magnetic bend field. The energy of the beam is changed by moving the longitudinal stochastic-cooling pickups. The beam moves away from the central orbit, and the range of energies is limited but appropriate for narrow resonances.

Since the magnetic field is constant, beam-energy differences can be calculated independently of ΔL , directly from the revolution-frequency spectra and the phase-slip factor, according to Eq. 2.9. A pivot run is chosen (subscript p). The rf frequency of this run is used as a reference to calculate the energy for particles in the rf bucket in other runs. These particles have revolution frequency f_i^{rf} and the energy is calculated as follows:

$$w_i^{\text{rf}} - w_p^{\text{rf}} = -\frac{1}{\eta} \frac{(\beta_p^{\text{rf}})^2 (\gamma_p^{\text{rf}})^2 m^2 f_i^{\text{rf}} - f_p^{\text{rf}}}{w_p^{\text{rf}} f_p^{\text{rf}}}. \quad (2.11)$$

For the scan at constant magnetic field, this relation is used instead of Eq. 2.7. Once the energy for particles at f_i^{rf} is known, the full energy spectrum within each run is obtained from Eq. 2.9, as usual. For the constant-field scan, the energy distributions may be obtained directly from the pivot energy by calculating $w - w_p^{\text{rf}}$, instead of using Eq. 2.11 first and then Eq. 2.9. The two-step procedure is chosen because it is faster to rescale the energy spectra than to re-calculate them from the frequency spectra when fitting for η . Numerically, the difference between the two calculations is negligible. Moreover, the two-step procedure exposes how the width depends on η .

Using this alternative energy measurement, the width and area determined from scans at constant magnetic field are negatively correlated with η . The increasing width with increasing η is still present, as it is in scans at nearly constant orbit. But the dominant effect is that a larger η brings the energy

points in the excitation curve closer to the pivot point, making the width smaller.

The constant-orbit and the constant-field scan can be combined. The resulting width has a dependence on η that is intermediate between the two. An appropriate luminosity distribution can make the resulting curve practically horizontal. The combined measurement is dominated by the statistical uncertainty. Moreover, thanks to this complementary behavior, the width, area and phase-slip factor can be determined in a maximum-likelihood fit where η is also a free parameter. Errors and correlations are then obtained directly from the fit.

2.4.4 Line shapes

The discussion so far was focused on the determination of Breit-Wigner resonance parameters. One might also wish to determine the line shape of resonances near the open charm threshold. The question then arises: How narrow should the beam be in order to distort the line shape by less than a given amount?

The distortion of the line shape can be characterized by the maximum difference d between the physical cross section $\sigma_{\text{phys}}(w)$ and the observed cross section $\sigma_{\text{obs}}(w)$ (arising from the convolution of the physical cross section with the $\bar{p}p$ energy distribution in the center of mass $B(w)$), divided by the physical cross section at the peak $\sigma_{\text{phys}}^{\text{peak}}$:

$$d \equiv \max_w |\sigma_{\text{phys}}(w) - \sigma_{\text{obs}}(w)| / \sigma_{\text{phys}}^{\text{peak}} \quad (2.12)$$

Figure 2.20 shows the distortion d as a function of the ratio between the FWHM of the energy distribution (assumed to be Gaussian) and the FWHM of the resonance (a Breit-Wigner, in this example). For instance, if a distortion of less than 10% is needed, then the FWHM ratio needs to be smaller than 0.43. If the FWHM of the resonance is $\Gamma = 1$ MeV, the rms of the energy distribution in the center of mass needs to be smaller than 0.18 MeV, corresponding to a momentum spread of 0.8×10^{-4} at 6 GeV/c (see also Fig. 2.18).

2.4.5 Achievable precision

From the above discussion, it is clear that some features of the machine are essential for precision measurements. Here is a list of the most important requirements:

- low-noise horizontal and vertical BPMs, with fluctuations corresponding to less than 0.1 mm in the orbit length;
- small lattice differences between the energy of the calibration resonance and the energies of interest;
- absolute rf voltage calibration to within a few percent;
- motorized longitudinal cooling pickups, for active feedback on energy drifts and for constant-field scans.

Table 2.3 summarizes the sources of statistical and systematic uncertainty in the resonance parameters. Statistical errors were normalized to \mathcal{N} , the product of detector efficiency ε , total integrated luminosity $\mathcal{L} \equiv \sum \mathcal{L}_i$, and peak cross section $\sigma_p \equiv \sigma_{\text{BW}}(M)$: $\mathcal{N} \equiv \varepsilon \mathcal{L} \sigma_p = 10^4$, in this example. Statistical uncertainties are affected by how the total integrated luminosity \mathcal{L} is spent. Here we assume that the optimal distribution is used [41]. For the numbers in the table, it is also assumed that the beam width is negligible, and so they represent lower limits for a given \mathcal{N} . The uncertainty in the width is the one that is most affected by a larger beam energy spread. Its dependence on the ratio between energy spread and resonance width is shown in Fig. 2.19.

- longitudinal Schottky pickups;

References

- [1] M. Büscher et al., The Moscow-Jülich Frozen-Pellet Target, in *Hadron Spectroscopy*, edited by A. Reis, C. Göbel, J. D. S. Borges, and J. Magnin, volume 814 of *American Institute of Physics Conference Series*, pages 614–620, 2006.
- [2] C. Ekstroem et al., Nucl. Instrum. Meth. **A371**, 572 (1996).
- [3] A. V. Boukharov et al., Phys. Rev. Lett. **100**, 174505 (2008).
- [4] Technical report, ATLAS Technical Design Report 11, CERN/LHCC 98-13.
- [5] Technical report, CMS Technical Design Report 5, CERN/LHCC 98-6.
- [6] B. Ketzer, Q. Weitzel, S. Paul, F. Sauli, and L. Ropelewski, Nucl. Instrum. Meth. **A535**, 314 (2004).
- [7] H. Staengle et al., Nucl. Instrum. Meth. **A397**, 261 (1997).
- [8] K. Mengel et al., IEEE Trans. Nucl. Sci. **45**, 681 (1998).
- [9] R. Novotny et al., IEEE Trans. Nucl. Sci. **47**, 1499 (2000).
- [10] M. Hoek et al., Nucl. Instrum. Meth. **A486**, 136 (2002).
- [11] Technical Proposal, CERN/LHC 9.71.
- [12] Technical Proposal, 1994, CERN/LHCC 94-38, LHCC/P1.
- [13] E. Auffray et al., Moscow, 1999.
- [14] P. Abbon et al., Nucl. Instrum. Meth. **A577**, 455 (2007).
- [15] N. Akopov et al., Nucl. Instrum. Meth. **A479**, 511 (2002).
- [16] G. S. Atoyan et al., Nucl. Instrum. Meth. **A320**, 144 (1992).
- [17] G. David et al., Performance of the PHENIX EM calorimeter, Technical report, PHENIX Tech. Note 236, 1996.
- [18] A. Golutvin, (1994), HERA-B Tech. Note 94-073.
- [19] LHCb Technical Proposal CERN LHCC 98-4, LHCC/P4, 1998.
- [20] I.-H. Chiang et al., (1999), KOPIO Proposal.
- [21] H. Morii, (2004), Talk at NP04 Workshop at J-PARC.
- [22] G. Atoyan et al., Test beam study of the KOPIO Shashlyk calorimeter prototype, in *Proceedings of "CALOR 2004"*, 2004.
- [23] T. A. Armstrong et al., Phys. Lett. **B385**, 479 (1996).
- [24] Baseline Technical Report, subproject HESR, Technical report, Gesellschaft für Schwerionen (GSI), Darmstadt, 2006.
- [25] O. Boine-Frankenheim, R. Hasse, F. Hinterberger, A. Lehrach, and P. Zenkevich, Nucl. Instrum. Meth. **A560**, 245 (2006).
- [26] V. Parkhomchuk, Nucl. Instrum. Meth. **A441**, 9 (2000).
- [27] A. H. Sørensen, Introduction to intrabeam scattering, in *CERN Accelerator School: General accelerator physics*, number CERN-87-10, page 135, 1987.
- [28] F. Hinterberger, T. Mayer-Kuckuk, and D. Prasuhn, Nucl. Instrum. Meth. **A275**, 239 (1989).
- [29] F. Hinterberger and D. Prasuhn, Nucl. Instrum. Meth. **A279**, 413 (1989).
- [30] D. Reistad et al., Calculations on high-energy electron cooling in the HESR, in *Proceedings of COOL 07 — Workshop on Beam Cooling and Related Topics*, pages 44–48, Bad Kreuznach, Germany, 2007.
- [31] H. Stockhorst et al., Stochastic Cooling Developments for the HESR at FAIR, in *Proc. of the European Accelerator Conference EPAC08*, number THP055, page 3491, Genoa, Italy, 2008.
- [32] A. Lehrach, O. Boine-Frankenheim, F. Hinterberger, R. Maier, and D. Prasuhn, Nucl. Instrum. Meth. **A561**, 289 (2006).
- [33] F. Hinterberger, Monte carlo simulations of Thin Internal Target Scattering in Ceslius, in *Beam-Target Interaction and Intra-beam Scattering in the HESR Ring: Emittance, Momentum Resolution and Luminosity*, Bericht des Forschungszentrum Jülich, 2006, Jül-Report No. 4206.

- [34] W.-M. Yao et al., Journal of Physics **G33**, 1 (2006).
- [35] A. Lehrach, IKP Annual Report **Jül-4234**, 138 (2006).
- [36] D. McGinnis, G. Stancari, and S. J. Werkema, Nucl. Instrum. Methods A **506**, 205 (2003).
- [37] M. Andreotti et al., Phys. Lett. B **654**, 74 (2007).
- [38] T. A. Armstrong et al., Phys. Rev. D **47**, 772 (1993).
- [39] D. C. Kennedy, Phys. Rev. D **46**, 461 (1992).
- [40] V. M. Aulchenko et al., Phys. Lett. B **573**, 63 (2003).
- [41] A. Pesce, *Studio della distribuzione ottimale di luminosità per la misura dei parametri di risonanza in fisica delle particelle* (BSc Thesis, in Italian), 2007.

3 Software

The offline software which has been devised for the PANDA Physics Book benchmark studies follows an object oriented approach, and most of the code has been written in C++. Several well-tested software tools and packages from other HEP experiments are used and have been adapted to the PANDA needs. The software contains

- event generators with accurate decay models for the individual physics channels as well as for the relevant background channels,
- particle tracking through the complete PANDA detector by using the GEANT4 transport code,
- the digitisation which models the signals of the individual detectors and their processing in the front-end-electronics,
- the reconstruction and identification of charged and neutral particles, providing lists of particle candidates for the physics analysis and
- user friendly high level analysis tools which allow to make use of vertex and kinematic fits and to reconstruct extensive decay trees very easily.

3.1 Event Generation

For generating events representing the benchmark reactions, EvtGen [1] was used. It allows to generate the resonances of interest, taking into account the known decay properties, including angular distributions, polarisation, etc., and allows user defined decay models.

For the simulation of the generic annihilation background, the Dual Parton Model based generator, DPM, was used in the case of $\bar{p}p$, and the Ultra-relativistic Quantum Molecular Dynamic model, UrQMD, in case of $\bar{p}N$, which are described in more detail in the following.

3.1.1 EvtGen Generator

EvtGen was first developed within the BaBar collaboration, and originally it was designed for the needs of studies at B-meson factories. The modular design allows an easy extension to other physics

channels, and meanwhile EvtGen has been adapted and used for ATLAS [2] and PANDA studies, too.

EvtGen makes use of the formalism of spin density matrices. This enables the inclusion of spin effects into the simulation, and allows the user to study angular distributions of particles in the final state.

The input data for each decay process are passed to the code as a complex amplitude. In cases where more than one complex amplitude are involved for the same process, these are added before the decay probabilities are calculated. Consequently, interference terms, which are of significant importance in many channels studied with PANDA, are included.

The package also uses a novel *nodal* decay algorithm, where each decay step is treated independently, addressing the problem of cascade decays. In a conventional Monte Carlo generator, kinematics for the whole chain would be generated at once, and the accept-reject decision applied on the result. This method is inefficient as a rejection leads to the whole chain being regenerated from scratch. The node-wise method of EvtGen avoids this by generating kinematics for each step separately. This approach does lead to increasingly complex spin density matrices being attached to the amplitudes for each node, but the computation time required to calculate these is very much less than what would be needed to continually re-generate kinematics for the whole decay tree.

EvtGen is controlled by means of a decay table, which lists all possible decay processes, their branching ratios and the decay model. A user decay table can be written to override the default table and, thereby, exclude unwanted processes.

3.1.2 Dual Parton Model

The Dual Parton Model [3] is a synthesis of the Regge theory, topological expansions of QCD $1/N_f$ or $1/N_c$, and ideas from the parton model. The Regge theory gives the energy dependence of hadron-hadron cross sections assuming various exchanges of particles between projectile and target in the t -channel. The cross sections are in a correspondence with diagrams of $1/N$ expansion. The diagrams describe creation of unstable intermediate s -channel states – quark-gluon strings or colour tubes.

The main objects of the model are constituent quarks having masses $\sim 300\text{--}350$ MeV, strings, and string junctions for baryons. It is assumed that mesons consist of a quark and an anti-quark which are coupled by colour forces. The vortex lines of the field are concentrated in a small space region forming a string-like configuration. So, mesons are considered as strings with small masses.

Baryons are assumed to consist of three quarks. Two possible string configurations in baryons were considered: triangle and Mercedes star configurations [4, 5, 6, 7, 8, 9, 10]. Three strings are joined in the central point in the Mercedes star case and give the string junction.

Various processes are possible in baryon-antibaryon interactions. Some of them are shown in Fig. 3.1 where string junctions are presented by dashed lines. The diagram of Fig. 3.1a represents a process with string junction annihilation and creation of three strings. The diagram 3.1b describes quark-antiquark annihilation and string creation between diquark and anti-diquark. Quark-antiquark and string junctions annihilation is shown in Fig. 3.1c. Finally, one string is created in the process of Fig. 3.1 e. After fragmentation of the strings, hadrons appear in the same way as in e^+e^- annihilation. One can assume that excited strings with complicated configuration are created in processes 3.1d and 3.1f. If the collision energy is sufficiently small, glueballs can be formed in the process 3.1f. Mesons with constituent gluons can be created in the process 3.1d.

The pomeron exchange is responsible for 2 strings formation and diffraction dissociation (Fig. 3.1g and 3.1h). They are dominant at high energies.

In the simplest approach it is assumed that the cross sections of the processes have an energy dependence given in Fig. 3.1 where s is the square of the total energy in the centre-of-mass system (CMS). Some of the processes (3.1d, 3.1f) have not a well-defined energy dependence of the cross sections. Since it is usually assumed that their cross sections are small, we have neglected them.

A calculation of the cross sections is a rather complex procedure (see [11, 12]) because there are interactions in initial and final states. Here we follow the approach developed in Ref. [12]. The cross sections calculated by us have a complicated energy dependence. To reproduce it we have parametrised

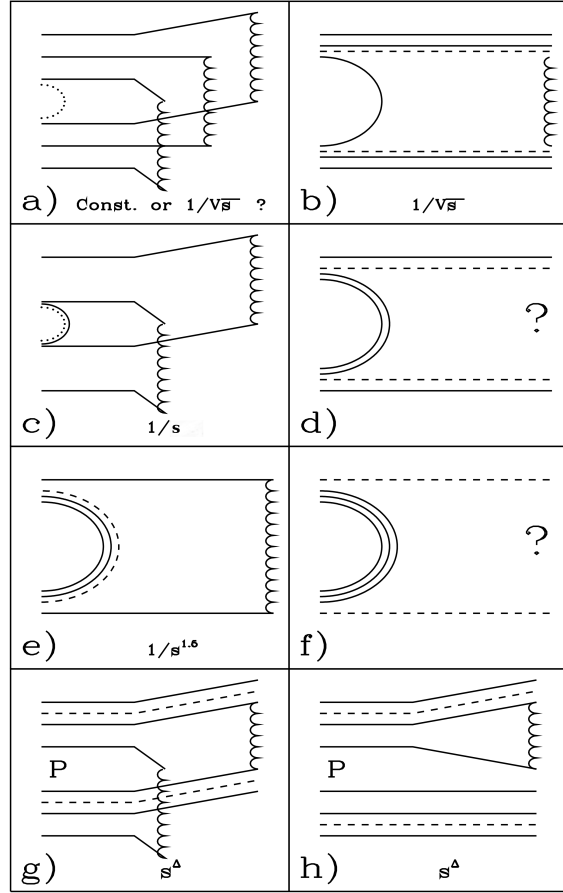


Figure 3.1: Possible processes in $\bar{p}p$ -interactions and their estimated energy dependencies. The question marks mean that the corresponding estimations are absent.

the cross sections of Fig. 3.1 in the following form:

$$\begin{aligned}
 \sigma_a &= 51.6/s^{0.5} - 58.8/s + 16.4/s^{1.5}, \\
 \sigma_b &= 77.4/s^{0.5} - 88.2/s + 24.6/s^{1.5}, \\
 \sigma_c &= 93/s - 106/s^{1.5} + 30/s^2, \\
 \sigma_d &= \sigma_e = \sigma_f = 0, \\
 \sigma_g &= 18.6/s^{0.08} - 33.5/s^{0.5} + 30.8/s, \\
 \sigma_h &= 0,
 \end{aligned}$$

where only the leading terms correspond to that shown in Fig. 3.1. All cross sections are given in mb with s in GeV^2 .

String masses are determined by kinematic properties of quarks and anti-quarks at their ends. According to Ref. [3] we assume the following probability distributions, dW_i , in the processes 3.1a, 3.1c

and 3.1g:

$$\begin{aligned} dW_a &\propto x_+^{-\alpha_R(0)} dx_+, \\ dW_c &\propto x_+^{-\alpha_R(0)} (1-x_+)^{-\alpha_R(0)} dx_+, \\ dW_g &\propto x_+^{-\alpha_R(0)} (1-x_+)^{\alpha_R(0)-2\alpha_N(0)} dx_+, \end{aligned}$$

where x_+ is the light-cone momentum fraction of quarks, and $\alpha_R(0)$ is the intercept of the non-vacuum reggeon trajectory.

The transverse momentum distribution of quarks has been chosen in the form:

$$d^2W = B^2 e^{-Bp_T} d^2p_T, \quad B = 4.5 \text{ (GeV}/c)^{-1},$$

where p_T is the transverse momentum, and B is the adjusted parameter.

The strings fragment into hadrons. The mechanism of the fragmentation is like the one applied in the LUND model [13, 14]. Here we use a code proposed by S. Ritter [15] with fragmentation functions (hadron distributions on light-cone momentum) taken from Refs. [16, 17]. Strings with small masses are considered as hadrons, and we put them on the mass-shell.

After the string fragmentation all unstable hadrons decay. We simulate the processes with the help of the code DECAY [18].

The corresponding event generator has been developed and tested successfully. It gives a possibility to simulate the inelastic interactions as well as the elastic $\bar{p}p$ -scattering.

3.1.3 UrQMD

The Ultra-relativistic Quantum Molecular Dynamic model (UrQMD) [19, 20] is a microscopic model based on a phase space description of nuclear reactions. It describes the phenomenology of hadronic interactions at low and intermediate energies ($\sqrt{s} < 5 \text{ GeV}$) in terms of interactions between known hadrons and their resonances. At higher energies, $\sqrt{s} > 5 \text{ GeV}$, the excitation of colour strings and their subsequent fragmentation into hadrons are taken into account in the UrQMD model.

The model is based on the covariant propagation of all hadrons considered on the (quasi-)particle level on classical trajectories in combination with stochastic binary scattering, colour string formation and resonance decay. It represents a Monte Carlo solution of a large set of coupled integro-differential equations for the time evolution of the various phase space densities of particle species $i = N, \Delta, \Lambda$, etc.. The main ingredients of the model are the

cross sections of binary reactions, the two-body potentials and decay widths of resonances.

In the UrQMD model, the total cross section σ_{tot} depends on the isospins of colliding particles, their flavor and the c.m. energy. The total and elastic proton-proton and proton-neutron cross sections are well known [21]. Since their functional dependence on \sqrt{s} shows a complicated shape at low energies, UrQMD uses a lookup-table for those cross sections. The neutron-neutron cross section is assumed to be equal to the proton-proton cross section (isospin-symmetry). In the high energy limit ($\sqrt{s} \geq 5 \text{ GeV}$) the CERN/HERA parametrisation for the proton-proton cross section is used [21].

Baryon resonances are produced in two different ways, namely: *hard production* - $N + N \rightarrow \Delta N, \Delta\Delta, N^*N$, etc. and *soft production* - $\pi^- + p \rightarrow \Delta^0, K^- + p \rightarrow \Lambda^* \dots$

The cross sections of s -channel resonances formation are fitted to measured data. Partial cross sections are used to calculate the relative weights for the different channels.

There are six channels for the excitation of non-strange resonances in the UrQMD model, namely $NN \rightarrow N\Delta_{1232}, NN^*, N\Delta^*, \Delta_{1232}\Delta_{1232}, \Delta_{1232}N^*$, and $\Delta_{1232}\Delta^*$. The Δ_{1232} is explicitly listed, whereas higher excitations of the Δ resonance have been denoted as Δ^* . For each of these 6 channels specific assumptions have been made with respect to the form of the matrix element, and the free parameters have been adjusted to the available experimental data.

Meson-baryon (MB) cross sections are dominated by the formation of s -channel resonances, *i.e.* the formation of a transient state of mass $m = \sqrt{s}$, containing the total c.m. energy of the two incoming hadrons. On the quark level such a process implies that a quark from the baryon annihilates an antiquark from the incoming meson. At c.m. energies below 2.2 GeV, intermediate resonance states get excited. At higher energies the quark-antiquark annihilation processes become less important. There, t -channel excitations of the hadrons dominate, where the exchange of mesons and Pomeron exchange determine the total cross section of the MB interaction [22].

To describe the total meson-meson (MM) reaction cross sections, the additive quark model and the principle of detailed balance, which assumes the reversibility of the particle interactions, are used.

Resonance formation cross sections from the measured decay properties of the possible resonances up to c.m. energies of 2.25 GeV for baryon resonance

and 1.7 GeV in the case of MM and MB reactions have been calculated based on the principle. Above these energies collisions are modelled by the formation of an s -channel string or, at higher energies (beginning at $\sqrt{s} = 3$ GeV), by one or two t -channel strings. In the strangeness channel elastic collisions are possible for those meson-baryon combinations which can not form a resonance, while the creation of t -channel strings is always possible at sufficiently large energies. At high collision energies both cross sections become equal due to quark counting rules.

A parametrisation proposed by Koch and Dover [23] is used in the UrQMD model for the baryon-antibaryon annihilation cross section. It is assumed that the antiproton-neutron annihilation cross section is identical to the antiproton-proton annihilation cross section.

The potential interaction is based on a non-relativistic density-dependent Skyrme-type equation of state with additional Yukawa- and Coulomb potentials. The Skyrme potential consists of a sum of two- and a three-body interaction terms. The two-body term, which has a linear density dependence models the long range attractive component of the nucleon-nucleon interaction, whereas the three-body term with its quadratic density dependence is responsible for the short range repulsive part of the interaction. The parameters of the components are connected with the nuclear equation of state. Only the hard equation of state has been implemented into the current UrQMD model.

At the beginning of an event generation a target nucleus is modelled according to the Fermi-gas ansatz. The wave-function of the nucleus is defined as the product of nucleon wave-functions. A nucleon wave-function is represented by the Gauss function in the configuration and momentum space. In configuration space, the centroids of the Gaussians are randomly distributed within a sphere with radius $R(A)$, where $R(A)$ is the nucleus radius. The initial momenta of the nucleons are randomly chosen between 0 and the local Thomas-Fermi momentum.

The impact parameter of a collision is sampled according to the quadratic measure ($dW \sim bdb$). At given impact parameter, b , the centres of projectile and target are placed along the collision axis in such a manner that the distance between the surfaces of the projectile and the target is equal to 3 fm. Momenta of nucleons are transformed in the system where the projectile and target have equal velocities directed in different directions of the axis. After that the time propagation starts. During the calculation, at the beginning of each time step each particle is checked whether it will collide within that

time step. A collision between two hadrons will occur if $d < \sqrt{\sigma_{\text{tot}}}/\pi$, where d and σ_{tot} are the impact parameter and the total cross section of the two hadrons, respectively. After each binary collision or decay the outgoing particles are checked for further collisions within the respective time step.

The hadron-hadron interactions at high energies are simulated in 3 stages. According to the cross sections, probabilities of interaction are defined (elastic, inelastic, antibaryon-baryon annihilation etc.), and a type of interaction is sampled. In the case of inelastic collisions with string excitation, the kinematic characteristics of strings are determined. The strings between quark and diquark (antiquark) from the same hadron are produced. The strings have the continuous mass distribution $f(M) \propto 1/M$ with the masses M , limited by the total collision energy \sqrt{s} : $M_1 + M_2 \leq \sqrt{s}$. The remaining energy is equally distributed between the longitudinal momenta of two produced strings.

The second stage of hadron-hadron interactions is related to string fragmentation. The fragmentation functions used in the UrQMD model are different from the ones in the well-known LUND model [24].

The formation time of created hadrons is taken into account in hadron-nucleus and nucleus-nucleus interactions.

The decay of the resonances proceeds according to the branching ratios compiled by the Particle Data Group [25]. The resonance decay products have isotropic distributions in the rest frame of the resonance. If a resonance is among the outgoing particles, its mass must first be determined according to a Breit-Wigner mass-distribution. If the resonance decays into $N > 2$ particles, then the corresponding N -body phase space is used to calculate the momenta of the final particles.

The Pauli principle is applied to hadronic collisions or decays by blocking the final state if the outgoing phase space is occupied.

The final state of a baryon-antibaryon annihilation is generated via the formation of two meson-strings. The available c.m. energy of the reaction is distributed in equal parts to the two strings which decay in the rest frame of the reaction. On the quark level this procedure implies the annihilation of a quark-antiquark pair and the reordering of the remaining constituent quarks into newly produced hadrons (additionally taking sea-quarks into account). This model for the baryon-antibaryon annihilation thus follows the topology of a rearrangement graph.

The collision term in the UrQMD model con-

tains 55 different baryon species (including nucleon, delta and hyperon resonances with masses up to 2.25 GeV) and 32 different meson species (including strange meson resonances with masses up to 1.9 GeV), which are supplemented by their corresponding anti-particle and all isospin-projected states. The states can either be produced in string decays, s-channel collisions or resonance decays. For excitations with masses larger than 2 GeV, a string picture is used. Full baryon/antibaryon symmetry is included: The number of implemented baryons therefore defines the number of antibaryons in the model, and the antibaryon-antibaryon interaction is defined via the baryon-baryon interaction cross sections.

A very important improvement of the UrQMD model was proposed in Ref. [26] where the model was coupled with the Statistical Multifragmentation (SM) Model [27]. According to Ref. [26], the UrQMD calculation is carried out up to a time scale referred to as the transition time $t_{tr} \sim 100\text{fm}/c$. The positions of the nucleons are then used to calculate the distribution of mass and charge numbers of pre-fragments. In determining the mass and charge numbers of the pre-fragments, the minimum spanning tree method [28] is employed. A pre-fragment is formed if the distances between nucleons are lower than 3 fm. The total energy of each pre-fragment is determined in its rest frame by the Lorentz transformation. The excitation energy of a hot pre-fragment is calculated as the difference between the binding energy of the hot pre-fragment and the binding energies of this pre-fragment in the ground state. The decay of the pre-fragments is described by the SM model.

We use the combination of the models for estimation of neutron production in \bar{p} -interactions with nuclear targets.

3.2 Particle Tracking and Detector Simulation

The detector simulation is subdivided into two steps. The first step is the propagation of the generated particles through the \bar{P} ANDA detector by using the GEANT4 transport code [29, 30]. It takes into account the full variety of interactions and decays that the different kinds of particles may undergo. The output of this first step is a collection of hits, which contain mainly the intersection points and energy losses of all particles in the individual detector parts. Based on this information the digitisation step follows, which models the signals and

their processing in the front-end-electronics of the individual detectors, producing a digitised detector response as similar as possible to beam data. This design ensures that in the future the *same* reconstruction code can be used for Monte Carlo and for beam data. For performance reasons for some detectors an effective smearing was used, which was derived from Monte Carlo calculations using a full digitisation.

3.2.1 Detector Setup

The geometry description of the \bar{P} ANDA detector is based on the detector description database developed by the CMS experiment [31]. It provides interfaces between the geometry information stored in Extensible Markup Language (XML) files and the corresponding transient objects of the individual applications. The used XML schema consists of type-safe XML constructs, abstract types, and hierarchical inheritance structures. This allows an easy integration into a C++ environment.

Tools have been developed which are able to convert technical drawings created by widely used Computer Aided Design (CAD) programs directly into the XML based detector description. This makes it very easy to add and remove geometries or to update modifications of specific detector parts in the simulation.

The simulations have been done with the complete setup which was already described in detail in Sec. 2.2. The still not finally established Time-Of-Flight (TOF) and the Forward RICH detectors have not been considered, and the Straw Tube option has been used for the central tracker device. The Muon detector consists only of two scintillator layers instead of a multilayer scenario within the iron yoke which was the most favoured option during the implementation phase of the geometry into the software. For the $\bar{p}p$ reactions the pellet scenario as an internal target has been chosen taking into account the material budget of the target pipe and the pumping stations. The interaction point has been considered with a spread of $\sigma=0.275$ mm in each direction.

Fig. 3.2 shows the contributions of the subdetectors to the material which a particle has to traverse to reach the EMC as a function of θ . The material thicknesses are presented in units of the corresponding radiation lengths X_0 .

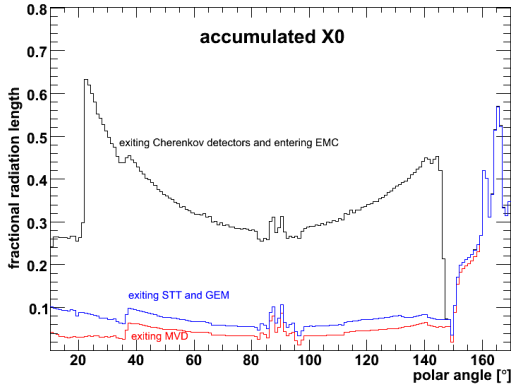


Figure 3.2: Contributions of the subdetectors to the material budget in front of the EMC in units of a radiation length X_0 as a function of the polar angle θ .

3.2.2 Digitisation

3.2.2.1 Readout of the Tracking Devices

3.2.2.1.1 Silicon Readout of the MVD The Micro Vertex Detector (MVD) makes use of two different silicon detector types, silicon strip and pixel detectors. The readout of the silicon devices is for both types different and is treated differently in the digitisation scheme. The signal in the sensor is formed by using the local trajectory within the detector material to calculate the corresponding channel relative to the readout matrix of the sensor. The hit position on the sensor surface defines the channel number and the deposited energy the charge collected by the electronics. The channel mapping of the trajectory is done on both sides of the sensor. In the case of the pixel detectors, the trajectory is projected to the surface and depending on its relative orientation, all excited pixel cells are calculated and the charge signal is shared among all pixel cells depending on the fraction of the local track. Strip sensors will be sensitive on both sides and the formation of digitised channels is done independently on both sides of the sensor. The procedure is similar to the pixel case but done only in one dimension.

The size of the readout structures are defined by the size of the pixel cell or the spacing of the strips. These parameters can be changed interactively in order to test various settings and have to meet the dimensions of the sensor. The channel is assigned to a frontend and a common number of 128 channels per frontend have been chosen. In the case of the pixel detector the size of the ATLAS frontend chip was used as basis to assign a frontend num-

ber to a certain channel. Since the electronics chip is bump bonded onto the surface of the detector the number of pixel cells per frontend is defined by the dimension of the frontend chip. A threshold for the electronics signal can be set and was chosen as standard to an equivalent of 300 electrons which is a reasonable value for pixel detectors.

3.2.2.1.2 Straw Tube Tracker and Drift Chambers

The digitisation for the Straw Tube Tracker (STT) and the Drift Chambers (DCH) have been treated in a similar way. Both devices consist of wires inside an ArCO₂ gas mixture volume. If a charged particle traverses this gas volume, the local helix trajectory is derived from the corresponding GEANT4 intersection points. The drift time of the ionisation electrons is estimated from the smallest distance of this helix trajectory to the wire d_{poca} . The uncertainty of the drift time is taken into account by smearing d_{poca} with a Gaussian distribution with a standard deviation of $\sigma = 150 \mu\text{m}$ for the STT, and $\sigma = 200 \mu\text{m}$ for the DCH devices.

The average number of primary ionisation electrons is the total deposited energy in the gas volume divided by the ionisation energy of 27 eV for ArCO₂. The energy signal of a straw tube is finally calculated by taking into account Poisson statistics.

3.2.2.1.3 GEMs Readout Each GEM station consists of two detector planes. The distance between the detector planes is 1 cm. It has been assumed that each detector plane has two strip detector layers with perpendicular orientation to each other. The gas amplification process and the response of the strip detector has not been simulated in detail. Instead, the entry point of a charged track into the detector plane has been taken directly from GEANT4 and smeared with a Gaussian distribution of 70 μm width in each strip orientation direction.

3.2.2.2 Readout of the DIRC Detectors

The light propagation in the Cerenkov radiators, the signal processing in the front-end-electronics, and the reconstruction of the Cerenkov angle have been modelled in a single effective step.

The resolution of the reconstructed Cerenkov angle σ_C is mainly driven by the uncertainty of the single photon angle $\sigma_{C,\gamma}$ and the statistics of relatively small numbers of detected Cerenkov photons N_{ph} :

$$\sigma_C = \frac{\sigma_{C,\gamma}}{\sqrt{N_{ph}}}$$

A single photon resolution of $\sigma_{C,\gamma} = 10$ mrad was used, corresponding to the experience with existing DIRC detectors. The number of detected photons was calculated from the velocity, β , of charged particles passing through the quartz radiators and the path length L within the radiator, via:

$$N_{ph} = \epsilon 2\pi\alpha L \left(1 - \frac{1}{\beta^2 n_{quartz}^2}\right) \left(\frac{1}{\lambda_{min}} - \frac{1}{\lambda_{max}}\right),$$

where α is the fine structure constant and $n_{quartz} = 1.473$ the refraction index of quartz. The sensitive wavelength interval, $\lambda_{min}-\lambda_{max}$, was chosen to [280 nm, 350 nm], and a total efficiency of $\epsilon = 7.5\%$ was used to take into account the transmission and reflectivity losses as well as the quantum efficiency of the photo detectors. Fig. 3.3 shows the simulated number of photons for the Barrel DIRC as a function of the polar angle for 1 GeV/c pions. The average number of detected photons at a polar angle of 90° , 20, increases by a factor of 2 for very forward and backward directions.

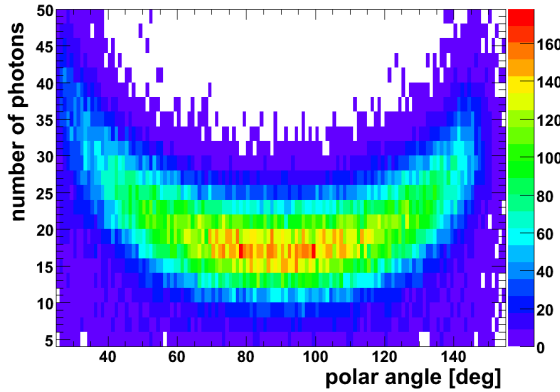


Figure 3.3: The number of detected Cerenkov photons versus the polar angle of pions with momenta of 1 GeV/c.

Fig. 3.4 shows the precision of the measured Cerenkov angle obtained with the digitisation and reconstruction procedure described above. A fit with a Gaussian distribution yields to a resolution of $\sigma = 2.33$ mrad.

3.2.2.3 EMC Scintillator Readout

For the EMC in the target spectrometer (TS EMC) reasonable properties of PbWO_4 crystals at the operational temperature of -25°C have been considered. A Gaussian distribution with a σ of 1 MeV has been used for the constant electronics noise. The statistical fluctuations were estimated by 80 photo electrons per MeV produced in the Large

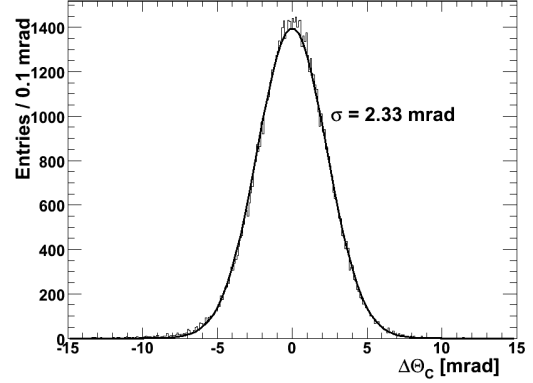


Figure 3.4: Difference between the reconstructed and expected Cerenkov angle $\Delta\Theta_C$ for single 1 GeV/c pions.

Area Avalanche Photo Diode (LAAPD). An excess noise factor of 1.38 has been used, corresponding to the measurements with the first LAAPD prototype at an internal gain of $M = 50$ (see [32]). This results in a photo statistics noise term of $0.41\%/\sqrt{E/\text{GeV}}$.

For the forward calorimeter (FW EMC) a Shashlyk detector consisting of lead-scintillator sandwiches is foreseen. Therefore, only a fraction of roughly 30% of the energy are deposited in the scintillator material. Based on this energy deposit the electronics noise with $\sigma = 3$ MeV has been considered which yields to a statistic noise term of $0.8\%/\sqrt{E/\text{GeV}}$.

3.2.2.4 Muon Detector Readout

Because the layout of the muon detector and its readout is still under investigation, a parametrised digitisation was used. The intersections of the particle tracks with the scintillators of the muon detectors were derived from the detector hits provided by the GEANT4 transport code. In the process of matching muon detector hits with reconstructed charged tracks, the uncertainties are dominated by the errors from the extrapolation of the reconstructed tracks to the muon detector, and therefore the finite position resolution of the muon detector was neglected. The algorithm that was used to deduce PID probabilities from the muon detector hits will be described in Sec. 3.3.3.1.4.

3.3 Reconstruction

3.3.1 Charged Particle Track Reconstruction

3.3.1.1 MVD Cluster Reconstruction

The MVD provides very precise space point measurements as a basis for the track and vertex reconstruction. The hit resolution of individual MVD measurements is shown in Fig. 3.5 in the case of the pixel detector.

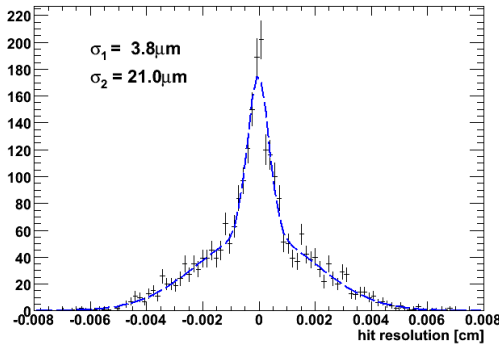


Figure 3.5: The resolution of the reconstructed hit position after clustering with respect to the simulated value.

The distribution in Fig. 3.5 shows the difference between the reconstructed position on the sensor and the generated Monte Carlo value. The broad contribution comes from hits where only one pixel is contributing to the hit cluster and the narrow contribution from multi hit clusters. In the latter case, charge weighting between the pixel cells in the cluster can be used to calculate the mean position of the hit. Without using the energy information, the resolution of the position measurement would be

$$\sigma_{geom} = p/\sqrt{12}$$

where p is the size of the readout structure. Using $100 \times 100 \mu\text{m}$ large pixel cells, the geometric resolution is $\sigma_{geom} = 28 \mu\text{m}$, which is the uncertainty of the broader distribution caused by single pixel clusters. For high momentum particles the hit resolution limits the overall track resolution whereas for low momentum particles the small angle scattering is the limiting factor.

3.3.1.2 Global Track Reconstruction

The track object provides information about a charged particle path through space. It contains

a collection of hits in the individual tracking sub-detectors. Each hit knows about the residual of the hit to a given reference trajectory and the precision of the measurement. For example, the hit residual of the STT is defined as the closest approach of the reference trajectory to the wire of the straw minus the actual drift distance. In case of hits in the MVD or in a GEM station, the residual is defined as the distance between the sensor and the reference track in the detector plane. An idealised pattern recognition has been used for track building based on Monte Carlo information to assign reconstructed hits to their original tracks. Tracks which contain less than eight detector hits were rejected.

The tracks in the target spectrometer are fitted with the Kalman Filter algorithm, which considers not only the measurements and their corresponding resolutions but also the effect of the interaction with the detector material, *i.e.* multiple scattering and energy loss. A detailed description of the implementation of the algorithm, which has been adapted from the reconstruction software of the BaBar Collaboration can be found in [33]. For simplification a constant magnetic field parallel to the z -axis has been assumed in the target spectrometer region. A typical choice for the parametrisation of the track in a solenoidal field is a five-parameter helix along the principle field direction z . The following parameter vector P is used:

$$P = (d_0, \phi_0, \omega, z_0, \tan \lambda)$$

where d_0 is the distance of closest approach to the origin in the x - y plane, signed by the angular momentum $\vec{r} \times \vec{p}$ at that point, ϕ_0 is the angle in the x - y plane at closest approach, and z_0 the distance of closest approach to the origin in the z projection. The parameter ω gives the curvature of the track in the x - y plane, and $\tan \lambda$ is the tangent of the track dip angle in the projection plane defined by the cylindrical coordinates ρ and z . The position of the particle as a function of the x - y plane projection of the flight length from the point of closest approach l is given by:

$$\begin{aligned} x &= \sin(\phi_0 + \omega \cdot l)/\omega - (1/\omega + d_0) \sin \phi_0 \\ y &= -\cos(\phi_0 + \omega \cdot l)/\omega - (1/\omega + d_0) \cos \phi_0 \\ z &= z_0 + l \cdot \tan \lambda \end{aligned}$$

The momentum of the track for a given magnetic field $(0,0,B)$ is then:

$$\begin{aligned} p_x &= q \cdot c \cdot B/\omega \cdot \cos(\phi_0 + \omega \cdot l) \\ p_y &= q \cdot c \cdot B/\omega \cdot \sin(\phi_0 + \omega \cdot l) \\ p_z &= q \cdot c \cdot B/\omega \cdot \tan \lambda \end{aligned}$$

The task of the track-fitting algorithm is to determine the optimal parameter vector and its covariance matrix as a function of the flight length l in order to create a representation of the track as a piecewise helix. In the physics analysis the particle position and momentum can then be accessed through this piecewise helix representation.

Tracks which have hits in the target spectrometer as well as in the drift chambers of the forward spectrometer are treated in the following way. From the hit residuals of the drift chambers a χ^2 is calculated, where the propagation of the track through space is done with a Runge-Kutta integration method. For minimising the χ^2 the package MINUIT [34] is used. The result of the fit is a five-parameter helix and its covariant matrix at $z = 1.9m$. This information serves as a constraint for the Kalman Filter fit, where also the hits in the target spectrometer are considered.

Multiple scattering and energy loss effects depend on the mass of the particle. Therefore, the tracks have been refitted separately for all five particle hypotheses (e , μ , π , K and p). This results in an adequate accuracy of the reconstructed kinematics assigned to the individual particle species.

3.3.1.3 Tracking Performance

In the following the track reconstruction efficiency, the momentum resolution, and the spatial resolution for reconstructed vertexes are shown, which were achieved for the chosen detector setup using the reconstruction software described above.

The upper histogram of Fig. 3.6 shows the obtained track efficiency as a function of the transverse momentum for single pions generated at a polar angle of 60° . The efficiency is here defined as the ratio between the number of tracks which fulfil only a low criterion on the accuracy of the reconstructed transverse momentum to the number of generated tracks. It is required that the difference between the reconstructed to the generated momentum is less than 3σ of its resolution. While above $p_t > 0.2 \text{ GeV}/c$ more than 90% of the tracks are well measured, the efficiency decreases to 70% for a transverse momentum of $0.1 \text{ GeV}/c$. These results are comparable to the track efficiency for real data obtained with the BaBar detector (Fig. 3.6 and [35]).

Fig. 3.7 illustrates the reconstructed momentum for pions of $1 \text{ GeV}/c$ momentum at a polar angle of 20° . This example yields to a momentum resolution of $\sigma_p/p = 1\%$.

The achieved vertex resolution is shown in Fig. 3.8

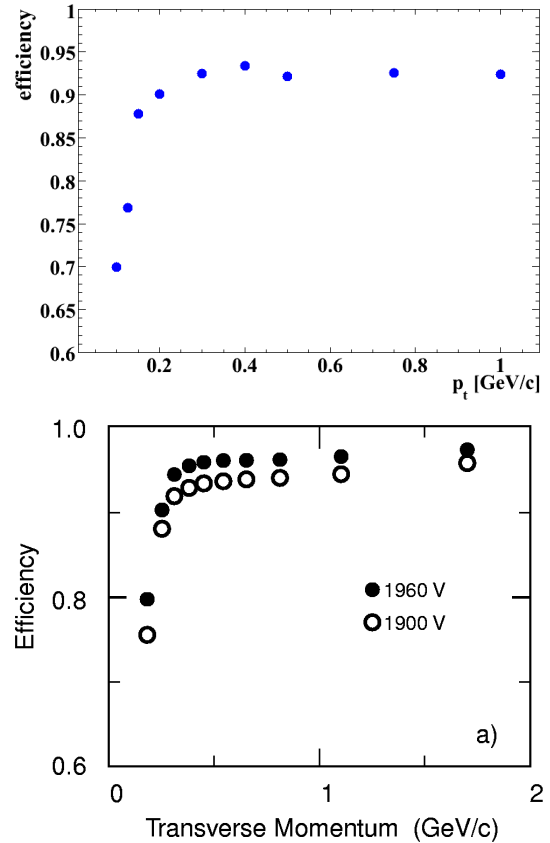


Figure 3.6: The track reconstruction efficiency as a function of the transverse momentum for pions at a polar angle of 60° (upper histogram).

The lower histogram was taken from [35] and illustrates the track reconstruction efficiency achieved at BaBar for two different operation modes of the central drift chamber.

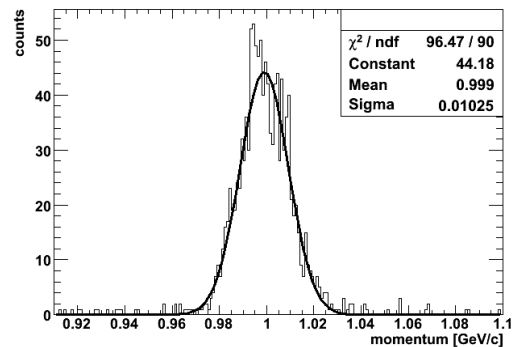


Figure 3.7: The momentum resolution for pions of $1 \text{ GeV}/c$ momentum at a polar angle of 20° .

for pions of $3 \text{ GeV}/c$ momentum. Here all tracking detectors were taken into account.

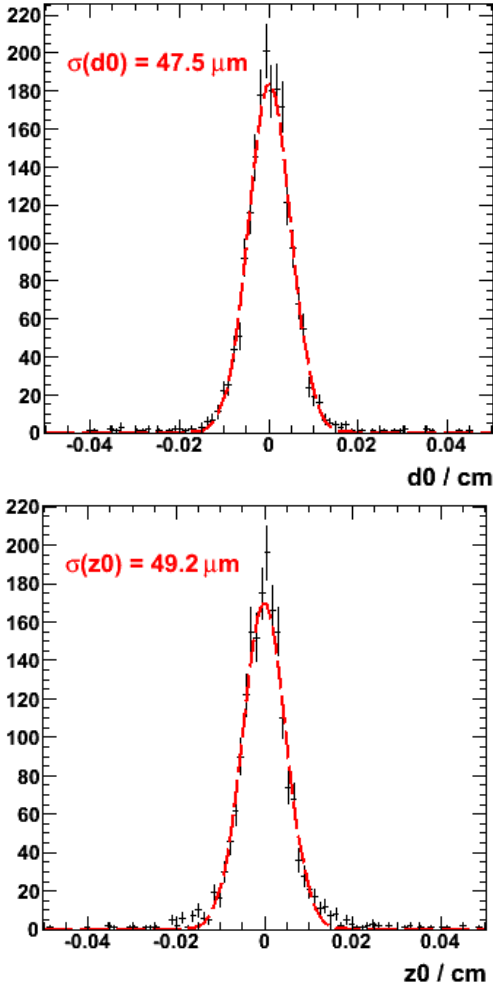


Figure 3.8: The achieved vertex resolution for pions of 3 GeV/c momentum.

3.3.2 Photon Reconstruction

3.3.2.1 Reconstruction Algorithm

A photon entering one scintillator module of the EMC develops an electromagnetic shower which, in general, extends over several modules. A contiguous area of such modules is called a cluster.

The energy deposits and the positions of all scintillator modules in a cluster allow a determination of the four vector of the initial photon. Most of the EMC reconstruction code used in the offline software is based on the cluster finding and bump-splitting algorithms which were developed and successfully applied by the BaBar experiment [35, 36].

The first step of the cluster reconstruction is the finding of a contiguous area of scintillator modules with energy deposit. The algorithm starts at the

module exhibiting the largest energy deposit. Its neighbours are then added to the list of modules if the energy deposit is above a certain threshold E_{xtl} . The same procedure is continued on the neighbours of newly added modules until no module fulfils the threshold criterion. Finally a cluster gets accepted if the total energy deposit in the contiguous area is above a second threshold E_{cl} .

The next step is the search for bumps within each reconstructed cluster. A cluster can be formed by more than one particle if the angular distances of the particles are small. In this case the cluster has to be subdivided into regions which can be associated with the individual particles. This procedure is called the *bump splitting*. A bump is defined by a local maximum inside the cluster: The energy deposit of one scintillator module E_{local} must be above E_{max} , while all neighbour modules have smaller energies. In addition the highest energy E_{Nmax} of any of the N neighbouring modules must fulfil the following requirement:

$$0.5(N - 2.5) > E_{Nmax} / E_{local} \quad (3.1)$$

The total cluster energy is then shared between the bumps, taking into account the shower shape of the cluster. For this step an iterative algorithm is used, which assigns a weight w_i to each scintillator module, so that the bump energy is defined as $E_b = \sum_i w_i E_i$. E_i represents the energy deposit in the i TH module and the sum runs over all modules within the cluster. The module weight for each bump is calculated by

$$w_i = \frac{E_i \exp(-2.5 r_i / r_m)}{\sum_j E_j \exp(-2.5 r_j / r_m)} \quad (3.2)$$

with

- r_m = Molière radius of the scintillator material,
- r_i, r_j = distance of the i TH and j TH module to the centre of the bump, respectively, and
- index j runs over all modules.

The procedure is iterated until convergence. The centre position is always determined from the weights of the previous iteration and convergence is reached when the bump centre stays stable within a tolerance of 1 mm.

The spatial position of a bump is calculated via a centre-of-gravity method. The radial energy distribution, originating from a photon, decreases mainly exponentially. Therefore, a logarithmic weighting with

$$W_i = \max(0, A(E_b) + \ln(E_i/E_b)) \quad (3.3)$$

	TS EMC	FW EMC
E_{xtl}	3 MeV	8 MeV
E_{cl}	10 MeV	15 MeV
E_{max}	20 MeV	10 MeV

Table 3.1: Reconstruction thresholds for the PbWO₄ and Shashlyk calorimeter.

was chosen, where only modules with positive weights are used. The energy dependent factor $A(E_b)$ varies between 2.1 for the lowest and 3.6 for the highest photon energies.

3.3.2.2 Reconstruction Thresholds

The optimal choice for the three photon reconstruction thresholds – as already explained in 3.3.2.1 – depends strongly on the light yield of the scintillator material and the electronics noise. To detect low energetic photons and to achieve a good energy resolution, the thresholds should be set as low as possible. On the other hand, the thresholds must be sufficiently high for a suppression of misleadingly reconstructed photons originating from the noise of the readout and from statistical fluctuations of the electromagnetic showers. The single crystal threshold was set to 3 MeV of deposited energy, corresponding to the energy equivalent of 3σ of the electronics noise (see Sec. 3.2.2.3). All reconstruction thresholds for the TS EMC as well as for the FW EMC are listed in Table 3.1.

3.3.2.3 Leakage Corrections

The sum of the energy deposited in the scintillator material of the calorimeters is in general less than the energy of the incident photon. While only a few percent is lost in the TS EMC, which mainly originates from energy losses in the material between the individual crystals, a fraction of roughly 70% of the energy is deposited in the absorber material for the Shashlyk calorimeter.

The reconstructed energy of the photon in the TS EMC is expressed as a product of the measured total energy deposit and a correction function which depends logarithmically on the energy and – due to the layout – also on the polar angle. Monte Carlo simulations using single photons have been carried out to determine the corrected photon energy $E_{\gamma,cor} = E * f(\ln E, \theta)$ with the correction func-

tion

$$f(\ln E, \theta) = \exp(a_0 + a_1 \ln E + a_2 \ln^2 E + a_3 \ln^3 E + a_4 \cos(\theta) + a_5 \cos^2(\theta) + a_6 \cos^3(\theta) + a_7 \cos^4(\theta) + a_8 \cos^5(\theta) + a_9 \ln E \cos(\theta))$$

Fig. 3.9 shows the result for the barrel part in the θ range between 22° and 90°.

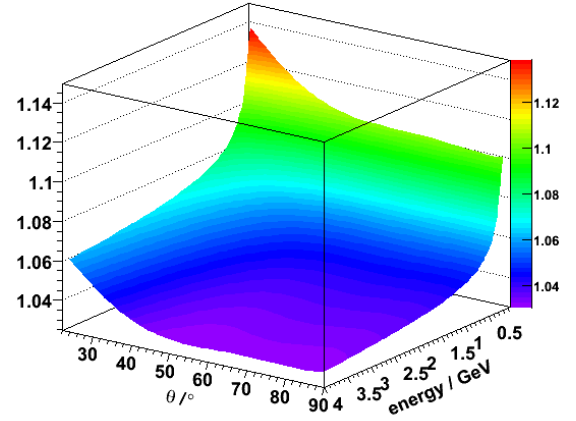


Figure 3.9: The leakage correction function for the barrel EMC in the θ range between 22° and 90°.

The energy leakage in the FW EMC is mainly driven by the huge amount of absorber material and is just slightly caused by the geometry. Therefore, a correction has been considered which only depends on the collected energy. Fig. 3.10 shows the resulting correction function for energies up to 5 GeV.

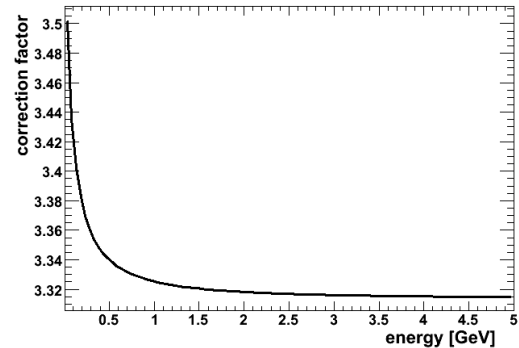


Figure 3.10: The leakage correction function depending on the deposited energy for the Shashlyk calorimeter.

3.3.3 Charged Particle Identification

Good particle identification for charged hadrons and leptons plays an essential role for PANDA and must be guaranteed over a large momentum range from 200 MeV/c up to approximately 10 GeV/c. Several subdetectors provide useful PID information for specific particle species and momenta. While energy loss measurements within the trackers obtain good criteria for the distinction between the different particle types below 1 GeV/c, the DIRC detector is the most suitable device for the identification of particles with momenta above the Cerenkov threshold. Moreover, in combination with the tracking detectors, the EMC is the most powerful detector for an efficient and clean electron identification, and the Muon detector is designed for the separation of muons from the other particle species. The best PID performance however can be obtained by taking into consideration all available information of all subdetectors.

The PID software is divided in two different parts. In the first stage the recognition is done for each detector individually, so that finally probabilities for all five particle hypothesis (e , μ , π , K and p) are provided. The probabilities are normalised uniquely by assuming same fluxes for each particle species.

In the second stage the global PID combines this information by applying a standard likelihood method. Based thereon, flexible tools can be used which allow an optimisation of efficiency and purity, depending on the requirements of the particular physics channel.

3.3.3.1 Subdetector PID

3.3.3.1.1 dE/dx Measurements The energy loss of particles in thin layers of material directly provides an access to the dE/dx . As can be seen directly from the Bethe-Bloch formula, for a given momentum particles of different types have different specific energy losses, dE/dx . This property can be used for particle identification, as illustrated in Fig. 3.11. The method however suffers from two limitations. First of all, at the crossing points, there is no possibility to disentangle particles. Secondly, the distribution of the specific energy loss displays a long tail which constitutes a limitation to the separation, especially when large differences exist between the different particle yields. Various methods have been worked out to circumvent this second limitation. In PANDA, two detectors will give access to a dE/dx measurement, the MVD detector setup, and the central spectrometer tracking system. In

the present status of the simulation, only the Straw Tube Tracker option has been investigated in detail. Although not discussed here, the TPC will also be able to give very good identification capabilities through dE/dx measurements.

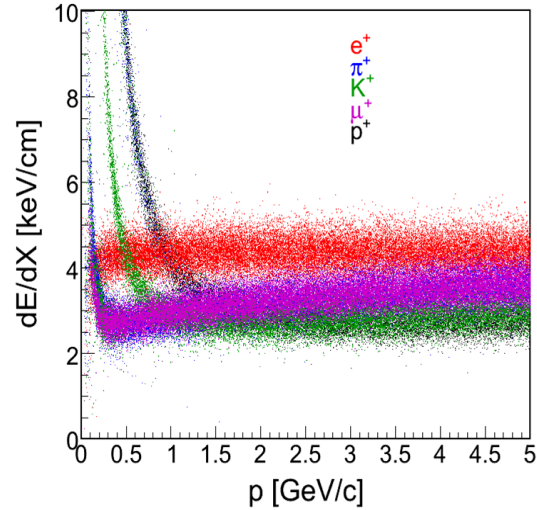


Figure 3.11: Typical truncated dE/dx plot as a function of momentum for the 5 particle types

3.3.3.1.1.1 MVD Although the number of reconstructed MVD hit points per track is limited to 4 in the barrel section and 5-6 in the forward domain the energy loss information provided by the readout electronics can be used as part of the particle identification decision. The ability of separating

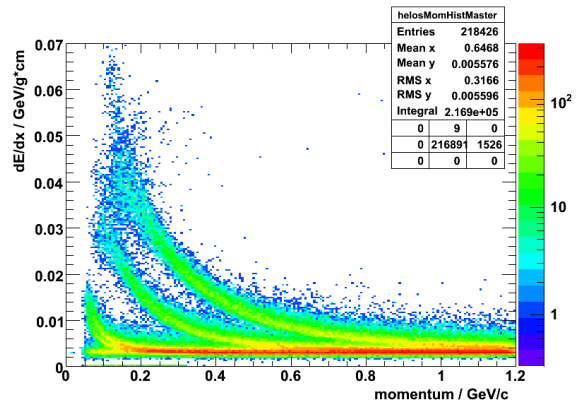


Figure 3.12: dE/dx information from the MVD versus track momentum for protons (upper band), kaons (middle) and pions/muons/electrons (lower).

different particle species relies on an accurate energy loss information and a good knowledge of the

track position with respect to the sensors. Contrary to the usual method of summing the individual hit measurements dE_i/dx_i to an energy loss information all hit measurements can be combined to a total quantity

$$S = \frac{\sum dE_i}{\sum dx_i} n_e^{-1}$$

where n_e^{-1} is the electron density in silicon. The dE_i are the energy information from the reconstructed hit and the dx_i are obtained by calculating the length of the reconstructed track traversing the sensor material. This method gives a slightly smaller spread of the Landau-smeared energy loss. Fig. 3.12 shows the calculated energy loss versus particle momentum for different particle types. Separation is possible only for protons (upper band) and kaons (middle) from the lowest band which is a superposition of pions, muons and electrons.

The width of the individual bands depends on the energy-loss distribution which varies with momentum. To reproduce the distribution all uncertainties are merged into a single Gaussian-distributed error which is added to the already Landau-distributed energy loss. The distribution has to be calculated using numerical integration of the convolution integral

$$w(s) = \int L(x) G(s-x) dx$$

with the parameters σ for the Gauss width, τ respectively for the Landau width and s , which is the most probable value of the Landau distribution. The used parametrisations for the distributions are

$$G_\sigma(x) = \frac{1}{\sqrt{2\pi}\sigma} e^{-x^2/\sigma^2}$$

for the Gauss distribution and

$$L_\tau(x) = \frac{1}{\pi\tau} \int_0^\infty e^{-t(\ln t - x/\tau)} \sin(\pi t) dt$$

for the scaled Landau distribution. For each particle type the parameters were obtained independently by generating 3×10^5 single particle events each over a momentum range from 50 MeV/c to 1.5 GeV/c. The energy loss distribution was fitted for 25 MeV/c bins to get the parameters \hat{s}_i , σ_i , τ_i for a given p_i . The width parameters σ and τ for protons are shown in Fig. 3.13 and the small inset shows the energy loss distribution for the momentum bin $\Delta p = 0.65 \dots 0.675$ GeV/c. For all particle types the evolution of the parameters $\hat{s}(p)$, $\sigma(p)$ and $\tau(p)$ are fitted with polynomials and used as a basis for the calculation of the particle hypothesis.

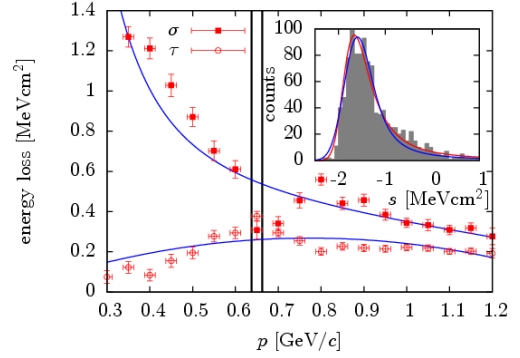


Figure 3.13: The change of the width parameters σ and τ for protons.

3.3.3.1.1.2 STT The energy loss of particles through thin layers of gas provides an opportunity for particle identification in a large domain of momentum. However, when thicknesses as low as a few mm of gas are considered, the fluctuations resulting from the relatively low number of primary collisions (less than 100 on a 1 cm Ar pathlength) give rise to an extended Landau tail in the energy loss distribution. To circumvent this phenomenon which could result into a dramatic reduction of PID capabilities, truncation methods associated to different averaging procedures are often used. The truncated arithmetic mean has been used in the framework of \bar{P} ANDA. Moreover, as straw tubes are cylindrical detectors, a path length determination is necessary to calculate a dE/dx . A transverse resolution of 150 μm was assumed. With the used hexagonal STT setup, particles pass 24 straw tubes on average in the angular range from 22° to 140° . This number decreases rapidly to 8 straw tubes at 14° .

A truncation parameter of 70, corresponding to keeping 70% of the smallest energy loss values, was found to be the best compromise between the resolution defined by the Gaussian fit and the tail still remaining after truncation. Parameters of the Gaussians (μ_i and σ_i) were obtained and tabulated for all particle types over the angular range $[14^\circ, 140^\circ]$ covered by the STT and for momenta ranging from a minimum of 400 MeV/c up to the maximum allowed by kinematics in $\bar{p}p$ collisions at 15 GeV/c. The dependence on the angle ϕ was not included in the simulation. However, the effect is expected to be important only in the two 6° wide ϕ angular regions at 90° and 270° . Outside the above mentioned limits, a priori probabilities are shared equally between all particle types e, μ, π, K and p . For a given triplet $(p, \theta, dE/dx_{trunc})$, five a priori

probabilities are calculated using the parameters of the Gaussians (μ_i, σ_i , $i = e, \mu, \pi, K$ and p), properly normalised. To take into account the role of possible non Gaussian tails, a lower limit on the likelihood was set to 1%. These likelihoods can then be directly combined with the ones from the other detectors to calculate a global likelihood.

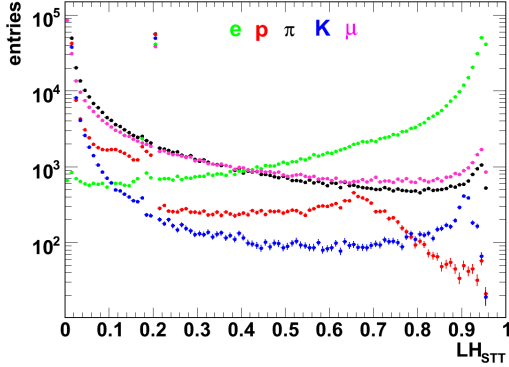


Figure 3.14: The distribution of the likelihoods for electron identification, averaged over the whole STT angular range in the $[0.2, 10.]$ GeV/ c momentum range. The peak at 0.2 corresponds to cases when all particle likelihoods are finally set to the same value of 0.2: this happens when all 5 first-guess likelihoods are below 1%.

Fig. 3.14 shows the likelihoods for being identified as electrons for particles with momenta between 0.2 GeV/ c and 10 GeV/ c and polar angles between 14° and 140° .

Whereas an efficiency above 98% is observed for electrons (see figure Fig. 3.15), the contamination rate, that is the probability for another type of particle (μ, π, K and p) to be identified as an electron varies between 1% and 16%. One should, however, note that these values are averaged over the polar angle: at forward angles, the contamination increases as the result of the strong decrease of the number of hits in the straw tubes.

3.3.3.1.2 PID with DIRC Charged tracks are considered if they can be associated with the production of Cerenkov light in the DIRC detector. Based on the reconstructed momentum, the reconstructed path length of the particle in the quartz radiator and the particle hypotheses the expected Cerenkov angles and its errors are estimated. Compared with the measured Cerenkov angle the likelihood and significance level for each particle species are calculated. As an example for the DIRC performance Fig. 3.16 shows the obtained kaon effi-

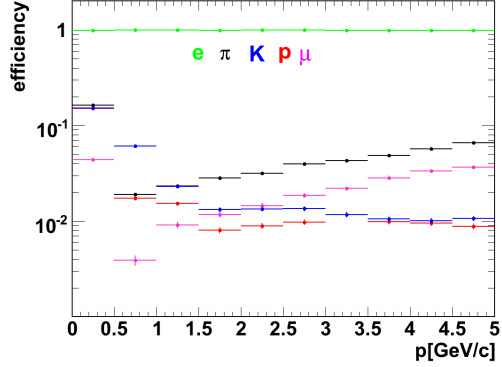


Figure 3.15: The efficiency for electrons in the momentum range between 0.2 GeV/ c and 10 GeV/ c and the contamination rates for the four other particle types, averaged over the whole STT angular range.

ciency and contamination rate by applying a **Loose** kaon criterion on the DIRC PID. The loose criterion corresponds to the kaon probability of 30%. While below the Cerenkov threshold of approximately 500 MeV/ c almost no kaon can be identified the efficiency above the threshold is more than 80% over the whole momentum range up to 5 GeV/ c . The fraction of pions misidentified as kaons is substantially less than 10^{-3} for momenta below 3 GeV/ c and increases up to 10% for 5 GeV/ c .

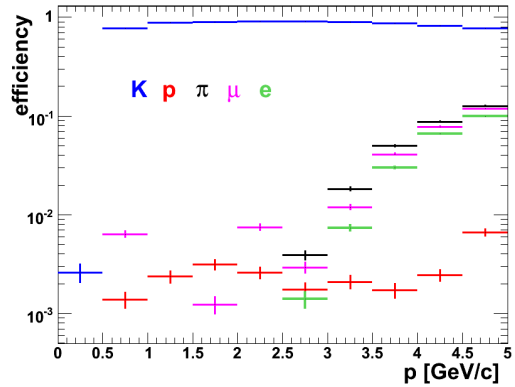


Figure 3.16: The kaon efficiency and contamination rate of the remaining particle species in different momentum ranges by using the DIRC information.

3.3.3.1.3 Electron Identification with the EMC The footprints of deposited energy in the calorimeter differ distinctively for electrons, muons and hadrons. The most suitable property is the de-

posited energy in the calorimeter. While muons and hadrons in general lose only a certain fraction of their kinetic energy by ionisation processes, electrons deposit their complete energy in an electromagnetic shower. The ratio of the measured energy deposit in the calorimeter to the reconstructed track momentum (E/p) will be approximately unity. Due to the fact that hadronic interactions can take place, hadrons can also have a higher E/p ratio than expected from ionisation. Figure Fig. 3.17 shows the reconstructed E/p fraction for electrons and pions as a function of the momentum.

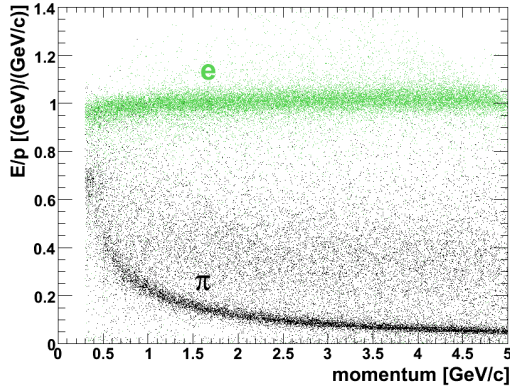


Figure 3.17: E/p versus track momentum for electrons (green) and pions (black) in the momentum range between 0.3 GeV/c and 5 GeV/c.

Furthermore, the shower shape of a cluster is helpful to distinguish between electrons, muons and hadrons. Since the chosen size of the scintillator modules corresponds to the Molière radius of the material, the largest fraction of an electromagnetic shower originating from an electron is contained in just a few modules. Instead, a hadronic shower with a similar energy deposit is less concentrated. These differences are reflected in the shower shape of the cluster, which can be characterised by the following properties:

- E_1/E_9 which is the ratio of the energy deposited in the central scintillator module and in the 3×3 module array containing the central module and the first innermost ring. Also the ratio between E_9 and the energy deposit in the 5×5 module array E_{25} is useful for electron identification.
- The lateral moment of the cluster defined by

$$mom_{LAT} = \frac{\sum_{i=3}^n E_i r_i^2}{\left(\sum_{i=3}^n E_i r_i^2 + E_1 r_0^2 + E_2 r_0^2\right)}$$

with

- n : number of modules associated to the shower
- E_i : deposited energy in the i TH module with $E_1 \geq E_2 \geq \dots \geq E_n$
- r_i : lateral distance between the central and the i TH module
- r_0 : the average distance between two modules.
- A set of Zernike moments which describe the energy distribution within a cluster by radial and angular dependent polynomials. An example is given in Fig. 3.18, where the Zernike moment 31 is depicted for each particle type.

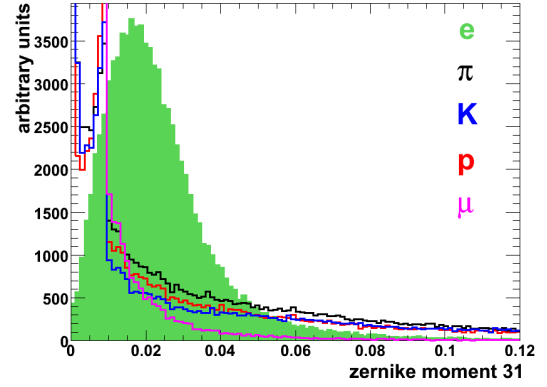


Figure 3.18: Zernike moment for electrons, muons and hadrons.

Since a lot of partially correlated EMC properties are suitable for electron identification, a Multilayer Perceptron (MLP) with 10 input nodes, 13 hidden nodes, and one output node has been applied. The advantage of a neural network is that it can provide a correlation between a set of input variables and one or several output variables without any knowledge of how the output formally depends on the input. The training of the MLP has been done with a data set of 850k single tracks for each particle species (e, μ , π , K and p) in the momentum range between 200 MeV/c and 10 GeV/c in such a way that the output values are constrained to be 1 for electrons and -1 for all other particle types. 10 input variables in total have been used, namely E/p , p , the polar angle θ of the cluster, and 7 shower shape parameters (E_1/E_9 , E_9/E_{25} , the lateral moment of the shower and 4 Zernike moments). The response of the trained network to a test data set of single particles in the momentum range between

300 MeV/c and 5 GeV/c is illustrated in Fig. 3.19. The logarithmically scaled histogram shows that an almost clean electron recognition with a quite small contamination of muons and hadrons can be obtained by applying a cut on the network output.

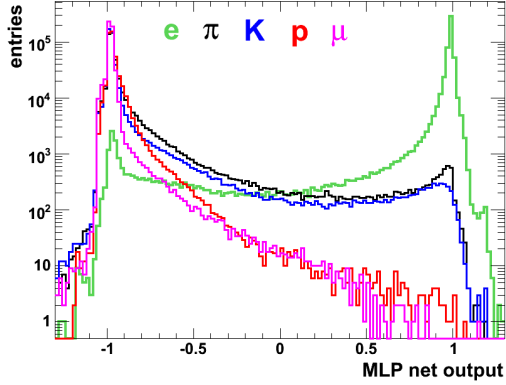


Figure 3.19: MLP network output for electrons and the other particle species in the momentum range between 300 MeV/c and 5 GeV/c.

For the global PID a correlation between the network output and the PID likelihood of the EMC has been calculated. Fig. 3.20 shows the electron efficiency and contamination rate as a function of momentum achieved by requiring an electron likelihood fraction of the EMC of more than 95%. For momenta above 1 GeV/c one can see that the electron efficiency is greater than 98% while the contamination by other particles is substantially less than 1%. For momenta below 1 GeV/c, the electron identification based solely on the EMC information has a poor efficiency and an insufficient purity.

3.3.3.1.4 PID with the Muon Detector The particle ID for the muon detector is based on an algorithm which quantifies for each reconstructed charged track the compatibility with the muon hypothesis. It propagates the charged particles from the tracking volume outward through the neighbouring detectors like DIRC and EMC and finally through the iron, where the scintillator layers of the muon device are located. This procedure takes into account the obtained parameters of the global tracking, the magnetic field as well as the muon energy loss in the material and the effects of multiple scattering. Then the extrapolated intersection points with the scintillators are compared with the detected muon hit positions. In case the distance between the expected and the detected hit is smaller than 12 cm, according to 4σ of the correspond-

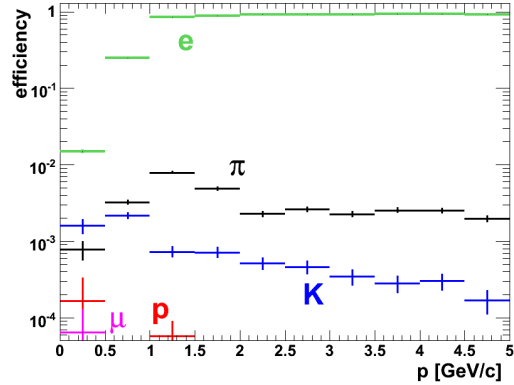


Figure 3.20: The electron efficiency and contamination rate for muons, pions, kaons and protons in different momentum ranges by using the EMC information.

ing distribution, the muon hit will be associated with the corresponding charged track. Fig. 3.21 shows an example for the obtained spatial resolution between the expected and the corresponding detected hits. The distribution of the distance in x-direction for generated single muons yields to a resolution $\sigma_x = 3.0$ cm. Based on the numbers of associated and expected muon hits, the likelihoods for each particle type are estimated.

The procedure results in a good muon identification for momenta above approximately 1 GeV/c. While electrons can be completely suppressed, a contamination rate of only a few percent can be achieved for hadrons.

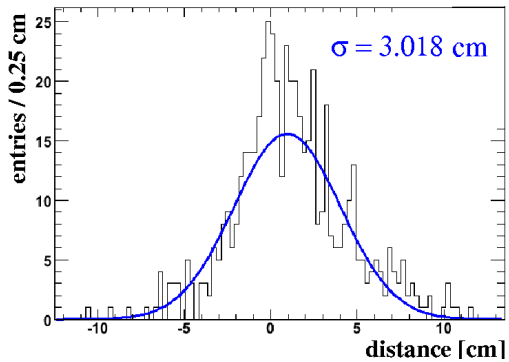


Figure 3.21: The distribution of the distance in x-direction between the expected hits obtained by the extrapolation and the corresponding detected hits in the muon detector. This figure illustrates an example for generated single muon particles hitting on specific layer within the barrel yoke.

3.3.3.2 Global PID

The global PID, which combines the relevant information of all subdetectors associated with one track, has been realised with a standard likelihood method. Based on the likelihoods obtained by each individual subdetector the probability for a track originating from a specific particle type $p(k)$ is evaluated from the likelihoods as follows:

$$p(k) = \frac{\prod_i p_i(k)}{\sum_j \prod_i p_i(j)}, \quad (3.4)$$

where the product with index i runs over all considered subdetectors and the sum with index j over the five particle types e , μ , π , K and p .

Due to the variety of requirements imposed by the different characteristics of the benchmark channels various kinds of particle candidate lists depending on different selection criteria on the global likelihood are provided for the analysis (see. Table 3.2). The usage of the so-called **VeryLoose** and **Loose** candidate lists allows to achieve good efficiencies, and the **Tight** and **VeryTight** lists are optimised to obtain a good purity with efficient background rejection. Fig. 3.22 represents the performance of the global PID for the **VeryTight** list for kaon and electron candidates, respectively.

particle	candidate list			
	VeryLoose	Loose	Tight	VeryTight
e	20 %	85 %	99 %	99.8 %
μ	20 %	45 %	70 %	85 %
π	20 %	30 %	55 %	70 %
K	20 %	30 %	55 %	70 %
p	20 %	30 %	55 %	70 %

Table 3.2: Selection criteria for the particle candidate lists provided for the analysis. The table represents the minimal values for the global likelihood (see. Eq. 3.4), which are required for the corresponding particle types.

3.4 Physics Analysis

The event data used for physics analysis is structured in three levels of detail:

- the small TAG level contains brief event summary data
- the Analysis Object Data (AOD) mainly consists of PID lists of particle candidates, and, in the case of MC data, also of MC truth data. Most analysis jobs run on AOD data.

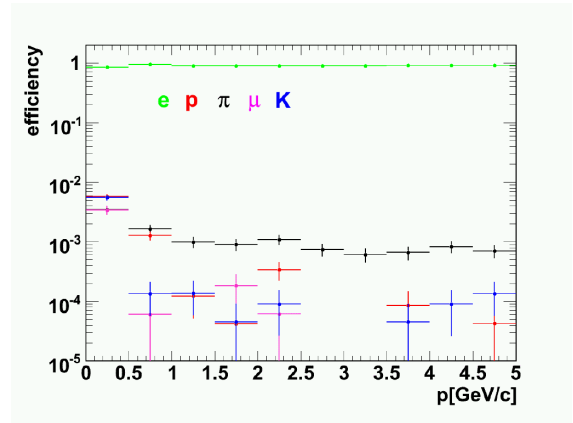
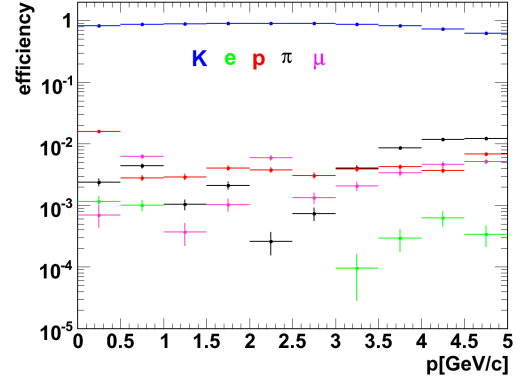


Figure 3.22: The kaon (upper histogram) and electron (lower histogram) efficiency with the contamination rate of the remaining particle species in different momentum ranges by applying **VeryTight** cuts on the global likelihood. The results are based on single particles generated within the θ range between 25° and 140° .

- the Event Summary Data (ESD), which holds all reconstruction objects down to the detector hits which are necessary to redo the track and neutral particle reconstruction, and to rebuild the PID information. The detailed ESD data is needed only by very few analysis jobs.

This event data design directly supports the typical analysis tasks, which usually can be subdivided into three steps:

- a fast event preselection that uses just the TAG data
- an event reconstruction and refined event selection step using the AOD data. In the event reconstruction, decay trees are built up, and geometrical and kinematic fits are applied on them. Cuts on the fit probabilities, invariant masses or kinematic properties of the candi-

dates are common to refine the event selection in this step. The output of this analysis step usually are n-tuple like data.

- in the last analysis step the event selection can be further refined by applying cuts on the n-tuple data, and histogram fits or partial wave analyses can be performed on the final set of events.

3.4.1 Analysis Tools

The used application framework provides filter modules which allow a TAG based event selection. For events which do not pass this selection, only the relative small TAG has to be read in. This yields in a significant speed up of the analysis jobs.

The analysis user has the choice to reconstruct decay trees, perform geometrical and kinematic fits, and to refine the event selection by using Beta, BetaTools and the fitters provided by the analysis software [37] directly in an application framework module, or by defining the analysis in a more abstract way using *SimpleComposition* tools. This TCL based high level analysis tool package provides an easy-to-learn user interface for the definition of an analysis task and the production of n-tuples, and it allows to set up analysis jobs without the need to compile any code. *SimpleComposition* as well as Beta, BetaTools and the geometric and kinematic fitters were taken over as well tested packages from BaBar, and adapted and slightly extended for PANDA.

For the exclusive benchmark channels it turned out that especially a 4C-fit of the reconstructed decay tree is a powerful tool to improve the data quality and to suppress background. 4C-fits and cuts on the results can also be defined in *SimpleComposition*. Fig. 3.23 shows an example of a drastic improvement of the mass resolution for a composite particle.

The last n-tuple based analysis steps were carried out utilising the ROOT [38] toolbox, which provides powerful, interactively usable instruments among others for cutting, histogramming, and fitting.

3.5 Data Production

The Monte Carlo data used for this document were produced in a centrally organised way. All simulation requests are stored in a MySQL database, and all job scripts and configuration files are produced automatically by Perl and PHP scripts. Also the

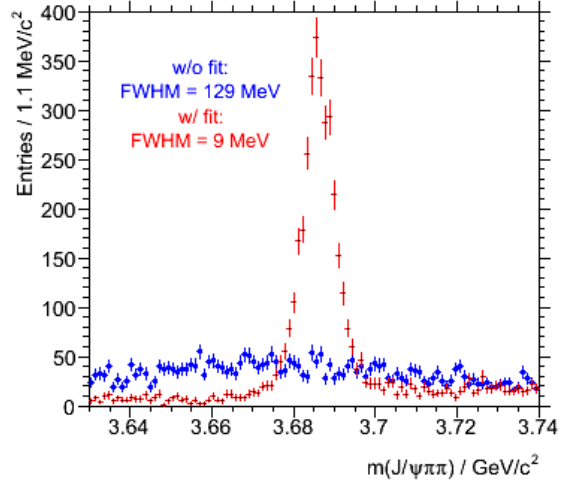


Figure 3.23: $J/\psi \pi^+ \pi^-$ mass spectra from $\bar{p}p \rightarrow \Psi(2S) \pi^+ \pi^- \rightarrow J/\psi 2\pi^+ 2\pi^-$ before and after applying a 4C-fit to the decay tree with requiring a common vertex for $J/\psi \rightarrow e^+ e^-$.

scanning of the log files of the simulation jobs is automated, and the determined job status is noted in the database, too.

The analysis users could get the actual status of the simulation production for an individual channel from a web page. With a tool available in the \bar{P} ANDA software they could configure the input of their analysis jobs and split an analysis task into an adequate number of jobs, which could run in parallel on one of the batch farms.

Because none of the involved computing sites listed in Table 3.3 had sufficient computing and storage resources available for \bar{P} ANDA, the data production for the simulation was distributed over four sites, namely the IPN in Orsay [39], the CCIN2P3 in Lyon, the Ruhr-Universität Bochum, and the GSI at Darmstadt. Table 3.3 lists the contributions of the sites to the simulation production. In total $22 \cdot 10^6$ signal events for 22 channels, $1002 \cdot 10^6$ dedicated background events including the dominant background reactions for the individual analyses and $280 \cdot 10^6$ generic background events were produced in 29 weeks. The typical event size was 3.5 kByte for AOD and TAG data, and 4.4 kByte for the ESD component.

The network bandwidth between the production sites was limited and did not allow to copy over analysis data from one site to another for a large number of events. Therefore, most analysis jobs ran at the site where the analysis data were produced.

site	events [10 ⁶]	stored data [TB]
Lyon	551	4.4
GSI	308	2.4
Orsay	149	1.2
Bochum	297	2.3

Table 3.3: Contributions of the computing sites to the Physics Book simulation production.

3.5.1 Filter on generator level

To achieve the relevant number of background events in a reasonable time, an event filter on the generator level has been applied for the data production of certain benchmark channels. The strategy is to consider only those background events which are possible candidates for passing all the selection criteria in the analysis. In particular the filter has been applied for benchmark channels including an J/ψ . In this case only events have been produced where the invariant mass of two charged particles (with the hypothesis that it was a e^+e^- pair) are within a certain J/ψ mass window. This method will now be explained and justified in detail for the example $J/\psi\eta$.

3.5.1.1 Validation of the generator filter method on the J/ψ analysis

In this analysis one relevant background channel is $\pi\pi\eta$. It had to be justified that the generated mass of the $\pi\pi$ system, with the pions falsely identified as electrons, can be limited to the J/ψ signal region.

A generator-level filter is applied in the following way. The four-vectors of the pions are recalculated with an electron mass hypothesis and are afterwards combined. The resulting invariant mass must lie within [2.8; 3.2] GeV/c^2 , corresponding to the J/ψ signal region. Another two data samples are created with the combined invariant mass between [2.4; 2.8] GeV/c^2 and [3.2; 3.6] GeV/c^2 , respectively, corresponding to the sideband regions below and above the J/ψ signal region.

10 million events have been generated for each of the three described mass regions at a beam momentum of $\bar{p}p = 8.6819 \text{ GeV}/c$.

The $\bar{p}p \rightarrow J/\psi\eta \rightarrow e^+e^-\gamma\gamma$ analysis module is run against the reconstructed $\pi\pi\eta$ data. The number of reconstructed entries in the signal region in dependence of the electron PID criteria is shown in Table 3.4. In Fig. 3.24 the resulting reconstructed $J/\psi\eta$ mass is shown after applying all cuts for events

$\mathcal{L}_{e^+e^-}$		reconstr. events		
e^\pm	e^\mp	SR	SB_l	SB_r
> 0%	> 0%	204269	0	0
> 0%	> 20%	18965		
> 20%	> 20%	338		
> 20%	> 85%	64		
> 85%	> 85%	3		
> 85%	> 99%	1		
> 99%	> 99%	0		

Table 3.4: Number of reconstructed $J/\psi\eta$ candidates from the background mode $\pi\pi\eta$, for different electron PID criteria, in three regions of the generated invariant $\pi\pi$ mass under electron mass hypothesis: J/ψ signal region SR and left and right J/ψ sideband regions (SB_l and SB_r , resp.).

from the J/ψ signal region. No PID requirements have been applied on the false electron candidates. About 200000 candidates are left out of 10 million. For events from the J/ψ sideband regions, there are no candidates left after applying the same selection criteria. Fig. 3.25 shows the reconstruction efficiency on the Monte Carlo truth level.

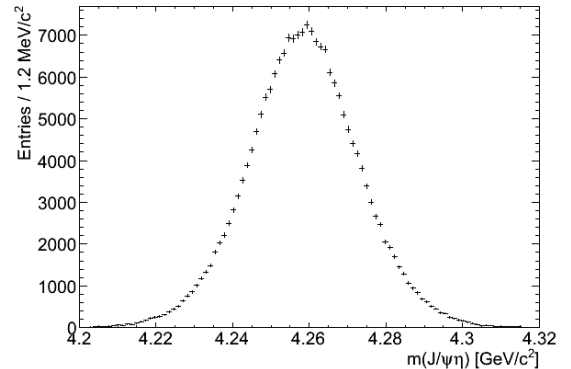


Figure 3.24: Reconstructed $J/\psi\eta$ mass from the background mode $\pi\pi\eta$, with the $\pi^+\pi^-$ mass (under electron mass hypothesis) within the J/ψ signal region.

In summary, one can limit the production to events whose generated $\pi\pi$ mass under electron mass hypothesis lies near the J/ψ mass. With a filter efficiency of 14%, the production time can be reduced by a factor of 7.

3.6 Software developments

The development of a next-generation simulation and analysis framework for

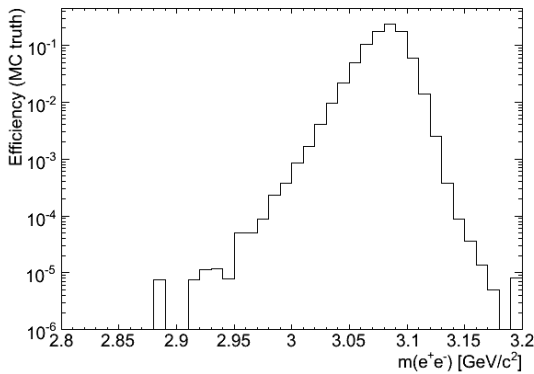


Figure 3.25: Reconstruction efficiency for wrongly identified e^+e^- pairs (Monte Carlo truth mass).

PANDA was initiated at the end of 2006. The new software infrastructure, called **PANDARoot**, is designed to improve the accessibility for beginning users and developers, to increase the flexibility to cope with future developments and to enhance synergy with other nuclear and high-energy physics experiments. In addition, it will provide a complete reconstruction and pattern-recognition chain to overcome the shortcomings of the older analysis framework. Most of the functionalities of the software infrastructure as described in the previous sections have been embedded in **PANDARoot** as well. Below, only the most important new elements of **PANDARoot** are described.

The core services for the detector simulation and offline analysis are provided by the **FAIRroot** framework [40], which is based on the object-oriented data analysis framework, **ROOT** [38], and the Virtual Monte-Carlo (**VMC**) interface [41]. **FAIRroot** enables the integration of a detailed magnetic-field map, advanced parameter handling with an interface to an Oracle database, the usage of a large set of event generators, presently **EvtGen**, **DPM**, **UrQMD**, and **Pluto**, and, since recently, a graphical tool to display reconstructed or Monte-Carlo based hits and tracks. Furthermore, a modular design of the framework is guaranteed via a task mechanism. With this, the developer can setup simulation, reconstruction, and analysis algorithms in well-separated and exchangeable tasks, which the user can exploit to compare different algorithms and methods for his or her application. Fig. 3.26 depicts the various ingredients of **FAIRroot** and its coupling to **ROOT**, **VMC**, and the two available branches, **PANDARoot** and **CBMroot**.

The **VMC** interface allows to perform easily, *e.g.* without the need to alter the user code, simu-

lations using various transport models, presently **Geant3** [42], **Geant4** [43], and **Fluka** [44]. For the modelling of the detector geometry, a vitalisation scheme, virtual geometry model (**VGM**), has been employed as well. The vitalisation concept foresees a transparent transition between older and newer transport models, thereby, improving the validity and lifetime of the framework significantly. Besides the option to run a simulation using one of the Monte-Carlo transport codes, the new framework includes a fast simulation package based on a parametrisation of the individual detector responses. The parametrisation is obtained by a comparison with the results from experimental data or from simulations using one of the full transport code. The fast-simulation package is used to generate large numbers of background events within an acceptable period of time.

Fig. 3.26 sketches the various simulation and analysis steps which are part of the **PANDARoot** framework. The new framework enables a complete reconstruction of tracks which does not depend upon the true origin of hits given by the Monte-Carlo transport code. For this, the information of the transport model is pre-processed to simulate the signals from the individual detector components. In Fig. 3.27 this procedure is indicated as *digitiser*. The data after this process represent the digitised detector response and are, therefore, comparable with experimental data. The following part, *reconstruction*, takes only this data as input to find tracks and to reconstruct the momenta, scattering angles, and the type of particle. Note that such an unbiased reconstruction procedure allows to study background due to fake tracks and pileup effects as well.

Efficient and fast algorithms, based on conformal mapping [45] or extended Riemann [46] techniques, can be exploited to find charged tracks, to correlate them with the information of various PID detectors of

PANDA. and to use as a pre-fit for a more precise track-fitter package. A track follower based on the well-tested **GEANE** package [42] combined with a generic Kalman filter provide a tool set to optimise the momentum reconstruction for charged particles. With these algorithms and tools, the new framework enables a realistic and complete track finding and pattern recognition.

For a complete particle identification, the propagation of Cerenkov photons is simulated and ring-finding algorithms for the **DIRC** are being implemented. Furthermore, for the global particle identification, multi-dimensional probability distribu-

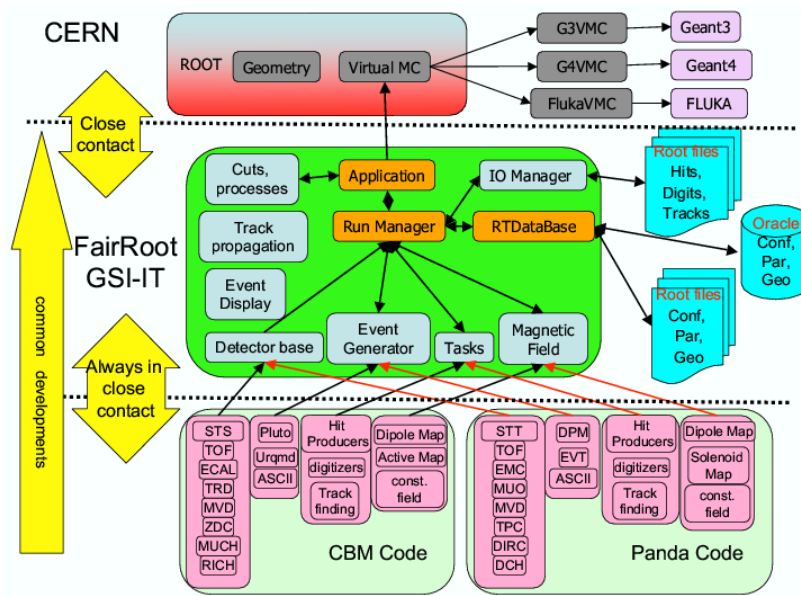


Figure 3.26: An illustration of the building blocks of FAIRroot. The framework inherits the functionalities of ROOT and Virtual Monte Carlo. The core elements of FAIRroot are indicated in the green box in the middle of the figure. The two boxes at the bottom of the figure represent the ingredients of the CBMroot and PANDARoot branches and both are based on FAIRroot.

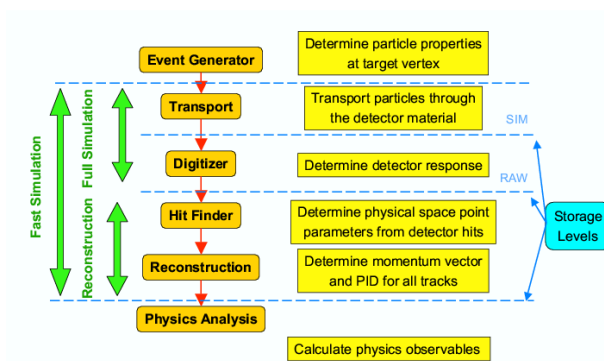


Figure 3.27: A sketch of the simulation and reconstruction chain of PANDARoot.

tions for the different particle types are provided using the k-nearest neighbourhood technique [47] together with a very fast multi-variate classification method based on self-organising maps [48].

For the higher-level analysis activities, the Rho package [49] have been embedded in the PANDARoot framework. The Rho package is an analysis tool kit which is optimised for interactive work and performance. It owes a lot to its predecessors, including

the BETA package [37], which has been described briefly in the previous sections. Unlike Beta, Rho is based on the solid fundamentals of the ROOT framework and runs interactively on all computing platforms supporting ROOT. The PANDARoot framework is enriched with vertex and kinematic fitting tools, based on the KFitter package from the Belle collaboration [50].

The PANDARoot framework is designed to run on a large variety of computing platforms. This has the advantage that the software can be employed easily on a GRID environment. The PANDA collaboration is presently expanding and maintaining an AliEN² GRID network [51] in synergy with the Alice collaboration and with the PANDARoot developments. A complete simulation and analysis chain has been tested successfully on the GRID which presently consists of about ten sites and gradually expanding. In addition, advanced monitoring tools, based on MonALISA, are being used in connection to the GRID and framework developments.

The development of the new simulation and analysis framework ran in parallel with the physics-benchmark simulations for this booklet. Hence, nearly all the channels were so-far studied using the predecessor of the PANDARoot framework. How-

ever, one of the electromagnetic channels, namely $\bar{p}p \rightarrow \gamma\gamma$, was simulated and analysed using PAN-DAroot. This channel depends primarily on the reconstruction code of the electro-magnetic calorimeter, which was successfully derived from the old framework, and, therefore, identical to the code which was used for the studies of all other channels. The new framework in combination with the GRID infrastructure will be used in the near future to perform simulations of an extended set of benchmark reactions.

References

- [1] D. J. Lange, Nucl. Instrum. Meth. **A462**, 152 (2001).
- [2] J. Catmor, R. Jones, and M. Smizanska, Development of the EvtGen package for the LHC and ATLAS, Proc. of CHEP2006, Mumbai, India, September 2006.
- [3] A. Capella, U. Sukhatme, C.-I. Tan, and J. Tran Thanh Van, Phys. Rept. **236**, 225 (1994).
- [4] X. Artru, Nucl. Phys. **B85**, 442 (1975).
- [5] G. C. Rossi and G. Veneziano, Nucl. Phys. **B123**, 507 (1977).
- [6] L. Montanet, G. C. Rossi, and G. Veneziano, Phys. Rept. **63**, 149 (1980).
- [7] T. T. Takahashi, H. Matsufuru, Y. Nemoto, and H. Suganuma, Phys. Rev. Lett. **86**, 18 (2001).
- [8] G. S. Bali, Phys. Rept. **343**, 1 (2001).
- [9] D. S. Kuzmenko and Y. A. Simonov, Phys. Atom. Nucl. **64**, 107 (2001).
- [10] D. S. Kuzmenko and Y. A. Simonov, Phys. Atom. Nucl. **66**, 950 (2003).
- [11] A. B. Kaidalov and P. E. Volkovitsky, Z. Phys. **C63**, 517 (1994).
- [12] V. V. Uzhinsky and A. S. Galoyan, hep-ph/0212369 (2002).
- [13] B. Andersson, G. Gustafson, and C. Peterson, Zeit. Phys. **C1**, 105 (1979).
- [14] B. Andersson, G. Gustafson, and T. Sjostrand, Zeit. Phys. **C6**, 235 (1980).
- [15] S. Ritter, Comput. Phys. Commun. **31**, 393 (1984).
- [16] A. B. Kaidalov, Yad. Fiz. **45**, 1452 (1987).
- [17] A. B. Kaidalov and O. I. Piskunova, Z. Phys. **C30**, 145 (1986).
- [18] K. Hanssger and S. Ritter, Comput. Phys. Commun. **31**, 411 (1984).
- [19] M. Bleicher et al., J. Phys. **G25**, 1859 (1999).
- [20] S. A. Bass et al., Prog. Part. Nucl. Phys. **41**, 225 (1998).

- [21] R. M. Barnett et al., Phys. Rev. **D54**, 1 (1996).
- [22] A. Donnachie and P. V. Landshoff, Phys. Lett. **B296**, 227 (1992).
- [23] P. Koch, B. Muller, and J. Rafelski, Phys. Rept. **142**, 167 (1986).
- [24] B. Andersson, G. Gustafson, and B. Soderberg, Z. Phys. **C20**, 317 (1983).
- [25] S. Eidelman et al., Phys. Lett. **B592**, 1+ (2004), <http://pdg.lbl.gov>.
- [26] K. Abdel-Waged, Phys. Rev. **C67**, 064610 (2003).
- [27] J. P. Bondorf, A. S. Botvina, A. S. Ilinov, I. N. Mishustin, and K. Sneppen, Phys. Rept. **257**, 133 (1995).
- [28] C. Hartnack et al., Eur. Phys. J. **A1**, 151 (1998).
- [29] J. Allison et al., IEEE Transactions on Nuclear Science **53**, 270 (2006).
- [30] S. Agostinelli et al., Nucl. Instrum. Meth. **A506**, 250 (2003).
- [31] P. Arce et al., Nucl. Instrum. Meth. **A502**, 687 (2003).
- [32] Technical report, Technical Design Report for the PANDA EMC, in progress.
- [33] D. Brown, E. Charles, and D. Roberts, The BaBar track fitting algorithm, Proc. Computing in High Energy Physics Conference, Padova, 2000.
- [34] F. James and M. Roos, Comput. Phys. Commun. **10**, 343 (1975).
- [35] B. Aubert et al., Nucl. Instrum. Meth. **A479**, 1 (2002).
- [36] P. Strother, *Design and application of the reconstruction software for the BaBar calorimeter*, PhD thesis, 1998, University of London and Imperial College, UK.
- [37] R. Jacobsen, Beta: A High Level Toolkit for BaBar Physics Analysis, 1997, presented at Conference on Computing in High Energy Physics, Berlin.
- [38] R. Brun and F. Rademakers, Phys. Res. **A389**, 81 (1996 1997).
- [39] Grille de Recherche d'Ile de France, <http://www.grif.fr>.
- [40] FairRoot, Simulation and Analysis Framework, <http://fairroot.gsi.de>.
- [41] Virtual Monte Carlo, <http://root.cern.ch/root/vmc>.
- [42] CERN Program Library W5013 (1991).
- [43] S. Agostinelli et al., Nucl. Instrum. Meth. **A506**, 250 (2003).
- [44] FLUKA, <http://www.fluka.org>.
- [45] P. Yepes, Nucl. Instr. and Meth. **A380**, 582 (1996).
- [46] R. Frühwirth, A. Strandlie, and W. Waltenberger, Nucl. Instr. and Meth. in Phys. Res. **A490**, 366 (2002).
- [47] R. Duda, P. Hart, and D. Stork, *Pattern Classification*, Wiley Interscience ISBN: 0-471-05669-3.
- [48] T. Kohonen, *Self-Organizing Maps*, Springer Series in Information Sciences, Springer, Berlin, Heidelberg, New York (1995,1997,2001).
- [49] Rho: A Set of Analysis Tools for ROOT, <http://savannah.fzk.de/websites/hep/rho/>.
- [50] Belle Kinematic Fitter, <http://hep.phys.s.u-tokyo.ac.jp/jtanaka/BelleSoft/KFitter/>.
- [51] Alien²@GRID, <http://alien.cern.ch>.

4 Physics Performance

COMMENT: Author(s): D. Bettoni, K. Peters

4.1 Overview

COMMENT: Author(s): D. Bettoni, K. Peters

The \bar{P} ANDA experiment will use the antiproton beam from the HESR colliding with an internal proton target and a general purpose spectrometer to carry out a rich and diversified hadron physics program.

The experiment is being designed to fully exploit the extraordinary physics potential arising from the availability of high-intensity, cooled antiproton beams. The aim of the rich experimental program is to improve our knowledge of the strong interaction and of hadron structure. Significant progress beyond the present understanding of the field is expected thanks to improvements in statistics and precision of the data.

Many experiments are foreseen in PANDA.

- The study of **QCD bound states** is of fundamental importance for a better, quantitative understanding of QCD. Particle spectra can be computed within the framework of non-relativistic potential models, effective field theories and Lattice QCD. Precision measurements are needed to distinguish between the different approaches and identify the relevant degrees of freedom. The measurements to be carried out in PANDA include charmonium, D meson and baryon spectroscopy. In addition to that PANDA will look for exotic states such as gluonic hadrons (hybrids and glueballs), multi-quark and molecular states.

- **Non-perturbative QCD Dynamics.**

In the quark picture hyperon pair production either involves the creation of a quark-antiquark pair or the knock out of such pairs out of the nucleon sea. Hence, the creation mechanism of quark-antiquark pairs and their arrangement to hadrons can be studied by measuring the reactions of the type $\bar{p}p \rightarrow \bar{Y}Y$, where Y denotes a hyperon. By comparing several reactions involving different quark flavours the OZI rule, and its possible violation, can

be tested for different levels of disconnected quark-line diagrams separately.

- **Study of hadrons in nuclear matter.** The study of medium modifications of hadrons embedded in hadronic matter is aimed at understanding the origin of hadron masses in the context of spontaneous chiral symmetry breaking in QCD and its partial restoration in a hadronic environment. So far experiments have been focussed on the light quark sector. The high-intensity \bar{p} beam of up to 15 GeV/c will allow an extension of this program to the charm sector both for hadrons with hidden and open charm. The in-medium masses of these states are expected to be affected primarily by the gluon condensate.
- **Hypernuclear physics.** Hypernuclei are systems in which up or down quarks are replaced by strange quarks. In this way a new quantum number, strangeness, is introduced into the nucleus. Although single and double Λ -hypernuclei were discovered many decades ago, only 6 double Λ -hypernuclei are presently known. The availability of \bar{p} beams at FAIR will allow efficient production of hypernuclei with more than one strange hadron, making \bar{P} ANDA competitive with planned dedicated facilities. This will open new perspectives for nuclear structure spectroscopy and for studying the forces between hyperons and nucleons.
- **Electromagnetic Processes.** In addition to the spectroscopic studies described above \bar{P} ANDA will be able to investigate the structure of the nucleon using electromagnetic processes, such as Deeply Virtual Compton Scattering (DCVS) and the process $\bar{p}p \rightarrow e^+e^-$, which will allow the determination of the electromagnetic form factors of the proton in the timelike region over an extended q^2 region.
- **Electroweak Physics.** With the high-intensity antiproton beam available at HESR a large number of D-mesons can be produced. This gives the possibility to observe rare weak decays of these mesons allowing to study electroweak physics by probing predictions of the Standard Model and searching for enhancements introduced by processes beyond the Standard Model.

In this chapter we will discuss in detail the various items of the \bar{P} ANDA physics program and we will describe the Monte Carlo simulations which have been carried out on a number of benchmark channels to study acceptances, resolutions, background rejection. In order to perform these studies a number of tools have been developed, which are described in detail in the previous chapter, and which include a full simulation of the detector response and a series of sophisticated reconstruction and analysis tools. These studies have allowed us to obtain reliable estimates for the performance of the \bar{P} ANDA experiment and the sensitivity of the various measurements.

4.2 QCD Bound States

COMMENT: Author(s): D. Bettoni, K. Peters, A. Gillitzer

4.2.1 The QCD Spectrum

The spectrum of charmonium, like bottomonium, is very similar (apart from the scale) to the spectrum positronium. It is therefore suggestive to assume that $c\bar{c}$ and $b\bar{b}$ (so called conventional mesons) can be understood in the strong interaction in an analogue way as positronium in electroweak interactions. This would imply a Coulomb-like potential and a term which takes care of linear confinement. But this $a/r + br$ potential arising mainly from the exchange of one gluon is by far not sufficient to explain the spectrum of hadrons. The coherent exchange of gluons which manifest in a gluon tube is an important aspect when one wants to understand the binding among strongly interacting particles. Together with mesic excitations and pure gluonic states which are possible in QCD they are usually present in the wave function of hadrons and are often referred to as Fock-States of the ground state meson. The Fock-States may decouple from the ground state and thus being individually observable as individual states. This happens if the lifetime of the objects allow a partitioning into individual objects (*e.g.* width smaller than the mass difference). We see this usually happening for the first rotational excitations of hadrons. For higher excitations they tend to end up in a continuum. Therefore the QCD spectrum is richer than that of the naive quark model (see Fig. 4.1). We distinguish conventional, gluonic and mesic hadrons. Conventional hadrons have been already discussed in Sec. 4.2.2. Gluonic hadrons fall into two categories: glueballs

and hybrids. Glueballs are predominantly excited states of glue while hybrids are resonances consisting largely of a quark, an antiquark, and excited glue. The properties of glueballs and hybrids are determined by the long-distance features of QCD and their study will yield fundamental insight into the structure of the QCD vacuum. Mesic hadrons are dimesons and/or tetra-quarks, often referred to as multi-quarks or baryonium. They may be viewed as a loosely bound meson-anti-meson system or a diquark-antidiquark ensemble.

The search for glueballs and hybrids has mainly been restricted to the mass region below $2.2 \text{ GeV}/c^2$. Experimentally, it would be very rewarding to go to higher masses because of the unavoidable problems due to the high density of normal $q\bar{q}$ mesons below $2.5 \text{ GeV}/c^2$.

In the search for glueballs, a narrow state at $1500 \text{ MeV}/c^2$, discovered in antiproton annihilations by Crystal Barrel [1, 2, 3, 4, 5], is considered the best candidate for the glueball ground state ($J^{PC} = 0^{++}$). However, the mixing with nearby conventional scalar $q\bar{q}$ states makes the unique interpretation as a glueball difficult.

Both cases indicate the problems of light quark spectroscopy due to large widths, deteriorated line-shapes and mixing among states. Thus heavy quarks states are decay modes give a more unbiased view to the spectrum of QCD states.

In the past decades many resonances have been associated with the quest of the existence of multi-quarks. The $a_0(980)$ and $f_0(975)$ were always believed to have a strong $K\bar{K}$. Now a lot of charmonium states are discussed in the same framework.

4.2.2 Charmonium

COMMENT: Author(s): D. Bettoni, M. Negrini

COMMENT: Referee(s): P. Gianotti

4.2.2.1 Introduction

Ever since its discovery in 1974 [6, 7] charmonium has been a powerful tool for the understanding of the strong interaction. The high mass of the c quark ($m_c \approx 1.5 \text{ GeV}/c^2$) makes it plausible to attempt a description of the dynamical properties of the $(c\bar{c})$ system in terms of non-relativistic potential models, in which the functional form of the potential is chosen to reproduce the asymptotic properties of the strong interaction. The free parameters in

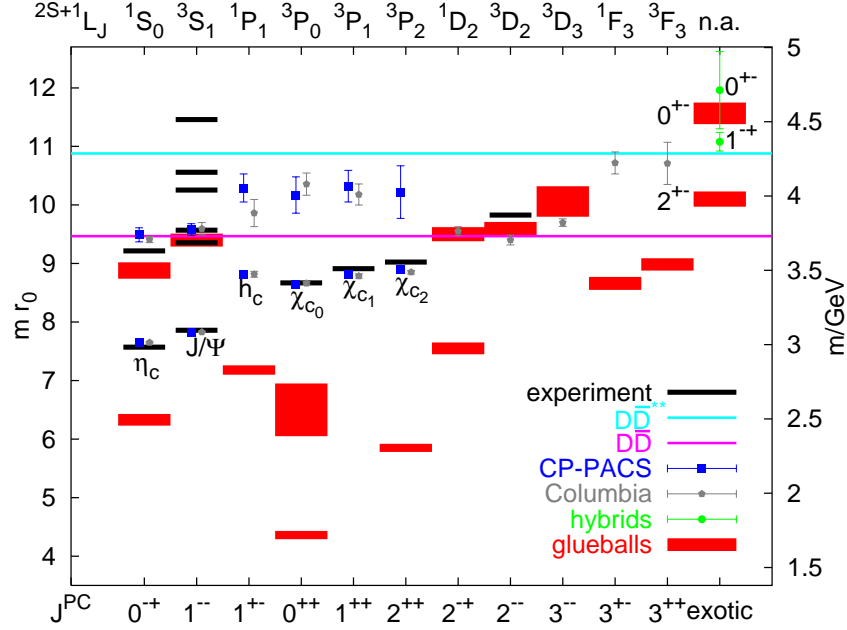


Figure 4.1: Charmonium spectrum from LQCD. See [?] for details.

these models are to be determined from a comparison with the experimental data.

Now, more than thirty years after the J/ψ discovery, charmonium physics continues to be an exciting and interesting field of research. The recent discoveries of new states (η'_c , $X(3872)$), and the exploitation of the B factories as rich sources of charmonium states have given rise to renewed interest in heavy quarkonia, and stimulated a lot of experimental and theoretical activities. The gross features of the charmonium spectrum are reasonably well described by potential models, but these obviously cannot tell the whole story: relativistic corrections are important and other effects, like coupled-channel effects, are significant and can considerably affect the properties of the $c\bar{c}$ states. To explain the finer features of the charmonium system, model calculations and predictions are made within various, complementary theoretical frameworks. Substantial progress in an effective field theoretical approach, labelled Non-Relativistic QCD (NRQCD) has been achieved in recent years. This analytical approach makes it possible to expect significant progress in lattice gauge theory calculations, which have become increasingly more capable of dealing quantitatively with non-perturbative dynamics in all its aspects,

starting from the first principles of QCD.

Experimental Study of Charmonium

Experimentally charmonium has been studied mainly in e^+e^- and $\bar{p}p$ experiments.

In e^+e^- annihilations direct charmonium formation is possible only for states with the quantum numbers of the photon $J^{PC} = 1^{--}$, namely the J/ψ , ψ' and $\psi(3770)$ resonances. Precise measurements of the masses and widths of these states can be obtained from the energy of the electron and positron beams, which are known with good accuracy. All other states can be reached by means of other production mechanisms, such as photon-photon fusion, initial state radiation, B-meson decay and double charmonium.

On the other hand all $c\bar{c}$ states can be directly formed in $\bar{p}p$ annihilations, through the coherent annihilation of the three quarks in the proton with the three antiquarks in the antiproton. This technique, originally proposed by P. Dalpiaz in 1979 [8], could be successfully employed a few years later at CERN and Fermilab thanks to the development of stochastic cooling. With this method the masses

and widths of all charmonium states can be measured with excellent accuracy, determined by the very precise knowledge of the initial $\bar{p}p$ state and not limited by the resolution of the detector.

The parameters of a given resonance can be extracted by measuring the formation rate for that resonance as a function of the c.m. energy E_{cm} , as explained in detail in section 2.4.1. As an illustra-

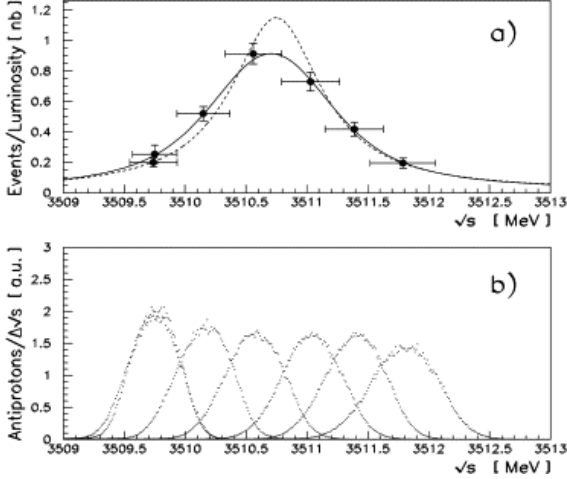


Figure 4.2: Resonance scan at the χ_{c1} carried out at Fermilab (a) and beam energy distribution in each data point (b).

tion of this technique we show in Fig. 4.2 a scan of the χ_{c1} resonance carried out at the Fermilab antiproton accumulator by the E835 experiment [9] using the process $\bar{p}p \rightarrow \chi_{c1} \rightarrow J/\psi\gamma$. For each point of the scan the horizontal error bar in (a) corresponds to the width of the beam energy distribution. The actual beam energy distribution is shown in (b). This scan allowed the E835 experiment to carry out the most precise measurement of the mass ($3510.719 \pm 0.051 \pm 0.019 \text{ MeV}/c^2$) and total width ($0.876 \pm 0.045 \pm 0.026 \text{ MeV}$) of this resonance.

The charmonium spectrum

The spectrum of charmonium states is shown in Fig. 4.3. It consists of eight narrow states below the open charm threshold (3.73 GeV) and several tens of states above the threshold.

All eight states **below $D\bar{D}$ threshold** are well established, but whereas the triplet states are measured with very good accuracy, the same cannot be said for the singlet states.

The η_c was discovered almost thirty years ago and many measurements of its mass and total width exist, with six new measurements in the last four

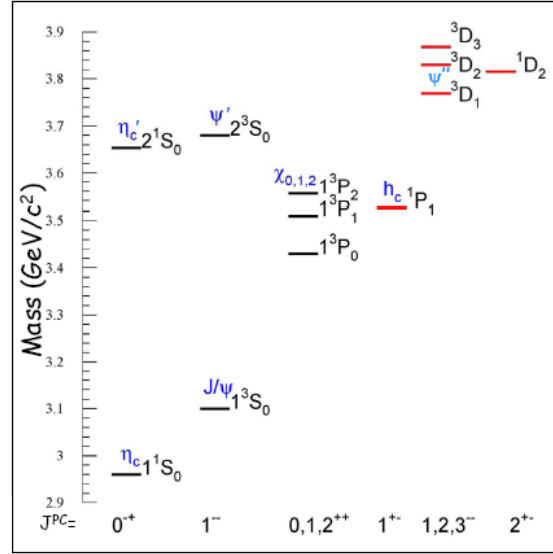


Figure 4.3: The charmonium spectrum.

years. Still the situation is far from satisfactory. The Particle Data Group (PDG) [10] value of the mass is $2980.4 \pm 1.2 \text{ MeV}/c^2$, an average of eight measurements with an internal confidence level of 0.026: the error on the η_c mass is still as large as $1.2 \text{ MeV}/c^2$, to be compared with few tens of keV/c^2 for the J/ψ and ψ' and few hundreds of keV/c^2 for the χ_{cJ} states. The situation is even worse for the total width: the PDG average is $25.5 \pm 3.4 \text{ MeV}$, with an overall confidence level of only 0.001 and individual measurements ranging from 7 MeV to 34.3 MeV. The most recent measurements have shown that the η_c width is larger than was previously believed, with values which are difficult to accommodate in quark models. This situation points to the need for new high-precision measurements of the η_c parameters.

The first experimental evidence of the $\eta_c(2S)$ was reported by the Crystal Ball collaboration [11], but this finding was not confirmed in subsequent searches in $\bar{p}p$ or e^+e^- experiments. The $\eta_c(2S)$ was finally discovered by the Belle collaboration [12] in the hadronic decay of the B meson $B \rightarrow K + \eta_c(2S) \rightarrow K + (K_s K^- \pi^+)$ with a mass which was incompatible with the Crystal Ball candidate. The Belle finding was then confirmed by CLEO [13] and BaBar [14] which observed this state in two-photon fusion. The PDG value of the mass is $3638 \pm 4 \text{ MeV}/c^2$, corresponding to a surprisingly small hyperfine splitting of $48 \pm 4 \text{ MeV}/c^2$, whereas the total width is only measured with an accuracy of 50%. The study of this state has just started and all its properties need to be measured with good ac-

curacy.

The 1P_1 state of charmonium (h_c) is of particular importance in the determination of the spin-dependent component of the $q\bar{q}$ confinement potential. The Fermilab experiment E760 reported an h_c candidate in the decay channel $J/\psi\pi^0$ [15], with a mass of $3526.2 \pm 0.15 \pm 0.2 \text{ MeV}/c^2$. This finding was not confirmed by the successor experiment E835, which however observed an enhancement in the $\eta_c\gamma$ [16] final state at a mass of $3525.8 \pm 0.2 \pm 0.2 \text{ MeV}/c^2$. The h_c was finally observed by the CLEO collaboration [17] in the process $e^+e^- \rightarrow \psi' \rightarrow h_c + \pi^0$ with $h_c \rightarrow \eta_c + \gamma$, in which the η_c was identified via its hadronic decays. They found a value for the mass of $3524.4 \pm 0.6 \pm 0.4 \text{ MeV}/c^2$. It is clear that the study of this state has just started and that many more measurements will be needed to determine its properties, in particular the width.

The region **above $D\bar{D}$ threshold** is rich in interesting new physics. In this region, close to the $D\bar{D}$ threshold, one expects to find the four $1D$ states. Of these only the 1^3D_1 , identified with the $\psi(3770)$ resonance, has been found. The $J = 2$ states (1^1D_2 and 1^3D_2) are predicted to be narrow, because parity conservation forbids their decay to $D\bar{D}$. In addition to the D states, the radial excitations of the S and P states are predicted to occur above the open charm threshold. None of these states have been positively identified.

The experimental knowledge of this energy region comes from data taken at the early e^+e^- experiments at SLAC and DESY and, more recently, at the B -factories, CLEO-c and BES. The structures and the higher vector states observed by the early e^+e^- experiments have not all been confirmed by the latest much more accurate measurements by BES [18, 19]. A lot of new states have recently been discovered at the B -factories, mainly in the hadronic decays of the B meson: these new states ($X, Y, Z \dots$) are associated with charmonium because they decay predominantly into charmonium states such as the J/ψ or the ψ' , but their interpretation is far from obvious. The situation can be roughly summarized as follows:

- the $Z(3931)$ [20], observed in two-photon fusion and decaying predominantly into $D\bar{D}$, is tentatively identified with the $\chi_{c2}(2P)$;
- the $X(3940)$ [21], observed in double charmonium events, is tentatively identified with the $\eta_c(3S)$;
- for all other new states ($X(3872)$, $Y(3940)$, $Y(4260)$, $Y(4320)$ and so on) the interpreta-

tion is not at all clear, with speculations ranging from the missing $c\bar{c}$ states, to molecules, tetraquark states, and hybrids. It is obvious that further measurements are needed to determine the nature of these new resonances.

The main challenge of the next years will be thus to understand what these new states are and to match these experimental findings to the theoretical expectations for charmonium above threshold.

Charmonium in $\bar{\text{P}}\text{ANDA}$

Charmonium spectroscopy is one of the main items in the experimental program of $\bar{\text{P}}\text{ANDA}$, and the design of the detector and of the accelerator are optimized to be well suited for this kind of physics. $\bar{\text{P}}\text{ANDA}$ will represent a substantial improvement over the Fermilab experiments E760 and E835:

- up to ten times higher instantaneous luminosity ($L = 2 \times 10^{32} \text{ cm}^{-2}\text{s}^{-1}$ in high-luminosity mode, compared to $2 \times 10^{31} \text{ cm}^{-2}\text{s}^{-1}$ at Fermilab);
- better beam momentum resolution ($\Delta p/p = 10^{-5}$ in high-resolution mode, compared with 10^{-4} at Fermilab);
- a better detector (higher angular coverage, magnetic field, ability to detect the hadronic decay modes).

At full luminosity $\bar{\text{P}}\text{ANDA}$ will be able to collect several thousand $c\bar{c}$ states per day. By means of fine scans it will be possible to measure masses with accuracies of the order of 100 keV and widths to 10 % or better. The entire energy region below and above open charm threshold will be explored.

4.2.2.2 Benchmark Channels

One of the main problems in the experimental study of charmonium spectroscopy in $\bar{p}p$ annihilation is the high hadronic background. It is therefore necessary to select those decays of charmonium which are less affected by background. In general we can identify four main classes of charmonium decay:

- **decays with a J/ψ in the final state:** $c\bar{c} \rightarrow J/\psi + X$, with $J/\psi \rightarrow e^+e^-$ or $J/\psi \rightarrow \mu^+\mu^-$. These channels can be used to identify states such as the χ_{cJ} , the ψ' or the $X(3872)$. The presence of the lepton pair in the final state makes these channels relatively clean, with the

main background coming from misidentified $\pi^+\pi^-$ pairs. The analysis of these channels relies on the positive identification of the lepton pair in the final state, with an invariant mass compatible with the J/ψ . In case of an exclusive analysis (e.g. $J/\psi\pi^+\pi^-$) a further improvement on the signal to background ratio can be obtained by means of a kinematical fit;

- **two- and three-photon decays** can be used to identify states such as the η_c , the η'_c or the h_c (via $h_c \rightarrow \eta_c + \gamma \rightarrow 3\gamma$). The main background comes from $\pi^0\gamma$ and $\pi^0\pi^0$ final states in which one or two photons are lost, either outside the calorimeter acceptance or below the calorimeter low-energy threshold. This background can be calculated by measuring the $\pi^0\gamma$ and $\pi^0\pi^0$ cross sections and then using Monte Carlo techniques to estimate the feed-down to $\gamma\gamma$ and 3γ . The analysis requires the presence of the required number of photons in the final state, with a veto on π^0 s and charged particles. Also in this case a kinematical fit can help improve the background situation;
- **decays to light hadrons.** As stated previously these decay modes are affected by a large hadronic background. In this case signal/background separation can be obtained by cutting on discriminating topological variables or angular distributions, whenever possible. An example of such decay is $h_c \rightarrow \eta_c\gamma \rightarrow \phi\phi\gamma$;
- **decays to $D\overline{D}$:** charmonium states above open charm threshold will generally be identified by means of their decay to $D\overline{D}$, unless forbidden by some conservation rule.

In what follows we will present a discussion of individual benchmark channels.

4.2.2.3 $\overline{\text{p}}\text{p} \rightarrow J/\psi + X$

A class of charmonium decays that will be studied at $\overline{\text{P}}\text{ANDA}$ presents a J/ψ in the final state resulting, for example, from de-excitation of a higher level charmonia with the emission of hadrons or photons. The existence of a J/ψ in the final state represents a clean signature for the signal. In what follows we present the study of the benchmark channels:

- $\overline{\text{p}}\text{p} \rightarrow J/\psi\pi^+\pi^- \rightarrow e^+e^-\pi^+\pi^-$;
- $\overline{\text{p}}\text{p} \rightarrow J/\psi\pi^0\pi^0 \rightarrow e^+e^-\gamma\gamma\gamma\gamma$;
- $\overline{\text{p}}\text{p} \rightarrow \chi_{c1,c2}\gamma \rightarrow J/\psi\gamma\gamma \rightarrow e^+e^-\gamma\gamma$;

- $\overline{\text{p}}\text{p} \rightarrow J/\psi\gamma \rightarrow e^+e^-\gamma$;
- $\overline{\text{p}}\text{p} \rightarrow J/\psi\eta$.

In all these cases the analysis strategy will focus on the detection of the $J/\psi \rightarrow e^+e^-$ in the final state, allowing an efficient rejection of the hadronic background, followed by the full event reconstruction. The first step in the analysis is the reconstruction of the J/ψ candidate starting from the lepton pair, following this strategy:

1. select one electron candidate from charged tracks with **Loose** PID criteria, and one electron candidate with **Tight** PID criteria;
2. kinematical fit of both electrons in order to reconstruct the J/ψ candidates with vertex constraint;
3. probability of J/ψ vertex fit: $P_{J/\psi} > 0.001$.

This strategy was followed for each benchmark channel, except for $J/\psi\eta$ where both electrons are identified with **Loose** PID criteria.

Fig. 4.4 shows the invariant mass distribution of the J/ψ candidates for $\overline{\text{p}}\text{p} \rightarrow Y(4260) \rightarrow J/\psi\pi^+\pi^-$. The results of the reconstructed J/ψ , at different center-of-mass energies and for several channels, are summarized in Table 4.1

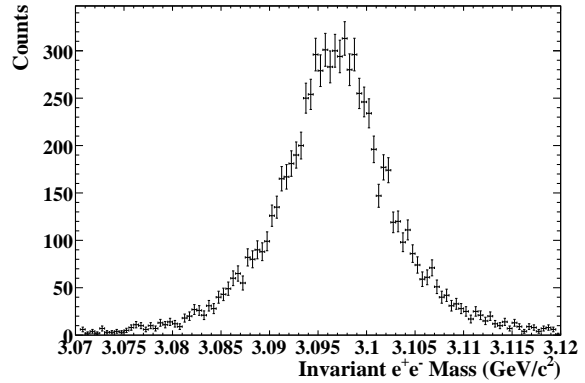


Figure 4.4: Invariant e^+e^- mass reconstructed at $\sqrt{s} = 4.260$ GeV.

We now turn to a detailed discussion of the five benchmark channels.

$\overline{\text{p}}\text{p} \rightarrow J/\psi\pi^+\pi^-$

The reaction $\overline{\text{p}}\text{p} \rightarrow J/\psi\pi^+\pi^- \rightarrow e^+e^-\pi^+\pi^-$ has been simulated for several center-of-mass energies. Event selection is done in the following steps:

Channel	Events	$\sqrt{s}(\text{GeV})$	Mean (GeV)	RMS (MeV)
$J/\psi\pi^+\pi^-$	25 k	3.526	3.097	2.5
	25 k	3.686	3.097	3.9
	25 k	3.872	3.097	4.3
	25 k	4.260	3.097	7.0
	25 k	4.600	3.097	5.7
	25 k	5.000	3.097	6.4
$J/\psi\pi^0\pi^0$	360 k	4.260	3.096	8.8
$\chi_{c1}\gamma$	20 k	3.686	3.096	6.8
	20 k	3.872	3.096	7.6
	20 k	4.260	3.095	8.3
$\chi_{c2}\gamma$	20 k	3.686	3.096	6.9
	20 k	3.872	3.096	7.5
	20 k	4.260	3.096	8.3
$J/\psi\gamma$	100 k	3.510	3.097	3.1
	100 k	3.556	3.097	3.4
	20 k	3.872	3.096	3.7
$J/\psi\eta$	40 k	3.638	3.093	7
	40 k	3.686	3.094	7
	40 k	3.872	3.096	6
	80 k	4.260	3.096	6

Table 4.1: Number of simulated events, mean value and RMS of the reconstructed J/ψ invariant mass distribution for each energy and channel analyzed, after 4C fit.

1. select a well reconstructed J/ψ in the event;
2. select two pion candidates from charged tracks with `VeryLoose` PID criteria;
3. kinematical fit of the $J/\psi\pi^+\pi^-$ candidates with vertex constraint;
4. probability of $J/\psi\pi^+\pi^-$ vertex fit: $P_{J/\psi\pi^+\pi^-} > 0.001$.

Fig. 4.5 shows the confidence level of the fit for the data simulated at $\sqrt{s} = 4.260$ GeV.

After this selection, the reconstruction efficiency and RMS of the invariant mass distribution are reported in Table 4.2.

As an example, we will discuss in more detail the results obtained for this channel at the energy of the resonance $Y(4260)$. This resonance was observed for the first time by BaBar in Initial State Radiation events [22], in the decay $Y(4260) \rightarrow J/\psi\pi^+\pi^-$. The natural quantum number assignment for this state is $J^{PC} = 1^{--}$ and one of its possible interpretation is a hybrid.

In Fig. 4.6 the invariant mass distribution for $Y(4260)$ candidates, obtained with the described selections, is presented.

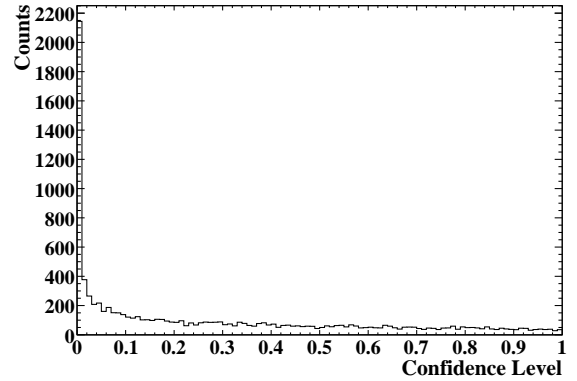


Figure 4.5: Confidence level of the kinematical fit to $J/\psi\pi^+\pi^-$ for the data simulated at $\sqrt{s} = 4.260$ GeV energy. The cut applied is $P_{J/\psi\pi^+\pi^-} > 0.001$.

In the simulation, the dipion invariant mass ($m_{\pi\pi}$) distribution was implemented according to the following parametrization [23]:

$$\frac{d\Gamma}{dm_{\pi\pi}} \propto PHSP \cdot (m_{\pi\pi}^2 - \lambda m_\pi^2)^2 \quad (4.1)$$

where PHSP is the phase-space factor, m_π is the pion mass and λ is a parameter that can be obtained from the data; in this analysis we used $\lambda = 4.0$

\sqrt{s} [GeV]	Eff [%]	RMS [MeV]
3.526	27.52	3.7
3.686	30.90	5.7
3.872	32.07	8.3
4.260	32.58	13.4
4.600	30.60	18.5
5.000	29.70	24.3

Table 4.2: Efficiencies and RMS of the reconstructed $J/\psi\pi^+\pi^-$ invariant mass distributions for each energy analyzed.

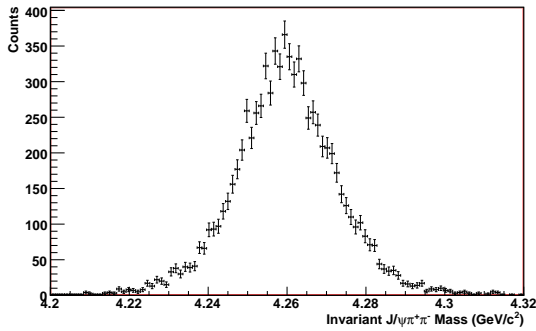


Figure 4.6: Invariant $J/\psi\pi^+\pi^-$ mass, in the case of $Y(4260)$ resonance.

[24]. This choice is motivated by measurements of $\psi(2S) \rightarrow J/\psi\pi^+\pi^-$, considering the fact that ψ' and $Y(4260)$ have the same quantum numbers.

Fig. 4.7 shows the $m_{\pi\pi}$ distribution after the recon-

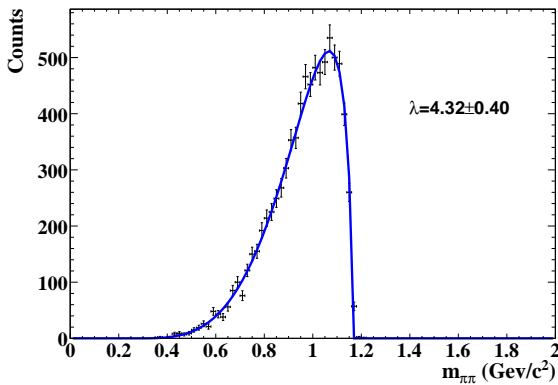


Figure 4.7: Invariant dipion mass of $Y(4260)$ candidates. The black line is the simulated and reconstructed data and the blue line is the fit with the theoretical function. The result of λ after the fit seems to be consistent with the input data.

struction. The blue line is the result of the fit with

the theoretical formula, which is consistent with the input data. The main background for this channel comes from $\bar{p}p \rightarrow \pi^+\pi^-\pi^+\pi^-$ where two pions may be misidentified as electrons and contaminate the signal.

The study of background contaminations is done only at the $Y(4260)$ energy. At $\sqrt{s} = 4.260$ GeV the cross section of the background reaction is approximately equal to 0.046 mb [25], while using available data from E835 experiment [24], we can estimate the cross section of $\bar{p}p \rightarrow Y(4260) \rightarrow J/\psi\pi^+\pi^- \rightarrow e^+e^-\pi^+\pi^-$ to be about 60 pb.

In order to estimate the signal/noise ratio, 55 M background filtered events were simulated (filter efficiency: 16.66%). Only 60 events satisfy the selection criteria, and present an invariant mass of the reconstructed J/ψ in the region between [2.8;3.2] GeV/c^2 , and none events show a peak at the J/ψ mass. We conclude that the signal/noise ratio is about 2, so this channel could be well identified in PANDA.

$\bar{p}p \rightarrow J/\psi\pi^0\pi^0$

With its excellent electromagnetic calorimeter \bar{P} ANDA will also be able to study the neutral dipion transition into $J/\psi\pi^0\pi^0$. In order to determine the acceptance and background rejection capability of the detector, Monte Carlo simulations have been done for this channel at $\sqrt{s} = 4.26$ GeV.

The event selection has been done in the following way. The J/ψ is reconstructed through the decay mode e^+e^- with the same cuts as described in the $J/\psi\pi^+\pi^-$ selection. Photons from π^0 candidates must have an energy deposit in the calorimeter larger than 20 MeV. After the 4C fit with $\text{CL} > 0.1\%$, only those events with $m(e^+e^-)$ within [3.07; 3.12] GeV/c^2 and $m(\gamma\gamma)$ within [120; 150] MeV/c^2 are accepted. In order to reduce background, the remaining events are fitted with $J/\psi\pi^0\pi^0$ and $J/\psi\eta\pi^0$ hypothesis. Only events with exactly one combination with $\text{CL}(J/\psi\pi^0\pi^0) > 0.1\%$ pass the event selection. Events with at least one $J/\psi\eta\pi^0$ combination with $\text{CL}(J/\psi\eta\pi^0) > 0.01\%$ are rejected.

The results are summarized in Table 4.3. Assuming a cross section for $\bar{p}p \rightarrow J/\psi\pi^0\pi^0 \rightarrow e^+e^-4\gamma$ of 30 pb [24], \bar{P} ANDA will be able to reconstruct in one day about 40 events, which is 5 times more than CLEO-c has observed [?] for this channel at $\sqrt{s} = 4.26$ GeV. The main background channels could be sufficiently suppressed. Only 1 from 250 million simulated $\pi^+\pi^-\pi^0\pi^0$ events pass the event selection, which results in a signal/background ratio

$S/B = 25$.

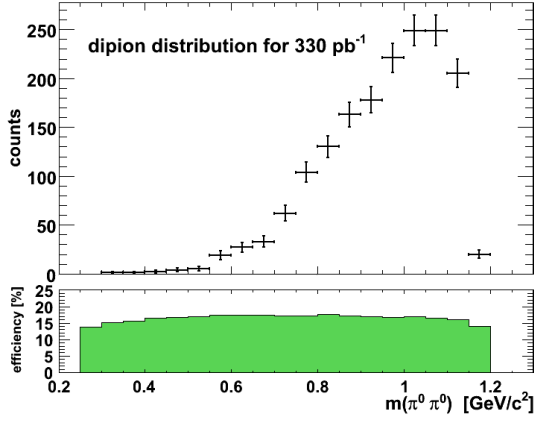


Figure 4.8: Invariant dipion mass of $J/\psi\pi^0\pi^0$ candidates.

The dipion mass distribution which is simulated with the same shape as that of the decay of $Y(4260) \rightarrow J/\psi\pi^+\pi^-$ is shown in Fig. 4.8. No strong efficiency variation in the $m_{\pi^0\pi^0}$ spectrum is visible.

$\bar{p}p \rightarrow \chi_c\gamma$

For the study of radiative decays to χ_c , it is possible to make use of the subsequent decay $\chi_c \rightarrow J/\psi\gamma$. Starting from the J/ψ sample it is possible to add a photon to reconstruct the χ_c candidate; a second photon is then added to fully reconstruct the final state.

We will consider the following processes:

$$\bar{p}p \rightarrow \chi_{c1,c2}\gamma \rightarrow J/\psi\gamma\gamma \rightarrow e^+e^-\gamma\gamma. \quad (4.2)$$

The event selection is done in the following steps:

1. select a well reconstructed J/ψ in the event;
2. select reconstructed photon candidates;
3. kinematic fit of the $\chi_{c1,c2}$ candidates with vertex constraint;
4. probability of $\chi_{c1,c2}$ vertex fit: $P_{\chi_{c1,c2}} > 0.001$;
5. probability of $\chi_{c1,c2}\gamma$ vertex fit: $P_{\chi_{c1,c2}\gamma} > 0.001$;
6. $\chi_{c1,c2}$ mass window: $[3.3, 3.7]$ GeV.

The results for the reconstructed $\chi_{c1,c2}$ are summarized in Table 4.4. Fig. 4.9 shows the χ_{c1} invariant

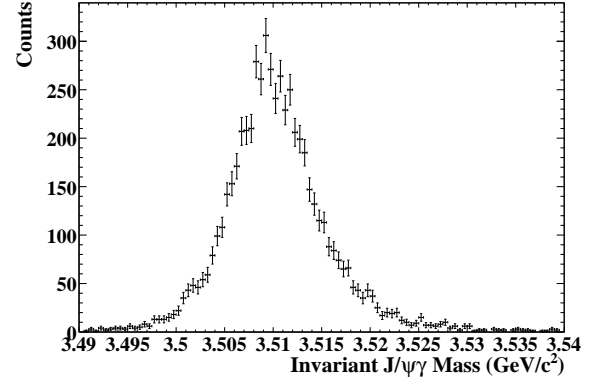


Figure 4.9: Invariant $J/\psi\gamma$ mass at $\sqrt{s} = 3.686$ GeV.

mass distribution reconstructed at $\sqrt{s} = 3.686$ GeV.

According to the selection cuts described above, a second photon is added to the reconstructed $\chi_{c1,c2}$ in order to reconstruct the complete final state, where it is possible to perform the kinematical fit to the $\bar{p}p$ 4-momentum. The results of the reconstructed $\chi_{c1,c2}\gamma$ are summarized in Table 4.5:

Fig. 4.10 shows the $\chi_{c1}\gamma$ candidates reconstructed at $\sqrt{s} = 3.686$ GeV.

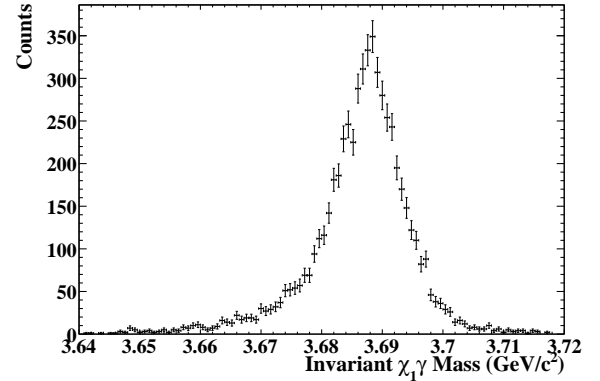


Figure 4.10: Invariant $\chi_{c1}\gamma$ mass at $\sqrt{s} = 3.686$ GeV.

The major background comes from $\bar{p}p \rightarrow \pi^+\pi^-\pi^0$. This study is done at the $Y(4260)$ and $X(3872)$ energies.

The cross section of the background reactions at $\sqrt{s}=4.260$ GeV is approximately equal to $30 \mu b$ [25], while at $\sqrt{s}=3.872$ GeV the cross section is about 0.29 mb [25].

36 million filtered events (filter efficiency: 13.5%) were analyzed at the $Y(4260)$ energy and, for the $\chi_{c1}\gamma$ final state, only 7 events pass the selection, while for $\chi_{c2}\gamma$ only 8 event satisfy the selection

channel	assumed σ	efficiency	
$\bar{p}p \rightarrow J/\psi\pi^0\pi^0 \rightarrow e^+e^-4\gamma$	30 pb	16.9 %	$n_{rec} = 40$ events / day
background reactions:			
$\bar{p}p \rightarrow \pi^+\pi^-\pi^0\pi^0 \rightarrow \pi^+\pi^-4\gamma$	50 μ b	1 / 250M	S/B = 25
$\bar{p}p \rightarrow J/\psi\eta\pi^0 \rightarrow e^+e^-4\gamma$	<30 pb	0 / 20K	S/B > 10 ³
$\bar{p}p \rightarrow J/\psi\omega\pi^0 \rightarrow e^+e^-5\gamma$	<10 pb	4 / 20K	S/B > 10 ³

Table 4.3: Simulation results for the channel $\bar{p}p \rightarrow J/\psi\pi^0\pi^0$. To save computing time $\pi^+\pi^-\pi^0\pi^0$ events with $m_{\pi^+\pi^-} < 2.4 \text{ GeV}/c^2$ or $m_{\pi^+\pi^-} > 3.4 \text{ GeV}/c^2$ are rejected without detector simulation.

$\sqrt{s}[\text{GeV}]$	χ_{c1}		χ_{c2}	
	Mean [GeV]	RMS [MeV]	Mean [MeV]	RMS [MeV]
3.686	3.510	5.5	3.556	5.5
3.872	3.509	6.9	3.556	6.1
4.260	3.510	7.0	3.556	7.4

Table 4.4: Mean value and RMS of the reconstructed $J/\psi\gamma$ candidates for each energy analyzed for the radiative decay of $\chi_{c1,c2}$.

$\sqrt{s}[\text{GeV}]$	χ_{c1}			χ_{c2}		
	Mean [GeV]	Eff [%]	RMS (MeV)	Mean [GeV]	Eff [%]	RMS [MeV]
3.686	3.687	28.88	7.6	3.686	29.13	8.5
3.872	3.875	29.98	14.3	3.873	28.78	10.8
4.260	4.262	28.61	15.5	4.262	29.26	15.4

Table 4.5: Mean value, efficiencies and RMS of the reconstructed $\chi\gamma$ candidates for each energy analyzed for the radiative decay of $\chi_{c1,c2}$.

criteria, corresponding to an effective background cross-section of 0.8 pb and 0.9 pb respectively. 68 million filtered events (filter efficiency: 12.7%) were analyzed at the X(3872) energy and, for the $\chi_{c1}\gamma$ final state, only 12 events pass the selection, while for $\chi_{c2}\gamma$ only 15 event satisfy the selection criteria, corresponding to an effective background cross-section of 6.5 pb and 8.1 pb respectively. Since the signal cross-section for these reactions is not known it is not possible to calculate a signal/background ratios. However these simulations show that for these channels a very good background suppression can be achieved.

$\bar{p}p \rightarrow J/\psi\gamma$

$\bar{p}p \rightarrow \chi_c \rightarrow J/\psi\gamma \rightarrow e^+e^-\gamma$ is the most important channel to study the radiative decay and the angular distribution of $\chi_c \rightarrow J/\psi\gamma$.

The first step is the reconstruction of a J/ψ from electron-positron decay and then, adding one photon, one can reconstruct the $J/\psi\gamma$ candidate. Event selection is done in the following steps:

1. select a well reconstructed J/ψ in the event;
2. select reconstructed photon candidates;
3. kinematic fit of the $J/\psi\gamma$ candidates with vertex constraint;
4. probability of $J/\psi\gamma$ vertex fit: $P_{J/\psi\gamma} > 0.001$.

According to the selection cuts described above, the results of the reconstructed $J/\psi\gamma$ are summarized in Table 4.6.

$\sqrt{s}[\text{GeV}]$	Mean [GeV]	Eff[%]	RMS [MeV]
3.510	3.512	44.47	10.5
3.556	3.557	45.10	11.0
3.872	3.874	37.96	15.3

Table 4.6: Mean value, efficiencies and RMS of the reconstructed $J/\psi\gamma$ candidates for each energy analyzed.

Fig. 4.11 shows the $J/\psi\gamma$ candidates reconstructed at $\sqrt{s} = 3.510 \text{ GeV}$.

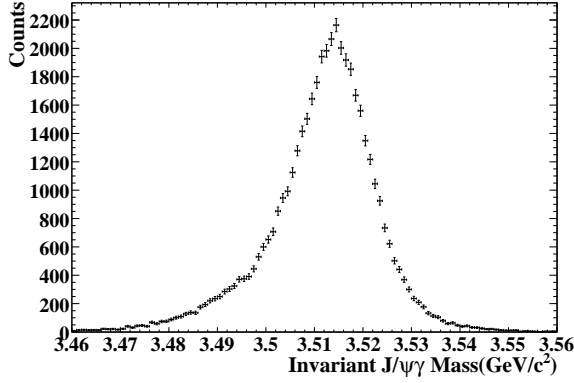


Figure 4.11: Invariant $J/\psi\gamma$ mass at $\sqrt{s} = 3.510$ GeV.

The major background comes from $\bar{p}p \rightarrow \pi^+\pi^-\pi^0$. The study of background contamination is done at the $X(3872)$ and χ_{c2} energies.

The cross section of the background reaction is approximately equal to 0.29 mb at $\sqrt{s} = 3.872$ GeV and 0.12 mb at $\sqrt{s} = 3.556$ GeV [25].

The cross section for $\bar{p}p \rightarrow \chi_{c2} \rightarrow J/\psi\gamma$ is, from E835 measurements, about 0.78 nb [9]. The number of simulated filtered background events was 26 M and 68 M at $\sqrt{s} = 3.556$ GeV and $\sqrt{s} = 3.872$ GeV, respectively. (filter efficiencies are 10.5% and 12.7% respectively). In the first case only 2 events pass the selection criteria, but if the constraint on the J/ψ invariant mass is applied, these events disappear. In the second case 13 events satisfy the selection criteria; also in this case, for many background events the 4C-fit does not converge so it is completely suppressed by the cut $CL > 0.1\%$.

Since no background events survive the selection we can set upper limits for the effective background cross-sections of 1.2 pb and 1.3 pb at the χ_{c2} and $X(3872)$ energies, respectively. For the χ_{c2} , where the signal cross section is known, this translates into a signal/background ratio $S/B > 660$.

$$\bar{p}p \rightarrow J/\psi\eta \rightarrow e^+e^-\gamma\gamma$$

The first step in the analysis of this channel is the reconstruction of a J/ψ via its electron decay; the second step is the reconstruction of a η candidate from two photons decay and then reconstruct the $J/\psi\eta$ candidate.

Event selection is done in the following steps:

1. select a well reconstructed J/ψ in the event;
2. select a well reconstructed η in the event;

3. kinematic fit with beam, J/ψ and η mass constraints;
4. J/ψ mass window: $[3.07;3.12]$ GeV/ c^2 ;
5. η mass window: $[0.535;0.565]$ GeV/ c^2 ;
6. probability of $J/\psi\eta$ vertex fit: $P_{J/\psi\eta} > 0.001$.

According to the selection cuts described above, the results of the reconstructed $J/\psi\eta$ are summarized in Table 4.7.

\sqrt{s} [GeV]	Mean [GeV]	Eff[%]	FWHM[MeV]
3.638	3.645	15.7	1
3.686	3.686	18.8	5
3.872	3.872	18.6	11
4.260	4.260	18.8	18

Table 4.7: Mean value, efficiencies and RMS of the reconstructed $J/\psi\eta$ candidates for each energy analyzed. These results are listed after a fit with mass constraint on J/ψ and η .

Fig. 4.12 shows the $J/\psi\eta$ candidates reconstructed at $\sqrt{s} = 4.260$ GeV.

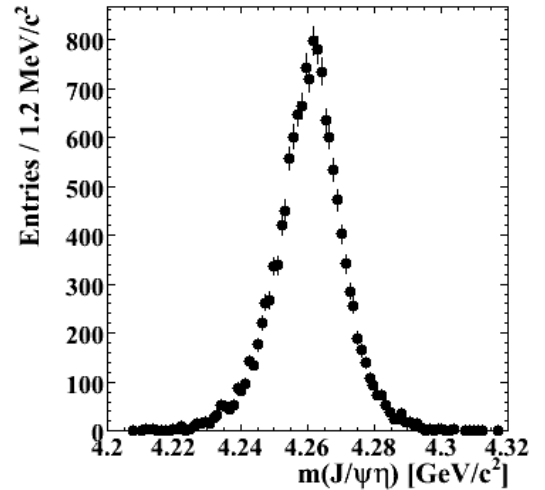


Figure 4.12: Invariant $J/\psi\eta$ mass at $\sqrt{s} = 4.260$ GeV.

For this signal channel we investigated the following background reactions:

- $\bar{p}p \rightarrow J/\psi\pi^0\gamma$
- $\bar{p}p \rightarrow J/\psi\pi^0\pi^0$
- $\bar{p}p \rightarrow J/\psi\eta\gamma$

- $\bar{p}p \rightarrow J/\psi\eta\pi^0$
- $\bar{p}p \rightarrow J/\psi\eta\eta$
- $\bar{p}p \rightarrow \pi^+\pi^-\eta$
- $\bar{p}p \rightarrow \pi^+\pi^-\pi^0$

with $\pi^0 \rightarrow \gamma\gamma$, $\eta \rightarrow \gamma\gamma$ and $J/\psi \rightarrow e^+e^-$. Most cross sections for decays including a J/ψ have not been measured yet.

The cross sections and branching fractions for the $J/\psi\eta$ signal and background modes are summarized in Table 4.8.

Table 4.9 presents the results of background contamination studies.

4.2.2.4 $\bar{p}p \rightarrow h_c \rightarrow \eta_c\gamma$

According to theoretical predictions and previous experimental observations [26], [27] one of the most promising decay modes for the observation of the h_c is its electromagnetic transition to the ground state of charmonium

$$h_c \rightarrow \eta_c + \gamma \quad (4.3)$$

where the energy of the photon is $E_\gamma = 503 \text{ MeV}$.

The η_c can be detected through many exclusive decay modes, neutral ($\eta_c \rightarrow \gamma\gamma$) or hadronic.

In order to estimate the signal cross-section we calculate the value of the Breit-Wigner formula at the resonance peak E_R :

$$\sigma_p = \frac{3\pi}{k^2} B_{\bar{p}p} B_{\eta_c\gamma} \quad (4.4)$$

where $k^2 = (E_R^2 - 4m_p^2)/4$ and the B s represent the branching ratios into the initial and final states.

Using the value measured by E835 $\Gamma_{\bar{p}p} B_{\eta_c\gamma} = 10 \text{ eV}$ and assuming a value of 0.5 MeV for the h_c width we obtain $\sigma_p = 33 \text{ nb}$.

$h_c \rightarrow \eta_c + \gamma \rightarrow 3\gamma$

We first consider the process $h_c \rightarrow 3\gamma$. This decay mode was observed at Fermilab by E835 [26]. It is characterized by a fairly clean final state, but the low value of the $\eta_c \rightarrow \gamma\gamma$ branching ratio ($4.3 \cdot 10^{-4}$) results in a relatively low event rate in comparison with the hadronic decay modes of η_c .

The main contributors to the background for the 3γ final state are γ s from the π^0 , η , η' decay in $\gamma\gamma$ decay modes: the loss of one or more γ s outside the detector acceptance or below the energy threshold

of the calorimeter can result in a 3γ final state. The background channels considered in this analysis are presented in Table 4.10 with the corresponding cross-sections measured by E760 and E835 over the angular range $|\cos(\theta)| < 0.6$ [28], [29].

The angular dependence for all the studied background channels is strongly peaked in the forward and backward direction, which is typical of two and three meson production in proton-antiproton annihilation. For the Monte Carlo study the angular dependence of the cross-section was parametrized by 6th or 7th order polynomials in $\cos(\theta)$. As an example we show the $\pi^0\pi^0$ angular distribution in Fig. 4.13.

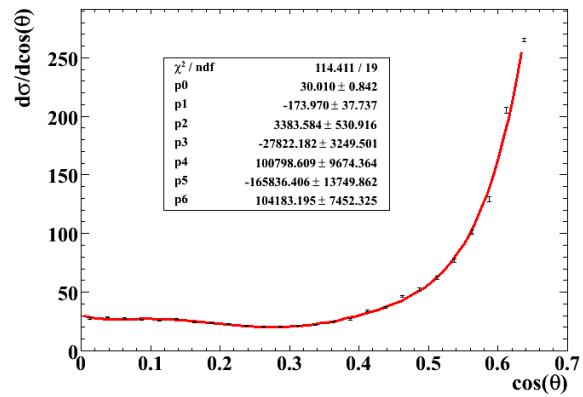


Figure 4.13: Angular dependence of $\pi^0\pi^0$ cross-section with parametrisation used in Monte-Carlo simulation.

The number of Monte Carlo events used for this analysis for signal and all the background channels are shown in Table 4.10.

The event selection is done in the following steps:

1. An η_c candidate is formed by pairing γ 's with an invariant mass in the window $[2.6; 3.2] \text{ GeV}$. The third γ is added to this pair to form the h_c candidate.
2. A 4C-fit to beam energy-momentum is applied to the h_c candidate and the information on the h_c and the updated information on the daughter γ 's are stored into the root ntuple.
3. The following cuts are applied at the ntuple level to suppress the background.
 - (a) Events with 3 γ 's were selected. This cut keeps 47% of all signal events, whereas it rejects more than 90% of all background events (with the exception of the $\pi^0\gamma$ channel).

Reaction $\bar{p}p \rightarrow$	\sqrt{s} [GeV]	σ	B
$J/\psi\eta$	3.638	σ_s	$2.34\% \times B(\eta_c(2S) \rightarrow J/\psi\eta)$
$J/\psi\pi^0\pi^0$	3.638	σ_b	5.78%
$J/\psi\pi^0\gamma$	3.638	σ_b	5.84%
$J/\psi\eta\gamma$	3.638	σ_b	2.32%
$J/\psi\eta$	3.686	σ_s	0.07%
$J/\psi\pi^0\pi^0$	3.686	σ_b	5.78%
$J/\psi\pi^0\gamma$	3.686	σ_b	5.84%
$J/\psi\eta\gamma$	3.686	σ_b	2.32%
$J/\psi\eta$	3.872	σ_s	$2.34\% \times B(X(3872)) \rightarrow J/\psi\eta$
$J/\psi\eta\pi^0$	3.872	σ_b	2.30%
$J/\psi\pi^0\pi^0$	3.872	σ_b	5.78%
$J/\psi\pi^0\gamma$	3.872	σ_b	5.84%
$J/\psi\eta\gamma$	3.872	σ_b	2.32%
$\pi^+\pi^-\pi^0$	3.872	$290 \mu b$	98.80%
$J/\psi\eta$	4.260	σ_s	$2.34\% \times B(Y(4260)) \rightarrow J/\psi\eta$
$J/\psi\eta\eta$	4.260	σ_b	0.92%
$J/\psi\eta\pi^0$	4.260	σ_b	2.30%
$J/\psi\pi^0\pi^0$	4.260	σ_b	5.78%
$J/\psi\pi^0\gamma$	4.260	σ_b	5.84%
$J/\psi\eta\gamma$	4.260	σ_b	2.32%
$\pi^+\pi^-\eta$	4.260	$1.54 \mu b^1$	39.38%
$\pi^+\pi^-\pi^0\pi^0$	4.260	$50 \mu b$	97.61%
$\pi^+\pi^-\pi^0$	4.260	$30 \pm 10 \mu b^2$	98.80%

Table 4.8: σ_s denotes the cross section for the formation of a given resonance in $\bar{p}p$ events, B the branching fraction for the decay tree. σ_b is the cross section for the background mode in $\bar{p}p$ annihilation. 1) obtained from DPM generator. 2) measured value at 8.8 GeV/c.

Decay $\bar{p}p \rightarrow$	\sqrt{s} [GeV]	Suppression	Signal to noise
$J/\psi\pi^0\pi^0$	3.638	$> 10^5$	$6300\tilde{\sigma}/\sigma_b$
$J/\psi\pi^0\gamma$	3.638	$> 10^5$	$6200\tilde{\sigma}/\sigma_b$
$J/\psi\eta\gamma$	3.638	5	$1\tilde{\sigma}/\sigma_b$
$J/\psi\pi^0\pi^0$	3.686	$> 10^5$	$7600\tilde{\sigma}/\sigma_b$
$J/\psi\pi^0\gamma$	3.686	12500	$900\tilde{\sigma}/\sigma_b$
$J/\psi\eta\gamma$	3.686	400	$100\tilde{\sigma}/\sigma_b$
$J/\psi\eta\pi^0$	3.872	$> 10^5$	$18800\tilde{\sigma}/\sigma_b$
$J/\psi\pi^0\pi^0$	3.872	$> 10^5$	$75\tilde{\sigma}/\sigma_b$
$J/\psi\pi^0\gamma$	3.872	8300	$600\tilde{\sigma}/\sigma_b$
$J/\psi\eta\gamma$	3.872	2000	$400\tilde{\sigma}/\sigma_b$
$\pi^+\pi^-\pi^0$	3.872	$> 7 \cdot 10^7$	$1\tilde{\sigma}/nb$
$J/\psi\eta\eta$	4.260	$> 10^5$	$47700\tilde{\sigma}/\sigma_b$
$J/\psi\eta\pi^0$	4.260	$> 10^5$	$19000\tilde{\sigma}/\sigma_b$
$J/\psi\pi^0\pi^0$	4.260	$> 10^5$	$7600\tilde{\sigma}/\sigma_b$
$J/\psi\pi^0\gamma$	4.260	3600	$300\tilde{\sigma}/\sigma_b$
$J/\psi\eta\gamma$	4.260	3400	$600\tilde{\sigma}/\sigma_b$
$\pi^+\pi^-\eta$	4.260	$> 7 \cdot 10^7$	$500\tilde{\sigma}/nb$
$\pi^+\pi^-\pi^0\pi^0$	4.260	$> 1.4 \cdot 10^8$	$20\tilde{\sigma}/nb$
$\pi^+\pi^-\pi^0$	4.260	$> 1.7 \cdot 10^8$	$15\tilde{\sigma}/nb$

Table 4.9: The signal to noise ratios are given in terms of the unknown cross section $\tilde{\sigma}$ or $\tilde{\sigma}/nb$.

Channel	σ (nb)	number of events
$\bar{p}p \rightarrow h_c \rightarrow 3\gamma$		20 k
$\bar{p}p \rightarrow \pi^0\pi^0$	31.4	1.3 M
$\bar{p}p \rightarrow \pi^0\gamma$	1.4	100 k
$\bar{p}p \rightarrow \pi^0\eta$	33.6	1.3 M
$\bar{p}p \rightarrow \eta\eta$	34.0	1.3 M
$\bar{p}p \rightarrow \pi^0\eta'$	50.0	100 k

Table 4.10: The main background contributors to $h_c \rightarrow 3\gamma$ with corresponding cross-section integrated over $|\cos(\theta)| < 0.6$.

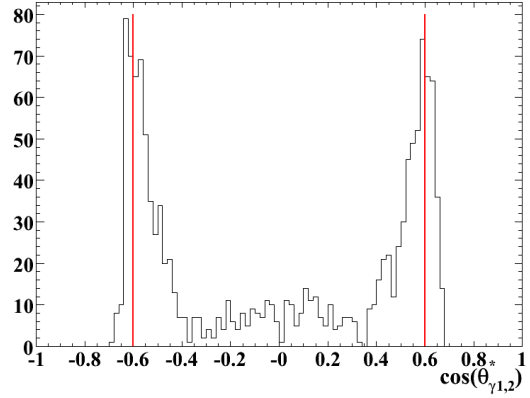


Figure 4.14: Distribution of reconstructed $\cos\theta$ of the γ in CM system for $\bar{p}p \rightarrow \pi^0\pi^0$ background.

- (b) Cut on the confidence level of the 4C-fit: $CL > 10^{-4}$.
- (c) Cut on the CM energy of the γ from the $h_c \rightarrow \eta_c\gamma$ (E_γ) radiative transition: $0.4 \text{ GeV} < E_\gamma < 0.6 \text{ GeV}$.
- (d) Angular cut $|\cos(\theta)| < 0.6$, to reject the background which is strongly peaked in the forward and backward directions. The $\cos(\theta)$ distributions for a background channel ($\pi^0\pi^0$) and for the signal are shown in Fig. 4.14 and Fig. 4.15, respectively.
- (e) The cut for invariant mass of combination $M(\gamma_1, \gamma_3) > 1.0 \text{ GeV}$ and $M(\gamma_2, \gamma_3) > 1.0 \text{ GeV}$ (the value of the cut is determined by the η' mass).

In Table 4.11 the selection efficiencies for different cuts are presented. Efficiencies are cumulative, *i.e.* applied one after another. Taking into account the signal cross-section $\sigma_{\bar{p}p \rightarrow h_c} = 33 \text{ nb}$ at resonance, branching ratio $\mathcal{B}(\eta_c \rightarrow \gamma\gamma) = 4.3 \cdot 10^{-4}$ and background cross-sections it results in the expected signal to background ratios presented in Table 4.12. The expected event rate for the luminosity in high luminosity mode $L = 2 \cdot 10^{32} \text{ cm}^{-2}\text{s}^{-1}$ is 20 events/day, and for high resolution mode with $L = 2 \cdot 10^{31} \text{ cm}^{-2}\text{s}^{-1}$ 2.0 events/day correspondingly.

$$h_c \rightarrow \eta_c\gamma \rightarrow \phi\phi\gamma$$

As a benchmark channel with a hadronic decay mode of the η_c we study the $\phi\phi$ final state with

Cut	h_c	$\pi^0\gamma$	$\pi^0\pi^0$	$\pi^0\eta$	$\eta\eta$	$\pi^0\eta'$
preselection	0.70	0.43	0.14	$8.2 \cdot 10^{-2}$	$4.0 \cdot 10^{-2}$	$8.5 \cdot 10^{-2}$
3 γ	0.47	0.31	$1.3 \cdot 10^{-2}$	$7.5 \cdot 10^{-3}$	$2.7 \cdot 10^{-3}$	$8.7 \cdot 10^{-3}$
$CL > 10^{-4}$	0.44	0.30	$9.9 \cdot 10^{-3}$	$4.9 \cdot 10^{-3}$	$7.2 \cdot 10^{-4}$	$5.7 \cdot 10^{-3}$
$E_\gamma [0.4;0.6]$ GeV	0.43	0.12	$3.9 \cdot 10^{-3}$	$2.0 \cdot 10^{-3}$	$2.8 \cdot 10^{-4}$	$2.3 \cdot 10^{-3}$
$ \cos(\theta) < 0.6$	0.22	$9.2 \cdot 10^{-2}$	$2.7 \cdot 10^{-3}$	$1.1 \cdot 10^{-3}$	$7.0 \cdot 10^{-5}$	$7.5 \cdot 10^{-4}$
$m_{12}^2, m_{23}^2 > 1.0$ GeV	$8.1 \cdot 10^{-2}$	0	0	0	0	0

Table 4.11: Selection efficiencies for $h_c \rightarrow 3\gamma$ and its background channels.

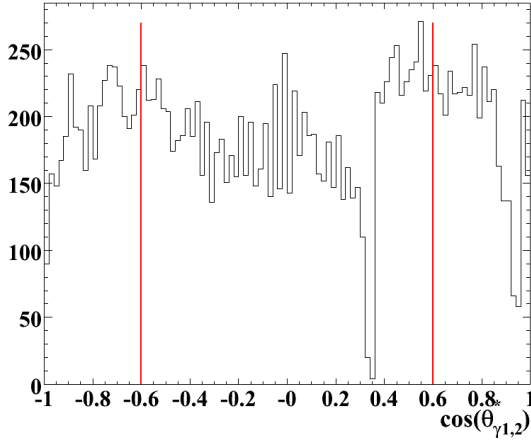


Figure 4.15: Distribution of reconstructed $\cos\theta$ of the γ in CM system from $h_c \rightarrow \eta_c\gamma$.

Channel	S/B ratio
$\bar{p}p \rightarrow \pi^0\pi^0$	> 94
$\bar{p}p \rightarrow \pi^0\gamma$	> 164
$\bar{p}p \rightarrow \pi^0\eta$	> 88
$\bar{p}p \rightarrow \eta\eta$	> 87
$\bar{p}p \rightarrow \pi^0\eta'$	> 250

Table 4.12: Signal to background ratio for $h_c \rightarrow 3\gamma$ and different background channels.

$\mathcal{B} = 2.6 \cdot 10^{-3}$. We detect the ϕ through the decay correspondingly $\phi \rightarrow K^+K^-$, with $\mathcal{B} = 0.49$ [30].

For the exclusive decay mode considered in this study:

$$\bar{p}p \rightarrow h_c \rightarrow \eta_c\gamma \rightarrow \phi\phi\gamma \rightarrow K^+K^-K^+K^-\gamma$$

the following 3 reactions are considered as the main contributors to the background:

1. $\bar{p}p \rightarrow K^+K^-K^+K^-\pi^0$,

2. $\bar{p}p \rightarrow \phi K^+K^-\pi^0$,

3. $\bar{p}p \rightarrow \phi\phi\pi^0$.

With one photon from the π^0 decay undetected these reactions have the same final state particles as the studied h_c decay. As in the case of the three photon decay discussed above, it is crucial to have as low an energy threshold as possible in order to effectively reject this background.

Additional possible source of background is $\bar{p}p \rightarrow K^+K^-\pi^+\pi^-\pi^0$. This reaction could contribute to background due to pion as kaon misidentification.

There are no experimental measurements, to our best knowledge, of the cross-sections for the first three background reactions, which are supposed to be main contributors to background. The only way to estimate their cross-sections was found to use the DPM (Dual Parton Model) event generator [31]. $2 \cdot 10^7$ events were generated with DPM at beam momentum $p_z = 5.609$ GeV/c, which corresponds to the studied h_c resonance. The corresponding numbers of events are 115 and 12 for the first two background channels. No events for the $\bar{p}p \rightarrow \phi\phi\pi^0$ reaction were observed. With the total $\bar{p}p$ cross-section at this beam momentum of 60 mb the cross-sections for the corresponding background channels are estimated at 345 nb, 60 nb and below 3 nb, respectively.

For $\bar{p}p \rightarrow K^+K^-\pi^+\pi^-\pi^0$ the cross-section was estimated by extrapolation from lower energy according to the total inelastic cross-section. It gives an estimation $\sigma = 30\mu\text{b}$.

The number of analysed events are presented in Table 4.13.

For the $\bar{p}p \rightarrow K^+K^-\pi^+\pi^-\pi^0$ channel 15 millions out of 20 millions events were simulated with filter on invariant mass of the pair of two kaons. The events with $m(K^+K^-)$ in the range [0.95;1.2] GeV were selected. The efficiency of the filter is 29.9 %, which gives effective number of simulated events ~ 55 M.

Channel	N of events
$\overline{\text{p}}\text{p} \rightarrow h_c \rightarrow \phi\phi\gamma$	20 k
$\overline{\text{p}}\text{p} \rightarrow K^+K^-K^+K^-\pi^0$	6.2 M
$\overline{\text{p}}\text{p} \rightarrow \phi K^+K^-\pi^0$	200 k
$\overline{\text{p}}\text{p} \rightarrow \phi\phi\pi^0$	4.2 M
$\overline{\text{p}}\text{p} \rightarrow K^+K^-\pi^+\pi^-\pi^0$	5 M + 15 M
	100 k

Table 4.13: The numbers of analysed events for h_c decay

The following selection criteria were applied:

- ϕ candidates were defined as K^+ , K^- pairs with invariant mass in the window [0.8; 1.2] GeV. Two ϕ candidates in one event with invariant mass in the window [2.6;3.2] GeV defined an η_c candidate which, combined with a neutral candidate, formed an h_c candidate.
- A 4C-fit to beam energy-momentum was applied to the h_c candidate, which was stored to a root ntuple together with the updated information on its decay products.
- The following cuts are performed at the ntuple level for additional background suppression:
 - cut on the confidence level of the 4C-fit to beam energy-momentum, $CL > 0.05$,
 - η_c invariant mass [2.9;3.06] GeV,
 - E_γ within [0.4;0.6] GeV,
 - ϕ invariant mass [0.99;1.05] GeV,
 - no π^0 candidates in the event, *i.e.* no 2 γ invariant mass in the range [0.115;0.15] GeV with 2 different low energy γ thresholds: 30 MeV and 10 MeV.

The efficiencies of the various cuts are given in Table 4.14 for the signal and three of considered background channels.

Assuming the h_c production cross-section of 33 nb at resonance, one obtains the signal to background ratios given in Table 4.15.

For the $\overline{\text{p}}\text{p} \rightarrow \phi\phi\pi^0$ background channel the reduction of low energy γ -ray threshold from 30 MeV to 10 MeV gives a 19% improvement in the signal to background ratio, for the $\overline{\text{p}}\text{p} \rightarrow \phi K^+K^-\pi^0$ the corresponding improvement is 33%.

With the final signal selection efficiency of 25% and the assumed luminosity in high luminosity mode of $L = 2 \cdot 10^{32} \text{ cm}^{-2}\text{s}^{-1}$ the expected signal event rate is 92 events/day. For the high resolution

mode with $L = 2 \cdot 10^{31} \text{ cm}^{-2}\text{s}^{-1}$ the expected signal event rate is 9 events/day.

4.2.2.5 $\overline{\text{p}}\text{p} \rightarrow D\overline{D}$

The main focus of this benchmark study is to assess the ability to separate the charm signal from the large hadronic background. In addition to the detection of charmonium states above the $D\overline{D}$ threshold this is important for other major parts of the $\overline{\text{PANDA}}$ physics program, such as open charm spectroscopy, the search for charmed hybrids decaying to $D\overline{D}$ and the investigation of rare decays and CP violation in the D meson sector.

In order to study the tracking and PID reconstruction capabilities of the proposed $\overline{\text{PANDA}}$ detector, two benchmark channels have been chosen with decays containing only charged particles (charge conjugated states included):

- $\overline{\text{p}}\text{p} \rightarrow D^+D^-$ with the decay $D^+ \rightarrow K^-\pi^+\pi^+$
- $\overline{\text{p}}\text{p} \rightarrow D^{*+}D^{*-}$ with the sequential decays $D^{*+} \rightarrow D^0\pi^+$ and $D^0 \rightarrow K^-\pi^+$

Both channels were simulated at a beam energy corresponding to $\sqrt{s} = m_{c\bar{c}}$, the $\Psi(3770)$ for the D^+D^- channel and the $\Psi(4040)$ for the $D^{*+}D^{*-}$ channel, respectively. The production is done directly into a $D\overline{D}$ pair, which corresponds to ≈ 40 MeV above the particular $D\overline{D}$ threshold.

The charm production cross sections close to threshold in $\overline{\text{p}}\text{p}$ annihilations are unknown. To estimate the $D\overline{D}$ production cross section a Breit-Wigner approach can be used to calculate the resonant cross section, where the unknown branching ratios to $\overline{\text{p}}\text{p}$ are estimated by scaling the known ratio $J/\psi \rightarrow \overline{\text{p}}\text{p}$ [32]. This method estimates only the strength of the resonance contribution to the cross section. The strength of the $D\overline{D}$ continuum production is unknown and to account for its contribution, the known decay branchings $c\bar{c} \rightarrow D\overline{D}$ have been set to 100%, which leads to assumptions for the cross sections of:

$$\sigma(\overline{\text{p}}\text{p} \rightarrow \Psi(3770) \rightarrow D^+D^-) = 3.9 \text{ nb}$$

for the first channel, and

$$\sigma(\overline{\text{p}}\text{p} \rightarrow \Psi(4040) \rightarrow D^{*+}D^{*-}) = 0.9 \text{ nb}$$

for the second channel, respectively. Taking into account the branching ratios of the considered D meson decays, the expected ratio R between the signal and the total $\overline{\text{p}}\text{p}$ cross section within this analysis

Selection criteria	signal	$4K\pi^0$	$\phi K^+K^-\pi^0$	$\phi\phi\pi^0$	$K^+K^-\pi^+\pi^-\pi^0$
pre-selection	0.51	$9.8 \cdot 10^{-3}$	$1.3 \cdot 10^{-2}$	$4.9 \cdot 10^{-2}$	$9.0 \cdot 10^{-6}$
$CL > 0.05$	0.36	$1.5 \cdot 10^{-3}$	$2.0 \cdot 10^{-3}$	$7.0 \cdot 10^{-3}$	$4.0 \cdot 10^{-8}$
$m(\eta_c), E_\gamma$	0.34	$4.1 \cdot 10^{-4}$	$5.2 \cdot 10^{-4}$	$1.8 \cdot 10^{-3}$	0
$m(\phi)$	0.31	$4.5 \cdot 10^{-6}$	$1.2 \cdot 10^{-4}$	$1.7 \cdot 10^{-3}$	0
$no \pi^0(30 MeV)$	0.26	$2.7 \cdot 10^{-6}$	$4.5 \cdot 10^{-5}$	$9.2 \cdot 10^{-4}$	0
$no \pi^0(10 MeV)$	0.24	$1.8 \cdot 10^{-6}$	$3.0 \cdot 10^{-5}$	$7.1 \cdot 10^{-4}$	0

Table 4.14: Efficiency of different event selection criteria.

channel	Signal/Background
$\bar{p}p \rightarrow K^+K^-K^+K^-\pi^0$	8
$\bar{p}p \rightarrow \phi K^+K^-\pi^0$	8
$\bar{p}p \rightarrow \phi\phi\pi^0$	> 10
$\bar{p}p \rightarrow K^+K^-\pi^+\pi^-\pi^0$	> 12

Table 4.15: Signal to background ratio for different h_c background channels

channel	D^+D^-	$D^{*+}D^{*-}$
decay	$D^\pm \rightarrow K^\mp \pi^\pm \pi^\pm$ (9.2 %)	$D^{*+} \rightarrow D^0 \pi^+$ $D^0 \rightarrow K^- \pi^+$ (67.7 %) (3.8 %)
R	4×10^{-10}	1×10^{-11}

Table 4.16: Definition of the $D\bar{D}$ physics channels, relevant decay branching ratios and the expected ratio between signal and total $\bar{p}p$ cross section.

can be calculated. The values obtained are listed in Table 4.16 together with the branching ratios of the individual D meson decays used in this analysis.

Using a value of 60 mb for the total $\bar{p}p$ cross section at the $D\bar{D}$ threshold the relevant production cross section will thus be suppressed at least by ten orders of magnitude.

The event selection requires all six charged tracks to be detected. D meson candidates are defined by means of loose mass windows of $\Delta m = \pm 0.3 \text{ GeV}/c^2$ before vertex fitting is done. For the D^+D^- channel three charged tracks are fitted to a common vertex and both D^\pm meson candidates are combined to the initial system, which has to meet kinematically the beam four-momentum. The confidence level for the kinematic fit is required to be $CL_{kin} > 0.01$. In events with more than two D^\pm candidates the best two are selected according to the χ^2 value from the vertex fit and the momentum of the candidate, which should be closer to the kinematically allowed

region. Fig. 4.16 shows the invariant mass distribution of the D^\pm candidates. The signal sample is free of combinatorial background and the distribu-

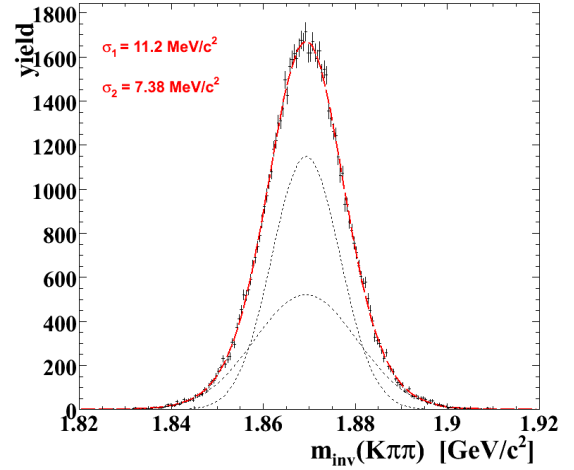


Figure 4.16: Invariant D^\pm mass distribution of $\bar{p}p \rightarrow D^+D^-$ signal events.

tion is well described by a fit containing a superposition of two Gaussian components (shown in the plot as dashed lines) with the individual widths of $\sigma_1 = 11.2 \text{ MeV}/c^2$ and $\sigma_2 = 7.4 \text{ MeV}/c^2$. The overall signal efficiency at this stage is $\epsilon = 39.9\%$.

For the $D^{*+}D^{*-}$ channel, again a loose mass window is set in the preselection of the D^0 candidate. A kaon and a pion track are combined and if a common vertex is found, a pion is combined to the previously selected D^0 candidate to reconstruct the corresponding $D^{*\pm}$ meson. If both $D^{*\pm}$ are found, the event is fitted kinematically to the four-momentum of the beam-target system. A confidence level $CL_{kin} > 0.01$ is required. The invariant masses of both D mesons are shown in Fig. 4.17. The right side shows the D^0 invariant mass and the line shape is well described by a fit containing two Gaussian components with values $\sigma_1 = 15.2 \text{ MeV}/c^2$ and $\sigma_2 = 28.3 \text{ MeV}/c^2$. The left side of Fig. 4.17 shows the invariant mass distribution of the $D^{*\pm}$

channel	D^+D^-	$D^{*+}D^{*-}$	Ratio to $\bar{p}p$
DPM	100 M	-	-
$3\pi^+3\pi^-\pi^0$	50 M	43 M	2.5×10^{-2}
$3\pi^+3\pi^-$	10 M	14 M	5×10^{-3}
$K^+K^-2\pi^+2\pi^-$	1 M	10 M	5×10^{-4}

Table 4.17: Background channels for the $D\bar{D}$ analysis with the corresponding number of simulated events and the ratio between the cross section for that channel and the total $\bar{p}p$ cross section.

candidates after a 5C kinematic fit.

This additional mass constraint can be imposed since the whole decay tree gets fitted. Together with the beam four-momentum constraint, the individual widths of the two Gaussian components are $\sigma_1 = 0.75 \text{ MeV}/c^2$ and $\sigma_2 = 0.29 \text{ MeV}/c^2$. Without the additional constraint the width of the D^* mass distribution would be of the same order as the D^\pm mass resolution. The efficiency for the 5C-fit gets only slightly reduced from $\epsilon_{signal,4C} = 27.4 \%$ to $\epsilon_{signal,5C} = 24.0 \%$.

In order to understand the general features of the analysis the Dual Parton Model (DPM) was used to produce background coming from $\bar{p}p$ annihilations. Only inelastic collisions including multi-prong events have been simulated. Because of the small ratio between the $D\bar{D}$ cross section and the total $\bar{p}p$ cross section, a very large number of events needs to be generated. For this reason this general study was carried out only for the D^+D^- channel: 10^8 events were produced to test the analysis, *e.g.* for the acceptance of events containing charged track multiplicities equal or larger than six and to check for possible detector-related effects.

In a second stage, in order to evaluate the ability to suppress the background to a sufficient level, a detailed study of specific background reactions was performed. This includes channels with six charged tracks in the final state, which could be kinematically interpreted as signal events. The selected channels and the relative ratio to the total $\bar{p}p$ cross section are given in Table 4.17:

To study the background arising from channels with charged kaons and pions the non-resonant production of $K^+K^-2\pi^+2\pi^-$ has been analysed, which has at least a 10^6 times higher cross section than the D^+D^- signal channel close to the production at threshold. Fig. 4.18 compares the longitudinal vs. the transverse momentum component of the D meson candidate for signal (left) and background events (right). A constraint on the D^\pm momentum

via the definition of a wide window in the two-dimensional momentum plane gives a reduction factor of ≈ 26 for background events. The cut has been chosen to reject mainly those background events with too large transverse momenta, which would result in lower values for the invariant D^\pm mass. The remaining events leave a non-peaking background distribution in the mass region defined by the loose mass window from the preselection. Thus, the remaining background will be kinematically similar to signal events and can not be separated further by kinematical constraints.

Background events will be produced prompt at the interaction point and can be in principle separated by finding the D^\pm decay vertices located separated from the primary interaction point. Since the $D\bar{D}$ production was studied close to threshold and due to the fixed-target character of the experiment, the direction of the D^\pm mesons will be close to the beam axis with a small opening angle. The uncertainty in the location of the primary vertex is determined by the size of the beam spot along the beam which is of the order of $\sigma_{z,prim} \approx 500 \mu\text{m}$. On the other hand, using the tracking system, a much better resolution can be obtained for the D^\pm decay vertex: $\sigma_{x,y} \approx 35 \mu\text{m}$ in the transverse plane and $\sigma_z \approx 80 \mu\text{m}$ in beam direction, respectively. The reconstructed decay position of both D^\pm candidates can be used to reject background events. Fig. 4.19 shows the beam axis projection of the difference vector of the two D^\pm meson decay vertices for signal events (black histogram) and for $K^+K^-2\pi^+2\pi^-$ background events (hatched histogram). Since the simulation requirement for the $D\bar{D}$ channels is already high, the amount of simulated background events was chosen to meet the level of signal generation, under the conservative cross section assumption given above. The shape of the background distribution has been scaled by a factor 10^5 , which is symbolized by an additional blue dashed line in Fig. 4.19 and would correspond to an equal amount of produced signal and background events. The vertical arrow represents a $\Delta z = 0.088 \text{ cm}$ cut, where the area below both distributions is equal. This would correspond to a signal to background ratio of 1 : 1. The remaining signal efficiency after the additional vertex cut is $\epsilon_{\Delta z}(D^+D^-) = 7.8 \%$. The shape of the background distribution can be assumed to be the same like the blue shaded region, since only vertex constraints determine the shape of the background distribution. An increase of the Δz cut can further enhance the signal to background ratio.

The cross sections for the pionic channels are according to Table 4.17 a factor of fifty larger com-

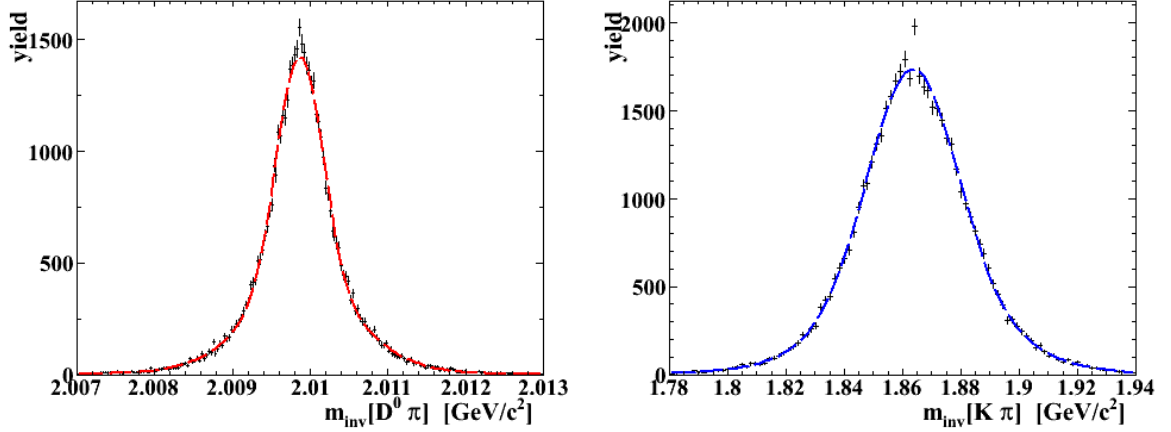


Figure 4.17: Invariant mass distributions of the $D^{*\pm}$ candidate (left) and the D^0 candidates (right).

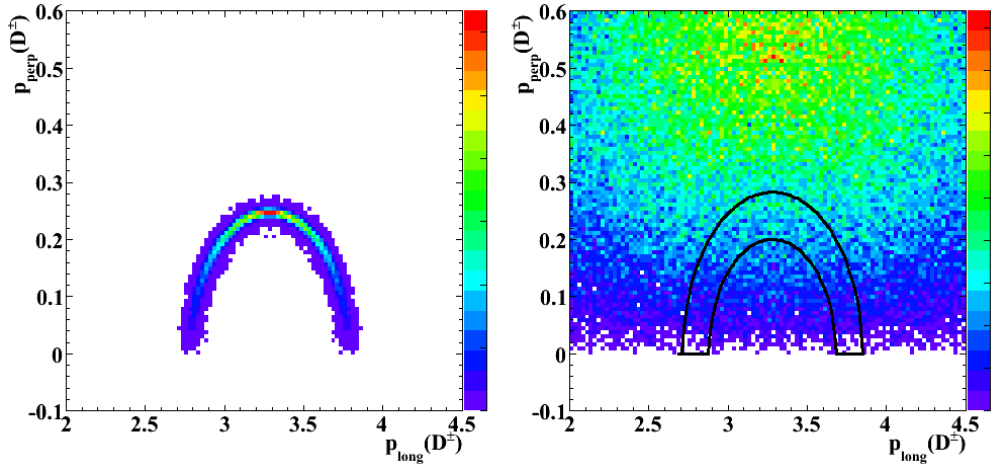


Figure 4.18: Momentum components of D^\pm candidates for signal events (left) and for background events of the reaction $\bar{p}p \rightarrow K^+K^-2\pi^+2\pi^-$ background (right). The surrounded region shows the allow momentum range for D^\pm candidates.

pared to the $\bar{p}p \rightarrow K^+K^-2\pi^+2\pi^-$ background reaction. For both channels all produced events could be suppressed completely, even without demanding a larger kaon probability in the D^\pm reconstruction. To obtain the efficiency for background events some cuts have been relaxed, e.g. the influence of the D^\pm momentum cut has been estimated in an analysis without kinematic fit.

For the benchmark channel $\bar{p}p \rightarrow 3\pi^+3\pi^-\pi^0$ the kinematic suppression of this channel is stronger compared to the $3\pi^+3\pi^-$ channel, although the cross section for this particular channel is a factor of five larger. The π^0 is not reconstructed and in most cases the event does not fit to the initial beam momentum. For the $3\pi^+3\pi^-$ channel, the suppression factor caused by the kinematic fit for

background events was estimated to be $\approx 2.6 \cdot 10^{-4}$, whereas for the $3\pi^+3\pi^-\pi^0$ channel it was estimated to $\approx 4.4 \cdot 10^{-4}$, respectively. For both channels no vertex constraints has been used. At this level the expected signal to background ratio are better than 2 : 1. Table 4.18 gives an overview about the obtained efficiencies and the resulting signal to background ratios. According to the investigation of the $K^+K^-2\pi^+2\pi^-$ channel and additional cut to the reconstructed D^\pm vertex positions would strongly increase the signal to background ratio.

For the second charmed benchmark channel $\bar{p}p \rightarrow D^{*+}D^{*-}$ in total 10^7 events for the background reaction $K^+K^-2\pi^+2\pi^-$ have been analysed. For the generation of the background channels for this physics channel, a prefilter has been used, which fil-

selection		efficiency		signal/background	
selection	D^+D^-	$3\pi^+3\pi^-$	$3\pi^+3\pi^-\pi^0$	$\frac{D^+D^-}{3\pi^+3\pi^-}$	$\frac{D^+D^-}{3\pi^+3\pi^-\pi^0}$
preselection	0.43	$5.4 \cdot 10^{-3}$	$9.6 \cdot 10^{-4}$	-	-
4C-fit	0.40	$1.4 \cdot 10^{-6}$	$4.2 \cdot 10^{-7}$	0.02	0.015
D^\pm momentum	0.40	$< 1.1 \cdot 10^{-8}$	$< 3.6 \cdot 10^{-9}$	> 2.7	> 1.8
K LH > 0.3	0.23	$< 1.8 \cdot 10^{-9}$	$< 1.7 \cdot 10^{-9}$	> 6.4	> 2.9

Table 4.18: Expected signal to background ratios for the D^+D^- channel to $3\pi^+3\pi^-(\pi^0)$ background events.

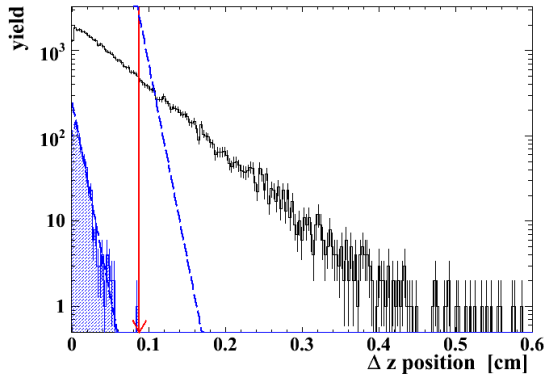


Figure 4.19: Distribution of the difference of both reconstructed D mesons as projection onto the beam axis. Upper curve for signal lower for remaining background events (see text for details).

tered those events, which does not have a D^0 and a $D^{*\pm}$ candidate in the event. Only $\approx 15\%$ of all events passed the filter. For this preselection a wide mass window of $\Delta m = 0.5$ GeV/ c has been set. All simulated events could be suppressed by the analysis. This corresponds to a signal to background ratio of $S/B \approx 1 : 3$. According to the analysis of this background channel for the D^+D^- signal, an additional suppression factor of 10 could be obtained by applying a cut on the difference of the D^0 decay vertices of $\Delta z = 200 \mu\text{m}$. This constraint would reduce the signal efficiency from $\epsilon = 24.0\%$ to $\epsilon = 12.7\%$ and the signal to background ratio would improve to $\approx 3 : 2$.

To estimate the contributions of the pionic background channels $\bar{p}p \rightarrow 3\pi^+3\pi^-(\pi^0)$ to the background of the $D^{*+}D^{*-}$ signal channel, the total of $5.7 \cdot 10^7$ background channels have been simulated (according to Table 4.17). This corresponds to a total of $3.5 \cdot 10^8$ events and no event passes the analysis for both background channels. To estimate the influence of the suppression of the kinematic fit, the pionic background channel have been analysed without kinematic fit and only a few events survive the preselection including vertex

fits. The efficiencies to suppress the background are given in Table ???. Assuming at least a factor of $\epsilon_{5C-kin} \approx 10^{-4}$ for the influence of the kinematic fit on the background suppression, the expected signal to background ratio for the pionic channels would than be larger than $S : N > 12$. This assumption is still very conservative, since the additional constraint on the D^0 mass in the kinematic fit could not be estimated and would increase the suppression factor for this background source. Therefore, the contribution to the expected hadronic background from the pionic channels is expected to be small.

In a general attempt the annihilation background was simulated using the DPM background generator. A total number of 10^8 events have been defined in order to study possible other background sources. So far 24×10^6 events have been produced and analysed and no event survived the selection cuts.

Assuming the reaction cross sections of charmonium production above the DD threshold to be in the order of 3 nb for the D^+D^- and 0.9nb for the $D^{*+}D^{*-}$ production the expected numbers of reconstructed events per year of \bar{P} ANDA operation are at least 1.5×10^4 and 1.4×10^3 , respectively. For these estimations a efficiency of $\epsilon = 7.8\%$ for the D^+D^- channel and $\epsilon = 24.0\%$ have been used. These values are obtained by using only the dominant charged decays of D mesons. Including further decay channels should significantly improve the signal efficiency.

4.2.2.6 h_c width measurement

In order to assess the ability to measure narrow widths we report a study of the sensitivity of \bar{P} ANDA to the determination of the h_c width. For this purpose we performed Monte Carlo simulations of energy scans around the resonance. Events were generated at 10 different energies around the h_c mass, each point corresponding to 5 days of running the experiment in high luminosity mode.

The expected shape of the measured cross-section is the convolution of the Breit-Wigner resonance curve

selection		efficiency		signal/background	
selection	$D^{*+}D^{*-}$	$3\pi^+3\pi^-$	$3\pi^+3\pi^-\pi^0$	$\frac{D^{*+}D^{*-}}{3\pi^+3\pi^-}$	$\frac{D^{*+}D^{*-}}{3\pi^+3\pi^-\pi^0}$
preselection	0.27	$5.0 \cdot 10^{-7}$	$7.5 \cdot 10^{-8}$	-	-
5C-fit	0.24	$5.0 \cdot 10^{-11}$	$7.5 \cdot 10^{-12}$	≥ 10	≥ 14

Table 4.19: Expected signal to background ratios for the $D^{*+}D^{*-}$ channel to $3\pi^+3\pi^-(\pi^0)$ background events.

$\Gamma_{R,MC}$ [MeV]	$\Gamma_{R,reco}$ [MeV]	$\Delta\Gamma_R$ [MeV]
1	0.92	0.24
0.75	0.72	0.18
0.5	0.52	0.14

Table 4.20: Reconstructed h_c width.

with the normalised beam energy distribution and an added background term. The expected number of events at the i th data point is

$$\nu_i = \left[\varepsilon \times \int L dt \right]_i \times \left[\sigma_{bkgd}(E) + \frac{\sigma_p \Gamma_R^2 / 4}{(2\pi)^{1/2} \sigma_i} \times \int \frac{e^{-(E-E')^2/2\sigma_i^2}}{(E' - M_R)^2 + \Gamma_R^2/4} dE' \right] \quad (4.5)$$

where σ_i is the beam energy resolution at the i th data point, Γ_R and M_R the resonance width and mass, L the luminosity and ε is an overall efficiency and acceptance factor. To extract the resonance parameters the likelihood function $-\ln \mathcal{L}$ is minimized assuming Poisson statistics, where

$$\mathcal{L} = \prod_{j=1}^N \frac{\nu_j^{n_j} e^{-\nu_j}}{n_j!} \quad (4.6)$$

For our simulation we assumed a signal to background ratio of 8:1 and we used the signal reconstruction efficiency of the $h_c \rightarrow \eta_c \gamma \rightarrow \phi \phi \gamma$ channel. The simulated data were fitted to the expected signal shape with 4 free parameters: E_R , Γ_R , σ_{bkgd} , σ_p . The background was assumed to be energy independent. The study has been repeated for 3 different values of the total width: $\Gamma_R = 0.5, 0.75, 1.0$ MeV. The results of the fit for 0.5 MeV and 1.0 MeV are presented in Fig. 4.20. The extracted Γ_R 's with errors are summarized in Table 4.20.

4.2.2.7 Angular distributions in the radiative decay of χ_c

The measurement of the angular distribution in the radiative decays of the χ_c states provides information on the multipole structure of the radiative de-

cay and the properties of the $\bar{c}c$ bound state. The process $\bar{p}p \rightarrow J/\psi \gamma \rightarrow e^+e^-\gamma$ is dominated by the dipole term $E1$. $M2$ and $E3$ terms arise in the relativistic treatment of the interaction between the electromagnetic field and the quarkonium system. They contribute to the radiative width at the few percent level.

The coupling between the set of χ states and $\bar{p}p$ is described by four independent helicity amplitudes:

- χ_{c0} is formed only through the helicity 0 channel;
- χ_{c1} is formed only through the helicity 1 channel;
- χ_{c2} can couple to both.

The angular distributions of the χ_{c1} and χ_{c2} are described by four independent parameters: $a_2(\chi_{c1}), a_2(\chi_{c2}), B_0^2(\chi_{c2}), a_3(\chi_{c2})$.

The fractional electric octupole amplitude, $a_3 \approx E3/E1$ can contribute only to the χ_{c2} decays, and is predicted to vanish in the single quark radiation model if the J/ψ is pure S -wave.

For the fractional $M2$ amplitude a relativistic calculation yields [33]:

$$a_2(\chi_{c1}) = -\frac{E_\gamma}{4m_c}(1 + \kappa_c) = -0.065(1 + \kappa_c) \quad (4.7)$$

$$a_2(\chi_{c2}) = -\frac{3}{\sqrt{5}} \frac{E_\gamma}{4m_c}(1 + \kappa_c) = -0.096(1 + \kappa_c) \quad (4.8)$$

where κ_c is the anomalous magnetic moment of the c -quark.

Fig. 4.21 shows the angles used in the description of the angular distribution:

- θ is the polar angle of the J/ψ with respect to the antiproton in the $\bar{p}p$ center of mass system;
- θ' is the polar angle of the positron in the J/ψ rest frame with respect to the J/ψ direction in the χ_c rest system;
- ϕ' is the azimuthal angle between the J/ψ decay plane and the χ_c plane.

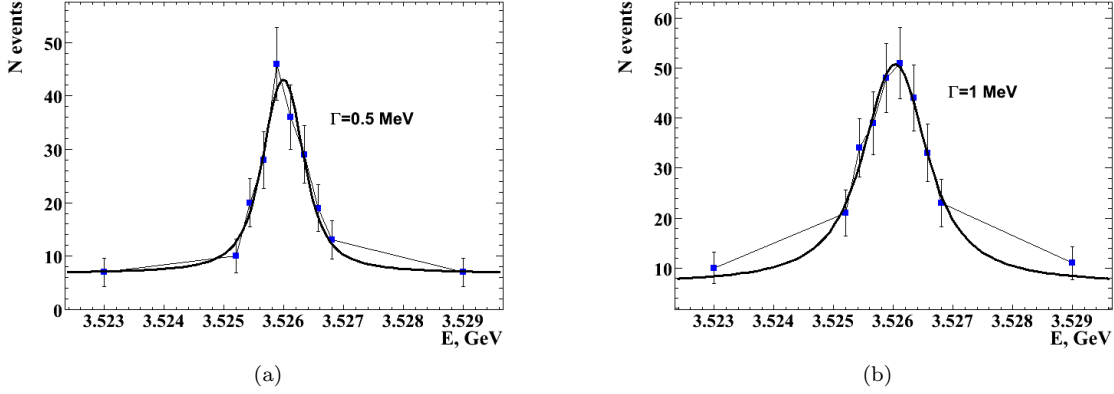


Figure 4.20: Fit of h_c resonance for $\Gamma = 0.5$ MeV (a) and $\Gamma = 1$ MeV (b)

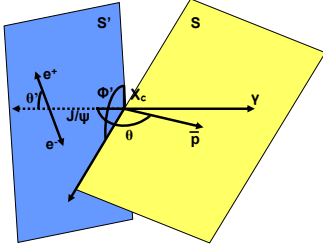


Figure 4.21: Definition of the angles for the angular distribution of the radiative decay of the χ_c .

The theoretical value of the ratio between $a_2(\chi_{c1})$ and $a_2(\chi_{c2})$ is predicted to be independent of the c -quark mass and anomalous magnetic moment:

$$\left(\frac{a_2(\chi_1)}{a_2(\chi_2)}\right)_{Th} = \frac{\sqrt{5} E_\gamma(\chi_1 \rightarrow J/\psi\gamma)}{3 E_\gamma(\chi_2 \rightarrow J/\psi\gamma)} = 0.676 \quad (4.9)$$

E835 measured for the first time this ratio and the result is [34]:

$$\left(\frac{a_2(\chi_1)}{a_2(\chi_2)}\right)_{E835} = -0.02 \pm 0.34 \quad (4.10)$$

While the value of $a_2(\chi_{c2})$ agrees well with the predictions of a simple theoretical model, the value of $a_2(\chi_{c1})$ is lower than expected (for $\kappa_c=0$) and the ratio between the two, which is independent of κ_c is $\approx 2\sigma$ away from the prediction. This could indicate the presence of competing mechanisms, lowering the value of the M2 amplitude at the χ_{c1} . Further, high

statistics measurements of these angular distributions are needed to solve this question.

In order to do that, following the results of E835, a new model of angular distribution was implemented using the following parameters for the decay of χ_{c1} :

- production amplitudes: $B_0=0$;
- decay amplitude: $a_2 = 0.002 \pm 0.032 \pm 0.004$;

and for the decay of χ_{c2} :

- production amplitudes: $B_0^2 = 0.16_{-0.10}^{+0.09} \pm 0.01$;
- decay amplitude: $a_2 = -0.076_{-0.050}^{+0.054} \pm 0.009$ and $a_3 = 0.020_{-0.044}^{+0.055} \pm 0.009$.

The angular distributions for the three angles can be approximately written, for the χ_{c1} , as:

$$\begin{aligned} \overline{W}(\cos\theta) &\sim 1 - \frac{1}{3} \cos^2 \theta \\ \overline{W}(\cos\theta') &\sim 1 - \frac{1}{3} \cos^2 \theta' \end{aligned}$$

and for the χ_{c2} :

$$\begin{aligned} \overline{W}(\cos\theta) &\sim 1 - \frac{1}{3} \cos^2 \theta \\ \overline{W}(\cos\theta') &\sim 1 + \frac{1}{13} \cos^2 \theta' \\ \overline{W}(\phi') &\sim 1 - \frac{8}{71} \cos 2\phi' \end{aligned}$$

Fig. 4.22 and 4.23 present the results obtained for the $\cos\theta$, $\cos\theta'$ and ϕ' distributions after the generation and reconstruction of the events for the decay of $\chi_{c1,2} \rightarrow J/\psi\gamma$. The top plots show the angle distributions corrected with the efficiency, which is presented in the lower part of the plot.

The dip in the efficiency around $\cos(\theta) \sim -0.4$ corresponds to events in which the photons are emitted

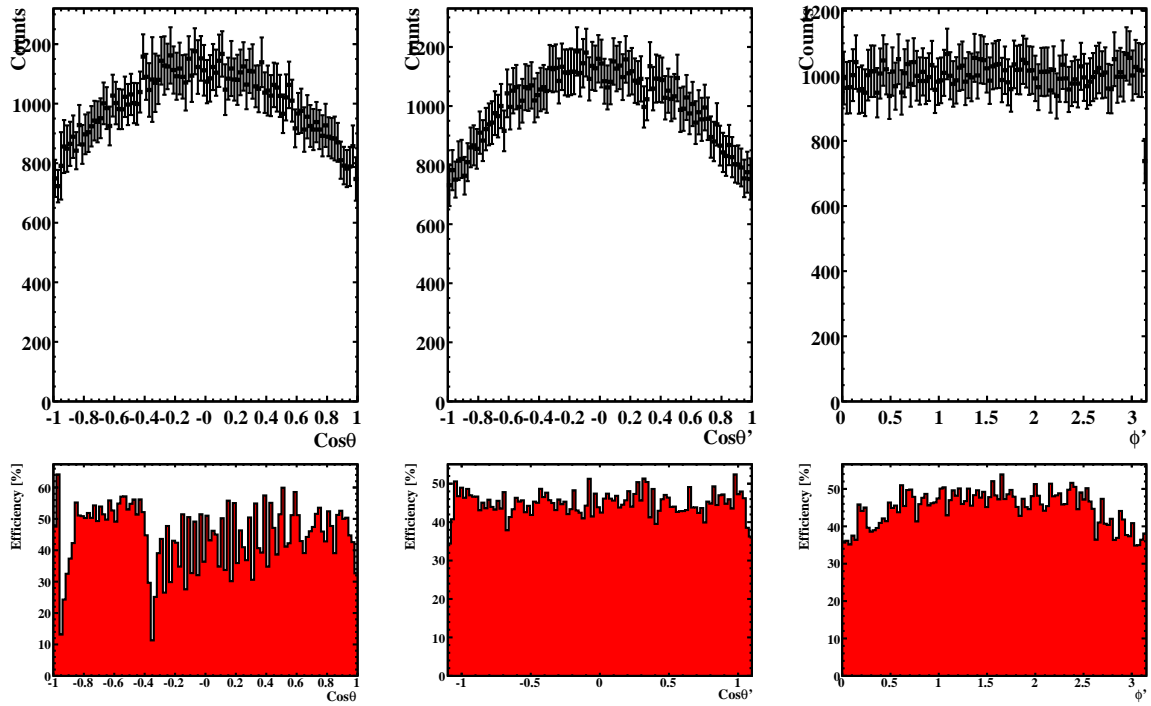


Figure 4.22: Results for $\cos\theta$, $\cos\theta'$ and ϕ' after the generation and reconstruction of the events for χ_{c1} decay.

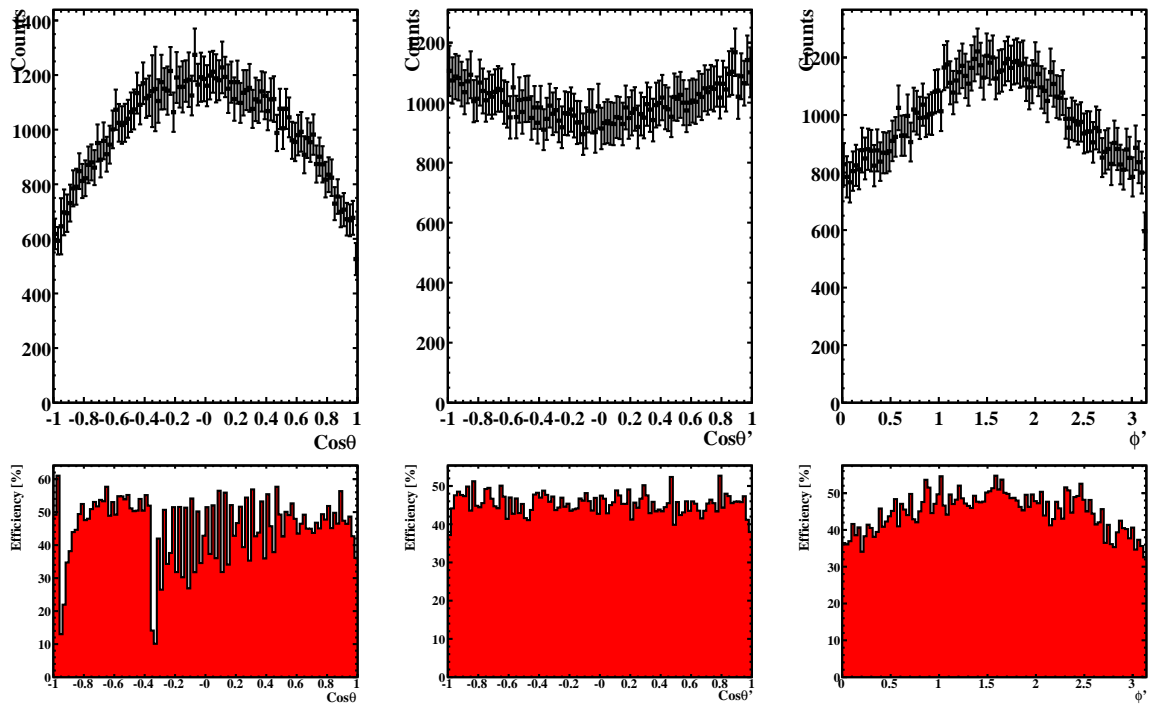


Figure 4.23: Results for $\cos\theta$, $\cos\theta'$ and ϕ' after the generation and reconstruction of the events for χ_{c2} decay.

at a polar angle in the laboratory system of $\sim 20^\circ$, in the transition zone between the target and for-

ward electromagnetic calorimeters. The projected angular distributions, after efficiency correction, are consistent with the observation from E835.

4.2.3 Exotic Excitations

COMMENT: Author(s): K. Peters
COMMENT: Referee(s): F. Iazzi

4.2.3.1 Hybrids - Gluonic Excitation of $q\bar{q}$ states

COMMENT: Author(s): K. Peters
COMMENT: Referee(s): F. Iazzi

The glue tube (often referred to as flux-tube) adds degrees of freedom which may manifest in vibrations of the tube. The higher the excitation the more units of angular momentum are carried. These different levels of excitation can be translated into different potentials, one for each mode. Fig. 4.24 shows this together with the corresponding wave functions.

Hybrids with exotic quantum numbers

The additional degrees of freedom (*e.g.* the vibration of the glue tube) manifest themselves also in a contribution to the quantum numbers of the topology. In the simplest scenario this corresponds to adding the quantum numbers of a gluon ($J^P=1^+$ or 1^- depending on if it is a colour-electric or colour-magnetic excitation) to a simple $q\bar{q}$ pair. Therefore they are often referred to as hybrids. This procedure creates *e.g.* for S-wave mesons 8 lowest lying hybrid states (see Table 4.21).

An important experimental aspect here is that 3 out of these 8 states exhibit quantum numbers which can not be formed by a normal $q\bar{q}$ pair. Therefore these quantum numbers are called exotic.

The most promising results for gluonic hadrons have come from antiproton annihilation experiments. Two particles, first seen in πN scattering [36, 37] with exotic $J^{PC} = 1^{-+}$ quantum numbers, $\pi_1(1400)$ [38] and $\pi_1(1600)$ [39] are clearly seen in $\bar{p}p$ annihilation at rest (for a more detailed list of observations see Table 4.22).

4.2.3.1.1 Charmonium Hybrids

Exotic charmonia are expected to exist in the 3–5 GeV/ c^2 mass region where they could be resolved and identified unambiguously.

Predictions for hybrids come mainly from calculations based on the bag model, flux tube model, and constituent gluon model and, recently, with increasing precision, from LQCD [48, 49]. For hybrids, the theoretical results qualitatively agree, lending support to the premise that the predicted properties

$(q\bar{q})_8$	Gluon	
	1^- (TM)	1^+ (TE)
$^1S_0, 0^{-+}$	1^{++}	1^{--}
$^3S_1, 1^{--}$	$0^{+-} \leftarrow$ exotic	0^{-+}
	1^{+-}	$1^{-+} \leftarrow$ exotic
	$2^{+-} \leftarrow$ exotic	2^{-+}

Table 4.21: The coupling of spins leads to 8 hybrid states for each pair of pseudoscalar and vector mesons with equal isospin. Even in this simple case three J^{PC} combination are not allowed for conventional $q\bar{q}$ pairs.

are realistic. Charmonium hybrids can be expected since the effect of an extra gluonic degree of freedom in meson-like systems is evident in the confining potentials for the $c\bar{c}g$ system (*e.g.* as derived from LQCD calculations in the Born-Oppenheimer approximation [49]).

The discussions have only been centred around the lowest-lying charmonium hybrids. Four of these states ($J^{PC} = 1^{--}, 0^{-+}, 1^{-+}, 2^{-+}$) correspond to a $c\bar{c}$ pair with $J^{PC} = 0^{-+}$ or 1^{--} , coupled to a gluon in the lightest mode with $J^{PC} = 1^{--}$. The other four states ($J^{PC} = 1^{++}, 0^{+-}, 1^{+-}, 2^{+-}$) with the gluon mode $J^{PC} = 1^{-+}$ are probably heavier. All models agree that the lightest exotic state would be 1^{-+} . Predictions for the mass are listed in Table 4.23. In addition to the lightest exotic state there are seven other hidden charmed hybrids to be discovered. The well accepted picture is that the quartet $1^{--}, (0,1,2)^{-+}$ is lower in mass than $1^{++}, (0,1,2)^{+-}$. The expected splitting is about 100–250 MeV from 1^{-+} to 0^{+-} [?, ?]. In addition there is fine-splitting within the hybrid triplets, so that the levels are spread over a few hundred MeV (*e.g.* 4.14 GeV/ c^2 for 0^{-+} and 4.52 GeV/ c^2 for 2^{-+}) [?, ?] which was verified by lattice QCD [?]. The actual signature is therefore not just an individual state, but also the pattern of states.

Charmonium hybrids are likely to be narrower since open-charm decays are forbidden or suppressed below the $D\bar{D}_j^* + c.c.$ (often referred to as DD^{**}) threshold. From experiments at LEAR we know that production rates of such $q\bar{q}$ states are similar to those of states with exotic quantum numbers. Thus, we estimate that the cross sections for the formation and production of charmonium hybrids will be similar to those of normal charmonium states which is in the order of 120 pb ($\bar{p}p \rightarrow J/\psi\pi^0$ [50]), in agreement with theoretical predictions [51]. The naming definitions of Table 4.24 are used for the subsequent discussions.

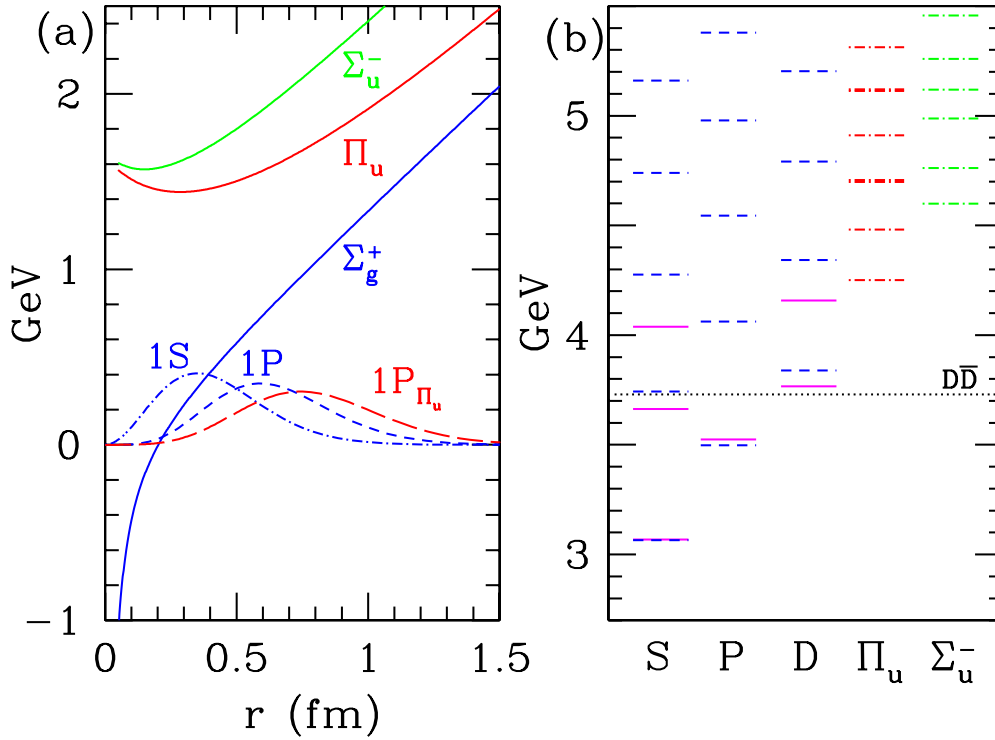


Figure 4.24: (a) Heavy quarkonium potentials and wave functions for different excitation levels from LQCD. Σ denotes normal one gluon exchange while the excited Π potentials are the lowest lying hybrid potentials. In that case, the attraction is not mediated by a single gluon but a string of gluons which carry angular momentum. (b) shows the charmonium spectrum from LQCD. The conventional charmonium states are on the right while the hybrids are found in column Π_u and Σ_u^- . See [35] for details.

Experiment	Exotic	J^{PC}	Mass [MeV/ c^2]	Width [MeV/ c^2]	Decay	Refs.	
E852	$\pi_1(1400)$	1^{-+}	1359	$^{+16}_{-14}$ $^{+10}_{-24}$	314	$^{+31}_{-29}$ $^{+9}_{-66}$	$\eta\pi$ [40]
Crystal Barrel	$\pi_1(1400)$	1^{-+}	1400	$\pm 20 \pm 20$	310	± 50 $^{+50}_{-30}$	$\eta\pi$ [38]
Crystal Barrel	$\pi_1(1400)$	1^{-+}	1360	± 25	220	± 90	$\eta\pi$ [41]
Obelix	$\pi_1(1400)$	1^{-+}	1384	± 28	378	± 58	$\rho\pi$ [42]
E852	$\pi_1(1600)$	1^{-+}	1593	± 8 $^{+29}_{-47}$	168	± 20 $^{+150}_{-12}$	$\rho\pi$ [43]
E852	$\pi_1(1600)$	1^{-+}	1597	± 10 $^{+45}_{-10}$	340	$\pm 40 \pm 50$	$\eta'\pi$ [43]
Crystal Barrel	$\pi_1(1600)$	1^{-+}	1590	± 50	280	± 75	$b_1\pi$ [44]
Crystal Barrel	$\pi_1(1600)$	1^{-+}	1555	± 50	468	± 80	$\eta'\pi$ [39]
E852	$\pi_1(1600)$	1^{-+}	1709	$\pm 24 \pm 41$	403	$\pm 80 \pm 115$	$f_1\pi$ [45]
E852	$\pi_1(1600)$	1^{-+}	1664	$\pm 8 \pm 10$	185	$\pm 25 \pm 28$	$\omega\pi\pi$ [46]
E852	$\pi_1(2000)$	1^{-+}	2001	$\pm 30 \pm 92$	333	$\pm 52 \pm 49$	$f_1\pi$ [45]
E852	$\pi_1(2000)$	1^{-+}	2014	$\pm 20 \pm 16$	230	$\pm 32 \pm 73$	$\omega\pi\pi$ [46]
E852	$h_2(1950)$	2^{+-}	1954	± 8	138	± 3	$\omega\pi\pi$ [47]

Table 4.22: Light states with exotic quantum numbers. The experiment E852 at BNL was performed with a pion beam on a hydrogen target, while Crystal Barrel was a $p\bar{p}$ spectroscopy experiment at LEAR.

Production vs. Formation

Formation experiments would generate non-exotic charmonium hybrids with high cross sections while production experiments would yield a charmonium

hybrid together with another particle, such as a π or an η . In $p\bar{p}$ annihilation, production experiments are the only way to obtain charmonium hybrids with exotic quantum numbers. It is envisaged

(a)	$m(c\bar{c}g), 1^{-+}$	Group	Ref.
	$4\,390 \pm 80 \pm 200$	MILC97	[52]
	$4\,317 \pm 150$	MILC99	[53]
	4 287	JKM99	[54]
	$4\,369 \pm 37 \pm 99$	ZSU02	[55]
(b)	$m(c\bar{c}g, 1^{-+}) - m(c\bar{c}, 1^{--})$	Group	Ref.
	$1\,340 \pm 80 \pm 200$	MILC97	[52]
	$1\,220 \pm 150$	MILC99	[53]
	$1\,323 \pm 130$	CP-PACS99	[56]
	1 190	JKM99	[54]
	$1\,302 \pm 37 \pm 99$	ZSU02	[55]

Table 4.23: Hybrid masses (a) and mass differences (b) from quenched LQCD. The results for the lightest J^{PC} exotic cluster around the threshold for $D\bar{D}^{**} + c.c.$ production.

$\tilde{\chi}_{c1} 1^{++}$	$\tilde{\psi} 1^{--}$
$\tilde{h}_{c0} 0^{+-} \leftarrow \text{exotic}$	$\tilde{\eta}_{c0} 0^{-+}$
$\tilde{h}_{c1} 1^{+-}$	$\tilde{\eta}_{c1} 1^{-+} \leftarrow \text{exotic}$
$\tilde{h}_{c2} 2^{+-} \leftarrow \text{exotic}$	$\tilde{\eta}_{c2} 2^{-+}$

Table 4.24: Lowest lying charmonium hybrids corresponding to the definitions as in Table 4.21.

that the first step of exploring charmonium hybrids would consist of production measurements at the highest antiproton energy available ($E_{\bar{p}} = 15 \text{ GeV}$, $\sqrt{s} = 5.46 \text{ GeV}/c^2$) and studying all possible production channels available to cover exotics and non-exotic states. The next step would consist of formation measurements by scanning the antiproton energy in small steps in the regions where promising hints of hybrids have been observed in the production measurements, thus having a second check on the static properties like the J^{PC} assignment as well as mass and width.

The discovery of such a reaction would necessitate a very good charmonium reconstruction efficiency. Thus, apart from the benchmark channels used for conventional charmonium, the charmed hybrid production in the mode $\bar{p}p \rightarrow \tilde{\eta}_{c1}\eta \rightarrow \chi_{c1}\pi^0\pi^0\eta$ ($\tilde{\eta}_{c1}$ is often referred to as ψ_g) has also been used to study the detector performance in multi-body charmonium reactions (see Sec. ??).

Proposed Measurements

The main goal is to measure all low lying charmonium hybrid states. From the 8 states, it is possible to measure 7 of them using three channels with a

charmonium final state. The possible reactions are

$$p\bar{p} \rightarrow \tilde{\eta}_{c0,1,2}\eta \rightarrow \chi_{c1}\pi^0\pi^0\eta \quad (4.11)$$

$$p\bar{p} \rightarrow \tilde{h}_{c0,1,2}\eta \rightarrow J/\psi\pi^0\pi^0\eta \quad (4.12)$$

$$p\bar{p} \rightarrow \tilde{\psi}\eta \rightarrow J/\psi\omega[\pi^0 \text{ or } \eta] \quad (4.13)$$

Since the final states $\chi_{c1}\pi^0\pi^0\eta$ with $\chi_{c1} \rightarrow J/\psi\gamma$ and $J/\psi\pi^0\pi^0\eta$ are very similar in terms of multiplicity and photon energies, the slightly more complicated channel (4.12) with a radiative charmonium decay and a charmonium hybrid mass of $4.3 \text{ GeV}/c^2$ is used to test the sensitivity of the detector. Although a charmonium final state is likely an open charm final state may also be possible and 7 of the already mentioned 8 states may be accessed with the final state DD^* . Thus the reactions

$$p\bar{p} \rightarrow [\tilde{\eta}_{c0,1,2}, \tilde{h}_{c0,1,2}, \tilde{\chi}_{c1}]\eta \rightarrow DD^*\eta \quad (4.14)$$

should be measured and will be also used as a benchmark channel with a charmonium hybrid mass of about $4.3 \text{ GeV}/c^2$. In order to ensure reasonable event statistics, D decays with high yields have to be combined. In both cases, the charmonium and the open charm channels are detailed partial wave decomposition has to be performed to disentangle the different waves. Since the experimental findings $Y(3940)$ and $Y(4320)$ are also discussed in the framework of hybrids, *e.g.* as vector charmonium hybrid candidates [?] they are also used as benchmark channels.

4.2.3.2 Glueballs - Gluonic Excitation of the QCD vacuum

LQCD calculations make rather detailed predictions for the glueball mass spectrum in the

quenched approximation disregarding light quark loops [57]. For example, the calculated width of approximately $100 \text{ MeV}/c^2$ [58] for the ground-state glueball matches the experimental results. LQCD predicts the presence of about 15 glueballs, some with exotic quantum numbers in the mass range accessible to the HESR.

Glueballs with exotic quantum numbers are called oddballs which cannot mix with normal mesons. As a consequence, they are predicted to be rather narrow and easy to identify experimentally [59]. It is conceivable that comparing oddball properties with those of non-exotic glueballs will reveal deep insight into the presently unknown glueball structure since the spin structure of an oddball is different [59]. The lightest oddball, with $J^{PC} = 2^{+-}$ and a predicted mass of $4.3 \text{ GeV}/c^2$, would be well within the range of the proposed experimental program. Like charmonium hybrids, glueballs can either be formed directly in the $\bar{p}p$ -annihilation process, or produced together with another particle. In both cases, the glueball decay into final states like $\phi\phi$ or $\phi\eta$ would be the most favorable reaction below $3.6 \text{ GeV}/c^2$ while $J/\psi\eta$ and $J/\psi\phi$ are the first choice for the more massive states.

The indication for a tensor state around $2.2 \text{ GeV}/c^2$ was found in the experiment of *Jetset* collaboration at LEAR [60]. The acquired statistics was not sufficient for the complementary reactions to be determined. We plan to measure the $\bar{p}p \rightarrow \phi\phi$ channel with statistics of two orders of magnitude higher than in the previous experiments. Moreover, other reactions of two vector particle production, such as $\bar{p}p \rightarrow \omega\omega, K^*\bar{K}^*, \rho\rho$ will be measured. However, the best candidate for the pseudo-scalar glueball ($\eta_L(1440)$), studied comprehensively at LEAR by the Obelix collaboration [61, 62, 63, 64, 65], is not widely accepted to be a glueball signal because the calculations of LQCD predict its mass above $2 \text{ GeV}/c^2$. Therefore, new data on many glueball states are needed to make a profound test of different model predictions.

It is worth stressing again that $\bar{p}p$ -annihilations present a unique possibility to search for heavier glueballs since alternative methods have severe limitations. The study of glueballs is a key to understanding long-distance QCD. Every effort should be made to identify them uniquely.

Light Glueballs

Since decades light meson spectroscopy experiments tried to identify the lowest lying glueball states. Many high statistics experiments have been performed which delivered excellent information about

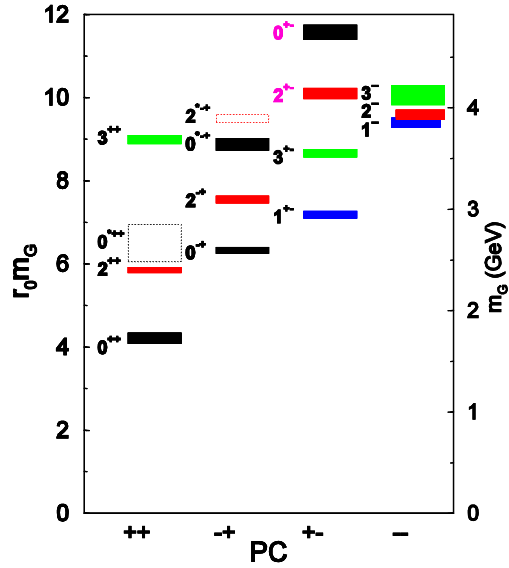


Figure 4.25: Glueball prediction from LQCD calculations. See [66, 57] for details. While the region of the ground-state glueball was investigated in the LEAR era (in particular by Crystal Barrel) are the tensor glueball and the spin exotic glueballs with $J^{PC} = 0^{+-}$ and 2^{+-} important research topics for \bar{P} ANDA.

the scalar and pseudoscalar waves. Nevertheless, due to the unavoidable mixing problem and the large widths arising from missing or smooth damping functions pinning down of the scalar glueballs will very difficult.

In light quark domain the tensor glueball is the best candidate to look at from experimental means. There is potential mixture from two nonets (3P_2 and 3F_2) which sums up to 5 expected isoscalar states, but $SU_F(3)$ forbids $\phi\phi$ decays to first order for the conventional $q\bar{q}$ states, while there is no suppression for a potential glueball. The mass for the glueball is expected in the range from $2.0 \text{ GeV}/c^2$ to $2.5 \text{ GeV}/c^2$. Thus the benchmark reaction is $p\bar{p} \rightarrow f_2(2000 - 2500) \rightarrow \phi\phi$.

Heavy Oddballs

Since glueballs don't have to obey any OZI rule, they may decay in any open channel. For glueballs above the open charm pair production threshold also decays in to D mesons and its excitations should be easily possible. The width is completely unknown. Since a lot of channels are potentially open, the heavy glueballs could be extremely wide. Nevertheless it is known from many other reactions, that nature seems to invest more likely in mass rather than in breakup-momentum, thus giving the

opportunity to look for oddballs in *e.g.* DD^* decays. Decays of this kind are investigated for the search for charmonium hybrids. The final state to look at is then $DD^*\eta$ or $DD^*\pi^0$. The lightest oddballs are $J^{PC} = 2^{+-}$ and 1^{+-} (spectroscopic name $b_{0,2}(4000 - 5000)$). Since they would appear in the same open charm final states as charmonium hybrids, the conclusions for these hybrid channels apply also to the oddball search.

4.2.3.3 Multiquarks - Mesic Excitation of $q\bar{q}$ states

COMMENT: Author(s): K. Peters

COMMENT: Referee(s): F. Iazzi

It is an widely accepted paradigm, that mesic excitations are present in the wave functions of QCD bound states, like the pion cloud around the nucleons. The mesic excitation is - if at all - expected to be loosely bound, thus resulting in extremely large widths. In the vicinity of strong thresholds this may be different and states with a potentially large additional mesic component can become substantially more narrow if they appear sub-threshold. This is for example seen in the $a_0(980)$ and $f_0(975)$ pair, which are believed to be the ground state $I = 1$ and $I = 0$ scalar mesons, but strongly attracted by the $K\bar{K}$ threshold and with large (may be dominating) $K\bar{K}$ component in the wave function.

In the case of the extremely narrow $X(3872)$ the DD^* threshold has a dramatic impact on its wave function and dynamics. As discussed in the previous section it was discovered in typical charmonium reactions, but it does not really fit very well in any potential model. One solution could be that it is dominated by a DD^* bound state. Various calculations show, that depending on the kind of object, the different dispersive effects would manifest in different lineshapes [?, ?] (see also Fig. 4.26).

4.2.3.4 Benchmark Channels

Study of $\bar{p}p \rightarrow \tilde{\eta}_{c1}\eta \rightarrow \chi_{c1}\pi^0\pi^0\eta$

For the production of ψ_g in $\bar{p}p \rightarrow \psi_g\eta$ it is assumed that the cross section is in the same order of magnitude as for the process $\bar{p}p \rightarrow \psi(2S)\eta$ including conventional charmonium. The cross section for this reaction is given in Ref. [?] to be (33 ± 8) pb at $\sqrt{s} = 5.38$ GeV and is calculated from the crossed process $\psi(2S) \rightarrow \eta\bar{p}p$ observed in e^+e^- annihilation.

The final state with 7 photons and an e^+e^- lepton pair originating from J/ψ decays has a distinctive signature and separation from light hadron background should be feasible. A source of background are events with hidden charm, in particular events including a J/ψ meson. This type of background has been studied by analysing $\bar{p}p \rightarrow \chi_{c0}\pi^0\pi^0\eta$, $\bar{p}p \rightarrow \chi_{c1}\pi^0\eta\eta$, $\bar{p}p \rightarrow \chi_{c1}\pi^0\pi^0\pi^0\eta$ and $\bar{p}p \rightarrow J/\psi\pi^0\pi^0\pi^0\eta$. The hypothetical hybrid state is absent in these reactions, but the χ_{c0} and χ_{c1} mesons decay via the same decay path as for the signal. Therefore these events have a similar topology as signal events and could potentially pollute the $\tilde{\eta}_{c1}$ signal.

Reaction	σ	\mathcal{B}
$\bar{p}p \rightarrow$		
$\tilde{\eta}_{c1}\eta$	33 pb	$1.63\% \times \mathcal{B}(\tilde{\eta}_{c1} \rightarrow \chi_{c1}\pi^0\pi^0)$
$\chi_{c0}\pi^0\pi^0\eta$		0.059%
$\chi_{c1}\pi^0\eta\eta$		0.648%
$\chi_{c1}\pi^0\pi^0\pi^0\eta$		1.61%
$J/\psi\pi^0\pi^0\pi^0\eta$		4.51%

Table 4.25: Cross sections for signal and background reactions. The table lists also the product of branching fractions for the subsequent particle decays.

The number of analysed signal and background events is summarized in Table 4.26.

Reaction	Events
$\bar{p}p \rightarrow$	
$\tilde{\eta}_{c1}\eta$	$2 \cdot 10^5$
$\chi_{c0}\pi^0\pi^0\eta$	$2 \cdot 10^5$
$\chi_{c1}\pi^0\eta\eta$	$2 \cdot 10^5$
$\chi_{c1}\pi^0\pi^0\pi^0\eta$	$2 \cdot 10^5$
$J/\psi\pi^0\pi^0\pi^0\eta$	$2 \cdot 10^5$

Table 4.26: Number of analysed signal and background events. The J/ψ decays with equal branching fraction of 50% into e^+e^- and $\mu^+\mu^-$.

Photon candidates are selected from the clusters found in the EMC with the reconstruction algorithm explained in Sec. ???. Two photon candidates are combined and accepted as π^0 and η candidates if their invariant mass is within the interval $[115;150]$ MeV/ c^2 and $[470;610]$ MeV/ c^2 , respectively.

From the J/ψ and photon candidates found in an event $\chi_{c1} \rightarrow J/\psi\gamma$ candidates are formed, whose invariant mass is within the range $[3.3;3.7]$ GeV/ c^2 . From these $\chi_{c1}\pi^0\pi^0\eta$ candidates are created,

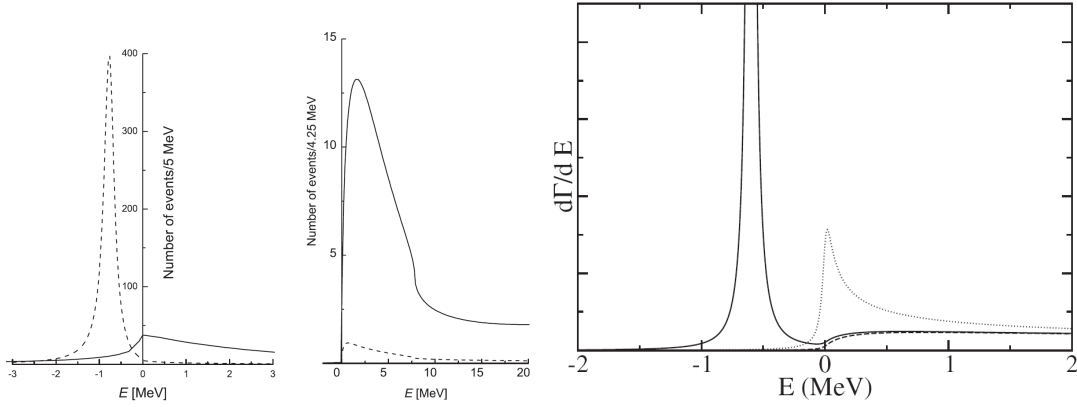


Figure 4.26: Dispersive effects on the $X(3872)$ from various authors: (left) Hanhardt et al. [67] and (right) Braaten et al. [?]. The left figure shows differential rates for the $J/\psi\pi^+\pi^-$ (first plot) and $D^0\bar{D}^{*0}$ (second plot) for large $J/\psi\pi^+\pi^-$ yield (solid curves) and $D^0\bar{D}^{*0}$ dominance (dashed curves). The right figure shows the line shapes near the $D^0\bar{D}^{*0}$ threshold for $X(3872)$ in the $D^0\bar{D}^{*0}$ channel. The line shapes are shown for three different model settings corresponding to a bound state (solid line), virtual state (dashed line), and smooth excitation (dotted line).

where the same photon candidate does not occur more than once in the final state. The corresponding tracks and photon candidates of the final state are kinematically fitted by constraining their momentum and energy sum to the initial $\bar{p}p$ system and the invariant lepton candidates mass to the J/ψ mass. Accepted candidates must have a confidence level of $CL > 0.1\%$ and the invariant mass of the $J/\psi\gamma$ subsystem should be within the range $[3.49; 3.53] \text{ GeV}/c^2$, whereas the invariant mass of the η candidates must be within the interval $[530; 565] \text{ MeV}/c^2$. A FWHM of $13 \text{ MeV}/c^2$ and $9 \text{ MeV}/c^2$ is observed for the η and χ_{c1} signal respectively (Figs. ??) after the kinematic fit.

For the final event selection the same kinematic fit is repeated with additionally constraining the invariant χ_{c1} , π^0 and η mass to the corresponding nominal mass values. Candidates having a confidence level less than 0.1% are rejected.

At this stage of the analysis 8.2% of the event are reconstructed, whereas for a fraction of 5.3% of the reconstructed events more than one $\chi_{c1}\pi^0\pi^0\eta$ combination is found per event. To ensure an unambiguous reconstruction of the total event, events with a candidate multiplicity higher than one are rejected.

The invariant $\chi_{c1}\pi^0\pi^0$ mass obtained after application of all selection criteria is shown in Fig. ?. The $\tilde{\eta}_{c1}$ signal has a FWHM of $30 \text{ MeV}/c^2$. The reconstruction efficiency is determined from the

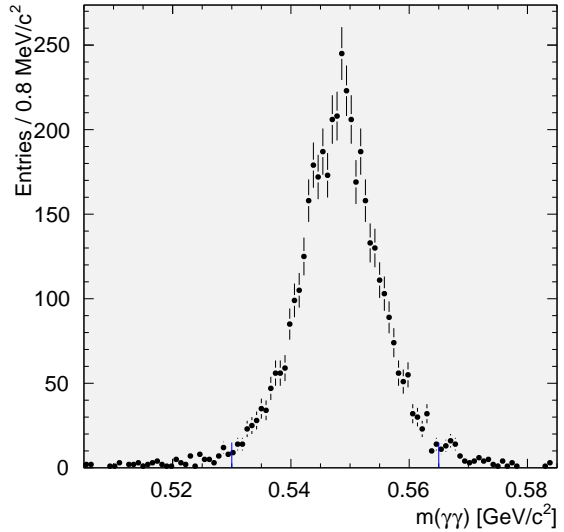


Figure 4.27: Invariant $\eta \rightarrow \gamma\gamma$ mass obtained after the kinematic fit with a momentum and energy constraint on the initial $\bar{p}p$ system as described in the text.

number of $\tilde{\eta}_{c1}$ signal entries in the mass range $4.24 - 4.33 \text{ GeV}/c^2$. The reconstruction efficiency is found to be 6.83% ($J/\psi \rightarrow e^+e^-$) and 5.06% ($J/\psi \rightarrow \mu^+\mu^-$).

The background suppression is estimated from the number of accepted background events after application of all selection criteria having a valid $\tilde{\eta}_{c1}$ candidate whose invariant mass is within the same

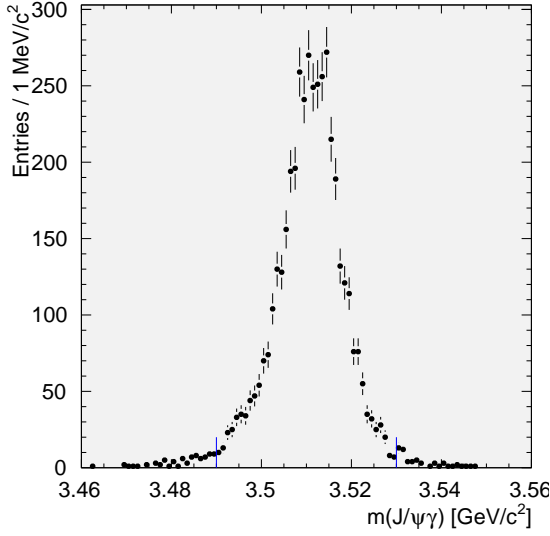


Figure 4.28: Invariant $\chi_{c1} \rightarrow J/\psi\gamma$ mass obtained after the kinematic fit with a momentum and energy constraint on the initial $\bar{p}p$ system as described in the text. The J/ψ is reconstructed from the e^+e^- decay mode.

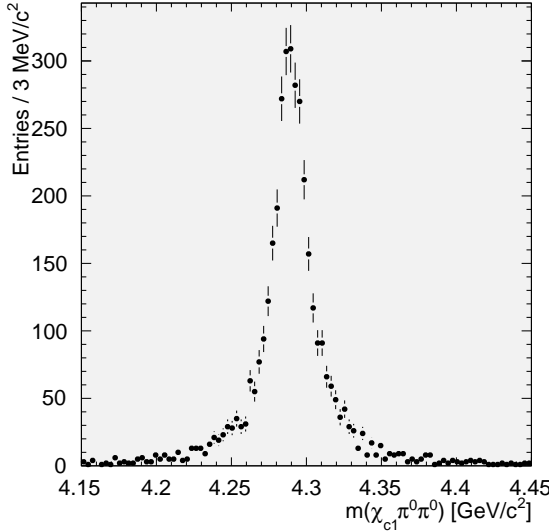


Figure 4.29: Invariant $\chi_{c1}\pi^0\pi^0$ mass obtained for the $J/\psi \rightarrow e^+e^-$ channel after application of all selection criteria.

interval used to determine the reconstruction efficiency for signal events. In Table 4.27 the suppression for the individual background channels is listed together with the expected signal to background ratio S/B , which is reported in terms of

$$\mathcal{R} = \frac{\sigma_S \mathcal{B}(\tilde{\eta}_{c1} \rightarrow \chi_{c1}\pi^0\pi^0)}{\sigma_B} \quad (4.15)$$

given by the unknown signal (background) cross section σ_S (σ_B) and the branching fraction for

the $\tilde{\eta}_{c1} \rightarrow \chi_{c1}\pi^0\pi^0$ decay. Depending on the background channel and reconstructed J/ψ decay mode S/B is varying between 110 – 10100 \mathcal{R} . For $\bar{p}p \rightarrow \chi_{c1}\pi^0\pi^0\pi^0\eta$ only a lower limit $> 5530 \mathcal{R}$ ($J/\psi \rightarrow e^+e^-$) is obtained. If the cross sections σ_B for the background processes are not enhanced by more than an order of magnitude over $\sigma_S \mathcal{B}(\tilde{\eta}_{c1} \rightarrow \chi_{c1}\pi^0\pi^0)$ very low contamination of the signal from these processes is expected.

Background reactions including no charm but light mesons in the final state have not been investigated yet. The studies of the background types performed for the charmonium states presented in this document proof that a clean reconstruction via the $J/\psi \rightarrow e^+e^-$ decay mode is possible. Therefore the reconstruction of the $\tilde{\eta}_{c1}$ state via this decay should yield also a sufficient background suppression. Since the results of the other studies showed also that the reconstruction via $J/\psi \rightarrow \mu^+\mu^-$ is presently not feasible the analysis is restricted to the $J/\psi \rightarrow e^+e^-$ decay mode only. Then the expected number of reconstructed events per day is given by

$$N = \sigma_S \mathcal{B}(\tilde{\eta}_{c1} \rightarrow \chi_{c1}\pi^0\pi^0) \times 9.62 \text{ nb}^{-1} \quad (4.16)$$

As afore said the cross section for $\bar{p}p \rightarrow \psi(2S)\eta$ is expected to be 33 pb. Assuming the same cross section for the production of the charmonium hybrid state this becomes $N = 0.32 \mathcal{B}(\tilde{\eta}_{c1} \rightarrow \chi_{c1}\pi^0\pi^0)$ events per day.

Study of $\bar{p}p \rightarrow \tilde{\eta}_{c1}\eta \rightarrow DD^*\eta$

Two possible background reactions including open charm decays leading to a similar event topology as signal events have been investigated. The first is $\bar{p}p \rightarrow D^0\bar{D}^{*0}\pi^0$, where the recoil η is absent and the D and D^* mesons decay via the same decay path as for signal events. Secondly the reaction $\bar{p}p \rightarrow D^0\bar{D}^{*0}\eta$ is investigated, where the recoil η is present but either the D^0 or the \bar{D}^{*0} meson (from $\bar{D}^{*0} \rightarrow \bar{D}^0\pi^0$ decay) is decaying into $K^-\pi^+\pi^0\pi^0$ and $K^+\pi^-\pi^0\pi^0$. This D^0 decay mode is listed in PDG as seen and it is assumed for this study that it's branching fraction is 5%, comparable in the order of magnitude to other D meson decay modes including a charged kaon. The product of branching fractions for the background and signal reactions are shown in Table 4.28. π^0 and η are selected in the standard way discussed before. Pions and kaons are selected from charged particles in the event by applying a likelihood based selection algorithm, where a likelihood value of $\mathcal{L} > 0.2$ is required to accept a candidate as a pion or kaon. All possible $K^+\pi^-\pi^0$ combinations having an invariant mass in the range

Reaction	$\eta_{e^+e^-}$	$\eta_{\mu^+\mu^-}$	$S/N_{e^+e^-}$	$S/N_{\mu^+\mu^-}$
$\bar{p}p \rightarrow$	$[10^3]$	$[10^3]$	$[10^3]$	$[10^3]$
$\chi_{c0}\pi^0\pi^0\eta$	5.33	7.27	10.1 \mathcal{R}	10.2 \mathcal{R}
$\chi_{c1}\pi^0\eta\eta$	26.6	26.8	4.57 \mathcal{R}	3.41 \mathcal{R}
$\chi_{c1}\pi^0\pi^0\pi^0\eta$	> 80	79.9	> 5.53 \mathcal{R}	4.09 \mathcal{R}
$J/\psi\pi^0\pi^0\pi^0\eta$	9.98	6.26	0.25 \mathcal{R}	0.11 \mathcal{R}

Table 4.27: Background suppression η and the ψ_g signal to background ratio S/N for the individual background reactions in terms of \mathcal{R} as defined in Eq. ??.

Reaction	\mathcal{B}
$\bar{p}p \rightarrow$	\mathcal{B}
$\tilde{\eta}_{c1}\eta$	$0.47\% \times \mathcal{B}(\psi_g \rightarrow D^0\bar{D}^{*0})$
$D^0\bar{D}^{*0}\eta$	$3.2\% \times \mathcal{B}(D^0 \rightarrow K^-\pi^+\pi^0\pi^0) = 0.16\%^*$
$D^0\bar{D}^{*0}\pi^0$	1.17%

Table 4.28: The product of branching fractions for the subsequent particle decays for signal and background reactions. For the branching fraction marked with an asterisk (*) $\mathcal{B}(D^0 \rightarrow K^-\pi^+\pi^0\pi^0) = 5\%$ is assumed.

[1.7;2.2] GeV/c^2 in an event are formed and fitted by applying a π^0 mass constraint and requiring a common vertex for the tracks of the two charged candidates. A confidence level $CL > 0.1\%$ is required to accept the candidates as $D^0 \rightarrow K^+\pi^-\pi^0$ candidates. These are then used to form $D^0\pi^0$ candidates having an invariant mass in the interval [1.95;2.05] GeV/c^2 , which are kinematically fitted applying a π^0 mass constraint. If the fit yields a confidence level $CL > 0.1\%$ the $D^{*0} \rightarrow D^0\pi^0$ candidate is accepted for further selection. Afterwards $D^0\bar{D}^{*0}\eta$ combinations are formed and fitted by constraining the final state particles' four-vectors to the initial $\bar{p}p$ system momentum and energy. Furthermore the invariant $\gamma\gamma$ mass of the π^0 candidates in the decay tree is constrained to the π^0 mass. A confidence level of $CL > 0.1\%$ is required.

A confidence level of $CL > 0.1\%$ is required. The resulting invariant $D^0 \rightarrow K^-\pi^+\pi^0$ and $D^{*0} \rightarrow \bar{D}^0\pi^0$ mass is shown in Figs. 4.30 and 4.31. For final event selection the fit is repeated but with additional mass constraints on the D^0 , D^{*0} and η candidates. Candidates leading to a confidence level lower than 0.1% are discarded.

A $\chi_{c1}\pi^0\pi^0\eta$ candidate multiplicity higher than one is observed in 9.5% of the reconstructed events. In order to avoid unambiguities in later analysis events with a higher multiplicity than one are rejected. To estimate the reconstruction ef-

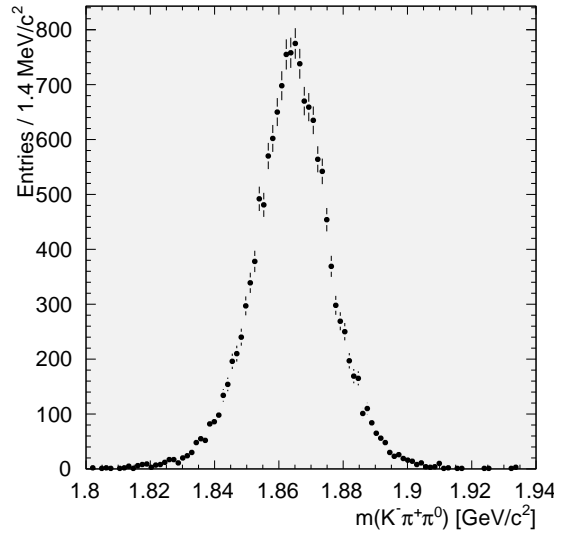


Figure 4.30: Invariant $K^-\pi^+\pi^0$ mass obtained after the kinematic fit of the $D^0\bar{D}^{*0}\eta$ candidates explained in the text.

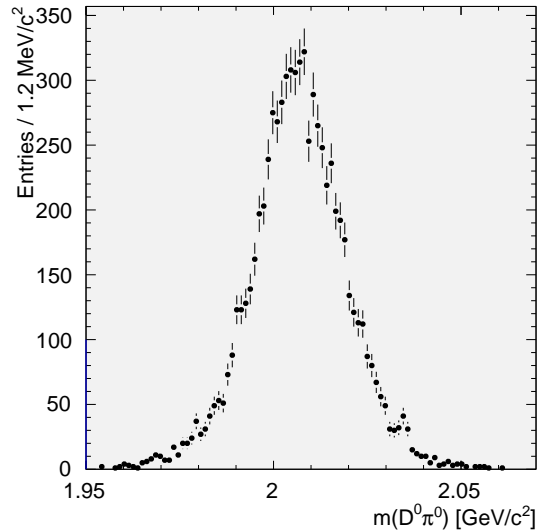


Figure 4.31: Invariant $D^0\pi^0$ mass obtained after the kinematic $D^0\bar{D}^{*0}\eta$ fit as explained in the text.

efficiency only the correct combinations are considered. The event yield is determined as the number of $D^0\bar{D}^{*0}$ signal entries falling in the mass window $[4.24; 4.33] \text{ GeV}/c^2$.

The obtained $D^0\bar{D}^{*0}$ invariant mass distribution is shown Fig. 4.32. A signal width (FWHM) of $22.5 \text{ MeV}/c^2$ is observed. The reconstruction efficiency is 5.17%.

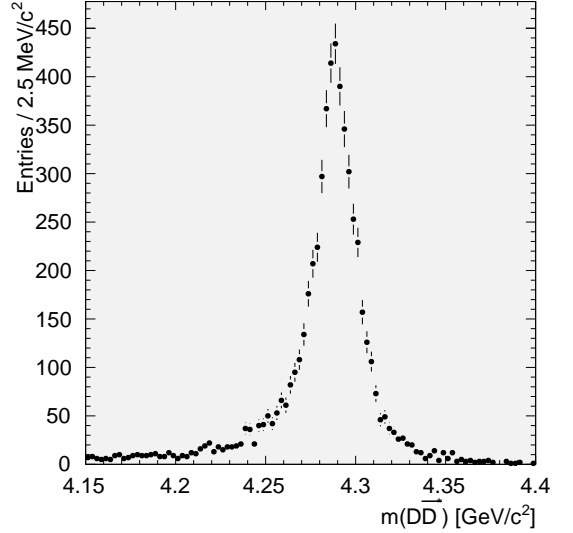


Figure 4.32: Invariant $D^0\bar{D}^{*0}$ mass obtained after the kinematic fit with a momentum and energy constraint on the initial $\bar{p}p$ system as described in the text.

The background reactions $\bar{p}p \rightarrow D^0\bar{D}^{*0}\eta$ (with $D^0 \rightarrow K^+\pi^-\pi^0\pi^0$) and $\bar{p}p \rightarrow D^0\bar{D}^{*0}\pi^0$ could be suppressed by a factor $> 1.6 \cdot 10^5$. Assuming equal cross sections for these processes and signal events and a branching fraction for $D^0 \rightarrow K^+\pi^-\pi^0\pi^0$ (which is listed by the PDG as seen) in the order of 5% the expected signal to noise ratio can be expressed by

$$\begin{aligned} \frac{S}{N} &> \frac{\mathcal{B}(\tilde{\eta}_{c1} \rightarrow D^0\bar{D}^{*0}) \times 0.47\% \times 5.17\%}{(0.16\% + 1.17\%) \times 5 \cdot 10^{-6}} \quad (4.17) \\ &= \mathcal{B}(\tilde{\eta}_{c1} \rightarrow D^0\bar{D}^{*0}) \times 2.9 \cdot 10^3, \quad (4.18) \end{aligned}$$

where the term $\mathcal{B}(\tilde{\eta}_{c1} \rightarrow D^0\bar{D}^{*0})$ is the unknown branching fraction for the decay $\tilde{\eta}_{c1} \rightarrow D^0\bar{D}^{*0}$.

With the assumed cross section of 30 pb and design luminosity $\mathcal{L} = 2 \cdot 10^{32} \text{ cm}^{-2} \text{ s}^{-1}$ the expected number of reconstructed events per day is given by

$$N = \mathcal{B}(\tilde{\eta}_{c1} \rightarrow D^0\bar{D}^{*0}) \times 0.14. \quad (4.19)$$

If one defines the significance as $s = S/\sqrt{S+B}$ one yields with the assumptions made above the

following formula

$$s = \frac{\sigma_S \epsilon \mathcal{B}_S \sqrt{\mathcal{L}t}}{\sqrt{(\sigma_S \epsilon \mathcal{B}_S + \sigma_B \eta \mathcal{B}_B) \sqrt{\mathcal{L}t}}}, \quad (4.20)$$

where σ_S and σ_B are the signal and background cross sections, \mathcal{B}_S and \mathcal{B}_B label the product of branching ratios for signal and background reactions and the time of data taking is given by t . The significance is shown in dependence of t in Fig. 4.33, where the above assumptions on the cross sections ($\sigma_S = \sigma_B$) and the branching fraction $\mathcal{B}(D^0 \rightarrow K^- \pi^+ \pi^0 \pi^0) = 5\%$ have been made. The branching fraction $\mathcal{B}(\tilde{\eta}_{c1} \rightarrow D^0 \bar{D}^{*0})$ has been set to 1, 0.30 and 0.13. Assuming that PANDA will run half of its lifetime (corresponding to ≈ 850 days) at a beam momentum of $15 \text{ GeV}/c$ a significance > 5 can be reached only if the branching fraction $\mathcal{B}(\tilde{\eta}_{c1} \rightarrow D^0 \bar{D}^{*0})$ is above 30%. This corresponds to a total of ≈ 30 reconstructed events. To be sensitive to lower branching fractions the D^0 , D^{*0} and the recoil η mesons have to be reconstructed from other decay modes and decays into $D^+ \bar{D}^{*-}$ have to be taken into account also.

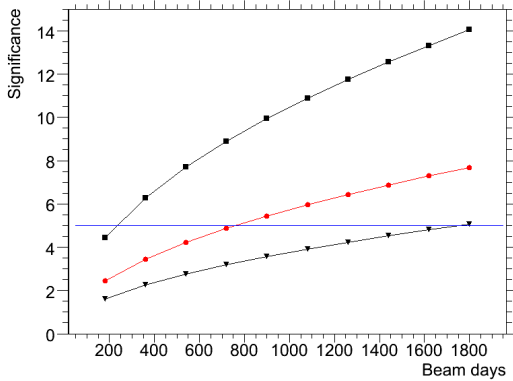


Figure 4.33: Expected significance for the reaction $\bar{p}p \rightarrow \tilde{\eta}_{c1}\eta$ in dependence of the beam time. The significance is shown for three values of the branching fraction $\mathcal{B}(\tilde{\eta}_{c1} \rightarrow D^0 \bar{D}^{*0})$: 1 (black squares), 0.3 (red circles) and 0.13 (black triangles). The blue line marks a significance level of 5.

In conclusion this study proves that the reconstruction of an object of a mass of $\approx 4 \text{ GeV}/c^2$ decaying to open charm produced in $\bar{p}p$ annihilation at $15 \text{ GeV}/c$ with a recoiling η meson leading to a final state with high photon multiplicity is feasible. The low branching fractions of D mesons make the inclusion of other decay modes necessary to be sensitive for lower $\tilde{\eta}_{c1}$ branching fractions, but these decays

should be detectable with similar efficiency as the decay mode presented in this study.

Study of $Y(3940) \rightarrow J/\psi\omega$ system in $\bar{p}p$ formation

In the following an exclusive study of the formation of $Y(3940)$ in $\bar{p}p$ annihilation is presented. The J/ψ is reconstructed from its decays to e^+e^- and $\mu^+\mu^-$, whereas the ω is reconstructed via the $\pi^+\pi^-\pi^0$ decay mode.

As possible sources of background the reactions

- $\bar{p}p \rightarrow \psi(2S)\pi^0$ ($\psi(2S) \rightarrow J/\psi\pi^+\pi^-$)
- $\bar{p}p \rightarrow J/\psi\rho^0\pi^0$ ($\rho^0 \rightarrow \pi^+\pi^-$)
- $\bar{p}p \rightarrow J/\psi\rho^+\pi^-$ ($\rho^+ \rightarrow \pi^0\pi^+$)
- $\bar{p}p \rightarrow \pi^+\pi^-\pi^0\rho^0$ ($\rho^0 \rightarrow \pi^+\pi^-$)
- $\bar{p}p \rightarrow \pi^+\pi^-\pi^-\rho^+$ ($\rho^+ \rightarrow \pi^0\pi^+$)
- $\bar{p}p \rightarrow \pi^+\pi^-\omega$ ($\omega \rightarrow \pi^+\pi^-\pi^0$)

have been considered.

None of the cross sections for these reactions have been measured in the energy range of the $Y(3940)$. The cross sections for the reactions $\bar{p}p \rightarrow \pi^+\pi^-\pi^0\rho^0$ and $\bar{p}p \rightarrow \pi^+\pi^-\omega$ have been measured in the \sqrt{s} energy range between 2.14 and 3.55 GeV [?]. They are shown in Fig. 4.34 in dependence of \sqrt{s} . The data can be fitted by an exponential function $\sim \exp(-\sqrt{s})$ and the cross sections at $\sqrt{s} = 3.94 \text{ GeV}/c^2$ are estimated by extrapolating this function. The obtained values are presented in Table 4.29. In addition the cross sections are extracted from the DPM event generator applying the technique described above. The results are shown in Fig. 4.34 and Table 4.29 together with data. The extracted cross sections from the generator underestimate the data over the whole energy range. At $\sqrt{s} = 3.94 \text{ GeV}$ the extracted values are ≈ 3 times lower than the values derived from extrapolating the fit functions. The reason for the observed deviation is not known and needs further investigation. However, in this study the values derived from the extrapolation are applied.

For the channels including charmonium states one has to distinguish between the formation process $\bar{p}p \rightarrow Y(3940)$ followed by the subsequent $Y(3940)$ decay on the one hand and direct production of a charmonium state with an associated recoil meson on the other hand. While the observed decay of the $Y(3940)$ into $J/\psi\omega$ is considered to be isospin conserving, a decay into $\psi(2S)\pi^0$ is isospin violating and thus expected to be suppressed. Here the

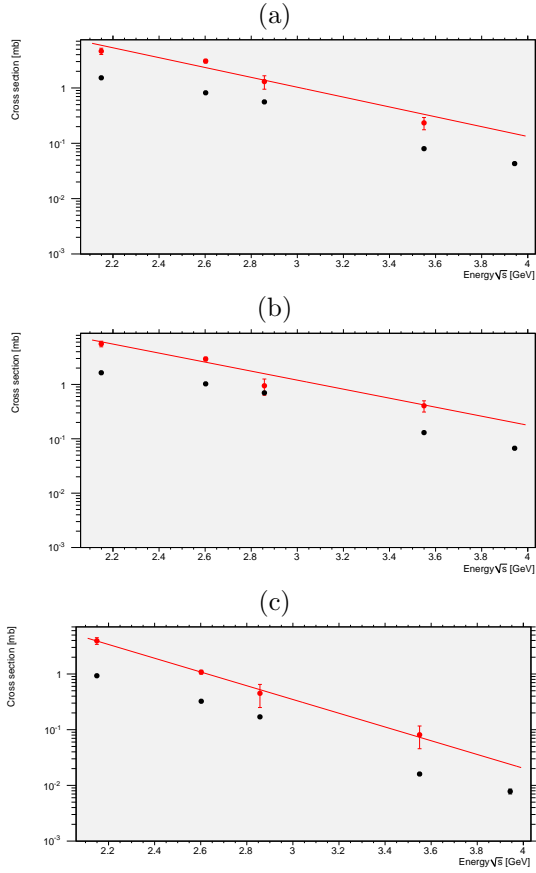


Figure 4.34: Cross sections for the reactions a) $\bar{p}p \rightarrow \pi^+\pi^-\pi^0\rho^0$, b) $\bar{p}p \rightarrow \pi^+\pi^-\pi^-\rho^+$ and c) $\bar{p}p \rightarrow \pi^+\pi^-\omega$ in dependence of \sqrt{s} . The measured cross sections (red dots) are overlaid by the result of a fit using a function $\sim \exp(-\sqrt{s})$, which is applied to extrapolate the cross section towards $\sqrt{s} = 3.94$ GeV. Also shown are the cross sections derived from the DPM event generator (black).

Reaction	Cross section at $\sqrt{s} = 3.94$ GeV	
$\bar{p}p \rightarrow$	Extr. [μb]	DPM [μb]
$\pi^+\pi^-\pi^0\rho^0$	149	43.3 ± 1.9
$\pi^+\pi^-\pi^-\rho^+$	198	67.7 ± 2.3
$\pi^+\pi^-\omega$	23.9	7.87 ± 0.8

Table 4.29: Cross sections for the background reactions under study. Listed are the values obtained from the extrapolation of measurements in the \sqrt{s} range 2.15 – 3.55 GeV and the corresponding values extracted from the DPM generator.

non-resonant reaction $\bar{p}p \rightarrow \psi(2S)\pi^0$ is considered as a possible source of background. Ref. [?] quotes the cross section for this process to be less than 55 pb. In this study a value of 55 pb is assumed for this process as a conservative estimate. Background

could also arise from hypothetical isospin conserving $Y(3940)$ decays into $J/\psi\rho\pi$, with a possible intermediate resonance decaying into $\rho\pi$. Since the time-scales of the two processes are distinct, less interference between the final states is expected and the background is considered to be incoherent to signal. For the branching fractions of the $Y(3940)$ into $J/\psi\rho^0\pi^0$ and $J/\psi\rho^+\pi^-$ a ratio of 1 : 2 is assumed, a decay pattern which is expected for an isoscalar state.

Table 4.30 summarizes the assumed cross sections and the branching fractions of the signal and background reactions under study.

Reaction	σ	\mathcal{B}
$\bar{p}p \rightarrow$		
$Y \rightarrow J/\psi\omega$	σ_S	$10.4\% \times \mathcal{B}(Y \rightarrow J/\psi\omega)$
$\pi^+\pi^-\pi^0\rho^0$	$149 \mu\text{b}^*$	100 %
$\pi^+\pi^-\pi^-\rho^+$	$198 \mu\text{b}^*$	100 %
$\pi^+\pi^-\omega$	$23.9 \mu\text{b}^*$	100 %
$\psi(2S)\pi^0$	55 pb	3.73 %
$Y \rightarrow J/\psi\rho\pi$	σ	$11.7\% \times \mathcal{B}(Y \rightarrow J/\psi\rho\pi)$

Table 4.30: Cross sections for signal and background reactions. The table lists also the branching ratios for the subsequent particle decays. The cross sections marked by an asterisk (*) take already the branching ratios of subsequent particle decays into account and the corresponding branching ratios are listed therefore as 100 %. The reaction $Y \rightarrow J/\psi\rho\pi$, which has its own relevance, is treated as background here.

The number of analysed signal and background events is summarized in Table 4.31. Signal events have been generated with phase space distribution for the reaction $Y(3940) \rightarrow J/\psi\omega$. For the $\omega \rightarrow \pi^+\pi^-\pi^0$ a proper angular distribution is considered (OMEGA_DALITZ decay model from EvtGen event generator)[?]. The background reactions $\bar{p}p \rightarrow \pi^+\pi^-\omega$ and $\bar{p}p \rightarrow \pi^+\pi^-\pi\rho$ require a large amount of data. To simulate the demanded number of events within a sufficient time a J/ψ mass filter technique is applied and the number of events analyzed for these reactions has to be corrected by the filter efficiency, which is also listed in Table 4.31.

The $J/\psi\omega$ system is reconstructed by combining the J/ψ candidates found in an event with $\omega \rightarrow \pi^+\pi^-\pi^0$ candidates. To form the latter, two candidates of opposite charge, both identified as pions having a likelihood value $\mathcal{L} > 0.2$ are combined together with $\pi^0 \rightarrow \gamma\gamma$ candidates, composed from two photon candidates having an invariant mass in the range [115; 150] MeV/ c^2 .

Reaction $\bar{p}p \rightarrow$	Events	Filter eff.
$J/\psi\omega$	$4 \cdot 10^4$	100%
$\pi^+\pi^-\pi^0\rho^0$	$8.49 \cdot 10^6$	0.77%
$\pi^+\pi^-\pi^-\rho^+$	$8.49 \cdot 10^6$	0.81%
$\pi^+\pi^-\omega$	$9.9 \cdot 10^6$	9.15%
$J/\psi\pi^-\rho^+$	$5 \cdot 10^5$	100%
$J/\psi\pi^0\rho^0$	$5 \cdot 10^5$	100%
$\psi(2S)\pi^0$	$1.6 \cdot 10^5$	100%

Table 4.31: Summary of analysed events and the J/ψ mass filter efficiency. For channels including charmonium states no filter is applied and the J/ψ is decaying to e^+e^- and $\mu^+\mu^-$ with equal branching fraction of 50%.

All combinations of an event are fitted by constraining the sum of the four-momenta of the final state particles to the initial beam energy and momentum and constraining the origin of the charged final state particles to a common vertex. Combinations where the fit yields a confidence level less than 0.1% are not considered for further analysis. The invariant mass of the J/ψ and ω candidates obtained after the fit are shown in Figs. 4.35 and 4.36. The J/ψ and ω signal has a FWHM of $9 \text{ MeV}/c^2$ and $16.5 \text{ MeV}/c^2$, respectively. An ω mass window of $[750; 810] \text{ MeV}/c^2$ is applied to cleanly select $J/\psi\omega$ candidates. For the final event selection the accepted candidates are fitted under the $J/\psi\omega$ hypothesis, where on top of the $\bar{p}p$ four-momentum constraint mass constraints are applied to the J/ψ and π^0 candidates. Only candidates where the fit yields a confidence level $\mathcal{L} > 0.1\%$ are considered further.

To suppress background arising from $\bar{p}p \rightarrow \psi(2S)\pi^0$ reactions events are rejected, where the invariant $J/\psi\pi^+\pi^-$ mass of the $J/\psi\omega$ candidates falls into to the interval $[3.6725; 3.7] \text{ GeV}/c^2$ around the $\psi(2S)$ mass. The invariant $J/\psi\pi^+\pi^-$ mass is shown in Fig. 4.37 for signal and background events.

At this stage of the analysis in 0.16% of the analysed signal events more than one $J/\psi\omega$ candidate is found. The ambiguity is solved by selecting the combination in the event which is leading to the highest confidence level for the fit assuming the $J/\psi\omega$ hypothesis. In 65% of the cases the selected combination is corresponding to the generated combination and thus is the correct one. In total a negligible fraction of $6 \cdot 10^{-4}$ out of the signal events is reconstructed in the wrong combination.

The reconstruction efficiency is estimated separately for events reconstructed via the two different J/ψ decay modes. Only the correct combinations are considered. The efficiency is found to be 14.7%

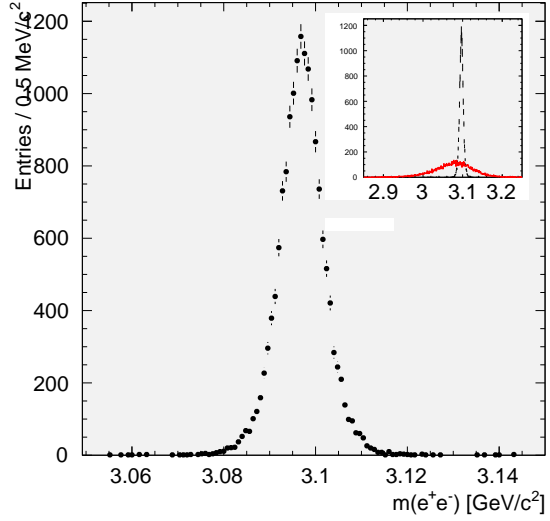


Figure 4.35: Invariant $J/\psi \rightarrow e^+e^-$ mass obtained after the kinematic fit of $J/\psi\omega$ candidates applying the constraints on the initial $\bar{p}p$ four-momentum. The inset shows the same signal (black) compared to the distribution obtained before the fit (red) in an extended mass region.

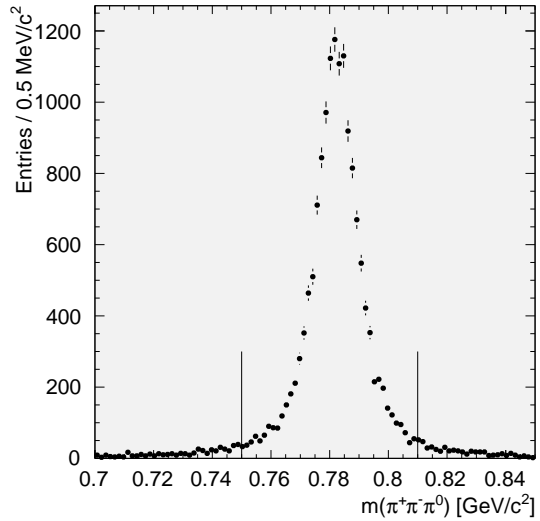


Figure 4.36: Invariant $\pi^+\pi^-\pi^0$ mass obtained after the kinematic fit of $J/\psi\omega$ (with $J/\psi \rightarrow e^+e^-$) candidates with constraints on the initial $\bar{p}p$ four-momentum. The ω mass window applied for selection is indicated by the vertical lines.

($J/\psi \rightarrow e^+e^-$) and 13.2% ($J/\psi \rightarrow \mu^+\mu^-$). The invariant $J/\psi\omega$ mass distribution obtained from a kinematic fit similar to the final fit applying the J/ψ and π^0 mass constraints, but removing the constraint on the beam momentum and energy is shown in Fig. 4.38. The signal width (FWHM) is found to be $14.4 \text{ MeV}/c^2$.

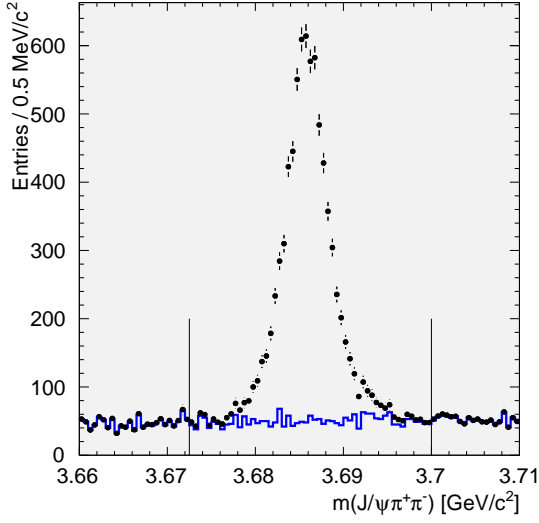


Figure 4.37: Invariant $J/\psi\pi^+\pi^-$ ($J/\psi \rightarrow e^+e^-$) mass of the accepted J/ψ candidates for signal and $\psi(2S)\pi^0$ background events. The background distribution is shown on top of the signal distribution (shaded) and is normalized to the signal cross section and branching fraction according to Table 4.30. The vertical lines indicate the mass region used for the $\psi(2S)$ veto.

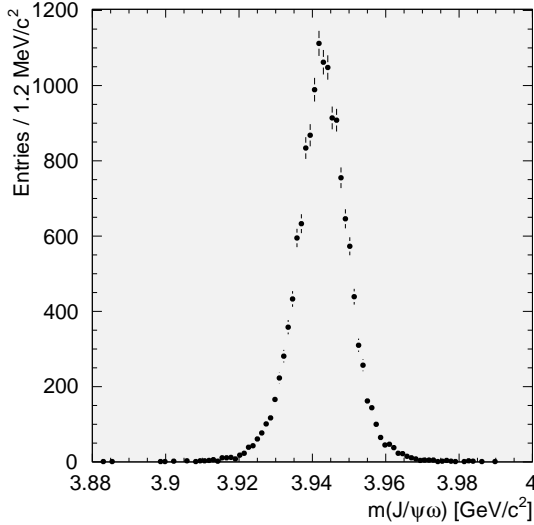


Figure 4.38: Invariant $J/\psi\omega$ mass distribution obtained after the kinematic fit applying the constraints described in the text.

In order to estimate the pollution of the signal from the considered background reactions, background events are analysed likewise as signal events and the number of reconstructed $J/\psi\omega$ candidates is determined. The suppression η for a certain background reaction is defined as the fraction of generated and accepted events and is given in Table 4.32 for the individual background channels. The expected signal

to noise ratio is then given by

$$\frac{S}{N} = \frac{\sigma_s}{\sigma_B} \frac{\mathcal{B}_S}{\mathcal{B}_B} \frac{\epsilon}{\eta^{-1}}, \quad (4.21)$$

where σ_s (σ_B) is the cross section and \mathcal{B}_S (\mathcal{B}_B) is the product of branching fractions for signal (background) reactions, and ϵ is the signal reconstruction efficiency. Since the cross section σ_S and the branching fraction $\mathcal{B}(Y \rightarrow J/\psi\omega)$ for the signal process $\bar{p}p \rightarrow Y \rightarrow J/\psi\omega$ is not known the signal to noise ratio is reported with respect to the product $\tilde{\sigma} = \sigma_S \mathcal{B}(Y \rightarrow J/\psi\omega)$. Table 4.32 summarizes the expected ratio S/B together with the suppression for the various background reactions.

A very good background suppression better than $1 \cdot 10^9$ and $1 \cdot 10^8$ is achieved for the channels $\bar{p}p \rightarrow \pi^+\pi^-\pi\rho$ and $\bar{p}p \rightarrow \pi^+\pi^-\omega$, respectively if the J/ψ is reconstructed from its e^+e^- decay mode. Here the expected signal to noise ratio is better than $34 - 40\tilde{\sigma}/\text{nb}$, depending on the background channel. If the $J/\psi \rightarrow \mu^+\mu^-$ decay mode is considered a background suppression in the order of 10^5 ($\bar{p}p \rightarrow \pi^+\pi^-\omega$) and 10^7 ($\bar{p}p \rightarrow \pi^+\pi^-\pi\rho$) is obtained, yielding a S/B of $0.008\tilde{\sigma}/\text{nb}$ and $0.74\tilde{\sigma}/\text{nb}$ respectively. The first ratio is insufficient and the separation of muons and pions has to be clearly improved before the $J/\psi \rightarrow \mu^+\mu^-$ channel becomes measurable.

For the $\psi(2S)\pi^0$ background a S/B of $24.8\tilde{\sigma}/\text{pb}$ ($J/\psi \rightarrow e^+e^-$) and $25.5\tilde{\sigma}/\text{pb}$ ($J/\psi \rightarrow \mu^+\mu^-$) is obtained. Thus the expected signal pollution is very low. For the two $J/\psi\rho\pi$ channels a suppression by a factor of 20–28 is observed and the expected S/B for the sum of the two $J/\psi\rho\pi$ charge combinations is $5.58\mathcal{B}$ ($J/\psi \rightarrow e^+e^-$) and $5.73\mathcal{B}$ ($J/\psi \rightarrow \mu^+\mu^-$), where $\mathcal{B} = \mathcal{B}(Y \rightarrow J/\psi\omega)/\mathcal{B}(Y \rightarrow J/\psi\rho\pi)$.

Both reactions can be disentangled performing a partial wave analysis, which is out of the scope of this document. However, it should be noted that the $\omega \rightarrow \pi^+\pi^-\pi^0$ decay has a distinct angular distribution from the decay $\rho\pi$ with $\rho \rightarrow \pi\pi$. The ω helicity angle θ_h is defined as the angle between the π^+ and π^0 momentum computed in the $\pi^+\pi^-$ centre of mass system. For signal events the $\cos\theta_h$ distribution is $\sim \sin^2\theta_h$. The reconstructed θ_h distribution for signal and background events is shown in Fig. 4.39 together with the reconstruction efficiency in dependence of $\cos\theta_h$. The efficiency distribution shows no prominent structures and is homogeneous with respect to statistical uncertainties. A linear fit to the efficiency distribution yields a gradient consistent with zero within statistical errors. Thus the angle θ_h can be cleanly reconstructed without significant distortion due to an inhomogeneity of

Reaction	$\eta_{e^+e^-}$	$\eta_{\mu^+\mu^-}$	$S/N_{e^+e^-}$	$S/N_{\mu^+\mu^-}$
$\pi^+\pi^-\pi^0\rho^0$	$> 1.1 \cdot 10^9$	$2.63 \cdot 10^7$	$> 56.5 \tilde{\sigma}/\text{nb}$	$1.19 \tilde{\sigma}/\text{nb}$
$\pi^+\pi^-\pi^-\rho^+$	$> 1.05 \cdot 10^9$	$1.84 \cdot 10^7$	$> 40.6 \tilde{\sigma}/\text{nb}$	$0.63 \tilde{\sigma}/\text{nb}$
$\pi^+\pi^-\omega$	$> 1.08 \cdot 10^8$	$2.87 \cdot 10^5$	$> 34.6 \tilde{\sigma}/\text{nb}$	$0.008 \tilde{\sigma}/\text{nb}$
$\psi(2S)\pi^0$	$3.33 \cdot 10^3$	$3.80 \cdot 10^3$	$24.8 \tilde{\sigma}/\text{pb}$	$25 \tilde{\sigma}/\text{pb}$
$J/\psi\pi^-\rho^+$	25	28.3	$4.90 \mathcal{BR}$	$4.90 \mathcal{BR}$
$J/\psi\pi^0\rho^0$	22.1	25.2	$7.65 \mathcal{BR}$	$8.72 \mathcal{BR}$

Table 4.32: Observed background suppression η and the expected signal to noise ratio S/B for the investigated background reactions listed separately for J/ψ reconstructed from the e^+e^- and $\mu^+\mu^-$ decay mode. The ratio S/B is reported for $Y \rightarrow J/\psi\rho\pi$ with respect to the unknown ratio $\mathcal{B} = \mathcal{B}(Y \rightarrow J/\psi\omega)/\mathcal{B}(Y \rightarrow J/\psi\rho\pi)$ of the branching fractions for the reactions $\bar{p}p \rightarrow Y \rightarrow J/\psi\omega$ and $\bar{p}p \rightarrow Y \rightarrow J/\psi\rho\pi$.

the efficiency. The $\cos\theta_h$ distribution reconstructed from signal events shows the expected $\sim \sin^2\theta_h$ dependence, which is distinct from the distribution obtained for background events. The result for background events is derived assuming phase space distribution for the $Y \rightarrow J/\psi\rho\pi$ decay. Depending on the production process of the ρ meson its helicity and thus the angular distribution for $\rho \rightarrow \pi\pi$ can vary. The two scenarios where the ρ decay angle is $\sim \sin^2$ and $\sim \cos^2$ have been tested by weighting the generated events accordingly. The observed θ_h distributions are independent of the assumed $\rho \rightarrow \pi\pi$ angular distribution. In conclusion it is expected that the $J/\psi\omega$ and $J/\psi\rho\pi$ decay modes could be disentangled performing a partial wave analysis of the $J/\psi\pi^+\pi^+\pi^0$ final state. Since the reconstruction via the channel $J/\psi \rightarrow \mu^+\mu^-$ yields not a sufficient background suppression for $\bar{p}p \rightarrow \pi^+\pi^-\omega$, the analysis is restricted to the $J/\psi \rightarrow e^+e^-$ decay mode only. The number of reconstructed events per day running the accelerator at the $Y(3940)$ peak position and design luminosity of $\mathcal{L} = 2 \cdot 10^{32} \text{ cm}^{-2}\text{s}^{-1}$ is given by

$$N = \epsilon_S \tilde{\sigma} \int \mathcal{L} dt = 132 \tilde{\sigma} \text{ nb}^{-1}. \quad (4.22)$$

Study of $Y(4320) \rightarrow \psi(2S)\pi^+\pi^-$ system in formation

In this section the decay $\bar{p}p \rightarrow \psi(2S)\pi^+\pi^-$, $\psi(2S) \rightarrow J/\psi\pi^+\pi^-$, $J/\psi \rightarrow e^+e^-$ at a beam momentum of $p_{\bar{p}} = 8.9578 \text{ GeV}/c$ (corresponding to the $Y(4320)$ resonance) is examined.

The $J/\psi \rightarrow e^+e^-$ candidates are reconstructed as described above. Both daughter candidates from a J/ψ decay must be identified as electrons with a likelihood $\mathcal{L} > 85\%$. The decay $J/\psi \rightarrow \mu^+\mu^-$ is currently not examined. The likelihood value for the particle candidates identified as pions must be

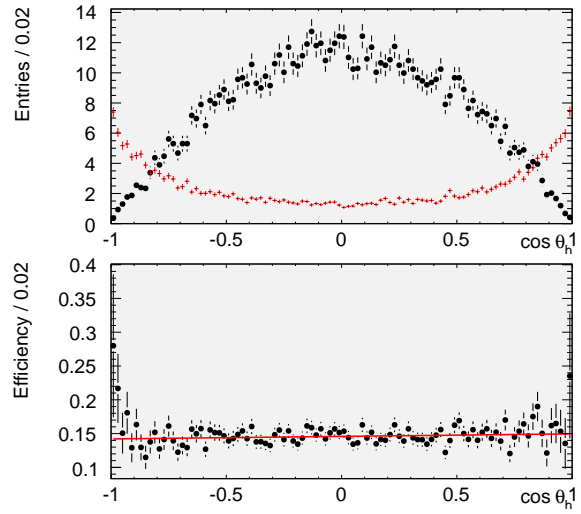


Figure 4.39: Distribution of the helicity angle θ_h (top) for signal (black) and $\bar{p}p \rightarrow J/\psi\rho\pi$ background (red) events. The distributions are normalized to the branching fraction $\mathcal{B}(Y \rightarrow J/\psi\omega)$ and $\mathcal{B}(Y \rightarrow J/\psi\rho\pi)$, respectively. Also shown is the reconstruction efficiency in dependence of θ_h (bottom). The red line is the result of a fit using a linear function.

$\mathcal{L} > 0.2$.

All combinations found in an event are kinematically fitted by constraining the sum of the four-vector of the final state particles to the initial beam energy and momentum and constraining the origin of the charged final state particles to originate from a common vertex. Also a mass constraint is applied on the J/ψ and $\psi(2S)$ candidates (mass and beam constraint - MBC). The fit is repeated with mass constraints only (M) and with beam/energy constraints only (only beam constraint - BC).

For accepted candidates the $\psi(2S)$ (BC) is required to be within the interval $[3.67 : 3.71] \text{ GeV}/c^2$ and the J/ψ mass (BC) to be within $[3.07 : 3.12] \text{ GeV}/c^2$. The confidence level of the fit (MBC) must be larger

than 0.1%. If more than one candidate in an event passes these selection criteria, the candidate with the highest confidence level is chosen and the others are rejected. Reconstructed $\psi(2S)\pi\pi$ candidates from the signal mode which are accepted by the criteria summarized above are checked if they are the correct combination.

The background channels are reconstructed in the same way and pass the same selection criteria as the signal modes, without an check for the right combination.

The reconstruction efficiency and the signal to noise ratio are examined separately for decays of $J/\psi \rightarrow e^+e^-$ and $\mu^+\mu^-$.

The $\psi(2S)\pi\pi$ signal region is defined as the interval from $[4.29 : 4.35]$ GeV/c^2 . The reconstruction efficiency is 14.9% ($J/\psi \rightarrow e^+e^-$) and 12.2% ($J/\psi \rightarrow \mu^+\mu^-$). The reconstructed signal has a mean of $4320 \text{ MeV}/c^2$ and a width (FWHM) of $13 \text{ MeV}/c^2$.

The cross section for the background mode $\bar{p}p \rightarrow 3\pi^+3\pi^-$ is $140 \mu\text{b}$ (measured at a beam momentum of $8.8 \text{ GeV}/c$). Suppression and signal to noise ratio are examined separately for $J/\psi \rightarrow e^+e^-$ and $J/\psi \rightarrow \mu^+\mu^-$. The suppression for this mode is $\eta_{e^+e^-} = 37 \cdot 10^6$ and $\eta_{\mu^+\mu^-} = 25 \cdot 10^6$. The signal to noise ratios are thus $S/N_{ee} = 700\tilde{\sigma}/\mu\text{b}$ and $S/N_{\mu^+\mu^-} = 400\tilde{\sigma}/\mu\text{b}$, where $\tilde{\sigma} = \sigma_S(\bar{p}p \rightarrow Y(4320))\mathcal{B}(Y(4320) \rightarrow \psi(2S)\pi^+\pi^-)$ is given in terms of the unknown signal cross section and branching fraction.

Reaction	Beam mom.	events	Filter eff.
$\bar{p}p \rightarrow$	$[\text{GeV}/c]$		$[\%]$
$\psi(2S)\pi^+\pi^-$	8.9578	20000	100
$3\pi^+3\pi^-$	8.9578	10^6	0.67

Table 4.33: Signal and background modes for the $\psi(2S)\pi^+\pi^-$ analysis. For the generator level filter, see Sec. 3.5.1.

Study of the formation process $\bar{p}p \rightarrow f_2(2000 - 2500) \rightarrow \phi\phi$ The primary goal of this study is to proof the feasibility of the reconstruction of exotic states decaying into the favoured decay channel $\phi\phi$ as a feasibility check for the long standing quest about the $\xi(2230)$. Since no explicit assumptions about the exotic particles properties like mass or angular momentum have been made the simulation considered here comprises non resonant reactions of the type $\bar{p}p \rightarrow \phi\phi$ without an intermediate resonance as a minimum bias approach. The detection of a possible resonant structure requires an energy scan around the region of interest in order to

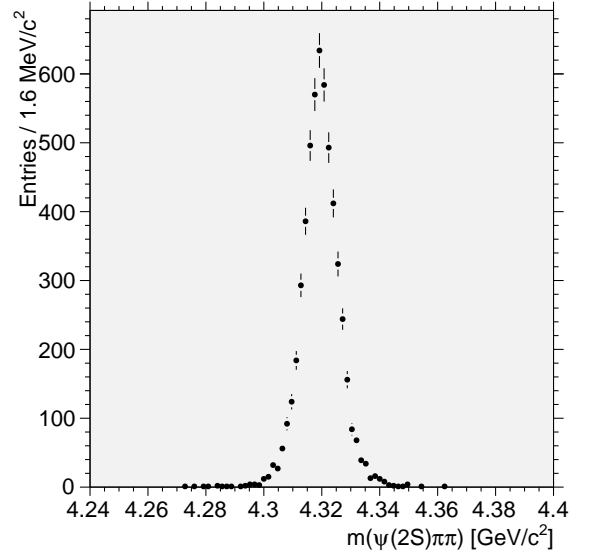


Figure 4.40: Invariant mass distribution for $\psi(2S)\pi\pi$ candidates.

measure the dynamic behaviour of the cross section $\sigma(\sqrt{s})$.

Thus this investigation consists of the following two parts:

1. Reconstruction of the signal
 - determination of efficiency of signal
 - estimate background level (signal to noise ratio S/B)
2. Simulation of an energy scan
 - estimate the expected energy dependent cross section with the efficiency measurement from above
 - estimate the required beam time to detect the signal with a significance of 10σ for different assumptions for the signal cross section

Goal of the reconstruction is to determine the number of reactions of the type

$$\bar{p}p \rightarrow \phi\phi \rightarrow K^+K^-K^+K^- \quad (4.23)$$

together with the reconstruction efficiency.

Under the assumption that the efficiency will not change very much for different energies in the region around 2.5 GeV signal as well as background events have been generated at $E_{cms} = 2.23 \text{ GeV}$ corresponding to an initial 4-vector

$$P_{\text{init}} = (p_x, p_y, p_z, E \cdot c) \quad (4.24)$$

$$= (0, 0, 1432, 2650) \text{ MeV}/c, \quad (4.25)$$

Reaction	σ	\mathcal{B}
$\bar{p}p \rightarrow$		
$\psi(2S)\pi^+\pi^-$	$\sigma_s(\bar{p}p \rightarrow Y(4320))$	$1.9\% \times \mathcal{B}(Y(4320) \rightarrow \psi(2S)\pi^+\pi^-)$
$3\pi^+3\pi^-$	140 μb	100%

Table 4.34: Cross sections and branching fractions for the $\psi(2S)\pi^+\pi^-$ signal and background modes. For the subsequent J/ψ decay we use to the sole branching fraction to one lepton type (the value for the branching fractions $\rightarrow e^+e^-$ and $\rightarrow \mu^+\mu^-$ are the same). The cross section for the background mode has been measured at a beam momentum of 8.8 GeV/c.

Decay	efficiency		suppression		Signal to noise	
$\bar{p}p \rightarrow$	ϵ_{S,e^+e^-}	$\epsilon_{S,\mu^+\mu^-}$	$\eta_{e^+e^-}$	$\eta_{\mu^+\mu^-}$	$S/N_{e^+e^-}$	$S/N_{\mu^+\mu^-}$
$\psi(2S)\pi^+\pi^-$	14.9%	12.2%	–	–		
$3\pi^+3\pi^-$	–	–	$37 \cdot 10^6$	$25 \cdot 10^6$	$700\tilde{\sigma}/\mu\text{b}$	$400\tilde{\sigma}/\mu\text{b}$

Table 4.35: Suppression η and signal to noise ratio for the background modes of the $\psi(2S)\pi^+\pi^-$ analysis, which are separately examined for the decay modes $J/\psi \rightarrow e^+e^-$ and $J/\psi \rightarrow \mu^+\mu^-$. The signal to noise ratios are given in terms of the unknown cross section $\tilde{\sigma}$.

additionally modified according to an relative jitter $p/dp = 10^{-5}$ accounting for the expected beam uncertainty. This is region where is has been found evidence for the tensor ($J^{PC} = 2^{++}$) glueball candidate $\xi(2230)$ by the BES experiment [68].

Signal events have been generated with the event generator `EvtGen` [?]. In order to determine the reconstruction efficiency with angular independent accuracy the events have been generated according to phase space resulting in flat angular distributions.

The simulated decay chain was

$$\bar{p}p \rightarrow \phi\phi \quad (4.26)$$

$$\phi \rightarrow K^+K^- \quad (4.27)$$

The particular decay chain leads to a branching ratio related reduction factor of

$$f_B = \mathcal{B}(\phi \rightarrow K^+K^-)^2 \cdot \underbrace{\mathcal{B}(f_2 \rightarrow \phi\phi)}_{\text{unknown!}} \quad (4.28)$$

$$= (0.492)^2 \cdot x < 0.242 \quad (4.29)$$

As a conservative estimate we will assume the branching ratio to be $\mathcal{B}(\text{Glueball} \rightarrow \phi\phi) = 0.2$ leading to a hypothetical factor $f_B = 0.05$.

Table 4.36 summarizes the datasets used for these studies.

The procedure for the reconstruction was:

1. Select kaon candidates from charged tracks with `VeryLoose` PID criterion¹

Channel	Number of events
$\bar{p}p \rightarrow \phi\phi$	50 k
DPM generic	10 M

Table 4.36: Datasets for the $\phi\phi$ feasibility study.

2. Create a list of ϕ candidates by forming all combinations of a negative with a positive charged kaon candidate
3. Kinematic fit of the single ϕ candidates with vertex constraint
4. Create $\bar{p}p$ candidates by forming any valid combination of two ϕ -candidates
5. Kinematic 4-constraint fit of the $\bar{p}p$ candidates with additional vertex constraint

Every of the so formed candidates had to fulfil the following requirements:

1. Probability of ϕ vertex fit: $P_\phi > 0.001$
2. Probability of $\bar{p}p$ kinematic fit: $P_{\bar{p}p} > 0.001$
3. ϕ mass window: $|m(K^+K^-) - m_{\text{PDG}}(\phi)| < 10 \text{ MeV}/c^2$
4. $\phi\phi$ mass window: $|m(\phi\phi) - 2.23\text{GeV}/c^2| < 30 \text{ MeV}/c^2$

The latter criterion defines the signal region being necessary to determine the efficiency. Fig. 4.41 (a),

¹ See section 3.3.3 for details.

(b) show the corresponding distributions according to the upper selection criteria for signal Monte Carlo data with kaon selection **VeryLoose**. The dashed lines in (b) as well as the box in (a) correspond to the selected mass windows. In plot (b) a superposition is shown of all reconstructed candidates.

In Fig. 4.41 (c), (d) the same plots are shown for generic background Monte Carlo data. No ϕ -signal is seen in the invariant masses $m(K^+K^-)$ in plot (c) and the signal window in (d) has only one entry, which disappears for tighter PID selection criteria. Therefore the conclusion concerning background level from generic hadronic reactions is limited for the time being. Nevertheless for cases without a single background event a limit is calculated with the assumption of one candidate in the signal region.

To find an optimum for the PID criterion the selection has been repeated for all available criteria **VeryLoose**, **Loose**, **Tight** and **VeryTight**. The results are summarized in Table 4.37. Since for the PID requirements **VeryLoose** and **Loose** only one event and for **Tight** and **VeryTight** no background event was observed in the signal region the optimum would be the most loose selection, since all calculations are based on one single background event in the region of interest. The expected signal-to-noise ratios extracted from this study vary between 1:6 and better than 1:9. These values are considered to have large uncertainties due to the direct influence of the relativ cross section of background with respect to the signal cross section σ_S , which has chosen to be $5 \cdot 10^6$.

It should be noted that only the order of magnitude of the efficiency, *i.e.* $\epsilon \approx 15\text{-}25\%$, is important, since it only serves as input for the simulation of the energy scan.

Besides the fact that there will be uncorrelated hadronic background due to misidentification or secondary particles the main obstacle for a high precision detection of a resonant structure in the cross section will probably be the total cross section of non-resonant

$$\bar{p}p \rightarrow \phi\phi \rightarrow K^+K^-K^+K^- \quad (4.30)$$

reactions being of the order of $\sigma_{\bar{p}p \rightarrow \phi\phi} \approx 3\text{-}4 \mu\text{b}$ in that energy region, which has been measured by the JETSET experiment as shown in Fig. 4.45. These have exactly the same signature as the signal reactions

$$\bar{p}p \rightarrow X \rightarrow \phi\phi \rightarrow K^+K^-K^+K^- \quad (4.31)$$

and thus are also kinematically not separable, *e.g.* by a 4 constraint fit. The only possibility to disentangle non-resonant from resonant reactions is to perform a spin-parity or partial-wave analysis (PWA). For that purpose it might be crucial to have a 'good' *i.e.* flat behaviour of the efficiency dependence with respect to the intrinsic appearing angles of the decay. These are

- the K-decay angle θ_{ϕ_1} of the first ϕ ,
- the K-decay angle θ_{ϕ_2} of the second ϕ and
- the angle ϕ_{plane} between the decay planes of the two ϕ -mesons, as illustrated in Fig. 4.42.

Since the initial $\bar{p}p$ system has been generated phase space distributed the decay angle distributions of the ϕ 's are expected to be flat.

The efficiency as function of these angles has been determined by dividing the distribution of reconstructed candidates by the distribution of the corresponding quantity of generated particles. Fig. 4.43 shows the results, in (a) for the ϕ -decay angle $\cos\theta_\phi$ and in (b) for the angle ϕ_{plane} between the decay planes.

It can be seen clearly that the efficiency is independent of any of the involved angles, thus making a potential PWA less difficult.

As previously indicated resonances in formation reactions can only be detected via an energy scan around the potential resonances pole mass. Close to that energy the total cross section will be enhanced according to the line shape of the resonance whose intensity could look like a Breit-Wigner distribution

$$BW(m) = A \cdot \frac{1}{\pi} \cdot \frac{\Gamma/2}{(m - m_R)^2 + (\Gamma/2)^2} \quad (4.32)$$

with Γ and m_R being its total width and pole mass respectively and A being an arbitrary amplitude. This enhancement has to be separated in particular from the non resonant part of the total cross section. The JETSET experiment performed a measurement of exactly this total cross section of the reaction $\bar{p}p \rightarrow \phi\phi$ leading to a value $\sigma_{\phi\phi} \approx 3\text{-}4 \mu\text{b}$, as shown in Fig. 4.45. For the following studies the empirical line fit shown has been considered as the background level upon which the signal shape has to be detected. The curve explicitly was chosen as

$$\sigma_{\text{non-res}}(m) = a + b \cdot m \quad (4.33)$$

with parameter values $a = 92.8 \mu\text{b}$ and $b = -40 \mu\text{b}/\text{GeV}/c^2$.

Figure of merit is the beam time necessary to measure the signal cross section with a significance

Channel	rel. X-sec	$\epsilon(\text{VL})[\%]$	$\epsilon(\text{L})[\%]$	$\epsilon(\text{T})[\%]$	$\epsilon(\text{VT})[\%]$
Signal	1	25.0	23.4	19.6	15.7
DPM generic	$5 \cdot 10^6$	$6.7 \cdot 10^{-5}$	$6.7 \cdot 10^{-5}$	$< 6.7 \cdot 10^{-5}$	$< 6.7 \cdot 10^{-5}$
$r = S : N$	–	1 : 6	1 : 6	$> 1 : 7$	$> 1 : 9$

Table 4.37: PID optimization summary. ϵ is the efficiency, VL, L, T, VT refer to the PID selection criteria described in the text.

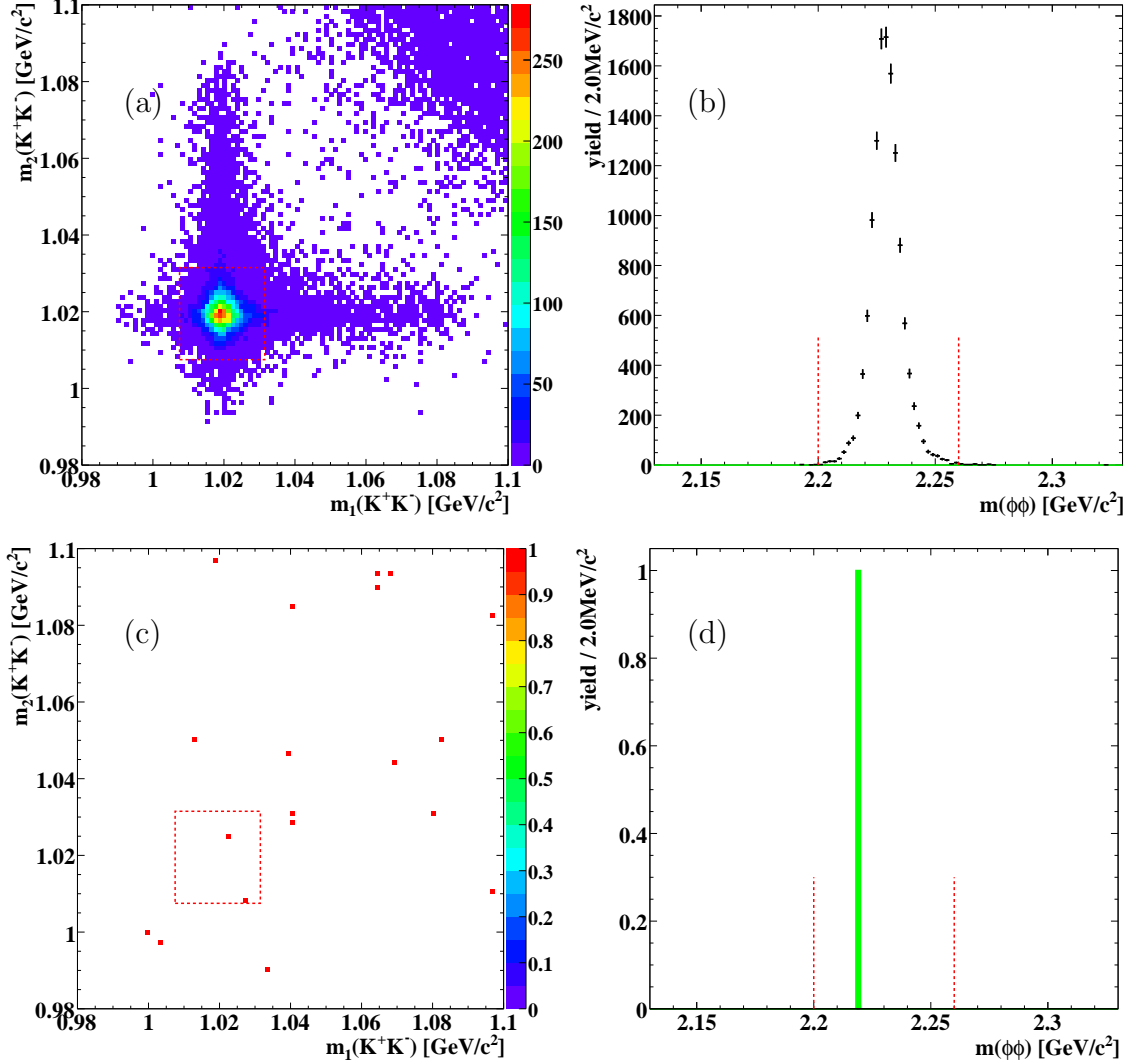


Figure 4.41: Distributions for reconstructed events for $\bar{p}p \rightarrow \phi\phi$. (a) 2D plot of invariant masses $m(\phi_1)$ vs. $m(\phi_2)$ for signal events, (b) invariant mass $m(\phi\phi)$ with MC truth match for signal events. (c), (d) The same distributions for reconstructed background events generated with the DPM generator. Black histogram corresponds to all reconstructed combinations, the shaded area represents combinations failing the MCT match.

$S = \sigma/\delta\sigma$ of 10σ , for now neglecting the background considerations for generic events discussed in the previous chapter.

The procedure for that purpose was:

1. Assumptions for parameters:

- Resonance pole mass: $m_{\text{pole}} = 2235 \text{ MeV}/c^2$
- Resonance full width: $\Gamma = 15 \text{ MeV}/c^2$

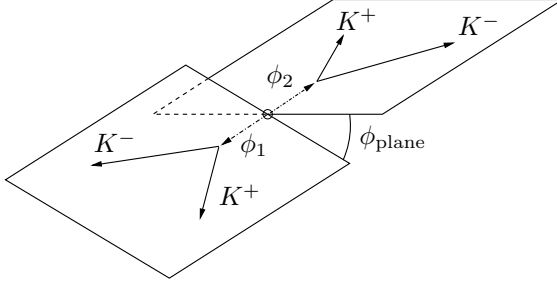


Figure 4.42: Angle ϕ_{plane} between the decay planes of the two ϕ 's.

- Resonance branching ratio to signal channel: $\mathcal{B}(f_2 \rightarrow \phi\phi) = 0.2$
 - Integrated luminosity: $L = 8.8 \text{ pb}^{-1}/\text{day}$
 - Energy window: $\pm 50 \text{ MeV}$ around pole mass
 - Number of equally distributed scan positions: $n = 25$
 - Reconstruction efficiency of $\phi\phi$ channel: $\epsilon = 0.25$
2. Vary signal cross section σ_S at pole mass between 1 nb and $1 \mu\text{b}$
 3. Determine the approximate total beam time T_b for the complete measurement to achieve significance of 10σ for the cross section measurement:

- Vary T_b arbitrarily and apply following steps until significance is 10σ
- Estimate number of expected background entries for each scan energy $E_i = m_i \cdot c^2$ as

$$B_i = \sigma_{\text{non-res}}(m_i) \cdot \epsilon \cdot \frac{T_b[d] \cdot L}{n} \quad (4.34)$$

- Estimate number of expected signal entries for E_i as

$$S_i = \frac{BW(m_i)}{BW(m_{\text{pole}})} \cdot \sigma_S \cdot \epsilon \quad (4.35)$$

$$\cdot \mathcal{B}(f_2 \rightarrow \phi\phi) \cdot \frac{T_b[d] \cdot L}{n} \quad (4.36)$$

- Set contents of bin number i of the scan histogram to $c_i = (S_i + B_i) \pm \sqrt{S_i + B_i}$
- Fit sum of signal function Eq. 4.32 and background function Eq. 4.33 to resulting histogram and compute the significance as $A/\delta A$, where A is the fitted amplitude for the resonant part of the fit model.

It turns out that the results reasonably behave according to statistics expectation, *i.e.* twice the beam time results in a precision improved by a factor $\sqrt{2}$. Fig. 4.44 shows some of the corresponding plots with the fits performed to the total cross section (a) as well as to the estimated background subtracted signal cross section determined as the difference of the total cross section and the background expectation computed from Eq. 4.33 (b). Both fits agree quite reasonable as expected. It seems surprising that in particular in Fig. 4.44 (a) no signal is visible at all whereas the fit result has quite a high significance. This is due to the assumed high precision of the data points reflected in the corresponding difference plots on the right hand side. Of course this evidently depends on the certainty of signal and background line shapes.

Table 4.38 summarizes the results for the studies above. The necessary beam times to achieve an accuracy of 10σ significance vary from infeasible hundreds to thousands of days with assumed signal cross section of $\sigma_S < 10 \text{ nb}$ down to comfortable "far less than a day" time windows for signal cross sections $\sigma_S > 100 \text{ nb}$.

σ_S [nb]	Beam time T_b (\approx)
1	13.7 y
5	200 d
10	50 d
100	12 h
500	0.5 h
1000	7.2 min

Table 4.38: Beam times needed to achieve a significance of 10σ .

It shall be emphasized at this point that the results might be too optimistic since idealized by the assumption of the correctness of the knowledge about the total cross section measurement. Therefore the given beam time estimates might be considerably sensitive to the uncertainties which clearly can be seen in Fig. 4.45.

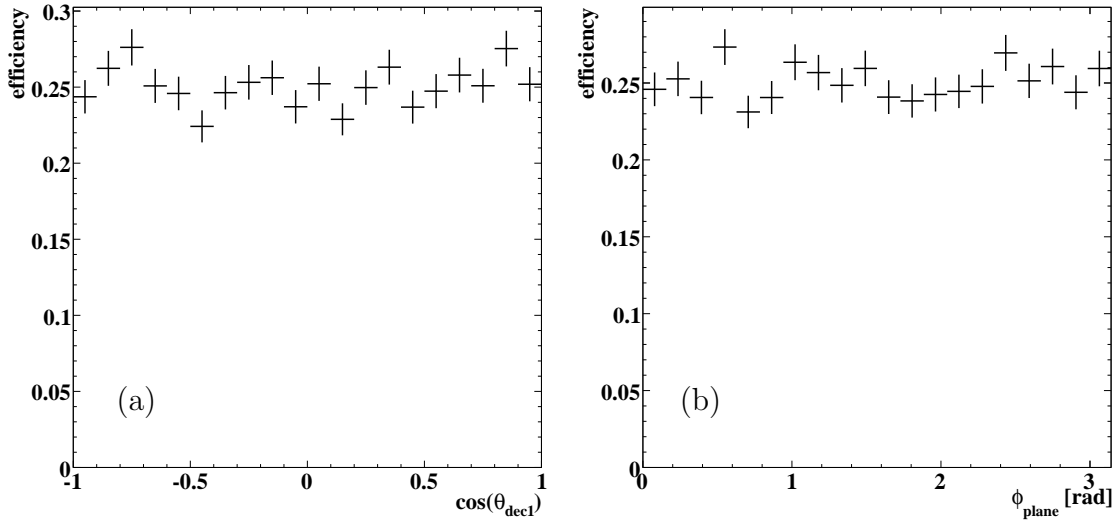


Figure 4.43: (a) Efficiency as function of the ϕ decay angle $\cos\theta_\phi$. (b) Efficiency as function of the angle ϕ_{plane} between the two decay planes.

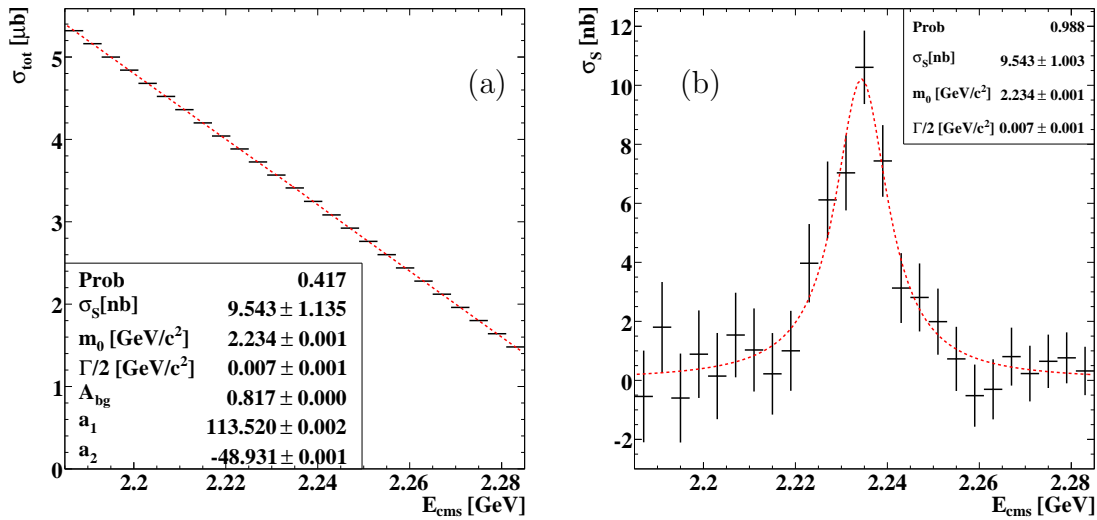


Figure 4.44: Fits to the total cross section (a) and the derived signal cross section (b) for a scan with $\sigma_S = 10$ nb and beam time according to Table 4.38.

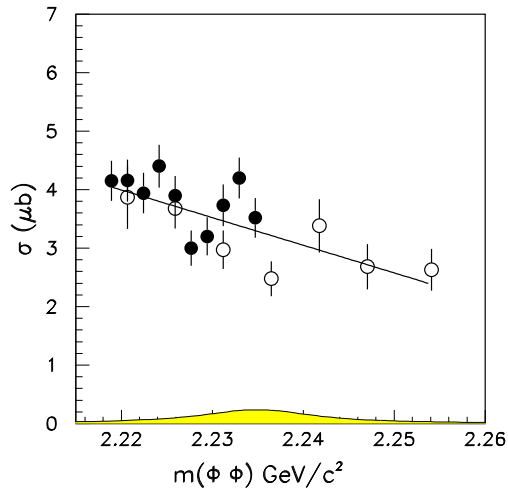


Figure 4.45: Cross section for the reaction $\bar{p}p \rightarrow \phi\phi$ measured by the JETSET experiment. The yellow curve represents a Breit-Wigner resonance, whose amplitude is at $CL = 95\%$ upper limit for the production of $f_J(2230)$ at a mass of $2235 \text{ MeV}/c^2$ and a width of $15 \text{ MeV}/c^2$ [69].

4.2.4 Heavy-Light Systems

COMMENT: Author(s): A. Gillitzer

COMMENT: Referee(s): K. Peters

Introduction

Consisting of a heavy and a light constituent, the D meson can be seen as the hydrogen atom of QCD. For the understanding of the strong interaction D mesons are very interesting objects since they combine the aspect of the heavy quark as a static color source on one side, and the aspect of chiral symmetry breaking and restoration due to the presence of the light quark on the other side. In the limit of infinite mass of the heavy quark (heavy quark limit), the states of heavy-light mesons are degenerate with respect to the spin degree of freedom of the heavy quark, and the total angular momentum of the light quark is conserved [70, 71]. In reality, the charm quark mass is not very much above the hadronic scale of ~ 1 GeV, but still, similar to the hyperfine splitting in the hydrogen atom induced by the proton spin, the spin orientation of the charm quark has only a small effect on the mass of the system.

Based on earlier observations of low-lying D meson states, the phenomenological quark model was thought to be able to describe the excitation spectra of heavy-light systems, and thus to predict also then unobserved D meson states with reasonable accuracy [71, 72, 73, 74]. According to the quark model systematics the lowest states are the S -wave states with the spin singlet $J^P = 0^-$ as ground state (D) and the spin triplet $J^P = 1^-$ as first excited state (D^*), followed by the P -wave states with $J^P = 0^+, 1^+, 1^+, 2^+$ (D_0, D_1, D'_1, D_2). The physical $J^P = 1^+$ doublet (D_1 with $j_q^P = \frac{1}{2}^+$, D'_1 with $j_q^P = \frac{3}{2}^+$; j_q is the total spin of the light quark) results from a mixing of 3P_1 and 1P_1 states, since in heavy-light systems the total spin $S = s_q + s_Q$ is not a good quantum number. The experimentally observed non-strange D meson spectrum [75] was consistent with this pattern of six states, although for some of the states no spin-parity assignments could be given. In the spectrum of charmed strange mesons the only states known with established spin-parity assignments before the recent discoveries were the pseudoscalar ground state D_s and the first excited vector state D_s^* . Apart from this, a $D_s(2536)$ and a $D_s(2573)$ state had been observed [75].

Recent discoveries

The series of new observations in the charmonium spectrum at B and charm factories was accompanied by exciting new experimental results on the spectrum of open charm mesons, starting with the unexpected discovery of a narrow $D_s(2317)$ state observed in the decay mode $D_s^+\pi^0$ by BaBar [76] in e^+e^- annihilation data at energies near 10.6 GeV. Shortly after, this state was confirmed by CLEO [77] and Belle [78]. At the same time, CLEO found a new, also narrow state $D_s(2460)$ [77] decaying to $D_s^+\pi^0$. This state was subsequently also seen by Belle [78], and confirmed by BaBar [79, 80]. The width of both states is small since the $D_s(2317)$ is lying below the DK threshold, and the $D_s(2460)$ is below the D^*K threshold. Thus the $D_s(2317)$ state cannot decay by kaon emission, and, with $J^P = 1^+$, decay with kaon emission is also forbidden for the $D_s(2460)$ state. Decay to $D_s^{(*)}$ with single pion emission is isospin forbidden. The properties of the two states were further studied in [81, 82]. [82] gives upper limits of the width $\Gamma < 3.8$ MeV for the $D_s(2317)$ state and $\Gamma < 3.5$ MeV for the $D_s(2460)$ state. The observed decay modes are consistent with spin-parity assignments $J^P = 0^+$ for the $D_s(2317)$ state and $J^P = 1^+$ for the $D_s(2460)$ state, respectively. The so far observed decay modes are [83] $D_s(2317)^+ \rightarrow D_s^+\pi^0$ and $D_s(2460)^+ \rightarrow D_s^+\pi^0, D_s^+\gamma, D_s^+\pi^+\pi^-$. Very recently, another D_s meson state decaying into DK at a mass of 2.86 GeV/ c^2 and a larger width of ~ 47 MeV was observed at BaBar [84].

Theoretical Interpretation

These observations attracted much interest both in the theoretical and the experimental hadron physics community, since the new states don't fit well into the quark model predictions for heavy-light systems in contrast to the previously known D meson states. The $D_s(2317)$ state is typically 150 MeV or more below the quark model expectation. In particular, it has been considered very difficult to reproduce the mass difference between the 0^+ and the 1^+ state within the quark model [85]. Fig. 4.46 shows a comparison between the observed D_s spectrum and quark model calculations [73, 74] together with the DK and D^*K thresholds.

Long before the discovery of the new states, a model based on chiral symmetry was developed for heavy-light systems that predicted the mass splitting of the $0^- - 0^+$ and $1^- - 1^+$ to be related to the light constituent quark mass [86, 87]. Since in that ap-

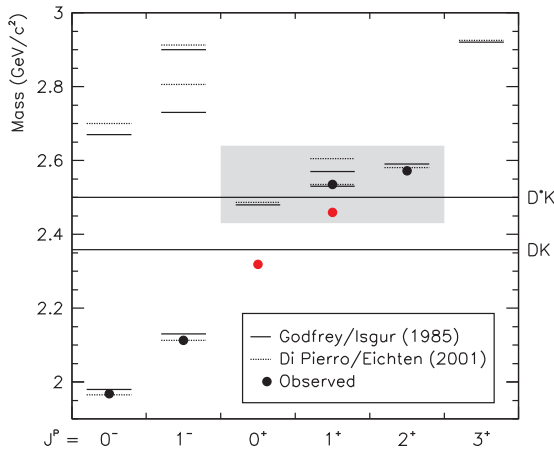


Figure 4.46: The D_s meson spectrum as predicted by Godfrey and Isgur [73] (solid lines) and Di Pierro and Eichten [74] (dashed lines). Experimental values are shown by points, the DK and D^*K thresholds as horizontal lines. The figure is taken from [82].

proach the D mesons, like the light quark fields in QCD, transform linearly under chiral $SU(3)$ rotations the spectrum shows a doublet structure. After the discovery of the new states the scheme was applied to the new D_s states [88, 89] and shown to explain the low $D_s(2317)$ mass and the identical hyperfine splitting in the $0^- - 1^-$ and $0^+ - 1^+$ doublets. Such results indicate the importance of chiral symmetry for the understanding of the open-charm meson spectrum.

The discovery of the scalar and axial-vector open-charm states triggered a series of theoretical works studying the new states in various frameworks. For a recent review focusing on approaches with active quark degrees of freedom see Ref. [85]. The possibility that these states could have a simple $c\bar{s}$ structure is discussed in Refs. [90, 91]. The predicted level scheme of typical quark models may, however, suggest that the scalar and axial-vector D_s mesons have an exotic non- $c\bar{s}$ structure. For instance tetraquark models for D_s states assume strong $[c\bar{s}] [u\bar{u} + d\bar{d}]$ or $[cq] [\bar{s}\bar{q}]$ components in the wave function [92, 93, 94, 95, 96, 97, 98, 99]. However, tetraquark models usually predict a large number of states in addition to the $q\bar{q}$ meson states for which there is little experimental evidence. In Refs. [100, 101, 102] the relevance of higher Fock states involving mesonic degrees of freedom for the scalar states was investigated applying resonating group methods to a quark model. The possibility that the scalar D_s may be a molecular DK state was discussed in Ref. [103].

First systematic computations where open-charm resonances are generated in terms of hadronic degrees of freedom were based on the chiral Lagrangian written down for the Goldstone bosons and the pseudo-scalar and vector D -meson ground states [104, 105]. The approach is consistent with the heavy-quark symmetry that arises in the limit of large charm quark mass. A natural explanation of the scalar and axial vector spectrum was achieved, where for instance the scalar D_s states are coupled-channel molecules with important DK but also ηD_s components. In contrast to the chiral-doubling approach of Ref. [86, 87] the chiral Lagrangian assumes the D meson fields to transform non-linearly under chiral transformation. As a consequence the arising spectrum is not necessarily grouped into chiral doublets. In fact the leading order chiral interaction predicts weak attraction in exotic non $c\bar{q}$ channels. The existence of such states depend on the character of sub-leading order terms in the chiral Lagrangian. A recent study [106] predicts exotic signals in the ηD^* and πD channels.

D Spectroscopy at $\overline{\text{PANDA}}$

An important quantity possibly allowing to distinguish between the different pictures is the decay width of the two D_s states [106, 107, 108, 109, 110, 111]. So far their widths are only constrained by upper limits of a few MeV due to detector resolution, which is not sensitive enough to draw conclusions on their internal structure. In the following, a different experimental approach to determine the narrow widths of these states is discussed. Very close to threshold the energy dependence of the production cross section for a narrow resonance can be calculated in a model-independent way [112], and this function is sensitive to the resonance width. Provided the beam energy is sufficiently well known, thus the width of a narrow resonance can be determined in a measurement of the energy dependence of the production cross section around the energy threshold, without requiring the corresponding detector resolution in the reconstruction of the resonance from the final state. With $\delta p/p \simeq 10^{-5}$ the \overline{p} momentum spread in the HESR is sufficiently small to allow the measurement of the D_{sJ} widths in a threshold scan of the reaction $\overline{p}p \rightarrow \overline{D}_s D_{sJ}$ at $\overline{\text{PANDA}}$ down to values of ~ 100 keV.

As an example, the study of the D_{s0} width is specifically discussed in the following sections related to simulation studies which have been performed for this report. Future investigations of the D and D_s meson spectra at $\overline{\text{PANDA}}$ have however a wider

scope beyond this specific aspect. If an exotic structure of the newly found states as molecular or tetraquark states should be established, an experimental D meson spectroscopy program should search for the then missing quark model states with the identical quantum numbers. Further insight is expected from a comprehensive study of the decay modes of both D and D_s mesons including also modes with small branching fraction. Recent theoretical studies have proposed to measure the partial widths for various radiative decays of the new D_s states, since these are predicted to be distinctly different for a molecular or $Q\bar{q}$ structure [106, 110, 111, 113, 114, 115, 116, 117]. This requires to measure both the branching fractions for the radiative transition and the total width of the decaying state which is certainly an ambitious goal. For not too small total widths and transition probabilities this may however be possible.

So far only S and P wave states have been observed in both the D and the D_s spectrum. Information on states with D wave and higher angular momenta are still missing. This is likely to be due to the limitation in angular momentum in the production process of D mesons studied up to now, that is by e^+e^- annihilation or by B meson decays. In contrast very high partial waves are available in the $\bar{p}p$ entrance channel which should also enhance the population of states with high L values. As was discussed very recently [118], the exploration of the region of states with high angular momenta could be an important step to clarify the question whether or not chiral symmetry is restored in hadrons at high excitation energies.

Simulated Signal Channels

For this report simulation studies focus on the identification of the $D_{s0}(2317)$ and the determination of its width, based on the reaction channel $\bar{p}p \rightarrow D_s^\pm D_{s0}^*(2317)^\mp$. The recoiling $D_{s0}^*(2317)$ is identified inclusively without specifying its decay mode, as will be discussed below. Signal events have been generated which the event generator `EvtGen`[119] with the intrinsic width of the $D_{s0}^*(2317)$ set to $\Gamma = 0.1$ MeV for the study of signal reconstruction. A data set for signal events (=Signal 1) was generated in the following way:

$$\bar{p}p \rightarrow D_s^\pm D_{s0}^*(2317)^\mp \quad (4.37)$$

$$D_s^\pm \rightarrow \phi\pi^\pm, \quad \phi \rightarrow K^+K^- \quad (4.38)$$

$$D_{s0}^*(2317)^\mp \rightarrow \text{anything} \quad (4.39)$$

A second data set with equal number of events (=Signal 2) was generated completely inclusive, *i.e.*

$$\bar{p}p \rightarrow D_s^\pm D_{s0}^*(2317)^\mp \quad (4.40)$$

$$D_s^\pm \rightarrow \text{anything} \quad (4.41)$$

$$D_{s0}^*(2317)^\mp \rightarrow \text{anything} \quad (4.42)$$

in order to allow for an independent determination of the reconstruction efficiency.

Since the $D_{s0}^*(2317)$ width with its present upper experimental limit $\Gamma < 3.5$ MeV [83] is smaller than the detector resolution, it cannot be measured directly. Instead, it can be deduced from a measurement of the shape of the excitation function of $D_{s0}^*(2317)$ production very close to threshold. The simulation studies thus also address an energy scan of the signal channel around the threshold energy and explore how well the shape of the excitation function can be determined.

Background Channels

In order to estimate the background level several specific reaction channels with a D_s meson in the final state with identical decay mode as the signal events have been investigated. To fill the available phase space at the threshold of the signal channel of 354 MeV, background channels with pions or photons in addition to the second D_s meson have been considered. Furthermore, a generic hadronic background sample created using the event generator `DpmGen` based on the dual parton model [120] has been analyzed. Table 4.39 lists the investigated data sets. The data sets were generated at 5 MeV above the nominal $D_s^\pm D_{s0}^*(2317)^\mp$ threshold.

Analysis Strategy

Corresponding to the goal of the simulation study of $D_{s0}^*(2317)^\mp$ production the analysis consists of two separated steps:

1. Reconstruct the signal at given energy:
 - determine the efficiency of the signal reconstruction
 - estimate the background level (signal to noise ratio S/N)
2. Simulate the energy dependence:
 - generate the relevant distributions for the signal events based on the results from step 1 at selected energies, and determine the number of signal and background events

Channel	Number of events
$\bar{p}p \rightarrow D_s^\pm D_{s0}^*(2317)^\mp$ (Signal 1)	40 k
$\bar{p}p \rightarrow D_s^\pm D_{s0}^*(2317)^\mp, D_s^\pm \rightarrow \text{any}$ (Signal 2)	40 k
$\bar{p}p \rightarrow D_s^\pm D_s^\mp \pi^0$	40 k
$\bar{p}p \rightarrow D_s^\pm D_s^\mp 2\pi^0$	40 k
$\bar{p}p \rightarrow D_s^\pm D_s^\mp \pi^+ \pi^-$	40 k
$\bar{p}p \rightarrow D_s^\pm D_s^{*\mp}$	40 k
$\bar{p}p \rightarrow D_s^\pm D_s^{*\mp} \pi^0$	40 k
$\bar{p}p \rightarrow D_s^\pm D_s^\mp \gamma$	40 k
$\bar{p}p \rightarrow D_s^\pm D_s^{*\mp} \gamma$	40 k
DPM generic	10.5 M

Table 4.39: The data sets to evaluate signal reconstruction efficiency and signal-to-noise ratio.

- determine the shape of the excitation function
- deduce width and mass of the $D_{s0}^*(2317)^\mp$ state

$$f_{\mathcal{B},\text{excl}} = \underbrace{\mathcal{B}(D_{s0}^*(2317) \rightarrow D_s \pi^0)}_{\text{unknown}} \cdot \mathcal{B}(D_s^\pm \rightarrow \phi \pi^\pm)^2 \cdot \mathcal{B}(\phi \rightarrow K^+ K^-)^2 \cdot \mathcal{B}(\pi^0 \rightarrow 2\gamma) < 4.6 \cdot 10^{-4}.$$

These analysis steps will be briefly discussed in the following.

Exclusive and inclusive signal reconstruction

The optimum signal to noise ratio is achieved in a full exclusive reconstruction of all particles emerging in the decay chains of the primary particles produced in the reaction. On the other hand, due to the small branching ratios involved the signal event rate based on a single decay chain will be very small. In the simulation studies these small branching ratios reduce the significance of the achieved background suppression factor at given size of the analyzed background sample. Therefore, as will be argued below, a different approach using inclusive $D_{s0}^*(2317)$ identification is pursued here.

The D_s^\pm meson has many decay branches. As channel with reasonable efficiency and with characteristic strangeness content the $D_s^\pm \rightarrow \phi \pi^\pm$ decay branch with $\phi \rightarrow K^+ K^-$ was selected. The combined branching ratio is

$$f_{\mathcal{B},D_s} = \mathcal{B}(D_s^\pm \rightarrow \phi \pi^\pm) \cdot \mathcal{B}(\phi \rightarrow K^+ K^-) = 0.044 \cdot 0.492 = 0.022.$$

Since the only known decay channel of the $D_{s0}^*(2317)$ is the isospin violating $D_{s0}^*(2317) \rightarrow D_s^\pm \pi^0$ decay (with unknown branching fraction) one also needs to reconstruct the $\pi^0 \rightarrow 2\gamma$ and the second D_s^\pm in the above channel for a full exclusive reconstruction resulting in the total branching ra-

The branching ratio $\mathcal{B}(D_{s0}^*(2317) \rightarrow D_s \pi^0)$ is expected to be very close to one. With the assumption of $\sigma = 1$ nb signal cross section at threshold, an integrated luminosity of about $\mathcal{L} = 9000/\text{nb}$ per day and efficiency $\epsilon \approx 0.2$ this results in an expected number of efficiency and branching ratio corrected signal reactions of

$$N_{\text{excl}} = \sigma \cdot \mathcal{L} \cdot \epsilon \cdot f_{\mathcal{B},\text{excl}} \approx 9000 \cdot 0.2 \cdot 4.6 \cdot 10^{-4} = 0.8 \text{ detected signals/day.}$$

Such low event rates would require a very long running time for the measurement of the excitation function. It therefore doesn't seem promising to only use this specific final state for the identification of the $\bar{p}p \rightarrow D_s^\pm D_{s0}^*(2317)^\mp$ reaction, but to include an as large as possible number of specific channels in the decay chain in order to increase the event rate in the exclusive reconstruction.

The task to simulate many different channels is however beyond the scope of this report. The simulations are therefore focused on the question whether an inclusive reconstruction of the D_s^\pm decay with the identification of the recoiling $D_{s0}^*(2317)^\mp$ via the missing mass method, which would result in higher event rates, yields sufficient background suppression for signal identification. To enhance the signal to background ratio kinematic correlations in the event are exploited, as discussed below. In case of the inclusive reconstruction the expected number of reactions which can be detected is estimated to

be

$$\begin{aligned} N_{\text{incl}} &= \sigma \cdot \mathcal{L} \cdot \epsilon \cdot f_{B, D_s} < 9000 \cdot 0.2 \cdot 0.022 = \\ &= 40 \text{ detected signals/day.} \end{aligned}$$

Hence, to collect a reasonable number like 500 events only around two weeks of beam time would be required.

Event selection criteria

D_s^\pm candidates were created in the following way:

1. Select kaon candidates from charged tracks with **VeryLoose** PID criterion² (will be tightened later for better S/B ratio)
2. Create a list of ϕ candidates by forming all combinations of a negative with a positive charged kaon candidate
3. Kinematic fit of the single ϕ candidates with vertex constraint
4. Select pion candidates from charged tracks with **VeryLoose** PID criterion
5. Combine ϕ candidates with pion candidates to form D_s^\pm candidates
6. Kinematic fit of the D_s^\pm candidates with vertex constraint

On the candidates preselected in this way the following requirements were applied in addition:

1. Probability of ϕ vertex fit: $P_\phi > 0.001$
2. Probability of D_s^\pm vertex fit: $P_{D_s} > 0.001$
3. ϕ mass window: $|m(K^+K^-) - m_{\text{PDG}}(\phi)| < 10 \text{ MeV}/c^2$
4. ϕ decay angle³: $|\cos \theta_{\text{dec}}| > 0.5$
5. D_s^\pm mass window: $|m(\phi\pi^\pm) - m_{\text{PDG}}(D_s^\pm)| < 30 \text{ MeV}/c^2$

Fig. 4.47 shows the D_s^\pm missing mass spectrum obtained with the selection criteria listed above. The black histogram represents all reconstructed candidates whereas the green filled area corresponds to candidates failing the so called Monte Carlo Truth (MTC) match⁴. Both D_s^\pm and $D_{s0}^*(2317)^\mp$ peaks are reconstructed with a resolution of about 10–15 MeV/c^2 .

In a completely exclusive analysis a 4-constraint fit to the sum of the 4-momenta of the final state particles as given by the 4-momentum vector of the

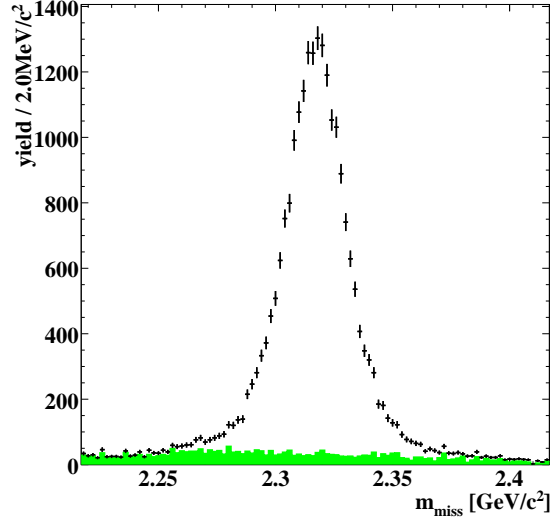


Figure 4.47: Missing mass spectrum obtained for the D_s^\pm candidates based on the known 4-momentum of the initial $\bar{p}p$ system. The black histogram corresponds to all reconstructed combinations of the required particles in the final state, the green filled area represents those combinations which fail the MCT match criterion (explanation see text).

initial $\bar{p}p$ state in general improves the signal quality significantly. As the $D_{s0}^*(2317)$ decay is not reconstructed, this is not possible here. However, the reconstructed D_s^\pm and $D_{s0}^*(2317)^\mp$ masses are kinematically anti-correlated as a consequence of their production very close to the threshold energy. This correlation, as shown in Fig. 4.48 (left) is exploited in order to enhance the signal to noise ratio. The peak of the $m_{\text{sum}} = m(D_s^\pm) + m(D_{s0}^*(2317)^\mp)$ sum mass appears to have a width of about 1 MeV/c^2 only. Therefore in this analysis the sum mass m_{sum} is used as quantity to count the number of signal events. It will be demonstrated later that background channels exhibit a different behavior and can be reasonably well separated from the signal in this projection.

The obtained m_{sum} spectrum is fit with a Voigt distribution, *i.e.* a convolution of a Breit-Wigner with a Gaussian distribution, with phase space

2. See section 3.3.3 for details.

3. The decay angle is defined as the angle between the direction of motion of the reconstructed ϕ candidate in the laboratory frame and the direction of motion of one of the kaons in the frame of the ϕ .

4. The Monte Carlo Truth match checks whether or not a decay tree has been exactly reconstructed the way it was generated.

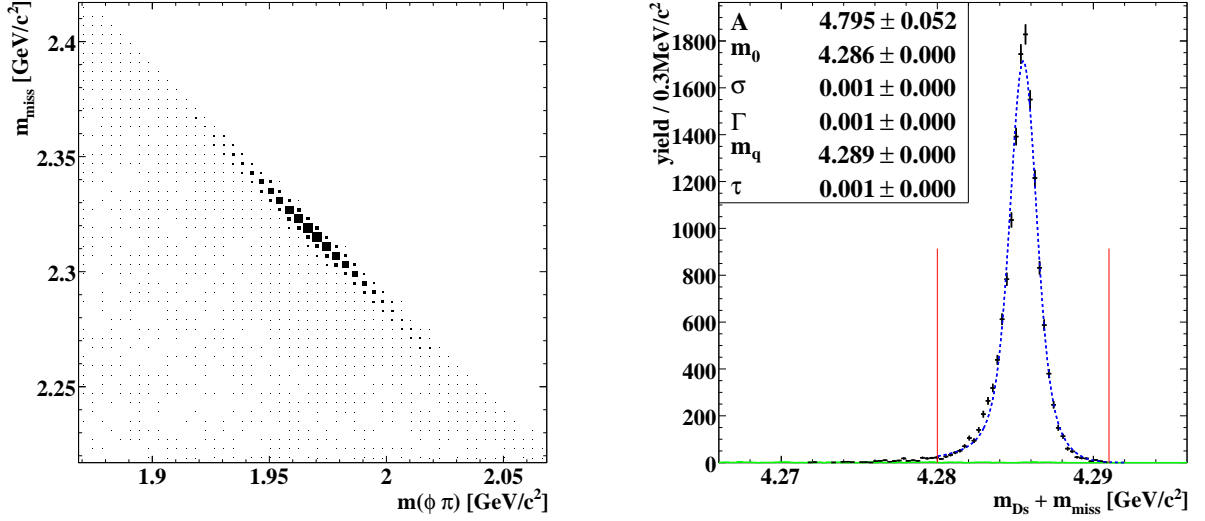


Figure 4.48: Reconstruction of signal events type 1. (Left) Correlation of missing mass and invariant D_s^\pm mass. (Right) The sum mass $m_{\text{miss}} + m(D_s^\pm)$. The number of signal events is evaluated as the number of entries in the interval between the vertical red lines.

damping⁵. However, due to the absence of background within the signal events the reconstruction efficiency can simply be determined by counting the number of events in the range

$$4280 \text{ MeV}/c^2 < m_{\text{sum}} < 4291 \text{ MeV}/c^2 \quad (4.43)$$

which is marked by the two vertical lines in Fig. 4.48 (right). For the particular example here with **VeryLoose** kaon identification we find $S = 14490$ entries in the signal region corresponding to an efficiency of $\epsilon = 36.2\%$. An efficiency of the same magnitude is independently found by the analysis of completely inclusive events (Signal 2), where also the recoiling D_s decays generically.

Background

Background channels as listed in Table 4.39 have been analyzed. Fig. 4.49 shows as an example background distributions due to the $\bar{p}p \rightarrow D_s^\pm D_s^\mp \pi^0$ reaction obtained for the **VeryLoose** kaon candidate selection. Left and right panels of Fig. 4.49 show the reconstructed D_s^\pm missing mass and the $m_{\text{sum}} = m(D_s^\pm) + m(D_{s0}^*(2317)^\mp)$ sum mass distributions, respectively. For this as well as the other specific background channels the m_{sum} distribution follows a phase space distribution which is well described by an Argus function⁶.

In the background sample generated with DPM - known to be inadequate for the simulation of charmed hadron production - no significant amount

of D_s^\pm mesons are correctly reconstructed. With the **VeryLoose** kaon candidate selection very few out of 5 M generated events are found in the m_{sum} window between 4280 MeV/c² and 4291 MeV/c².

Results

In order to find the selection criteria for the maximum signal significance many parameters have to be varied. At the present stage of the study only the influence of the kaon identification quality has been systematically analyzed.

Four different selection criteria **VeryLoose**, **Loose**, **Tight** and **VeryTight** based on a global PID likelihood function \mathcal{L} are available with requirements according to tab. 3.2.

All these four criteria for kaon identification were applied to the selection procedure, resulting in different numbers of residual candidates for signal and background in the m_{sum} signal region. The expected signal-to-noise ratio r_{SB} depending on the

5. This function is given by $f(m) = A \cdot \left[\int_{-\infty}^{+\infty} G(x'; m_0, \sigma) * BW(m - x'; m_0, \Gamma) dx' \right] \times \frac{1}{1 + \exp\left(\frac{m - m_q}{\tau}\right)}$ with a Gaussian $G(m)$, a non-relativistic Breit-Wigner function $BW(m)$, an intensity parameter A , running variable m , resonance pole mass m_0 , resonance width Γ , reconstruction resolution σ , phase space limit m_q and decay parameter τ (all except A in [GeV/c²]).

6. Here the Argus function is defined as $f_{\text{bg}}(m) = A_s \cdot m \cdot \sqrt{1 - (m/m_0)^2} \cdot \exp[c \cdot (1 - (m/m_0)^2)]$ with amplitude parameter A_s , phase space limit m_0 and shape parameter c .

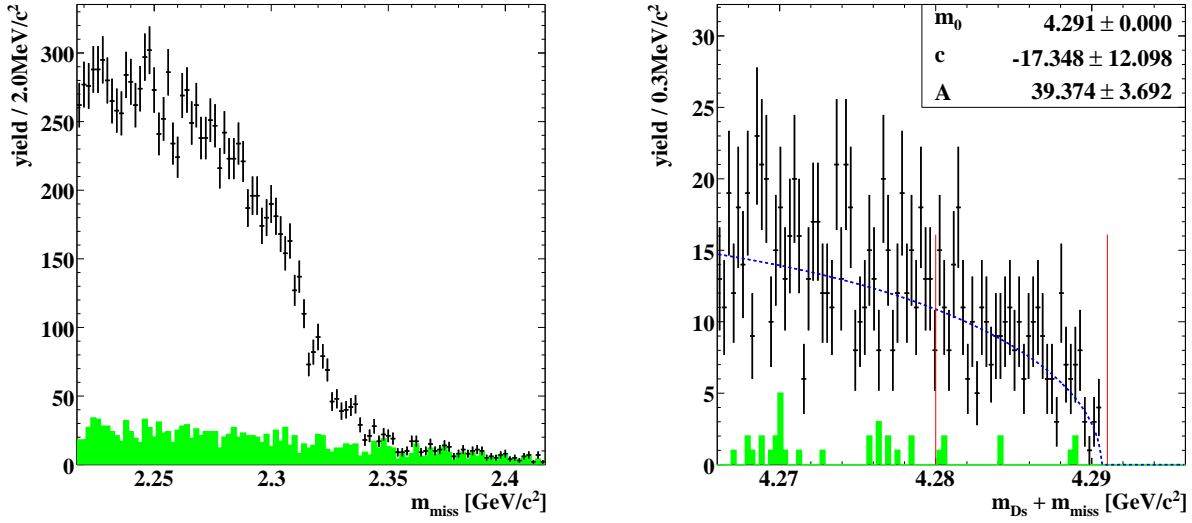


Figure 4.49: Background channel 1: $\bar{p}p \rightarrow D_s^\pm D_s^\mp \pi^0$. (Left) Reconstructed D_s^\pm missing mass distribution. (Right) Obtained sum mass distribution: the number of background events is evaluated in the interval $4280 \text{ MeV}/c^2 < 4291 \text{ MeV}/c^2$ as indicated by the vertical red lines. The black histogram corresponds to all reconstructed combinations of the required particles in the final state, the green filled area represents those combinations which fail the MCT match criterion (explanation see text).

Channel	rel. X-sec	$\epsilon(\text{VL})[\%]$	$\epsilon(\text{L})[\%]$	$\epsilon(\text{T})[\%]$	$\epsilon(\text{VT})[\%]$
Signal	1	36.2	28.1	21.0	19.0
$\bar{p}p \rightarrow D_s^\pm D_s^\mp \pi^0$	1	0.8	0.6	0.5	0.4
$\bar{p}p \rightarrow D_s^\pm D_s^\mp 2\pi^0$	1	6.9	5.2	4.0	3.6
$\bar{p}p \rightarrow D_s^\pm D_s^\mp \pi^+ \pi^-$	1	8.1	6.1	4.6	4.2
$\bar{p}p \rightarrow D_s^\pm D_s^{*\mp}$	1	0.0	0.0	0.0	0.0
$\bar{p}p \rightarrow D_s^\pm D_s^{*\mp} \pi^0$	1	3.7	2.8	2.1	1.9
$\bar{p}p \rightarrow D_s^\pm D_s^\mp \gamma$	0.1	0.6	0.4	0.3	0.3
$\bar{p}p \rightarrow D_s^\pm D_s^{*\mp} \gamma$	0.1	1.1	0.9	0.6	0.6
DPM generic	10^6	$2.5 \cdot 10^{-4}$	$4.5 \cdot 10^{-5}$	$1.9 \cdot 10^{-5}$	$1.9 \cdot 10^{-5}$
r_{SB} (w/ DPM)	–	1 : 318	1 : 74	1 : 43	1 : 47
r_{SB} (w/o DPM)	–	1.86	1.90	1.89	1.88

Table 4.40: Results of the simulation studies of signal reconstruction and background suppression: ϵ denotes the signal reconstruction efficiency for the signal channel and the fake signal finding probability for the studied background channels, respectively. The resulting values for the signal-to-noise ratio r_{SB} including or excluding the generic DPM background are also given (see text).

PID selection criterion can only be given based on relative cross sections of the background channels as compared to that of the signal. Since all cross sections are unknown, as reference value for the signal and for all purely hadronic background channels 1 nb is assumed, whereas the reference value is scaled down by a factor 10 to 0.1 nb for channels with photons in the final state. The S/B ratio for all considered specific background channels based on this assumption is given in Table 4.40. The S/B ratio for the generic background obtained with DPM corresponds to an assumed ratio of the back-

ground to signal cross section of 10^6 . Using the signal selection criteria described above, 3 events out of $10.5 \cdot 10^6$ DPM background events are found in the signal region. For a kaon selection based on criterion **Tight** this corresponds to an expected ratio of $r_{SB} \approx 1 : 43$.

Although this value has a large statistical uncertainty, this indicates that it may be difficult to measure an excitation function based on the inclusive reconstruction method described above. Therefore, an even larger DPM background sample was also

analyzed with the exclusive reconstruction of the $D_s^\pm D_{s0}^*(2317)^\mp \rightarrow \phi\pi^\pm\pi^0\phi\pi^\mp$ decay chain. None of $4.0 \cdot 10^7$ DPM background events survived the signal selection cuts using the `VeryLoose` kaon selection criterion. Further background suppression can be expected from using a tighter kaon selection criterion, and particularly, from a cut on the D_s^+ and D_s^- decay vertices. Unfortunately, due to the small branching ratio to the final state, the non-observation of fake events only corresponds to an estimated lower limit of signal-to-background ratio $S/B > 1 : 623$. In order to obtain a more significant result on the achievable background suppression, much larger background samples have to be generated and analyzed. In addition, the same type of exclusive analysis needs to be repeated for different decay chains, in order to acquire a higher signal event rate. Both tasks are beyond the scope of the present report, and will be pursued in future studies.

Simulation of a Near-Threshold Energy Scan

Excitation function

At small excess energies above threshold governed by S -waves the energy dependence of the cross section for the reaction $a+b \rightarrow 1+2$ where the two final state particles ($i = 1, 2$) have Breit-Wigner spectral functions

$$\rho_i(m) = \frac{1}{\pi} \cdot \frac{\Gamma_i/2}{(m - m_{R_i})^2 + (\Gamma_i/2)^2} \quad (4.44)$$

with resonances pole mass and width m_{R_i} and Γ_i is given by the integral [121]

$$\sigma(s) = |M|^2 \int_{-\infty}^{+\infty} dm_1 \int_{-\infty}^{+\infty} dm_2 \rho_1(m_1)\rho_2(m_2) \cdot p \cdot \Theta(\sqrt{s} - m_1 - m_2).$$

Here m_1 and m_2 are the running masses, \sqrt{s} is the total center-of-mass energy, M the matrix element of the process, and p the momentum of the two resonances in the center-of-mass frame. Substituting Breit-Wigner spectral functions with zero width for the D_s meson, and the center-of-mass momenta, one obtains a simplified relation for the energy dependence (with $m_d \equiv m(D_s)$) [121]:

$$\frac{\sigma(s)}{|M|^2} = \frac{\Gamma}{4\pi\sqrt{s}} \int_{-\infty}^{\sqrt{s}-m_d} dm \frac{\sqrt{[s - (m + m_d)^2] \cdot [s - (m - m_d)^2]}}{(m - m_R)^2 + (\Gamma/2)^2}. \quad (4.45)$$

Scan procedure

The simulated energy scan for this write-up is based on several simplifying assumptions.

Apart from the effects due to energy dependent shifts of the kinematic limit in the Argus function modelling the background distributions of the specific channels considered, the background level is assumed to be energy independent within the small energy range in which the excitation function is simulated. Also the signal reconstruction efficiency is assumed to be constant for all energy steps.

The momentum spread of the beam is only taken into account in a simplified way, namely by an additional contribution to the energy selected in the scan procedure. In a fully correct treatment the effective excitation function instead consists of a convolution of the energy spread with the theoretical excitation function for infinitely small momentum spread.

The following parameters are selected:

- The width $\Gamma_{D_{s0}}$ of the $D_{s0}^*(2317)$.
- The spent beam time T_{beam} for the complete measurement; a signal cross section of $\sigma_S = 1 \text{ nb}$ at threshold energy E_{thr} and an integrated luminosity of $\mathcal{L} = 9 \text{ pb}^{-1}/\text{day}$ is assumed.
- The energy region ΔE_{max} below and above the threshold to be scanned.
- The number n of the taken measurements within the energy scan ($\rightarrow \Delta E = 2 \cdot \Delta E_{\text{max}}/n$)
- The signal-to-noise ratio r_{SB}
- The signal reconstruction efficiency $\epsilon \cdot f_{\mathcal{B}, D_s}$

The number of signal events at each energy step is computed according to

$$S_i = \sigma(E_i/c^2) \cdot \frac{\mathcal{L}_{\text{tot}}}{n} \cdot \epsilon \cdot f_{\mathcal{B}, D_s} = \sigma_S \cdot \frac{f_{\text{ex}}(E_i + \delta E)}{f_{\text{ex}}(E_{\text{thr}})} \cdot \mathcal{L} \cdot \frac{T_{\text{beam}}}{n} \cdot \epsilon \cdot f_{\mathcal{B}, D_s}$$

where δE corresponds to the uncertainty of the beam energy, and is randomly selected within a gaussian distribution of 150 keV width, and f_{ex} is given by the value of the integral in equation 4.45.

The signal-to-background ratio r_{SB} listed above is valid at the highest energy E_n of the scan. According to the lower number of signal events at the lower energies within the scan the value of r_{SB} is scaled down appropriately, assuming constant background apart from a phase space correction.

Results

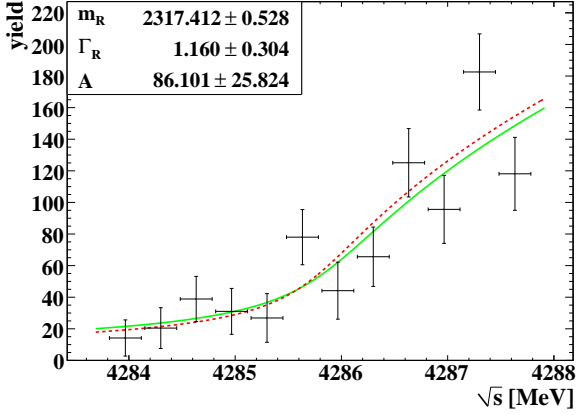


Figure 4.50: Fit of the excitation function obtained from the reconstructed signal events, shown by the full green line. The red dotted line shows the excitation function corresponding to the generated events.

So far a few combinations of parameters have been explored in the simulation of the energy scan of the $\bar{p}p \rightarrow D_s^\pm D_{s0}^*(2317)^\mp$ reaction. No attempt was made to find the global optimum of the procedure, which would require a systematic investigation of a high-dimensional parameter space. The result obtained for a specific parameter set is shown in Fig. 4.50. The selected parameters (scan 1) are:

- $T = 14$ d, $r_{SB} = 1 : 3$, $\Gamma = 1$ MeV/ c^2 , $\Delta E_{\max} = 2$ MeV, $n = 12$.

For this parameter set the fit yields

$$m = 2317.41 \pm 0.53 \text{ MeV}/c^2, \quad \Gamma = 1.16 \pm 0.30 \text{ MeV}/c^2, \quad (4.46)$$

to be compared with the input values $m = 2317.30$ MeV/ c^2 and $\Gamma = 1.00$ MeV/ c^2 , respectively.

The same procedure with a parameter set corresponding to a much smaller S/B ratio

- $T = 28$ d, $r_{SB} = 1 : 30$, $\Gamma = 0.5$ MeV/ c^2 , $\Delta E_{\max} = 1$ MeV, $n = 12$

did not allow to deduce a meaningful fit result for the $D_{s0}^*(2317)$ width.

4.2.5 Strange and Charmed Baryons

COMMENT: Author(s): A. Gillitzer

COMMENT: Referee(s): M. Lutz

Introduction

An understanding of the baryon excitation spectrum is one of the prime goals of non-perturbative QCD. In the nucleon sector, where most of the experimental information is available and where the experimental effort is still being concentrated, it is found that the agreement with quark model predictions is astonishingly small: some of the low-lying states are not at the energies predicted, whereas many of the predicted higher lying states have not been seen experimentally [122]. The latter aspect has been discussed as the problem of 'missing resonances' [123], and different explanations have been suggested. For example a quark-diquark structure of baryons would reduce the number of internal degrees of freedom, and thus the number of states. Another reason could be a lack of experimental sensitivity, since resonance excitation and detected final states have so far been largely based on pionic modes [122]. It is also not clear to which extent the observed states are three-quark excitations or governed by meson-baryon dynamics. In the approach of chiral coupled channel dynamics [124, 125, 126], based on the conjecture that the only genuine qqq states are the octet and decuplet ground states, it is attempted to describe all excited baryon states as dynamically generated resonances.

Strange Baryons

The question to which extent the excitation spectra of baryons consisting of light quarks (u, d, s) follow the systematics of $SU(3)$ flavor symmetry, requires knowledge not only on N^* and Δ spectra but also on those of all species of strange baryons, *i.e.* of Λ , Σ , Ξ , and Ω hyperons. However, as one adds strangeness as an additional degree of freedom to the baryonic constituents, the experimental data quality becomes increasingly poor. This is already the case for the Λ and Σ spectrum, where recent observations of new states [127, 128] are waiting for confirmation and interpretation. The data base is particularly scarce for $S = -2$ and $S = -3$ baryons. Ξ and Ω excited states have in general been seen as bumps in inclusive experiments only, without determination of spin and parity quantum numbers. The 2006 edition of the Review of Particle Physics [122] explicitly mentions that "noth-

ing of significance on Ξ resonances has been added since the 1988 edition". A large fraction of the data has been obtained with low statistics in bubble chamber experiments. Apart from the Ξ octet and decuplet ($\Xi(1530)P_{13}$) ground states spin and parity assignments only exist for the three-star resonances $\Xi(1820)D_{13}$ and $\Xi(2030)$, but their assignment is labelled as "merely educated guesses" in [122]. More recent information on masses, widths, and decay modes of the $\Xi^0(1690)$, $\Xi^-(1820)$, and $\Xi^-(1950)$ states was delivered by the WA89 experiment [129, 130]. The $\Xi^0(1690)$ state was also seen in Λ_c^+ decays at Belle [131] and at BaBar [132]. The latter study favors a spin 1/2 assignment to this state, and confirms the $J^P = 3/2^+$ assignment for the $\Xi^0(1530)$ state.

Almost nothing is known on the excitation spectrum of the Ω baryon: no assignment exists for any of the three seen excited states (one three-star, two two-star resonances). Table 4.41 gives an overview of the assignment of known baryonic states in the light quark sector [122].

Recent theoretical work on the Ξ and Ω spectrum is found in Refs [133, 134]. Due to the lack of experimental data, most of the calculated states have no experimental counterpart and their existence needs verification. Ref. [134] also estimates two-body decay widths, and obtains values of less than 50 MeV for some of the states.

Baryon Spectroscopy with \bar{P} ANDA

The \bar{P} ANDA experiment is well-suited for a comprehensive baryon spectroscopy program, in particular in the spectroscopy of (multi-)strange and possibly also charmed baryons. In $\bar{p}p$ collisions, a large fraction of the inelastic cross section is associated with channels resulting in a baryon antibaryon pair in the final state. As an example, at 3 GeV/c \bar{p} momentum the total $\bar{p}p$ cross section is 77 mb, the inelastic cross section is 53 mb, with a one to one ratio of baryonic final states and of annihilation into mesons. At higher \bar{p} momenta the yield of channels with baryonic final states exceeds that of the mesonic channels, *e.g.* at $p_{\bar{p}} = 12$ GeV/c the ratio is ~ 2.2 . To a large extent reactions with baryonic final states proceed via excited states giving access to the decay modes of the populated resonances and to the angular distributions of the decay particles. A particular benefit of using antiprotons in the study of (multi-)strange and charmed baryons is that in $\bar{p}p$ collisions no production of extra kaons or D mesons is required for strangeness or charm conservation, respectively. This reduces the energy threshold as

J^P	$(D, L_N^P) S$	Octet members			Singlets
$1/2^+$	$(56, 0_0^+)$	$1/2 N(939)$	$\Lambda(1116)$	$\Sigma(1193)$	$\Xi(1318)$
$1/2^+$	$(56, 0_2^+)$	$1/2 N(1440)$	$\Lambda(1600)$	$\Sigma(1660)$	$\Xi(?)$
$1/2^-$	$(70, 1_1^-)$	$1/2 N(1535)$	$\Lambda(1670)$	$\Sigma(1620)$	$\Xi(?)$ $\Lambda(1405)$
$3/2^-$	$(70, 1_1^-)$	$1/2 N(1520)$	$\Lambda(1690)$	$\Sigma(1670)$	$\Xi(1820)$ $\Lambda(1520)$
$1/2^-$	$(70, 1_1^-)$	$3/2 N(1650)$	$\Lambda(1800)$	$\Sigma(1750)$	$\Xi(?)$
$3/2^-$	$(70, 1_1^-)$	$3/2 N(1700)$	$\Lambda(?)$	$\Sigma(?)$	$\Xi(?)$
$5/2^-$	$(70, 1_1^-)$	$3/2 N(1675)$	$\Lambda(1830)$	$\Sigma(1775)$	$\Xi(?)$
$1/2^+$	$(70, 0_2^+)$	$1/2 N(1710)$	$\Lambda(1810)$	$\Sigma(1880)$	$\Xi(?)$ $\Lambda(?)$
$3/2^+$	$(56, 2_2^+)$	$1/2 N(1720)$	$\Lambda(1890)$	$\Sigma(?)$	$\Xi(?)$
$5/2^+$	$(56, 2_2^+)$	$1/2 N(1680)$	$\Lambda(1820)$	$\Sigma(1915)$	$\Xi(2030)$
$7/2^-$	$(70, 3_3^-)$	$1/2 N(2190)$	$\Lambda(?)$	$\Sigma(?)$	$\Xi(?)$ $\Lambda(2100)$
$9/2^-$	$(70, 3_3^-)$	$3/2 N(2250)$	$\Lambda(?)$	$\Sigma(?)$	$\Xi(?)$
$9/2^+$	$(56, 4_4^+)$	$1/2 N(2220)$	$\Lambda(2350)$	$\Sigma(?)$	$\Xi(?)$
Decuplet members					
$3/2^+$	$(56, 0_0^+)$	$3/2 \Delta(1232)$	$\Sigma(1385)$	$\Xi(1530)$	$\Omega(1672)$
$3/2^+$	$(56, 0_2^+)$	$3/2 \Delta(1600)$	$\Sigma(?)$	$\Xi(?)$	$\Omega(?)$
$1/2^-$	$(70, 1_1^-)$	$1/2 \Delta(1620)$	$\Sigma(?)$	$\Xi(?)$	$\Omega(?)$
$3/2^-$	$(70, 1_1^-)$	$1/2 \Delta(1700)$	$\Sigma(?)$	$\Xi(?)$	$\Omega(?)$
$5/2^+$	$(56, 2_2^+)$	$3/2 \Delta(1905)$	$\Sigma(?)$	$\Xi(?)$	$\Omega(?)$
$7/2^+$	$(56, 2_2^+)$	$3/2 \Delta(1950)$	$\Sigma(2030)$	$\Xi(?)$	$\Omega(?)$
$11/2^+$	$(56, 4_4^+)$	$3/2 \Delta(2420)$	$\Sigma(?)$	$\Xi(?)$	$\Omega(?)$

Table 4.41: Quark-model assignments for some of the known baryon states in flavor-spin SU(6) basis. Part of the spin-parity assignments are not well established and need confirmation (taken from [122]).

e.g. compared to pp collisions and thus the number of background channels. In addition, the requirement that the patterns found in baryon and antibaryon channels have to be identical reduces the systematic experimental errors. Strange, multi-strange and charmed baryons are characterized by their or their daughters' displaced decay vertices, which can be identified thanks to the good tracking capability of the \bar{P} ANDA tracking detectors (MVD, central tracker, tracking detectors of the forward spectrometer).

Production cross sections for Ξ resonances are expected to be of the same order as for ground state Ξ production, *i.e.* for the reaction $\bar{p}p \rightarrow \Xi\bar{\Xi}$ for which a cross section up to $2\mu\text{b}$ has been measured [135, 136]. The $\Xi^*(\bar{\Xi}^*)$ yields will thus be sufficiently high to allow good statistics studies analyzing the various Ξ^* decay modes such as $\Xi\pi$, $\Xi\pi\pi$, $\Lambda\bar{K}$, $\Sigma\bar{K}$, $\Xi\eta$, and others. Given the extremely scarce experimental information on the Ξ excitation spectrum available, the discovery potential of \bar{P} ANDA seems to be particularly large for Ξ resonances. One should also note that Ξ resonances are in general much narrower than nucleon or Δ resonances which helps to separate contributions of

different states.

The very poorly known Ω spectrum can also be studied, however the creation of an additional $s\bar{s}$ pair has to be paid by a reduction of the cross section. No experimental data exist for the reaction $\bar{p}p \rightarrow \Omega\bar{\Omega}$, its predicted maximum cross section is $\sim 2\text{nb}$ [137], to our knowledge the only existing theoretical estimate. Some confidence in this prediction may be drawn from the consistency of calculated cross sections with experimental data for other binary reactions in $\bar{p}p$ collisions [137]. At a luminosity of $10^{32}\text{cm}^{-2}\text{s}^{-1}$ a cross section of 2nb would still correspond to ~ 700 produced $\Omega\bar{\Omega}$ pairs per hour which allows to identify excited Ω states and their most important decay modes.

For all non-charmed baryons the HESR energy range is sufficient to access excitation energies up to the continuum regime, and thus to populate the complete discrete part of the spectrum. Depending on the hyperon resonances and their decay modes to be studied, the \bar{p} beam momentum should be chosen such that the excess energy above the threshold for the respective final state is as low as possible in order to limit the number of partial waves and to facilitate the separation of different resonances.

Also for $\bar{p}p \rightarrow \bar{\Lambda}_c\Lambda_c, \bar{\Sigma}_c\Sigma_c, \bar{\Lambda}_c\Sigma_c/\Lambda_c\bar{\Sigma}_c$ reactions no experimental data exist. For the $\bar{\Lambda}_c^+\Lambda_c^+$ final state [137] predicts a cross section up to $0.2\mu\text{b}$ which is much larger than for $\Omega\bar{\Omega}$. However, the decay length of the Λ_c^+ hyperon is only $c\tau(\Lambda_c^+) = 60\mu\text{m}$, which is too short to be detected by its displaced vertex. It has only few percent branching for channels with a Λ hyperon in the final state which could be easily identified by its delayed decay. Thus, in order to estimate the capability of \bar{P} ANDA to identify final states with charmed baryons, detailed simulations of these channels are being planned. One should also note that for charmed baryon resonances the range of excitation energies accessible is restricted due to the kinematic limit at the HESR of $\sqrt{s} = 5.5\text{GeV}$, which allows to populate excitation energies up to 0.93GeV and 0.76GeV above the Λ_c and Σ_c ground states, respectively.

Recent theoretical studies using a chiral coupled channel approach [138, 139] predict the existence of narrow crypto-exotic baryon resonances with hidden charm. In particular, these calculations find a narrow resonance at $3.52\text{GeV}/c^2$ being a coupled-channel bound state of $\eta_c\Lambda$ and $\bar{D}\Sigma_c$ which should dominantly decay to $\eta'N$. Whereas the exotic or crypto-exotic baryon resonances for systems with open charm ranging from $C = -1$ to $C = +3$ also found as dynamically generated states in the same approach [138, 139] are not accessible within

the HESR energy range, we see a good perspective to confirm or to rule out the existence of narrow crypto-exotic baryons with hidden charm in the mass range between $3 \text{ GeV}/c^2$ and $4 \text{ GeV}/c^2$ in the PANDA experiment.

Benchmark Channels

In the context of baryon spectroscopy, the reaction

$$\bar{p}p \rightarrow \Xi^+ \Xi^- \pi^0$$

with

$$\Xi^- \rightarrow \Lambda \pi^-, \Lambda \rightarrow p \pi^-$$

(and *c.c.*) has been chosen as benchmark channel for the simulation studies. As a first step, the events have been generated isotropically over the phase space. The goal of these simulation studies is to reconstruct $\Xi^- \pi^0$ pairs (and *c.c.*) as one of the daughter states in the decay of Ξ resonances, to deduce the acceptance function of the PANDA detector - and thus the capability to determine the population of the three-body final state across the full Dalitz plot, and to explore the suppression of the presumed dominant background channels. The capability of identifying specific Ξ resonances with their quantum numbers in the presence of a continuum distribution and other Ξ resonances in the same final state involves a partial wave analysis, which is beyond the scope of the studies for this report.

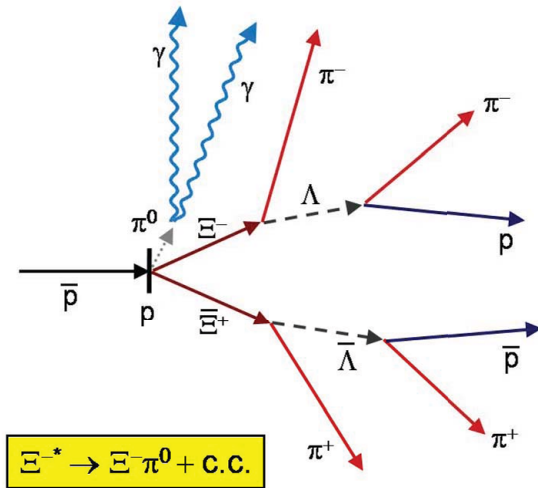


Figure 4.51: Schematic illustration of the investigated $\bar{p}p \rightarrow \Xi^+ \Xi^- \pi^0$ reaction with the considered decay branches. The reaction is characterized by four delayed decay vertices.

In order to take into account possible interactions of the charged Ξ baryons with the detector material and their bending in the magnetic field within their propagation before decay ($c\tau = 4.9 \text{ cm}$), their decays are not generated on event generator level but within the GEANT4 detector simulation.

The selected antiproton beam momentum is $p_{\bar{p}} = 6.57 \text{ GeV}/c$ corresponding to a maximum $\Xi\pi$ invariant mass of $2.45 \text{ GeV}/c^2$. For the $\bar{p}p \rightarrow \Xi\Xi$ reaction at this incident momentum Ref. [137] predicts a cross section of about $0.3 \mu\text{b}$. In the following this value is also used as estimate for the $\bar{p}p \rightarrow \Xi\Xi\pi^0$ reaction, taking into account that the predicted $\Xi\Xi$ cross section is below the measured value.

Background Reactions

The following background channels are considered:

- $\bar{p}p \rightarrow \bar{\Lambda}\Lambda\pi^+\pi^-\pi^0 \rightarrow \bar{p}p\pi^+\pi^-\pi^+\pi^-\pi^0$
- $\bar{p}p \rightarrow \bar{\Sigma}(1385)^+\Sigma(1385)^-\pi^0 \rightarrow \bar{\Lambda}\Lambda\pi^+\pi^-\pi^0 \rightarrow \bar{p}p\pi^+\pi^-\pi^+\pi^-\pi^0$
- $\bar{p}p \rightarrow \bar{p}p\pi^+\pi^-\pi^+\pi^-\pi^0$
- DPM generic background

The background channel (a) is expected to be the main background source since it has the identical final state as the signal, and since it also has the same intermediate state characterized by a $\Lambda\bar{\Lambda}$ pair. This background will be suppressed by requiring the Ξ and Ξ delayed decays according to a decay length $c\tau = 4.9 \text{ cm}$ visible in a kink in the charged particle track. In addition good $\Lambda\pi^-$ ($\bar{\Lambda}\pi^+$) invariant mass resolution helps to distinguish the Ξ^- (Ξ^+) mass peak from the $\Lambda\pi^-$ ($\bar{\Lambda}\pi^+$) continuum. The cross section for this channel is not known. For the reactions $\bar{p}p \rightarrow \bar{\Lambda}\Lambda\pi^+\pi^-$ and $\bar{p}p \rightarrow \bar{\Lambda}\Lambda 2\pi^+ 2\pi^-$ Ref. [140] lists a measured cross section of $(59 \pm 12) \mu\text{b}$ and $(8 \pm 4) \mu\text{b}$ at $p_{\bar{p}} = 6.93 \text{ GeV}/c$, respectively. In the following a cross section of $70 \mu\text{b}$ for process (a) is assumed.

In reality, intermediate and final states of channel (a) are expected to have some contribution from $\Sigma(1385)^-$ (and *c.c.*) production according to channel (b). Even if this fraction is small, it might be of concern due to the relatively close masses of $\Sigma(1385)^-$ and Ξ^- to be reconstructed from $\Lambda\pi^-$ pairs (and *c.c.*). The cross section for this channel is also not known. For the reaction $\bar{p}p \rightarrow \bar{\Sigma}(1385)^-\Sigma(1385)^+$ Ref. [140] lists a measured cross section of $(14 \pm 3) \mu\text{b}$ at $p_{\bar{p}} = 5.7 \text{ GeV}/c$. In the following a cross section of $20 \mu\text{b}$ for process (b) is assumed.

Channel (c) is expected to have the largest cross section of the specific background reactions considered here, however it has no delayed decays and should be suppressed very efficiently by requiring delayed Λ and $\bar{\Lambda}$ vertices. For this channel Ref. [140] lists a cross section of $(280 \pm 30) \mu\text{b}$ at $p_{\bar{p}} = 6.94 \text{ GeV}/c$. In the following a cross section of $300 \mu\text{b}$ for process (c) is assumed.

Analysis Strategy

The following selection criteria are chosen in order to discriminate signal and background events:

1. p and π^- (\bar{p} and π^-) are fitted to a common vertex with χ probability $P > 0.001$. Proton candidates are selected from charged tracks with **VeryLoose** PID criteria, pion candidates from all charged tracks.
2. The mass of Λ , $\bar{\Lambda}$ candidates has to fulfill the condition $1.105 \text{ GeV}/c^2 < m_{\Lambda} < 1.125 \text{ GeV}/c^2$.
3. Λ and π^- ($\bar{\Lambda}$ and π^+) are fitted to a common vertex with χ probability $P > 0.001$.
4. The mass of Ξ^- , $\bar{\Xi}^+$ candidates has to fulfill the condition $1.31 \text{ GeV}/c^2 < m_{\Xi} < 1.33 \text{ GeV}/c^2$.
5. 2γ candidates with $E > 25 \text{ MeV}$ each are combined to a π^0 candidate within a mass window $110 \text{ MeV}/c^2 < m_{\pi^0} < 160 \text{ MeV}/c^2$.
6. Ξ^- and $\bar{\Xi}^+$ are fitted to a common vertex with the assumption that the π^0 is emitted from the same vertex. In addition constraints on the total 4-momentum are set. Combinations with χ probability $P < 0.001$ are rejected.
7. Only events containing exactly one combination of particles fulfilling all criteria listed above are further considered.
8. The Ξ^- , $\bar{\Xi}^+$ decay vertices have to fulfill the condition that the sum of their distances from the interaction point is larger than 2 cm.
9. The complete event is refitted with mass constraints on the Ξ^- , $\bar{\Xi}^+$, Λ , $\bar{\Lambda}$, and π^0 .

Simulation Results

For the signal and all background channels the $\bar{p}p\pi^+\pi^-\pi^+\pi^-\pi^0$ final state has been investigated.

Channel	Number of events
$\bar{p}p \rightarrow \bar{\Xi}^+\Xi^-\pi^0$	$8.13 \cdot 10^5$
$\bar{p}p \rightarrow \bar{\Lambda}\Lambda\pi^+\pi^-\pi^0$	$8 \cdot 10^5$
$\bar{p}p \rightarrow \bar{\Sigma}(1385)^-\Sigma(1385)^+\pi^0$	$8 \cdot 10^5$
$\bar{p}p \rightarrow \bar{p}p\pi^+\pi^-\pi^+\pi^-\pi^0$	$3 \cdot 10^5$
DPM generic	$2 \cdot 10^7$

Table 4.42: Number of events simulated for signal and background channels. For the signal and the specific background channels the number refers to the $\bar{p}p\pi^+\pi^-\pi^+\pi^-\pi^0$.

The size of the analyzed signal and background samples is given in Table 4.42.

Table 4.43 shows the signal efficiency and the number of remaining background events depending of the cut condition on the sum of the distances of the Ξ and $\bar{\Xi}$ decay vertices from the interaction point $D_{\Xi\bar{\Xi}}^{(IP)} = \text{dist}(\bar{\Xi} - \text{IP}) + \text{dist}(\Xi - \text{IP})$. The selection $D_{\Xi\bar{\Xi}}^{(IP)} > 2 \text{ cm}$ is used for further analysis. With this selection the signal reconstruction efficiency is about 16%. Taking into account a luminosity of $\mathcal{L} = 9000/\text{nb}$ per day, a cross section $\sigma = 0.3 \mu\text{b}$, and the branching fraction of the final state, this corresponds to $1.7 \cdot 10^5$ reconstructed signal events per day.

Based on the selection criteria, 4 remaining events are found in the background channel $\bar{p}p \rightarrow \bar{\Lambda}\Lambda\pi^+\pi^-\pi^0$, whereas no events survive the selection criteria in the other specific background channels and in the DPM generic background sample. Based on the cross sections assumed for signal and background channels as given above, the resulting values for signal-to-background ratio are much larger than one in all cases:

- (a) $S/B = 135$ for $\bar{p}p \rightarrow \bar{\Lambda}\Lambda\pi^+\pi^-\pi^0$
- (b) $S/B > 1896$ for $\bar{p}p \rightarrow \bar{\Sigma}(1385)^-\Sigma(1385)^+\pi^0$
- (c) $S/B > 47$ for $\bar{p}p \rightarrow \bar{p}p\pi^+\pi^-\pi^+\pi^-\pi^0$
- (d) $S/B > 19$ for DPM generic.

Fig. 4.52 shows the invariant mass resolution in the reconstruction of a $\Xi^-\pi^0$ pair which is relevant for the determination of width and pole position of Ξ resonances as a function of the $\Xi^-\pi^0$ invariant mass. Fig. 4.53, showing the ratio of the number of reconstructed events relative to that of the generated Monte Carlo events in a Dalitz plot of the $\bar{\Xi}^+\Xi^-\pi^0$ final state, demonstrates that the reconstruction efficiency varies smoothly across the 3-body phase space at average values of $\sim 15\%$.

Channel	$\epsilon(D_{\Xi\Xi}^{(IP)} > 2 \text{ cm})$	$\epsilon(D_{\Xi\Xi}^{(IP)} > 4 \text{ cm})$	$\epsilon(D_{\Xi\Xi}^{(IP)} > 6 \text{ cm})$
$\bar{p}p \rightarrow \Xi\Xi\pi^0$	15.8%	15.0%	13.9%
	$N_B(D_{\Xi\Xi}^{(IP)} > 2 \text{ cm})$	$N_B(D_{\Xi\Xi}^{(IP)} > 4 \text{ cm})$	$N_B(D_{\Xi\Xi}^{(IP)} > 6 \text{ cm})$
$\bar{p}p \rightarrow \bar{\Lambda}\Lambda\pi^+\pi^-\pi^0$	4	2	1
$\bar{p}p \rightarrow \bar{\Sigma}(1385)^-\Sigma(1385)^+\pi^0$	0	0	0
$\bar{p}p \rightarrow \bar{p}p\pi^+\pi^-\pi^+\pi^-\pi^0$	0	0	0
DPM generic	0	0	0

Table 4.43: Signal efficiency and remaining number of background events depending on the cut condition on the Ξ and Ξ decay vertices (explanation see text).

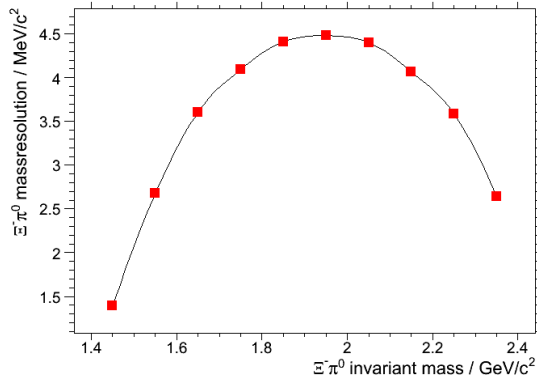


Figure 4.52: Resolution achieved in the invariant mass of reconstructed $\Xi\pi^0$ pairs as a function of the $\Xi\pi^0$ invariant mass.

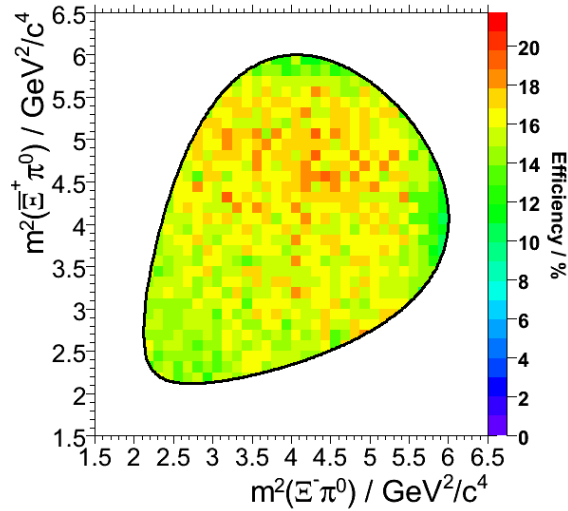


Figure 4.53: Dalitz plot showing the reconstruction efficiency for the $\bar{p}p \rightarrow \Xi^+\Xi^-\pi^0$ reaction.

4.3 Non-perturbative QCD Dynamics

An effective description of reactions in hadron physics relies on the identification of the relevant degrees of freedom. At highest energies quark and gluon degrees of freedom seem to describe the observed reactions very accurately. The energy regime for $\bar{p}p$ collisions at HESR is well suited to study the onset of hadron degrees of freedom. In this regime both *ansätze* are viable. Thus they can be experimentally tested separately and compared to each other.

In the quark picture hyperon pair production either involves the creation of a quark-antiquark pair or the knock out of such pairs out of the nucleon sea. Hence, the creation mechanism of quark-antiquark pairs and their arrangement to hadrons can be studied by measuring the reactions of the type $\bar{p}p \rightarrow \bar{Y}Y$, where Y denotes a hyperon. By comparing several reactions involving different quark flavours the OZI rule [141, 142, 143], and its possible violation, can be tested for different levels of disconnected quark-line diagrams separately.

The parity violating weak decay of most ground state hyperons introduces an asymmetry in the distribution of the decay particles. This is quantified by the decay asymmetry parameter and gives access to spin degrees of freedom for these processes, both to the antihyperon/hyperon polarisation and spin correlations. One open question is how these observables relate to the underlying degrees of freedom.

All strange hyperons, as well as single charmed hyperons are energetically accessible in $\bar{p}p$ collisions at HESR. A systematic investigation of these reactions will bring new information on single/multiple strangeness and charm production and its dependence on spin observables. This is particularly true above 2 GeV/c where practically nothing is known about the differential distributions and spin observables. The large amount of observables accessible and high statistics \bar{P} ANDA data will allow for a partial wave analysis. Thus it will be possible to pin down relevant quantum numbers, coupling constants and possibly find new resonances.

4.3.1 Previous Experiments

The $\bar{p}p \rightarrow \bar{\Lambda}\Lambda$ process can be considered as a prototype reaction in the study of production of strangeness. This reaction exhibits strong polarisation phenomena and spin correlation parameters

can be extracted when both the $\bar{\Lambda}$ and Λ are reconstructed. The PS185 experiment at LEAR has provided high quality data on the $\bar{p}p \rightarrow \bar{\Lambda}\Lambda$ reaction from threshold (1.436 GeV/c) up to 2 GeV/c [144] which was the maximum momentum of LEAR (see Fig. 4.54). The data above 2 GeV/c are dominated by low statistics bubble chamber experiments and no data exist above 7 GeV/c. Little, if anything, is known about the $\bar{p}p \rightarrow \bar{Y}Y$ reaction in the multiple strangeness sector. Only total cross sections based on a few events have been measured in the double strangeness channel, *i.e.* the production of Ξ hyperons [145]. Nothing at all is known about this reaction for charmed hyperons. All the available data on the total cross section for the $\bar{p}p \rightarrow \bar{Y}Y$ reaction is summarised in Fig. 4.54. The high statistics data samples from PS185 comprises 40k completely reconstructed $\bar{p}p \rightarrow \bar{\Lambda}\Lambda$ events [146]. Corresponding bubble chamber experiments have, at most, a few hundred complete events [145]. There is one counter experiment at 6 GeV/c with comparable statistics to PS185 [147], but normally only one hyperon could be reconstructed for the events which meant that no spin correlation could be measured.

One example which shows the strength of hyperon pair production in $\bar{p}p$ annihilations is the following: By measuring spin correlations in the PS185 experiment, it has been shown that the $\bar{\Lambda}\Lambda$ pairs are practically always produced in a triplet state [144]. It is natural to associate this with the spin degrees of freedom in the creation process of the $s\bar{s}$ pair since the spin of the Λ hyperon is primarily carried by its strange quark. In other words, the $s\bar{s}$ pair is predominantly created in a triplet state. The LEAR data were taken near threshold; and one should verify that this feature persists as one goes up in momentum transfer into the more perturbative region. Both meson-exchange models and models based on the constituent quark model have been applied to the near threshold data from LEAR and both give a relatively good description of the main features of the data [148, 149]. The triplet state is produced by assuming that the $s\bar{s}$ pair is created with the quantum number of the vacuum, 3P_0 , or with the gluon quantum number, 3S_1 , for the quark based models. Alternatively, it has been suggested that $s\bar{s}$ pairs may be extracted from the nucleon or antinucleon sea instead of being created in the reaction itself [150]. In this scenario the triplet state would reflect the fact that the $s\bar{s}$ pairs are polarised in the nucleon sea. In meson-exchange models, the triplet state is interpreted as being due to a strong tensor force generated by the exchange of K and K^* mesons.

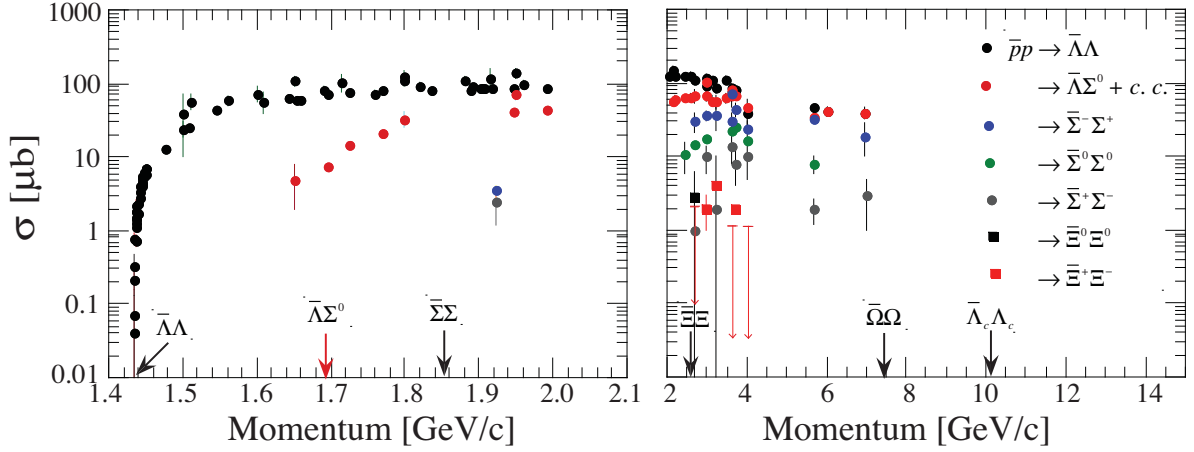


Figure 4.54: Total cross sections for the $\bar{p}p \rightarrow \bar{Y}Y$ reaction in the momentum range of the HESR. The figure to the left is an expanded view of the threshold region, which reveals channels of single strangeness production. The figure to the right shows the experimental situation for momenta above 2 GeV/c [144, 145]. The absence of error bars for some $\bar{\Xi}^+\Xi^-$ points are because they are missing in reference [135]. The upper limits in red also refer to this channel. The arrows pointing to the momentum axis indicate the threshold momenta for the different hyperon families.

4.3.2 Experimental Aims

As seen from Fig. 4.54 any measurement of hyperon pair production in the PANDA energy regime will significantly improve the data set. Even in $\bar{\Lambda}\Lambda$ production, where a large data set exists, data points at momenta above 2 GeV/c and a cross check at low momenta would help understanding the production mechanism. For all other hyperon pairs PANDA will provide the first conclusive insights on the behaviour of the total cross section and first differential cross sections. The very first measurements can be provided for the pair production of charmed hyperons.

Spin observables for the $\bar{\Xi}\Xi$ reaction can be extracted similarly to the $\bar{\Lambda}\Lambda$ case. This will allow for detailed comparisons between the $s\bar{s}$ and $s\bar{s}s\bar{s}$ creation processes. A comparison between the $\bar{\Lambda}\Lambda$ channel, which filters isospin $I = 0$, to the $\bar{\Lambda}\Sigma^0$ channel (including its charge conjugate channel), which forces $I = 1$, gives opportunities to study the isospin dependence of strangeness production. In the naïve quark model the spin of the Σ^0 is opposite to that of its constituent strange quark. This should lead to differences in the spin correlations if they are related to the spin state of the created $s\bar{s}$ -pair. Studies on the production of charmed hyperons will allow for detailed comparisons between the $\bar{c}c$ and the $s\bar{s}$ creation processes. This may help to disentangle the perturbative contributions from the non-perturbative ones, as the charm production will be mainly probing the hard processes while the

strangeness production will be influenced by non-perturbative effects.

4.3.3 Reconstruction of the $\bar{p}p \rightarrow \bar{Y}Y$ Reaction

Two-body kinematics together with the relatively long lifetime of strange hyperons makes the identification and reconstruction of $\bar{Y}Y$ events rather straightforward. The identification of these reaction channels involve practically always the reconstruction of a $\bar{\Lambda}\Lambda$ pair as can be seen from the main decay channels listed in Table 4.44.

The PANDA detector allows for the reconstruction of both neutral and charged hyperons, due to its capabilities to track charged particles, to detect photons and discriminate between almost all stable particles. For neutral hyperons with charged decay modes, *e.g.* the $\Lambda \rightarrow p\pi^-$ decay channel, the decay vertex outside the interaction region is reconstructed. Neutral strange hyperons, apart from the Λ , are accompanied by photons, which will be detected in the electro-magnetic calorimeter. The reconstruction of charged hyperons involve the identification of tracks from the interaction region that exhibit a “kink” that signals the hyperon decay.

A good understanding of the response and reconstruction of tracks that originate well outside of the interaction region is important for these studies. This is further emphasised when extracting spin observables. The parity violating weak decay of hy-

Table 4.44: Properties of strange and charmed ground state hyperons [151] that are energetically accessible at \bar{P} ANDA. The hyperon, its valence quark composition, mass, decay length $c\tau$, main decay mode, branching ratio \mathcal{B} and the decay asymmetry parameter α_Y are listed.

Hyperon	Quarks	Mass [MeV/ c^2]	$c\tau$ [cm]	Main decay	\mathcal{B} [%]	α_Y
Λ	uds	1116	8.0	$p\pi^-$	64	+0.64
Σ^+	uus	1189	2.4	$p\pi^0$	52	-0.98
Σ^0	uds	1193	$2.2 \cdot 10^{-9}$	$\Lambda\gamma$	100	-
Σ^-	dds	1197	2.4	$n\pi^-$	100	-0.07
Ξ^0	uss	1315	8.7	$\Lambda\pi^0$	99	-0.41
Ξ^-	dss	1321	4.9	$\Lambda\pi^-$	100	-0.46
Ω^-	sss	1672	2.5	ΛK^-	68	-0.03
Λ_c^+	udc	2286	$6.0 \cdot 10^{-3}$	$\Lambda\pi^+$	1	-0.91(15)
Σ_c^{++}	uuc	2454		$\Lambda_c^+\pi^+$	100	
Σ_c^+	udc	2453		$\Lambda_c^+\pi^0$	100	
Σ_c^0	ddc	2454		$\Lambda_c^+\pi^-$	100	
Ξ_c^+	usc	2468	$1.2 \cdot 10^{-2}$	$\Xi^-\pi^+\pi^+$	seen	
Ξ_c^0	dsc	2471	$2.9 \cdot 10^{-3}$	$\Xi^-\pi^+$	seen	-0.6(4)
Ω_c^0	ssc	2697	$1.9 \cdot 10^{-3}$	$\Omega^-\pi^+$	seen	

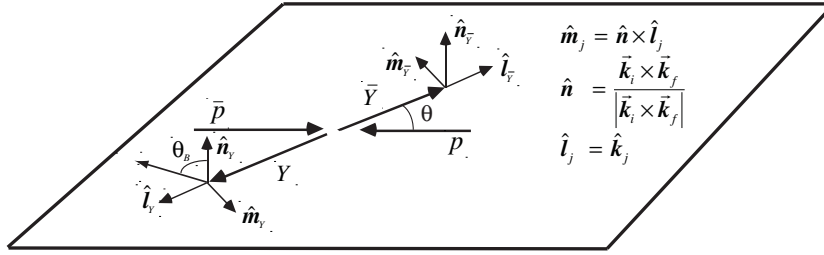


Figure 4.55: Coordinate system for the $\bar{p}p \rightarrow \bar{Y}Y$ reaction. θ is the centre-of-mass (CM) scattering angle, \vec{k}_i and \vec{k}_f are the initial \bar{p} beam and the final antihyperon momentum vectors in the CM system, respectively. These two vectors define the scattering plane and also the pseudovector $\vec{n} = \vec{k}_i \times \vec{k}_f$ which is normal to the scattering plane. These vectors are then used to define a coordinate system for the antihyperon/hyperon rest frame with one axis along \vec{n} and the two other axes in the scattering plane. The direction of the j^{th} particle momentum \vec{k}_j ($j = \bar{Y}$ or Y) in the CM system is taken as the \hat{l}_j axis. The handiness of the coordinate system is taken to be right handed.

perons gives a decay distribution in its own rest frame according to

$$I(\theta_B) = \frac{1}{4\pi} (1 + \alpha_Y P^Y \cos \theta_B), \quad (4.47)$$

where θ_B is the baryon emission angle with respect to the spin direction of the decaying hyperon, α_Y is the decay asymmetry parameter (listed in Table 4.44) and P^Y is the hyperon polarisation. The coordinate system used in the analysis is given in Figure 4.55. The axes are chosen such that a maximum use of parity conservation can be made.

Spin observables can be extracted for all strange hyperons, with the exception of Σ^- and Ω^- where

the decay asymmetry parameter is too small. The Σ^0 hyperon decays via the parity conserving electromagnetic interaction but spin observables can be extracted from the subsequent $\Lambda \rightarrow p\pi^-$ decay via

$$I(\theta_p) = \frac{1}{4\pi} \left(1 - \frac{1}{3} \alpha_\Lambda P^{\Sigma^0} \cos \theta_p \right). \quad (4.48)$$

The measured cross sections for production of single and doubly strange hyperons range from a μb to a hundred μb . These cross sections are comfortably high with hundred thousands of events produced per hour already at nominal luminosity. Nothing is experimentally known of the cross section for triple strangeness production, *i.e.* the reaction

$\bar{p}p \rightarrow \bar{\Omega}^+ \Omega^-$. The only existing theoretical estimate predicts maximum cross section of ~ 2 nb [152] which would correspond to ~ 700 produced $\bar{\Omega}^+ \Omega^-$ pairs per hour at a luminosity of $10^{32} \text{cm}^{-2} \text{s}^{-1}$. This is sufficient for a measurement of the total cross section and the differential angular distribution. No spin observables will be directly accessible for this reaction due to the very small decay asymmetry parameter.

There are two estimates for the cross section of the $\bar{p}p \rightarrow \bar{\Lambda}_c^- \Lambda_c^+$ reaction. At 15 GeV/c one predicts it to be as high as $0.1 \mu\text{b}$ [152] whereas the other estimates one order of magnitude lower cross section [?]. The asymmetry parameter in the $\Lambda_c^+ \rightarrow \Lambda \pi^+$ decay is comfortably large to access spin observables. The challenges in studying this reaction via this decay channel is that its branching ratio is only 1%. In fact, all decay channels for the Λ_c^+ have branching ratios of the order of 1% or less [151]. The decay length $c\tau$ of the Λ_c^+ cannot be used to identify the reaction as it is only $60 \mu\text{m}$. However, the Λ_c^+ and its antiparticle decay into Λ and $\bar{\Lambda}$, which have a long decay length. The reaction may be identified against a large background as it is possible to additionally pin down the interaction vertex by the reconstruction of the charged pions from the Λ_c^+ decay.

It is worthwhile to note that the decay pattern given for all charmed hyperons listed in Table 4.44 will always lead to the appearance of a Λ particle. It is therefore important to acquire a good understanding of the reconstruction of Λ particles in $\bar{\text{P}}\text{ANDA}$.

4.3.3.1 Benchmark channels

Among the variety of channels of hyperon pair production accessible at $\bar{\text{P}}\text{ANDA}$, the channels $\bar{p}p \rightarrow \bar{\Lambda}\Lambda$ and $\bar{\Xi}^+ \Xi^-$ have been chosen to prove our principle ability to reconstruct the angular and polarisation distributions. These channels exhibit the following features which make them well suited for a case study.

- $\bar{p}p \rightarrow \bar{\Lambda}\Lambda$. Though well studied close to threshold this basic channel provides an essential tool to understand the reconstruction capabilities for all hyperon pair production reactions at $\bar{\text{P}}\text{ANDA}$. This is mainly due to the fact that most hyperons decay such that a $\bar{\Lambda}(\Lambda)$ particle is produced in an intermediate state (see Table 4.44). This is also the case for the excited baryons (see sec. 4.2.5). Hence, a detailed understanding of the reconstruction and identification of $\bar{\Lambda}$ or Λ particles in $\bar{\text{P}}\text{ANDA}$ de-

tor is very important for many aspects of the $\bar{\text{P}}\text{ANDA}$ physics programme. The reconstruction of the $\bar{\Lambda}(\Lambda)$ decay products (mostly from $\bar{\Lambda} \rightarrow \bar{p}\pi^+$ and $\Lambda \rightarrow p\pi^-$) differs from ordinary charged particle reconstruction in $\bar{\text{P}}\text{ANDA}$ as the charged particles do not stem from the interaction point. This displaced vertex poses a challenge to reconstruction algorithms and special attention has to be drawn to background reduction. The extension and comparison of the well measured near-threshold data to higher momenta makes the study of this channel also interesting in its own right.

- $\bar{p}p \rightarrow \bar{\Xi}^+ \Xi^-$. This channel probes the tracking capability near the interaction region to a much larger extent than the Λ pair production. This will also be a reaction where $\bar{\text{P}}\text{ANDA}$ will provide first differential distributions. For the simulation we therefore assumed an isotropic distribution in the CM system to investigate how well this can be reconstructed with $\bar{\text{P}}\text{ANDA}$.

Study of the $\bar{p}p \rightarrow \bar{\Lambda}\Lambda$ Reaction.

Monte Carlo data for this reaction have been generated and analysed at three incoming momenta, 1.64 GeV/c, 4 GeV/c and 15 GeV/c. Approximately 10^6 events were generated for each of the three beam momenta. The lowest momentum corresponds to the near threshold region where high quality data exist from the PS185 experiment at LEAR. The data for this momentum were generated according to the experimental angular distribution [146]. An empirical function composed of two exponentials and four parameters in total was used to generate the corresponding angular distributions at the two higher momenta as suggested in Ref. [147],

$$d\sigma/dt' = ae^{bt'} + ce^{dt'} \quad (4.49)$$

Here, $t' = -\frac{1}{2}t'_{max}(1 - \cos\theta_{CM})$ is the reduced four-momentum transfer squared, where mass effects are removed from the full four momentum transfer

$$t = m_p^2 + m_\Lambda^2 - \frac{s}{2} + \frac{1}{2}t'_{max} \cos\theta_{CM} \quad (4.50)$$

with $t'_{max} = \sqrt{(s - 4m_p^2)(s - 4m_\Lambda^2)}$.

The polarisation was assumed to follow a $\sin 2\theta_{CM}$ dependence for all momenta. The reconstruction of the events was done consecutively in the following steps:

1. Identified pairs of antiprotons(protons) and $\pi^+(\pi^-)$ are fitted to a common vertex under

the hypothesis of stemming from a $\bar{\Lambda}(\Lambda)$. The χ^2 of the fit is then required to be > 0.001 .

2. The invariant $\bar{p}\pi^+$ and $p\pi^-$ masses of the reconstructed $\bar{\Lambda}$ and Λ , respectively, are required to be within about 4σ of the Λ mass, *i.e.* $1.11 \text{ GeV}/c^2 \leq M \leq 1.12 \text{ GeV}/c^2$. (See also figure 4.56.)
3. The remaining events are fitted to the $\bar{p}p \rightarrow \bar{\Lambda}\Lambda$ hypothesis in a tree-fit. Again, the χ^2 of the fit is then required to be > 0.001 .
4. Finally, cuts on the $\bar{\Lambda}$ and Λ vertices are applied. An effective cut on the displaced vertices is found to be the requirement that the sum of both path lengths is above 2 cm.

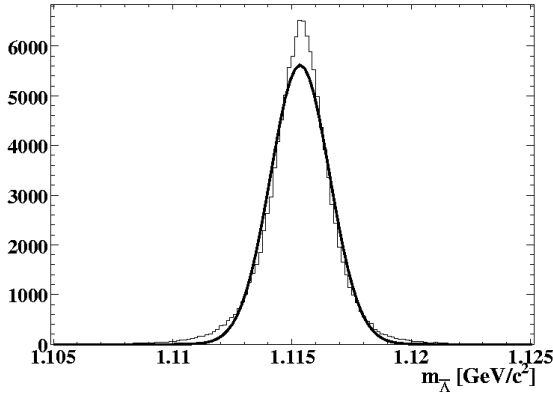


Figure 4.56: Reconstructed $\bar{p}\pi^+$ invariant mass for $\bar{\Lambda}$ candidates from the $\bar{p}p \rightarrow \bar{\Lambda}\Lambda$ reaction at 1.64 GeV/c (histogram) and a Gaussian fit to the distribution (smooth curve). The distributions at 4 and 15 GeV/c show a similar behaviour.

These criteria result in global reconstruction efficiencies of 0.11, 0.24 and 0.14 for the $\bar{p}p \rightarrow \bar{\Lambda}\Lambda$ reaction in the charged decay mode at 1.64 GeV/c, 4 GeV/c and 15 GeV/c, respectively. The reason for the lower efficiency at 1.64 GeV is that there are many pions produced with momenta below 50 MeV/c at this momentum. These cannot be reconstructed as will be shown in the discussion on polarisation below. The lower efficiency at 15 GeV/c is primarily due to a higher loss of tracks in the beam pipe. This is a result of the very forward peaked angular distribution. The reconstructed $\bar{\Lambda}$ mass at 1.64 GeV/c is shown in figure 4.56. The $\bar{\Lambda}$ mass is reconstructed obtaining a sigma of $1.2 \text{ MeV}/c^2$ at this momentum. Similar mass resolutions are obtained at the higher momenta.

The spatial distributions of decay vertices for isotropically generated $\bar{\Lambda}$ events are shown in figure 4.57. The upper figure shows the distribution at 1.64 GeV/c and the lower figure the corresponding distribution at 15 GeV/c. This illustrates the origin of the charged tracks from the $\bar{\Lambda}\Lambda$ reaction. A rather smooth dependency on the vertex position in the reconstruction efficiency is found (apart from obvious geometrical constraints). The decay vertices are reconstructed with a sigma ranging from 0.6 mm at 1.64 GeV/c to 2.8 mm at 15 GeV/c. The z component of the vertex is dominating the uncertainty and this naturally increases with higher beam momenta as the particles are emitted in smaller angles.

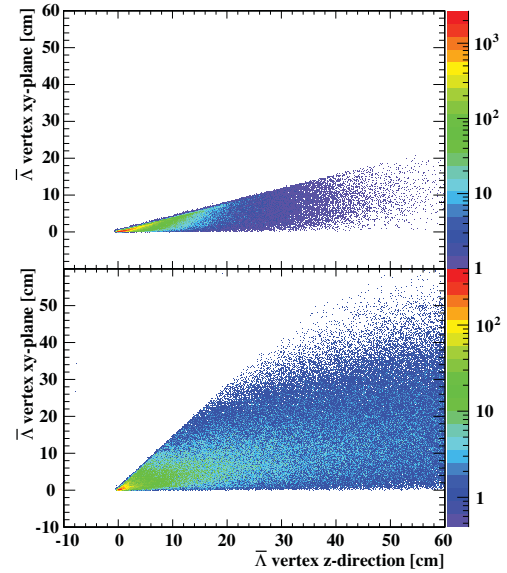


Figure 4.57: $\bar{\Lambda}$ decay vertex coordinates at beam momenta of 1.64 GeV/c (upper panel) and 15 GeV/c (lower panel) for phase space distributed events.

Center-of-mass angular distributions for the outgoing $\bar{\Lambda}$ at 1.64 GeV/c and 4 GeV/c are shown in figure 4.58. The Monte Carlo generated events are the black histograms and the angular dependencies are taken from references [146] and [147], respectively. The red histograms show the corresponding reconstructed angular distributions (multiplied by a factor of 10 to account roughly for the overall efficiency). It is seen that the experimental acceptance covers the whole angular region for this reaction at 1.64 GeV/c. The lack of events at higher angles at 4 GeV/c is due to the exponential fall off of the generated angular distribution (see Eq. 4.49) and this is further emphasized at 15 GeV/c. The loss in the very forward direction is due to losses of events with tracks in the beam pipe region. It has been

verified that the acceptance is covering the full angular region at the two higher momenta as well, by analysing Monte Carlo event samples with isotropic CM angular distributions. This means that, after acceptance correction, the full center-of-mass angular distributions of the outgoing hyperons can be deduced for this reaction over the full momentum range of HESR.

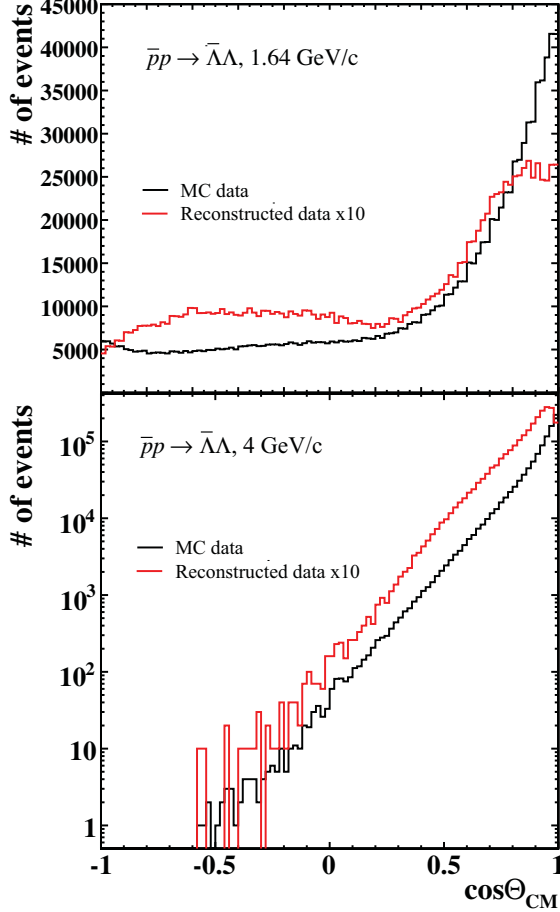


Figure 4.58: Centre-of-mass angular distributions for the $\bar{\Lambda}$ hyperon from the $\bar{p}p \rightarrow \bar{\Lambda}\Lambda$ reaction at 1.64 GeV/c (upper figure) and 4 GeV/c (lower figure). The Monte Carlo generated angular distributions are shown in black; the reconstructed angular distributions (multiplied by a factor of ten) are shown in red.

The analysis of spin observables require the knowledge of the angular distribution of the hyperon decay particles, the proton and pion, in the rest frame of the hyperon. This angular distribution is isotropic for the unpolarised case. The coordinate system that is used for this reconstruction is given in figure 4.55. It should be noted that the axes of this coordinate system vary from event to event. In this coordinate system the projections onto the $\hat{\mathbf{l}}$

and $\hat{\mathbf{m}}$ axes are isotropic independently of the hyperon polarisation. The distribution along the $\hat{\mathbf{n}}$ axis will exhibit a slope equal to $\alpha_{\Lambda} P^{\Lambda}$. Here α_{Λ} is the decay asymmetry parameter and P^{Λ} is the polarisation (see Eq. 4.47). CP conservation requires that $P^{\Lambda} = P^{\bar{\Lambda}}$. Figure 4.60 shows the projections of the decay antiproton emission vector along the $\hat{\mathbf{l}}$, $\hat{\mathbf{n}}$ and $\hat{\mathbf{m}}$ axes for reconstructed non-polarised events at 1.64 GeV/c. These distributions are clearly non-isotropic for all projections which shows that the $\bar{\text{P}}\text{ANDA}$ acceptance is inhomogeneous for these reactions. Such distributions will therefore be used for acceptance corrections in the extraction of the polarisation. The non-isotropies are related to an inefficiency to reconstruct low-energy pions in $\bar{\text{P}}\text{ANDA}$.

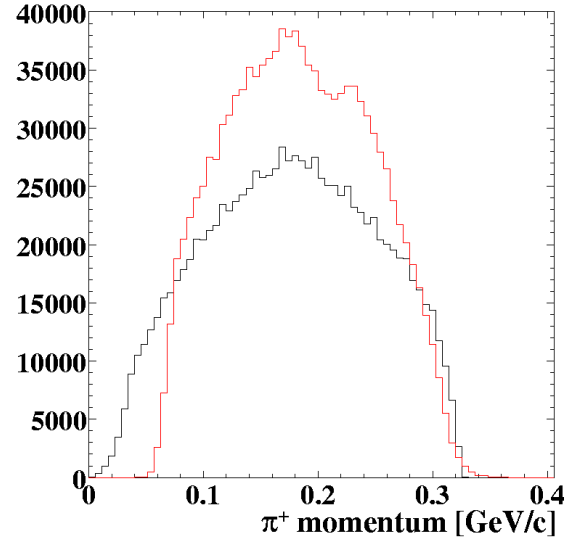


Figure 4.59: Absolute value of the pion momentum in the laboratory system from the $\bar{\Lambda}$ decay 1.64 GeV/c. The black histogram is Monte Carlo data and the red histogram shows the reconstructed events. The histogram for the reconstructed has been multiplied by a factor of ten.

That low-energy pions cannot be reconstructed efficiently can be seen in figure 4.59 which shows the absolute value of the π^+ momentum in the laboratory system from the $\bar{\Lambda}$ decay at 1.64 GeV/c. The black histogram shows the Monte Carlo generated events and the red histogram shows the momenta from the reconstructed events multiplied by a factor of ten. It is clear from this picture that pions with momenta lower than about 50 MeV/c are not reconstructed. This is also the origin of the non-isotropies in figure 4.60. The same pattern is seen at higher momenta, but the magnitude of the effect decreases with increasing beam momentum since the amount of low energy pions decreases with increasing beam

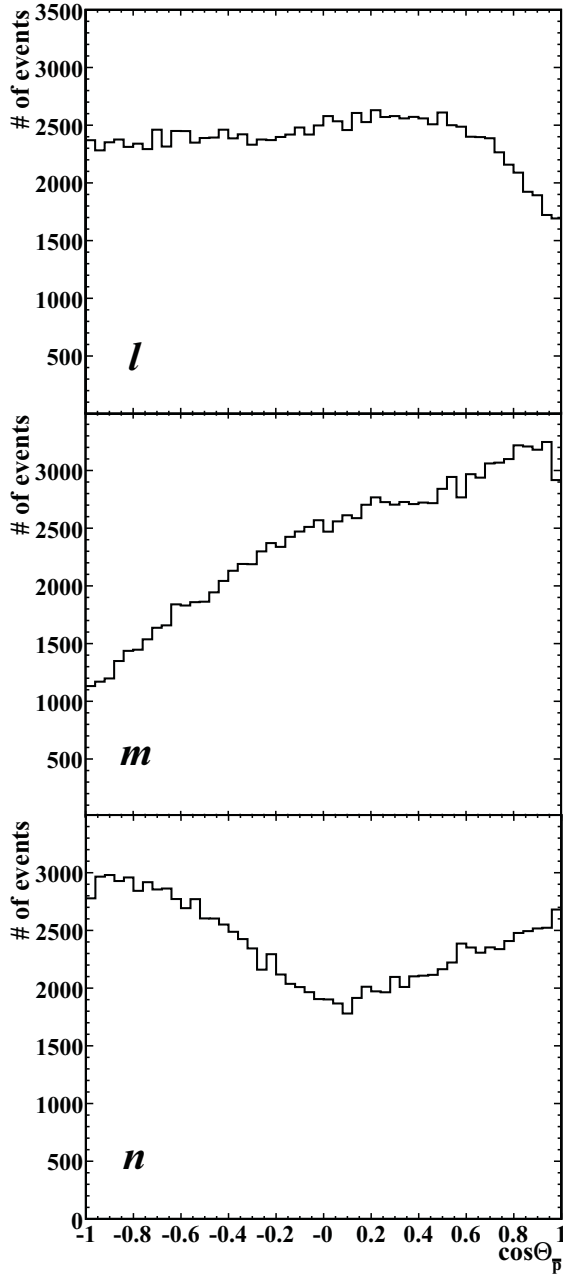


Figure 4.60: Angular distributions of \bar{p} from the $\bar{\Lambda} \rightarrow \bar{p}\pi^+$ decay reconstructed in the \bar{P} ANDA acceptance in the hyperon rest frame according to the coordinate system defined in figure 4.55.

momentum.

The polarisation distributions are extracted by applying the method of moments [153] with acceptance correction functions from non-polarised data in bins of $\cos\theta_{CM}$. The polarisation is finally extracted using both hyperon polarisations, *i.e.* $(P^{\bar{\Lambda}} + P^{\Lambda})/2$. The extracted polarisations at 1.64 GeV/ c and 4 GeV/ c are shown in figure 4.61 together with

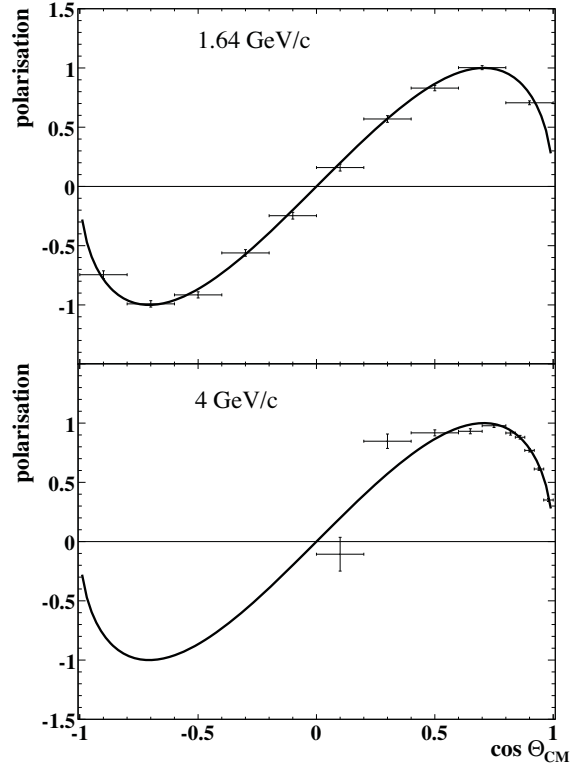


Figure 4.61: Reconstructed polarisation from $\bar{p}p \rightarrow \bar{\Lambda}\Lambda$ reaction at 1.64 GeV/ c (upper figure) and 4 GeV/ c (lower figure). The solid line is the $\sin 2\theta_{CM}$ function that is used to generate the polarisation.

the superimposed $\sin 2\theta_{CM}$ function which is used to generate the polarisation data. The large error bars at the higher angles at 4 GeV/ c are due to the functional form for the angular distribution which strongly suppresses events at large CM emission angles. This is further emphasised at 15 GeV/ c where reasonable statistics is only acquired at the uppermost angular bins. The background for this channel is treated in section 4.3.3.2.

Study of the $\bar{p}p \rightarrow \bar{\Xi}^+\Xi^-$ Reaction.

$4 \cdot 10^6$ Monte Carlo events have been generated and analysed at 4 GeV/ c for this reaction. This momentum was chosen because it is also used for analysing events for the $\bar{\Lambda}\Lambda$ channel. No experimental information on angular distributions are available for the $\bar{p}p \rightarrow \bar{\Xi}^+\Xi^-$ channel. The production of two $s\bar{s}$ quark-pairs in this reaction will most likely lead to a less steep angular distribution than in the $\bar{\Lambda}\Lambda$ case. An isotropic CM angular distribution was therefore chosen. The reconstructed angular distribution will then directly give the angular acceptance for the process. A $\sin 2\theta_{CM}$ function was used

for the polarisation. The reaction was studied in the $\Xi^+ \rightarrow \bar{\Lambda}\pi^+ \rightarrow \bar{p}\pi^+\pi^+$ ($\Xi^- \rightarrow \Lambda\pi^- \rightarrow p\pi^-\pi^-$) decay channel which is illustrated in figure 4.62.

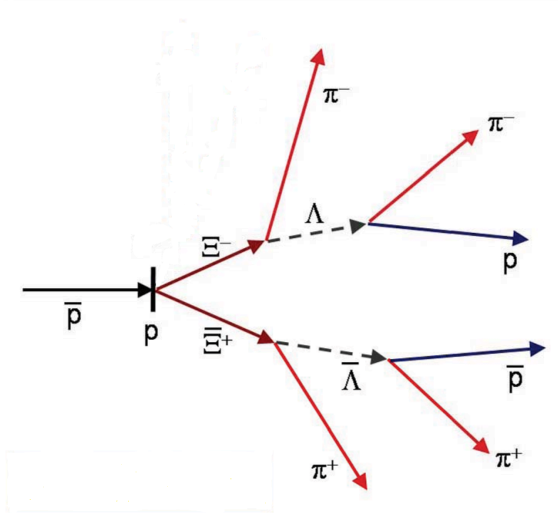


Figure 4.62: Schematic illustration of the topology for the investigated $\bar{p}p \rightarrow \Xi^+\Xi^-$ reaction. The characteristic pattern of this reaction is four separated decay vertices

The reconstruction was made in the following steps:

1. Identified pairs of antiprotons(protons) and $\pi^+(\pi^-)$ are fitted to a common vertex under a $\bar{\Lambda}(\Lambda)$ hypothesis. The χ^2 of the fit is then required to be > 0.001 .
2. The invariant $\bar{p}\pi^+$ masses of the reconstructed $\bar{\Lambda}$ and Λ are required to be close to the Λ mass, $1.11 \text{ GeV}/c^2 \leq M \leq 1.12 \text{ GeV}/c^2$.
3. Pairs of $\bar{\Lambda}(\Lambda)$ and $\pi^+(\pi^-)$ are fitted to a common vertex under a $\Xi^+(\Xi^-)$ hypothesis. The χ^2 of the fit is then required to be > 0.001 .
4. The invariant mass of the reconstructed Ξ^+ and Ξ^- are required to be close to the Ξ^- mass, *i.e.* $1.31 \text{ GeV}/c^2 \leq M \leq 1.33 \text{ GeV}/c^2$.
5. The remaining events are fitted to the $\bar{p}p \rightarrow \Xi^+\Xi^-$ hypothesis in a tree-fit. The χ^2 of the fit is then required to be > 0.001 .

These criteria result in an overall reconstruction efficiency of about 0.17. The reconstructed invariant Ξ^+ mass is shown in figure 4.63. The Ξ^+ mass is reconstructed with a sigma of $2.1 \text{ MeV}/c^2$. The sigma of reconstructed Λ mass is $1.7 \text{ MeV}/c^2$. The Ξ and Λ decay vertices are reconstructed with a sigma of

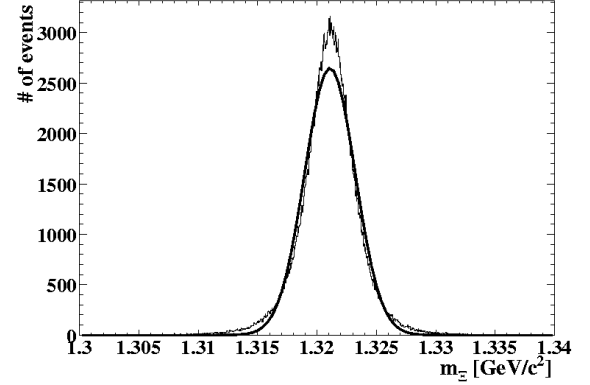


Figure 4.63: Reconstructed Ξ^+ mass for the $\bar{p}p \rightarrow \Xi^+\Xi^-$ reaction at $4 \text{ GeV}/c$.

5.2 mm and 4.7 mm, respectively. The dominating contribution is the resolution in the z direction.

The reconstructed Ξ^+ centre-of-mass angular distribution is shown in figure 4.64. The acceptance does not vary more than a factor of two over the full angular range which means that the distribution can be extracted with small statistical uncertainties in all angular bins. The dip in the forward and backward directions are primarily related to events where one track is lost in the beam pipe region. One must correct for the bending of the charged Ξ tracks in the transverse direction to get the correct production momentum vector. This is done by applying the formula [151]

$$R = \frac{p_{\perp} B}{0.3} \quad , \quad (4.51)$$

where R is the radius of curvature in meters, p_{\perp} the momentum component in the transverse direction in GeV/c and B the magnetic field in tesla. This correction improves the resolution in the x and y components of the production momentum vector of the Ξ particles from $5.3 \text{ MeV}/c$ to $1.9 \text{ MeV}/c$.

The analysis of polarisation is done in the same way as for the $\bar{\Lambda}\Lambda$ case described in the previous section. Here one analyses the distribution of the Ξ decay particles, Λ and π , in the Ξ rest frame. The cosine distributions of the $\bar{\Lambda}$ distribution look quite similar to the corresponding \bar{p} distribution for the $\bar{\Lambda}\Lambda$ case. Figure 4.65 shows the extracted polarisation, using $P = (P^{\Xi^+} + P^{\Xi^-})/2$. The generated polarisation is very well reproduced by the reconstructed events when corrected for the PANDA acceptance.

Channel 1.64 GeV/c	Rec. eff.	σ [μb]	Signal
$\bar{p}p \rightarrow \bar{\Lambda}\Lambda$	0.11	64	1
$\bar{p}p \rightarrow \bar{p}p\pi^+\pi^-$	$1.2 \cdot 10^{-5}$	~ 10	$4.2 \cdot 10^{-5}$
Channel 4 GeV/c			
$\bar{p}p \rightarrow \bar{\Lambda}\Lambda$	0.23	~ 50	1
$\bar{p}p \rightarrow \bar{p}p\pi^+\pi^-$	$< 3 \cdot 10^{-6}$	$3.5 \cdot 10^3$	$< 2.2 \cdot 10^{-3}$
$\bar{p}p \rightarrow \bar{\Lambda}\Sigma^0$	$5.1 \cdot 10^{-4}$	~ 50	$2.2 \cdot 10^{-3}$
$\bar{p}p \rightarrow \bar{\Lambda}\Sigma(1385)$	$< 3 \cdot 10^{-6}$	~ 50	$< 1.3 \cdot 10^{-5}$
$\bar{p}p \rightarrow \bar{\Sigma}^0\Sigma^0$	$< 3 \cdot 10^{-6}$	~ 50	$< 1.3 \cdot 10^{-5}$
Channel 15 GeV/c			
$\bar{p}p \rightarrow \bar{\Lambda}\Lambda$	0.14	~ 10	1
$\bar{p}p \rightarrow \bar{p}p\pi^+\pi^-$	$< 1 \cdot 10^{-6}$	$1 \cdot 10^3$	$< 2 \cdot 10^{-3}$
$\bar{p}p \rightarrow \bar{\Lambda}\Sigma^0$	$2.3 \cdot 10^{-3}$	~ 10	$1.6 \cdot 10^{-2}$
$\bar{p}p \rightarrow \bar{\Lambda}\Sigma(1385)$	$3.3 \cdot 10^{-5}$	60	$1.4 \cdot 10^{-3}$
$\bar{p}p \rightarrow \bar{\Sigma}^0\Sigma^0$	$3.0 \cdot 10^{-4}$	~ 10	$2.1 \cdot 10^{-3}$
DPM	$< 1 \cdot 10^{-6}$	$5 \cdot 10^4$	$< .09$
Channel 4 GeV/c			
$\bar{p}p \rightarrow \bar{\Xi}^+\Xi^-$	0.17	~ 2	1
$\bar{p}p \rightarrow \bar{\Sigma}^+(1385)\Sigma^-(1385)$	$< 1 \cdot 10^{-6}$	~ 60	$< 2 \cdot 10^{-4}$

Table 4.45: Background for $\bar{p}p \rightarrow \bar{\Lambda}\Lambda$ and $\bar{p}p \rightarrow \bar{\Xi}^+\Xi^-$. The reconstruction efficiencies give the probability for generated background events to be identified as a physics event. The cross sections are taken from refs. [146, 145] or extrapolated from the latter. The cross sections and branching ratios into the charged decay mode is taken into account in the signal number which gives the normalised probability for a background reaction event to be identified as a physics event.

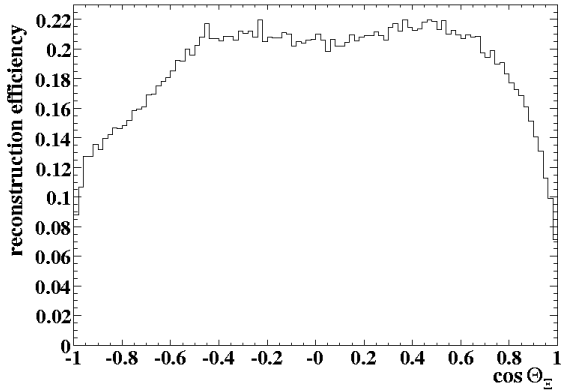


Figure 4.64: Centre-of-mass angular distribution for the $\bar{p}p \rightarrow \bar{\Xi}^+\Xi^-$ reaction at 4 GeV/c from isotropically generated events reconstructed in the PANDA acceptance.

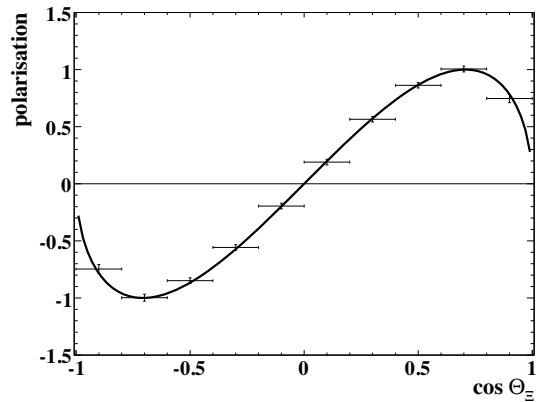


Figure 4.65: Reconstructed polarisation for the $\bar{p}p \rightarrow \bar{\Xi}^+\Xi^-$ reaction at 4 GeV/c. The solid line is the $\sin 2\theta_{\text{CM}}$ function used to generate the polarisation.

4.3.3.2 Background Reactions

The PS185 experiment at LEAR showed that the $\bar{p}p \rightarrow \bar{\Lambda}\Lambda$ reaction can be extracted with low background near the threshold. The background was of the order of (5-10) % which primarily came from quasi-free production on carbon from the CH_2 tar-

get [146]. We therefore anticipate a much lower background in this kinematical region when using pure hydrogen pellets. The remaining background reactions that have been considered for the $\bar{p}p \rightarrow \bar{\Lambda}\Lambda$ channel are:

- (a) $\bar{p}p \rightarrow \bar{p}p\pi^+\pi^-$

- (b) $\bar{p}p \rightarrow \bar{\Lambda}\Sigma^0$
- (c) $\bar{p}p \rightarrow \bar{\Lambda}\Sigma(1385)$
- (d) $\bar{p}p \rightarrow \bar{\Sigma}^0\Sigma^0$
- (e) Dual Parton Model (DPM)

These channels could potentially mimic the $\bar{\Lambda}\Lambda$ channel by producing a $\bar{p}p\pi^+\pi^-$ system in the final state. It should be noted that channels (b), (c) and (d) are of interest in their own right, but are treated here as a background. The only hyperon channel that is energetically accessible at 1.64 GeV/c is the $\bar{\Lambda}\Lambda$ channel and therefore was only reaction (a) considered at this momentum. At 4 GeV/c there are several hyperons channels with a $\bar{\Lambda}\Lambda$ pair present as a result of Σ^0 decays in addition to reaction (a). The same reactions were studied at 15 GeV/c together with the DPM. 1M events were generated and analysed for reaction (a) at 1.64 GeV/c and 15 GeV/c and the DPM. 300k events were generated and analysed for the other background channels at all momenta and reaction (a) at at 4 GeV. The result of this background study is summarised in Table 4.45.

At 1.64 GeV/c we can expect a background well below 1 %, as anticipated from the PS185 results. The background will be somewhat higher at 4 GeV/c due to the increase of the cross section for reaction (a) and the presence of several neutral hyperon channels. The result is that we can expect a background of the order of a percent at this momentum. Due to the large inelastic cross section the largest source of background at the highest momentum is assumed to stem from the DPM process. This background would not be greater than a few percent, however. Hyperon resonances, not considered here, could be additional sources of background. This background and the Σ^0 channels would be suppressed by applying a χ^2 test on these hypotheses.

The $\bar{p}p \rightarrow \bar{\Xi}^+\Xi^-$ channel involves four well separated decay vertices. Thus any background channel with a different decay pattern can be suppressed imposing a constraint on this pattern. A channel which has the same $\bar{\Lambda}\Lambda\pi^+\pi^-$ final state is the

$$\bar{p}p \rightarrow \Sigma^+(1385)\Sigma^-(1385)$$

reaction. We therefore consider it as the main source of background. This channel has one order of magnitude higher cross section. However, the contamination from the 1 M events generated and analysed is negligible as can be seen in Table 4.45. The low level of remaining background is also confirmed in the background studies made for

the $\bar{p}p \rightarrow \bar{\Xi}^+\Xi^-\pi^0$ channel at a somewhat higher momentum in section 4.2.5 where more background channels were studied.

4.3.3.3 Simulation Results

This study shows that the benchmark channels $\bar{p}p \rightarrow \bar{\Lambda}\Lambda$ and $\bar{p}p \rightarrow \bar{\Xi}^+\Xi^-$ can be well reconstructed in \bar{P} ANDA. There is acceptance over the full angular range and the whole momentum range of HESR for the $\bar{\Lambda}\Lambda$ channel. The same will most likely hold true also for the Σ^0 channels due to the kinematical similarities. There is also full CM acceptance for the $\bar{\Xi}^+\Xi^-$ channel at 4 GeV/c, and most likely over the full momentum range from threshold.

Acceptance corrections have to be applied to obtain the final results due to the loss of particles in the beam pipe direction and the loss of pions below 50 MeV/c. The angular differential cross section and the polarisation can be extracted to high precision after those corrections.

The count rates will be high for the studied channels. Table 4.46 gives the expected count rates for the benchmark channels in their charged decay mode channels in \bar{P} ANDA at a luminosity of $2 \cdot 10^{32} \text{cm}^{-2}\text{s}^{-1}$, ranging from a few 10 per second for the $\bar{\Xi}^+\Xi^-$ channel up to a thousand per second for the $\bar{\Lambda}\Lambda$ channel.

Momentum [GeV/c]	Reaction	Rate [s ⁻¹]
1.64	$\bar{p}p \rightarrow \bar{\Lambda}\Lambda$	580
4	$\bar{p}p \rightarrow \bar{\Lambda}\Lambda$	980
	$\bar{p}p \rightarrow \bar{\Xi}^+\Xi^-$	30
15	$\bar{p}p \rightarrow \bar{\Lambda}\Lambda$	120

Table 4.46: Estimated count rates into their charged decay mode for the benchmark channels at a luminosity of $2 \cdot 10^{32} \text{cm}^{-2}\text{s}^{-1}$

The high count rate together with the expected low background, not more than a few percent, makes the study of antihyperon-hyperon pairs very promising.

4.4 Hadrons in the Nuclear Medium

COMMENT: Author(s): A. Gillitzer

COMMENT: Referee(s): V. Metag

The study of hadron properties at finite nuclear densities has a long history. As the most fundamental aspect, the change of hadron masses inside the nuclear medium has been proposed to reflect a modification of the chiral symmetry breaking pattern of QCD due to the finite density, and thus to be an indicator of changes of quark condensates. In particular, attractive mass shifts reflecting the reduced quark pair condensate at finite density have been predicted for vector mesons [154, 155]. As the ongoing theoretical discussion on this issue (see recent review articles like [156]) demonstrates, the relation between the nuclear density dependence of in-medium masses and chiral condensates is however not a direct one. Furthermore, it is important to note that in-medium mass shifts of hadrons, reflecting the real part of a nuclear potential, are driven by low energy interactions. The most significant medium effects are thus expected for hadrons which are at rest or have a small momentum relative to the nuclear environment, whereas the non-observation of mass shifts at high momenta not necessarily implies the absence of nuclear potentials. For experimental studies of hadron in-medium properties therefore appropriate conditions of the reaction kinematics have to be selected. Due to the released annihilation energy of almost 2 GeV/c antiprotons are particularly well suited to implant produced hadrons at rest or at low momentum inside the nuclear environment.

Numerous experiments using proton-nucleus, photon-nucleus, or nucleus-nucleus collisions have been, at least partially, devoted to deduce in-medium mass shifts or nuclear potentials of hadrons in the light quark sector (u,d,s), both for vector mesons [157, 158, 159, 160, 161, 162], and for pseudoscalar mesons [163, 164, 165, 166, 167, 168, 169, 170, 171]. Only in part of the experiments the mesons were studied at low momenta relative to the nuclear environment, where possibly significant medium effects may be expected.

Besides the mass shift also the change of the width of hadrons inside the nuclear medium is an important observable. In general the width will increase due to the opening of decay channels which are not accessible in the vacuum. The measurement of the modification of a hadron's width in the nuclear medium therefore yields information on its inelas-

tic interactions, which is otherwise very difficult to access for unstable hadrons. In the case of very short-lived mesons decaying inside the nucleus, the in-medium width may be measured directly. As an alternative approach, the measurement of the transparency ratio determined from the production cross section with different target nuclei allows to deduce the in-medium width of mesons [172, 173].

4.4.1 In-Medium Properties of Charmed Hadrons

The energy range of the HESR and the detection capabilities of the \bar{P} ANDA detector in principle allow to extend this type of studies into the sector of charmed hadrons by using antiproton-nucleus collisions as entrance channel. The in-medium properties of both D mesons and charmonium states have been studied theoretically in different approaches (for a review on the earlier work see [174]). In analogy to the K/\bar{K} splitting in nuclear matter phenomenological estimates using a quark-meson coupling model [175, 176] predict an in-medium mass splitting between \bar{D} and D mesons of about 100 MeV, and an attractive D meson (D^+ , D^0) potential with a depth of more than -100 MeV at normal nuclear density $\rho = \rho_0$. A downward shift of the $D\bar{D}$ average mass by about 50 MeV was obtained in a QCD sum rule estimate [177]. The QCD sum rule analysis of Refs. [174, 178] predicts a $D^+ - D^-$ mass splitting of more than 50 MeV with the a downward shift of the D^+/D^- average mass by about the same order of magnitude at $\rho = \rho_0$. A more involved coupled channel approach [179, 180, 181] reveals a complicated structure of D^+ mesons (and equivalently D^0 mesons) which is not appropriately described by two simple parameters denoting in-medium mass and width, respectively. Inside the nuclear medium the inelastic charm exchange channels $DNN \rightarrow \Lambda_c N$ and $DN \rightarrow \pi \Lambda_c$ are open at threshold resulting in a low mass component reflecting Λ_c -hole excitation. Nuclear binding effects for charmonium have been studied theoretically almost 20 years ago [182], but the binding effect was later found to be rather small, namely between 5 and 10 MeV for J/ψ and η_c states [183, 184]. Large attractive mass shifts of ~ 100 MeV in normal nuclear matter were predicted for higher-lying charmonium states resulting from the QCD second order Stark effect due to the change of the gluon condensate [185, 186].

Different experimental methods were discussed to observe signals of the D meson mass modification in nuclear matter. It was proposed [176] to

study subthreshold production of D and \bar{D} mesons in antiproton-nucleus collisions, where reduced in-medium masses should be visible in an enhancement of the production cross section. A lowering of the in-medium $D\bar{D}$ threshold has been predicted to result in a dramatic increase of the $\psi(2S)$ and $\psi(3770)$ width, since in free space these states are rather narrow due to their vicinity to the $D\bar{D}$ threshold [177]. Using a Multiple Scattering Monte Carlo approach [187] it was however found that the collisional width of these charmonium states in the nuclear medium is much larger than their width in free space already for unchanged D/\bar{D} masses. Taking the collisional width and D/\bar{D} rescattering into account, no effect of attractive nuclear potentials survived in the $D\bar{D}$ channel, and only a very small effect in the di-lepton channel.

It has also been proposed to study the elementary DN and $\bar{D}N$ interaction more directly in $\bar{p}d$ collisions by using the spectator nucleon in the deuteron as secondary target, as discussed for the elastic $D\bar{D}N$ cross section in [188]. Inelastic channels with charm exchange like $\bar{p}d \rightarrow \Lambda_c N(\pi)$ or $\bar{p}d \rightarrow \Sigma_c N(\pi)$ might also be studied. Recently, the $\bar{D}N$ interaction with its energy dependence was studied in a combined meson exchange and quark-gluon dynamics approach [189]. It was found that the $\bar{D}N$ cross section is by about a factor two larger than the KN cross section within the range up to about 150 MeV above threshold. In the nucleon rest frame this corresponds to a \bar{D} momentum of about 1.4 GeV/c.

Due to the high mass of charmed hadrons, it is very difficult to realize the conditions at which their medium properties are experimentally accessible. Despite the energy release of 1.9 GeV/c, direct annihilation processes in antiproton-nucleus collisions kinematically don't fulfill the condition of low momentum required to be sensitive to nuclear medium effects. At threshold the D/\bar{D} meson momentum is 3.2 GeV/c. Lower D/\bar{D} momenta can be reached by using backward production at higher beam energies, but at the highest HESR beam momentum of 15 GeV/c the minimum D/\bar{D} momentum is still 1.67 GeV/c. The interesting regime of momenta below 1 GeV/c can only be reached in complicated two- or multi-step reactions with correspondingly small cross sections. Qualitatively, the same holds for charmonium states produced in $\bar{p}A$ collisions. Presently it is neither known to which extent the discussed observables are still sensitive to nuclear potentials at high D/\bar{D} or charmonium momenta relative to the nuclear medium, or if more complicated processes slowing down charmed hadrons

inside a nucleus can be experimentally identified. Therefore the study of possible mass modifications of charmed hadrons in nuclear matter is considered as a long term physics goal based on further theoretical studies on the reaction dynamics, and on the exploration of the experimental capability to identify more complicated processes. It will however not be in the focus of the physics program during the first years of PANDA operation.

4.4.2 Charmonium Dissociation

Apart from the determination of nuclear potentials of charmed hadrons, specific well-defined problems exist to which the study of antiproton-nucleus collisions with \bar{P} ANDA can contribute valuable information. As an important issue in this respect we see the still open question of the $J/\psi N$ dissociation cross section. This cross section is as yet experimentally unknown, except for indirect information deduced from high-energy J/ψ production from nuclear targets. A $J/\psi N$ cross section $\sigma_{J/\psi N} = 3.5 \pm 0.8$ mb has been deduced by measuring J/ψ photo-production from nuclei with a mean photon energy of 17 GeV/c [190]. The J/ψ momentum in the nuclear rest frame was not explicitly determined. In [191] the authors analyzed proton-nucleus collisions with beam energies between 200 and 800 GeV/c and found as absorption cross section $\sigma = 7.3 \pm 0.6$ mb, also without explicitly specifying the J/ψ momentum in the nuclear rest frame. In an analysis of recent measurements of J/ψ and ψ' production in pA collisions at 400 and 450 GeV/c [192, 193] the NA50 Collaboration finds $\sigma_{abs}(J/\psi) = 4.6 \pm 0.6$ mb and $\sigma_{abs}(\psi') = 10.0 \pm 1.5$ mb. The authors of [193] explicitly mention the energy dependence of J/ψ and ψ' absorption as a still open question. Recently, nuclear shadowing effects of J/ψ mesons were also studied in $d + Au$ collisions in the PHENIX experiment at RHIC at the much higher energy $\sqrt{s_{NN}} = 200$ GeV/c, resulting in a deduced J/ψ breakup cross section of $\sigma_{breakup} = 2.8^{+1.7}_{-1.4}$ mb [194, 195].

Apart from being a quantity of its own interest, the $J/\psi N$ dissociation cross section is closely related to the attempt of identifying quark-gluon plasma (QGP) formation in ultra-relativistic nucleus-nucleus collisions. A significant additional, so-called anomalous suppression of the J/ψ yield in high-energy nucleus-nucleus collisions had been predicted due to color screening of $c\bar{c}$ pairs in a QGP environment [196]. In fact, the CERN-SPS experiments have observed a J/ψ suppression effect increasing with the size of the interacting nuclear system, and interpreted this as signature for QGP

formation [197, 198, 199]. The validity of such an interpretation is however based on the knowledge of the "normal" suppression effect due to J/ψ dissociation in a hadronic environment. Nuclear J/ψ absorption can so far only be deduced from models [200, 201, 202] since the available data do not cover the kinematic regime relevant for the interpretation of the J/ψ suppression effect seen in the SPS heavy ion data, since *e.g.* $J/\psi N$ dissociation processes will in general occur at higher relative momenta in 400 GeV/c pA collisions than in 158 GeV/c/u Pb + Pb collisions with partial stopping of the nuclear matter. Ref. [201] gives a range from ~ 1 mb to ~ 7 mb for the uncertainty of the estimated values of the J/ψ -nucleon cross section. In cold nuclear matter J/ψ mesons can dissociate via the reaction $J/\psi N \rightarrow \bar{D}\Lambda_c$ at $p_{\text{lab}} \geq 1.84$ GeV/c, whereas dissociation via $J/\psi N \rightarrow D\bar{D}N$ requires $p_{\text{lab}} \geq 5.17$ GeV/c. Therefore the $J/\psi N$ dissociation cross section will be strongly momentum dependent, and it is important to supply experimental information on this dependence particularly at lower momenta.

4.4.3 J/ψ N Dissociation Cross Section in $\bar{p}A$ Collisions

In antiproton-nucleus collisions the $J/\psi N$ dissociation cross section can be determined for momenta around 4 GeV/c with very little model dependence, in contrast to its values deduced from the previous studies as discussed in section 4.4.2. The J/ψ momentum inside the nuclear medium is constrained by the condition that the $\bar{p}p \rightarrow J/\psi$ formation proceeds 'on resonance' with a target proton ($p_{\bar{p}} = 4.1$ GeV/c). The determination of the $J/\psi N$ dissociation cross section is, in principle, straight forward: the J/ψ production cross section is measured for different target nuclei of mass number ranging from light (d) to heavy (Xe or Au), by scanning the \bar{p} beam momentum across the J/ψ yield profile whose width is essentially given by the internal target nucleon momentum distribution. The internal nuclear momentum distribution is sufficiently well known. The J/ψ is identified by its decay branch to $\mu^+\mu^-$ or e^+e^- . The attenuation of the J/ψ yield per effective target proton as a function of the target mass is a direct measure for the $J/\psi N$ dissociation cross section, which can be deduced by a Glauber type analysis. Note that a study of $\bar{p}d$ collisions 'on the J/ψ resonance' allows an exclusive measurement of the final state, and thus with the spectator neutron as secondary target should give direct access to the cross section for specific $J/\psi n$ reactions [188].

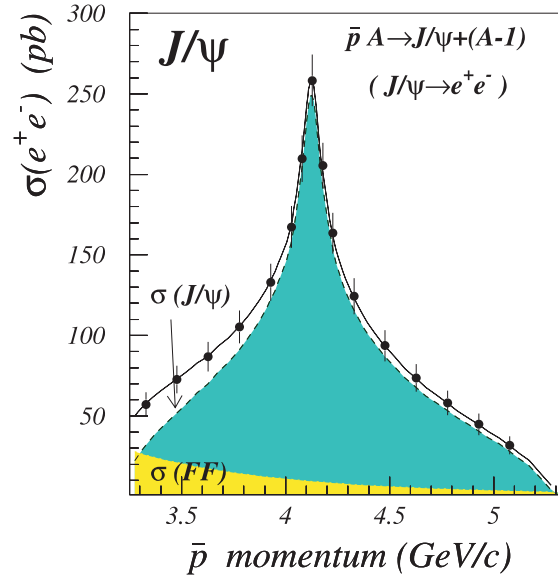


Figure 4.66: Simulated cross section for resonant J/ψ production on nuclear protons with internal Fermi momentum distribution as a function of the antiproton momentum [203].

In a second step these studies may be extended to higher charmonium states like the ψ' ($\psi(2S)$) which requires \bar{p} momenta around 6.2 GeV/c for resonant production. This would also allow to determine the cross section for the inelastic process $\psi' N \rightarrow J/\psi N$ [204] which is also relevant for the interpretation of the ultra-relativistic heavy ion data. Measurement of ψ' production on nuclear targets is more difficult since the ψ' yield will be considerably smaller than that of J/ψ . Neglecting absorption, the estimated ratio of the production cross sections is $\sigma_{\bar{p}A \rightarrow \psi' X} / \sigma_{\bar{p}A \rightarrow J/\psi X} \simeq 0.03$, based on the Breit-Wigner formula with the known [151] widths and $\bar{p}p$ branching ratios. Absorption effects will further reduce this ratio, since due to the larger size of the ψ' a larger absorption cross section is expected than for J/ψ . At low momenta in the nuclear rest frame the lower thresholds for dissociation processes will also play an important role and enhance the ratio of ψ' to J/ψ absorption. In contrast to the $J/\psi N$ system as discussed above, the $\psi' N \rightarrow \bar{D}\Lambda_c$ channel is already open at threshold, and the dissociation via $J/\psi N \rightarrow D\bar{D}N$ is also open at the \bar{p} momenta chosen for resonant ψ' production (in the nucleon rest frame the ψ' threshold momentum for $D\bar{D}$ dissociation is 1.28 GeV/c).

Benchmark Channels

The simulation studies for this report, in the context of antiproton nucleus collisions, focus on aspects relevant for the determination of the J/ψ -nucleon dissociation cross section. The reaction studied is:

$$\bar{p} \text{ } ^{40}\text{Ca} \rightarrow J/\psi X \rightarrow e^+ e^- X$$

The incident \bar{p} momentum is $4.05 \text{ GeV}/c$, corresponding to resonant J/ψ formation with a proton at rest in the target nucleus. Goal of the simulations is to study the identification of the J/ψ signal in e^+e^- pairs, and to explore the suppression of presumed dominant background channels. No attempt is made at the present stage to simulate the full experiment required to determine the $J/\psi N$ dissociation cross section, and to estimate its achievable statistical and systematic errors. The full experiment will comprise the measurement of absolute cross sections for J/ψ production on a series of target nuclei ranging from very light to heavy (*e.g.* ^2H , N , Ne , Ar , Kr , Xe) including a \bar{p} momentum scan across the J/ψ excitation function in each case.

A dedicated event generator for the reaction $\bar{p} A \rightarrow J/\psi X$ [205] has been used to generate 80 thousand events of the signal channel. The event generator includes realistic Fermi momentum distributions and average nuclear binding effects of the nuclear target protons, as well as \bar{p} and J/ψ absorption in the nuclear medium.

Various criteria are conceivable to select the $J/\psi \rightarrow e^+e^-$ signal events. They are briefly listed in the following, whereas a more detailed discussion of the conditions used in the simulation is presented later.

- at least one e^+e^- pair candidate in the event
- the invariant mass of the e^+e^- pair is close to the J/ψ mass, *i.e.* $|M_{e^+e^-} - M_{J/\psi}| < \delta M$
- the longitudinal e^+e^- pair momentum is close to the \bar{p} beam momentum:
 $|p_{z,e^+} + p_{z,e^-} - p_{\bar{p}}| < \delta p_z$
- the transverse e^+e^- pair momentum is small, and given by the Fermi momentum:
 $\left[(p_{x,e^+} + p_{x,e^-})^2 + (p_{y,e^+} + p_{y,e^-})^2 \right]^{\frac{1}{2}} < \delta p_t$
- as a consequence of the quasi two-body reaction kinematics on a slowly moving target proton, the e^+e^- pair is approximately coplanar with the beam axis, with a 180° difference between the e^+ and e^- azimuthal angles:
 $|\phi_{e^+} - \phi_{e^-} - \pi| < \delta \phi$

- with J/ψ formation no energy is available for the production of other hadrons or for high momentum transfer. In particular, the event does not contain pions or high energy nucleons above a few 10 MeV. The maximum energy of detected nucleons is given by the excitation energy of the proton hole created by the $\bar{p}p$ annihilation (*i.e.* the binding energy of the struck proton).

Background Reactions

As compared to resonant J/ψ formation with an antiproton hitting a free target proton at a cross section of $\sim 5 \mu\text{b}$, J/ψ production on a nucleus is reduced roughly by a factor 1000 due to the nuclear Fermi momentum, and thus the peak cross section is estimated to be a few nb. In contrast, the total antiproton-nucleus cross section, dominated by annihilation and inelastic hadronic processes on target nucleons, is approximately given by the geometrical cross section of the order of 1 b. Taking into account the $\sim 6\%$ branching for the e^+e^- decay, the rate of hadronic background reactions is almost 10 orders of magnitude larger than that of the J/ψ signal. Obviously, it is not possible to simulate the detector response for a sample of unspecific background events which is large enough to test background suppression at a relative signal level below 10^{-9} . The background suppression and signal detection capability can therefore only be estimated by using extrapolations based on certain assumptions.

Annihilation of antiprotons with one of the nuclear target protons into $\pi^+ \pi^-$ pairs without creation of other particles or high momentum transfer to target nucleons is considered to be the most dangerous background channel to a dileptonic J/ψ signal. Experimental data on the reaction $\bar{p}p \rightarrow \pi^+ \pi^-$ at energies above the LEAR energy range are scarce. Ref [140] lists a total cross section of $7 \pm 5 \mu\text{b}$ at $p_{\bar{p}} = 4 \text{ GeV}/c$. Angular distributions for $\bar{p}p \rightarrow \pi^+ \pi^-$ have been measured up to \bar{p} momentum $p_{\bar{p}} = 0.78 \text{ GeV}/c$ [206] whereas for $\bar{p}p \rightarrow \pi^0 \pi^0$ differential cross sections at total $\bar{p}p$ center-of-mass energies in the charmonium mass range have been measured by the Fermilab E760 and E835 experiments for part of the angular range [207, 208].

Samples of 26.4 million background events for $4.05 \text{ GeV}/c$ \bar{p} on ^{40}Ca have been created by using the UrQMD event generator [209, 210] in the standard version (*i.e.* statistical de-excitation of the system by emission of low energy particles is neglected). This sample is representative for unspecific back-

ground in $\bar{p}A$ collisions. Since it is difficult to decide which event patterns create background in the di-leptonic J/ψ signal at a level below 10^{-9} no filter to the UrQMD events has been applied before propagation through the detector. In addition a sample of $3 \cdot 10^7$ $\bar{p}p \rightarrow \pi^+\pi^-$ background events was generated. Since at the considered energy no experimental data on $\pi^+\pi^-$ angular distributions in $\bar{p}p$ collisions exist, the parametrization of the $\pi^0\pi^0$ angular distribution measured by the E835 experiment was used [208].

4.4.3.1 Simulation Results

The first step in the analysis is the computation of the invariant mass of selected pairs of e^- and e^+ candidates. Four e^\pm candidate lists have been defined - the **VeryLoose**, **Loose**, **Tight**, and **VeryTight** lists. In Fig. 4.67 the e^+e^- invariant mass distributions using the different lists are displayed.

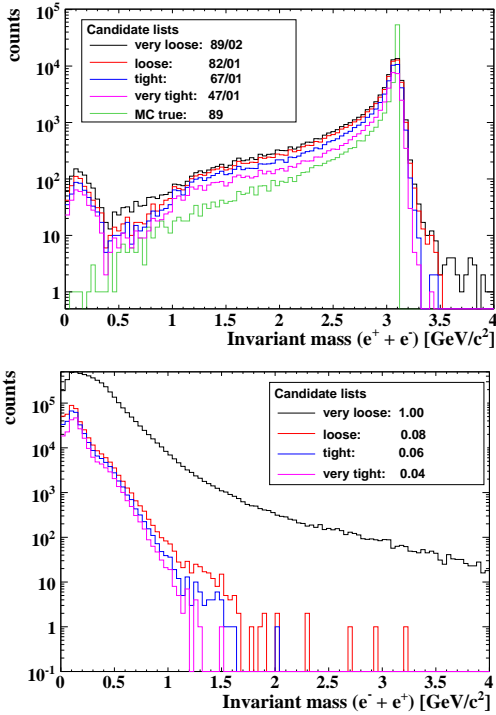


Figure 4.67: Reconstructed invariant mass distribution of e^+e^- pair candidates for the signal events (upper panel) and for the UrQMD background events (lower panel).

The upper panel contains the signal events, whereas the lower panel shows the corresponding distributions obtained for the UrQMD background events. The two numbers given in the legend of the upper

panel are the percentages of reconstructed true and fake J/ψ mesons, respectively, at a minimum reconstructed mass of $2.0 \text{ GeV}/c^2$.

The green line, labelled with *MC true*, represents the true mass distribution for the **VeryLoose** list. The reconstruction efficiency decreases from $\sim 89\%$ with the **VeryLoose** list to $\sim 47\%$ with the **VeryTight** list. With the available statistics the number of fake J/ψ meson candidates in the considered invariant mass region is zero for all cases. In the lower panel, showing the background distributions, the number in the legend is the fraction of reconstructed fake J/ψ mesons with respect to the number obtained with the **VeryLoose** list. The mass distribution decreases strongly with increasing mass. Except for the **VeryLoose** list there are only few background events in the mass range above $2 \text{ GeV}/c^2$. With the available number of simulated background events, using the **Loose** list 5 background events survive in this mass range. With the **Tight** list 1 event, with the **VeryTight** list no background event is found above $2 \text{ GeV}/c^2$.

A realistic ratio of the numbers of background and signal events reflecting the cross section ratio of 10^{10} may however require additional cuts for further background suppression. The simple topology of the signal events helps to select the signal events from the dominating background. The typical features which can be exploited to suppress the background are listed below:

1. the two leptons emerge from the main vertex
2. the total momentum approximately equals the incident \bar{p} momentum ($P_z(e^+) + P_z(e^-) \approx P_z(\bar{p})$)

The total perpendicular momentum approximately vanishes ($P_\perp(e^+) \approx -P_\perp(e^-)$) which implies that

3. in the center of mass system the angle between the two leptons $\Phi(e^+, e^-)$ is $\sim 180^\circ$
4. the absolute values of the perpendicular momenta of the two leptons is approximately equal ($|P_\perp(e^+)| \approx |P_\perp(e^-)|$)

The momentum relations are only approximately valid because of the Fermi-motion of the protons in the target nuclei.

The cuts deduced from these characteristic features are shown in Fig. 4.68. The panels on the left side contain the signal events, whereas the right side panels show the background events using the **Loose**

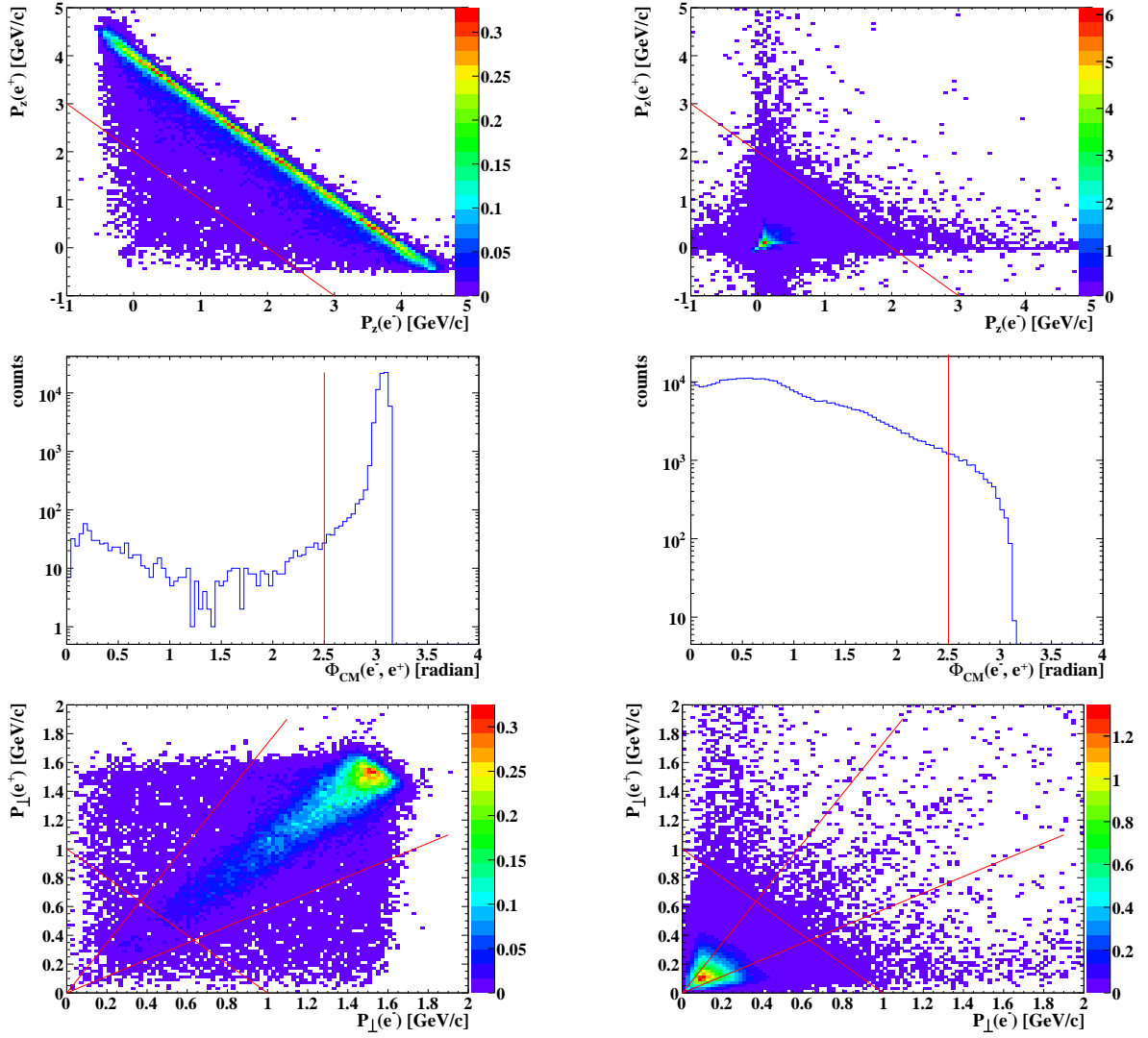


Figure 4.68: Distributions used to suppress the background: Left panels are for signal events, right panels show the UrQMD background distributions. Upper panels show the longitudinal momentum of e^- versus that of e^+ , middle panels show the azimuthal angle $\phi(e^+, e^-)$ between e^+ and e^- in the center of mass system, and lower panels show the perpendicular momentum of e^- versus that of e^+ . The red lines represent cuts to enhance the signal to background ratio. The 2D-histograms are normalized to contain 100 events.

list. The red lines represent possible cuts to separate signal and background. The used cuts are explicitly given in Table 4.47. In addition, not shown in the figure, a condition in the $x - y$ plane on the primary interaction vertex at the target can be set.

The efficiencies of these cuts in combination with the Loose e^\pm candidate list are listed in Table 4.47. In case of the signal the numbers represent the fraction of true J/ψ mesons which are reconstructed and accepted by the given cut in the invariant mass range above $2 \text{ GeV}/c^2$. In case of the background the given fraction is the number of accepted e^+e^- pairs with a reconstructed invariant mass above $2 \text{ GeV}/c^2$

relative to the number of simulated events.

The combination of all four cuts efficiently enhances the signal to background ratio. Figure 4.69 shows the invariant mass distribution after application of the combined cut. With the given statistics no UrQMD background events are left in the investigated mass range. Therefore the fraction of accepted UrQMD background events shown in Table 4.47 represents a lower limit for the achievable background suppression. On the other hand 73% of the true J/ψ mesons are accepted. Note that this combination of Loose list and software cuts is considerably more efficient than simply using a more

Table 4.47: Definition of cuts and their selection efficiency in combination with the Loose e^\pm candidate list for the $J/\psi \rightarrow e^+e^-$ signal, the generic UrQMD, and specific background channel $\pi^+\pi^-$. The numbers are computed for e^+e^- invariant masses above a minimum mass of $2 \text{ GeV}/c^2$. v_x, v_y are the x, y coordinates of the primary vertex.

cut	fraction accepted		
	signal	background	
		UrQMD	$\pi^+\pi^-$
$\sqrt{v_x^2 + v_y^2} < 1 \text{ mm}$	0.77	$3.8 \cdot 10^{-8}$	$4.1 \cdot 10^{-6}$
$P_z(e^+) + P_z(e^-) > 2.0 \text{ GeV}/c$	0.77	$2.3 \cdot 10^{-7}$	$4.9 \cdot 10^{-6}$
$\Phi(e^+, e^-) > 2.5 \text{ rad}$	0.77	$1.5 \cdot 10^{-7}$	$4.9 \cdot 10^{-6}$
$[P_\perp(e^+) + P_\perp(e^-)] > 1 \text{ GeV}/c$ & $ \arctan\left(\frac{P_\perp(e^+)}{P_\perp(e^-)}\right) - 45^\circ < 15^\circ$	0.73	$3.8 \cdot 10^{-8}$	$2.8 \cdot 10^{-6}$
combined ($IM_{e^+e^-} > 2.0 \text{ GeV}/c^2$)	0.73	$< 3.8 \cdot 10^{-8}$	$2.4 \cdot 10^{-6}$

stringent list to enhance the signal to background relation.

The black line in Fig. 4.69 shows an estimate of the remaining background with $8 \cdot 10^{14}$ simulated UrQMD background events (10^{10} times the number of signal events). The distribution is assumed to follow an exponential function which was fit to the Loose list distribution shown in the lower panel of Fig. 4.67 and was scaled accordingly. This estimate indicates that also with the realistic relation of signal and background events it should be possible to measure J/ψ production in antiproton-nucleus collisions with acceptable signal to background ratio.

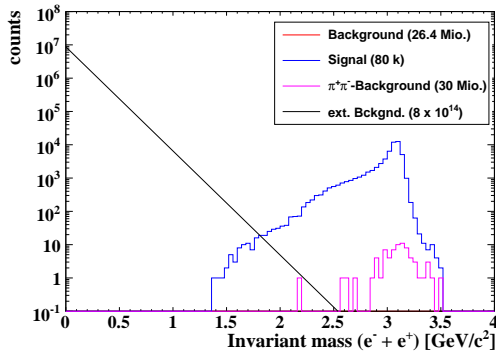


Figure 4.69: Invariant mass distribution of e^+e^- pair candidates for signal (blue), UrQMD background (red), and $\pi^+\pi^-$ background (magenta) events. The estimated distribution for an UrQMD background sample scaled up to 10^{10} times the number of signal events is shown by the black line.

In addition, as specific background channel, the reaction $\bar{p}p \rightarrow \pi^+\pi^-$ at the same incident momentum of $4.05 \text{ GeV}/c$ has been studied. To mimic the contribution of this 2-charged-pion annihilation channel with a nuclear target, the momentum

of the target proton was smeared isotropically according to a Gaussian distribution with a width of $\sigma_p = 180 \text{ MeV}/c$. Assuming $\sigma_{\bar{p}p \rightarrow \pi^+\pi^-} = 10 \mu\text{b}$ at the upper limit within the experimental uncertainty [140] together with an $A^{2/3}$ scaling for the nuclear target and a signal cross section of 0.1 nb , a suppression factor of minimum 10^{-5} is required to keep the signal level above possible background due the $\pi^+\pi^-$ channel. The right most column in Table 4.47 shows the fraction of $\pi^+\pi^-$ pairs which are erroneously accepted as e^+e^- pairs from J/ψ decay.

The corresponding invariant mass spectrum of $\pi^+\pi^-$ pairs accepted out of 30 million generated $\bar{p}p \rightarrow \pi^+\pi^-$ events is represented in Fig. 4.67 by the magenta distribution.

The suppression factor of $2.4 \cdot 10^{-6}$ obtained with the combined cut is smaller than the required value and indicates that a signal-to-background ratio with respect to the $\pi^+\pi^-$ channel above one can be achieved.

4.4.4 Antibaryons and antikaons Produced in $\bar{p}A$ Collisions

Although not covered in the simulation section of this write-up, it is worth mentioning that the special kinematics of \bar{p} induced reactions combined with the detection capabilities of \bar{P} ANDA opens the opportunity to study the in-medium properties of a number of hadrons in the light quark sector which can be produced at rest or at very small momenta inside nuclei. This is *e.g.* the case for \bar{p} , $\bar{\Lambda}$, and \bar{K} , for which the nuclear potential is a quantity of interest, but could not be determined experimentally up to now.

The antiproton-nucleon interaction at low energies is dominated by annihilation. As a consequence of

the strong absorption effects constraints deduced from the energy levels of antiprotonic atoms or from low energy antiproton-nucleus scattering on the depth of the real part of the \bar{p} nuclear potential have large uncertainties. In theoretical work G parity transformation has been proposed as a concept to provide a link between the NN and $N\bar{N}$ interaction at most for distances where the meson exchange picture is applicable [211], whereas at short distances the quark-gluon structure of baryons may question the validity of this approach. Based on G parity transformation relativistic mean field models predict a depth of the \bar{p} nuclear potential as large as -700 MeV [212, 213, 214]. The depth of phenomenological potentials deduced from antiprotonic atoms [215, 216, 217] and from sub-threshold antiproton production in nucleus-nucleus and in proton-nucleus collisions [218, 219, 220]. ranges at lower values, typically between -100 and -350 MeV. Therefore better experimental constraints on the nuclear antiproton potential, which may help to elucidate the role of the quark-gluon structure of baryons for the short-range baryon-antibaryon force, are needed.

The study of antiproton-nucleus collisions at high energy opens new opportunities: in this case the antiproton can penetrate into the interior of the nucleus, and probe the nuclear potential quasi at rest by backward scattering from a nuclear proton. An attractive \bar{p} potential will be visible in forward protons having a higher momentum than the incident antiproton which is a very sensitive signature. The cross section for $\bar{p}A \rightarrow pX$ with a recoil proton at $\theta \simeq 0^\circ$ is expected to be comfortably large despite nuclear absorption effects for the incident antiproton and the outgoing recoil proton. The nuclear antiproton potential reflects itself in the missing mass distribution of the fast forward proton.

The same method of low recoil momentum production is applicable for $\bar{\Lambda}$ antihyperons in the reaction $\bar{p}p \rightarrow \bar{\Lambda}\Lambda$ on a nuclear proton with Λ emission close to 0° . This may for the first time give access to the properties of $\bar{\Lambda}$ antihyperons inside nuclei, since no experimental information on the nuclear potential of antihyperons exists so far.

In addition, for larger momenta of the produced hadrons, quantitative information on the 'difference' between baryon and antibaryon potentials and hence on the potential of antibaryons may be obtained via exclusive antibaryon-baryon pairs produced close to threshold after an antiproton-proton annihilation within a complex nucleus [221]. Once these hyperons leave the nucleus and are detected, their asymptotic momentum distributions will re-

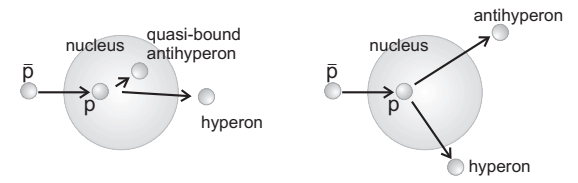


Figure 4.70: Schematic illustration of reactions giving access to the nuclear potential of $\bar{\Lambda}$ antihyperons: recoilfree $\bar{\Lambda}$ production with Λ missing mass measurement (left), and comparison of Λ and $\bar{\Lambda}$ transverse momentum distribution (right).

fect the depth of the respective potentials. A deeply attractive potential for one species could result in a momentum distribution of antihyperons which is very different from that of the coincident hyperon. Thus event-by-event momentum correlation of coincident baryon-antibaryon pairs can provide a direct and quantitative probe for the nuclear potentials. Fig. 4.70 schematically illustrates both experimental approaches to access nuclear potentials of $\bar{\Lambda}$ antihyperons as described above. Both methods may be used in the same experiment to study baryon and antibaryon in-medium properties over a larger range of momenta.

Due to its mass being very close to that of the nucleon, recoilfree production is also possible for the ϕ meson, and hence also for the antikaon as one of the decay particles emitted at very low momentum in the ϕ rest frame. This may give access to the nuclear potential for ϕ mesons and for antikaons. We therefore propose to explore the reaction $\bar{p}p \rightarrow \phi\phi \rightarrow K^+K^-K^+K^-$ at $\theta \simeq 0^\circ$ on nuclear target protons.

In these reactions the produced slow hadrons are very likely to be absorbed in the nuclear medium and not to be detected directly. However a measurement of the ϕ or ϕK^+ missing mass may allow to identify the reaction channel, and to deduce the in-medium properties of ϕ or K^- mesons, respectively. In the latter case it is experimentally challenging to detect and identify a low momentum K^+ meson.

4.5 Hypernuclear Physics

COMMENT: Author(s): J. Pochodzalla, A. Feliciello, F. Iazzi

COMMENT: Referee(s): F. Maas

Quantum Chromo Dynamics (QCD) is the theory of the force responsible for the binding of nucleons and nuclei and thus of a significant fraction of the ordinary matter in our universe. While the internal structure of hadrons and the spectra of their excited states are important aspects of QCD, it is at least equally important to understand how nuclear physics emerges in a more rigorous way out of QCD and how nuclear structures - nuclei on the small scale and dense stellar objects on the large scale - are formed [222]. For example, the presence of hyperons in neutron star cores is expected to lower the maximum mass of neutron (*e.g.* ref.[223]). Recent measurements of a few large masses of pulsars in binaries with white dwarfs could be used to put additional (astrophysical) constraints on the hyperon-nucleon interaction (*e.g.* ref.[223]). However, there is at present no clear picture emerging as to what kind of matter exists in the cores of neutron stars [224, 225, 226].

A hyperon bound in a nucleus offers a selective probe of the hadronic many-body problem as it is not restricted by the Pauli principle in populating all possible nuclear states, in contrast to neutrons and protons. On one hand a strange baryon embedded in a nuclear system may serve as a sensitive probe for the nuclear structure and its possible modification due to the presence of the hyperon. On the other hand properties of hyperons may change dramatically if implanted inside a nucleus. Therefore a nucleus may serve as a laboratory offering a unique possibility to study basic properties of hyperons and strange exotic objects. Thus hypernuclear physics represents an interdisciplinary science linking many fields of particle, nuclear and many-body physics (Fig. 4.71).

4.5.1 Physics Goals

4.5.1.1 Hypernuclei probing Nuclear Structure

While it is difficult to study nucleons deeply bound in ordinary nuclei, a Λ hyperon not suffering from Pauli blocking can form deeply bound hypernuclear states which are directly accessible in experiments. In turn, the presence of a hyperon inside the nuclear medium may give rise to new nuclear structures which cannot be seen in normal nuclei con-

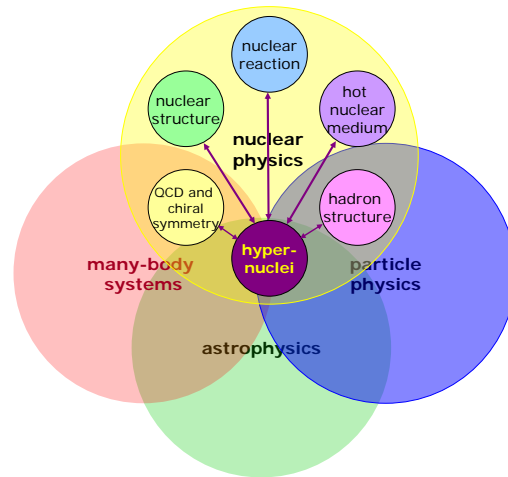


Figure 4.71: Hypernuclei and their link to other fields of physics.

sisting only of nucleons. Furthermore, a comparison of ordinary nuclei and hypernuclei may reveal new insights in key questions in nuclear physics like for example the origin of the nuclear spin-orbit force [227].

An important goal is to measure the level spectra and decay properties of hypernuclei in order to test the energies and wave functions from microscopic structure models. Indeed recent calculations of light nuclei based on modern nucleon-nucleon potentials, which also incorporate multi-nucleon interactions, are able to describe the excitation spectra of light nuclei with a very high precision of 1-2% [228, 229, 230, 231]. A challenging new approach to hyperon interactions and structure of hypernuclei is the relativistic density functional theory. This is a full quantum field theory enabling an *ab initio* description of strongly interacting many-body system in terms of mesons and baryons by deriving the in-medium baryon-baryon interactions from free space interactions by means of Dirac-Brueckner theory [232, 233]. The field theoretical approach is also the appropriate starting point for the connection to QCD-inspired descriptions based for example on chiral effective field theory (χEFT) [234, 235]. At present, χEFT is well understood for low-energy meson-meson [236] and meson-baryon dynamics in the vacuum [237, 238] and infinite nuclear matter [239, 240]. A task left for the future is to obtain the same degree of understanding for processes in a finite nuclear environment. Present nuclear structure calculations of the light nuclei in χEFT [231, 241, 242, 243] signal significant progress.

It is this progress made in our theoretical understanding of nuclei which nurtures the hope that detailed information on excitation spectra of hypernuclei and their structure will provide unique information on the hyperon-nucleon and - in case of double hypernuclei – on the hyperon-hyperon interactions.

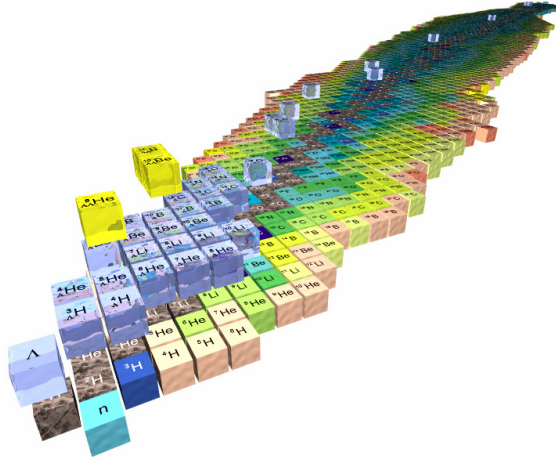


Figure 4.72: Present knowledge on hypernuclei. Only very few individual events of double hypernuclei have been detected and identified so far.

4.5.1.2 Hypernuclei: Baryon-Baryon Interaction

While the nucleon-nucleon scattering was extensively studied since the 50's, direct experimental investigations for the YN interactions are still very sparse. Because of their short lifetimes, hyperon targets are not available. Low-momentum hyperons are very difficult to produce and hyperon-proton scattering is only feasible via the double-scattering technique [244, 245]. There are only a few hundreds low-momentum Λ - N and Σ^\pm - N scattering events available and there is essentially no data on Ξ - N or Ω - N scattering.

In single hypernuclei the description of hyperons occupying the allowed single-particle states is without the complications encountered in ordinary nuclei, like pairing interactions and so on. The strength of the Λ - N strong interaction may be extracted with a description of single-particle states by rather well known wave functions. Furthermore, the decomposition into the different spin-dependent contributions may be analyzed. For these contributions, significantly different predictions exist for example from meson exchange-current and quark models.

It is also clear that a detailed and consistent understanding of the quark aspect of the baryon-

baryon forces in the $SU(3)$ space will not be possible as long as experimental information on the hyperon-hyperon channel is not at our disposal. Since scattering experiments between two hyperons are impractical, the precise spectroscopy of multi-strange hypernuclei at PANDA will provide a unique approach to explore the hyperon-hyperon interaction. So far only very few individual events of double hypernuclei have been detected and identified (Fig. 4.72).

4.5.1.3 Hypernuclei: Weak Decays

Once a hypernucleus has reached its ground state, it can only decay via a strangeness-changing weak interaction. Because of the low Q -value for free- Λ mesonic decay at rest of only 40 MeV, the mesonic decay of a $\Lambda \rightarrow N\pi$ bound in a nucleus ($B_\Lambda \geq -27$ MeV; see e.g. Ref. [246]) is disfavored by the Pauli principle and is only for light nuclei still sizable (see Fig. 4.73). In contrast, processes like $\Lambda N \rightarrow NN$ and $\Lambda\Lambda \rightarrow \Lambda N$ are allowed, opening a unique window for the four-baryon, strangeness non-conserving interaction. Moreover, in double hypernuclei hyperon induced non-mesonic weak decays $\Lambda\Lambda \rightarrow \Lambda N$ and $\Lambda\Lambda \rightarrow \Sigma N$ are possible [247, 248, 249] giving unique access to the $\Lambda\Lambda K$ coupling.

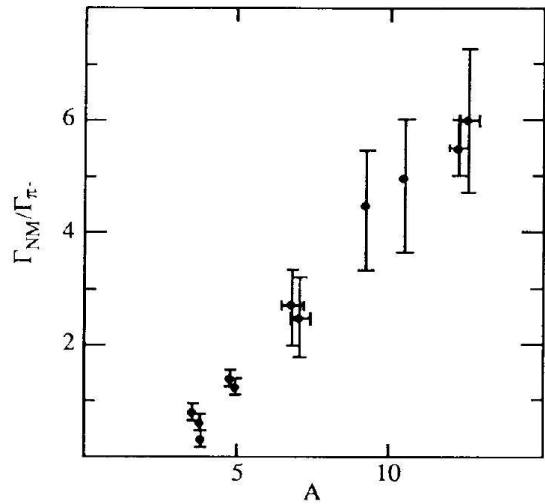


Figure 4.73: Measured ratio of nonmesonic ($\Lambda N \rightarrow NN$) to mesonic ($\Lambda \rightarrow N\pi$) hypernuclear decay widths as a function of the nuclear mass [250].

In the simulation presented below we consider only the case of two subsequent pionic decays which amounts to typically 10% of all weak decays of the light double hypernuclei (c.f. Fig. 4.73). Consider-

ing in the future also non-mesonic decays the event statistics may therefore increase significantly.

4.5.1.4 Multi-Strange Atoms

It is interesting to note that the different $S=-2$ systems - Ξ^- -atoms and single Ξ^- -hypernuclei on one side and double $\Lambda\Lambda$ hypernuclei on the other side - provide complementary information on the baryon force: on the one-meson exchange level strange mesons with $I=1/2$ do not contribute to the Ξ - N interaction. On the other hand, only strange mesons act in the ΞN - $\Lambda\Lambda$ coupling while only non-strange mesons contribute in the Λ - Λ interaction [251, 252]. Indeed, hyperatoms created during the capture process of the hyperon will supply additional information on the hyperon-nucleus interaction. X-rays from π^- , K^- , \bar{p} and Σ^- atoms have already been studied in several experiments in the past. At J-PARC first precise studies of Ξ^- -atoms are planned [253]. At \bar{P} ANDA not only Ξ^- atoms but also Ω^- atoms can be studied for the first time thus providing unique information on the nuclear optical potential of Ω^- baryons. The Ω hyperon is particularly interesting because due to its long lifetime and its spin of $3/2$ it is the only 'elementary' baryon with a non-vanishing spectroscopic quadrupole moment. Since the quadrupole moment of the Ω is mainly determined by the one-gluon exchange contribution to the quark-quark interaction [254, 255] its measurement represents a unique benchmark for our understanding of the quark-quark interaction.

4.5.1.5 Hypernuclei: Doorway to Exotic Quark States

The claimed observation of pentaquark states places also the question for other exotic quark states on the agenda. Thus the possible existence of an $S=-2$ six quark (uuddss) H -dibaryon [256, 257] represents another challenging topic of $\Lambda\Lambda$ hypernuclear physics. Because of their long lifetimes double Λ hypernuclei may serve as 'breeder' for the H -particle. Although some theories predict the H -dibaryon to be stable ([258] and references therein), the observation of several double hypernuclei makes the existence of a strongly bound free H -dibaryon unlikely. However, since the mass of the H -particle might drop inside a nucleus [258] and due to hyperon mixing [259, 260, 261, 262] it might be possible to observe traces of a H -dibaryon even if it is unbound in free space by a detailed study of the energy levels in double hypernuclei.

4.5.2 Experimental Integration and Simulation

In the \bar{P} ANDA experiment, bound states of Ξ hypernuclei will be used as a gateway to form double Λ hypernuclei [263]. The production of low momentum Ξ^- hyperons and their capture in atomic levels is therefore essential for the experiment. At \bar{P} ANDA the reactions $\bar{p} + p \rightarrow \Xi^- \bar{\Xi}^+$ and $\bar{p} + n \rightarrow \Xi^- \bar{\Xi}^0$ followed by re-scattering of the Ξ^- within the primary target nucleus will be employed (Fig. 4.74). After stopping the Ξ^- in an external secondary target, the formed Ξ hypernuclei will be converted into double Λ hypernuclei. This two-step production mechanism requires major additions to the usual simulation package PandaRoot as well as the \bar{P} ANDA setup (Fig. 2.8 in Sec. 2.2). Mandatory for this experiment is a modular and highly flexible setup of the central \bar{P} ANDA detector:

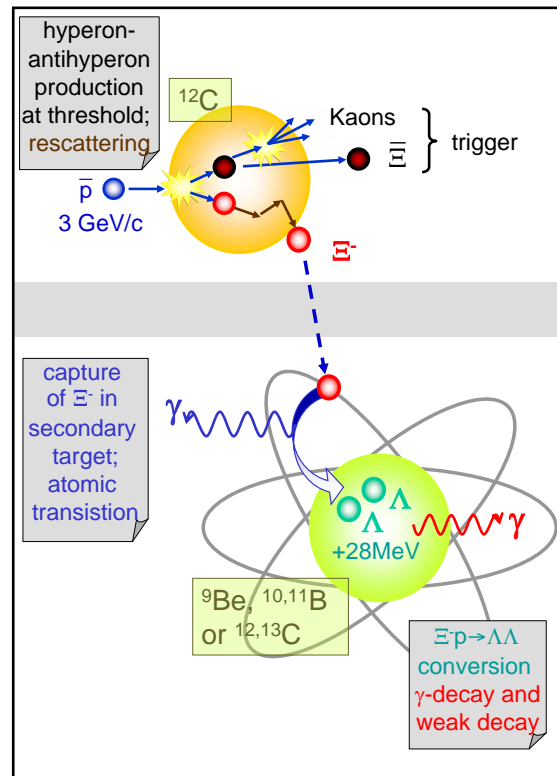


Figure 4.74: Various steps of the double hypernucleus production in \bar{P} ANDA.

- A primary carbon target at the entrance to the central tracking detector of \bar{P} ANDA. To avoid unnecessary radiation damage to the micro vertex detectors surrounding the nominal target region, these detectors will be removed during the hypernucleus runs.

- A small secondary active sandwich target composed of silicon detectors and ^9Be , $^{10,11}\text{B}$ or $^{12,13}\text{C}$ absorbers to slow down and stop the Ξ^- and to identify the weak decay products.
- To detect the γ -rays from the excited double hypernuclei an array of 15 n-type Germanium triple Cluster-arrays will be added. To maximize the detection efficiency the γ -detectors must be arranged as close as possible to the target. Hereby the main limitation is the load of particles from \bar{p} -nucleus reactions. Since the γ -rays from the slowly moving hypernuclei is emitted nearly isotropic the Ge-detectors will be arranged at backward angles.

4.5.2.1 Simulation of Hyperon Production

At present high statistics production of hyperon-antihyperon pairs in antiproton-nucleus are not practical within full microscopic transport calculations like UrRQMD. We therefore employed an event generator [264] which is based on an Intra Nuclear Cascade model and which takes as a main ingredient the rescattering of the antihyperons and hyperons in the target nucleus into account.

Target nuclei with larger mass are more efficient for rescattering of the produced primary particles and hence for the emission of low momentum Ξ^- hyperons. However, heavier targets increase the neutron and x-ray background in the germanium detectors. Furthermore, Coulomb scattering in heavy primary targets leads to significant losses of antiprotons. Therefore it is foreseen to use thin carbon micro-ribbons [265] as a primary target in the HESR ring. For the present simulations 10^6 $\Xi^- \bar{\Xi}^-$ pairs were generated. At the incident momentum of 3 GeV/c we expect a cross section per nucleon of $2\mu\text{b}$ [266]. For comparison, at PANDA a luminosity of $10^{32}\text{cm}^{-2}\text{s}^{-1}$ for $\bar{p}+^{12}\text{C}$ reactions corresponds to about 700000 produced $\Xi^- \bar{\Xi}^-$ pairs per hour. Out of the produced 1 million pairs, 50505 contain low momentum Ξ^- with momentum less than 500 MeV/c.

4.5.2.2 Deceleration of Ξ^- Hyperons in a Secondary Target

In order to limit the number of possible transitions and thus to increase the possible signal to background ratio, the experiment will focus on light secondary target nuclei with mass number $A_0 \leq 13$. Since the identification of the double hypernuclei has to rely on the unique assignment of the detected γ -transitions, different isotopically enriched light absorbers (^9Be , $^{10,11}\text{B}$, $^{12,13}\text{C}$) will be used. In

the following we consider as an example the case of ^{12}C absorbers in all four quadrants of the secondary target.

The geometry of the target (see Fig. 2.9 in Sec. 2.2) is essentially determined by the lifetime of the hyperons and their stopping time in solid material: only hyperons with momenta smaller than about 500 MeV/c have a non-negligible chance to be stopped prior to their free decay. From 50505 pro-

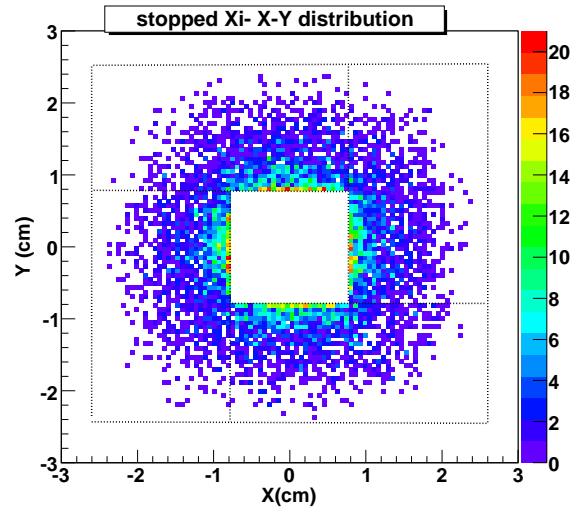


Figure 4.75: Layout out the secondary sandwich target used in the present simulations. The figure marks the stopping points of the Ξ^- hyperons within the target in the x-y plane transverse to the beam direction. The rectangles indicate the outlines of the four target segments. All four segments are equipped with ^{12}C absorbers.

duced events which contained a Ξ^- with a laboratory momentum less than 500 MeV/c, 7396 hyperons are stopped within the secondary target. The majority of the hyperons are stopped in the most inner layers of the sandwich structure (Fig. 4.75). The typical momenta of these stopped Ξ^- are in the range of 200 MeV/c (see lower part of Fig. 4.76).

Recently Yamada and co-workers studied within the framework of the doorway double- Λ hypernuclear picture [267] the production of double- Λ hypernuclei for stopped Ξ^- particles in ^{12}C [268]. Per stopped Ξ^- they predict a total double- Λ hypernucleus production probability of 4.7%. An even larger probability of 11.1% was recently obtained by Hirata *et al.* within the Antisymmetrized Molecular Dynamics approach [269, 270]. Since the present studies concentrate on the production of double hypernuclei, a full microscopic simulation of the atomic cascade and capture of the Ξ^- hyperons is not performed. For the final rate estimate we as-

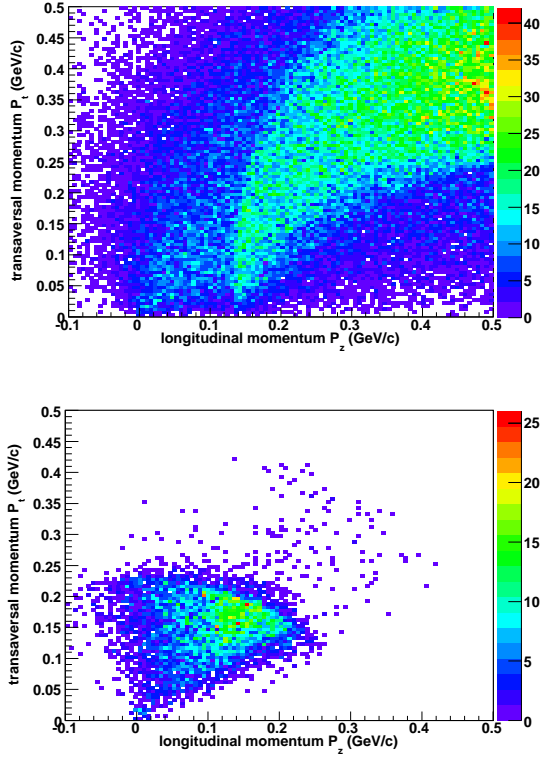


Figure 4.76: Transverse vs. longitudinal momentum distribution of Ξ^- with transverse and longitudinal momenta less than 500 MeV/c (upper part) and those stopped within the secondary target (lower part).

sume a $\Xi^- p \rightarrow \Lambda\Lambda$ conversion probability of only 5%. Of course for the study of hyperatoms the simulations need to be complemented in this aspect.

4.5.2.3 Population of Excited States in Double Hypernuclei

For light nuclei even a relatively small excitation energy may be comparable with their binding energy. Model calculations [271, 272, 252] show that the width for the conversion of a Ξ^- and a proton into two Λ 's is around 2–5 MeV, i.e. the conversion is rather fast and takes less than 100 fm/c. In this case we assume that the principal mechanism of de-excitation is the explosive decay of the excited nucleus into several smaller clusters. To describe this break-up process we have developed [273] a model which is similar to the famous Fermi model for particle production in nuclear reactions [274]. In the microcanonical model we consider all possible break-up channels, which satisfy the mass number, hyperon number (i.e. strangeness), charge, en-

ergy and momenta conservations, and take into account the competition between these channels. Previously, this model was applied rather successfully for the description of break-up of conventional light nuclei in nuclear reactions initiated by protons, pions, antiprotons and ions [275, 276, 277, 278]. The precision was around 20–50% for the description of experimental yields of different fragments. This precision is sufficient for the present analysis of hypernucleus decay, since the main uncertainty is in unknown masses and energy levels of the produced hyperfragments.

For double hypernuclei the experimental information is restricted to a few cases only [279, 280, 281, 282, 283]. Except for the ${}^6_{\Lambda\Lambda}\text{He}$ nucleus reported in Ref. [283] the interpretation of the observed events is however not unique [284, 285, 286, 287, 288]. Furthermore no direct experimental information on possible excited states is at hand (see e.g. discussion in Ref. [287]). Therefore, theoretical predictions of bound and excited states of double hypernuclei by Hiyama and co-workers [287] were used in the present model calculation for nuclei with mass number $6 \leq A_0 \leq 10$. For the mirror nuclei ${}^5_{\Lambda\Lambda}\text{H}$ and ${}^5_{\Lambda\Lambda}\text{He}$ there seems to be a consensus that these nuclei are indeed bound [260, 262, 289, 290, 291]. In view of the theoretical uncertainties, we assumed in our calculations a value for the Λ - Λ bond energy $\Delta B_{\Lambda\Lambda} = 1$ MeV for both nuclei. In case of ${}^4_{\Lambda\Lambda}\text{H}$ the experimental situation is ambiguous [282, 288] and also the various model calculations predict an unbound [292] or only slightly bound nucleus [293, 294, 291].

Also for heavier nuclei several particle stable excited states are expected [268]. The groundstate mass of these double hypernuclei was estimated from the known masses of single hypernuclei and adopting a fixed value for $\Delta B_{\Lambda\Lambda}$ of 1 MeV. Furthermore, the calculations of Hiyama and co-workers [287] signal that in the mass range relevant for this work the level structure of particle stable double hypernuclei resembles the level scheme of the corresponding core nucleus. The excitation spectrum of double hypernuclei with $A \geq 11$ was therefore assumed to be given by that of the corresponding core nucleus. Only states below the lowest particle decay threshold were considered in the present calculations.

For hypernuclei with a single Λ particle, we use the experimental masses and excited states which are summarized in various reviews (e.g. Ref. [295, 246]). In case of the production of conventional nuclear fragments in a break-up channel, we adopt their experimental ground states masses, and take into account their excited states, which are stable re-

spective to emission of nucleons (see nuclear tables, e.g. [296]). Masses of fragments in excited states were calculated by adding the corresponding excitation energy to their ground state masses.

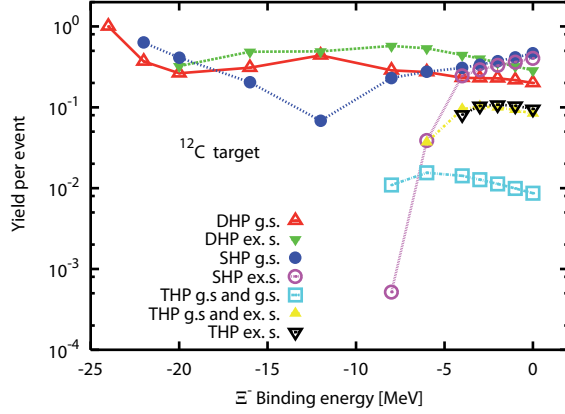


Figure 4.77: Production probability of ground (g.s.) and excited states (ex.s.) in conventional nuclear fragments and in one single (SHP), twin (THP) and double hypernuclei (DHP) after the capture of a Ξ^- in a ^{12}C nucleus and its conversion into two Λ hyperons predicted by a statistical decay model.

The main reaction which we analyze is the break-up of an excited hypernucleus with double strangeness produced after absorption of stopped Ξ^- . Unfortunately, the excitation energies of the produced hypernuclei are not well known, since this conversion may happen at different energy levels, and a part of the released energy may be lost. The maximum energy available in this case is $E_{max} = (M(\Xi^-) + M_{target})c^2$. In order to take into account a possible reduction of this energy because of the Ξ^- binding the calculations were performed for a range of energies less than E_{max} .

The Fermi break-up events were generated by comparing probabilities of all possible channels with Monte-Carlo methods. The Coulomb expansion stage was not considered explicitly for such light systems. The momentum distributions of the final break-up products were obtained by a random generation over the whole accessible phase space, determined by the total kinetic energy, taking into account exact energy and momentum conservation laws. For this purpose we applied a very effective algorithm proposed by G.I. Kopylov [297].

Fig. 4.77 shows as an example the production of ground (g.s.) and excited (ex.s.) states of conventional nuclear fragments as well as single (SHP), twin (THP) and double (DHP) hypernuclei in case of a ^{12}C target as a function of the assumed Ξ^- binding energy. According to these calculations ex-

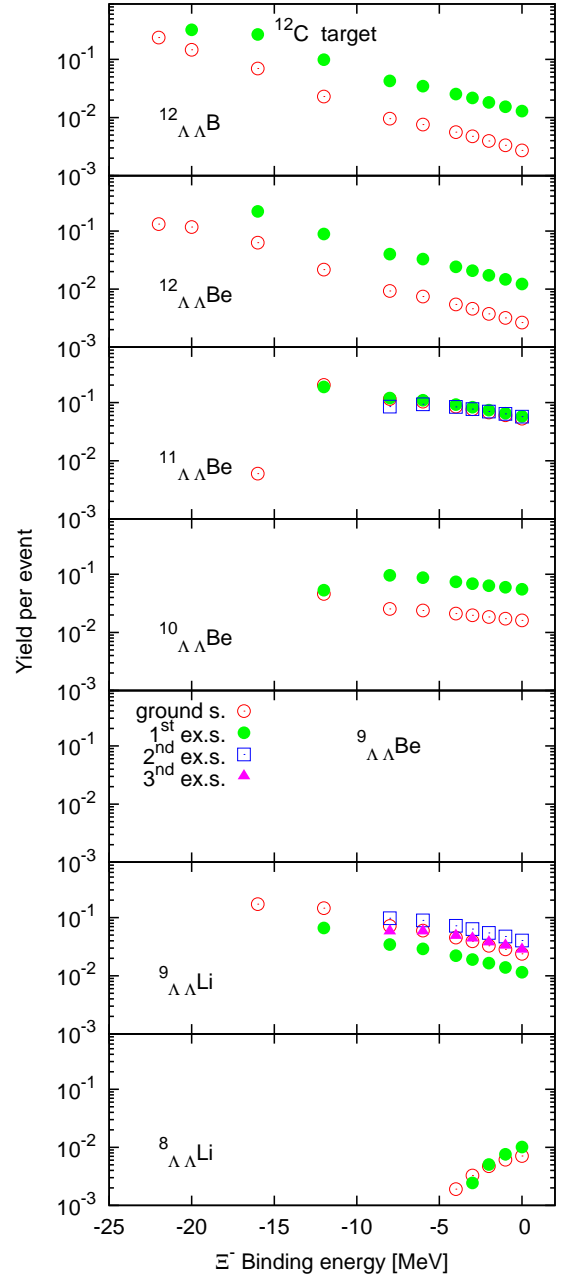


Figure 4.78: Production probability of ground and excited states of accessible double hypernuclei after the capture of a Ξ^- in a ^{12}C nucleus and the Ξ^- conversion into two Λ hyperons. Excited states in $^{11}_{\Lambda\Lambda}\text{Be}$, $^{10}_{\Lambda\Lambda}\text{Be}$ and $^9_{\Lambda\Lambda}\text{Li}$ dominate over a wide range of the Ξ^- binding energy.

cited states in double hypernuclei (green triangles) are produced with significant probability. Fig. 4.78 shows the population of the different accessible double hypernuclei. For the ^{12}C target, excited states in $^{11}_{\Lambda\Lambda}\text{Be}$, $^{10}_{\Lambda\Lambda}\text{Be}$ and $^9_{\Lambda\Lambda}\text{Li}$ dominate over a wide range

of the assumed Ξ^- binding energy.

Very little is established experimentally on the interaction of Ξ hyperons with nuclei. Various analyses (see e.g. [298, 299]) suggest a nuclear potential well depth around 20 MeV. Calculations of light Ξ atoms [300] predict that the conversion of the captured Ξ^- from excited states with correspondingly small binding energies dominates. In a nuclear emulsion experiment a Ξ^- capture at rest with two single hyperfragments has been observed [301] which was interpreted as $\Xi^- + C \rightarrow {}^4_{\Lambda}H + {}^9_{\Lambda}Be$ reaction. The deduced binding energy of the Ξ^- varied between 0.62 MeV and 3.70 MeV, depending whether only one out of the two hyperfragments or both fragments were produced in an excited particle stable state. Therefore for the present simulation of the γ -ray spectra a Ξ^- binding energy of 4 MeV was adopted. As can be seen from Fig. 4.78 this choice of the binding energy is not crucial for the final γ -ray yield.

4.5.2.4 Gamma detection

In the next step the excited particle stable states of double hypernuclei as well as excited states of conventional nuclei and single hypernuclei produced during the decay process deexcite via γ -ray emission. For the high resolution spectroscopy of excited hypernuclear states a position sensitive Germanium γ -array [302] has been implemented in the standard PANDA framework PandaRoot (see Fig. 2.8). To describe the response of these detectors, processes which are relevant for the interaction of the emitted photons with matter such as pair production, Compton scattering and the photoelectric effect have been taken into account.

Fig. 4.79 shows the total energy spectrum summed over all germanium detectors for all events where a Ξ^- has been stopped in the secondary target. Note, that the size of the bins (50 keV) in this plot is significantly larger than the resolution of the germanium detectors expected even for high data rates at normal conditions (3.4 keV at 110 kHz [303]). Even after 100 days of operation at \bar{P} ANDA and an integrated neutron fluence of about $6 \cdot 10^9$ neutrons/cm², we expect a degradation of the resolution by less than a factor of 3 to no more than 10 keV [304]. Several peaks seen in the spectrum around 1, 1.68 and 3 MeV are associated with γ -transitions in various hypernuclei. However, for a clear assignment of these lines obviously additional experimental information will be needed.

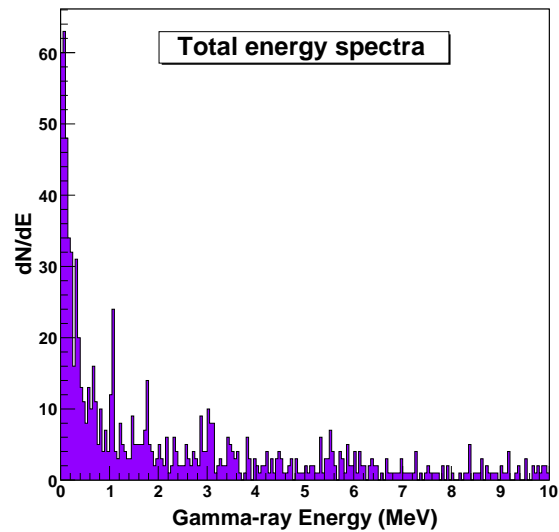


Figure 4.79: Total γ -ray spectrum resulting from the decay of double hypernuclei produced in a ${}^{12}\text{C}$ target and detected in the germanium array and before additional cuts. The statistics of the simulations corresponds to a data taking time of about two weeks.

4.5.2.5 Weak decays of Hypernuclei

For the light hypernuclei relevant for the planned experiments the non-mesonic and mesonic decays are of similar importance. In the following we will focus on the case of two subsequent mesonic weak decays of the produced double and single hypernuclei. For the light nuclei discussed below this amounts to about 10% of the total decay width (see Fig. 4.73). Since the momenta of the two pions are strongly correlated their coincident measurement provides an effective method to tag the production of a double hypernucleus. Moreover, the momenta of the two pions are a fingerprint of the hypernucleus respective its binding energy.

In \bar{P} ANDA the pions are tracked in the silicon strip detectors of the secondary target. In the present configuration silicon strip detectors with a pitch of $100\mu\text{m}$ and a two-dimensional readout are implemented. For the reconstruction the standard software package of \bar{P} ANDA was applied. Since most Ξ^- stop in the first few millimeters of the secondary target, the efficiency for tracking both pions produced in the subsequent weak decays is rather high. After the statistical decay of the 7396 produced excited Ξ^- hypernuclei, 14883 charged tracks are reconstructed out of which 8133 tracks are assigned as a π^- candidate.

The upper part of Fig. 4.80 shows the momentum correlation of all negative pion candidates from the

secondary ^{12}C target. The various bumps corresponding to different double hypernuclei are marked by different colors. The good separation of the different double hypernuclei provides an efficient selection criterion for their decays.

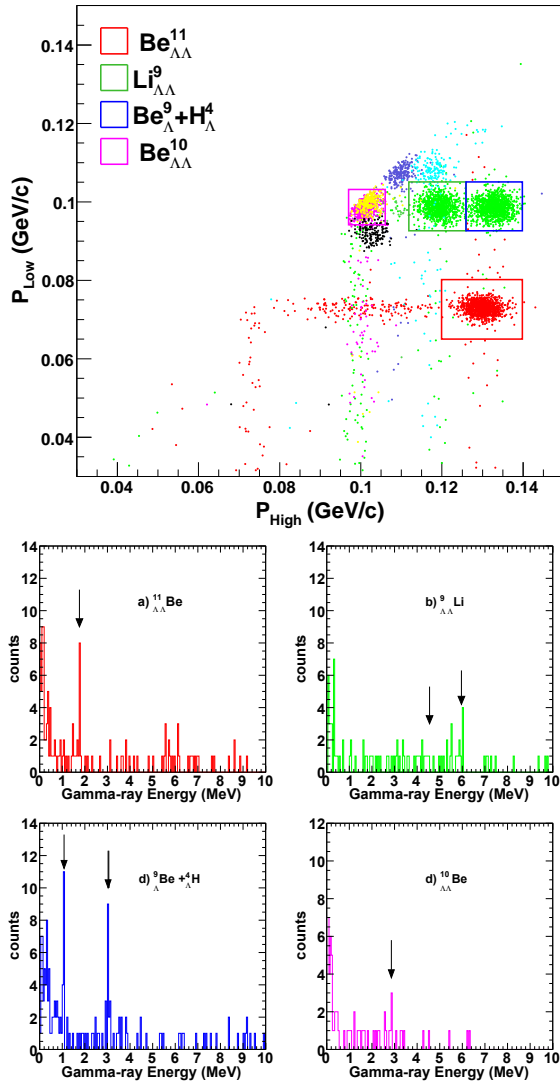


Figure 4.80: Upper part: Momentum correlation of all negative pion candidates resulting from the decay of double hypernuclei in a secondary ^{12}C target. Lower part: γ -spectrum detected in the Ge-array by cutting on the two pion momenta. The expected γ -transition energies from single and double hypernuclei are marked by the arrows.

The lower parts of Fig. 4.80 show the γ -ray spectra gated on the four regions indicated in the two-dimensional scatter plot. In the plots (a) and (d) the 1.684 MeV $\frac{1}{2}^+$ and the 2.86 MeV 2^+ states of $^{11}_{\Lambda\Lambda}\text{Be}$ and $^{10}_{\Lambda\Lambda}\text{Be}$, respectively, can clearly be identified. Because of the limited statistics in the present

simulations and the decreasing photopeak efficiency at high photon energies, the strongly populated high lying states in $^9_{\Lambda\Lambda}\text{Li}$ at 4.55 and 5.96 MeV cannot be identified in (b). The two dominant peaks seen in part (c) result from the decays of excited single hyperfragments produced in the $\Xi^- + C \rightarrow ^4_{\Lambda}H + ^9_{\Lambda}Be$ reaction, i.e. $^4_{\Lambda}H$ at an excitation energy of 1.08 MeV [305, 306] and $^9_{\Lambda}Be$ at an excitation energy of 3.029 and 3.060 MeV [307, 308].

In the present simulation several intermediate steps, which do not effect the kinematics and hence the detection of the decay products, have not been considered on an event-by-event basis. Of course, these points are relevant for the final expected count rate:

- a capture and conversion probability of the Ξ^- of 5-10%.
- typical probability of a double mesonic decay of 10% (c.f. Fig. 4.73).
- availability of data taking 50% .

With these additional factors taken into account, the spectra shown in Fig. 4.80 correspond to a running time at PANDA of about two weeks. It is also important to realize that gating on double non-mesonic weak decays or on mixed weak decays may significantly improve the final rate by up to a factor 10.

4.5.2.6 Background

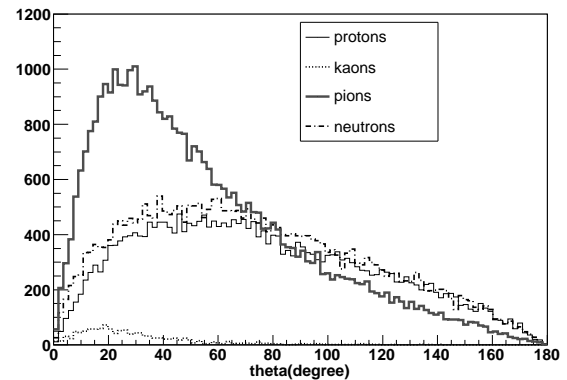


Figure 4.81: Distribution of produced particles from background reactions. The Germanium detectors will be affected mainly by particles emitted at backward axial angle.

Particles produced simultaneously with the double hypernuclei do not significantly disturb the γ -ray detection. The main limitation is the load of the

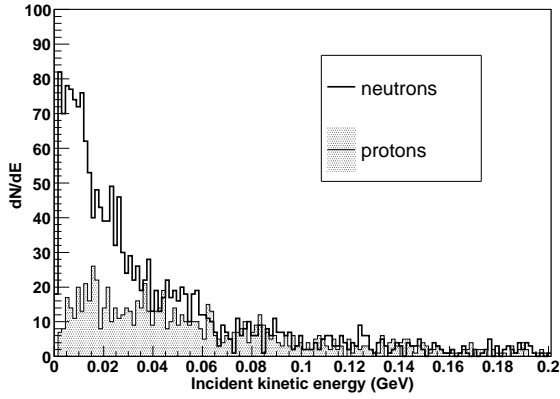


Figure 4.82: Incident kinetic energy of protons and neutrons entering the Germanium detector surface. The main contribution to a possible radiation damage of the detector is provided by neutrons.

Cluster-array by the high particles rate from uncorrelated background reactions. The $\bar{p}p \rightarrow \Xi^- \bar{\Xi}$ cross section of $2\mu b$ is about a factor 2500 smaller than the inelastic $p\bar{p}$ cross section of 50mb at 3 GeV/c. Charged particles and low energy neutrons which are emitted into the region covered by the Ge detectors will undergo electromagnetic and nuclear interactions and will thus contribute to the signal of the detector. The total energy spectra in the crystal has been obtained summing up event by event the energy contributions of the particles impinging on the Ge array.

Background reactions have been calculated by using the UrQMD+SMM [309] event Generator. At present, it is not possible to simulate the detector response for a sample of unspecific background events which is large enough to test background suppression in all details. The background suppression and signal detection capability can therefore only be estimated by using extrapolations based on simplified assumptions. For the present analysis 10000 $\bar{p} + {}^{12}C$ interactions at 3 GeV/c were generated. Most of the produced charged and neutrals particles are emitted into the forward region not covered by the Germanium array (see Fig. 4.81). Charged particles emitted into backward axial angles are very low in kinetic energy, and will be absorbed to a large fraction in the material surrounding the primary target. More critical are neutrons emitted into the backward direction which also contribute to the radiation damage of the detector. Fig. 4.82 shows the kinetic energy distribution of protons and neutrons entering the surface of the Germanium detectors.

The total energy spectra resulting from the back-

ground simulation have been filtered by using the same technique as it was done for the signal events. Particularly the same cuts on correlated pion candidates have been applied to the background events, in order to obtain the corresponding background spectrum for each of the hypernuclei channels. For ${}^{11}_{\Lambda\Lambda}Be$ as well as ${}^{10}_{\Lambda\Lambda}Be$ only one single event survived the cuts. Both of these events had an energy deposition in the germanium detector exceeding 10 MeV significantly.

Several further improvements of the background suppression are expected by exploring the topology of the sequential weak decays. This includes the analysis of tracks not pointing to the primary target, multiplicity jumps in the detector planes and the energy deposition in the secondary target. Furthermore kaons detected in the central detector of $\bar{P}ANDA$ at forward angles can be used to tag the Ξ^- production.

4.6 The structure of the nucleon using electromagnetic processes

COMMENT: Author(s): M.P. Bussa, M. Düren, F. Maas, M. Maggiora

4.6.1 Distribution amplitudes in hard exclusive $p\bar{p}$ -annihilation

Introduction

A wide area of the physics program of $\bar{\text{PANDA}}$ concerns studies of the non-perturbative region of QCD. However, the experimental setup foreseen offers the opportunity to study also a certain class of hard exclusive processes that give insight into an intermediate region, which marks the transition towards increasingly important perturbative QCD effects.

In the recent years, the theoretical framework of generalized parton distributions (GPDs) has been developed, which allows treating hard exclusive processes in lepton scattering experiments on a firm QCD basis [310, 311, 312, 313]. This is possible under suitable conditions where one can factorize short and long distance contributions to the reaction mechanism. Being related to non-diagonal matrix elements, GPDs do not represent any longer a mere probability, but rather the interference between amplitudes describing different parton configurations of the nucleon, thus giving access to various momentum correlations. Their importance was first stressed in studies of deeply virtual Compton scattering (DVCS)[314, 315, 316], for which it could be rigorously proven that the QCD handbag diagram (see Fig. 4.83) dominates the process in certain kinematical domains and that factorization holds, *i.e.* that the process is divided into a hard perturbative QCD process and a soft part of the diagram which is parameterized by GPDs. The application of perturbative QCD is possible in DVCS due to the hard scale defined by the large virtuality Q^2 of the exchanged photon. A second example for the application of the handbag formalism is wide angle Compton scattering (WACS). Here the hard scale is related to the large transverse momentum of the final state photons.

The important question which arises is whether the concepts that are used in lepton scattering experiments have universal applicability and can therefore be used in studies of $p\bar{p}$ -annihilation processes

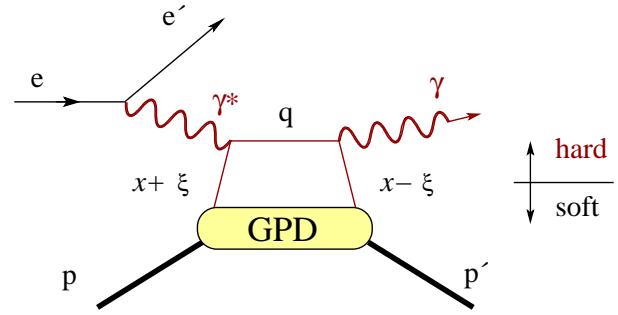


Figure 4.83: DVCS can be described by the handbag diagram, as there is factorization between the upper ‘hard’ part of the diagram which is described by perturbative QCD and QED, and a lower ‘soft’ part that is described by GPDs.

with the crossed kinematics. The crossed diagram of WACS is the process $p\bar{p} \rightarrow \gamma\gamma$ with emission of the two final state photons at large polar angle in the CM system (see Fig. 4.84). It can be shown that

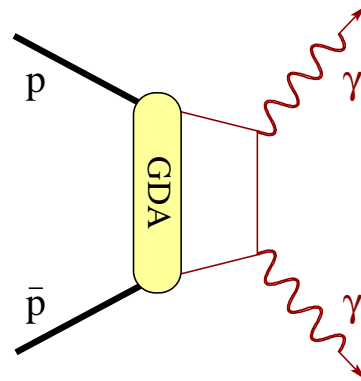


Figure 4.84: The handbag diagram may describe the inverted WACS process $p\bar{p} \rightarrow \gamma\gamma$ at $\bar{\text{PANDA}}$ energies.

the handbag approach is not appropriate to describe the crossed channel WACS neither at very small nor at very large energies [317, 318]. However, there are strong arguments and first experimental indications that the handbag approach is appropriate at the intermediate energy regime where $\bar{\text{PANDA}}$ operates [319, 320], even though a rigorous proof of factorization has not been achieved yet. The corresponding amplitudes that parameterize the soft part of the annihilation process (*i.e.* the counterparts of GPDs) are called generalized distribution amplitudes (GDAs). The measurement of the process $p\bar{p} \rightarrow \gamma\gamma$ as a function of s and t is an experimental challenge, due to the smallness of the cross section. The high luminosity and the excellent de-

tector, especially the 4π electromagnetic calorimeter, should enable \bar{P} ANDA to separate this process from the large hadronic background.

A second, much more abundant process that can be described in terms of handbag diagrams is $p\bar{p} \rightarrow \pi^0\gamma$. In contrast to WACS, in this case one photon is replaced by a pseudoscalar meson, but otherwise the theoretical description is similar. First experimental results from the Fermilab experiment E760 indicate that the handbag approach is appropriate to accommodate the data in the range $s \sim 8.5 - 13.5 \text{ GeV}^2$ [319].

The handbag approach (*i.e.* the factorization assumption) is suitable for the description of further reactions, like $p\bar{p} \rightarrow M\gamma$ where M is any neutral meson (*e.g.* a ρ^0) or $p\bar{p} \rightarrow \gamma^*\gamma$, where γ^* decays into an e^+e^- or $\mu^+\mu^-$ -pair. The latter process is described by the crossed diagram of DVCS. Unfortunately, the factorization proof in DVCS $\gamma^*p \rightarrow \gamma p$ is not applicable for the crossed diagram $p\bar{p} \rightarrow \gamma^*\gamma$, as the virtuality Q^2 of the final state γ^* is limited to be smaller than s , in contradiction to the assumption made in the proof of factorization of this diagram in DVCS kinematics.

In a complementary theoretical approach, the process $p\bar{p} \rightarrow \gamma^*\gamma$ is not described by the handbag diagram but by so-called transition distribution amplitudes (TDAs) [321] that parameterize the transition of a proton into a (virtual) photon according to the diagram in Fig. 4.85.

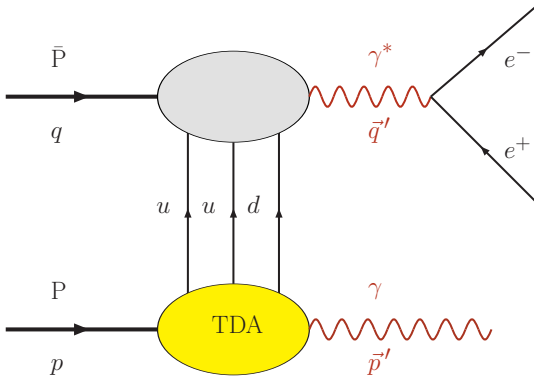


Figure 4.85: The production of a hard virtual photon (upper part) is a hard sub-process that is claimed to factorize from the lower part, which can be described by a hadron to photon transition distribution amplitude (TDA).

The theoretical understanding of GPDs and related unintegrated distributions is just at its beginning. There is an extended experimental endeavor by lepton scattering experiments at DESY, CERN and

JLAB to get access to these powerful distributions. \bar{P} ANDA has the chance to join this quest for an improved description of the nucleon structure by measuring the crossed-channel counterparts of these distributions in hard exclusive processes with various final states in a new kinematical region. New insights into the applicability and universality of these novel QCD approaches can be expected.

Crossed-channel Compton scattering

It has been argued [322] that the crossed-channel Compton scattering, namely exclusive proton-antiproton annihilation into two photons, $p\bar{p} \rightarrow \gamma\gamma$ can also be described in a generalized parton picture at large s with $|t|, |u| \sim s$. The two photons are predominantly emitted in the annihilation of a single “fast” quark and antiquark originating from the proton and antiproton. The new double distributions, describing the transition of the $p\bar{p}$ system to a $q\bar{q}$ pair, can be related to the timelike nucleon form factors; by crossing symmetry they are also connected with the usual quark/antiquark distributions in the nucleon. With a model for the double partonic distributions one can compute the $p\bar{p} \rightarrow \gamma\gamma$ amplitude from the handbag graphs of Fig. 4.84. The result for the helicity-averaged differential cross section is

$$\frac{d\sigma}{d\cos\theta} = \frac{2\pi\alpha_{\text{em}}^2}{s} \frac{R_V^2(s) \cos^2\theta + R_A^2(s)}{\sin^2\theta} \quad (4.52)$$

with the energy dependency of the squared form factors $R_V^2(s)$ and $R_A^2(s)$ depicted in Fig. 4.86.

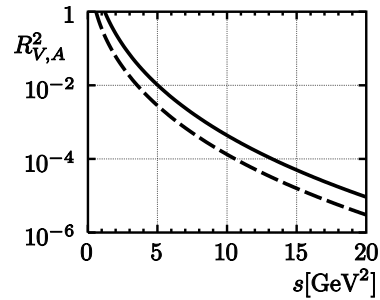


Figure 4.86: The squared form factors $R_V^2(s)$ (solid line) and $R_A^2(s)$ (dashed line), as calculated from the double distribution model (Fig. 2 of ref. [322])

Recent measurements of the time-reversed process $\gamma\gamma \rightarrow p\bar{p}$ by the BELLE collaboration [320] tend to confirm the predicted asymptotic behavior at higher energies, however at intermediate energies (2.5 – 4 GeV) they can not be entirely explained by the existing theoretical models.

Hard exclusive meson production

Besides detecting $p\bar{p} \rightarrow \gamma\gamma$, hard exclusive meson production, like $p\bar{p} \rightarrow \gamma\pi^0$, can also provide valuable information about the structure of the proton. In treating this process, one can adopt as start-

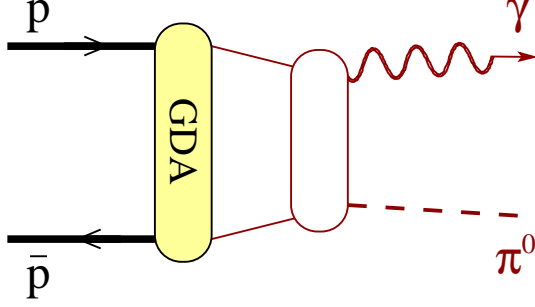


Figure 4.87: The handbag contribution to $p\bar{p} \rightarrow \gamma\pi^0$ at large but non-asymptotic s . The blob on the right hand side represents the parameterized general dynamics for $q\bar{q} \rightarrow \gamma\pi^0$

ing point the assumption of the handbag factorization of the amplitude for the kinematical region $s, -t, -u \gg \Lambda^2$ (see Fig. 4.87), where Λ is a typical hadronic scale of the order of 1 GeV, as in [319]. A comparison with existing Fermilab E760 data [323] concerning both the energy dependence of the integrated cross section and angular distribution of the differential cross section makes it possible to have a reliable prediction for the differential cross section of $p\bar{p} \rightarrow \gamma\gamma$ at PANDA, as shown in Fig. 4.88.

Simulation of $p\bar{p} \rightarrow \gamma\gamma$ and $p\bar{p} \rightarrow \gamma\pi^0$

In order to test the possibility of detection of both the $p\bar{p} \rightarrow \gamma\gamma$ and $p\bar{p} \rightarrow \gamma\pi^0$ reactions, Monte Carlo simulations were run within the PANDARoot framework. The main goal of these studies was to estimate the ability of the PANDA detector system to separate useful physics events from the background.

The main background for the crossed channel Compton scattering $p\bar{p} \rightarrow \gamma\gamma$ comes from reactions with neutral hadrons in the final states, like $p\bar{p} \rightarrow \pi^0\pi^0$ or $p\bar{p} \rightarrow \gamma\pi^0$. After a comparison of the various cross sections of interest at PANDA energies, given in Fig. 4.89, it can be concluded that the number of the exclusive background events considered is roughly three (respectively two) orders of magnitudes higher than the number of the events of interest. This result has been taken into account all along our studies.

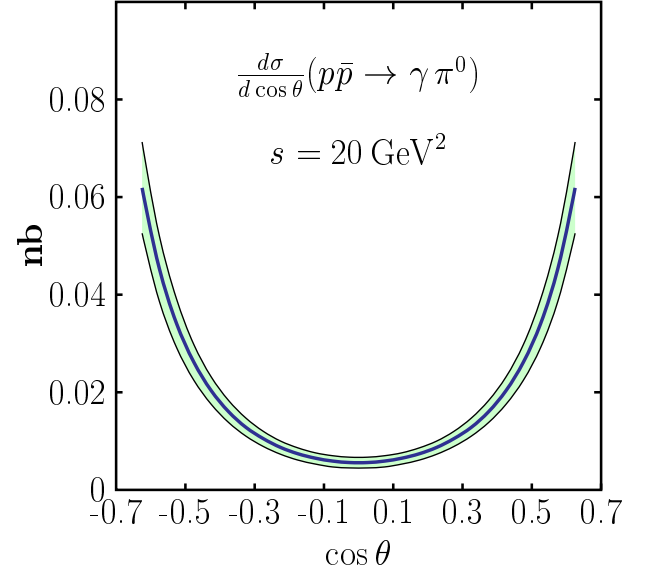


Figure 4.88: Cross section prediction for the angular distribution at $s = 20 \text{ GeV}^2$ for PANDA taken from ref. [319].

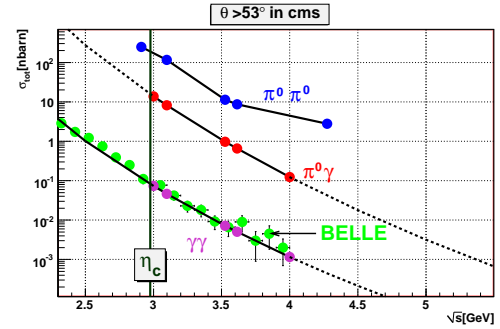


Figure 4.89: Cross sections for processes with $\gamma\gamma$, $\pi^0\gamma$ and $\pi^0\pi^0$ in the final state, for different PANDA energies. The results correspond to particles with $|\cos(\theta)| < 0.6$ in the center of mass system (Refs. [324, 319, 320]).

The background has a significant constituent originating in reactions with charged particles in the final states. These events are supposed to be vetoed by the detector subsystems that are sensitive to charged particles, however a systematic study of them was not yet performed.

In order to test the detector response, $\gamma\gamma$, $\pi^0\gamma$ and $\pi^0\pi^0$ events were generated using EvtGen. For the angular distribution of $\gamma\gamma$ events Eq. 4.52 fitted to the BELLE data [320] was used, for $\pi^0\gamma$ results similar to the one in Fig. 4.88 in [319] were considered, the $\pi^0\pi^0$ distribution follows the one given by Ong and Van de Wiele [324]. The center of

mass angle of the generated particles was limited by $|\cos(\theta)| < 0.6$.

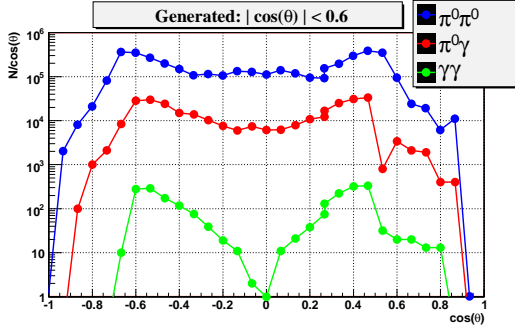


Figure 4.90: Angular distribution of generated particles in the center of mass system, as seen by the detector.

Fig. 4.90 gives the distribution of reconstructed events in the electromagnetic calorimeter. The influence of the asymmetric detector system is clearly visible, which introduces a difference between the angular distribution of particles moving in forward or backward direction. Noticeably, detected particles seem to be found also outside the $|\cos(\theta)| < 0.6$ angular limit, a feature caused by the finite digitization in the detector.

For the reconstruction of $\gamma\gamma$ events the following algorithm was used:

- Identify all the bumps in the electromagnetic calorimeter and order them according to their energy in the center of mass system.
- Associate single photons with the first two bumps of highest cms-energy.
- Evaluate the kinematic factor

$$K_{\gamma\gamma} \sim \sqrt{|\vec{p}_{\bar{p}} - \vec{p}_{\gamma_1} - \vec{p}_{\gamma_2}|^2 + |E_L - E_{\gamma_1} - E_{\gamma_2}|^2} \times \left(\frac{1}{\sqrt{\vec{p}_{\gamma_1}^2 + E_{\gamma_1}^2}} + \frac{1}{\sqrt{\vec{p}_{\gamma_2}^2 + E_{\gamma_2}^2}} \right) \quad (4.53)$$

Events with $\gamma\pi^0$ in the final state are reconstructed in a slightly different way:

- Order the bumps in the EMC as above.
- Associate a single photon to the first one, the photons from π^0 to the next two of them.
- Evaluate the kinematic factor $K_{\gamma\pi^0}$ similar to Eq. 4.53

First a comparison of the kinematic factors for the signal and background is performed, followed by a cut on the value of the kinematic factor in order to further eliminate possible misidentifications. Finally, a cut on the number of hits in the EMC is applied to differentiate between photons and pions.

In Fig. 4.91 and 4.92 preliminary results on the separability of $\gamma\gamma$, $\gamma\pi^0$ and $\pi^0\pi^0$ events are presented. Five different $\bar{p}p$ center of mass energies ($\sqrt{s} = 2, 2.5, 3.5, 4$ and 5.5 GeV) were considered, and for all energies 1000 events of the type $\gamma\gamma$, and 10,000 events of the types $\pi^0\gamma$ and $\pi^0\pi^0$ were generated in the $|\cos(\theta)| < 0.6$ angular interval. A full simulation of the detector system was performed and the event recognition algorithms with the corresponding cuts were applied.

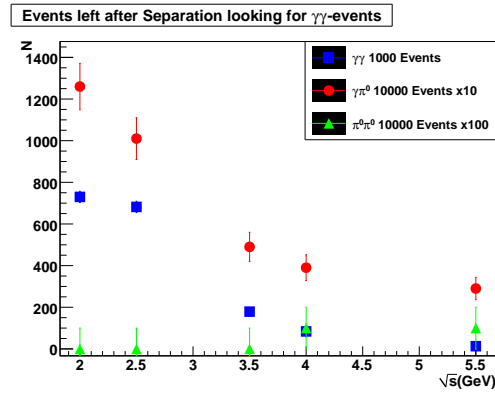


Figure 4.91: Separation of $\gamma\gamma$ events from the neutral background $\gamma\pi^0$ and $\pi^0\pi^0$ is not yet possible with the current selection algorithms. The number of misidentified $\gamma\pi^0$ ($\pi^0\pi^0$) events and their statistical error were magnified by a factor 10^2 , (10^3) to match the limited Monte Carlo statistics to the abundance of the background in the experiment.

To obtain a realistic picture, the ratio of the cross sections (see Fig. 4.89) for the various processes involved must be taken into account, when evaluating the possibility of detecting an useful physics signal. Therefore, lacking the necessary Monte Carlo statistics, the numbers of $\pi^0\gamma$ and $\pi^0\pi^0$ events misidentified as $\gamma\gamma$ have to be multiplied by factors of 10 and 100, respectively (see Fig. 4.91). A similar approach was taken while identifying $\pi^0\gamma$ events (Fig. 4.92). In this case the number of misidentified $\pi^0\pi^0$ events (and its error) were multiplied only by a factor of 10.

After this selection and normalization, the $\gamma\gamma$ signal is still dominated by pion background, which means that the separation algorithms are not sufficient to isolate this class of events. The studies are still very

preliminary and only simple cuts were applied, so that we are positive that more sophisticated cuts in future will improve the situation.

The separation of exclusive $\gamma\pi^0$ events is possible up to about 4 GeV after applying the above simple cuts as shown in Fig. 4.92.

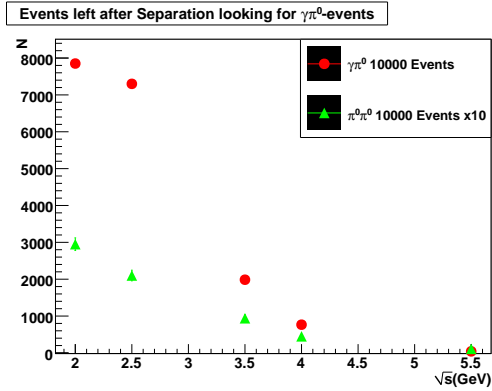


Figure 4.92: Separation of $\gamma\pi^0$ events from the neutral background. The number of misidentified $\pi^0\pi^0$ events and their statistical error was magnified by factor 10.

Conclusions

First simulation results suggest that the interesting process of $p\bar{p} \rightarrow \gamma\gamma$ is hard to measure, and simple selection criteria are not sufficient to isolate the signal. More sophisticated analysis methods have to be developed to measure the $\gamma\gamma$ cross section. The $p\bar{p} \rightarrow \gamma\pi^0$ simulations suggest that this exclusive reaction can be successfully measured at PANDA. The performance of the EMC plays a crucial role for the measurement of these processes. A more detailed study of the event recognition algorithms and the applied cuts, as well as considerably increased Monte Carlo statistics are required for more precise predictions.

4.6.2 Transverse Parton Distribution Functions in Drell-Yan Production

COMMENT: Author(s): M.P. Bussa, M. Maggiora

COMMENT: Referee(s): D. Bettoni

Theoretical introduction

In a Drell-Yan (DY) process $\bar{p}^{(\dagger)}p^{(\dagger)} \rightarrow \mu^+\mu^-X$ two (eventually polarised) hadrons H_1 and H_2 annihilate into a lepton-antilepton pair $\bar{l}l$; hadrons carry momenta P_1 and P_2 respectively ($P_{1,2}^2 = M_{1,2}^2$) and spins S_1, S_2 ($S_{1,2} \cdot P_{1,2} = 0$), the $\bar{l}l$ momenta being k_1, k_2 ($k_{1,2}^2 \sim 0$). Relevant kinematic variables are the initial squared energy in the center-of-mass (CM) frame $s = (P_1 + P_2)^2$, and the time-like momentum transfer $q^2 \equiv Q^2 = (k_1 + k_2)^2 \geq 0$ directly related to the final state invariant mass ($Q^2 \equiv M_{\bar{l}l}^2$).

In the DIS regime, defined by the limit $Q^2, s \rightarrow \infty$ with limited $0 \leq \tau = Q^2/s \leq 1$, a DY process can be described factorising an elementary annihilation process $\bar{q}q \rightarrow \bar{l}l$ with two soft correlation functions describing the annihilating antiparton (1) and parton (2) distributions in the parent hadrons:

$$\begin{aligned} \bar{\Phi}(p_1; P_1, S_1) &= \int \frac{d^4z}{(2\pi)^4} e^{-ip_1 \cdot z} \langle P_1 S_1 | \bar{\psi}(z) \psi(0) | P_1, S_1 \rangle, \\ \Phi(p_2; P_2, S_2) &= \int \frac{d^4z}{(2\pi)^4} e^{ip_2 \cdot z} \langle P_2, S_2 | \bar{\psi}(0) \psi(z) | P_2, S_2 \rangle. \end{aligned} \quad (4.54)$$

The dominant contribution in leading order is depicted in Fig. 4.93 [325], provided that M is constrained inside a range where the elementary annihilation can be safely assumed to proceed through a virtual photon converting into the final $\bar{l}l$.

At $Q^2 \rightarrow \infty$ the parton momenta $p_{1,2}$ are approximately aligned with the corresponding hadron and antihadron momenta $P_{1,2}$, the corresponding light-cone fractions of the parton momenta being $x_{1,2} = \frac{p_{1,2}}{P_{1,2}} \simeq \frac{Q^2}{2P_{1,2} \cdot q}$ ($q = p_{1,2}$, by momentum conservation [326]); momenta $\mathbf{p}_{1,2T}$ (often addressed in the literature as \mathbf{k}_\perp), the intrinsic transverse momenta of the partons in the parent hadron w.r.t. the axis defined by the corresponding hadron 3-momentum $\mathbf{P}_{s_{1,2}}$, are bound by the momentum conservation $\mathbf{q}_T = \mathbf{p}_{1T} + \mathbf{p}_{2T}$, where \mathbf{q}_T is the transverse momentum of the final lepton pair.

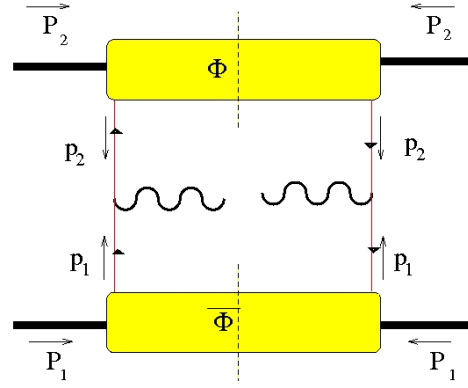


Figure 4.93: The leading-twist contribution to the Drell-Yan dilepton production [325]; the correlation functions for the annihilating hadrons $\bar{\Phi}$ and Φ can be parametrised considering explicitly their dependence on the transverse parton momenta \mathbf{p}_{1T} and \mathbf{p}_{2T} [327], thus leading to Eq. 4.57.

If $\mathbf{q}_T \neq 0$ the annihilation direction is not known and a convenient reference frame is needed; the Gottfried-Jackson (GJ) frame and the u -channel frame being other popular choices, the most commonly adopted frame is the so called Collins-Soper frame [328] (see fig. 4.94), defined by:

$$\hat{t} = \frac{q}{Q}, \quad \hat{z} = \frac{x_1 P_1}{Q} - \frac{x_2 P_2}{Q}, \quad \hat{h} = \frac{q_T}{|\mathbf{q}_T|} \quad (4.55)$$

where azimuthal angles lie in the plane perpendicular to \hat{t} and \hat{z} : ϕ and $\phi_{S_{1,2}}$ are respectively the angles of \hat{h} and of the nucleon spin $\mathbf{S}_{1,2T}$ with respect to the lepton plane.

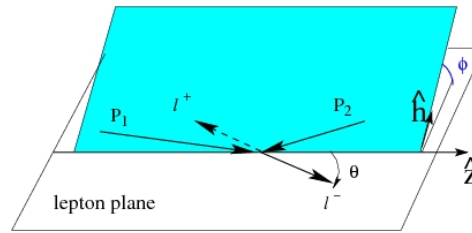


Figure 4.94: The Collins-Soper (CS) frame [328].

In collinear kinematics ($\mathbf{p}_{1,2T} \sim 0$, i.e. neglecting dependencies on the \mathbf{k}_\perp) a factorised pQCD approach cannot interpret experimental unpolarised cross sections for inclusive particle production in high-energy hadron-hadron production [329]; only recently NLO calculations including threshold resummation effects have been developed [330], in reasonable agreement with inclusive cross sections integrated over the hadron rapidity range, but the

rapidity-dependent case is still under investigation. Moreover the collinear kinematics approach fails in particular considering the DY production at low lepton-pair transverse momentum: no transverse momentum can be generated in the collinear LO approximation.

The role of parton's intrinsic transverse momentum has thus to be explicitly accounted for; since the early interest of Feynman and collaborators [331,

332] huge efforts have been dedicated to provide a full set of Transverse-Momentum Dependent (TMD) Parton Distribution Functions (PDF) and Fragmentation Functions (FF). The generalisation of the pQCD factorisation theorem to the TMD scenario has been formally proved for the DY processes [328]; at leading twist eight independent TMD PDF distributions are needed to describe the nucleonic structure and the nucleonic correlator can be parametrised as [327]:

$$\begin{aligned} \Phi(x, \mathbf{p}_T, S) = & \frac{1}{2} \left\{ f_1 \not{n}_+ + f_{1T}^\perp \frac{\epsilon_{\mu\nu\rho\sigma} \gamma^\mu n_+^\nu p_T^\rho S_T^\sigma}{M} + \left(S_L g_{1L} + \frac{\mathbf{p}_\perp \cdot \mathbf{S}_T}{M} g_{1T} \right) \gamma^5 \not{n}_+ \right. \\ & \left. + h_{1T} i\sigma_{\mu\nu} \gamma^5 n_+^\mu S_T^\nu \left(S_L h_{1L}^\perp + \frac{\mathbf{p}_\perp \cdot \mathbf{S}_T}{M} h_{1T}^\perp \right) \frac{i\sigma_{\mu\nu} \gamma^5 n_+^\mu p_T^\nu}{M} + h_1^\perp \frac{\sigma_{\mu\nu} p_T^\mu n_+^\nu}{M} \right\} \end{aligned} \quad (4.56)$$

where n_\pm are auxiliary light-like vectors, M is the nucleon mass, and all the TMD PDF's depend on x and $|\mathbf{p}_\perp|$ (e.g. $f_1 = f_1(x, \mathbf{p}_T^2)$). This form of the TMD approach is also addressed in the literature as Generalised Parton Model (GPM). Several notations are used for the TMD's nomenclature [333, 334]; in the one [335] adopted in Eq. 4.56, f , g and h refer respectively to unpolarised, longitudinally polarised and transversely polarised quarks, to longitudinal and transverse hadron polarisation (subscripts L and T), at leading twist (subscript 1), explicitly dependent on intrinsic momenta (apex \perp). The functions f_1 and h_1^\perp (a.k.a. Boer-Mulders, BM, function) are the distributions of respectively unpolarised and transversely polarised partons in unpolarised hadrons; f_{1T}^\perp (a.k.a. Sivers function) and h_{1T} (a.k.a. Transversity) the distributions of respectively unpolarised and transversely polarised partons in a transversely polarised nucleon.

The Transversity distribution h_{1T} is historically the first TMD PDF to be introduced [325] right for DY processes; it is a leading-twist distribution [336, 337], not diagonal in the parton helicity basis, since involves a helicity flipping mechanism at parton level. It is hence chirally-odd, since at leading twist chirality and helicity are identical, and this is reason why it cannot be accessed in DIS: QED and QCD for massless quarks conserve helicity, and thus h_{1T} pertains the "soft" domain where the chiral symmetry of QCD is (spontaneously) broken. To be measured in a (chirally-even) cross-section or asymmetry it needs another chiral-odd partner, in contrast with the unpolarised and the

helicity distribution functions, both chiral-even (see for a review also Refs. [338, 334]). It is linked to other TMD distributions by the well-known Soffer inequality ($2|h_{1T}| \leq (f_1 + g_{1L})$) [339]. As originally proposed in Ref. [325] the most promising source of information for h_{1T} is the double transverse spin asymmetry in DY processes, where it appears quadratically (Eq. 4.64), but h_{1T} can be accessed in the single-polarised DY as well, convoluted with h_1^\perp (Eq. 4.61). In the transverse spin basis h_{1T} is diagonal and can be interpreted as the difference between the probabilities to find a quark polarised along the transverse proton polarisation and against it. In a nucleon (and more generally in any spin $\frac{1}{2}$ hadron) it has no gluonic counterpart, due to the mismatch in the change of helicity units, and its evolution is hence decoupled from radiative gluons; it also decouples from charge-even $q\bar{q}$ configurations of the Dirac sea, because it is odd also under charge conjugation transformations. The prediction of its weaker evolution [338] could represent a basic test of QCD in the non-perturbative domain.

The Sivers function f_{1T}^\perp (originally suggested in [340, 341]) is a T-odd chirally-even \mathbf{p}_\perp -odd distribution describing how the distribution of unpolarised quarks is affected by the transverse polarisation of the parent proton, and is related to azimuthal asymmetries in single-polarised DY $\bar{p}p^\uparrow \rightarrow l^+l^-X$ (Eq. 4.61); a measurement of a non-vanishing asymmetry would be a direct evidence of the orbital angular momentum of quarks [342]. It appears at leading twist as well in semi-inclusive DIS (SIDIS) processes like $lp^\uparrow \rightarrow l'\pi X$ [343] or $pp^\uparrow \rightarrow \pi X$ [344],

where it is responsible of the so-called Sivers effect, the azimuthal asymmetric distribution of the detected pions depending on the direction of the target polarisation, since it is proportional [327, 333] to the function $\Delta^N f$ of Refs. [345, 346]. It is addressed in the literature as "Sivers function" as well.

The Boer-Mulders (BM) function h_1^\perp , proposed in Ref. [326] as a possible tool to explain the azimuthal asymmetry observed in unpolarised DY processes (Eq. 4.57 and Eq. 4.59), appears convoluted with h_{1T} in the single-polarised DY cross sections as well [326] (Eq. 4.61); it describes the influence of the quark transverse polarisation on its momentum distribution inside an unpolarised parent nucleon and, being a chirally-odd PDF, it cannot be extracted from DIS data [347]. Its relevance arises from the violation of the Lam-Tung sum rule [348, 349, 350] caused by a sizeable azimuthal asymmetry in the unpolarised DY cross section that cannot be explained neither by NLO QCD calculations [351] nor by higher twists or factorisation-breaking terms in NLO QCD [352, 353, 354].

It was stated before that the DY production at low lepton-pair transverse momentum can not be interpreted in the framework of collinear kinematics; the energy evolution of the spin and TMD distributions had been discussed in [355] resumming the large logarithms arising in perturbative calculations for SIDIS and DY process at low transverse momentum. To extend the validity of the TMD factorisation approach from the very small q_T range to the moderate transverse momentum region (yet with $q_T \ll Q$) soft gluon radiation has to be accounted for by the mean of Sudakov factors included by proper resummation; the outcome is a suppression of the TMD azimuthal asymmetries that becomes more important with rising energy [356].

It should be stressed that theoretical approaches other than the TMD formalism do exist; in particular the one considering twist-three effects in collinear pQCD, whose origin dates back to [357], allows to evaluate the azimuthal asymmetries in the framework of pQCD generalised factorisation theorems with the introduction of new twist-three quark-gluon correlator functions convoluted with

ordinary twist-two parton distribution functions and a short-distance hard scattering part; such functions do not have a simple partonic interpretation, being expectation values between hadronic states of three field operators. See Ref. [358] for a more detailed discussion of such functions and of their relation with SSA.

A comparison of the twist-three and of the TMD approaches [359, 360, 361, 362] to SIDIS and DY processes shows how both mechanisms, yet having different validity domains, describe the same physics in the overlapping kinematic region. In the twist-three approach domain (large lepton pair transverse momentum and photon virtuality: $\mathbf{q}_T, Q \gg \Lambda_{\text{QCD}}$) twist-three quark-gluon correlations can lead to the spin-dependent cross section; at $q_T \simeq \Lambda_{\text{QCD}} \ll Q$ single spin asymmetries (SSA) can be generated from spin-dependent TMD quark distributions; in the domain $q_T \simeq \Lambda_{\text{QCD}} \ll Q$, q_T is large enough for the asymmetry to be a twist-three effect but at the same time a $q_T \ll Q$ allows for the TMD factorisation formalism. The connections between such different formalisms lead to strong constraints on those phenomenological studies aiming at the dynamics underlying transverse SSA.

Experimental data and theoretical interpretations

We will focus herewith on the unpolarised and single-polarised DY processes, that can be accessed in the \bar{P} ANDA scenario respectively since the very beginning and when a polarised target will eventually become available; nevertheless double-polarised DY processes will be shortly addressed as well, being the most promising scenario to access transversity effects in the nucleon dynamics, even if in such a case an antiproton polarisation is needed, and such a polarisation can eventually be provided only in later FAIR stages.

The unpolarised case: $\bar{p}p \rightarrow l^+l^-X$

The TMD leading-twist parametrisation of $\bar{\Phi}$ and Φ [327] leads to the following fully differential cross section for the unpolarised DY process [326]:

$$\frac{d\sigma^o}{d\Omega dx_1 dx_2 d\mathbf{q}_T} = \frac{\alpha^2}{12Q^2} \sum_f e_f^2 \left\{ (1 + \cos^2 \theta) \mathcal{F} \left[\bar{f}_1^f f_1^f \right] + f \sin^2 \theta \cos 2\phi \mathcal{F} \left[\left(2\hat{\mathbf{h}} \cdot \mathbf{p}_{1T} \hat{\mathbf{h}} \cdot \mathbf{p}_{2T} - \mathbf{p}_{1T} \cdot \mathbf{p}_{2T} \right) \frac{\bar{h}_1^{\perp f} h_1^{\perp f}}{M_1 M_2} \right] \right\}, \quad (4.57)$$

α being the fine structure constant, e_f the charge of a parton with flavour f . The TMD PDF's are

convoluted with their antiparton partners according to:

$$\mathcal{F} \left[\bar{f}_1^f f_1^f \right] \equiv \int d\mathbf{p}_{1_T} d\mathbf{p}_{2_T} \delta(\mathbf{p}_{1_T} + \mathbf{p}_{2_T} - \mathbf{q}_T) \left[\bar{f}_1^f(x_1, \mathbf{p}_{1_T}) f_1^f(x_2, \mathbf{p}_{2_T}) + (1 \leftrightarrow 2) \right]. \quad (4.58)$$

Cross section (4.57), when considered differential in $\sqrt{\tau}$ and x_F only ($\tau = x_1 x_2$ and the Feymann parameter $x_F = x_1 - x_2$) scales as $d^2\sigma/d\sqrt{\tau}dx_f \sim 1/s$, influencing the choice of the kinematical set-up, while after integrating on all the kinematic variables but the angular distribution, at leading order in α_s becomes:

$$\frac{1}{\sigma^o} \frac{d\sigma^o}{d\Omega} = \frac{3}{4\pi} \frac{1}{\lambda + 3} \left(1 + \lambda \cos^2 \theta + \mu \sin^2 \theta \cos \phi + \frac{\nu}{2} \sin^2 \theta \cos 2\phi \right) \quad (4.59)$$

In a naive parton model approach the assumption of massless quarks leads to a transversely polarised virtual photon, so that $\lambda = 1$, $\mu = \nu = 0$ and $d\sigma/d\cos\theta \sim 1 + \cos^2\theta$; such predictions are confirmed by both LO and NLO perturbative QCD calculations [351]. The so called Lam-Tung rule [363, 364, 365] $\lambda = 1 - 2\nu$, analogous to the Callan-Gross relation in DIS, should hold in any reference frame and be unaffected by first-order QCD corrections [365], even if it could be influenced by parton intrinsic motions and other "soft" effects.

Experimental data from NA3 [366] and NA10 [348, 349] Collaborations at CERN and from the E615 [350] Collaboration at Fermilab for muon pairs production with π^- beams at different momenta ($140 \div 286 \text{ GeV}/c$) on 2H and W targets have shown no evidence of a CM energy dependence or a nuclear dependence of the angular distribution parameters λ , μ and ν . Data for the former two parameters, leading to $\lambda \sim 1$ and $\mu \sim 0$ as predicted, are mostly independent of the considered kinematic region, except a slight reduction of λ at high x_1 (the light-cone fraction of the parton in the pion) that has been interpreted with higher-twist effects [354, 367]. But these experimental data show a relevant $\cos 2\phi$ dependence with a deviation from zero for ν at high q_T , depending on \sqrt{s} , that tops at larger q_T values $\nu \sim 0.30$ in CERN data [349] and $\nu \sim 0.73$ in Fermilab data [350], clearly departing from pQCD expectations. Other mechanisms, like higher twists or factorisation breaking terms at NLO, are not able to explain such a relevant violation of the Lam-Tung relation [352, 353, 354].

This is not the case if we consider the TMD approach, where the convolution of the two BM func-

tions $h_1^{\perp f}$ and $\bar{h}_1^{\perp f}$ in the last term of Eq. 4.57 allows for a leading-twist (hence large) $\cos 2\phi$ azimuthal dependence [326]. Since the BM function describes the transverse polarisation of partons in unpolarised hadrons, it is intimately connected to the orbital motion of the parton inside the hadron; the product $\bar{h}_1^{\perp} h_1^{\perp}$ brings a change of two units in the orbital angular momentum, leading to an angular dependence on 2ϕ .

Other mechanisms, like the role of QCD-vacuum structure in hadron-hadron scattering [368, 351, 369], has been considered as well, and more recently the $\cos 2\phi$ azimuthal dependence of the unpolarised DY process $p\bar{p} \rightarrow \mu^+\mu^-X$ has been studied in the quark-diquark spectator approach [370].

Very recent data from E866/NuSea [371] Collaboration at FNAL for muon pairs production with a $800 \text{ GeV}/c$ proton beam on 2H haven't shown any significant $\cos 2\phi$ azimuthal dependence, constraining thus those theoretical models predicting larger azimuthal dependencies originating from QCD vacuum effects, and pointing toward an almost vanishing sea-quark BM function, much smaller than that related to valence quarks [327].

Moreover contributions to a $\cos 2\phi$ azimuthal asymmetry for DY dilepton production with (anti)nucleon on nuclear targets could arise from the nuclear distortion of the hadronic projectile wave function, typically a spin-orbit effect occurring on the nuclear surface [372]; this effect, expected to be on the percent level, should be added to the one originating from the elementary hard event.

The single-polarised case: $\bar{p}p^\uparrow \rightarrow \mu^+\mu^-X$

When one of the annihilating hadrons is transversely polarised, in a TMD approach at leading-twist a further polarised term shows up in the cross section:

$$\frac{d\sigma}{d\Omega dx_1 dx_2 d\mathbf{q}_T} = \frac{d\sigma^o}{d\Omega dx_1 dx_2 d\mathbf{q}_T} + \frac{d\Delta\sigma^\uparrow}{d\Omega dx_1 dx_2 d\mathbf{q}_T} \quad (4.60)$$

where $d\sigma^o/d\Omega dx_1 dx_2 d\mathbf{q}_T$ is the unpolarised cross section defined in Eq. 4.57. The polarised $d\Delta\sigma^\uparrow/d\Omega dx_1 dx_2 d\mathbf{q}_T$ [326]:

$$\begin{aligned}
\frac{d\Delta\sigma^\uparrow}{d\Omega dx_1 dx_2 d\mathbf{q}_T} &= \frac{\alpha^2}{12sQ^2} \sum_f e_f^2 |\mathbf{S}_{2T}| \left\{ (1 + \cos^2\theta) \sin(\phi - \phi_{S_2}) \mathcal{F} \left[\hat{\mathbf{h}} \cdot \mathbf{p}_{2T} \frac{\bar{f}_1^f f_{1T}^{\perp f}}{M_2} \right] \right. \\
&\quad - \sin^2\theta \sin(\phi + \phi_{S_2}) \mathcal{F} \left[\hat{\mathbf{h}} \cdot \mathbf{p}_{1T} \frac{\bar{h}_1^{\perp f} h_{1T}^f}{M_1} \right] \\
&\quad \left. - \sin^2\theta \sin(3\phi - \phi_{S_2}) \mathcal{F} \left[\left(4\hat{\mathbf{h}} \cdot \mathbf{p}_{1T} (\hat{\mathbf{h}} \cdot \mathbf{p}_{2T})^2 - 2\hat{\mathbf{h}} \cdot \mathbf{p}_{2T} \mathbf{p}_{1T} \cdot \mathbf{p}_{2T} - \hat{\mathbf{h}} \cdot \mathbf{p}_{1T} \mathbf{p}_{2T}^2 \right) \frac{\bar{h}_1^{\perp f} h_{1T}^f}{2M_1 M_2^2} \right] \right\} \quad (4.61)
\end{aligned}$$

depends explicitly on the Siverson function $f_{1T}^{\perp f}$, on the Transversity h_{1T}^f and on the BM function $h_{1T}^{\perp f}$; sum is extended on the parton flavour f .

Eq. 4.61 shows how a powerful tool can be the Drell-Yan production of muon pairs, since selecting the proper angular dependence both the BM and the Siverson functions can be accessed. A spin asymmetry weighted by $\sin(\phi - \phi_{S_2})$ leads to the convolution of $f_{1T}^{\perp f}$ with the known distribution f_1^f in a mechanism similar to the Siverson effect in DIS with lepton beams [341]. The asymmetry defined weighting for $\sin(\phi + \phi_{S_2})$ leads to the convolution of h_{1T}^f with $h_1^{\perp f}$ in a mechanism similar to the Collins effect [373]; since $h_1^{\perp f}$ contribute at leading twist to the unpolarised cross section as well (Eq. 4.57), a combined analysis of the $\cos 2\phi$ and $\sin(\phi + \phi_{S_2})$ moments of azimuthal asymmetries respectively in the unpolarised and in the single-polarised Drell-Yan cross sections should allow for the determination of both PDF's at the same time in a single experimental scenario.

The Siverson function was originally expected to vanish [373] in DY, due to parity and time reversal invariance in the light-cone gauge, but the role of the presence of Wilson lines had been reconsidered [374] since under time-reversal the future-pointing Wilson lines are replaced by past-pointing Wilson lines. The corresponding transverse gauge link is responsible of the gauge invariance of TMD parton distributions [375] and at the same time of the attractive final state interactions (FSI) in SIDIS and of the repulsive initial state interactions (ISI) in DY [373, 376]. Since in the latter case the past-pointing Wilson lines allow as well an appropriate factorisation of the Drell-Yan process [374, 377], the correct result is not a vanishing Siverson function in DY, but rather a Siverson function showing opposite signs in SIDIS and in DY:

$$f_{1T}^{\perp f}|_{\text{SIDIS}} = f_{1T}^{\perp f}|_{\text{DY}} \quad (4.62)$$

preserving hence the universality of the TMD spin-

dependent PDF's. Huge theoretical efforts have been aimed to investigate the role of the gauge links in TMD distributions [378, 375, 379, 380, 355, 381], with a focus on the gauge invariance of the TMD PDF's and on the proper QCD factorisation at leading twist for SIDIS and DY processes; the evaluation of the Siverson function in the DY di-lepton production could allow for a strong test on the universality of the TMD PDF's.

As pointed out by theoretical predictions based on the Siverson effect from SIDIS experimental data, large SSA are expected for DY processes at the large energy scale foreseen in the later phases of the FAIR project [382, 383, 384, 382, 385], while the Siverson asymmetry at RHIC could be measured only at high rapidity and should be strongly sensitive to the sea-quark Siverson distributions [385].

Two TMD mechanisms has been discussed until now, that could lead to transverse SSA's in the DY process $\bar{p}p^\uparrow \rightarrow \mu^+\mu^-X$: the Siverson effect and the Boer-Mulders effect (which involves also the Transversity distribution); in such exclusive process, and this is the main advantage with respect to inclusive processes like $pp \rightarrow h + X$, the measurement of the lepton-pair angular distribution automatically allows to select one specific effect. A systematic calculation of all leading-twist PDF's in the nucleon has been performed in the framework of a diquark spectator model [386]. But other mechanisms that could also generate SSA's in the DY process had been proposed in the literature [387, 388, 389, 390], based on higher twist quark-gluon correlation functions in a generalised pQCD factorisation theorem approach [391]: in such cases the asymmetries depend on the angle between the proton polarisation direction and the final lepton pair plane [328], and vanish upon corresponding angular integrations.

The Siverson function f_{1T}^{\perp} has recently attracted the deepest interests in the spin physics community. Besides being a T-odd TMD PDF, it describes how

the distribution of unpolarised quarks is distorted by the transverse polarisation of the parent hadron, and as such it contains informations on the orbital motion of hidden confined partons and their spatial distribution [392]. Besides, it offers a natural link between microscopic properties of confined elementary constituents and hadronic measurable quantities, such as the nucleon anomalous magnetic moment [393]. And the prediction of Eq. 4.62 is a strong test of the universality of TMD PDF's.

Recently, very precise data for SSA involving f_{1T}^\perp (the Sivers effect) have been obtained for the SIDIS process on transversely polarised protons [394, 395, 396]. Three different parametrisation of f_{1T}^\perp [382, 384, 397] have been extracted from the HERMES data (see for a comparison among the various approaches Ref. [398]), showing a relevant non zero effect. On the contrary COMPASS data for non-identified [399, 400] and identified hadrons [401] show small effects, compatible with zero within the statistical errors, interpreted in term of a cancellation between the u- and d-quark contributions [401, 402, 403, 404]. Although SIDIS data by HERMES and COMPASS do not constraint the large transverse momentum region, at lower transverse momentum they show a serious conflict as

long as Sivers effects are concerned, in particular considering the latest data from COMPASS [405] that show Sivers asymmetries compatible with zero both for positive and negative hadrons.

New efforts are in progress either to explain the non zero Sivers effects in $p-p$ collisions by the mean of scalar and spin-orbit re-scattering terms [406], either to account for the new data from COMPASS updating the present parametrisations [407]. An independent evaluation of the Sivers distribution f_{1T}^\perp in the single-polarised DY processes at FAIR would certainly contribute to the present (and probably long lasting) challenge to the spin physics community.

The dream option: $\bar{p}^\uparrow p^\uparrow \rightarrow \mu^+ \mu^- X$

The fully polarised case is the simplest scenario to extract the Transversity function h_{1T} , and it requires a reasonable antiproton polarisation; such a dream option could be accessed only in the very last stage of the FAIR project, as proposed in [408] and in [409].

In a TMD approach at leading twist the fully polarised cross section, after integrating upon $d\mathbf{q}_T$, becomes [410]:

$$\begin{aligned} \frac{d\sigma^{\uparrow\uparrow}}{dx_1 dx_2 d\Omega} = & \frac{\alpha^2}{12q^2} \left[(1 + \cos^2 \theta) \sum_f e_f^2 \bar{f}_1^f(x_1) f_1^f(x_2) + \sin^2 \theta \cos 2\phi \frac{\tilde{\nu}(x_1, x_2)}{2} \right. \\ & \left. + |\mathbf{S}_{T1}| |\mathbf{S}_{T2}| \sin^2 \theta \cos(2\phi - \phi_{s_1} - \phi_{s_2}) \sum_f e_f^2 \bar{h}_{1T}^f(x_1) h_{1T}^f(x_2) + (1 \leftrightarrow 2) \right] \quad (4.63) \end{aligned}$$

where ϕ_{s_i} is the azimuthal angle of the transverse spin of hadron i as it is measured with respect to the lepton plane in a plane perpendicular to \hat{z} and \hat{t} of the CS frame (Fig. 4.94); the contribution from

$h_{1T}^{\perp f}$ is hidden in the function $\tilde{\nu}$, while to access the Transversity distribution h_{1T}^f a double spin asymmetry can be defined:

$$A_{TT} = \frac{d\sigma^{\uparrow\uparrow} - d\sigma^{\uparrow\downarrow}}{d\sigma^{\uparrow\uparrow} + d\sigma^{\uparrow\downarrow}} = |\mathbf{S}_{T1}| |\mathbf{S}_{T2}| \frac{\sin^2 \theta}{1 + \cos^2 \theta} \cos(2\phi - \phi_{s_1} - \phi_{s_2}) \frac{\sum_f e_f^2 \bar{h}_{1T}^f(x_1) h_{1T}^f(x_2) + (1 \leftrightarrow 2)}{\sum_f e_f^2 \bar{f}_1^f(x_1) f_1^f(x_2) + (1 \leftrightarrow 2)} \quad (4.64)$$

The asymmetry depends at leading order on h_{1T}^f squared, without contribution from sea-quark PDF's nor convolution with fragmentation func-

tions as in SIDIS, providing then the best possible scenario to access Transversity.

The asymmetry in Eq. 4.64 could in principle be

accessed at RHIC as well, in the polarised DY process $p^\uparrow p^\uparrow \rightarrow l^+ l^- X$, the first process suggested to access Transversity at leading order [325]. But in such a case it would depend on sea-quark PDF's, since it would involve the Transversity of an antiquark in a transversely polarised proton. Moreover, NLO simulations in the RHIC CM energy range [411, 412] have shown an A_{TT} strongly suppressed by QCD evolution and by a Soffer bound on the percent level. On the contrary making use of the FAIR's antiproton beams the asymmetry would involve Transversities of valence partons only [413, 414].

Total cross section

The full expression of the leading-twist differential cross section for the Drell-Yan $H_1^{(\uparrow)} H_2^{(\uparrow)} \rightarrow l^+ l^- X$ process can be found in the Appendix of Ref. [326]

The clear systematics in the literature showing a production of Drell-Yan pairs distributed with $\langle |\mathbf{q}_T| \rangle > 1 \text{ GeV}/c$ and depending on \sqrt{s} , suggests that sizeable QCD corrections are needed beyond a simple Quark Parton Model (QPM) approach, since confinement alone induces much smaller quark intrinsic transverse momenta. The involved higher order Feynman diagrams typically show $q\bar{q}$ annihilations into gluons or quark-gluon scattering [350]. Two main levels of approximation had been used in the literature [415]. The first one is the so-called Leading-Log Approximation (LLA), where the leading logarithmic corrections to the DY cross section can be re-summed at any order in the strong coupling constant α_s , introducing in the PDF's an additional scale dependence on M_{ll}^2 . The so-called DGLAP evolution can be obtained by describing the functions with parameters explicitly depending on $\log M^2$ (see Ref. [416] and Apps. A, B and D in Ref. [350] for further details). The second approximation level in the QCD higher order corrections, the so-called Next-to-Leading-Log Approximation (NLLA), is performed including in the calculation all processes at first order in α_s involving a quark, an antiquark and a gluon [415], and leads to sizeable effects, approximately doubling the pure QPM cross-section. Such a corrections is roughly independent of x_F and M^2 (except for the kinematical upper limits) and it is usually indicated as the K factor. K -factors depend on the choice of the parametrisation of the distribution functions through their normalisation [417], and

scale as $\sqrt{\tau}$ [350].

The azimuthal asymmetries, which are defined as ratios of cross sections, should be pretty robust w.r.t. such kind of QCD corrections, since the corrections in the numerator and in the denominator should approximately compensate each other [411].

But this is not the case if we consider the (un)polarised cross-section. DY processes at high CM energy show reduced K -factors, but the relevant role of higher-order perturbative QCD corrections [418], in terms of the available fixed-order contributions as well as of all-order soft-gluon re-summations, leads to large enhancements of the unpolarised DY dilepton production in the \bar{P} ANDA kinematic regime, due to soft gluon emission near partonic threshold; the unpolarised cross section for DY dilepton production at \bar{P} ANDA energies is thus matter of investigation itself, and could provide information on the relation of perturbative and non-perturbative dynamics in hadronic scattering [418].

The \bar{P} ANDA scenario

The unpolarised and the single-polarised Drell-Yan $\bar{p}p^{(\uparrow)} \rightarrow \mu^+ \mu^- X$ can be investigated with the \bar{P} ANDA spectrometer (the former case since the very beginning, the latter *if* a polarised target would be developed) and the HESR antiproton beam. In such a scenario a beam energy of 15 GeV on the protons at rest in the fixed target can provide a center of mass energy up to $s \simeq 30 \text{ GeV}^2$.

The handbag diagram of Fig. 4.93 is the dominant contribution only for a CM energy s much bigger than the involved hadron masses. Moreover the dilepton mass M_{ll} should not belong to the hadronic resonance region, in order to select for the elementary process an annihilation into a virtual photon; this is the reason why the DY di-lepton production is usually investigated in the so-called "safe region": $4 \text{ GeV} \leq M_{ll} \leq 9 \text{ GeV}$, between the ψ' and the first Υ resonance.

In the DIS regime we can define, in terms of the light-cone momentum fractions, the parameter $\tau = x_1 x_2$ and the invariant $x_F = x_1 - x_2$ (fraction of the total available longitudinal momentum in the collision CM frame); the unpolarised cross section $d\sigma^0$ of Eq. 4.57, kept differential in $M_{ll}^2 \equiv Q^2$ and integrated upon $d\tau$:

$$\frac{d\sigma^o}{dM^2 dx_F} = \frac{4\pi\alpha^2}{9} \frac{1}{M^2 s(x_1 + x_2)} \sum_f e_f^2 \left[\bar{f}_1^f(x_1) f_1^f(x_2) + (1 \leftrightarrow 2) \right] \quad (4.65)$$

shows the scaling in the CM energy s experimentally confirmed [419] and the enhanced production of di-lepton pairs at lower M_{ij}^2 .

In the $\bar{\text{PANDA}}$ scenario the upper limit of the "safe region" $M < 9 \text{ GeV}$ is beyond the accessible kinematic region: since for a \bar{p} beam on a p fixed target is $M^2 = \tau s = \tau 2M_p(M_p + E_{\bar{p}}) \sim \tau 2M_p E_{\bar{p}}$, even considering the limit $\tau \sim 1$, i.e. the case in which all the available CM energy is transferred to the virtual photon, an $M \sim 9 \text{ GeV}$ would correspond to an antiproton beam energy $E_{\bar{p}} \sim 40 \text{ GeV}$. The lower cut $M > 4 \text{ GeV}$ selects then a phase space region $0.5 \lesssim \tau \lesssim 1$ limited to very high values of both x_1 and x_2 . To release the constraint on the lower cut, the $1.5 \text{ GeV} \leq M \leq 2.5 \text{ GeV}$ portion of the di-lepton mass spectrum can be considered as well: a region not overlapping the ϕ and J/ψ resonances, that leads to two major benefits in the $\bar{\text{PANDA}}$ scenario: a wider accessible τ range (as shown in Fig. 4.95) and a larger cross section (see Eq. 4.65 and Ref. [420]).

The expected integrated cross section for $\bar{p}p \rightarrow l^+l^-X$ at $s = 30 \text{ GeV}^2$ in the $1.5 \text{ GeV} \leq M \leq 2.5 \text{ GeV}$ is $\sigma_{1.5 \leq M \leq 2.5}^0 \sim 0.8 \text{ nb}$ [420]; assuming the design luminosity of the High Resolution mode (see Tab. 2.1 in Sec. 2.3.1) $L = 2 \cdot 10^{32} \text{ cm}^{-2} \text{ s}^{-1}$, the expected rate for the DY production of μ -couples would hence be:

$$R = 2 \cdot 10^{32} \text{ cm}^{-2} \text{ s}^{-1} \times 0.8 \cdot 10^{-33} \text{ cm}^{-2} = 0.16 \text{ s}^{-1} \quad (4.66)$$

The cross section at $s = 30 \text{ GeV}^2$ is expected to drop dramatically in the "safe-region" to $\sigma_{4 \leq M \leq 9}^0 \sim 0.4 \text{ pb}$ [420]; since the resulting rate for the DY processes would be incompatible with a detailed investigation in the $\bar{\text{PANDA}}$ framework, the focus will be herewith on the $1.5 \text{ GeV} \leq M \leq 2.5 \text{ GeV}$ region only.

Simulations

The investigation of the (un)polarised DY $\bar{p}p^{(1)} \rightarrow \mu^+\mu^-X$ process in the scenario and with the kinematic conditions described above in this section is certainly a difficult task; to probe its feasibility Monte-Carlo simulations have been performed, based on the event generator kindly provided us by A. Bianconi (a more detailed description of such a generator can be found in Ref. [420, 421]). This

is the very same event generator involved in the feasibility studies performed for the polarised DY $\pi^\pm p^\dagger \rightarrow \mu^+\mu^-X$ process at the CM energy $\sqrt{s} \sim 14 \text{ GeV}$ reachable at COMPASS [422, 423], and for the polarised DY $pp^\dagger \rightarrow \mu^+\mu^-X$ process at the CM energy $\sqrt{s} = 200 \text{ GeV}$ reachable at the Relativistic Heavy-Ion Collider (RHIC) of BNL [424].

The main goal of the Monte-Carlo simulations reported herewith is to estimate the number of events required for the DY program at $\bar{\text{PANDA}}$, in order to access unambiguous information on the PDF's of interest, namely the BM function h_1^\perp in the $\bar{p}p \rightarrow \mu^+\mu^-X$ process and the Siverts function f_{1T}^\perp , the Transversity h_{1T} and the h_1^\perp again in the $\bar{p}p^\dagger \rightarrow \mu^+\mu^-X$ process. The effects of the kinematic cuts above described and of the acceptance introduced by the $\bar{\text{PANDA}}$ spectrometer, and the possibility to probe the dependence of the experimental asymmetries on the kinematics have to be investigated as well.

An estimation of the fully polarised case is beyond the scope of the present discussion; see Ref. [425, 413, 414] for the predictions of double-spin asymmetries in different experimental scenarios at FAIR in the case of the fully polarised DY process.

For each one of the two investigated processes 480K events have been generated at $s = 30 \text{ GeV}^2$ in order to satisfy the following kinematic cuts: a di-lepton invariant mass $1.5 \text{ GeV} \leq M \leq 2.5 \text{ GeV}$, a di-lepton transverse momentum $q_T > 1 \text{ GeV}/c$, and a polar angle for the μ^+ in the CS frame $60^\circ \leq \theta_{\mu^+}^{CS} \leq 120^\circ$. The second cut, together with the rejection factor introduced by the iron in the magnet, is necessary to select the DY signal events from the hadronic background, as will be discussed later in this section; the latter cut is aimed to select the azimuthal $\theta_{\mu^+}^{CS}$ -region where the azimuthal asymmetries are expected to be larger (at $\theta_{\mu^+}^{CS} \sim \frac{\pi}{2}$ [420]).

If the simulations had included also events in the safe-region ($4 \text{ GeV} \leq M \leq 9 \text{ GeV}$) the phase space for large $\tau = x_1 x_2$ would have been anyway scarcely populated, since the virtual photon introduces a $1/M^2 \propto 1/\tau$ factor in the cross section of Eq. 4.65, which thus decreases for increasing τ (with $0 \leq \tau \leq 1$). The PDF's become hence negligible for $x_1 x_2 \rightarrow 1$ and events accumulate in the phase space

part corresponding to small τ .

This is indeed the case of Fig. 4.95, reporting the x_1 vs x_2 scatter-plot for the generated sample of unpolarised DY di-lepton production. The upper right corner of the figure corresponds to the limit $\tau \rightarrow 1$, when all the available CM energy is transferred to the virtual photon, and is depleted by the cut $1.5 \text{ GeV} \leq M \leq 2.5 \text{ GeV}$; such a cut selects the region $0.075 \leq \tau \leq 2.1$, and the distribution becomes more and more dense approaching the lower ridge. The line bisecting the plot at 45° corresponds to $x_F \sim 0$; parallel lines above and below indicate $x_F > 0$ and $x_F < 0$, corresponding in the laboratory frame respectively to "forward" (small $\theta_{\mu^+}^{LAB}$) and "backward" (large $\theta_{\mu^+}^{LAB}$) events.

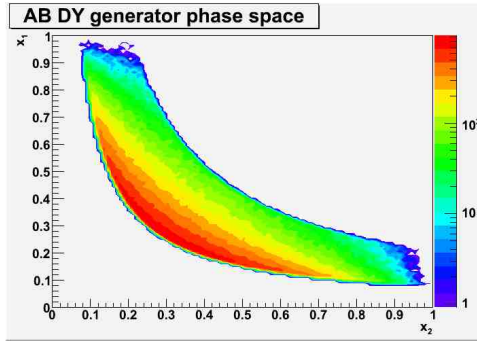


Figure 4.95: The correlation between the two light-cone momentum fractions of the parton momenta $x_{1,2}$ for the 480K DY events generated with the Andrea Bianconi's generator [420] for the unpolarised $\bar{p}p \rightarrow l^+l^-X$ processes at $s = 30 \text{ GeV}^2$ in the following kinematic conditions: a di-lepton invariant mass $1.5 \leq M_{ll}^2 \leq 2.5 \text{ GeV}$, a transverse momentum of the lepton pair $q_T > 1 \text{ GeV}/c$ and a polar angle for the μ^+ in the Collins-Soffer frame $60^\circ \leq \theta_{\mu^+}^{CS} \leq 120^\circ$.

The azimuthal asymmetry related in the CS frame to the $\cos 2\phi$ term of Eq. 4.57 and Eq. 4.59 (an asymmetry that leads to the BM function h_1^\perp) has been evaluated for muon pairs with transverse momentum $1 < q_T < 2 \text{ GeV}/c$ or $2 < q_T < 3 \text{ GeV}/c$ in x_p bins (x_p being the light-cone momentum fraction of the parton in the proton) over the range $0.2 < x_p < 0.8$, where according to the phase space distribution of Fig. 4.95 the statistics is reasonably large. The asymmetry $A^{\cos 2\phi}$ has been obtained considering all the 480K unpolarised $\bar{p}p \rightarrow l^+l^-X$ events generated by the Andrea Bianconi's generator [420], tuned to reproduce the most recent experimental data available in the literature [350]. For each x_p bin and q_T cut two event samples are stored, corresponding respectively to positive and

negative values of $\cos 2\phi$; the resulting asymmetry $A^{\cos 2\phi} = (U - D)/(U + D)$ between cross sections with positive (U) and negative (D) values of $\cos 2\phi$ is shown in Fig. 4.96. Error bars represent statistical errors only; since the asymmetry has been evaluated considering the whole sample of the generated events, both the asymmetry itself and its error bars shown in Fig. 4.96 are not folded with the acceptance of the PANDA spectrometer.

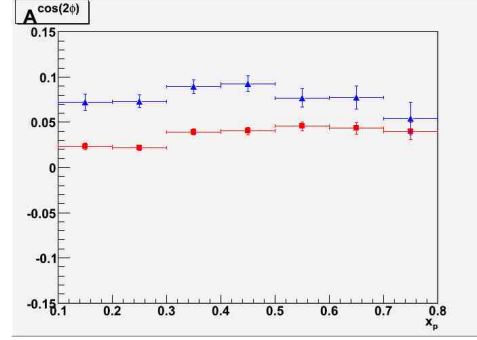


Figure 4.96: The azimuthal asymmetry between cross sections related to positive and negative values of the $\cos 2\phi$ term in Eq. 4.57 for 480K events of the unpolarised DY process $\bar{p}p \rightarrow l^+l^-X$ in the same kinematic conditions of Fig. 4.95. The asymmetry is evaluated in x_p bins for a di-lepton pair transverse momentum $1 \leq q_T \leq 2 \text{ GeV}/c$ (squares) or $2 \leq q_T \leq 3 \text{ GeV}/c$ (triangles). Error bars reflect statistical errors only.

The azimuthal asymmetry related to h_1^\perp is hence expected to be not negligible, experimentally measurable in the PANDA energy range, with errors good enough to allow for the investigation of the dependence of the asymmetry on the relevant kinematic variables such as the transverse momentum of the lepton pair q_T . Such an investigation is of uttermost importance in order to probe the existence of a possible inversion of the trend in the energy dependence of the asymmetries, to balance soft and hard effects in this kind of processes.

In the case of the single-polarised DY process $\bar{p}p^\uparrow \rightarrow \mu^+\mu^-X$ two different SSA's can be defined; a first one, $A_T^{\sin(\phi-\phi_{S_2})}$, weighted by the factor $\sin(\phi-\phi_{S_2})$ (Eq. 4.61) and related to the Sivers function f_{1T}^\perp ; a second one, $A_T^{\sin(\phi+\phi_{S_2})}$, weighted by the factor $\sin(\phi+\phi_{S_2})$ (Eq. 4.61) and related to the convolution of the Transversity h_{1T} with the BM function h_1^\perp . The single-polarised DY sample have been generated under the assumptions described in Sec. A of [420] but assuming the simpler functional hypothesis $\langle h_1(x_p) \rangle / \langle f_1(x_p) \rangle = 1$. The procedure to determine the two asymmetries is the analogous of

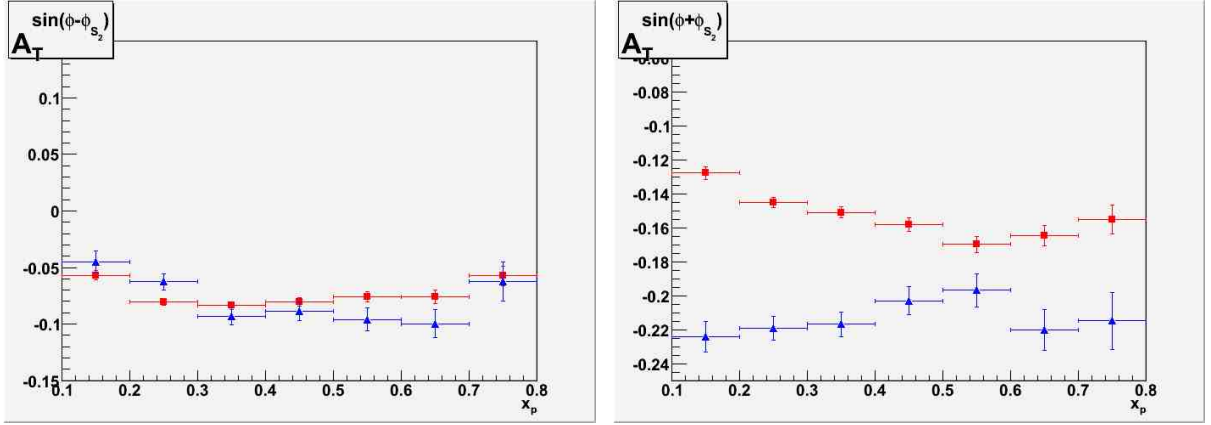


Figure 4.97: The single-spin azimuthal asymmetries $A_T^{\sin(\phi - \phi_{S_2})}$ and $A_T^{\sin(\phi + \phi_{S_2})}$ between cross sections related to positive and negative values respectively of the two $\sin(\phi - \phi_{S_2})$ and $\sin(\phi + \phi_{S_2})$ terms in Eq. 4.61, for 480K events of the single-polarised DY process $\bar{p}p^\uparrow \rightarrow l^+l^-X$ in the same kinematic conditions of Fig. 4.95. The asymmetries are evaluated in x_p bins for a di-lepton pair transverse momentum $1 \leq q_T \leq 2 \text{ GeV}/c$ (squares) or $2 \leq q_T \leq 3 \text{ GeV}/c$ (triangles). Error bars reflect statistical errors only.

that used to evaluate the unpolarised asymmetry: for each x_p bin four sample of events are stored, for positive (U_\pm) and negative (D_\pm) values of the factors respectively $\sin(\phi + \phi_{S_2})$ and $\sin(\phi - \phi_{S_2})$. The resulting asymmetries $A_T^{\sin(\phi \pm \phi_{S_2})} = (U_\pm - D_\pm)/(U_\pm + D_\pm)$ are plotted in Fig. 4.97 in x_p bins in the range $0.2 < x_p < 0.8$, separately for muon pairs with transverse momentum $1 < q_T < 2 \text{ GeV}/c$ or $2 < q_T < 3 \text{ GeV}/c$. The asymmetries have been obtained considering the whole sample of 480K events generated for the single-polarised DY process and are hence not affected by the spectrometer acceptance; error bars represent statistical errors only.

Under the assumptions above described the asymmetry $A_T^{\sin(\phi + \phi_{S_2})}$ is expected to be relevant, and also in this case the investigation of the dependence of the asymmetry on the di-lepton transverse momentum q_T should be possible. This is not the case for the asymmetry $A_T^{\sin(\phi - \phi_{S_2})}$, predicted to be much smaller and with a strongly reduced dependence on q_T .

For each one of the two simulated DY processes the generated events have then been propagated through the PANDA spectrometer (Sec. 2.2) in order to evaluate the global acceptance introduced by the experimental layout, i.e. the geometrical acceptance and the events' loss due to the material budgets, in particular the ones introduced by the Electromagnetic Calorimeter and by the iron of the magnet (in which the muon detectors will be embedded).

The iron shield is mandatory in order to separate

the muon couples produced in the investigated DY processes from the pion couples coming from the hadronic background; in fact the required combined rejection factor that has to be provided by the experimental apparatus itself and by the events' reconstruction is very large. The total $\bar{p}p$ annihilation cross section in the PANDA energy range is $\sigma_{\bar{p}p} \sim 50 \text{ mb}$; once accounted for its diffractive component, the global cross section for pion production in the final state is of the order of some tens of mb . Since the DY expected cross section [420] is of the order of the nb , the required rejection factor is $\sim 10^7$.

The extended simulations needed to investigate the background rejection are actually still in progress. Nevertheless their preliminary indications point toward a scheme in which the required rejection factor could be achieved by the mean of: the depletion of the pions' sample due to their interaction with the iron in the PANDA solenoid; a set of kinematic cuts in order to select in the event reconstruction stage the DY processes (the most effective ones being the requirement of a di-muon pair transverse momentum $q_T \geq 1 \text{ GeV}/c$ and of a reaction vertex in the target region); a kinematically constrained refit of the final state in order to reject the residual contamination from the hadronic background. To balance the best possible background rejection and the minimum DY events loss, the geometry of the iron in the barrel and in the endcap of the solenoid has to be segmented, in order to host embedded muon counters. The minimum iron thickness required to achieve such a large rejection factor determines the

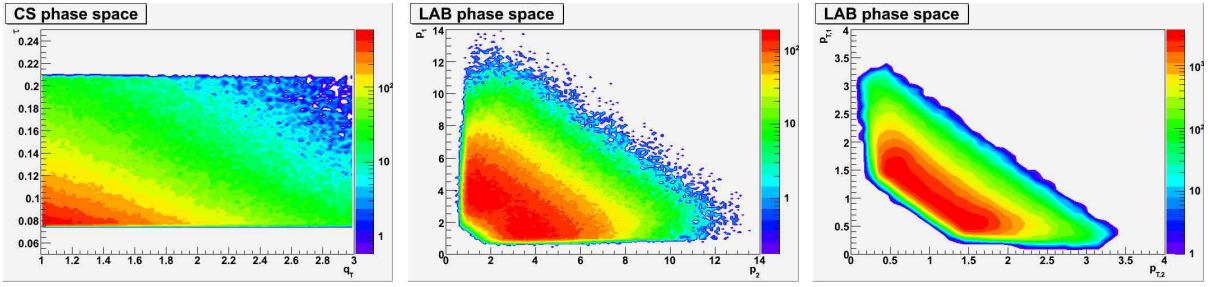


Figure 4.98: Estimated kinematic acceptance for the unpolarised DY process in the same kinematic conditions of Fig. 4.95. A "Montecarlo through" has been performed considering the preliminary estimation of the minimum iron thickness required to resolve the DY signal from the hadronic background. Left panel shows the accessible τ region and the events accumulating toward low values of the transverse momentum of the lepton pair q_T in the Collins-Soper frame. The central and the right panels show the scatter plots respectively of the momenta and of the transverse momenta of the two outgoing muons in the laboratory Frame frame.

preliminary global acceptance of the apparatus for the DY processes.

The preliminary indications for such an acceptance from the extended simulation in progress, point to a reduction by a factor of ~ 2 of the total cross-section σ^0 quoted above in this section. That would rescale Eq. 4.66 to the corresponding rate expected for those DY muon pairs that can be detected and resolved from the hadronic background in these kinematic conditions by the \bar{P} ANDA spectrometer: $R = 2 \cdot 10^{32} \text{cm}^{-2} \text{s}^{-1} \times 0.8 \cdot 10^{-33} \text{cm}^{-2} \times \frac{1}{2} = 0.08 \text{s}^{-1}$, i.e. $\sim 200K$ events/month, not accounting for the various experimental efficiencies.

The plots in Fig. 4.98 show few of the most rele-

vant kinematic distributions for those unpolarised DY events surviving the (preliminarily estimated) minimum iron thickness required to resolve the DY signal from the hadronic background; i.e., those kinematic distributions are folded with the global acceptance of the \bar{P} ANDA spectrometer.

The most unwanted effect of the \bar{P} ANDA spectrometer acceptance is the introduction of sizeable fake instrumental asymmetries, heavily depending on the geometrical cut introduced in the muons polar angle distribution in the laboratory frame by the hole in the endcap around the beam pipe (varying on the azimuthal angle $\phi_{\mu_{\pm}}^{LAB}$ but being in the average $\theta_{\mu_{\pm}}^{LAB} \geq 7^\circ$). Such an effect will have to be carefully accounted for in the analysis stage and can be par-

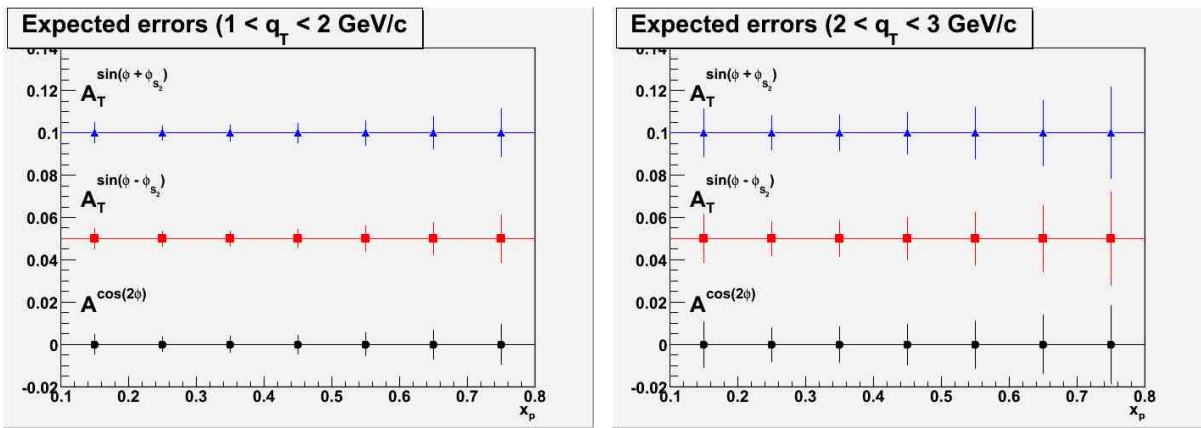


Figure 4.99: The statistical errors for the asymmetries of Figures 4.96 and 4.97 expected once they are folded with the \bar{P} ANDA global acceptance (see text for a more detailed discussion), for a di-lepton pair transverse momentum $1 \leq q_T \leq 2 \text{ GeV}/c$ (left panel) or $2 \leq q_T \leq 3 \text{ GeV}/c$ (right panel). The "Montecarlo through" has been performed for each one of the two sets of 480K events generated for unpolarised and single-polarised DY processes, in the same kinematic conditions of Fig. 4.95, considering the preliminary estimation of the minimum iron thickness required to resolve the DY signal from the hadronic background.

tially reduced including in the considered DY sample also those events for which (one of) the outgoing muons can be detected in the Forward Spectrometer (FS) (See Sec. 2.2)..

The plots in Fig. 4.99 show the expected statistical errors for the three considered azimuthal asymmetries once the effects of the preliminary $\bar{\text{PANDA}}$ acceptance, and namely the consequent reduction in the statistics, are accounted for. The estimated errors show how the $\bar{\text{PANDA}}$ spectrometer should be able to detect and experimentally evaluate the above described azimuthal asymmetries, even if they were rather small.

Conclusions

The DY production of muon pairs is an excellent tool to access transverse spin effects within the nucleon. As stated before in this Section, the double-polarised case would really be a "dream option", allowing to access the Transversity distribution h_{1T} directly and without any convolution with other PDF's; unfortunately it is beyond the initial scope

of the $\bar{\text{PANDA}}$ physics program. But even considering the unpolarised and the single-polarised cases only, the Boer-Mulders distribution h_1^\perp and the Sivers distribution f_{1T}^\perp could be accessed as well, and in a single experimental scenario. To access the latter a polarised target is needed, an element not yet included in the present $\bar{\text{PANDA}}$ layout but by many indicated as an almost necessary upgrade, while the former can be accessed since the very beginning of the $\bar{\text{PANDA}}$ activities.

A DY program in $\bar{\text{PANDA}}$, besides addressing the present excitement in the spin physics community driven by the discrepancies among the most recent SIDIS data for the Sivers function, would allow for the evaluation of three of the most hunted PDF's in a kinematic region where the valence contributions are expected to be dominant.

A large rejection factor is needed to resolve the DY processes from the hadronic background; a detailed evaluation of the hadronic background in the $\bar{\text{PANDA}}$ scenario is in progress, in order to complete the feasibility studies relative to the spin physics program.

4.6.3 Electromagnetic Form Factors in the Time-like Region

COMMENT: Author(s): F. Maas

COMMENT: Referee(s): D. Bettoni

4.6.3.1 Introduction

The electromagnetic probe is an excellent tool to investigate the structure of the nucleon. The \bar{P} ANDA-experiment offers the unique possibility to make a precise determination of the electromagnetic form factors in the time-like region with unprecedented accuracy. The electric (G_E) and magnetic (G_M) form factors of the proton parameterize the hadronic current in the matrix element for elastic electron scattering ($e^- + p \rightarrow e^- + p$) and in its crossed process annihilation ($\bar{p}p \rightarrow e^+e^-$) as shown in Fig. 4.100. The form factors (FF) measured in electron scattering are intimately connected with those measured in the annihilation process. Moreover they are observables that can probe our understanding of the nucleon structure in the regime of nonperturbative QCD as well as at higher energies where perturbative QCD applies.

The interaction of the electron with the nucleon is described by the exchange of one photon with space-like four momentum transfer q^2 . The lepton vertex is described completely within QED and on the nucleon vertex, the structure of the nucleon is parameterized by two real scalar functions depending on one variable q^2 only. These real functions are the Dirac form factor $F_1^{p,n}$ and the Pauli form factor $F_2^{p,n}$, or as a linear combination of $F_{1,2}^{p,n}$ the Sachs form factors $G_E^{p,n}$ and $G_M^{p,n}$. The standard way of writing the matrix element for elastic electron proton scattering in the framework of one-photon exchange is:

$$M = \frac{e^2}{q^2} \bar{u}(k_2) \gamma_\mu u(k_1) \bar{u}(p_2) [F_1(q^2) \gamma_\mu + i \frac{\sigma_{\mu\nu} q^\nu}{2m_p} F_2(q^2)] u(p_1), \quad (4.67)$$

$k_1(p_1)$ and $k_2(p_2)$ are the four-momenta of the initial and final electron (nucleon) represented by the spinors $\bar{u}(k)$ ($\bar{u}(p)$) and $u(k)$ ($u(p)$), m_p is the nucleon mass, $q = k_1 - k_2$, $q^2 < 0$. Applying crossing symmetry yields the matrix element for $\bar{p}p \rightarrow e^+e^-$ where $k_2(p_2)$ changes sign so that $q^2 = s$.

The matrix elements are analytic functions of the four momentum transfer q^2 ranging from $q^2 = -\infty$ to $q^2 = +\infty$. While in electron scattering the form factors can be accessed in the range of negative q^2

(space-like), the annihilation process allows to access positive q^2 (time-like) starting from the threshold of $q^2 = 4m_p^2$. Unitarity of the matrix element requires that space-like form factors are real functions of q^2 while for time-like q^2 they are complex functions. In the Breit frame, space-like FFs have

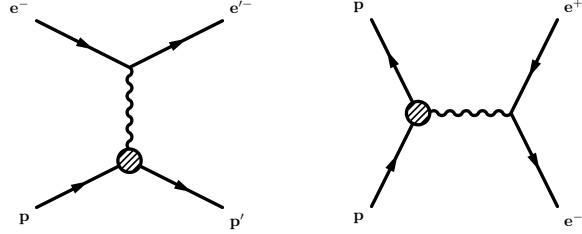


Figure 4.100: Feynman diagrams for elastic electron scattering (left) and its crossed channel annihilation $\bar{p}p \rightarrow e^+e^-$ (right) which will be measured with the \bar{P} ANDA-detector.

concrete interpretations, since they are the Fourier transforms of the spatial charge (G_E) and the magnetization distribution (G_M) of the proton. Their slope at $q^2 = 0$ directly yields the charge and magnetization radius of the proton. In time-like region, their Fourier transform corresponds to the response of the nucleon in the time domain. That way two complementary aspects of nucleon structure can be studied and ask for a full and complete description of the electromagnetic form factors over the full kinematical range of q^2 .

Impact from electron scattering data

The experimental determination of the electromagnetic form factors of the nucleon has triggered large experimental programs at all major facilities since they have long served as one of the testing grounds for our understanding of nucleon structure ranging from the low- q^2 regime of QCD up to the high energy perturbative regime. Basically all models of nonperturbative QCD, which are using effective degrees of freedom, have been used to estimate the nucleon form factors. For example different constituent quark models, skyrmion type of models, bag models and more recently a framework like chiral perturbation theory and lattice gauge theory have been applied.

Due to its analyticity space-like and time-like form factors are intimately connected by the application of dispersion relations which are an application of Cauchy's integral formula. Perturbative QCD

makes predictions for the large q^2 behavior of the connection between space-like region and time-like region. Space-like form factors are connected to the recent developments using nonperturbative generalized parton distributions.

The interest in the time-like form factors of the nucleon has been renewed by the recent measurement at JLAB using the polarization transfer and target asymmetry method, showing that the ratio of $R = G_E/G_M$ deviates from unity and is in contrast to the results derived from Rosenbluth separation technique [?, 426, 427, 428]. While this discrepancy is most probably connected with radiative corrections, it has been shown, that the polarization transfer method is much less sensitive to those effects. It seems that G_E is approaching zero around a q^2 of $8 (\text{GeV}/c)^2$ while G_M follows a dipole form factor indicating that the charge distribution has a hard surface in contrast to the magnetization distribution. This surprising result has reopened the question on the determination of G_E and G_M in the time-like domain which are complex functions. Almost all experiments so far have determined $|G_E|/|G_M|$ in the time-like domain using the hypothesis of equality between G_E and G_M which now is largely questioned now due to the JLAB results. Only two experiments had enough statistics to determine the ratio of $|G_E|/|G_M|$ independently from any hypothesis and which have so far reached contradicting results with large experimental uncertainties. The determination of the electromagnetic form factors in the time-like domain at low to intermediate momentum transfer is therefore regarded to be an open question.

Existing data on time-like form factors

The $\overline{\text{PANDA}}$ experiment offers a unique opportunity to determine the moduli of the complex form factors in the time-like domain, by measuring the angular distribution of the process $\overline{\text{p}}\text{p} \rightarrow e^+e^-$ in a q^2 range from about $5 (\text{GeV}/c)^2$ up to $22 (\text{GeV}/c)^2$.

The differential cross section for unpolarised initial and final states of the process $\overline{\text{p}}\text{p} \rightarrow e^+e^-$ is [429]:

$$\frac{d\sigma}{d\cos\theta} = \frac{\pi\alpha^2(\hbar c)^2}{8m_p^2\sqrt{\tau}(\tau-1)} [|G_M|^2 (1 + \cos^2\theta) + \frac{|G_E|^2}{\tau} (1 - \cos^2\theta)] \quad (4.68)$$

with $\tau = q^2/4m_p^2$. A measurement of this differential cross section over a wide range of $\cos\theta$ allows an independent determination of the moduli $|G_E^p(q^2)|$ and $|G_M^p(q^2)|$ of the electromagnetic

form factors and has been attempted by a number of experiments [429, 430, 431]. Fig. 4.101 gives a sum-

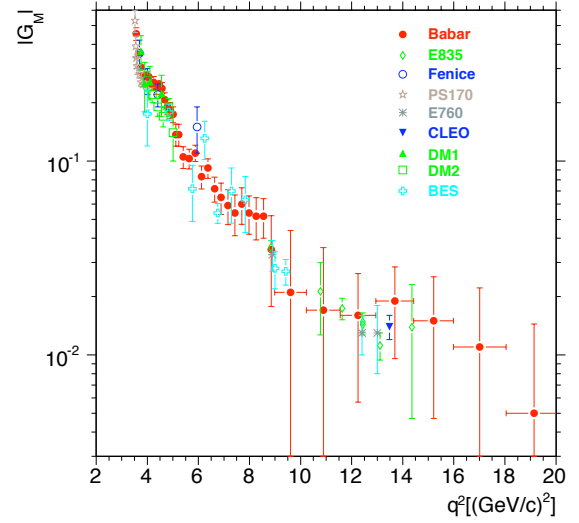


Figure 4.101: World data on the modulus $|G_M|$ of the time-like magnetic form factor extracted from different experiments using $\overline{\text{p}}\text{p} \rightarrow e^+e^-$, $e^+e^- \rightarrow \overline{\text{p}}\text{p}$, and $e^+e^- \rightarrow \gamma\overline{\text{p}}\text{p}$. In all cases, the hypothesis of $R = |G_E|/|G_M| = 1$ has been used to analyse the data.

mary on the world data on the modulus $|G_M|$ of the time-like magnetic form factor extracted from different experiments using $\overline{\text{p}}\text{p} \rightarrow e^+e^-$, $e^+e^- \rightarrow \overline{\text{p}}\text{p}$, and $e^+e^- \rightarrow \gamma\overline{\text{p}}\text{p}$. In all cases, the hypothesis of $|G_E| = |G_M|$ has been used to analyse the data using the integrated differential cross section.

So far only two experiments have collected enough statistics in order to analyse the angular distribution and extract $|G_E|$ and $|G_M|$ independently (see Fig. 4.102).

The $\overline{\text{PANDA}}$ experiment is planned to have unprecedented luminosity and rich particle identification capabilities, which are necessary in order to discriminate against the very large background of $\overline{\text{p}}\text{p} \rightarrow \pi^-\pi^+$ which is about 10^6 times higher in cross section. We show here the strategy how to reach a $\pi^-\pi^+$ rejection factor of about 10^8 using the particle identification capabilities of each detector.

Any possible two-photon exchange contribution in the time-like domain, which is regarded to be one of the radiative correction processes responsible for the discrepancy between Rosenbluth and polarization transfer method, can be detected in the same measurement since it introduces a forward-backward asymmetry in the angular distribution which otherwise is symmetric in one-photon exchange.

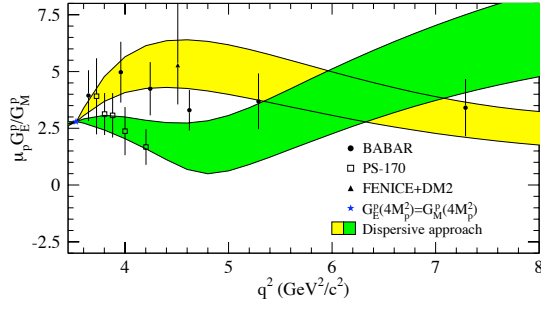


Figure 4.102: The data from the LEAR experiment PS170 and recent BABAR data have been alternatively used as an input to a dispersion relation analysis of the electromagnetic form factors. The recent data from JLAB have been used as an input for the space-like region. The green band gives the dispersion relation fit result on $|G_E|/|G_M|$ when using the PS170 data in the time-like region and the yellow band gives the result for the BABAR data. The present accuracy in the ratio of $R = |G_E|/|G_M|$ is of order 50% while a future measurement using the \bar{P} ANDA experiment at the design luminosity yields a statistical error of order few % or better after 10^7 s in this region of q^2 .

A large experimental activity is coming from B -factory e^+e^- -colliders where the energy is fixed to a $b\bar{b}$ -resonance. The process of initial state radiation $e^+e^- \rightarrow \bar{p}p\gamma$ (ISR), where the variable energy γ from an initial state electron is used in order to "scan" the q^2 of the virtual photon probing the form factors, is used at those B-factories. The BABAR experiment has recently published results for the ratio $R = |G_E|/|G_M|$, but is penalized by the fact, that the luminosity for $e^+e^- \rightarrow \bar{p}p\gamma$ is then suppressed by factors of 10^5 to 10^6 as compared to the direct e^+e^- -luminosity and cannot so far compete with the proposed measurement at \bar{P} ANDA.

An analogous process to ISR would be the emission of a π by one of the $\bar{p}p$ in the initial state which would lower the q^2 of the virtual photon at the annihilation vertex. That way, one could reach the otherwise inaccessible range below the threshold and measure the form factors down to lower q^2 . Vector meson dominance and hypothetical baryonium states could be accessed that way. Another possible extension of the program could be a possibility to access the axial form factor in time-like domain, by using a neutron (deuteron) target [432]. In analogy to electro-pion production, the chiral Ward-identities could be used here to extract the axial form factor in the time-like domain, for which no data exist at all. We have performed first estimates of cross sections for both, subthreshold electromagnetic form factors and axial form factor measure-

ment, but more theoretical work and simulations is necessary.

4.6.3.2 Simulations

Time-like form factors (TLFF) measurements through the reaction $\bar{p}p \rightarrow e^+e^-$ (or $\mu^+\mu^-$) require the complete identification of the 2 outgoing leptons. The shape of the angular distribution provides a direct access to the moduli of the two proton form factors $|G_M|$ and $|G_E|$ (see 4.6.3.1). We have studied two aspects concerning the determination of $|G_M|$ and $|G_E|$ with the \bar{P} ANDA detector: the background conditions which will eventually limit the purity of the lepton signal and the sensitivity to the shape of the angular distribution after reconstructing the lepton signal in the \bar{P} ANDA detector. The integrated cross section of the signal reaction $\bar{p}p \rightarrow e^+e^-$ was modeled by a fit to the world data where the following Ansatz for G_M had been used (see details in [433]):

$$|G_M| = \frac{a}{\left(1 + \frac{q^2}{m_a^2}\right)} G_D \quad (4.69)$$

$$G_D = \frac{1}{\left(1 + \frac{q^2}{m_d^2}\right)^2},$$

$$m_a^2 = 3.6 \text{ GeV}^2,$$

$$m_d^2 = 0.71 \text{ GeV}^2$$

G_D denotes the usual dipole-form factor, $a = 22.5$ is a normalisation constant and m_a is an additional parameter describing the deviation from a dipole. $m_a^2 = 3.6 \pm 0.9 \text{ GeV}^2$. m_d is the usual dipole-mass parameter.

The upper plot of Fig. 4.103 shows the magnetic time-like proton form factor $|G_M|$ which has been used in the signal simulations described here. The lower part of Fig. 4.103 shows the integrated absolute cross section dependence versus q^2 . The plot shows the individual contributions of $|G_E|$ and $|G_M|$ to the total cross section. One sees that the sensitivity to the electric form factor decreases with increasing q^2 due to the kinematic factor $1/\tau$ in front of $|G_E|$ ($\tau = \frac{q^2}{4m_p^2}$ (see Equ. 4.68)).

Due to the fact that the world data on time-like form factors have been analysed under the assumption that $|G_E| = |G_M|$, we can determine and fit the absolute integrated cross section as shown in Fig. 4.103. The knowledge of the ratio $R = |G_E|/|G_M|$ at present is very limited, dispersion theory allows values between 0 and 3 for certain q^2 -

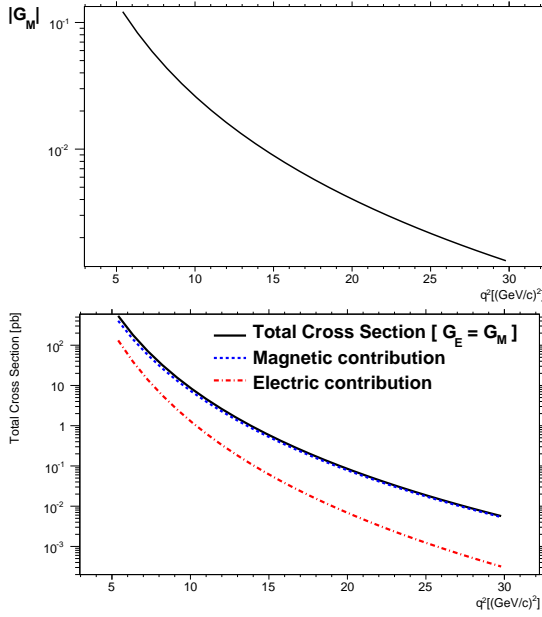


Figure 4.103: The upper plot shows the modulus of the magnetic time-like proton form factor $|G_M|$ which has been used in the simulations of the process $\bar{p}p \rightarrow e^+e^-$ described here. The lower plot gives the integrated $\bar{p}p \rightarrow e^+e^-$ cross section as a function of q^2 . Also shown is the cross section contribution from magnetic and electric form factors under the assumption of $|G_E| = |G_M|$.

values (see Fig. ??). In order to study the sensitivity to the ratio of $|G_E|/|G_M|$ we have taken the measured cross section to estimate the total number of counts and have created different angular distributions according to the model for $|G_E|/|G_M|$ under consideration. Fig. 4.104 shows angular distributions for several assumptions on $|G_E|/|G_M|$. Table 4.48 summarizes the simulated event numbers reached for the signal simulation ($\bar{p}p \rightarrow e^+e^-$ and $\bar{p}p \rightarrow \mu^+\mu^-$) and the most important background channels ($\bar{p}p \rightarrow \pi^+\pi^-$, $\bar{p}p \rightarrow \pi^0\pi^0$).

Reactions with 2 oppositely charged particles ($\pi^+\pi^-$ and K^+K^-) represent the most important background reactions to cope with. The thickness of the electromagnetic calorimeter (about 20 radiation lengths X_0) corresponds to slightly more the one nuclear interaction length λ_0 , so that we expect for about 30% of the pions nuclear reactions among which are charge exchange reactions. This completely taken into account in the determination PID-likelihood.

The cross sections of the processes with $\pi^+\pi^-$ or K^+K^- in the final state are of the same order of magnitude. However, the kaon mass is substantially

q^2 [GeV ²]	e^+e^-	$\mu^+\mu^-$	$\pi^+\pi^-$	$\pi^0\pi^0$
5.4	4×10^6	4×10^6	-	-
7.21	4×10^6	4×10^6	-	-
8.21	4×10^6	4×10^6	10^8	3×10^6
11.03	4×10^6	4×10^6	-	-
12.9	4×10^6	4×10^6	-	-
13.9	4×10^6	-	10^8	3×10^6
16.7	4×10^6	4×10^6	2.10^8	3×10^6
22.3	4×10^6	-	-	-

Table 4.48: The number of simulated events reached for the simulation of the signal ($\bar{p}p \rightarrow e^+e^-$ and $\bar{p}p \rightarrow \mu^+\mu^-$) and for the background reactions ($\bar{p}p \rightarrow \pi^+\pi^-$ and $\bar{p}p \rightarrow \pi^0\pi^0$). For the signal case we have created 10^6 -events each for the cases $|G_E| = 0$, $|G_E| = |G_M|$ and $|G_E| = 3|G_M|$ plus an isotropic e^+e^- -distribution for acceptance and efficiency corrections. We have studied three cases for the final state of $\pi^0\pi^0$: a) both π^0 decay into 2 gammas, b) one of the final state $\pi^0\pi^0$ is decaying to 100% into $e^+e^-\gamma$ (Dalitz decay) and, c) both final state $\pi^0\pi^0$ do 100 % Dalitz decay.

higher than the pion mass, so rejection through PID and kinematical constraints is more efficient for the K^+K^- channel.

Consequently, the $\pi^+\pi^-$ background channel was simulated as the first step. The corresponding angular distributions (see Fig. 4.105) were taken from measured data and extrapolated where necessary [434, 435, 436, 437, 438]. The ratio of $\pi^+\pi^-$ to e^+e^- cross sections, which varies from 10^5 at $|\cos\theta_{CM}| = 0$ up to $3 \cdot 10^6$ at $|\cos\theta_{CM}| = 0.8$, is then properly taken into account in the simulation.

Three-body final state background reactions involving 2 opposite charged hadrons and a neutral massive particle (π^0 or heavier meson) are much easier to separate, since kinematical considerations can then provide additional constraints which can be used to cut very efficiently the corresponding background. They have not yet been simulated.

The background events from $\pi^+\pi^-$ and $\pi^0\pi^0$ were analyzed under the hypothesis of having an e^+e^- -pair. Analogously, the $\pi^+\pi^-$ events have been re-analysed under the hypothesis of having a $\mu^+\mu^-$ -pair. The same analysis cuts and kinematical fit constraints have then been applied to the e^+e^- signal sample ($\mu^+\mu^-$ -sample respectively) in order to create the signal distributions. Different cuts on the PID were used as described in Sec. 3.3.3, corresponding to different thresholds on the global likelihood (see Table 3.2).

Special attention has been paid to the $\pi^0\pi^0$ channel.

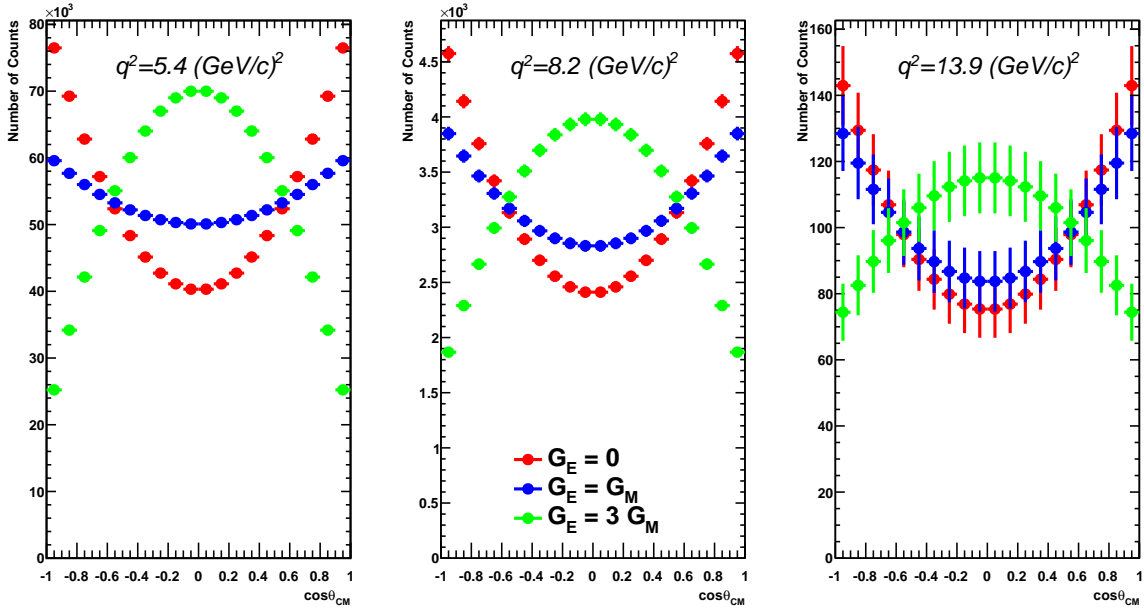


Figure 4.104: Event generator distributions (events before particle tracking and reconstruction) for $\bar{p}p \rightarrow e^+e^-$ for three different values of q^2 . The three different distributions in each plot show the angular distribution in the center of mass frame (CMS), for the different models: $|G_E| = 0$ (red), $|G_E| = |G_M|$ (blue) and $|G_E| = 3|G_M|$ (green). The number of expected counts for each model at the same q^2 are the same. The error bars denote the statistical errors where no efficiency correction has been taken into account.

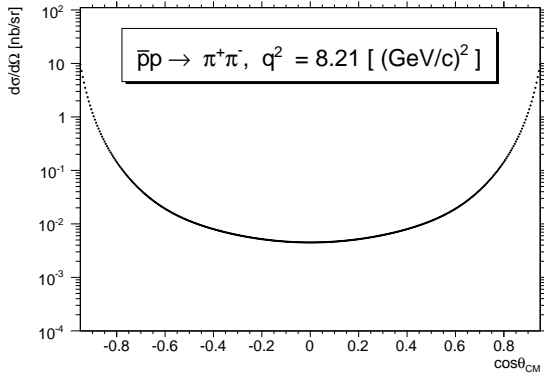


Figure 4.105: Angular distribution of $\bar{p}p \rightarrow \pi^+\pi^-$ as used in the simulation. The phenomenological fit to data has been further symmetrized in $\cos\theta$.

The photons from the main π^0 -decay can eventually convert to e^+e^- -pairs in the PANDA detector, notably in the beam pipe before the tracking detectors. Those e^+e^- -pairs fulfill all PID cuts but can very efficiently be suppressed by the kinematical constraints. In addition, we studied the case of one (two respectively) π^0 decaying via the Dalitz-channel ($\pi^0 \rightarrow e^+e^-\gamma$). The e^+e^- from Dalitz decay again fulfill all PID cuts for electrons, but again,

can be efficiently rejected due to kinematical constraints. One should note, that the branching ratio for Dalitz decay is of order 1%, i.e. the probability that both π^0 decay via the Dalitz process is about 10^{-4} .

Extensive simulations have been made for the e^+e^- -channel and are discussed below (see Table 4.48). Measuring the $\mu^+\mu^-$ channel could be a very interesting and complementary channel too which we studied at different q^2 -values. However, the rather low separation power provided by the MVD, the DIRC and the ECAL in connection with the insufficient iron yoke thickness or to the in-flight decaying pions result in a much too low rejection power of the $\pi^+\pi^-$ background channel.

4.6.3.3 Background analysis

Separating e^+e^- from $\pi^+\pi^-$ In the analysis of the process $\bar{p}p \rightarrow e^+e^-$, the most severe background comes from two pion final states, namely $\bar{p}p \rightarrow \pi^+\pi^-$ and $\bar{p}p \rightarrow \pi^0\pi^0$. The large ratio of the cross section for pion final states versus lepton final states (of order 10^6) requires a large event sample of order 10^8 in order to show that the lepton signal pollution by pion final states is below 1%. For this

reason, we have simulated the background processes for $\pi^+\pi^-$ final states with very high statistics only at 3 incident momenta, where we have chosen a low momentum, a medium momentum value and the highest momentum value, where we can access form factors: $3.3 \text{ GeV}/c$ ($q^2 = 8.21 \text{ GeV}^2$), $5.84 \text{ GeV}/c$ ($q^2 = 13.9 \text{ GeV}^2$), and $7.86 \text{ GeV}/c$ ($q^2 = 16.7 \text{ GeV}^2$) (see Table 4.48). The effect of different cuts in the global PID are shown in Table 4.49. For the $\bar{p}p \rightarrow e^+e^-$ -signal processes, particles at CMS-angles of $|\cos\theta_{CM}| > 0.8$, one of the electrons hits the forward spectrometer, which is less powerful concerning the e^+e^- reconstruction. Since we don't use this region of CMS-angle for our simulations of the signal channel, $\pi^+\pi^-$ events were simulated only in a restricted range ($[-0.8, 0.8]$) of $\cos\theta_{CM}$ values. Outside this interval, there are no data on measured $\bar{p}p \rightarrow \pi^+\pi^-$ cross sections and the extrapolation by phenomenological models introduces large uncertainties due to the steep rise of the cross section in this $\cos\theta_{CM}$ region. However, as will be shown in the next subsection, the acceptance for the signal is very low close to $|\cos\theta_{CM}| = 1$ and this limitation is then not relevant.

$q^2((\text{GeV}/c)^2)$	8.2	13.8	16.7
no cut	10^8	10^8	$2 \cdot 10^8$
VL	46.8	???	140 k
L	425	???	3 k
T	31	???	120
VT	2	???	6
CL^*	$8 \cdot 10^5$	$1 \cdot 10^6$	$2.5 \cdot 10^6$

Table 4.49: Number of $\pi^+\pi^-$ events, misidentified as e^+e^- , left after the different cuts applied for 3 different q^2 values. The CL^* cut requires 2 kinematical fit conditions to be fulfilled, namely $CL \geq 0.001$ and $CL_{e^+e^-} \geq 10CL_{\pi^+\pi^-}$. Please note that the suppression factor of about 100 from the CL^* cut is independent from the cut in the PID-probability. By requiring both, PID-cut and CL^* cut, we expect a total suppression factor of order 10^9 to 10^{10} .

Fig. 4.106 displays the effect of the different PID cuts. Only the **VeryTight** cut, corresponding to a global likelihood greater than 99.8% (and at least a 10% minimum likelihood on each subdetector) on both positive and negative charged candidates can be used. Combining one **VeryTight** with one **Tight** candidate is by far not efficient enough to suppress the background. Additionally the Confidence Level (CL^*) cut resulting from the kinematic refit was used to efficiently reduce the background. This CL^* cut requires 2 conditions to be fulfilled, namely $CL \geq 0.001$ and $CL_{e^+e^-} \geq 10CL_{\pi^+\pi^-}$. It gives an in-

dependent rejection factor of the order of 100, only slightly depending on energy. The contamination of signal e^+e^- events by background $\pi^+\pi^-$ ones is given for all 3 simulated q^2 values in Table 4.49. Using **VeryTight** cuts together with the conditions CL^* then allows to reach an overall rejection factor greater than 10^9 up to 10^{10} . Within these conditions, the contamination of the e^+e^- signal by $\pi^+\pi^-$ will be well below 1% and will therefore not affect the precision for extracting the magnetic and the electric proton form factors.

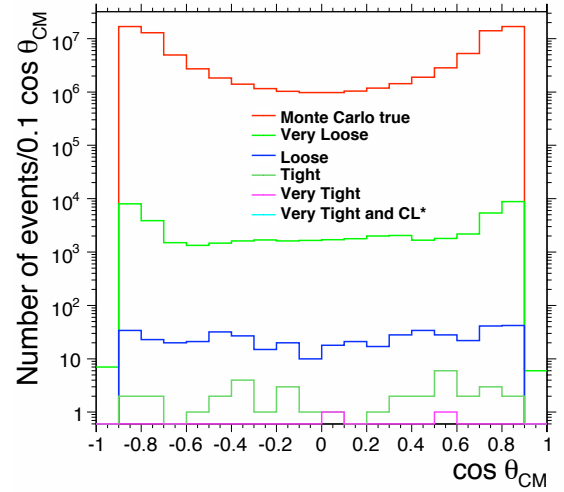


Figure 4.106: Center of mass distribution of pions misidentified as electrons after the different PID cuts. The CL^* cut provides an independent rejection factor of the order of 100, thus rejecting very efficiently the 2 remaining events after the VT cut.

The contamination of signal events by background $\pi^0\pi^0$ ones is shown in the figure Fig. ???. In this case, electrons are indeed detected and correctly identified as such. They originate from 3 different channels, namely the double π^0 Dalitz decay, one π^0 Dalitz decay associated to a photon conversion from the other π^0 , or 2 photon conversions from the 2 π^0 . The first one scales as the π^0 Dalitz decay branching ratio $\Gamma_{\gamma e^+e^-}$ squared, The second one scales as $\Gamma_{\gamma e^+e^-}$ times the conversion probability in the detector material. the third one scales as the conversion probability squared. In all cases the final state is a 6-body one ($2e^+, 2e^-, 2\gamma$). From the first case, shown on the left part of the figure, one can deduce that kinematical constraints and \bar{P} ANDA hermeticity provide a rejection of at least a factor 10^4 . This factor applies as well to the case with 2 photon conversion. As a result, we can say that the $\pi^0\pi^0$ channel can be rejected by a factor close to 10^8 .

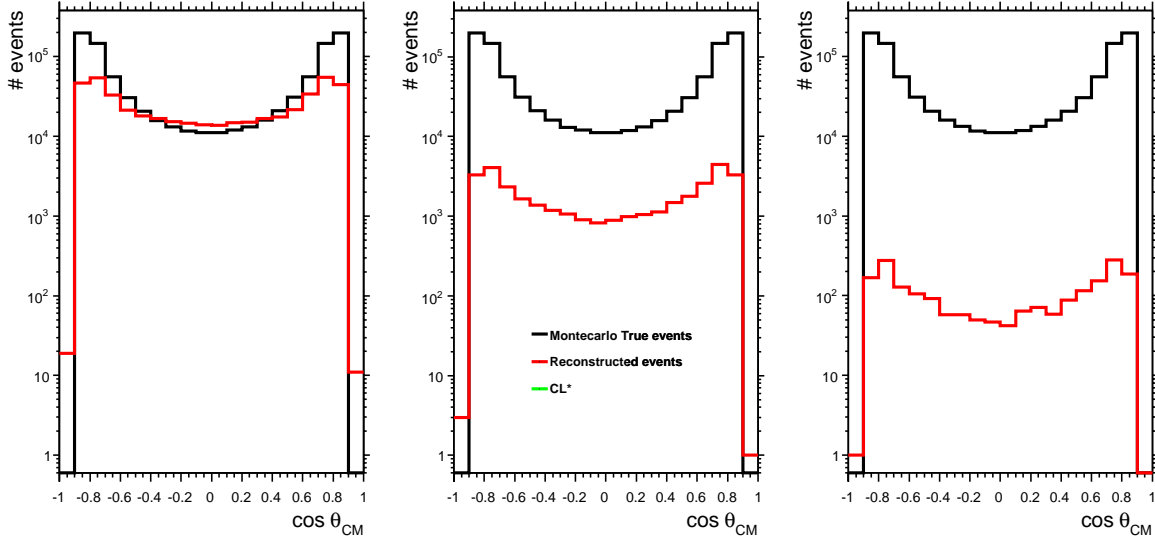


Figure 4.107: Center of mass distribution of events after different cuts for the 3 different channels (see text). The top curves are the π^0 angular distributions whereas the other curves display the angular distribution of electrons

Separating $\mu^+\mu^-$ from $\pi^+\pi^-$ The same full-scale simulations were used to analyse the rejection of $\pi^+\pi^-$ when using the PID cuts adapted to the selection of $\mu^+\mu^-$ pairs. There are two major effects that limit our ability to discriminate the $\mu^+\mu^-$ signal from the background $\pi^+\pi^-$: the in-flight decay of pions and the insufficient iron yoke thickness. In the former case muons from decaying pions in the close vicinity of the target behave like true muons. In the later case, the background is due to pions which did not interact strongly with iron and are detected by the muon counters. However, since pion and muon masses are not very different, particle identification through specific energy loss dE/dx or Cerenkov radiation is of very little help. The calorimeter provides only a rejection factor on pions, but is however of the order of 2/3. The overall pion rejection factor, after using the **VeryTight** and the CL^* cuts corresponding to muons, is of the order of 10^5 at $q^2 = 8.21(\text{GeV}/c)^2$ and gets worse with increasing q^2 . Given the ratio of the background to signal cross section, similar to the electron case, it will not be possible to extract the $\mu^+\mu^-$ channel.

Signal analysis

e^+e^- channel. Signal events for the processes $\bar{p}p \rightarrow e^+e^-$ and $\bar{p}p \rightarrow \mu^+\mu^-$ have been simulated. The electromagnetic form factors span the regime from nonperturbative QCD to perturbative

QCD at higher energies that is why we simulated events at 8 different energies. In the simulations presented here, we concentrate on the extraction of the ratio $|G_E|/|G_M|$. Due to the kinematical factor $1/\tau$ in front of $|G_E|$, the sensitivity to $|G_E|$ from the cross section measurement decreases with rising beam momentum (see Fig. 4.103). Table 4.50 gives the expected number of events for different antiproton beam momenta. For a given q^2 we used the same total number of expected events for the different assumptions on the ratio $|G_E|/|G_M|$. We have

p GeV/c	q^2 $(\text{GeV}/c)^2$	number of events
1.70	5.40	1230000
2.87	7.43	134000
3.30	8.21	68400
4.85	11.03	9450
5.86	12.90	3310
6.37	13.84	2050
7.88	16.66	587
10.9	22.29	83

Table 4.50: Expected counting rates expected for e^+e^- corresponding to an integrated luminosity of $2fb^{-1}$ (10^7s corresponding to about 4 months at $L = 2 \cdot 10^{32} \text{cm}^{-2} \text{s}^{-1}$)

applied the same cuts concerning particle identification and kinematical constraints as for the background channels described in the previous para-

graph. Fig. 4.108 indicates the reconstruction efficiency as a function of $\cos\theta_{CM}$ for different cuts for $q^2 = 8.21 (GeV/c)^2$. For the **VeryTight** cut, one can note the important drop corresponding to the loss of the PID capabilities. Holes or drops in the spectrum correspond to regions where detector transitions occur, *e.g.* transition between the barrel part of the calorimeter and the forward end cap at $\theta_{lab} = 22^\circ$ ($|\cos\theta_{CM}| = 0.33$) or loss of STT dE/dx identification at $\theta_{lab} = 14^\circ$ ($|\cos\theta_{CM}| = 0.67$). Fig. 4.109 shows the total reconstruction efficiency,

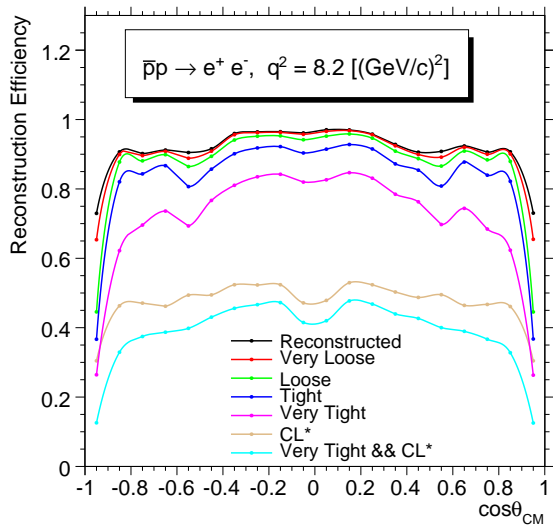


Figure 4.108: Reconstruction efficiency as a function of $\cos\theta_{CM}$ at one example of beam energy corresponding to $q^2 = 8.21 (GeV/c)^2$ for the different different PID cuts and kinematical constraints. The values quoted are averaged over a bin interval of 0.1, but still show the drop in efficiency at the transitions between barrel and forward end cap detector parts.

integrated over an interval in $\cos\theta_{CM}$ of $[-0.8, 0.8]$. The reconstruction efficiency decreases for large q^2 values. In addition to the drop in reconstruction efficiency, the cross section decreases with rising q^2 and the sensitivity for $|G_E|$ decreases too. For a q^2 above $14 (GeV/c)^2$ a measurement of the total cross section will still be possible with unprecedented accuracy, yielding a determination of $|G_M|$. An e^+e^- angular distribution is shown for $q^2 = 8.21 (GeV/c)^2$ for one model assumption ($|G_E| = |G_M|$) in Fig. 4.110. The event generator output is shown together with the reconstructed event distribution. We apply acceptance and reconstruction efficiency corrections, determined from an independent isotropic e^+e^- distribution. We have simulated the e^+e^- distributions for all q^2 -values given in table Table 4.48 and for all three assumptions on $|G_E|/|G_M|$ plus isotropic case. Reconstruc-

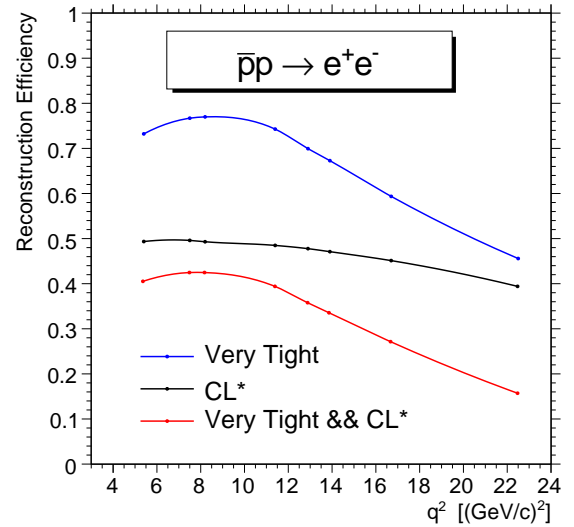


Figure 4.109: Overall integrated reconstruction efficiency as a function of q^2 applying kinematical constraints and PID cuts, integrated over an interval in $\cos\theta_{CM}$ of $[-0.8, 0.8]$ (red curve). The effect of applying the kinematical constraints only (CL^* , black curve) and PID cuts only (blue curve) are shown separately .

tion efficiency corrections have been determined for every q^2 from the isotropic e^+e^- distribution. We fitted every resulting e^+e^- -distribution with a linear 2 parameter function in order to determine the error on R . Fig. 4.111 summarizes the results for the case $|G_E| = |G_M|$. The yellow band represents a parametrisation of the errors of the fits on R . The results for the cases $|G_E| = 0$ and $|G_E| = 3|G_M|$ are similar. It shows that the separation of the 2 Form Factors can be made almost up to $14 GeV^2$. In the low q^2 region, $\bar{P}ANDA$ will be able to improve the error bars by an order of magnitude compared to the most recent BaBar data, and will consequently severely constrain the theoretical predictions which today display quite a large dispersion.

$\mu^+\mu^-$ channel. Measuring the $\mu^+\mu^-$ channel could be a very interesting and complementary channel to e^+e^- . It was studied at different q^2 values and corresponding efficiencies were determined. Their $\cos\theta_{CM}$ behaviour is different from the e^+e^- channel, since they are strongly dependent on the geometry of the muon counters and on the thickness of the iron yoke. At high q^2 , the average efficiency is only slightly smaller than for e^+e^- , but drops dramatically at low q^2 , reaching values below 10% over an extended $\cos\theta_{CM}$ interval at $q^2 = 5.4 (GeV/c)^2$.

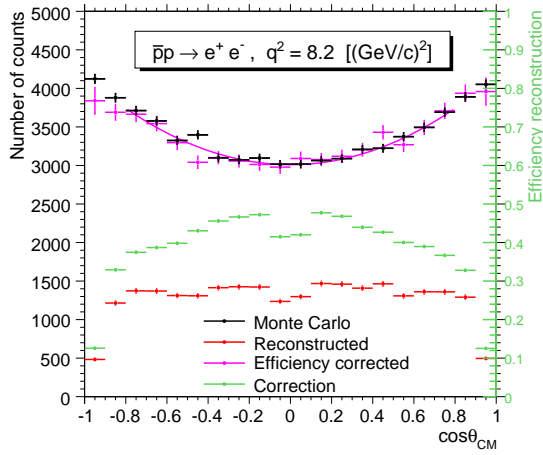


Figure 4.110: The figure shows the angular distribution of e^+e^- pairs in the center of mass system. The black symbols denote the distribution at the output of the event generator (Monte Carlo). The red symbols denote the distribution of the reconstructed e^+e^- -pairs. An acceptance and reconstruction efficiency correction (green) has been determined from an isotropically in the CM distributed e^+e^- data sample (right scale). The angular distribution of the reconstructed and efficiency corrected e^+e^- pairs in the center of mass system at $q^2 = 8.21(\text{GeV}/c)^2$ (red points). The corrected angular distribution, fits nicely to the Monte Carlo one, the ratio $R = |G_E|/|G_M|$ is extracted from a fit to the angular distribution. Only statistical errors have been taken into account.

4.6.3.4 Conclusion

In extended simulations, we have shown, that it is possible to reject the most important background process $\bar{p}p \rightarrow \pi^+\pi^-$ with a rejection factor of at least 10^9 . The resulting contamination of the signal process $\bar{p}p \rightarrow e^+e^-$ data sample is expected to be well below 1 % and can therefore be completely neglected.

Our studies have been performed without explicit assumptions on the accuracy of a luminosity measurement. For this we can extract the ratio $R = |G_E|/|G_M|$ with unprecedented precision up to $14 (\text{GeV}/c)^2$. A factor 10 improved experimental precision is expected with respect to present world data. Fig. 4.112 shows the expected accuracy on the \bar{P} ANDA measurements in comparison with the world data, under the assumption that $R = 1$. With a precise luminosity measurement, we can not only determine the ratio R but also the absolute and differential cross section up to $22 (\text{GeV}/c)^2$. Moreover separate determination of $|G_E|$ and $|G_M|$ can be made below $14 (\text{GeV}/c)^2$.

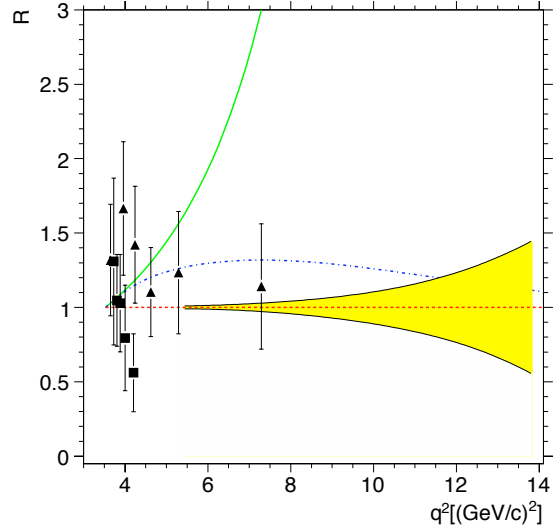


Figure 4.111: The expected error of the ratio $R = |G_E|/|G_M|$ is given as a function of q^2 . The yellow band represents the errors from the fits to the efficiency corrected e^+e^- distributions at the 8 q^2 values and is plotted up to $q^2 = 14(\text{GeV}/c)^2$. The results for the cases $|G_E| = 0$ and $|G_E| = 3|G_M|$ look similar. The data points from PS170 and BABAR are shown as well as two theoretical expectations for $R = |G_E|/|G_M|$. In the low q^2 region, \bar{P} ANDA will be able to improve the error bars by an order of magnitude.

In contrast to the e^+e^- case, the situation for the process $\bar{p}p \rightarrow \mu^+\mu^-$ is different. Due to the similar mass of muon and pion PID capabilities are not sufficient to arrive at a clean separation of pions against muons. Our simulations show, that a measurement of the electromagnetic form factors using muons is much less promising. Further studies are required.

Polarisation degree of freedom, either on the target side or with transversely polarised \bar{p} -beam would allow to access the imaginary part of the complex form factors. For example with a transversely polarised target only one could already determine the phase difference of the two form factors.

4.7 Electroweak Physics

COMMENT: Author(s): L. Schmitt

COMMENT: Referee(s): O. Scholten

With the high-intensity antiproton beam available at HESR a large number of D-mesons can be produced. This gives the possibility to observe rare weak decays of these mesons allowing to study

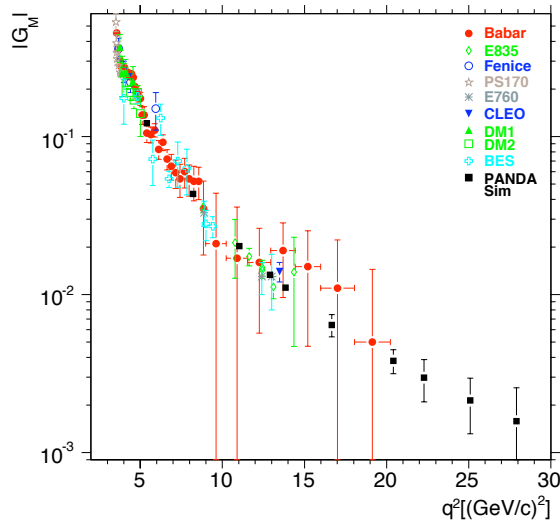


Figure 4.112: Present world data on $|G_M|$ (extracted using the hypothesis $R = |G_E|/|G_M| = 1$) are shown together with the expected accuracy by measuring $\bar{p}p \rightarrow e^+e^-$ with the PANDA experiment at FAIR. Each point corresponds to an integrated luminosity of 2 fb^{-1} .

electroweak physics by probing predictions of the Standard Model and searching for enhancements introduced by processes beyond the Standard Model. Since the studied processes are very rare and small deviations are looked for statistics is the main factor in this class of measurements. This implies to perform them at highest possible luminosity, best by even extending the antiproton production rate beyond the anticipated $2 \times 10^7/\text{s}$. However a longterm parasitic measurement in parallel to spectroscopy and other topics whenever D mesons are produced can also provide an interesting statistics over some years.

4.7.1 CP-Violation and Mixing in the Charm-Sector

\mathcal{CP} violation [439] has been observed in neutral kaon and in neutral B meson decays [440, 441]. Recently BaBar has seen evidence for mixing of D and \bar{D} [442]. The observed lifetime differences are however in no contradiction to the Standard Model.

In the standard model, \mathcal{CP} violation arises from a single phase entering the Cabbibo-Kobayashi-Maskawa (CKM) matrix. As a result, two elements of this matrix, i.e. V_{ub} and V_{td} have large phases. The elements have small magnitudes and involve the third generation and \mathcal{CP} violation is small in the K^0 system. The violation is predicted to be even smaller in the D^0 system [443]. Thus, a devia-

tion from the small standard model effect indicating "new physics" can be more easily distinguished in experiments in the D meson system. An enhanced mass difference of mixing D and \bar{D} mesons would constitute a deviation from the Standard Model. However lifetime difference mostly occur through long range interaction of common final states and can be enhanced simply by a strong phase.

Working with D mesons produced at the $D\bar{D}$ threshold has advantages arising from the strong correlation of the $D\bar{D}$ pair which is kept in the hadronization process. Formed near threshold, asymmetries are not expected in the production process and the observation of one D meson reveals the quantum numbers of the other one when produced in a charge symmetric environment (flavor tagging). Thus, flavor mixing of $D\bar{D}$ and \mathcal{CP} violation can be searched for in analogy to methods in the B -system produced on the $\Upsilon(4S)$ [444].

The two-body channels $\bar{p}p \rightarrow \psi(3770) \rightarrow D\bar{D}$ and $\bar{p}p \rightarrow \psi(4040) \rightarrow D^*\bar{D}^*$ may serve to investigate the open charm reconstruction abilities of PANDA. As shown in section 4.2.2.5 D mesons can be reconstructed well in PANDA. The open question is the value of the production cross-section for $p\bar{p} \rightarrow D\bar{D}$. In section 4.2.2.5 a very conservative estimate derived from the decay width $J/\Psi \rightarrow p\bar{p}$ of about 3 nb was given. On the other hand Kroll in studies for SuperLEAR calculated a cross section of up to 200 nb for this process [445]. For a measurement of $\alpha_{CP} \sim 10^{-3}$ as predicted by the Standard Model the production of 10^9 D meson pairs would be required, which at a production cross section of 200 nb would correspond to 3 years of running at $L = 2 \cdot 10^{32} \text{ cm}^{-2}\text{s}^{-1}$, but would be out of reach at the conservative lower limit of the cross section.

4.7.2 CP-Violation in Hyperon Decays

In self-analyzing two-body decays of hyperons the polarization of the mother particle can be obtained directly from the daughters. In these decays the orbital angular momentum of the final state can be $L = 0, 1$, in other words the decay amplitude can be an S -wave or a P -wave. Having two amplitudes, interference can occur and \mathcal{CP} -violating phases can enter. There are two characteristic parameters, which govern the decay dynamics: The quantity α denotes the asymmetry of the decay angular distribution, the quantity β gives the decay-baryon polarization. With these quantities and the decay width Γ , \mathcal{CP} asymmetries can be formed [446]:

$$A = \frac{\alpha\Gamma + \bar{\alpha}\bar{\Gamma}}{\alpha\Gamma - \bar{\alpha}\bar{\Gamma}} \approx \frac{\alpha + \bar{\alpha}}{\alpha - \bar{\alpha}} \quad B = \frac{\beta\Gamma + \bar{\beta}\bar{\Gamma}}{\beta\Gamma - \bar{\beta}\bar{\Gamma}} \approx \frac{\beta + \bar{\beta}}{\beta - \bar{\beta}} \quad D = \frac{\Gamma + \bar{\Gamma}}{\Gamma - \bar{\Gamma}}$$

For the asymmetry A , standard model predictions are of the order $\approx 2 \times 10^{-5}$. Some models beyond the standard model predict CP asymmetries of the order of several 10^{-4} . To reach the standard model limit about 10^{10} hyperon decays have to be reconstructed, which could be done within one year under ideal conditions. The detector for this experiment requires good vertex reconstruction, excellent particle identification both in forward direction and at large angles and reliable long term stability.

4.7.3 Rare Decays

The study of rare decays can open a window onto physics beyond the standard model since it probes the violation of fundamental symmetries. Lepton flavor number violating decays, *e.g.* $D^0 \rightarrow \mu e$ or $D^\pm \rightarrow \pi \mu e$, could be searched for. Flavor changing neutral currents like in the decay $D^0 \rightarrow \mu^+ \mu^-$ can occur in the standard model through box graphs or weak penguin graphs with branching fractions smaller than 10^{-15} . However, the signatures of the decays are clean leaving hope for their observation, if processes exist that boost the decay branch.

References

- [1] C. Amsler et al., Phys. Lett. **B342**, 433 (1995).
- [2] C. Amsler et al., Phys. Lett. **B353**, 571 (1995).
- [3] A. Abele et al., Phys. Lett. **B385**, 425 (1996).
- [4] A. Abele et al., Eur. Phys. J. **C19**, 667 (2001).
- [5] C. Amsler et al., Phys. Lett. **B340**, 259 (1994).
- [6] J. Aubert et al., Phys. Rev. Lett. **33**, 1404 (1974).
- [7] J. Augustin et al., Phys. Rev. Lett. **33**, 1406 (1974).
- [8] P. Dalpiaz, Charmonium and other onia at minimum energy, in *Karlsruhe 1979, Proceedings, Physics With Cooled Low Energetic Antiprotons*, edited by H. Poth, pages 111–124, 1979.
- [9] M. Andreotti et al., Nucl. Phys. B **717**, 34 (2005).
- [10] W.-M. Yao et al., J. of Phys. G **33**, 1 (2006).
- [11] C. Edwards et al., Phys. Rev. Lett. **48**, 70 (1982).
- [12] S. Choi et al., Phys. Rev. Lett. **89**, 102001 (2002).
- [13] D. Asner et al., Phys. Rev. Lett. **92**, 142001 (2004).
- [14] B. Aubert et al., Phys. Rev. Lett. **92**, 142002 (2004).
- [15] T. Armstrong et al., Phys. Rev. Lett. **69**, 2337 (1992).
- [16] M. Andreotti et al., Phys. Rev. D **72**, 032001 (2005).
- [17] J. Rosner et al., Phys. Rev. Lett. **95**, 102003 (2005).
- [18] J. Bai et al., Phys. Rev. Lett. **84**, 594200 (2000).
- [19] J. Bai et al., Phys. Rev. Lett. **88**, 101802 (2002).

- [20] S. Uehara et al., Phys. Rev. Lett. **96**, 082003 (2006).
- [21] K. Abe et al., Phys. Rev. Lett. **94**, 182002 (2005).
- [22] B. et al., Phys. Rev. Lett. **95**, 142001 (2005).
- [23] B. T.N.Pham and T. Truong, Phys. Lett. **B61**, 183 (1976).
- [24] M. Negrini, *Measurement of the branching ratios $\psi' \rightarrow J\psi X$ in the experiment E835 at FNAL*, PhD thesis, University of Ferrara, 2003.
- [25] V. Flaminio et al., CERN-HERA **70-03** (1970).
- [26] M. Andreotti et al., Phys. Rev. **D72**, 032001 (2005).
- [27] J. L. Rosner et al., Phys. Rev. Lett. **95**, 102003 (2005).
- [28] M. Andreotti et al., Phys. Rev. **D72**, 112002 (2005).
- [29] T. A. Armstrong et al., Phys. Rev. **D56**, 2509 (1997).
- [30] W. M. Yao et al., J. Phys. **G33**, 1 (2006).
- [31] A. Capella et al., Phys. Rept. **236**, 225 (1994).
- [32] P. collaboration, PANDA Technical Progress Report, Technical report, FAIR-ESAC, 2005.
- [33] H. G. K.J. Sebastian and F. L. Ridener, Phys. Rev. **D45**, 3163 (1992).
- [34] M. A. et al., Phys. Rev. **D65**, 05002 (2002).
- [35] K. Juge, J. Kuti, and C. Morningstar, Phys. Rev. Lett. **90**, 161601 (2003).
- [36] D. Thompson et al., Phys. Rev. Lett. **79**, 1630 (1997).
- [37] G. Adams et al., Phys. Rev. Lett. **81**, 5760 (1998).
- [38] A. Abele et al., Phys. Lett. **B423**, 175 (1998).
- [39] J. Reinhardt, Nucl. Phys. **A692**, 268c (2001).
- [40] S. U. Chung et al., Phys. Rev. **D65**, 072001 (2002).
- [41] A. Abele et al., Phys. Lett. **B446**, 349 (1999).
- [42] P. Salvini et al., Eur. Phys. J. **C35**, 21 (2004).
- [43] E. I. Ivanov et al., Phys. Rev. Lett. **86**, 3977 (2001).
- [44] S. U. Chung and E. Klempt, Phys. Lett. **B563**, 83 (2003).
- [45] J. Kuhn et al., Phys. Lett. **B595**, 109 (2004).
- [46] M. Lu et al., hep-ex/0405044.
- [47] G. Adams, Talk given at the First GHP Meeting of the APS, Chicago, 2004.
- [48] P. Chen, X. Liao, and T. Manke, Nucl. Phys. Proc. Suppl. **94**, 342 (2001).
- [49] C. Michael, in *Proceedings of "Heavy Flavours 8"*, 1999.
- [50] R. Cester, in *Proceedings of the "Super LEAR Workshop"*, pages 91–103, Zürich, 1991.
- [51] M. Gaillard, L. Maiani, and R. Petronzio, Phys. Lett. **B110**, 489 (1982).
- [52] C. Bernard et al., Phys. Rev. **D56**, 7039 (1997).
- [53] C. Bernard et al., Nucl. Phys. (Proc. Suppl.) **B73**, 264 (1999).
- [54] K. Juge, J. Kuti, and C. Morningstar, Phys. Rev. Lett. **82**, 4400 (1999).
- [55] Z.-H. Mei and X.-Q. Luo, Int. J. Mod. Phys. **A18**, 5713 (2003), hep-lat/0206012.
- [56] T. Manke et al., Nucl. Phys. (Proc. Suppl.) **B82**, 4396 (1999).
- [57] C. Morningstar and M. Peardon, Phys. Rev. **D60**, 34509 (1999).
- [58] J. Sexton, A. Vaccarino, and D. Weingarten, Phys. Rev. Lett. **75**, 4563 (1995).
- [59] P. Page, in *Proceedings of the "pbar2000 Workshop"*, edited by D. Kaplan and H. Rubin, pages 55–64, Chicago, 2001.
- [60] R. Jones, in *Proceedings of the workshop "Gluonic excitations"*, Jefferson Lab, 2003, in print.

- [61] A. Bertin et al., Phys. Lett. **B400**, 187 (1995).
- [62] A. Bertin et al., Phys. Lett. **B385**, 493 (1996).
- [63] A. Bertin et al., Phys. Lett. **B400**, 226 (1997).
- [64] C. Cicalo et al., Phys. Lett. **B462**, 453 (1999).
- [65] F. Nichitiu et al., Phys. Lett. **B545**, 261 (2002).
- [66] C. Morningstar and M. Peardon, Phys. Rev. **D56**, 4043 (1997).
- [67] C. Hanhart, Y. S. Kalashnikova, A. E. Kudryavtsev, and A. V. Nefediev, Phys. Rev. **D76**, 034007 (2007).
- [68] J. Z. Bai et al., Phys. Rev. Lett. **76**, 3502 (1996).
- [69] C. Evangelista et al., Phys. Rev. **D57**, 5370 (1998).
- [70] A. De Rujula, H. Georgi, and S. L. Glashow, Phys. Rev. Lett. **37**, 785 (1976).
- [71] N. Isgur and M. B. Wise, Phys. Rev. Lett. **66**, 1130 (1991).
- [72] S. Godfrey and R. Kokoski, Phys. Rev. **D43**, 1679 (1991).
- [73] S. Godfrey and N. Isgur, Phys. Rev. **D32**, 189 (1985).
- [74] M. Di Pierro and E. Eichten, Phys. Rev. **D64**, 114004 (2001).
- [75] K. Hagiwara et al., Phys. Rev. **D66**, 010001 (2002).
- [76] B. Aubert et al., Phys. Rev. Lett. **90**, 242001 (2003).
- [77] D. Besson et al., Phys. Rev. **D68**, 032002 (2003).
- [78] P. Krokovny et al., Phys. Rev. Lett. **91**, 262002 (2003).
- [79] B. Aubert et al., Phys. Rev. **D69**, 031101 (2004).
- [80] B. Aubert et al., Phys. Rev. Lett. **93**, 181801 (2004).
- [81] K. Abe et al., Phys. Rev. Lett. **92**, 012002 (2004).
- [82] B. Aubert et al., Phys. Rev. **D74**, 032007 (2006).
- [83] <http://pdglive.lbl.gov>.
- [84] B. Aubert, Phys. Rev. Lett. **97**, 222001 (2006).
- [85] E. Swanson, Phys. Rept. **429**, 243 (2006).
- [86] M. A. Nowak, M. Rho, and I. Zahed, Phys. Rev. **D48**, 4370 (1993).
- [87] W. A. Bardeen and C. T. Hill, Phys. Rev. **D49**, 409 (1994).
- [88] W. A. Bardeen, E. J. Eichten, and C. T. Hill, Phys. Rev. **D68**, 054024 (2003).
- [89] M. A. Nowak, M. Rho, and I. Zahed, Acta Phys. Polon. **B35**, 2377 (2004).
- [90] R. N. Cahn and J. D. Jackson, Phys. Rev. **D68**, 037502 (2003).
- [91] O. Lakhina and E. S. Swanson, Phys. Lett. **B650**, 159 (2007).
- [92] K. Terasaki, Phys. Rev. **D68**, 011501 (2003).
- [93] A. Hayashigaki and K. Terasaki, Prog. Theor. Phys. **114**, 1191 (2006).
- [94] H.-Y. Cheng and W.-S. Hou, Phys. Lett. **B566**, 193 (2003).
- [95] L. Maiani, F. Piccinini, A. D. Polosa, and V. Riquer, Phys. Rev. Lett. **93**, 212002 (2004).
- [96] L. Maiani, F. Piccinini, A. D. Polosa, and V. Riquer, Phys. Rev. **D71**, 014028 (2005).
- [97] Y.-Q. Chen and X.-Q. Li, Phys. Rev. Lett. **93**, 232001 (2004).
- [98] M. E. Bracco, A. Lozea, R. D. Matheus, F. S. Navarra, and M. Nielsen, Phys. Lett. **B624**, 217 (2005).
- [99] M. Nielsen, R. D. Matheus, F. S. Navarra, M. E. Bracco, and A. Lozea, AIP Conf. Proc. **814**, 528 (2006).
- [100] E. van Beveren and G. Rupp, Phys. Rev. Lett. **91**, 012003 (2003).
- [101] D. S. Hwang and D.-W. Kim, Phys. Lett. **B601**, 137 (2004).
- [102] D. S. Hwang and D. W. Kim, J. Phys. Conf. Ser. **9**, 63 (2005).

- [103] T. Barnes, F. E. Close, and H. J. Lipkin, Phys. Rev. **D68**, 054006 (2003).
- [104] E. E. Kolomeitsev and M. F. M. Lutz, Phys. Lett. **B582**, 39 (2004).
- [105] J. Hofmann and M. F. M. Lutz, Nucl. Phys. **A733**, 142 (2004).
- [106] M. Lutz and M. Soyeur, arXiv:hep-ph/0710.1545.
- [107] F. P. Sassen and S. Krewald, Int. J. Mod. Phys. **A20**, 705 (2005).
- [108] F.-K. Guo, S. Krewald, and U.-G. Meißner, arXiv:hep-ph/0712.2953.
- [109] F. Sassen, PhD thesis, Universität Bonn, 2005.
- [110] A. Faessler, T. Gutsche, V. E. Lyubovitskij, and Y.-L. Ma, Phys. Rev. **D76**, 014005 (2007).
- [111] A. Faessler, T. Gutsche, V. E. Lyubovitskij, and Y.-L. Ma, Phys. Rev. **D76**, 114008 (2007).
- [112] C. Hanhart, priv. comm., 2005.
- [113] T. Mehen and R. P. Springer, Phys. Rev. **D70**, 074014 (2004).
- [114] F. E. Close and E. S. Swanson, Phys. Rev. **D72**, 094004 (2005).
- [115] P. Colangelo and F. De Fazio, Phys. Lett. **B570**, 180 (2003).
- [116] P. Colangelo, F. De Fazio, and A. Ozpineci, Phys. Rev. **D72**, 074004 (2005).
- [117] X. Liu, Y.-M. Yu, S.-M. Zhao, and X.-Q. Li, Eur. Phys. J. **C47**, 445 (2006).
- [118] M. Shifman and A. Vainshtein, Phys. Rev. **D77**, 034002 (2008).
- [119] D. J. Lange, Nucl. Instrum. Meth. **A462**, 152 (2001).
- [120] A. Capella, U. Sukhatme, C.-I. Tan, and J. Tran Thanh Van, Phys. Rept. **236**, 225 (1994).
- [121] C. Hanhart, priv. comm., 2006.
- [122] W. M. Yao et al., J. Phys. **G33**, 1 (2006).
- [123] E. Klempt, Phys. Rev. **C66**, 058201 (2002).
- [124] M. F. M. Lutz and E. E. Kolomeitsev, Nucl. Phys. **A700**, 193 (2002).
- [125] M. F. M. Lutz and E. E. Kolomeitsev, Nucl. Phys. **A730**, 110 (2004).
- [126] E. E. Kolomeitsev and M. F. M. Lutz, Phys. Lett. **B585**, 243 (2004).
- [127] I. Zychor et al., Phys. Rev. Lett. **96**, 012002 (2006).
- [128] M. I. Adamovich et al., Eur. Phys. J. **C50**, 535 (2007).
- [129] M. I. Adamovich et al., Eur. Phys. J. **C5**, 621 (1998).
- [130] M. I. Adamovich et al., Eur. Phys. J. **C11**, 271 (1999).
- [131] K. Abe et al., Phys. Lett. **B524**, 33 (2002).
- [132] V. Ziegler, PhD thesis, University of Iowa, 2007, report SLAC-R-868.
- [133] U. Löring, B. C. Metsch, and H. R. Petry, Eur. Phys. J. **A10**, 447 (2001).
- [134] V. Guzey and M. V. Polyakov, arXiv:hep-ph/0512355, 2005.
- [135] C. Baltay et al., Phys. Rev. **140**, B1027 (1965).
- [136] B. Musgrave, Nuov. Cim. **35**, 735 (1965).
- [137] A. B. Kaidalov and P. E. Volkovitsky, Z. Phys. **C63**, 517 (1994).
- [138] J. Hofmann and M. F. M. Lutz, Nucl. Phys. **A763**, 90 (2005).
- [139] M. F. M. Lutz and J. Hofmann, Int. J. Mod. Phys. **A21**, 5496 (2006).
- [140] V. Flaminio, W. Moorhead, D. Morrison, and N. Rivoire, Report CERN-HERA 84-01, 1984.
- [141] S. Okubo, Phys. Lett. **5**, 165 (1963).
- [142] G. Zweig, CERN report TH-401.
- [143] J. Iizuka, Prog. Theor. Phys. Suppl. **38**, 21 (1966).
- [144] T. Johansson, Antihyperon-hyperon production in antiproton-proton collisions, in *AIP Conf. Proc. Eight Int. Conf. on Low Energy Antiproton Physics*, page 95, 2003.
- [145] CERN-HERA **84-01**.

- [146] P. D. Barnes et al., Phys. Rev. C **54**, 1877 (1996).
- [147] H. Becker et al., Nucl. Phys. B **141**, 48 (1978).
- [148] E. Klempt et al., Phys. Rept. **368**, 119 (2002).
- [149] M. Alberg, Nucl. Phys. A **692**, 47c (2001).
- [150] M. Alberg, J. Ellis, and D. Kharzeev, Phys. Lett. B **356**, 113 (1995).
- [151] W.-M. Yao et al., J. Phys. G **33**, 1 (2006).
- [152] A. Kaidalov and P. Volkovitsky, Z. Phys. C **63**, 517 (1994).
- [153] A. Frodesen, O. Skjeggstad, and H. Tøfte, *Probability and Statistics in Particle Physics*, Universitetsforlaget, Bergen, 1979.
- [154] G. Brown and M. Rho, Phys. Rev. Lett. **66**, 2720 (1991).
- [155] T. Hatsuda and S. Lee, Phys. Rev. C **46**, 34 (1992).
- [156] U. Mosel, arXiv:0801.49701 [hep-ph], 2008.
- [157] D. Trnka et al., Phys. Rev. Lett **94**, 191303 (2005).
- [158] M. Naruki et al., Phys. Rev. Lett. **96**, 092301 (2006).
- [159] R. Muto et al., Phys. Rev. Lett. **98**, 042501 (2007).
- [160] R. Nasseripour et al., Phys. Rev. Lett **99**, 262302 (2007).
- [161] G. Agakishiev et al., Phys. Rev. Lett **75**, 1272 (1995).
- [162] R. Arnaldi et al., Phys. Rev. Lett. **96**, 162302 (2006).
- [163] T. Yamazaki et al., Z. Phys. A **355**, 219 (1996).
- [164] H. Geissel et al., Phys. Rev. Lett. **88**, 122301 (2002).
- [165] K. Suzuki et al., Phys. Rev. Lett. **92**, 072302 (2004).
- [166] J. G. Messchendorp et al., Phys. Rev. Lett. **89**, 222302 (2002).
- [167] M. Nikipelov et al., Phys. Lett. B **540**, 207 (2002).
- [168] Z. Rudy et al., Eur. Phys. J. A **15**, 303 (2002).
- [169] R. Barth et al., Phys. Rev. Lett. **78**, 4007 (1997).
- [170] F. Laue et al., Phys. Rev. Lett. **82**, 1640 (1999).
- [171] M. Pfeiffer et al., Phys. Rev. Lett. **92**, 252001 (2004).
- [172] M. Kotulla et al., Phys. Rev. Lett. **100**, 192302 (2008).
- [173] T. Ishikawa et al., Phys. Lett. **B608**, 215 (2005).
- [174] W. Weise, in *Proc. Int. Workshop on the Structure of Hadrons*, Hirschegg, Austria, 2001.
- [175] K. Tsushima, D. Lu, A. Thomas, K. Saito, and R. Landau, Phys. Rev. C **59**, 2824 (1999).
- [176] A. Sibirtsev, K. Tsushima, and A. Thomas, Eur. Phys. J. A **6**, 351 (1999).
- [177] A. Hayashigaki et al., Phys. Lett. B **487**, 96 (2000).
- [178] P. Morath, PhD thesis, TU München, 2001.
- [179] L. Tolós, J. Schaffner-Bielich, and A. Mishra, Phys. Rev. C **70**, 025203 (2004).
- [180] M. Lutz and C. Korpa, Phys. Lett. B **633**, 43 (2006).
- [181] T. Mizutani and A. Ramos, Phys. Rev. C **74**, 065201 (2006).
- [182] S. Brodsky, I. Schmidt, and G. de Téramond, Phys. Rev. Lett. **64**, 1011 (1990).
- [183] S. Brodsky and G. Miller, Phys. Lett. B **412**, 125 (1997).
- [184] F. Klingl et al., Phys. Rev. Lett. **82**, 3396 (1999).
- [185] S. Lee and C. Ko, Prog. Theor. Phys. Suppl. **149**, 173 (2003).
- [186] S. Lee, in *Proc. 10th Int. Conf. on Hadron Spectroscopy (Hadron'03)*, Aschaffenburg, 2003, [arXiv:nucl-th/0310080].
- [187] Y. Golubeva, E. Bratkovskaya, W. Cassing, and L. Kondratyuk, Eur. Phys. J. A **17**, 275 (2003).

- [188] W. Cassing, Y. Golubeva, and L. Kondratyuk, *Eur. Phys. J. A* **7**, 279 (2000).
- [189] J. Haidenbauer, G. Krein, U.-G. Meißner, and A. Sibirtsev, *Eur. Phys. J. A* **33**, 107 (2007).
- [190] R. Anderson et al., *Phys. Rev. Lett.* **38**, 263 (1977).
- [191] D. Kharzeev, C. Lourenco, M. Nardi, and H. Satz, *Z. Phys. C* **74**, 307 (1997).
- [192] B. Alessandro et al., *Eur. Phys. J.* **C33**, 31 (2004).
- [193] B. Alessandro et al., *Eur. Phys. J. C* **48**, 329 (2006).
- [194] S. S. Adler et al., *Phys. Rev. Lett.* **96**, 012304 (2006).
- [195] A. Adare et al., *Phys. Rev.* **C77**, 024912 (2008).
- [196] T. Matsui and H. Satz, *Phys. Lett. B* **178**, 416 (1986).
- [197] B. Alessandro et al., *Eur. Phys. J. C* **39**, 335 (2005).
- [198] R. Arnaldi et al., *Eur. Phys. J. C* **43**, 167 (2005).
- [199] R. Arnaldi et al., *Phys. Rev. Lett.* **99**, 132302 (2007).
- [200] A. Sibirtsev, K. Tsushima, and A. W. Thomas, *Phys. Rev.* **C63**, 044906 (2001).
- [201] A. Sibirtsev, K. Tsushima, and A. Thomas, *Phys. Rev. C* **75**, 064903 (2007).
- [202] J. Hilbert, N. Black, T. Barnes, and E. Swanson, *Phys. Rev. C* **75**, 064907 (2007).
- [203] K. Seth, in *Proc. Int. Workshop on the Structure of Hadrons*, Hirschegg, Austria, 2001.
- [204] L. Gerland, L. Frankfurt, and M. Strikman, *Phys. Lett. B* **619**, 95 (2005).
- [205] A. Sibirtsev, 2008, priv. communication.
- [206] T. Tanimori et al., *Phys. Rev. Lett.* **55**, 1835 (1985).
- [207] T. A. Armstrong et al., *Phys. Rev.* **D56**, 2509 (1997).
- [208] M. Andreotti et al., *Phys. Rev. Lett.* **91**, 091801 (2003).
- [209] M. Bleicher et al., *J. Phys.* **G25**, 1859 (1999).
- [210] S. A. Bass et al., *Prog. Part. Nucl. Phys.* **41**, 225 (1998).
- [211] A. Faessler, G. Lubeck, and K. Shimizu, *Phys. Rev.* **D26**, 3280 (1982).
- [212] T. Bürvenich et al., *Phys. Lett. B* **542**, 261 (2002).
- [213] I. N. Mishustin, L. M. Satarov, T. J. Bürvenich, H. Stöcker, and W. Greiner, *Phys. Rev.* **C71**, 035201 (2005).
- [214] A. Larionov, I. Mishustin, L. Satarov, and W. Greiner, arXiv:0802.1845 [nucl-th] (2008).
- [215] C.-Y. Wong, A. Kerman, G. Satchler, and A. Mackellar, *Phys. Rev. C* **29**, 574 (1984).
- [216] C. Batty, E. Friedman, and A. Gal, *Phys. Rept.* **287**, 385 (1997).
- [217] E. Friedman, A. Gal, and J. Mareš, *Nucl. Phys. A* **761**, 283 (2005).
- [218] S. Teis, W. Cassing, T. Maruyama, and U. Mosel, *Phys. Rev. C* **50**, 388 (1994).
- [219] C. Spieles et al., *Phys. Rev.* **C53**, 2011 (1996).
- [220] A. Sibirtsev, W. Cassing, G. I. Lykasov, and M. V. Rzyanin, *Nucl. Phys.* **A632**, 131 (1998).
- [221] J. Pochodzalla, *Phys. Lett.* **B669**, 306 (2008).
- [222] W. Greiner, *Int. Journal of Modern Physics E* **5**, 1 (1995).
- [223] P. Haensel, A.Y.Potekhin, and D. Yakovlev, *Neutron Stars 1. Equation of state and structure*, Springer, 2007.
- [224] F. Weber, R. Negreiros, and P. Rosenfield, *Springer Lecture Notes*, arXiv:arXiv:0705.2708.
- [225] T. K. Jha, H. Mishra, and V. Sreekanth, *Phys. Rev. C* **77**, 045801 (2008).
- [226] H. Dapo, B.-J. Schäfer, and J. Wambach, arXiv:0811.29391 [nucl-th].

- [227] N. Kaiser and W. Weise, Phys. Rev. C **71**, 015203 (2005).
- [228] R. B. Wiringa and S. C. Pieper, Phys. Rev. Lett. **89**, 182501 (2002).
- [229] S. C. Pieper, R. B. Wiringa, and J. Carlson, Phys. Rev. C **70**, 054325 (2004).
- [230] S. C. Pieper, Quantum Monte Carlo Calculations of Light Nuclei, in *Lecture notes for Course CLXIX - "Nuclear Structure far from Stability: New Physics and new Technology"*, 2007, arXiv:0711.1500v1 [nucl-th].
- [231] I. Stetcu, B. Barrett, and U. van Kolck, Phys. Rev. C **73**, 037307 (2006).
- [232] C. Keil, F. Hofmann, and H. Lenske, Phys. Rev. C **61**, 06401 (2000).
- [233] F. Hofmann, C. Keil, and H. Lenske, Phys. Rev. C **64**, 034314 (2001).
- [234] S. Beane, P. Bedaque, A. Parreno, and M. Savage, Nucl. Phys. A **747**, 55 (2005).
- [235] M. Savage, Baryon-baryon interactions from the lattice, in *Proc. of the IX International Conference on Hypernuclear and Strange Particle Physics*, edited by J. Pochodzalla and T. Walcher, page 301, SIF and Springer-Verlag Berlin Heidelberg, 2007, arXiv: 0612063 [nucl-th].
- [236] A. G. Nicola and J. Pelaez, Phys. Rev. D **65**, 054009 (2002).
- [237] M. Lutz and E. Kolomeitsev, Nucl. Phys. A **700**, 193 (2002).
- [238] H. Polinder, J. Haidenbauer, and U.-G. M. M. ner, Nucl. Phys. A **779**, 244 (2006).
- [239] L. Tolos, A. Ramos, and E. Oset, Phys. Rev. C **74**, 015203 (2006).
- [240] M. Lutz, C. Korpa, and M. Moeller, Nucl. Phys. A **808**, 124 (2008).
- [241] I. Stetcu, B. Barrett, and U. van Kolck, Phys. Lett. B **653**, 358 (2007).
- [242] B. Borasoy, E. Epelbaum, H. Krebs, D. Lee, and U.-G. Meißner, Eur. Phys. J. A **31**, 105 (2007).
- [243] P. Navratil et al., Light nuclei from chiral EFT interactions, in *Proceedings of the 20th European Conference on Few-Body Problems in Physics (EFB20)*, 2007.
- [244] Y. Kondo et al., Nucl. Phys. A **676**, 371 (2000).
- [245] J. Ahn et al., Phys. Lett. B **633**, 214 (2006).
- [246] O. Hashimoto and H. Tamura, Prog. Part. Nucl. Phys. **57**, 566 (2006).
- [247] K. Itonaga, T. Ueda, and T. Motoba, Nucl. Phys. A **691**, 197c (2001).
- [248] A. Parreno, A. Ramos, and C. Bennhold, Nucl. Phys. A **65**, 015205 (2001).
- [249] K. Sasaki, T. Inoue, and M. Oka, Nucl. Phys. A **726**, 349 (2003).
- [250] J. Dubach, G. B. Feldman, B. R. Holstein, and L. de la Torre, Ann. Phys. **249**, 146 (1996).
- [251] T. Motoba, Nucl. Phys. A **691**, 231c (2001).
- [252] T. Rijken and Y. Yamamoto, arXiv:hep-ph/0207358v1.
- [253] K. Tanida et al., Plan for the measurement of Ξ^- -atomic X rays at J-PARC, in *Proc. of the IX International Conference on Hypernuclear and Strange Particle Physics*, edited by J. Pochodzalla and T. Walcher, page 145, SIF and Springer-Verlag Berlin Heidelberg, 2007.
- [254] A. Buchmann, Z. Naturforschung **52**, 877 (1997).
- [255] A. Buchmann and R. F. Lebed, Phys. Rev. D **67**, 016002 (2003).
- [256] R. Jaffe, Phys. Rev. Lett. **38**, 195 (1977).
- [257] R. Jaffe, Phys. Rev. Lett. **38**, 617E (1977).
- [258] T. Sakai, K. Shimizu, and K. Yazaki, Prog. Theor. Phys. Suppl. **137**, 121 (2000).
- [259] T. Yamada and C. Nakamoto, Phys. Rev. C **62**, 034319 (2000).
- [260] K. S. Myint, S. Shinmura, and Y. Akaishi, Eur. Phys. J. A **16**, 21 (2003).
- [261] I. Afnan and B. Gibson, Phys. Rev. C **67**, 017001 (2003).
- [262] I. Filikhin, A. Gal, and V. Suslov, Phys. Rev. C **68**, 024002 (2003).
- [263] J. Pochodzalla, Nucl. Phys. A **754**, 430c (2005).

- [264] F. Ferro, M. Agnello, F. Iazzi, and K. Szymanska, Nucl. Phys. A **789**, 209 (2007).
- [265] W. R. Lozowski, D. Steski, H. Huang, and C. Naylor, Nucl. Instr. and Meth. in Physics Research A **590**, 157 (2008).
- [266] P. V. A.B. Kaidalov, Z. Phys. C **63**, 517 (1994).
- [267] T. Yamada and K. Ikeda, Nucl. Phys. **A585**, 79c, 1995.
- [268] T. Yamada and K. Ikeda, Phys. Rev. C **56**, 3216 (1997).
- [269] Y. Hirata, Y. Nara, A. Ohnishi, T. Harada, and J. Randrup, Nucl. Phys. A **639**, 389c (1998).
- [270] Y. Hirata, Y. Nara, A. Ohnishi, T. Harada, and J. Randrup, Prog. Theor. Phys. **102**, 89 (1999).
- [271] D. Millener, C. Dover, and A. Gal, Prog. Theor. Phys. Suppl. **117**, 307 (1994).
- [272] K. Ikeda et al., Prog. Theor. Phys. **91**, 747 (1994).
- [273] A. S. Lorente, A. Botvina, and J. Pochodzalla, (in preparation).
- [274] E. Fermi, Progr. Theor. Phys. **5**, 570 (1950).
- [275] J. Bondorf, A. Botvina, A. Iljinov, I. Mishustin, and K. Sneppen, Phys. Rep. **257**, 133 (1995).
- [276] A. Botvina, Y. Golubeva, and A. Iljinov, INR, P-0657, Moscow (1990).
- [277] A. Botvina et al., Z. Phys. A **345**, 413 (1993).
- [278] A. Sudov et al., Nucl. Phys. A **554**, 223 (1993).
- [279] M. Danysz et al., Nucl. Phys. **49**, 121 (1963).
- [280] D. Prowse, Phys. Rev. Lett **17**, 782 (1966).
- [281] S. Aoki et al., Prog. Theor. Phys. **85**, 1287 (1991).
- [282] J. Ahn et al., Phys. Rev. Lett. **87**, 132504 (2001).
- [283] H. Takahashi et al., Phys. Rev. Lett. **87**, 212501 (2001).
- [284] M. Danysz et al., Nucl. Phys. **49**, 121 (1963).
- [285] R. Dalitz et al., Proc. R. Soc. Lond. A **426**, 1 (1989).
- [286] C. Dover, D. Millener, A. Gal, and D. Davis, Phys. Rev. C **44**, 1905 (1991).
- [287] E. Hiyama et al., Phys. Rev. C **66**, 024007 (2002).
- [288] S. Randeniya and E. Hungerford, Phys. Rev. C **76**, 064308 (2007).
- [289] D. Lanskoj and Y. Yamamoto, Phys. Rev. C **69**, 014303 (2004).
- [290] M. Shoeb, Phys. Rev. C **69**, 054003 (2004).
- [291] H. Nemura, S. Shinmura, Y. Akaishi, and K. S. Myint, Phys. Rev. Lett. **94**, 202502 (2005).
- [292] I. Filikhin and A. Gal, Phys. Rev. Lett. **89**, 172502 (2002).
- [293] H. Nemura, Y. Akaishi, and K. S. Myint, Phys. Rev. C **67**, 051001(R) (2003).
- [294] M. Shoeb, Phys. Rev. C **71**, 024004 (2005).
- [295] H. Bando, T. Motoba, and J. Zofka, Int. J. Mod. Phys. **A5**, 4021 (1990).
- [296] F. Ajzenberg-Selove, Nucl. Phys. A **433**, 1 (1985).
- [297] G. Kopylov, *Principles of resonance kinematics*, Moscow, 1970.
- [298] C. Dover and A. Gal, Ann. Phys. **147**, 309 (1983).
- [299] E. Friedman and A. Gal, Phys. Report **452**, 89 (2007).
- [300] C. J. Batty, E. Friedman, and A. Gal, Phys. Rev. C **59**, 295 (1999).
- [301] S. Aoki et al., Phys. Lett. B **355**, 45 (1995).
- [302] A. S. Lorente et al., Nucl. Inst. Meth A **573**, 410 (2007).
- [303] M. Kavatsyuk et al., GSI Annual report (2007).
- [304] P. Leleux et al., Astronomy and Astrophysics **411**, L85 (2003).
- [305] A. Bamberger et al., Nucl. Phys. B **60**, 1 (1973).

- [306] M. Bedjidian et al., Phys. Lett. **62**, 467 (1976).
- [307] M. May et al., Phys. Rev. Lett. **51**, 2085 (1983).
- [308] H. Akikawa et al., Phys. Rev. Lett. **88**, 082501 (2002).
- [309] A. Galoyan, Private Communication.
- [310] A. V. Belitsky and A. V. Radyushkin, Phys. Rept. **418**, 1 (2005).
- [311] X. Ji, Ann. Rev. Nucl. Part. Sci. **54**, 413 (2004).
- [312] M. Diehl, Phys. Rept. **388**, 41 (2003).
- [313] K. Goeke, M. V. Polyakov, and M. Vanderhaeghen, Prog. Part. Nucl. Phys. **47**, 401 (2001).
- [314] X.-D. Ji, Phys. Rev. Lett. **78**, 610 (1997).
- [315] A. V. Radyushkin, Phys. Lett. **B380**, 417 (1996).
- [316] X.-D. Ji, Phys. Rev. **D55**, 7114 (1997).
- [317] A. V. Radyushkin, Phys. Rev. **D58**, 114008 (1998).
- [318] M. Diehl, T. Feldmann, R. Jakob, and P. Kroll, Eur. Phys. J. **C8**, 409 (1999).
- [319] P. Kroll and A. Schafer, Eur. Phys. J. **A26**, 89 (2005).
- [320] C.-C. Kuo et al., Phys. Lett. **B621**, 41 (2005).
- [321] J. P. Lansberg, B. Pire, and L. Szymanowski, Nucl. Phys. **A782**, 16 (2007).
- [322] A. Freund, A. V. Radyushkin, A. Schafer, and C. Weiss, Phys. Rev. Lett. **90**, 092001 (2003).
- [323] T. A. Armstrong et al., Phys. Rev. **D56**, 2509 (1997).
- [324] S. Ong and J. Van der Wiele, private communication .
- [325] J. P. Ralston and D. E. Soper, Nucl. Phys. **B152**, 109 (1979).
- [326] D. Boer, Phys. Rev. **D60**, 014012 (1999).
- [327] D. Boer and P. J. Mulders, Phys. Rev. **D57**, 5780 (1998).
- [328] J. C. Collins and D. E. Soper, Phys. Rev. **D16**, 2219 (1977).
- [329] C. Bourrely and J. Soffer, Eur. Phys. J. **C36**, 371 (2004).
- [330] D. de Florian and W. Vogelsang, Phys. Rev. **D71**, 114004 (2005).
- [331] R. D. Field and R. P. Feynman, Phys. Rev. **D15**, 2590 (1977).
- [332] R. P. Feynman, R. D. Field, and G. C. Fox, Phys. Rev. **D18**, 3320 (1978).
- [333] A. Bacchetta, U. D'Alesio, M. Diehl, and C. A. Miller, Phys. Rev. **D70**, 117504 (2004).
- [334] V. Barone, A. Drago, and P. G. Ratcliffe, Phys. Rept. **359**, 1 (2002).
- [335] P. J. Mulders and R. D. Tangerman, Nucl. Phys. **B461**, 197 (1996).
- [336] X. Artru and M. Mekhfi, Z. Phys. **C45**, 669 (1990).
- [337] R. L. Jaffe and X.-D. Ji, Phys. Rev. Lett. **67**, 552 (1991).
- [338] R. L. Jaffe, (1996).
- [339] J. Soffer, Phys. Rev. Lett. **74**, 1292 (1995).
- [340] D. W. Sivers, Phys. Rev. **D41**, 83 (1990).
- [341] D. W. Sivers, Phys. Rev. **D43**, 261 (1991).
- [342] U. Etschenbroich, G. Schnell, and R. Seidl, (2004).
- [343] A. V. Efremov, K. Goeke, and P. Schweitzer, Phys. Lett. **B568**, 63 (2003).
- [344] M. Anselmino, M. Boglione, U. D'Alesio, E. Leader, and F. Murgia, Phys. Rev. **D71**, 014002 (2005).
- [345] M. Anselmino, M. Boglione, and F. Murgia, Phys. Lett. **B362**, 164 (1995).
- [346] M. Anselmino, A. Drago, and F. Murgia, (1997).
- [347] R. L. Jaffe and X.-D. Ji, Phys. Rev. Lett. **71**, 2547 (1993).
- [348] S. Falciano et al., Z. Phys. **C31**, 513 (1986).
- [349] M. Guanziroli et al., Z. Phys. **C37**, 545 (1988).

- [350] J. S. Conway et al., Phys. Rev. **D39**, 92 (1989).
- [351] A. Brandenburg, O. Nachtmann, and E. Mirkes, Z. Phys. **C60**, 697 (1993).
- [352] A. Brandenburg, S. J. Brodsky, V. V. Khoze, and D. Mueller, Phys. Rev. Lett. **73**, 939 (1994).
- [353] K. J. Eskola, P. Hoyer, M. Vanttinen, and R. Vogt, Phys. Lett. **B333**, 526 (1994).
- [354] E. L. Berger and S. J. Brodsky, Phys. Rev. Lett. **42**, 940 (1979).
- [355] A. Idilbi, X.-d. Ji, J.-P. Ma, and F. Yuan, Phys. Rev. **D70**, 074021 (2004).
- [356] D. Boer, Nucl. Phys. **B603**, 195 (2001).
- [357] G. L. Kane, J. Pumplin, and W. Repko, Phys. Rev. Lett. **41**, 1689 (1978).
- [358] U. D'Alesio and F. Murgia, Prog. Part. Nucl. Phys. **61** **2008**, 394 (2008).
- [359] X. Ji, J.-W. Qiu, W. Vogelsang, and F. Yuan, Phys. Rev. Lett. **97**, 082002 (2006).
- [360] X. Ji, J.-w. Qiu, W. Vogelsang, and F. Yuan, Phys. Rev. **D73**, 094017 (2006).
- [361] X. Ji, J.-W. Qiu, W. Vogelsang, and F. Yuan, Phys. Lett. **B638**, 178 (2006).
- [362] Y. Koike, W. Vogelsang, and F. Yuan, Phys. Lett. **B659**, 878 (2008).
- [363] C. S. Lam and W.-K. Tung, Phys. Rev. **D18**, 2447 (1978).
- [364] C. S. Lam and W.-K. Tung, Phys. Lett. **B80**, 228 (1979).
- [365] C. S. Lam and W.-K. Tung, Phys. Rev. **D21**, 2712 (1980).
- [366] J. Badier et al., Zeit. Phys. **C11**, 195 (1981).
- [367] E. L. Berger, Z. Phys. **C4**, 289 (1980).
- [368] O. Nachtmann and A. Reiter, Z. Phys. **C24**, 283 (1984).
- [369] D. Boer, A. Brandenburg, O. Nachtmann, and A. Utermann, Eur. Phys. J. **C40**, 55 (2005).
- [370] L. P. Gamberg and G. R. Goldstein, Phys. Lett. **B650**, 362 (2007).
- [371] L. Y. Zhu et al., Phys. Rev. Lett. **99**, 082301 (2007).
- [372] A. Bianconi and M. Radici, J. Phys. **G31**, 645 (2005).
- [373] J. C. Collins, Nucl. Phys. **B396**, 161 (1993).
- [374] J. C. Collins, Phys. Lett. **B536**, 43 (2002).
- [375] A. V. Belitsky, X. Ji, and F. Yuan, Nucl. Phys. **B656**, 165 (2003).
- [376] S. J. Brodsky, D. S. Hwang, and I. Schmidt, Phys. Lett. **B530**, 99 (2002).
- [377] S. J. Brodsky, D. S. Hwang, and I. Schmidt, Nucl. Phys. **B642**, 344 (2002).
- [378] X.-d. Ji and F. Yuan, Phys. Lett. **B543**, 66 (2002).
- [379] X.-d. Ji, J.-p. Ma, and F. Yuan, Phys. Rev. **D71**, 034005 (2005).
- [380] X.-d. Ji, J.-P. Ma, and F. Yuan, Phys. Lett. **B597**, 299 (2004).
- [381] A. Idilbi, X.-d. Ji, and F. Yuan, Phys. Lett. **B625**, 253 (2005).
- [382] M. Anselmino et al., Phys. Rev. **D72**, 094007 (2005).
- [383] A. V. Efremov, K. Goeke, S. Menzel, A. Metz, and P. Schweitzer, Phys. Lett. **B612**, 233 (2005).
- [384] W. Vogelsang and F. Yuan, Phys. Rev. **D72**, 054028 (2005).
- [385] J. C. Collins et al., Phys. Rev. **D73**, 094023 (2006).
- [386] A. Bacchetta, F. Conti, and M. Radici, (2008).
- [387] N. Hammon, O. Teryaev, and A. Schafer, Phys. Lett. **B390**, 409 (1997).
- [388] D. Boer, P. J. Mulders, and O. V. Teryaev, Phys. Rev. **D57**, 3057 (1998).
- [389] D. Boer and P. J. Mulders, Nucl. Phys. **B569**, 505 (2000).
- [390] D. Boer and J.-w. Qiu, Phys. Rev. **D65**, 034008 (2002).
- [391] J.-w. Qiu and G. Sterman, Phys. Rev. **D59**, 014004 (1999).

- [392] M. Burkardt and D. S. Hwang, Phys. Rev. **D69**, 074032 (2004).
- [393] M. Burkardt and G. Schnell, Phys. Rev. **D74**, 013002 (2006).
- [394] A. Airapetian et al., Phys. Rev. Lett. **94**, 012002 (2005).
- [395] M. Diefenthaler, AIP Conf. Proc. **792**, 933 (2005).
- [396] M. Diefenthaler, (2007).
- [397] J. C. Collins et al., (2005).
- [398] M. Anselmino et al., (2005).
- [399] V. Y. Alexakhin et al., Phys. Rev. Lett. **94**, 202002 (2005).
- [400] E. S. Ageev et al., Nucl. Phys. **B765**, 31 (2007).
- [401] M. Alekseev et al., (2008).
- [402] A. Courtoy, S. Scopetta, and V. Vento, (2008).
- [403] A. V. Efremov, K. Goeke, and P. Schweitzer, Czech. J. Phys. **56**, F181 (2006).
- [404] A. V. Efremov, K. Goeke, and P. Schweitzer, Phys. Rev. **D73**, 094025 (2006).
- [405] S. Levorato, (2008).
- [406] A. Bianconi, J. Phys. **G35**, 115003 (2008).
- [407] M. Anselmino et al., (2008).
- [408] V. Abazov et al., ASSIA LOI, The structure of the nucleon: A study of spin-dependent interactions with antiprotons, hep-ex/0507077, 2004.
- [409] PAX LOI, <http://www.fz-juelich.de/ikp/pax>.
- [410] R. D. Tangerman and P. J. Mulders, Phys. Rev. **D51**, 3357 (1995).
- [411] O. Martin, A. Schafer, M. Stratmann, and W. Vogelsang, Phys. Rev. **D57**, 3084 (1998).
- [412] V. Barone, T. Calarco, and A. Drago, Phys. Rev. **D56**, 527 (1997).
- [413] A. V. Efremov, K. Goeke, and P. Schweitzer, Eur. Phys. J. **C35**, 207 (2004).
- [414] M. Anselmino, V. Barone, A. Drago, and N. N. Nikolaev, Phys. Lett. **B594**, 97 (2004).
- [415] G. Altarelli, R. K. Ellis, and G. Martinelli, Nucl. Phys. **B157**, 461 (1979).
- [416] A. J. Buras and K. J. F. Gaemers, Nucl. Phys. **B132**, 249 (1978).
- [417] E. Anassontzis et al., Phys. Rev. **D38**, 1377 (1988).
- [418] H. Shimizu, G. Sterman, W. Vogelsang, and H. Yokoya, Phys. Rev. **D71**, 114007 (2005).
- [419] G. Moreno et al., Phys. Rev. **D43**, 2815 (1991).
- [420] A. Bianconi and M. Radici, Phys. Rev. **D71**, 074014 (2005).
- [421] A. Bianconi, Nucl. Instrum. Meth. **A593**, 562 (2008).
- [422] A. Bianconi and M. Radici, Phys. Rev. **D73**, 114002 (2006).
- [423] A. Bianconi and M. Radici, J. Phys. **G34**, 1595 (2007).
- [424] A. Bianconi and M. Radici, Phys. Rev. **D73**, 034018 (2006).
- [425] A. Bianconi and M. Radici, Phys. Rev. **D72**, 074013 (2005).
- [426] O. Gayou et al., Phys. Rev. Lett. **88**, 092301 (2002).
- [427] O. Gayou et al., Phys. Rev. C **71**, 055202 (2005).
- [428] M. Jones et al., Phys. Rev. C **74**, 035201 (2006).
- [429] A. Zichichi et al., Nuovo Cim. **24**, 170 (1962).
- [430] M. Ambrogiani et al., Phys. Rev. **D60**, 032002 (1999), and references therein.
- [431] B. Aubert et al., Phys. Rev. **D73**, 012005 (2006).
- [432] C. Adamuscin, E. Kuraev, E. Tomasi-Gustafsson, and F. Maas, Phys.Rev. **C75**, 045205 (2007).
- [433] E. Tomasi-Gustafsson and M. P. Rekalov, Phys.Lett. **B504**, 291 (2001).
- [434] E. Eisenhandler et al., Nucl. Phys. B **96**, 109 (1975).
- [435] T. Buran et al., Nucl. Phys. B **116**, 51 (1976).

- [436] T. Berglund et al., Nucl. Phys. B **137**, 276 (1978).
- [437] R. Dulude et al., Phys. Lett **79B**, 329 (1978).
- [438] T. Armstrong et al., Phys. Rev. D **56**, 2509 (1997).
- [439] I. Bigi, Surveys High Energy Phys. **12**, 269 (1998).
- [440] B. Aubert et al., Phys. Rev. Lett. **87**, 091801 (2001).
- [441] K. Abe et al., Phys. Rev. Lett. **87**, 091802 (2001).
- [442] B. Aubert et al., Phys. Rev. Lett. **98**, 211802 (2007).
- [443] G. Burdman, hep-ph/9407378.
- [444] P. Harrison and H. Quinn, editors, *The Babar Physics Book*, SLAC, 1998, SLAC-R-504.
- [445] P. Kroll, Invited talk at SuperLEAR Workshop, Zurich, Switzerland, Oct 9-12, 1991.
- [446] N. H. Hamann, Prepared for SUPERLEAR Workshop, Zurich, Switzerland, 9-12 Oct 1991.

5 Summary and Outlook

COMMENT: Author(s): D. Bettoni, K. Peters

References

Acknowledgments

thanks....

ADC Analog to Digital Converter	ENC Equivalent Noise Charge
AGATA Advanced Gamma Tracking Array	Eoc End-of-Column
AGS Alternate Gradient Synchrotron	EPR Electron Paramagnetic Resonance
APD Avalanche Photo Diode	EU European Union
API Application Programming Interface	FADC Flash ADC
AS Advanced Switching	FAIR Facility for Antiproton and Ion Research
ASIC Application Specific Integrated Circuit	FE Front-End
BGO Bismuth Germanate	FEE Front-End Electronics
BNL Brookhaven National Laboratory	FET Field-Effect Transistor
BTCP Bogoroditsk Techno-Chemical Plant	FNAL Fermi National Laboratory
CA Certification Authority	FPGA Field Programmable Gate Array
CAD Computer Aided Design	FS Forward Spectrometer
CCE Charge Collection Efficiency	FZJ Forschungszentrum Jülich
CDR Conceptual Design Report	GEM Gas Electron Multiplier
CERN Conseil European pour la Recherche Nucleaire	GPD Generalized Parton Distribution
CLAS Cebaf Large Acceptance Spectrometer	GSI Gesellschaft für Schwerionenforschung
CKM Cabbibo-Kobayashi-Maskawa	GSS Generic Security Service, an authentication API aka Kerberos V5
CLAS CEBAF Large Acceptance Spectrometer	HC Hadron Calorimeter
COMPASS Common Muon Proton Apparatus for Structure and Spectroscopy	HESR High Energy Storage Ring
COSY Cooler Synchrotron	HFG Hermann von Helmholtz-Gemeinschaft Deutscher Forschungszentren
CT Central Tracker	HTS High Temperature Superconductors
CVS Code Versioning System	HV High Voltage
DAQ Data Acquisition	IBP In-Beam Polarimeter
DESY Deutsches Elektronensynchrotron	IP Interaction point
DIRC Detector for Internally Reflected Cherenkov Light	IHEP Institute for High Energy Physics
DLL Delay Lock Loop	INFN Istituto Nazionale di Fisica Nucleare
DPM Dual Parton Model	KVI Kernfysisch Versneller Instituut
DSP Digital Signal Processor	LAAPD Large Area APD
DVCS Deeply Virtual Compton Scattering	LEAR Low Energy Antiproton Ring
EGEE Enabling Grids for E-science in Europe	LEC Liquid Encapsulated Czochalski
ELT Enclosed Layout Transistors	LED Light Emission Diode
EMC Electromagnetic Calorimeter	LEGS Laser Electron Gamma Source
	LHC Large Hadron Collider

LNP Low Noise Preamplifier	SSL Secure Socket Layer
LOI Letter of Intent	STT Straw Tube Tracker
LP Low-Pass	TCS Trigger Control System
LQCD Lattice QCD	TDC Time to Digital Converter
MAPS Monolithic Active Pixel Sensor	TDS Time Distribution System
MDC Mini Drift Chamber	TJNAF Thomas Jefferson National Accelerator Facility
MIP Minimum Ionizing Particle	TOF Time-of-Flight Detector
MIRAC Mid Rapidity Calorimeter	TOP Time-of-Propagation
MUD Muon Detector	ToT Time-over-Threshold
MVD Micro Vertex Detector	TPC Time Projection Chamber
NIEL Non-Ionizing Energy Loss	TRD Transition Radiation Detector
NMR Nuclear Magnetic Resonance	TS Target Spectrometer
PCB Printed Circuit Board	TSL Thermostimulated luminescence
PCI Peripheral Component Interconnect	TSL The Svedberg Laboratory
PDR Preliminary Design Report	TTC Time Trigger and Control
PED Particle Energy Deposit	UrQMD Ultra-relativistic Quantum Molecular Dynamic
PID Particle Identification	VEGA Versatile and Efficient Gamma Detector
PLL Phase Lock Loop	VME Versa Module Eurocard
PMT Photomultiplier	WLS Wave Length Shift(er/ing)
PSI Paul Scherrer Institute	
PTS Pellet Test Station	
PWO Lead Tungstate	
QA Quality Assurance	
QCD Quantum Chromo Dynamics	
QED Quantum Electrodynamics	
RICH Ring Imaging Cherenkov Counter	
RPC Resistive Plate Chambers	
SASL Simple Authentication and Security Layer	
SCT Semiconductor Tracker	
SI Semi-insulating	
SICCAS Shanghai Institute of Ceramics, Chinese Academy of Sciences	
SLAC Stanford Linear Accelerator Center	
SMD Surface Mount Device	

List of Figures

1.1	The running of the strong coupling constant as function of the scale μ [1].	2	2.13	Schematic view of the HESR. Tentative positions for injection, cooling devices and experimental installations are indicated.	28
1.2	LQCD results divided by experimental values for selected quantities in hadronic physics. On the left the quenched calculations are shown, on the right the corresponding unquenched ones. While the former exhibit systematic deviations of some 10% from experiment, the latter are in impressive agreement with experiment.	4	2.14	Time dependent luminosity during the cycle $L(t)$ versus the time in the cycle. Different measures for beam preparation are indicated.	29
1.3	The LQCD glueball spectrum in pure SU(3) gauge theory [6].	5	2.15	Cycle average luminosity vs. cycle time at 1.5 (left) and 15 GeV/c (right). The maximum number of particles is limited to 10^{11} (solid line), and unlimited (dashed lines).	29
1.4	LQCD predictions for the charmonium, the glueball and the spin-exotic $\bar{c}c$ -glue hybrids spectrum in quenched lattice QCD.	7	2.16	Maximum average luminosity L_{\max} vs. atomic charge Z for three different beam momenta.	30
2.1	Artistic view of the \bar{P} ANDA Detector	14	2.17	$\psi(2S)$ resonance scans: the observed cross section (excitation curve) for each channel (filled dots); the expected cross section from the fit (open diamonds); the ‘bare’ resonance curves σ_{BW} from the fit (solid lines). The two bottom plots show the normalized energy distributions B_i (from Ref. [37]).	32
2.2	Side view of the target spectrometer	15	2.18	Kinematical factors used in the determination of the center-of-mass energy from the velocity of antiprotons in the rf bucket. Left vertical axis: partial derivatives of the center-of-mass energy w with respect to revolution frequency f and orbit length L . Right vertical axis: energy spread in the center of mass Δw for a given momentum spread $\Delta p/p$	33
2.3	Schematic of the target and beam pipe setup with pumps.	15	2.19	Statistical uncertainty in the resonance width as a function of the ratio between energy spread (Gaussian FWHM Γ_B) and resonance width Γ . The amount of data is $\mathcal{N} \equiv \varepsilon \mathcal{L} \sigma_p = 10^4$ in this example. An optimal luminosity distribution is assumed.	33
2.4	The Micro-vertex detector of \bar{P} ANDA	17	2.20	Distortion of the resonance shape as a function of the ratio between energy spread (Gaussian FWHM Γ_B) and resonance width Γ	33
2.5	Straw Tube Tracker in the Target Spectrometer	18			
2.6	GEM Time Projection Chamber in the Target Spectrometer	18			
2.7	The \bar{P} ANDA barrel and end-cap EMC	20			
2.8	Integration of the secondary target and the germanium Cluster-array in the \bar{P} ANDA detector. The beam enters from left.	21			
2.9	Layout out the secondary sandwich target. The active silicon layers provide also tracking information on the emitted weak decay products of the produced hypernuclei.	21			
2.10	Design of the γ -ray spectroscopy setup with 15 germanium cluster detector, each comprising 3 germanium crystals.	21			
2.11	Schematic overview of the luminosity monitor concept.	24			
2.12	Top view of the experimental area	26			

3.1	Possible processes in $\bar{p}p$ -interactions and their estimated energy dependencies. The question marks mean that the corresponding estimations are absent.	40	3.20	Electron efficiency and contamination rate for muons, pions, kaons and protons in different momentum ranges by using the EMC information.	54
3.2	Material budget in front of the EMC	44	3.21	The distribution of the distance in x-direction between the expected hits obtained by the extrapolation and the corresponding detected hits in the muon detector for generated single muon particles.	54
3.3	The number of detected Cerenkov photons versus the polar angle of pions	45	3.22	Kaon and electron efficiency with the contamination rate of the remaining particle species in different momentum ranges by applying VeryTight PID cuts	55
3.4	Difference between the reconstructed and the expected Cerenkov angle	45	3.23	Improving the $J/\psi\pi^+\pi^-$ mass resolution by applying a kinematic fit	56
3.5	Pixel hit resolution on sensor coordinates	46	3.24	Reconstructed $J/\psi\eta$ mass from the background mode $\pi\pi\eta$	57
3.6	Tracking reconstruction efficiency	47	3.25	Reconstruction efficiency for wrongly identified e^+e^- pairs (truth mass)	58
3.7	The momentum resolution for pions momentum of 1 GeV/c momentum at a polar angle of 20°	47	3.26	Functionality of FAIRroot	59
3.8	The vertex resolution for pions of $p = 3$ GeV/c momentum.	48	3.27	Flow diagram of PANDArroot	59
3.9	Leakage correction function for the barrel EMC in the θ range between 22° and 90°	49	4.1	Charmonium spectrum from LQCD	65
3.10	Leakage correction function depending on the deposited energy for the Shashlyk calorimeter	49	4.2	Resonance scan at the χ_{c1}	66
3.11	Typical truncated dE/dx plot	50	4.3	The charmonium spectrum.	66
3.12	dE/dx versus track momentum in the MVD for different particle species	50	4.4	Invariant e^+e^- mass reconstructed at $\sqrt{s} = 4.260$ GeV.	68
3.13	Width parameters of the energy loss information from the MVD	51	4.5	Confidence level of the kinematical fit to $J/\psi\pi^+\pi^-$ for the data simulated at $\sqrt{s} = 4.260$ GeV energy. The cut applied is $P_{J/\psi\pi^+\pi^-} > 0.001$	69
3.14	Distribution of the likelihood for electron identification.	52	4.6	Invariant $J/\psi\pi^+\pi^-$ mass, in the case of Y(4260) resonance.	70
3.15	Efficiency for electrons and contamination rate for the 4 other particle types.	52	4.7	Invariant dipion mass of Y(4260) candidates. The black line is the simulated and reconstructed data and the blue line is the fit with the theoretical function. The result of λ after the fit seems to be consistent with the input data.	70
3.16	Kaon efficiency and contamination rate of the remaining particle species in different momentum ranges by using the DIRC information	52	4.8	Invariant dipion mass of $J/\psi\pi^0\pi^0$ candidates.	71
3.17	E/p versus track momentum for electrons and pions	53	4.9	Invariant $J/\psi\gamma$ mass at $\sqrt{s} = 3.686$ GeV.	71
3.18	Zernike moment 31 for electrons, muons and hadrons.	53	4.10	Invariant $\chi_{c1}\gamma$ mass at $\sqrt{s} = 3.686$ GeV.	71
3.19	MLP network output for electrons and the other particle species in the momentum range between 300 MeV/c and 5 GeV/c.	54			

4.11 Invariant $J/\psi\gamma$ mass at $\sqrt{s} = 3.510$ GeV.	73	4.38 Invariant $J/\psi\omega$ mass distribution	99
4.12 Invariant $J/\psi\eta$ mass at $\sqrt{s} = 4.260$ GeV.	73	4.39 Distribution of the helicity angles in $J/\psi\omega$	100
4.13 Angular dependence of $\pi^0\pi^0$ cross-section with parametrisation used in Monte-Carlo simulation.	74	4.40 Invariant mass distribution for $\psi(2S)\pi\pi$ candidates.	101
4.14 Distribution of reconstructed $\cos\theta$ of the γ in CM system for $\bar{p}p \rightarrow \pi^0\pi^0$ background.	76	4.41 Reconstructed events for $\bar{p}p \rightarrow \phi\phi$	104
4.15 Distribution of reconstructed $\cos\theta$ of the γ in CM system from $h_c \rightarrow \eta_c\gamma$	77	4.42 Angle between ϕ decay planes.	105
4.16 Invariant D^\pm mass distribution of $\bar{p}p \rightarrow D^+D^-$ signal events	79	4.43 Angular dependent efficiencies	106
4.17 Invariant $D^{*\pm}$ and D^0 mass distributions	81	4.44 Cross section scan examples	106
4.20 Fit of h_c resonance for $\Gamma = 0.5$ MeV (a) and $\Gamma = 1$ MeV (b)	84	4.45 Cross section measurement $\bar{p}p \rightarrow \phi\phi$ by JETSET.	107
4.21 Definition of the angles for the angular distribution of the radiative decay of the χ_c	84	4.46 The D_s spectrum and quark model predictions	109
4.22 Results for $\cos\theta$, $\cos\theta'$ and ϕ' after the generation and reconstruction of the events for χ_{c1} decay.	85	4.47 Missing mass spectrum obtained for the D_s^\pm candidates	112
4.23 Results for $\cos\theta$, $\cos\theta'$ and ϕ' after the generation and reconstruction of the events for χ_{c2} decay.	85	4.48 Reconstruction of signal events type 1	113
4.24 Charmonium potentials and hybrid spectrum from LQCD	88	4.49 Background channel 1: $\bar{p}p \rightarrow D_s^\pm D_s^\mp \pi^0$	114
4.25 Glueball prediction from LQCD calculations	90	4.50 Fit of the excitation function obtained from the reconstructed signal events	116
4.26 Dispersive effects on the $X(3872)$	92	4.51 Schematic illustration of the investigated $\bar{p}p \rightarrow \bar{\Xi}^+\Xi^-\pi^0$ reaction	119
4.27 Invariant $\eta \rightarrow \gamma\gamma$ mass	92	4.52 $\Xi^-\pi^0$ invariant mass resolution	121
4.28 Invariant $\chi_{c1} \rightarrow J/\psi\gamma$ mass	93	4.53 Dalitz plot showing the $\bar{\Xi}^+\Xi^-\pi^0$ reconstruction efficiency	121
4.29 Invariant $\chi_{c1}\pi^0\pi^0$ mass	93	4.54 Total cross sections for the $\bar{p}p \rightarrow \bar{Y}Y$ reaction.	123
4.30 Invariant $K^-\pi^+\pi^0$ mass	94	4.55 Coordinate system for the $\bar{p}p \rightarrow \bar{Y}Y$ reaction.	124
4.31 Invariant $D^0\pi^0$ mass	94	4.56 Reconstructed $\bar{p}\pi^+$ invariant mass for $\bar{\Lambda}$ candidates from the $\bar{p}p \rightarrow \bar{\Lambda}\Lambda$ reaction.	126
4.32 Invariant $D^0\bar{D}^{*0}$ mass	95	4.57 $\bar{\Lambda}$ decay vertex distributions.	126
4.33 Expected significance for the reaction $\bar{p}p \rightarrow \tilde{\eta}_{c1}\eta$	96	4.58 CM angular distributions for the $\bar{p}p \rightarrow \bar{\Lambda}\Lambda$ reaction.	127
4.34 Background cross sections for $J/\psi\omega$	97	4.59 Pion momentum distributions in the laboratory system from the $\bar{\Lambda}$ decay 1.64 GeV/c.	127
4.35 Invariant $J/\psi \rightarrow e^+e^-$ mass obtained after the kinematic fit	98	4.60 Reconstructed \bar{p} angular distributions from the $\bar{\Lambda} \rightarrow \bar{p}\pi^+$ decay.	128
4.36 Invariant $\pi^+\pi^-\pi^0$ mass obtained after the kinematic fit	98	4.61 Reconstructed polarisations from the $\bar{p}p \rightarrow \bar{\Lambda}\Lambda$ reaction.	128
4.37 Invariant $J/\psi\pi^+\pi^-$ ($J/\psi \rightarrow e^+e^-$) mass	99	4.62 Topology of the $\bar{p}p \rightarrow \bar{\Xi}^+\Xi^-$ reaction.	129
		4.63 Reconstructed $\bar{\Xi}^+$ mass for the $\bar{p}p \rightarrow \bar{\Xi}^+\Xi^-$ reaction.	129

4.64 Reconstructed CM angular distribution for the $\bar{p}p \rightarrow \bar{\Xi}^+\Xi^-$ reaction. . .	130	4.77 Production probability of ground (g.s.) and excited states (ex.s.) in conventional nuclear fragments and in one single (SHP), twin (THP) and double hypernuclei (DHP) after the capture of a Ξ^- in a ^{12}C nucleus and its conversion into two Λ hyperons predicted by a statistical decay model. 145
4.65 Reconstructed polarisation for the $\bar{p}p \rightarrow \bar{\Xi}^+\Xi^-$ reaction.	130	4.78 Production probability of ground and excited states of accessible double hypernuclei after the capture of a Ξ^- in a ^{12}C nucleus and the Ξ^- conversion into two Λ hyperons. Excited states in $^{11}_{\Lambda\Lambda}\text{Be}$, $^{10}_{\Lambda\Lambda}\text{Be}$ and $^9_{\Lambda\Lambda}\text{Li}$ dominate over a wide range of the Ξ^- binding energy.
4.66 Simulated cross section for resonant J/ψ production on nuclear protons .	134	4.79 Total γ -ray spectrum resulting from the decay of double hypernuclei produced in a ^{12}C target and detected in the germanium array and before additional cuts. The statistics of the simulations corresponds to a data taking time of about two weeks. . . .
4.67 Reconstructed invariant mass distribution of e^+e^- pair candidates for signal and background	136	4.80 Upper part: Momentum correlation of all negative pion candidates resulting from the decay of double hypernuclei in a secondary ^{12}C target. Lower part: γ -spectrum detected in the Ge-array by cutting on the two pion momenta. The expected γ -transitions energies from single and double hypernuclei are marked by the arrows.
4.68 Distributions used to suppress the background	137	4.81 Distribution of produced particles from background reactions. The Germanium detectors will be affected mainly by particles emitted at backward axial angle.
4.69 Invariant mass distribution of e^+e^- pair candidates for signal, UrQMD, and $\pi^+\pi^-$ events	138	4.82 Incident kinetic energy of protons and neutrons entering the Germanium detector surface. The main contribution to a possible radiation damage of the detector is provided by neutrons.
4.70 Schematic illustration of reactions giving access to the nuclear potential of $\bar{\Lambda}$ antihyperons	139	4.83 DVCS can be described by the handbag diagram, as there is factorization between the upper ‘hard’ part of the diagram which is described by perturbative QCD and QED, and a lower ‘soft’ part that is described by GPDs.
4.71 Hypernuclei and their link to other fields of physics.	140	
4.72 Present knowledge on hypernuclei. Only very few individual events of double hypernuclei have been detected and identified so far.	141	
4.73 Measured ratio of nonmesonic ($\Lambda N \rightarrow NN$) to mesonic ($\Lambda \rightarrow N\pi$) hypernuclear decay widths as a function of the nuclear mass [250]. .	141	
4.74 Various steps of the double hypernucleus production in \bar{P} ANDA.	142	
4.75 Layout out the secondary sandwich target used in the present simulations. The figure marks the stopping points of the Ξ^- hyperons within the target in the x-y plane transverse to the beam direction. The rectangles indicate the outlines of the four target segments. All four segments are equipped with ^{12}C absorbers.	143	
4.76 Transverse vs. longitudinal momentum distribution of Ξ^- with transverse and longitudinal momenta less than 500 MeV/c (upper part) and those stopped within the secondary target (lower part).	144	

- 4.84 The handbag diagram may describe the inverted WACS process $p\bar{p} \rightarrow \gamma\gamma$ at \bar{P} ANDA energies. 149
- 4.85 The production of a hard virtual photon (upper part) is a hard subprocess that is claimed to factorize from the lower part, which can be described by a hadron to photon transition distribution amplitude (TDA). 150
- 4.86 The squared form factors $R_V^2(s)$ (solid line) and $R_A^2(s)$ (dashed line), as calculated from the double distribution model (Fig. 2 of ref. [322]) 150
- 4.87 The handbag contribution to $p\bar{p} \rightarrow \gamma\pi^0$ at large but non-asymptotic s . The blob on the right hand side represents the parameterized general dynamics for $q\bar{q} \rightarrow \gamma\pi^0$ 151
- 4.88 Cross section prediction for the angular distribution at $s = 20 \text{ GeV}^2$ for \bar{P} ANDA taken from ref. [319] 151
- 4.89 Cross sections for processes with $\gamma\gamma$, $\pi^0\gamma$ and $\pi^0\pi^0$ in the final state, for different \bar{P} ANDA energies. The results correspond to particles with $|\cos(\theta)| < 0.6$ in the center of mass system (Refs. [324, 319, 320]). 151
- 4.90 Angular distribution of generated particles in the center of mass system, as seen by the detector. 152
- 4.91 Separation of $\gamma\gamma$ events from the neutral background $\gamma\pi^0$ and $\pi^0\pi^0$ is not yet possible with the current selection algorithms. The number of misidentified $\gamma\pi^0$ ($\pi^0\pi^0$) events and their statistical error were magnified by a factor 10^2 , (10^3) to match the limited Monte Carlo statistics to the abundance of the background in the experiment. 152
- 4.92 Separation of $\gamma\pi^0$ events from the neutral background. The number of misidentified $\pi^0\pi^0$ events and their statistical error was magnified by factor 10. 153
- 4.93 Leading-twist contribution to the Drell-Yan dilepton production 154
- 4.94 The Collins-Soper frame 154
- 4.95 Light-cone momentum fractions scatter plot for unpolarised DY dilepton production. 162
- 4.96 The azimuthal asymmetry for the unpolarised DY process $\bar{p}p \rightarrow l^+l^-X$. 162
- 4.97 The azimuthal asymmetries for the single-polarised DY process $\bar{p}p^\uparrow \rightarrow l^+l^-X$ 163
- 4.98 \bar{P} ANDA acceptance for the unpolarised DY process $\bar{p}p \rightarrow l^+l^-X$ 164
- 4.99 Expected statistical errors for SSA in the (un)polarised DY process $\bar{p}p^{(\uparrow)} \rightarrow l^+l^-X$ folded with \bar{P} ANDA acceptance. 164
- 4.100 Feynman diagrams for elastics electron scattering (left) and its crossed channel $\bar{p}p \rightarrow e^+e^-$ (right) which will be measured with the \bar{P} ANDA-detector. 166
- 4.101 World data on the modulus $|G_M|$ of the time-like magnetic form factor extracted from different experiments using $\bar{p}p \rightarrow e^+e^-$, $e^+e^- \rightarrow \bar{p}p$, and $e^+e^- \rightarrow \gamma\bar{p}p$. In all cases, the hypothesis of $R = |G_E|/|G_M| = 1$ has been used to analyse the data. . . . 167
- 4.102 The data from the LEAR experiment PS170 and recent BABAR data have been alternatively used as an input to a dispersion relation analysis of the electromagnetic form factors. The recent data from JLAB have been used as an input for the space-like region. The green band gives the dispersion relation fit result on $|G_E|/|G_M|$ when using the PS170 data in the time-like region and the yellow band gives the result for the BABAR data. The present accuracy in the ratio of $R = |G_E|/|G_M|$ is of order 50% while a future measurement using the \bar{P} ANDA experiment at the design luminosity yields a statistical error of order few % or better after 10^7 s in this region of q^2 168
- 4.103 e^+e^- cross section as a function of q^2 . 169
- 4.104 e^+e^- cross section as a function of θ_{CMS} 170
- 4.105 Symmetrized angular distribution of $\pi^+\pi^-$ at 8.21. 170

4.106	Angular distribution of misidentified pions.	171
4.107	Distribution of misidentified π^0 . . .	172
4.108	e^+e^- reconstruction efficiency at $q^2 = 8.21 (GeV/c)^2$	173
4.109	Integrated e^+e^- reconstruction efficiency versus q^2	173
4.110	Reconstructed angular e^+e^- distribution at $q^2 = 8.21(GeV/c)^2$	174
4.111	precision on ratio G_E/G_M as a function of q^2	174
4.112	Present world data on $ G_M $ (extracted using the hypothesis $R = G_E / G_M = 1$) are shown together with the expected accuracy by measuring $\bar{p}p \rightarrow e^+e^-$ with the \bar{P} ANDA experiment at FAIR. Each point corresponds to an integrated luminosity of 2 fb^{-1}	175

List of Tables

2.1	Injection parameters, experimental requirements and operation modes.	28	4.10	The main background contributors to $h_c \rightarrow 3\gamma$	76
2.2	Upper limit for relative beam loss rate, $1/e$ beam lifetime $t_{\bar{p}}$, and maximum average luminosity L_{\max} for a H_2 pellet target.	29	4.11	Selection efficiencies for $h_c \rightarrow 3\gamma$ and its background channels.	77
2.3	Summary of the sources of uncertainty in the resonance parameters	32	4.12	Signal to background ratio for $h_c \rightarrow 3\gamma$ and different background channels.	77
3.1	Reconstruction thresholds for the $PbWO_4$ and Shashlyk calorimeter	49	4.13	The numbers of analysed events for h_c decay	78
3.2	Selection criteria for the particle candidate lists	55	4.14	Efficiency of different event selection criteria	79
3.3	Contributions of the computing sites to the Physics Book simulation production	57	4.15	Signal to background ratio for different h_c background channels	79
3.4	Number of reconstructed $J/\psi\eta$ candidates from the background mode $\pi\pi\eta$, for different electron PID criteria, in three regions of the generated invariant $\pi\pi$ mass under electron mass hypothesis	57	4.16	Definition of the $D\bar{D}$ physics channels, relevant decay branching ratios and the expected ratio between signal and total $\bar{p}p$ cross section	79
4.1	Number of simulated events, mean value and RMS of the reconstructed J/ψ	69	4.17	Background channels for the $D\bar{D}$ analysis and amount of simulated events	80
4.2	Efficiencies and RMS of the reconstructed $J/\psi\pi^+\pi^-$ invariant mass distributions	70	4.18	Signal to background ratio for the $\bar{p}p \rightarrow D^+D^-$ channel	82
4.3	results $J/\psi\pi^0\pi^0$	72	4.19	Signal to background ratio for the $\bar{p}p \rightarrow D^{*+}D^{*-}$ channel	83
4.4	Various properties of reconstructed $J/\psi\gamma$ candidates for the radiative decay of $\chi_{c1,c2}$	72	4.20	Reconstructed h_c width.	83
4.5	Various properties of reconstructed $\chi\gamma$ candidates for the radiative decay of $\chi_{c1,c2}$	72	4.21	The 8 lowest lying hybrid states	87
4.6	Various properties of reconstructed $J/\psi\gamma$ candidates	72	4.22	Light states with exotic quantum numbers	88
4.7	Various properties of reconstructed $J/\psi\eta$ candidates	73	4.23	LQCD predictions for the lightest spin exotic hybrid	89
4.8	Cross sections and branching fractions for the $J/\psi\eta$ signal and background modes.	75	4.24	Lowest lying charmonium hybrids corresponding to the definitions as in Table 4.21.	89
4.9	Suppression η and signal to noise ratio for the background modes of the $J/\psi\eta$ analysis.	75	4.25	Cross sections for the charmonium hybrid channel	91
			4.26	Signal and background events for the charmonium hybrid analysis	91
			4.27	$\psi_g\eta$ signal to background ratio	94
			4.28	Decay branching ratios for open charm production	94
			4.29	Cross sections from extrapolation and DPM event generator	97
			4.30	Cross sections for signal and background reactions	97

4.31	Summary of analysed events and the J/ψ mass filter efficiency. For channels including charmonium states no filter is applied and the J/ψ is decaying to e^+e^- and $\mu^+\mu^-$ with equal branching fraction of 50%.	98
4.32	Observed background suppression and the expected signal to noise ratio	100
4.33	Signal and background modes for the $\psi(2S)\pi^+\pi^-$ analysis. For the generator level filter, see Sec. 3.5.1.	101
4.34	Cross sections and branching fractions for the $\psi(2S)\pi^+\pi^-$ signal and background modes	102
4.35	Suppression η and signal to noise ratio for the background modes of the $\psi(2S)\pi^+\pi^-$ analysis	102
4.36	Datasets for the $\phi\phi$ feasibility study.	102
4.37	PID optimization summary.	104
4.38	Beam times needed to achieve a significance of 10σ	105
4.39	The data sets to evaluate signal reconstruction efficiency and signal-to-noise ratio	111
4.40	Results of the simulation studies of signal reconstruction and background suppression	114
4.41	Quark-model assignments for some of the known baryon states	118
4.42	Number of events simulated for signal and background channels	120
4.43	Signal efficiency and remaining number of background events	121
4.44	Properties of strange and charmed ground state hyperons	124
4.45	Background for $\bar{p}p \rightarrow \bar{\Lambda}\Lambda$ and $\bar{p}p \rightarrow \bar{\Xi}^+\Xi^-$	130
4.46	Estimated count rates into their charged decay mode for the design luminosity	131
4.47	Definition of cuts for the e^+e^- analysis	138
4.48	Electromagnetic form factor simulation statistics	169
4.49	Rejection efficiency for pions	171
4.50	Expected signal counting rates for e^+e^-	172